

FINAL REPORT

Simultaneous Inversion of UXO Parameters and Background Response

SERDP Project MR-1573

MARCH 2012

Leonard R. Pasion
Kevin Kingdon
Jon Jacobson
Nicolas Lhomme
Sky Research, Inc.

Douglas Oldenburg
University of British Columbia Geophysical Inversion Facility

This document has been cleared for public release



REPORT DOCUMENTATION PAGE			Form Approved OMB No. 0704-0188	
Public reporting burden for this collection of information is estimated to average 1 hour per response, including the time for reviewing instructions, searching existing data sources, gathering and maintaining the data needed, and completing and reviewing the collection of information. Send comments regarding this burden estimate or any other aspect of this collection of information, including suggestions for reducing this burden, to Washington Headquarters Services, Directorate for Information Operations and Reports, 1215 Jefferson Davis Highway, Suite 1204, Arlington, VA 22202-4302, and to the Office of Management and Budget, Paperwork Reduction Project (0704-0188) Washington, DC 20503.				
1. AGENCY USE ONLY (Leave blank)		2. REPORT DATE 3-7-2012	3. REPORT TYPE AND DATES COVERED Final Report 2011	
4. TITLE AND SUBTITLE Project MM-1573: Simultaneous Inversion of UXO Parameters and Background Response, Final Report			5. FUNDING NUMBERS W912HQ-07-C-0012	
6. AUTHOR(S) Leonard Pasion, Steve Billings, Kevin Kingdon, Jon Jacobson, Nicolas Lhomme (Sky Research, Inc.), Douglas Oldenburg (UBC-GIF)				
7. PERFORMING ORGANIZATION NAME(S) AND ADDRESS(ES) Sky Research, Inc., 445 Dead Indian Memorial Road, Ashland, OR 97520 University of British Columbia Geophysical Inversion Facility, Department of Earth and Ocean Sciences, 6339 Stores Road, University of British Columbia, Vancouver, B.C., V6T1Z4, Canada			8. PERFORMING ORGANIZATION REPORT NUMBER	
9. SPONSORING/MONITORING AGENCY NAME(S) AND ADDRESS(ES) Strategic Environmental Research and Development Program 901 North Stuart Street, Suite 303 Arlington, VA 22203-1821			10. SPONSORING/MONITORING AGENCY REPORT NUMBER	
11. SUPPLEMENTARY NOTES				
12a. DISTRIBUTION/AVAILABILITY STATEMENT Unclassified/Unlimited			12b. DISTRIBUTION CODE	
13. ABSTRACT (Maximum 200 words) Methods for processing data collected at sites with magnetic geology were developed. Instead of relying on filtering data directly to remove the background response, we use instrument position and orientation information to model the sensor response due to soils. Computational routines and techniques to simultaneously invert for the parameters of the buried object and the response of the background have been developed. The response of the magnetic geology is calculated by using an approximate multi-dipole representation of the transmitter. We verified our methods by processing both simulated and field data for the Geonics EM63 time domain electromagnetic sensor and the newly developed Man Portable Vector time domain electromagnetic sensor. Using data acquired over magnetic soil test pits at the Defense Research and Development Canada facility in Suffield, Alberta, we demonstrated an ability to accurately recover dipole parameters using the simultaneous inversion method. Numerical modeling code for solving Maxwell's equations was developed to quantify the effect of the topography on the EMI signal and to determine the validity of the assumption that the response of a target buried in a magnetic and conductive half-space is additive.				
14. SUBJECT TERMS Simultaneous inversion, background response, UXO, EMI, magnetics			15. NUMBER OF PAGES 160	
			16. PRICE CODE	
17. SECURITY CLASSIFICATION OF REPORT Unclassified	18. SECURITY CLASSIFICATION OF THIS PAGE Unclassified	19. SECURITY CLASSIFICATION OF ABSTRACT Unclassified	20. LIMITATION OF ABSTRACT Unlimited	

This report was prepared under contract to the Department of Defense Strategic Environmental Research and Development Program (SERDP). The publication of this report does not indicate endorsement by the Department of Defense, nor should the contents be construed as reflecting the official policy or position of the Department of Defense. Reference herein to any specific commercial product, process, or service by trade name, trademark, manufacturer, or otherwise, does not necessarily constitute or imply its endorsement, recommendation, or favoring by the Department of Defense.

TABLE OF CONTENTS

Abstract.....	i
Objective	i
Technical Approach	i
Results	i
Benefits	ii
List of Tables	iii
List of Figures	iv
List of Acronyms	xiv
Acknowledgements	1
Executive Summary.....	2
Overview/Objectives	4
1. Modeling of EMI sensor response for a compact metallic target in a magnetic setting.	9
Modeling the compact target using a point dipole model.....	9
MODELING GEOLOGIC SIGNAL DUE TO SENSOR MOTION OVER A MAGNETIC EARTH	11
MODELING GEOLOGY RELATED SENSOR NOISE WITH A SLOWLY SPATIALLY VARYING BACKGROUND GEOLOGY MODEL.....	15
Example: Modeling MTADS data at Camp Sibert, Alabama.....	16
Summary.....	18
2. Data processing Methods.....	24
Method One: Sequential Processing: Subtract soil response from observed data, then invert for target parameters	24
Example: Cued EM63 from Sibert	26
Example: Application of Sequential Processing using Geophex GEM3 Frequency Domain EMI Data.....	29
Method Two: Simultaneous Inversion Solution	44
Example: Dynamic, Cued Interrogation EM63 Data from the Camp Sibert Geophysical Proveout	44
Example: Dynamic EM63 Data from the Camp Sibert Geophysical Proveout	47
Simulations for determining the effectiveness of simultaneous estimation of target and background	47

Defining Metrics for comparing discrimination performance	51
Summary.....	57
3. A Method for Processing Data From Advanced EMI Sensors	59
Example of Modeling data from Multi-Static Sensors: MPV-MARK 1 Measurements at the Ashland, Oregon Airport.....	62
A method for processing data from Advanced Sensors	64
Processing Field Data collected at the Defence Research and Development Centre Magnetic Soil Test Facility	69
Description of Measurements	69
Inversion Results	70
4. Investigating the Effects of Soils with Complex Magnetic Susceptibility on EMI Measurements Using Numerical Modeling of Maxwell's Equations	82
Numerical modeling of Maxwell's equations using EH3D	82
Results 1: Additivity of Soil and Target Responses	85
Results 2: Studying the effect of small scale topography	89
Numerical Modeling Simple Topography: Comparison with Field Data.....	89
4.3 Modeling Simple Topography: Bump and Trench of Varying Size	91
Modeling Example: TEMTADS data.....	94
Simulations for Testing the Effect of Topography on Discrimination	97
Summary.....	98
5. Modeling the background response with dipole sources.....	101
Camp Sibert EM63 Multi Object Inversion.....	105
Modeling Background, Removing Background, Single Object Target Inversion	105
Camp Butner – M48 like targets	116
Camp Beale MetalMapper and TEMTADS 2x2 Multi Object Inversion	127
6. Conclusions.....	134
References	137
Appendices	140

ABSTRACT

OBJECTIVE

SERDP Project MM-1573 addressed the UXO Statement of Need MMSON-07-04, “Advanced Technologies for Detection, Discrimination and Remediation of Munitions and Explosives of Concern (MEC): UXO Technology”. In particular, this project addressed the problem identified in the SON of reduction of geological interference on UXO discrimination procedures through a new and innovative discrimination technology to substantially reduce the impact of geological effects on data collected by magnetic and electromagnetic (EMI) sensors.

The task of discriminating UXO from non-UXO items is more difficult when sensor data are collected at sites where an electromagnetically active host contributes a large background signal. In general, approaches to UXO discrimination assume that the object of interest is in free-space. Any influence of the background medium is assumed to have been removed by preprocessing or filtering the data. However, the spatial variations of the background signal can be the same size as UXO anomalies. These signal variations can result from small scale topography (due to bumps or dips in the surface), changes in the orientation and height of the sensor relative to the ground, and spatial variations in the electromagnetic properties of the soil (i.e. conductivity and magnetic susceptibility). A high pass filter to remove the geologic signal is often unable to remove smaller scale spatial variations. In addition, this filtering step often introduces artifacts that can bias estimates of the target parameters.

TECHNICAL APPROACH

We developed methods for processing data collected at sites with magnetic geology. Instead of relying on filtering data directly to remove the background response, we use instrument position and orientation information to model the sensor response due to soils. Computational routines and techniques to simultaneously invert for the parameters of the buried object and the response of the background have been developed. For electromagnetic induction (EMI) data, we simultaneously invert for geologic properties of the background response in addition to the target’s dipole parameters. The response of the magnetic geology is calculated by using an approximate multi-dipole representation of the transmitter. Numerical modeling code for solving Maxwell's equations was developed to quantify the effect of the topography on the EMI signal and to determine the validity of the assumption that the response of a target buried in a magnetic and conductive half-space is additive.

RESULTS

We verified our methods by processing both simulated and field data for the Geonics EM63 time domain electromagnetic sensor and the newly developed Man Portable

Vector time domain electromagnetic sensor. Using data acquired over magnetic soil test pits at the Defense Research and Development Canada (DRDC) research facility in Suffield, Alberta, we demonstrated an ability to accurately recover dipole parameters using the simultaneous inversion method. Numerical modeling code was used to study the two key assumptions of our approximate forward modeling: (1) the response of a target buried in a magnetic and conductive half-space is additive and (2) topography would not be essential. These studies confirmed that these assumptions would not significantly affect the accuracy of recovered target parameters.

BENEFITS

This research will provide tools that will improve upon the existing capabilities for discriminating between hazardous UXO and non-hazardous metallic items sites with magnetic geology. Numerical modeling code has been tested that allow for modeling different aspects of EMI at sites with magnetic geology.

LIST OF TABLES

Table 2.1. Summary of performance when inverting simulated data for a 37 mm projectile buried at 20 cm, a 60 mm mortar buried at 40 cm, and an 81 mm mortar buried at 40 cm.	57
Table 3.1. Bartington MS2D Magnetic Susceptibility measurements.....	72
Table 5.1. Recovered positions for different inversion scenarios attempted for target 2362.	117
Table 5.2. Recovered positions for different inversion scenarios attempted for target 3416.	119
Table 5.3. Recovered positions for different inversion scenarios attempted for target 3879.	121
Table 5.4. Recovered positions for different inversion scenarios attempted for target 272.	123
Table 5.5. Recovered positions for different inversion scenarios attempted for target 35.	125

LIST OF FIGURES

Figure 0.1. Geonics EM61 MKII time domain data acquired on Kaho'olawe Island, Hawaii. (a) In order to study the effect of topography, the instrument was placed on planks. (b) Data was taken with and without a steel nut placed in a small rivulet that ran underneath the planks. The large increases in magnitude at the ends of the line of data are due to the sensor moving from the planks to the ground. (c) The steel nut used in this experiment. (d) Distance from the top of the planks and the ground.....	7
Figure 0.2. Geonics EM63 data acquired at the Former Camp Sibert Geophysical Proveout area. Full coverage, dynamic data were acquired at using the Geonics EM63 (a). North-South lines were acquired at 0.5 m linespacing. The first time channel of data is gridded in (b). Evidence of tractor tracks running East-West can be seen in the data. In (c), we look at the raw and detrended data, elevation, pitch and roll along a line located at Easting=40m. There are peaks in the data (in particular between 20 and 30 m Northing) that correlate to lower elevation. The low elevation "valleys" are likely due to the EM63 wheels falling into the tractor "ruts", and thus moving closer to the ground.....	8
Figure 1.1. Sensitivity of the EMI response to a magnetic half-space as a function of sensor height. For this example we the sensor response at the center of a circular transmitter loop. The values plotted in (b) are normalized to unity at a height of 30 cm. Height variations of only a few centimeters can produce a significant change in the background signal	13
Figure 1.2. An example of the effect of the waveform on the theoretical step-off response. (a) MPV-MARK 1 data were acquired at the Ashland airport. The MPV-MARK 1 during this data collected had a finite on-time of approximately $\Delta t=25$ ms. (b) The theoretical $1/t$ step off response is modified due to the finite on-time of the MPV-MARK 1. The vertical component of the signal (black circles) follows the theoretical response due a rectangular pulse (plotted in red).....	13
Figure 1.3. Tilt and height testing modeling results. A Geonics EM-61 Mark 2 sensor was used to collect data on Kaho'olawe, Island at a number of different heights and tilt angles. The signal was calculated by representing the transmitter loop with 8 dipoles.	14
Figure 1.4. Fitting raw (i.e. non-detrended) data with a slowly spatially varying background geology. A regularized inversion is used to fit data with both a flat and smooth model.	19
Figure 1.5. Photo of the MTADS EM61 array. Three EM61 MKI sensors with 1m x 1m transmitter/receiver pairs are mounted on a trailer towed by a low noise vehicle. The three GPS sensors on the trailer provide positioning and orientation information	20
Figure 1.6. Example of modeling the MTADS soil response. The estimated ground clearance for Cell 644 is plotted in (a), which shows a total variation of 13 cm. The	

measured data and data predicted by the geology model is presented in (b). In the NS line there is an approximately 40 mV anomaly, and in the EW lines there is no significant anomaly. Data features in both the EW and NS lines are well modeled by the background signal modeling21

Figure 1.7. Example of modeling the MTADS soil response. For this example, the anomaly is in the EW lines. Variation in the ground clearance predicts a geologic anomaly of approximately 70 mV in the first time channel. The predicted soil response matches the measured data both when looking at the gridded images in (c) and (d), as well as along a line (e)22

Figure 1.8. Example of how detrending can produce inaccurate results. (a) plots the line of interest from Cell 809. (b) the raw elevation. (c) The detrended elevation was obtained by removing a linear trend. (d) The predicted soil response (blue line) is compared to the detrended EM61 first channel data (green line). Although the shape of the response is quite similar, there is an approximately 30 mV shift in the data magnitude. The need to apply a median filter to the data limits the application of the background modeling method to EM61 data.23

Figure 2.1. Geonics EM63 data acquired over a wrench. (a) The Geonics EM63 at Camp Sibert, Alabama. (b) Excavated object. (c) A gridded image of data at time channels 1 ($t = 0.18$ ms) and 20 ($t = 7.1$ ms).26

Figure 2.2. Application of a soil fitting procedure to the Geonics EM63 data in Figure 2.1(c). The elevation variations in (a) are correlated with the measured data in (b). A soil model is constructed by discretizing the surface, and then solving an underdetermined inverse problem that constructs a smooth model based on data outside the green circle. The soil model does a good job of predicting the soil response outside the green circle. The corrected data is shown in (e).28

Figure 2.3. The Geophex GEM3 sensor. A schematic of the GEM3 sensor head is shown in (a). A pair of transmitter coils are used to buck the primary field, such that the receiver coil is placed in a region of low transmit field. For the examples in this project, GEM3 were collected on a template. The template used at FLBGR is shown in (b).29

Figure 2.4. Demonstration of soil removal technique applied to Geophex GEM3 Frequency domain data. Excavation of this anomaly (Cell 29) produced a 0.50 cal. 32

Figure 2.5. Demonstration of soil removal technique applied to Geophex GEM3 Frequency domain data. Excavation of this anomaly (Cell 40) uncovered a 37 mm mortar.33

Figure 2.6. Data fit (left) and fitting recovered polarizabilities with the equation 2.6 (right) for cell 29, which contains a 0.50 cal.34

Figure 2.7. Data fit (left) and fitting recovered polarizabilities with the equation 2.6 (right) for cell 40, which contains 37 mm projectile.35

Figure 2.8. A comparison of different model parameters from Equation 2.6 when inverting GEM3 data collected at the FLBGR 20 mm range fan. For the transverse axis, the symbol represents the average of the parameters related to the two secondary polarizabilities and the endpoints of the line indicate the maximum and minimum values of that parameter.	36
Figure 2.9. A comparison of different model parameters from Equation 2.6 when applied to data corrected using a background soil model, and data corrected by subtracting a low order surface at each frequency.	37
Figure 2.10. Cued pattern for collecting GEM3 data at the Camp Sibert GPO.	38
Figure 2.11. Example of EMI data collected on the Camp Sibert GPO. The top two grids show the real and imaginary part of the secondary field at 90 Hz. The bottom left image is of the first time channel of Geonics EM63 time domain data.	39
Figure 2.12. Example of data collected in areas of the GPO. The presence of VRM soil results in a small offset in the imaginary or quadrature part of the data (red lines) and a large negative offset in the real (or in-phase) part of the data (blue lines).	41
Figure 2.13. Examples of Geophex GEM3 data acquired over targets buried at a depth greater than 1 m. The location of the data in the GPO is indicated by a white circle on the gridded data. At depths greater than 1 m the Geophex GEM3 is unable to sense the target, and is only sensitive to the soil. Plots of the individual soundings (real component in blue and imaginary component in red) possess the characteristics of viscous remnant magnetized soil.	42
Figure 2.14. Feature space plots when processing the Camp Sibert GEM3 data. For the Sibert data, the intact and partial 4.2 inch mortars cluster classes based on the amplitude k do not have same clear separation as for the FLBGR case. However, there is a very clear separation in the axial time constant τ that would allow for reliable discrimination between the 4.2 inch mortars and partial shells.	43
Figure 2.15. Simultaneous fitting example. The data from Figure 1 is inverted for dipole parameters and background soil model simultaneously. The background soil model is $G(x,y)=ax+by+c$. The top set of plots in (a) are for the first time channel, and the results for the 20th time channel are plotted in the lower set of plots. (b) Observed and predicted soundings are plotted at a couple of locations in the grid. (c) comparison of observed and predicted data in the first time channel.	45
Figure 2.16. Comparison of polarizabilities recovered using simultaneous inversion of background and dipole parameters with polarizabilities derived using TEMTADS in-air measurements. The data were inverted assuming axial symmetry (2 unique polarizabilities) and without any assumptions on symmetry (3 unique polarizabilities). For the 3 polarizability case, the primary polarizability is well constrained, but there is a difference in magnitude in one of the two secondary polarizabilities.	46

Figure 2.17. Examples of synthetic 60 mm mortar data. For this example the 60 mm mortar was buried at a depth of 40 cm, and pointed 20 degrees from North and 56 degrees from vertical. The first time channel is shown here. The data profiles are taken along the line indicated by the red arrows. The data filtered by estimating a soil model (c) has less correlated noise in the data.	49
Figure 2.18. A comparison of recovered polarizabilities for the 60 mm mortar buried in a host with a background response of 30 mV in the first time channel.	50
Figure 2.19. Feature space plots based on the inversion of Geonics EM63 data acquired at Camp Sibert.	53
Figure 2.20. Synthetic examples of characterizing the separation of cluster classes using an ROC curve. Clusters are generated by generating Gaussian distributions with unit standard deviation. The separation between clusters decreases from (a) to (d). The panels on the left plot a pair of features for two different target types (red and blue). The middle panels are histograms when projecting the clusters onto a line that connects the true parameters of the two target types.....	54
Figure 2.21. Comparison of processing data where there is a 30 mV background soil response. The blue cluster contains feature vectors from a 37 mm projectile. The red cluster contains feature vectors from 60 mm mortars.....	56
Figure 3.1. The geologic response of horizontal loop transmitters.	60
Figure 3.2. TEMTADS 2x2 data collected at Camp Beale, CA.	61
Figure 3.3. MPV-MARK 1 measurements made at the Ashland Municipal Airport. ...	63
Figure 3.4. Height and tilt test measurements using the MPV-MARK 1 sensor.	63
Figure 3.5. Steel cylinder used for simulations	66
Figure 3.6. An example of a survey used during MPV- Mark 1 simulations.....	66
Figure 3.7. An example of synthetically generated data as part of the MPV-Mark 1 simulations. The red dashed boxes indicate the components most sensitive to soil. .	67
Figure 3.8. A comparison of recovered polarizabilities when inverting the simulated data.....	68
Figure 3.9. Photos of samples taken from Cambodian soil pit for susceptibility measurements.	73
Figure 3.10. The DRDC Suffield magnetic soil test pits. The test pits were located in a heated greenhouse. The greenhouse resulted in two challenges during data collection: (1) GPS positioning was not possible and (2) the EMI sensors were sensitive to the metal frame of the structure. The Cambodian Soil pit is in the foreground.	73
Figure 3.11. Positioning was achieved by placing the MPV-MARK 1 on piece of plywood that was marked with a uniform 7 x 7 grid with a 15 cm spacing. The data acquisition pattern is shown in (b).	74

Figure 3.12. Photo of targets measured at the Cambodian soil pit and a photo of the inside of the DRDC magnetic soil test facility greenhouse.	74
Figure 3.13. Measurements taken with the artificially created mound.	75
Figure 3.14. Example of MPV-MARK 1 data collected at DRDC Suffield. For this example data were acquired over a 3 inch aluminum cylinder with a 40 mm diameter. The cylinder was horizontal and flush with the surface.	76
Figure 3.15. Results from inverting data acquired over a 4 inch steel cylinder buried in the Cambodian soil pit data.	77
Figure 3.16. Results from inverting data acquired over a 3 inch aluminum cylinder buried in the Cambodian soil pit data.	78
Figure 3.17. Data acquired over a simulated mound and void. (a) A simulated mound with dimensions of 60 x 13 x 11 cm was created. (b) A void was created by placing pieces of wood in the soil pit. The void measures 61 x 20 x 8 cm. (c) Both the mound and void does not produce a significant anomaly in the data. The brown line indicates the location of the mound and void along the line of data.	79
Figure 3.18. Results from a tilt test.	80
Figure 3.19. Results from inverting data acquired over synthetic soil. The black synthetic soil have large levels of instantaneous susceptibility (see Table 3.1) but a low level of viscous remnant magnetization.	81
Figure 4.1. The staggered grid used in EH3D finite volume methods.	83
Figure 4.2. The environment modeled in EH3D for validation tests.	84
Figure 4.3. EH3D correctly models the viscous remnant magnetization (VRM) response. Panel on the left shows the susceptibility values calculated based on soil measurements made at Kaho’olawe, Hawaii and the panel on the right illustrates both the analytical and EH3D solutions for a conductive only half-space and a conductive half-space with viscous remnant magnetism (VRM).	85
Figure 4.4. The environment modeled in EH3D for additivity tests.	87
Figure 4.5. Additivity illustrated through the imaginary component of the H field at 1668 Hz. Panel (a) shows the EH3D response generated for a target in a half-space, (b) the EH3D response for a half-space. Panel (c) displays the derived target in free space response obtained by differencing the top 2 panel responses. Finally, panel (d) displays the EH3D response for a target in a free space which is virtually identical to the adjacent derived response of panel (c). All four panels shown have identical limits on color scale. Half-space results used were the 0.1 S/m case.	87
Figure 4.6. Additivity is examined by comparing the response computed for a target in free space with a derived free space response obtained by differencing a target in half space response with a half-space response. There is a small difference between these	

computed and derived free space solutions due to the soil response from the target void.	88
Figure 4.7. Real and imaginary values of the H field for all frequencies modeled in EH3D with a target in a conductive half-space with viscous remnant magnetism (VRM) (top 2 panels) and a half-space with VRM (second row 2 panels). The third row of two panels plots the response due to soil replacing the target volume in free space. The bottom 2 panels plot the derived target in free space solution obtained by differencing the soundings at the center of the loop between the top row of panels and the middle row of panels. The EH3D computed solution for a target in free space is also plotted in the bottom row panels.	88
Figure 4.8. EH3D results for modeling MPV-MARK 1 data acquired over a single bump. The upper left panel illustrates the environment modeled in EH3D. The upper right panel shows the MPV-MARK 1 acquiring data over the single bump target. The bottom row of plots shows the three components of the fields both measured with the MPV-MARK 1 and modeled using EH3D.	90
Figure 4.9. EH3D results for modeling MPV-MARK 1 data acquired over a single trench. The upper left panel illustrates the environment modeled in EH3D. The upper right panel shows the single trench target. The bottom row of plots shows the three components of the fields both measured with the MPV-MARK 1 and modeled using EH3D.	90
Figure 4.10. EH3D model environment for two simple variations in topography including a bump (left panel) and trench (right panel).	92
Figure 4.11. EH3D results for modeling simple geologic variations. The top three panels illustrate the three components of the H fields for a series of bumps of increasing size. The bottom three panels the same fields for trenches of increasing dimensions. Physical properties and dimensions used for the modeling are described in Figure 4.10.	92
Figure 4.12. Plots comparing the simulated profiles over bumps and trenches for a 1m loop and 40cm loop. Y axes in the 40cm loop plots forced to match those of the 1m plots to help comparing the two loop sizes.	93
Figure 4.13. TEMTADS EMI Array. The TEMTADS array consists of a 25 transmitters with a receiver at the center of each transmitter. The transmitter fire sequentially and each of the 25 receivers record the secondary field, resulting in a total of 625 soundings measured.	94
Figure 4.14. EH3D results for three different Tx locations over a bump. Modeled sensor was comprised of 5 x 5 array of 40cm square loops with coincident Tx/Rx. The Tx locations are overlaid on the images of the real part of H. Tx locations correspond to center, middle right and lower right Rx/Tx loops. Target was a bump of dimensions 14cm x 14cm x 50cm.	95

Figure 4.15. TEMTADS data from SLO illustrating the difference between the observed response for a significant metallic target, a 4.2 inch mortar (on left) and a no contact cell presumed to be due to soil effects (on right).	96
Figure 4.16. Setup for testing effect of a mound of magnetic soil above a buried target. The mound runs North-South. The blue dots in (c) indicate the stations at which data soundings are acquired.	99
Figure 4.17. Recovered polarizabilities for a 40 mm projectile buried beneath a mound of magnetic soil.	100
Figure 4.18. Recovered polarizabilities for a 37 mm projectile buried beneath a mound of magnetic soil.	100
Figure 5.1. The MetalMapper (left) and Geonics EM61 (right) at Camp Butner.	102
Figure 5.2. Dynamic MetalMapper data and Geonics EM61 data acquired at Camp Butner. Only the middle 3 receivers of the MetalMapper are gridded above. The black dashed lines in (a) highlight the elevated levels of magnetic soil response at the site. The horizontal components of the signal are unaffected by the magnetic soils (gridded in (b) and (c)). The Geonics EM61 data in (d) were leveled using a demedian filter. .	102
Figure 5.3. Flagged anomalies for the Camp Butner site are shown in (a). The anomalies that produced estimated polarizabilities that are similar to the characteristic M48 polarizabilities and estimated depths greater than 40 cm are plotted in (c).	103
Figure 5.4. Examples of M48 type polarizabilities recovered from cued MetalMapper acquired at Camp Butner. The locations of the three anomalies are indicated in Figure 5.3. On the left is the recovered polarizability. The center panel indicates the location of the anomaly in size/decay feature space with a yellow circle. For the size/decay plot, the x axis has the size which is defined as the integrated value of the total polarizability, and the decay rate - ratio of total polarizability at early and late time - is plotted on the y axis. On the right is the predicted source location and depth. In each case the source depth is approximately 50 cm.	104
Figure 5.5. Camp Sibert GPO, background soil response is more problematic in the northeast portion of the grid.	106
Figure 5.6. Recovered polarizabilities from single object inversion (left) and multi object inversion (right) from the Camp Sibert GPO. Only detectable 4.2 inch mortars were included in the analysis. Green plot represents the library polarizability for a 4.2 inch mortar, the red curves indicate items that fall into the northeastern portion of the GPO where a stronger soil response is evident while the black curves are GPO items in the more benign southwest portion of the GPO.	107
Figure 5.7. First time channel and elevation for target 852. A moderate bump in the topography (along the line shown in magenta colour) leads to a lower amplitude in the data.	107

Figure 5.8. Modeling the background response for Camp Sibert target 852 using a single object inversion with an exclusive mask (top row). Once the background response is removed, reinvert with a single object inversion for the target response (bottom row).	108
Figure 5.9. Modeling the background response for Camp Sibert target 852 using a two object inversion with an exclusive mask (top row). Once the background response is removed, reinvert with a single object inversion for the target response (bottom row).	108
Figure 5.10. Modeling the background response for Camp Sibert target 852 using a three object inversion with an exclusive mask (top row). Once the background response is removed, reinvert with a single object inversion for the target response (bottom row).	109
Figure 5.11. Modeling target and background response for Camp Sibert target 852 simultaneously using a three object inversion with two dipoles constrained to depths between 5 and 10m to model the soil response.	109
Figure 5.12. Modeling the background response for Camp Sibert target 852 using a thin plate spline to calculate background values within the mask region. Single object inversions are shown with no background removed (top row) and after removing a background using a thin plate spline across the masked target region (bottom row).	110
Figure 5.13. Recovered polarizabilities for different inversion scenarios. Secondary polarizabilities are better resolved for the two and three object inversions where one unconstrained dipole models the target and remaining dipole(s) are constrained to be 5 to 10m deep to model the soil response.	110
Figure 5.14. Modeling target response for Camp Sibert target 1032 using a single object inversion with different masks (top 2 rows) and two and three object inversions (bottom 2 rows) with one unconstrained dipole modeling the target and additional dipole(s) constrained to depths between 5 and 10m modeling the soil response (bottom).	112
Figure 5.15. Target 808. Inverting Camp Sibert target 808 with different approaches to compensate for an elevated background response. Top row shows the single object inversion with no background removed. The middle row depicts results after removing a background response using a thin plate spline to calculate background values within the mask region. The bottom row shows a two object inversion with no background removed and one dipole forced deep between 5 and 10m.	113
Figure 5.16. Target 954. Inverting Camp Sibert target 954 with different approaches to compensate for background response. Top row shows the single object inversion with no background removed. The middle row depicts results after removing a background response using a thin plate spline to calculate background values within	

the mask region. The bottom row shows a two object inversion with no background removed and one dipole forced deep between 5 and 10m.	114
Figure 5.17. Target 997. Inverting Camp Sibert target 997 with different approaches to compensate for background response. Top row shows the single object inversion with no background removed. The middle row depicts results after removing a background response using a thin plate spline to calculate background values within the mask region. The bottom row shows a two object inversion with no background removed and one dipole forced deep between 5 and 10m.	115
Figure 5.18. Groundtruth for Camp Butner targets 2362 and 3879. Both items were small pieces of frag that when inverted produced polarizabilities that closely matched the M48 library polarizability	116
Figure 5.19. Target 2362. Recovered polarizabilities for MetalMapper cued data over target 2362. The original single and 2 object inversions are shown as well as two and three object inversions where the modeled dipoles are not constrained and again when one dipole is unconstrained and remaining dipole(s) are constrained to be deep (5-10m) to model the background soil response. Library polarizability is shown in blue with black, red, green illustrating single, two object and three object inversions.	118
Figure 5.20. Target 3416. Recovered polarizabilities for MetalMapper cued data over target 3416. The original single and 2 object inversions are shown as well as two and three object inversions where the modeled dipoles are not constrained and again when one dipole is unconstrained and remaining dipole(s) are constrained to be deep (5-10m) to model the background soil response. Library polarizability is shown in blue with black, red, green illustrating single, two object and three object inversions.	120
Figure 5.21. Target 3879. Recovered polarizabilities for MetalMapper cued data over target 3879. The original single and 2 object inversions are shown as well as two and three object inversions where the modeled dipoles are not constrained and again when one dipole is unconstrained and remaining dipole(s) are constrained to be deep (5-10m) to model the background soil response. Library polarizability is shown in blue with black, red, green illustrating single, two object and three object inversions.....	122
Figure 5.22. Groundtruth for Camp Butner target 272. This was the deepest M48 at the site and is shown for comparison purposes with the soil responses that emulate M48 polarizabilities.	123
Figure 5.23. Recovered polarizabilities for MetalMapper cued data over target 272. The original single and 2 object inversions are shown as well as two and three object inversions where the modeled dipoles are not constrained and again when one dipole is unconstrained and remaining dipole(s) are constrained to be deep (5-10m) to model the background soil response. Library polarizability is shown in blue with black, red, green illustrating single, two, and three object inversions.	124

Figure 5.24. Groundtruth for Camp Butner target 35. This was a high SNR M48 at the site and is shown for comparison purposes with the soil responses that emulate M48 polarizabilities.....	125
Figure 5.25. Recovered polarizabilities for MetalMapper cued data over target 35. The original single and 2 object inversions are shown as well as two and three object inversions where the modeled dipoles are not constrained and again when one dipole is unconstrained and remaining dipole(s) are constrained to be deep (5-10m) to model the background soil response. Library polarizability is shown in blue with black, red, green illustrating single, two, and three object inversions.	126
Figure 5.26. Photos of anomalies 438 and 1553. The red soil in the background of the anomaly 438 photo suggest the presence of iron rich, magnetic soil.	129
Figure 5.27. Anomaly 438. MetalMapper inversion results.	130
Figure 5.28. MetalMapper data fit when inverting anomaly 438.	131
Figure 5.29. Anomaly 438. Polarizabilities estimated from TEMTADS 2x2 data. Three sources produce the best result.	132
Figure 5.30. Anomaly 1553. Polarizabilities estimated from MetalMapper data. A three source model (bottom row) is required to extract the correct polarizabilities for the 0.50 cal bullet. The background response is modeled by a deep (1.2 m) and large dipole source (Model 3/3).	133

LIST OF ACRONYMS

ATC	Aberdeen Test Center
AUC	Area Under The Curve
BUD	Berkeley Unexploded Ordnance Discriminator
DRDC	Defense Research and Development Canada
ESTCP	Environmental Security Technology Certification Program
EM	Electromagnetic
EMI	Electromagnetic Induction
FLBGR	Former Lowry Bombing and Gunnery Range
GPO	Geophysical Proveout
IMU	Inertial Measurement Unit
MPV	Man Portable Vector sensor
MTADS	Multi-Sensor Towed Array Detection System
ROC	Receiver Operating Characteristic
SERDP	Strategic Environmental Research and Development Program
SNR	Signal-To-Noise Ratio
TEM	Time Domain Electromagnetic
TEMTADS	Transient Electromagnetic Towed Array Discrimination System
UXO	Unexploded Ordnance
UBC-GIF	University of British Columbia – Geophysical Inversion Facility
VRM	Viscous Remnant Magnetization

ACKNOWLEDGEMENTS

Funding of this work is provided through the Strategic Environmental Research and Development Program (SERDP) funded project “Simultaneous Inversion of UXO Parameters and Background Response (SERDP Project MM-1573)”. We thank Dr. Greg Oldenborger for his help in running the EH3D numerical modeling code. We also thank Roman Shekhtman for preparing a version of EH3D that models complex susceptibility and also for providing support when running the code on the UBC-GIF computer cluster. Time domain data from the Former Camp Sibert, San Luis Obispo and Camp Beale were acquired as part of the Environmental Security Technology Certification Program (ESTCP) Live-Site Demonstration program. We would also like to thank Kevin Russell and Wayne Sirovyak at the Defence Research and Development Canada (DRDC) facility in Suffield, Alberta for hosting us at the DRDC magnetic soil test facility.

EXECUTIVE SUMMARY

This report summarizes the research completed under the SERDP funded project SERDP MM1573 “Simultaneous Inversion of UXO Parameters and Background Response”. This project built on the work of SERDP MR-1414 “Improving Detection and Discrimination of UXO in Magnetic Environments” (MR-1414 Final Report, 2010). In SERDP MR-1414, the physical basis for viscous remnant magnetization (VRM) and how it affects EMI data was presented. We found that sensor movement (that is variations in the sensor ground clearance) and topography can produce significant variations in the EMI signal. By exploiting differences in the way EMI sensors respond to compact metallic targets and magnetic soil, we developed data processing approaches that improve the ability to detect targets at geologically hostile sites.

In SERDP MR-1414 we investigated the limitations of processing dynamically acquired data with a high-pass filter for discrimination. We observed that for data acquired over magnetic soils, inverting high-pass filter data did not sufficiently constrain estimated dipole parameters for reliable classification of UXO. In this project we developed and evaluated techniques where, instead of filtering the data, the background geologic sensor response is modeled.

Main results and findings:

- **Developed a method for modeling the EMI response of a sensor above viscous remnant magnetic earth.** Our method represents the EMI transmitter as a number of dipoles, and estimates the response by adding the response of the half-space to each dipole. The analytic solution of a dipole is calculated in the frequency domain, and is then converted to the time domain. The accuracy of the modeling was verified using field data measured by both traditional mono-static sensors (Geophex GEM3, Geonics EM61, MTADS array, and Geonics EM63) and more recently developed multi-static sensors (BUD, TEMTADS, and MPV-MARK 1).
- **A number of inversion approaches were developed that modeled that background soil response.**
 1. *Subtract soil response prior to inversion.* In this approach, we first solve for a smooth background susceptibility model. The background response is then calculated and subtracted from the measured data. The background corrected data is then inverted for dipole parameters. This technique was successfully demonstrated using both frequency domain data (GEM-3 at Fort Lowry Bombing and Gunnery Range and the Former Camp Sibert geophysical proveout) and time domain data (Geonics EM63 at the Former Camp Sibert).
 2. *Simultaneously solve for host parameters and target parameters:* In this approach, the target parameters and background response is solved for simultaneously. This approach was successfully demonstrated using Geonics EM63 TEM data acquired at the Former Camp Sibert and using Man Portable

Vector (MPV-Mark 1) TEM data collected at the Defence Research and Development Canada (DRDC) Suffield magnetic soil facility.

- **Processing methodologies extended to multi-static, multi-channel advanced EMI sensors.** Over the course of this project, SERDP and ESTCP funded the development of several EMI instruments designed specifically for discrimination (for example Gasperikova et al. 2007; Steinhurst et al. 2010; Prouty et al. 2011; Fernandez et al. 2011). These instruments have multiple transmitters for improved target illumination and are multi-static (i.e. have multiple receivers). In some cases these receivers measure three orthogonal components of the secondary field. The development of these instruments greatly improves our ability to discriminate in the presence of magnetic soils. Whereas the classic mono-static instruments are optimally coupled to the ground, the newer instruments have data components that are minimally-coupled to the ground, i.e. are relatively insensitive to the ground. A two stage inversion method was developed, where dipole parameters are first estimated using null-coupled components of the data. The estimated dipole parameters are then used as a starting model when simultaneously inverting all data components for soil and target parameters. The ability to estimate a good starting model increases the robustness of the simultaneous inversion algorithm. This method was demonstrated using MPV-MARK 1 data collected at the DRDC Suffield magnetic soil facility.
- **Simulations were used to demonstrate that modeling the background response as part of the inversion process improves discrimination.** Simulations for full coverage, dynamically acquired data used the Geonics EM63 sensor, while MPV-MARK 1 data simulations were used to test algorithms for advanced EMI sensors. For both data types, modeling the background response was shown to potentially improve discrimination ability.
- **Numerical modeling code for solving Maxwell's equations using complex magnetic susceptibility was successfully developed and tested.** The EH3D electromagnetic numerical modeling program developed at UBC-GIF was successfully modified to model complex magnetic susceptibility. The fields are calculated by discretizing the earth using a mesh of rectangular cells and then using a finite volume numerical solution to Maxwell's Equations. The code was first validated by comparing modeled results with analytic solutions for a half-space of VRM soil. The code was then used to calculate the effect of bumps and trenches on EMI data. Modeled results matched well with field data measured using the MPV-MARK 1 sensor.
- **Numerical modeling code verified that the electromagnetic interaction between UXO and the viscous remnant magnetic host material is not significant enough to be included in modeling.** EH3D was used to investigate whether there is significant electromagnetic interaction between the UXO and its host material or whether the signals are additive. We showed that the EM interaction between the host and a compact metallic object is minimal

for a specific example where a target is buried in a highly magnetic soil with VRM levels similar to those found on Kaho'olawe, Hawaii. Verifying that the signal is essentially additive was critical, as our "dipole + soil response" modeling method used in the simultaneous inversion relies on the assumption of additivity.

- **Effect of topography on recovered dipole polarizabilities is not significant.** When carrying out the simultaneous inversion, surface roughness is not modeled. Therefore, surface roughness has the potential to produce geologic noise that can bias polarizability estimates. We studied the effect of simple variations of surface roughness (i.e. bumps and trenches) on recovered dipole polarizabilities through inversions of simulated data. Simulated data were created by adding bump and trench responses calculated by EH3D to dipole responses. Inversions of this data showed that topography did not greatly affect the recovered polarizabilities, with the majority of the polarizability distortion occurring at early and late times.

At the start of this project, the general attitude was that UXO discrimination is not possible at sites with significant magnetic geology (Cargile, 2004). As a result of this project, a number of UXO discrimination methodologies have been developed specifically for geologically difficult sites. We believe that application of these algorithms, combined with the development of multi-static EMI sensors, discrimination success can be extended to sites with a large magnetic geology response.

OVERVIEW/OBJECTIVES

Detection and identification of unexploded ordnance (UXO) at sites with large geologic background signals can be very difficult. With the large frequency-dependent component of susceptibility at a "geologically hostile" site like Kaho'olawe Island, Hawaii, detection of UXO can be compromised due to geology-related sensor responses of the same order of magnitude as those from UXO (Figure 0.1). At sites with magnetic geology noise less extreme than Kaho'olawe, reliable detection may be possible, but discrimination can be challenging due to geology-related sensor noise biasing the recovered polarization tensor (Pasion et al. 2007). The standard approach to processing data collected in a magnetic geologic setting is to develop filtering techniques such that the background response can be estimated, and subsequently subtracted from the data.

These filtering methods generally assume that the geologic - and thus electromagnetic - properties of the host material are spatially slowly varying, while the anomalies of compact targets have a smaller spatial wavelength. The filtered data are then inverted assuming a physical model for a UXO in free space. One of the major difficulties with

the data filtering approach is the accuracy with which a high pass filter can remove the background response. In particular, movement of the transmitter and receiver relative to magnetic ground can produce significant small wavelength anomalies in the data (Walker et al. 2005 and Foley et al. 2005). Figure 0.2 contains a single line of Geonics EM-63, elevation data measured using GPS, and inertial measurement unit (IMU) data collected on the Camp Sibert Geophysical Proveout Area (GPO). The Geonics EM63 is a pulse-based multi-gate time domain electromagnetic induction instrument. The system consists of a 1 m x 1 m square transmitter coil and three coaxial 0.5 m x 0.5 m square receiver loops mounted on a two-wheel trailer. Measured decays are averaged over 26 geometrically spaced time gates, spanning the range from 177 μ s to 25.01 ms. Along the data line shown in Figure 0.2, there were no known UXO or metallic items. The EMI, elevation and IMU sensor data are clearly correlated. Of particular interest are the approximately 10 mV peaks in the first time channel between a Northing of 20 and 30 m. These peaks appear to be well correlated with lower elevation values. The lower elevation values correspond to instances where the Geonics EM63 cart was in a rut or depression in the ground, such that the sensor was closer to the magnetic ground. High pass filters will have limited success in cases where the geologic response produces anomalies of comparable wavelength to those from buried metallic objects. Least-squares inversion procedures are sensitive to correlated noise and can produce biased estimates of target parameters.

Rather than using a filter to eliminate the geologic response, we propose to use GPS and IMU information to directly model the data features caused by sensor movement. In this project, we developed a method of modeling the background geology response by assuming the underlying geology has smoothly varying magnetic characteristics. Parameters describing the amplitude and spatial variation of the geology and parameters characterizing a buried compact target can either be estimated simultaneously from electromagnetic induction sensor data, or sequentially. The best approach will depend on the type of data acquired.

There are a number of key factors to be addressed when developing a processing system that models both target and background parameters. Foremost, is the development of a forward model that (1) accurately models the background response and (2) is computationally efficient enough to be used in data inversion algorithms. In order to make the modeling tractable, there are a number of assumptions that are required. We investigated whether there is significant electromagnetic interaction between the UXO and its host material or whether the signals are additive. If the total signal can be adequately represented by the superposition of the two individual signals (i.e. the field of a UXO in free space, and the effect of a conductive host with topography and complex magnetic susceptibility) then there are many avenues by which data can be preprocessed to remove contaminating effects, or by which joint inversion of UXO and host parameters can be carried out.

In this project, we used a combination of numerical simulations and field data to investigate the different scientific questions posed in this research. Numerical simulations were used to assess the feasibility of the proposed processing schemes. In particular, simulated data with realistic background noise were inverted to assess the ability of the algorithms to estimate dipole polarizability parameters. Numerical modeling using a Maxwell's equation solver was used to understand how topography affects the EMI response and the additivity of the UXO and host material signals. When available, field data were used to test the forward modeling and inversion algorithms. Both controlled test stand measurements and field survey data were utilized for this purpose. Since ground clearance sensors are typically not used when collecting ground based EMI data, we were limited to estimating the ground clearance by using the GPS elevation measurement and assuming flat ground. Over the course of the project a number of advanced EMI sensors were developed by SERDP and ESTCP (for example Gasperikova et al. 2007; Steinhurst et al. 2010; Prouty et al. 2011; Fernandez et al. 2011). Towards the end of the project, our focus shifted from monostatic sensors (e.g. Geonics EM61/EM63 and the Geophex GEM3) to the newer multi-static sensors (e.g. the Man Portable Vector (MPV) sensor, TEMTADS, MetalMapper, Berkeley Unexploded Ordnance Discriminator(BUD)).

This document summarizes the work completed in SERDP MR-1573. We begin with an overview of the modeling techniques used in this project. For more detail on the modeling procedures, we direct the reader to the annual report for the project's first year since the majority of the modeling development was carried out in the first year of the project. We then present simultaneous and sequential inversion algorithms for solving both parameters of the background and dipole parameters. These algorithms are then tested using synthetic and field data. MPV-MARK 1 data collected at the Defense Research and Development Canada (DRDC) Suffield magnetic soil facility were used to test the algorithms designed for advanced sensors. The report concludes with numerical modeling of Maxwell's equations and applications to modeling the interaction between compact metallic bodies and magnetic soil, as well as the effect of small scale topography on sensor data. The appendix includes key reports and presentations funded as part of this project.

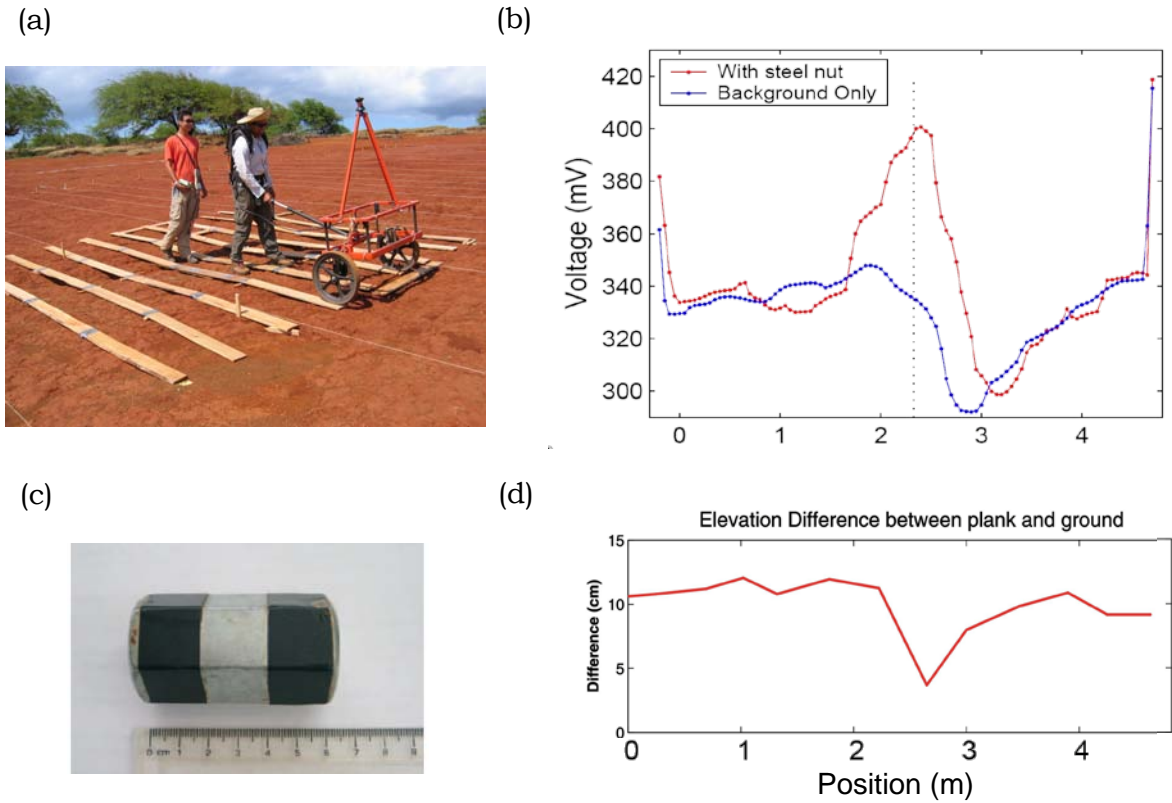
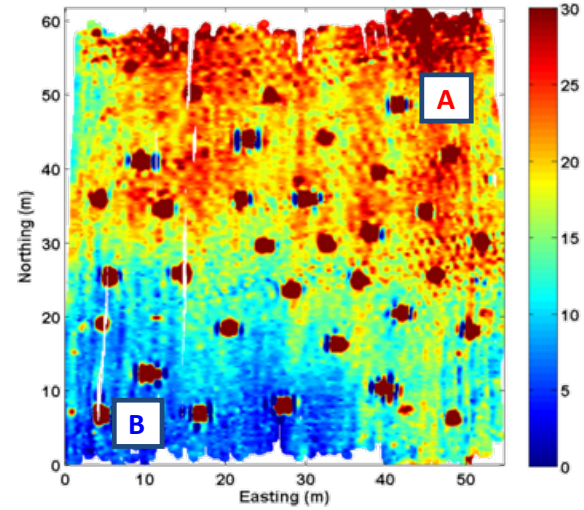


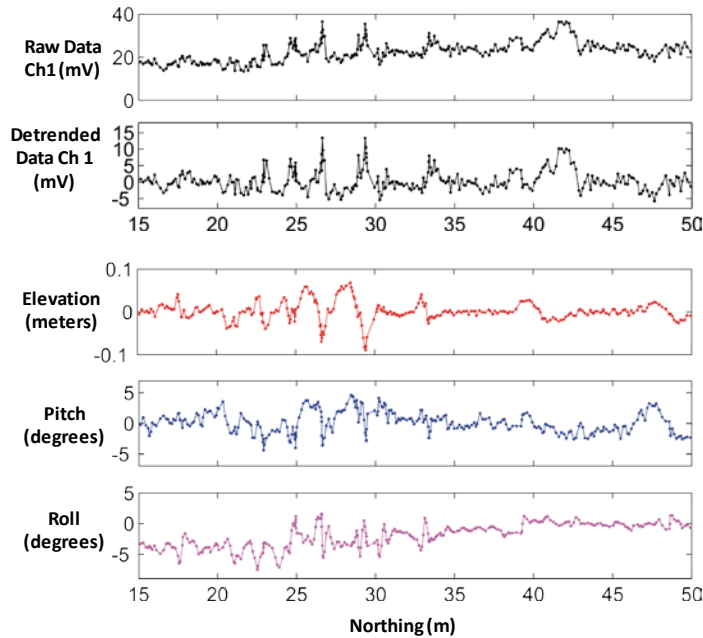
Figure 0.1. Geonics EM61 MKII time domain data acquired on Kaho’olawe Island, Hawaii. (a) In order to study the effect of topography, the instrument was placed on planks. (b) Data was taken with and without a steel nut placed in a small rivulet that ran underneath the planks. The large increases in magnitude at the ends of the line of data are due to the sensor moving from the planks to the ground. (c) The steel nut used in this experiment. (d) Distance from the top of the planks and the ground.



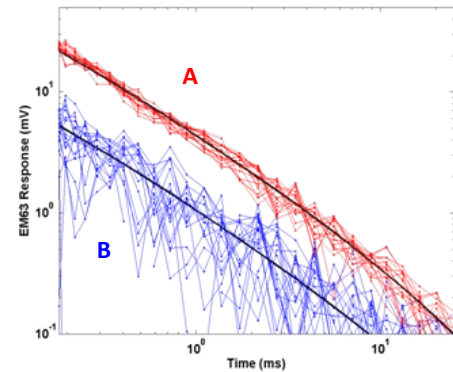
(a) Geonics EM63 sensor at the Former Camp Sibert Geophysical Proveout area



(b) Gridded Image of first time channel



(c) Comparison of raw and detrended first channel Geonics EM63 data with elevation, pitch and roll. The line at Easting = 40 m is plotted above.



(d) Soundings at high (A) and low (B) magnetic susceptibility areas of the grid.

Figure 0.2. Geonics EM63 data acquired at the Former Camp Sibert Geophysical Proveout area. Full coverage, dynamic data were acquired at using the Geonics EM63 (a). North-South lines were acquired at 0.5 m linespacing. The first time channel of data is gridded in (b). Evidence of tractor tracks running East-West can be seen in the data. In (c), we look at the raw and detrended data, elevation, pitch and roll along a line located at Easting=40m. There are peaks in the data (in particular between 20 and 30 m Northing) that correlate to lower elevation. The low elevation "valleys" are likely due to the EM63 wheels falling into the tractor "ruts", and thus moving closer to the ground.

1. MODELING OF EMI SENSOR RESPONSE FOR A COMPACT METALLIC TARGET IN A MAGNETIC SETTING.

Consider a target buried in a setting where the background geology is not negligible. The measured sensor data can be written as:

$$\mathbf{d}^{\text{obs}} = \mathbf{F}[\text{target}, \text{host}] + \text{noise}$$

where \mathbf{d}^{obs} is the observed sensor data and $\mathbf{d}^{\text{obs}} = \mathbf{F}[\text{target}, \text{host}]$ represents the forward model that is a function of the target and host. If the responses of the target and host are assumed to be additive, we can write:

$$\begin{aligned} \mathbf{d}^{\text{obs}} &= \mathbf{F}^{\text{bg}}[\text{host}] + \mathbf{F}^{\text{t}}[\text{target}] + \text{noise} \\ &= \mathbf{d}^{\text{bg}} + \mathbf{d}^{\text{target}} + \text{noise} \end{aligned} \tag{1.1}$$

where $\mathbf{d}^{\text{bg}} = \mathbf{F}^{\text{bg}}[\text{host}]$ is the response due to the background host and $\mathbf{d}^{\text{target}} = \mathbf{F}^{\text{t}}[\text{target}]$ is the response due to the target. In most cases $\mathbf{F}^{\text{t}}[\text{target}]$ is chosen to be a dipole model representation of the target.

MODELING THE COMPACT TARGET USING A POINT DIPOLE MODEL

In the EMI method, a time varying field illuminates a buried, conductive target. This illuminating – or primary – field induces currents in the target that subsequently decay, generating a decaying secondary field that is measured at the surface. These data are then used to estimate the position, orientation, and parameters related to the target’s material properties and shape. In the UXO community, it is commonly assumed that the secondary field can be accurately approximated as a point dipole (for example Gasperikova et al. 2009; Pasion and Oldenburg 2001; Bell et al. 2001; Baum 1999). The process of estimating the parameters of the dipole forward model from the data is called data inversion.

The dipole model assumes that the time-varying secondary magnetic field $\mathbf{B}(t)$, is due to a point dipole $\mathbf{m}(t)$ located at \mathbf{r} :

$$\mathbf{B}(t) = \frac{\mu_0}{4\pi} \frac{1}{r^3} \mathbf{m}(t) \cdot (3\hat{\mathbf{r}}\hat{\mathbf{r}} - \mathbf{I}) \tag{1.2}$$

where $\hat{\mathbf{r}} = \mathbf{r}/|\mathbf{r}|$ is the unit-vector pointing from the dipole to the observation point, \mathbf{I} is the 3 x 3 identity matrix, $\mu_0 = 4 \pi \times 10^{-7} \text{ H/m}$ is the permeability of free space and $r = |\mathbf{r}|$ is the distance between the center of the object and the observation point. The dipole induced by the interaction of the primary field \mathbf{B}_o and the buried target is given by:

$$\mathbf{m}(t) = \frac{1}{\mu_0} \mathbf{M}(t) \cdot \mathbf{B}_o \tag{1.3}$$

where $\mathbf{M}(t)$ is the target's polarization tensor. The polarization tensor is written as:

$$\mathbf{M}(t) = \begin{bmatrix} L_1(t) & 0 & 0 \\ 0 & L_2(t) & 0 \\ 0 & 0 & L_3(t) \end{bmatrix} \quad (1.4)$$

The polarization tensor reflects the characteristics of the buried target and is a function of the shape, size, and material properties of the target. The magnitude and decay of the polarization tensor elements is a function of the size and electromagnetic properties of the target. The relative sizes of the polarization tensor elements are indicative the target shape. If we order the polarization tensor elements such that $L_1 > L_2 > L_3$, then, for a steel body-of-revolution (BOR), $L_2 = L_3$ for a rod-like object and $L_1 = L_2$ for a plate-like object.

The model parameters of the dipole model (i.e. location, orientation, and polarization tensor elements) are estimated in a process known as data inversion. The objective of data inversion is to determine the set of parameters that most accurately predict the observed data. Typically, numerical optimization methods are used to determine the parameters that minimize a data misfit objective function. The dipole model is an ideal candidate for inversion because (1) the forward model is physics based with parameters that tell us something about the characteristics of the target and (2) the forward model is extremely fast to compute, which is important since numerical optimization can involve an extensive search of parameter space involving numerous calculations of the forward model.

Numerous factors affect the success of dipole inversion for UXO discrimination. Model parameters derived from dipole inversion are useful for discrimination when, for the different targets to be distinguished, they are sufficiently different. If the discrimination problem involves distinguishing between two targets that are similar in size and shape, then using the dipole model to discriminate between the two would be difficult since they would have similar model parameters. Data quality (e.g. signal to noise, data coverage, sensor positioning accuracy, etc.) is a key factor in discrimination since it controls the accuracy with which parameters can be estimated. As data quality decreases the ability to constrain parameters to the correct solution decreases. As a result, when processing poor quality data, the expected model parameters for two different targets may become indistinguishable. The development of a new generation of multi-channel, multi-illumination, and multi-static (i.e. multiple measurement receiver locations for a given transmitter) EMI sensors, along with improvements in positioning and orientation estimation technologies, have resulted in UXO survey data that result in more reliable recovery of dipole model parameters than could be achieved with traditional production level sensors (such as the Geonics EM61).

MODELING GEOLOGIC SIGNAL DUE TO SENSOR MOTION OVER A MAGNETIC EARTH

The background geology response is a function of the position (i.e. location and orientation) of the EMI sensor relative to the ground surface, topography, and the spatial distribution of the subsurface electromagnetic properties (i.e. conductivity and magnetic susceptibility). Accurate modeling of the electromagnetic response of the geology requires numerical modeling of Maxwell's equations, which can be computationally intensive and unsuitable for processing large numbers of target anomalies. Unfortunately, an analytic solution for the response of a loop at an arbitrary orientation over a conductive and magnetic subsurface is not available. Therefore we develop an approximate solution that has the same form as the solution for a horizontal circular transmitter loop over a half-space with viscous remnant magnetization.

For the case of a single loop over a complex permeable, but non-conducting, half-space, the solution for the magnetic field at the center of the loop is given by (for example Pasion et al. 2007)

$$H_z^s(\omega) = \frac{I}{4} \frac{a^2}{[a^2 + (2h)^2]^{3/2}} \chi(\omega). \quad (1.5)$$

where the current in the loop is I , the radius of the loop is a , the frequency dependent magnetic susceptibility of the half-space is $\chi(\omega)$, and the height of the loop over the half-space is h . If we assume a complex susceptibility defined by log-uniform distribution of time constants (where $\tau_2 \gg \tau_1$), then:

$$H_z^s(\omega) = \frac{I}{4} \frac{a^2}{[a^2 + (2h)^2]^{3/2}} \frac{\chi_o}{\ln(\tau_2/\tau_1)} \left(1 - \ln(\omega\tau_2) - i\frac{\pi}{2} \right). \quad (1.6)$$

A Fourier transform of the above expression can then be used to calculate the step-off response in the time domain:

$$\frac{\partial H}{\partial t} = \frac{I}{4} \frac{a^2}{[a^2 + (2h)^2]^{3/2}} \frac{\chi_o}{\ln(\tau_2/\tau_1)} \frac{1}{t}. \quad (1.7)$$

Equations (1.5)-(1.7) can be used to show the sensitivity of the EMI response as a function of changes in the ground clearance of the sensor. Figure 1.1 demonstrates how the measured signal changes as a function of transmitter height.

Therefore, for the simple case of a loop over a complex permeable, but non-conductive half-space, the response can be written as the product of three components:

$$V_s = A(h)G(\chi)f(t). \quad (1.8)$$

where $A(h)$ is a function of the sensor geometry and relative position to the half-space and is independent of the susceptibility, $G(\chi)$ is a function of the half-space susceptibility, and $f(t)$ is the temporal response of the geology (i.e. $f(t)$ is the convolution of the VRM response with the transmitter waveform - see Figure 1.2 for an example).

An approximate forward model can be constructed under the following assumptions:

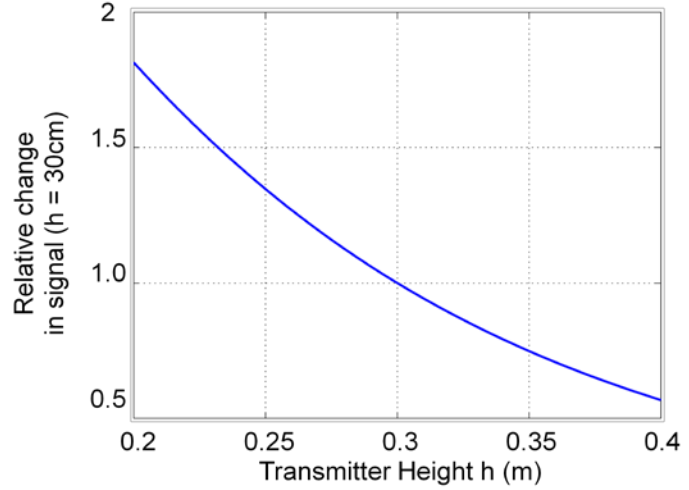
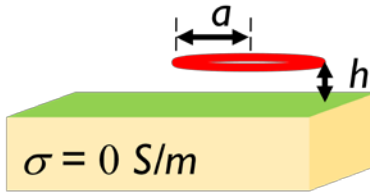
1. The response measured by a sensor moving over the ground can be approximated by a stationary receiver loop. That is, we assume that the receiver loop is moving slowly enough, that the signal due to a change in flux through the receiver loop due to the Rx loop's movement through the earth's field is small.
2. The geologic response will primarily be due to viscous remnant magnetization (VRM), and not conductivity. Modeling and field measurements at sites with VRM have shown that this assumption is valid for the time range and geometry of transmitter loops used in UXO sensors. We note that this assumption is not necessary, but does simplify the modeling,
3. The response of a loop with an arbitrary orientation can be approximated by Equation 1.8. That is, the function related to the sensor position and orientation can be separated from the function related to the geologic properties:

$$V_s = A(h, pitch, roll, yaw)G(\chi)f(t)$$

This assumption simplifies our calculations, since A and $f(t)$ are dependent only on survey and sensor parameters, and not the geologic properties of the subsurface. Therefore, when fitting data, the function A needs to be calculated only once at the start of processing rather than at each iteration when the inversion process searches model space.

4. Topography does not need to be modeled. We note that it is possible to introduce a ground clearance correction into the function A (Walker et al. 2005). However, information on surface topography is not usually available at the scale or resolution required.
5. The transmitter loop can be approximated as multiple dipole moments.

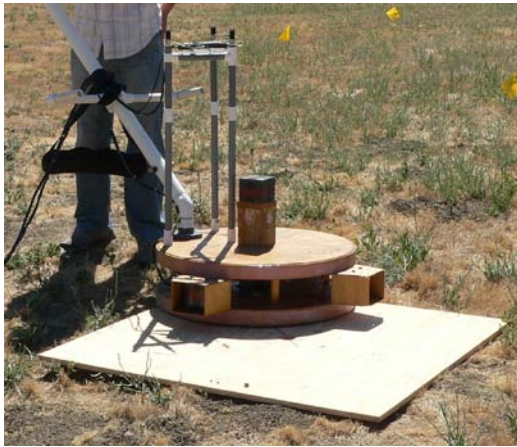
Figure 1.3 contains data measured using a Geonics EM-61 Mark2 pulse induction sensor that was modified to have a 10 msec transmitter on time. The data were taken on Kaho'olawe Island, Hawaii with the sensor at a number of heights and dip angles. We found that using 8 dipoles to model the transmitter sensor was sufficient to model the measured data. Not surprisingly, data collected with the transmitter loop close to the ground were less accurately modeled. When the loop is greater than 10 cm above the ground surface and less than 50 degrees from horizontal the data are accurately modeled using the multiple-dipole method



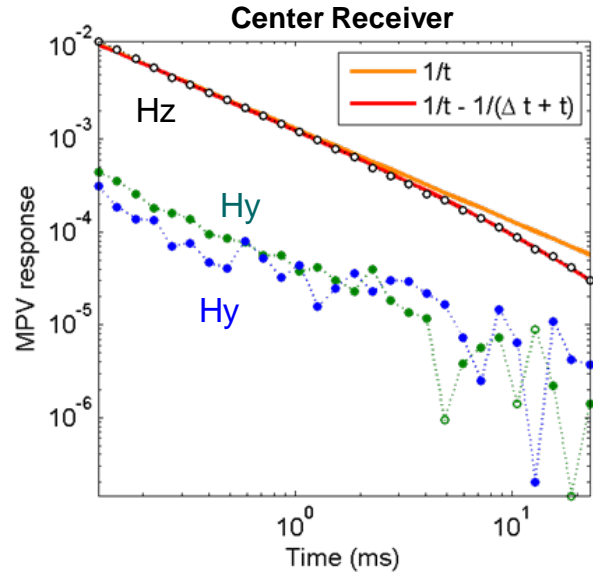
(a) Geometry of loop over $\frac{1}{2}$ space above the surface

(b) Relative change in signal for loop in (a). 30 cm

Figure 1.1. Sensitivity of the EMI response to a magnetic half-space as a function of sensor height. For this example we the model sensor response at the center of a circular transmitter loop. The values plotted in (b) are normalized to unity at a height of 30 cm. Height variations of only a few centimeters can produce a significant change in the background signal.



(a) The MPV-MARK 1 at the former Sky Research UXO test site



(b) Data recorded by the center receiver.

Figure 1.2. An example of the effect of the waveform on the theoretical step-off response. (a) MPV-MARK 1 data were acquired at the Ashland airport. The MPV-MARK 1 used during this data collection had a finite on-time of approximately $\Delta t = 25$ ms. (b) The theoretical $1/t$ step off response is modified due to the finite on-time of the MPV-MARK 1. The vertical component of the signal (black circles) follows the theoretical response due to a rectangular pulse (plotted in red).

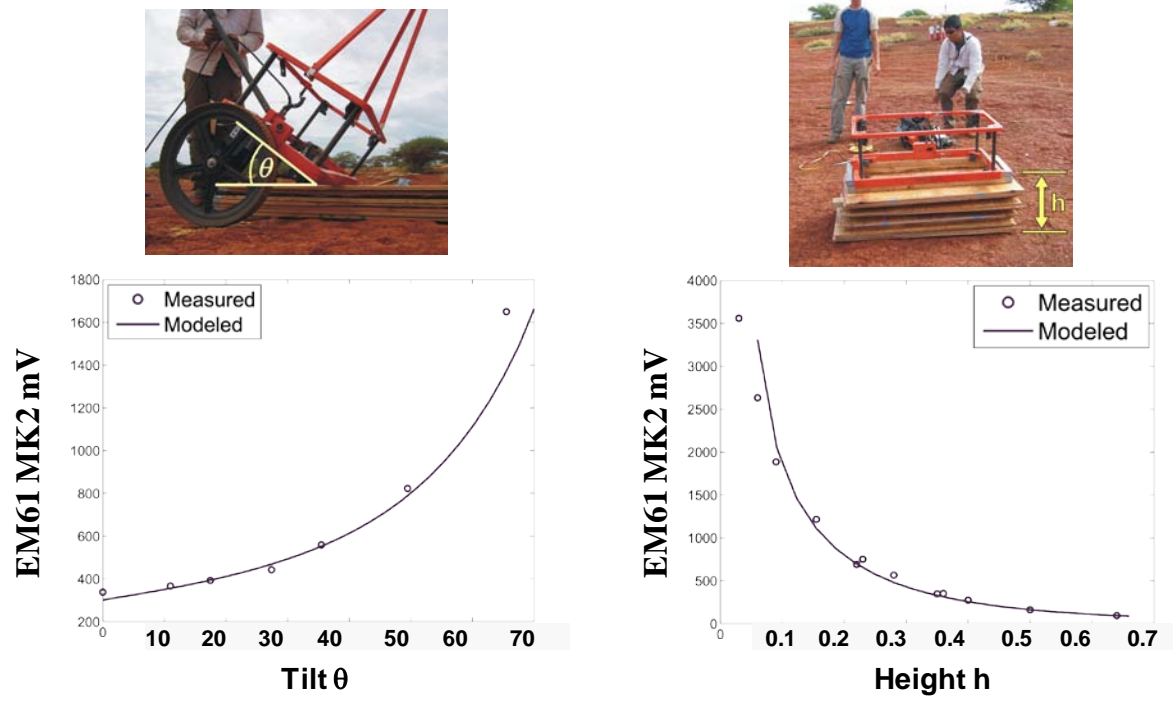


FIGURE 1.3. TILT AND HEIGHT TESTING MODELING RESULTS. A GEONICS EM-61 MARK 2 SENSOR WAS USED TO COLLECT DATA ON KAHO'OLawe, ISLAND AT A NUMBER OF DIFFERENT HEIGHTS AND TILT ANGLES. THE SIGNAL WAS CALCULATED BY REPRESENTING THE TRANSMITTER LOOP WITH 8 DIPOLES.

MODELING GEOLOGY RELATED SENSOR NOISE WITH A SLOWLY SPATIALLY VARYING BACKGROUND GEOLOGY MODEL

In this project we assume that the electromagnetic properties of the subsurface are slowly spatially varying. That is, small spatial wavelength features in the data can be attributed to the sensor motion $A(h, \text{pitch}, \text{roll}, \text{yaw})$ rather than sudden changes in the mineralogy (modeled by $G(\chi)$). The function $G(\chi)$ will be estimated in the data processing methods of this project. In order to make the inverse problem tractable, it is important that the geologic response can be attributed to a function $G(\chi)$ that can be parameterized by a simple model, such as a plane or constant.

In order to test this assumption, we again consider the line of EM-63 and IMU data plotted in Figure 0.2. Recall that the forward model for the soil can be written as:

$$d = A(h, \text{pitch}, \text{roll}, \text{yaw})G(\chi)f(t) \quad (5)$$

The data d is linearly dependent on the model $G(\chi)$, i.e. $Am = d$ where the variation in the data due to changes in sensor position and orientation is contained in the modeling matrix A , and the spatial behavior of the geology is contained in the model vector $m = G(\chi)$. Let us parameterize the geologic model $G(\chi)$ with 2 cm constant cells along the N-S direction. Since data are taken at approximately 10 cm intervals along each line, we have an under-determined problem for the model.

Tikhonov regularization is used to solve the under-determined linear inverse problem. The optimal geologic model is obtained through the following optimization problem:

$$\text{Minimize } \|d - Am\|^2 + \lambda \|Wm\|^2 \quad (6)$$

where λ is the trade-off parameter and W is the regularization matrix. The regularization matrix allows us to introduce features of the model that we know *a-priori*. Common choices for the regularization matrix are flatness, which is enforced using the first order finite difference matrix. Regularization for this choice of W thus balances the data fit with a measure of the slope of the recovered model. Another common choice for regularization is smoothness, which is enforced using the second order finite difference matrix. Once a Wm is chosen, the solution for m is:

$$m = (A^T A + \lambda W^T W)^{-1} A^T d \quad (7)$$

Figure 1.4 contains examples of fitting the data using either smooth or flat models to a line of Geonics EM-63 data collected on the Camp Sibert GPO. We do not here discuss how the trade-off parameter λ is selected, as our primary objective is to determine if the geologic properties in m can be slowly spatially varying while still being able to model the small wavelength variations in the data. Figure 1.4 plots the results of fitting the data with a flat model in (a) and a smooth model in (b). In both (a) and (b), the upper panel shows the fit to the first time channel of data and the lower panel

plots the recovered geology model. The flat model is nearly linear with Northing, while still fitting the main features in the data. The smooth and flat models have similar magnitudes. These results suggest that it may be possible to parameterize the background geology with simple models, such as a plane, within small spatial subsets of the data while still modeling small wavelength features.

EXAMPLE: MODELING MTADS DATA AT CAMP SIBERT, ALABAMA

Multi-Sensor Towed Array Detection System (MTADS) EMI data were collected at Camp Sibert, Alabama. The MTADS EMI consists of an array of three modified Geonics EM61 time domain electromagnetic sensors (Figure 1.5). Each EM61 sensor consists of coaxial 1 m x 1m transmitter/receiver pairs. These sensors are overlapped such that a 2 meter swath of data is acquired on each pass. The position, elevation, and orientation of the trailer were determined by using data from three GPS receivers that were placed on the MTADS trailer.

The MTADS EM61 data were acquired along lines in both North-South and East-West directions. Of the anomalies identified from the MTADS EM61 data, several produced empty holes when excavated. We suspected that several of these anomalies could be attributed to the presence of magnetic soils in the survey area. We would expect that small spatial wavelength anomalies due to the movement of the EMI sensors relative to the surface would be evident in the MTADS data.

A short study was carried out to determine the nature of targets selected from the MTADS data that were classified as “can’t analyze” and, upon excavation, resulted in empty holes. We investigate whether sensor motion could explain features in the data that complicated the initial analysis by modeling the MTADS system response over a half-space with complex magnetic susceptibility. We focused on anomalies where the sensor ground clearance varied by greater than 10 cm in the vicinity of the anomaly. The ground clearance was estimated by detrending the elevation data recorded by the three GPS antennas.

The MTADS sensor does not have an altimeter to measure the height of the sensor above the ground. Therefore, elevation data is used to estimate a ground clearance. We process the data on a “cell-by-cell” basis, i.e. we analyze a 5 m x 5 m portion of the total data set centered on the target anomaly. We assume that within each cell of data that the ground surface is flat, such that by removing a linear trend along each line of elevation data an estimate of the ground clearance will be computed.

There are a number of factors that affect the accuracy of our processing:

- The MTADS data analyzed here were first leveled using a median filter. The median filter produced artifacts in the data.
- The effect of topography was not included in the modeling. The same ruts and bumps on the ground surface that cause MTADS trailer elevation (and therefore, ground clearance) to change can also produce EM anomalies. That is,

a void beneath a sensor results in a decrease in amplitude while a bump produces an increase in the secondary field amplitude.

- In order to reduce computation time, the primary field generated by each of the EM61 sensors was generated with only 4 dipoles.
- We assume the magnetic susceptibility within a cell is constant. Data features produced by small spatial scale variations in magnetic susceptibility are not modeled.

The MTADS data were acquired along North-South and East-West lines. Many of the geology related anomalies on the site were due to ruts that ran along an East-West direction. When the MTADS trailer wheels would pass over these ruts, the distance between the magnetic soil and the sensors would decrease resulting in an increase in the signal measured by the sensors. These cross-track ruts were not as pervasive during EW traverses of the site. For data collected along the East-West direction, the sensor motion anomalies were generally much smaller in amplitude. An example of this type of anomaly was found in Cell 644 (Figures 1.6). The image in the upper left part of Figure 1.6(b) shows the first time channel of de-trended data. Figure 1.6(a) plots the ground clearance estimated by removing linear trends from the elevation data. Removal of a linear trend predicts that the ground clearance varies by about 13 cm for data collected along NS lines, and 5 cm for data collected along EW lines. By comparing Figures 1.6(a) and (b), we see that the regions where the MTADS ground clearance is predicted to be closer to the ground is correlated with higher amplitudes in the recorded signal. We have found that there may be a slight lag problem in the data, as we consistently achieve better correlation between the ground clearance data and the secondary field when lagging the position by a couple of points. The plots on the right side of figure 1.6(b) compare the data predicted by modeling the background with a constant magnetic susceptibility along a number profiles. We see that the general shape of the predicted data is similar to the measured data, which suggests that the anomaly of Cell 644 is due to presence of magnetic soils and the MTADS EMI sensors being closer to the ground during the NS traverse. There are smaller scale geology signals in the EW lines since there are smaller variations in the ground clearance of the sensors. The difference in magnitude between geology related anomalies detected along NS and EW lines suggests that it may be a good data feature to reduce geology anomalies. Indeed, simply discarding targets with EW data anomaly magnitude less than the detection threshold was shown to be an effective way of reducing the number of geology anomalies (Billings, 2008). Figure 1.7 provides a second example of how the modeling technique can accurately model the geologic response.

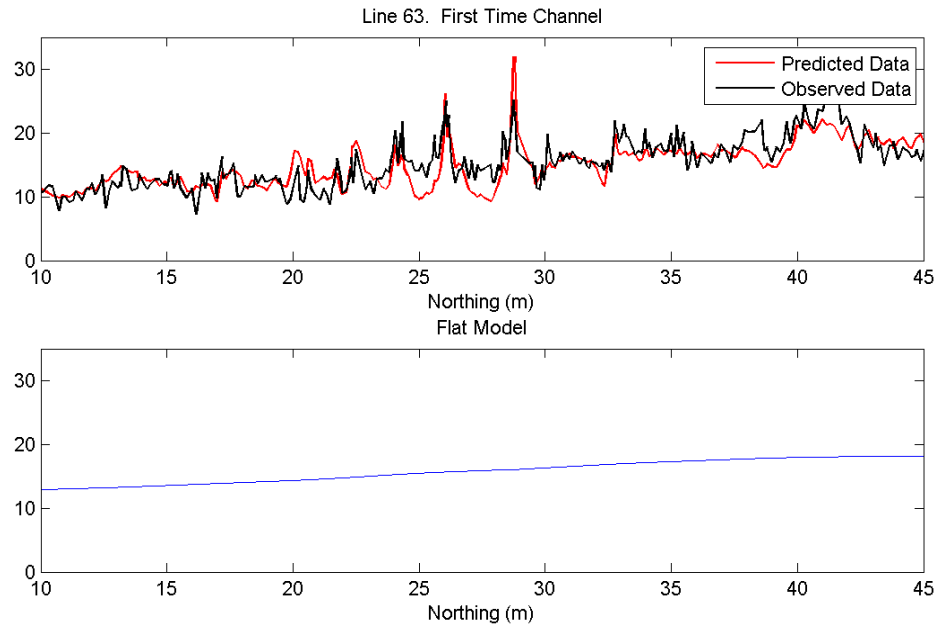
Figure 1.8 shows an example of how detrending can produce inaccurate results. For this example (Cell 809) the predicted soil response has a similar shape to the measured anomaly. However, the data magnitude is shifted by approximately 30 mV. The need to apply a detrending filter to MTADS data - and the resulting filtering

artifacts in the data - makes the MTADS data a poor candidate for applying a processing method where the background response is modeled.

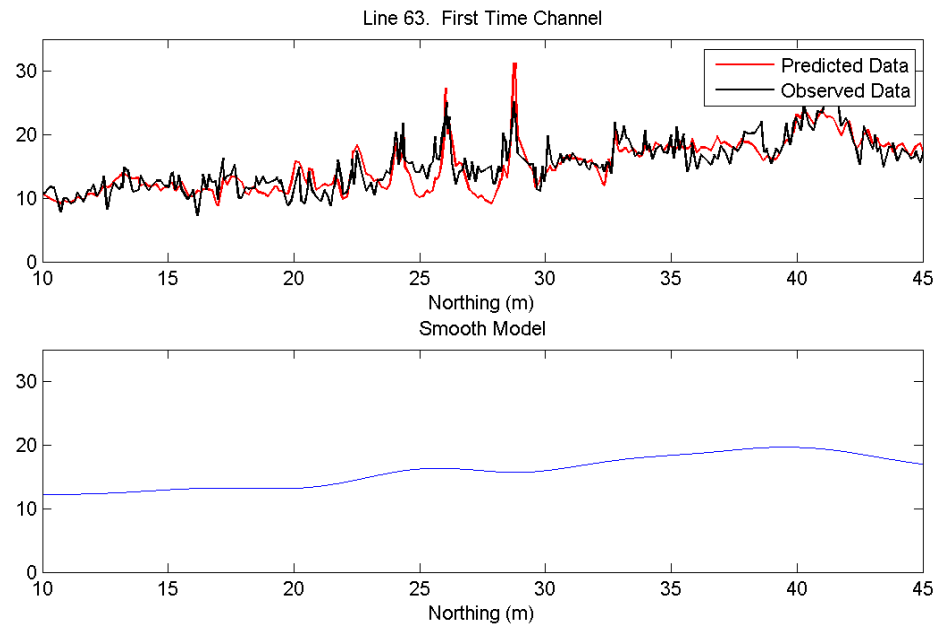
SUMMARY

In this chapter we summarized the geology modeling method developed in this project. The method is based on representing the transmitter as multiple dipoles. The analytic solution for a dipole over a magnetic and conductive half-space is then used to construct the measured secondary field. The validity of this model was initially established by comparing Geonics EM61 MK2 data collected at Kaho'olawe to the modeling results. We showed that geologic response measured using full coverage Geonics EM63 data acquired at the former Camp Sibert data could be predicted using the modeling approach here. Of note with the Geonics EM63 result, was that this example showed that many of the small length scale data features could be modeled using a slowly varying background magnetic susceptibility model. We concluded this chapter with an example of results from a study that looked at MTADS data related to the empty holes dug at the Former Camp Sibert. We showed that features in MTADS EMI anomalies could be due to sensor movement relative to the magnetic background at Camp Sibert.

The modeling technique developed here has the potential to reduce false alarms due to sensor movement. In addition this modeling will improve discrimination since a more complete forward model of the data could be incorporated into processing and inversion routines. In order for this modeling technique to be useful in a practical setting, better estimates of the ground clearance are required. In addition, sensors with minimal drift should be used, such that the need for applying a median filter to remove long spatial wavelength anomalies in the data is eliminated.



(a) Flat model data fitting result

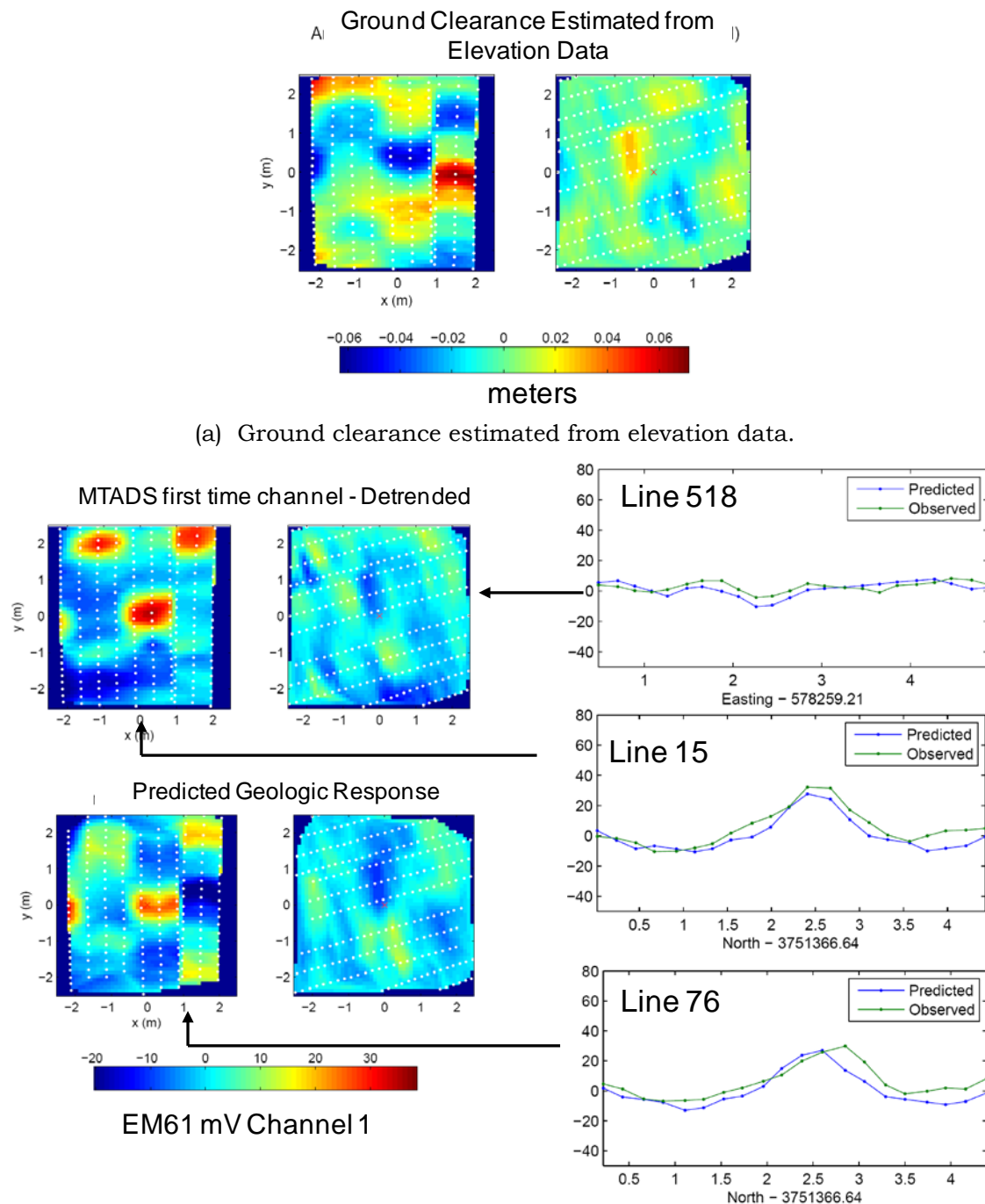


(b) Smooth model data fitting result

Figure 1.4. Fitting raw (i.e. non-detrended) data with a slowly spatially varying background geology. A regularized inversion is used to fit data with both a flat and smooth model.

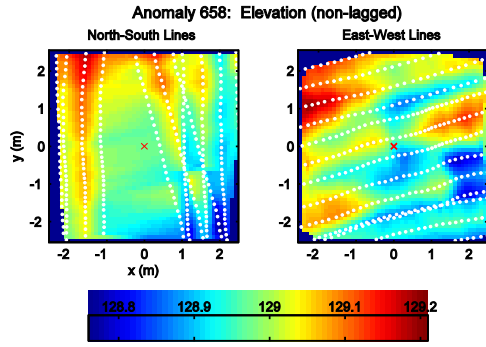


Figure 1.5. Photo of the MTADS EM61 array. Three EM61 MKI sensors with 1m x 1m transmitter/receiver pairs are mounted on a trailer towed by a low noise vehicle. The three GPS sensors on the trailer provide positioning and orientation information.

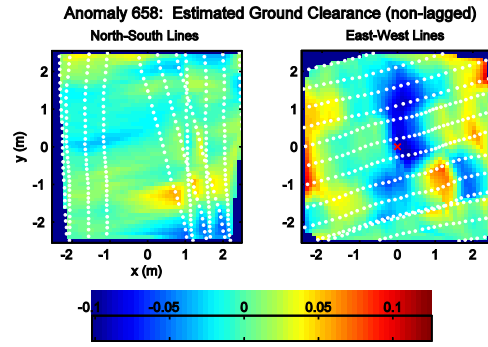


(b) Comparison of first time channel EM61 MKI data and the data modeled assuming a constant background geology

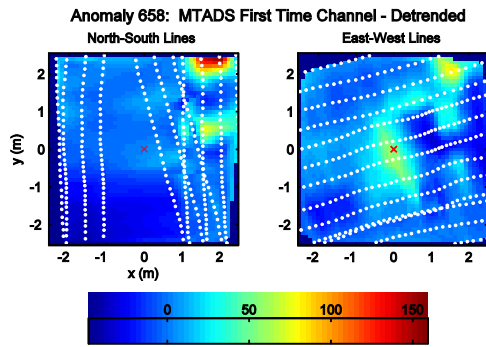
Figure 1.6. Example of modeling the MTADS soil response. The estimated ground clearance for Cell 644 is plotted in (a), which shows a total variation of 13 cm. The measured data and data predicted by the geology model is presented in (b). In the NS line there is an approximately 40 mV anomaly, and in the EW lines there is no significant anomaly. Data features in both the EW and NS lines are well modeled by the background signal modeling.



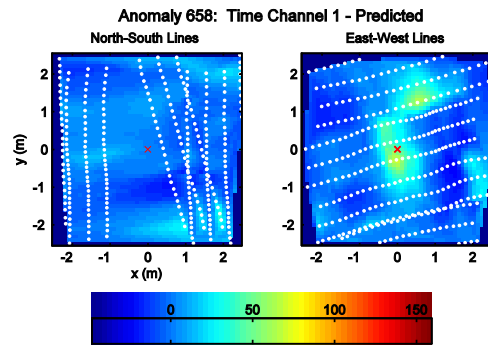
(a) Elevation recorded by GPS



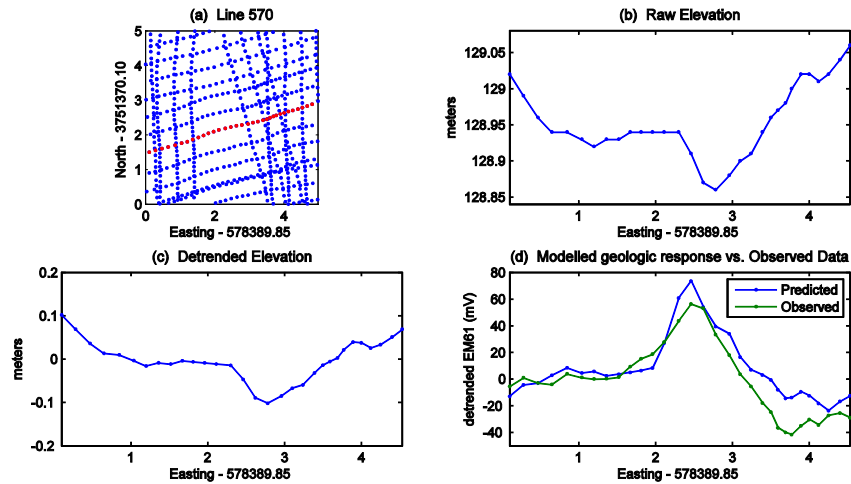
(b) Ground clearance estimated from elevation



(c) First time channel of MTADS data



(d) Data predicted by geology modeling



(e) Comparison of modeling along an EW profile

Figure 1.7. Example of modeling the MTADS soil response. For this example, the anomaly is in the EW lines. Variation in the ground clearance predicts a geologic anomaly of approximately 70 mV in the first time channel. The predicted soil response matches the measured data both when looking at the gridded images in (c) and (d), as well as along a line (e).

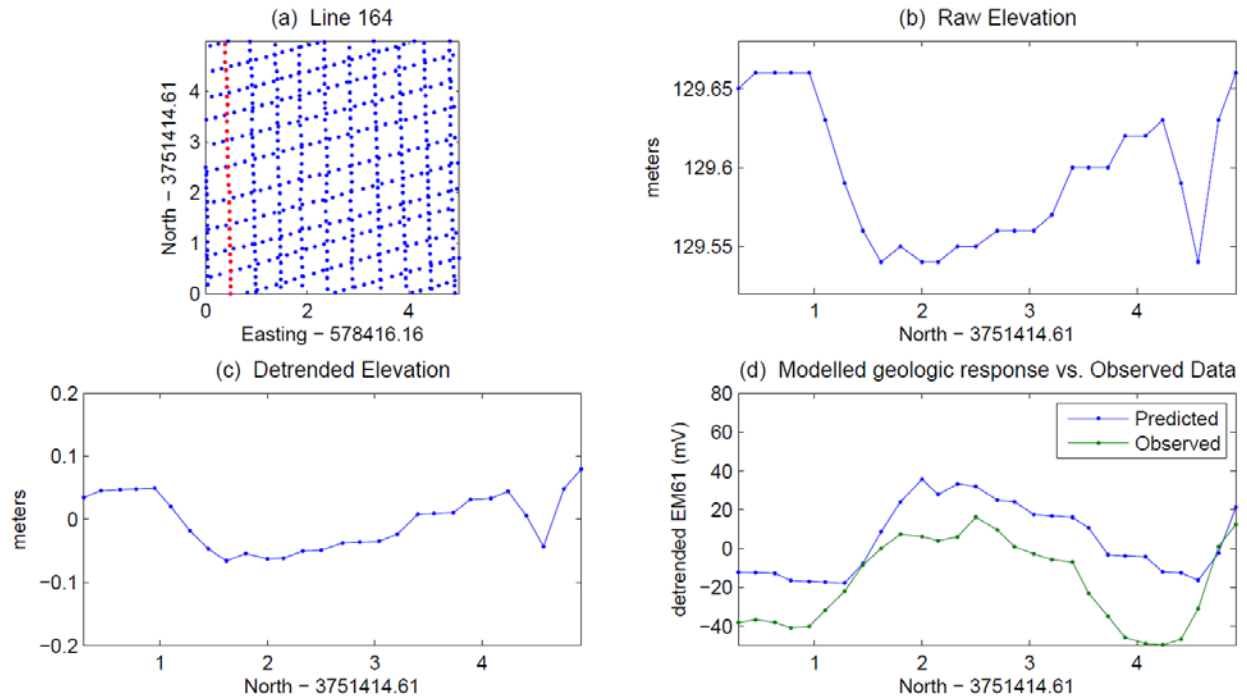


Figure 1.8. Example of how detrending can produce inaccurate results. (a) plots the line of interest from Cell 809. (b) the raw elevation. (c) The detrended elevation was obtained by removing a linear trend. (d) The predicted soil response (blue line) is compared to the detrended EM61 first channel data (green line). Although the shape of the response is quite similar, there is an approximately 30 mV shift in the data magnitude. The need to apply a median filter to the data limits the application of the background modeling method to EM61 data.

2. DATA PROCESSING METHODS

The standard method for processing data is to apply a high pass filter to the data. A common filter to use is a median filter where the filter window is larger than the maximum spatial size anomaly for a target of interest, and smaller than slowly varying geology related features in the data. In SERDP MR-1414 we tested the use of a 2D Butterworth filter applied to gridded full coverage data (Li et al. 2010). Also in SERDP 1414, we showed that a data filtering approach could be ineffective at removing background soil signal resulting from the movement of the transmitter and receiver relative to magnetic ground since the soil signals would produce data features that are the same spatial size or smaller than targets of interest.

In the previous chapter, we showed that GPS and IMU information could be used to directly model the small spatial wavelength features caused by sensor movement. In this project we want to determine if dipole polarizability parameters could be more accurately estimated by accounting for these sensor movements related signals in the forward model. We developed a number of different processing methods that incorporate this modeling.

In this chapter, we outline two methods that incorporate the modeling of the geologic response. The first approach is a sequential approach, where the first step is to estimate the magnetic susceptibility within the region of a target. The next step is to subtract the soil response calculated using the estimated magnetic susceptibility. To make the susceptibility estimation problem tractable, we assume that the underlying geology has smoothly varying magnetic characteristics. The final step of the sequential approach is to estimate target dipole parameters using the background corrected data. The second approach is a simultaneous inversion approach. Parameters describing the amplitude and spatial variation of the geology and parameters characterizing a buried compact target are simultaneously estimated from electromagnetic induction sensor data.

These inversion methods are demonstrated using Geonics EM63 pulse induction sensor data and Geophex GEM3 frequency domain data. Simulations using Geonics EM63 data are used to demonstrate the performance of the processing methods.

METHOD ONE: SEQUENTIAL PROCESSING: SUBTRACT SOIL RESPONSE FROM OBSERVED DATA, THEN INVERT FOR TARGET PARAMETERS

In this approach, the soil and target parameters are estimated in a two step procedure. We first define a region of interest that surrounds the anomaly. Soundings that are assumed to be from the background geology, and not from the buried target of interest, are then used to estimate the parameters \mathbf{m}_{soil} of a background soil model $G(x,y)$. The soil parameters are determined by solving the following optimization problem:

$$\text{Minimize } \phi(\mathbf{m}_{soil}) = \frac{1}{2} \left\| V_d^{-1/2} (\tilde{\mathbf{d}} - F[\mathbf{m}_{soil}]) \right\|^2 \quad (2.1)$$

where $\tilde{\mathbf{d}}$ are the data that do not have a contribution from the buried target and V_d is the data covariance matrix. When we choose a soil model that has many parameters, such that we have an underdetermined system to solve, we either regularize the inverse problem or solve the problem using truncated singular value decomposition. If the background soil properties function $G(x,y)$ can be parameterized with a simple function, then the problem is over determined. For example, if we assume that the background soil properties can vary spatially as a plane, then $G(x,y) = ax + by + c$. and the soil parameters are

$$\mathbf{m}_{soil} = [a, b, c] \quad (2.2)$$

Once the background soil model is estimated, the soil response is calculated (\mathbf{d}^{bg}). A background corrected data set is obtained by subtracting \mathbf{d}^{bg} from the observed data \mathbf{d}^{obs} .

The second step of the sequential method is to use the corrected data to invert for the dipole model by solving a second optimization problem:

$$\text{Minimize } \phi(\mathbf{m}_{target}) = \frac{1}{2} \left\| V_d^{-1/2} ((\mathbf{d}^{obs} - \mathbf{d}^{bg}) - F[\mathbf{m}_{target}]) \right\|^2 \text{ subject to } m_i^L \leq m_i \leq m_i^U \quad (2.3)$$

The accuracy with which the dipole model parameters \mathbf{m}_{target} are estimated is limited by the ability to estimate the background geology parameters \mathbf{m}_{soil} and its corresponding response \mathbf{d}^{bg} . The upper and lower constraints on the i^{th} target parameter are defined as m_i^U and m_i^L , respectively. Successful application of the sequential processing method therefore requires sufficient soundings collected near the target to accurately estimate \mathbf{m}_{soil} , but far enough away from the target such that the data $\tilde{\mathbf{d}}$ used to estimate the soil model is not contaminated by the target response.

The sequential approach is similar to the standard data filtering approach for removing background signal. Indeed, for a survey where ground clearance and sensor orientation is constant, the two approaches are essentially equivalent. The critical difference is that we are able to model sensor movement related features in the data that have a short length scale by incorporating the sensor ground clearance and orientation into the soil modeling function $F[\mathbf{m}_{soil}]$.

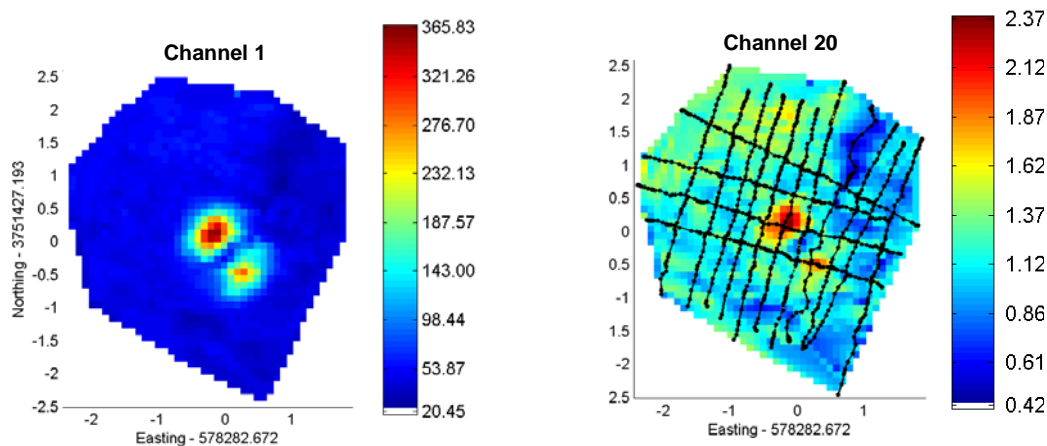
EXAMPLE: CUED EM63 FROM SIBERT



(a) The Geonics EM63 acquiring cued interrogation data



(b) Target 852: Wrench



(c) Gridded image at time channels 1 and 20

Figure 2.1. Geonics EM63 data acquired over a wrench. (a) The Geonics EM63 at Camp Sibert, Alabama. (b) Excavated object. (c) A gridded image of data at time channels 1 ($t = 0.18$ ms) and 20 ($t = 7.1$ ms).

At the Former Camp Sibert ESTCP Pilot discrimination study, anomalies of interest were chosen from a Geonics EM61 full coverage detection survey. Geonics EM63 data were acquired over an approximately 4m x 4m area centered on each picked target. To ensure good spatial coverage, a tarp with survey lines was centered on each target location (Figure 2.1(a)). The data were acquired in a dynamic mode with a Leica TPS

1260 Robotic Total Station provided positioning information, and a Crossbow AHRS-400 IMU was used for measuring the pitch, roll and yaw of the EM-63 cart. Figure 2.1(c) contains gridded images of time channel 1 and 20 data acquired over a wrench. At the first time channel the signal is dominated by the response of the wrench, while at time channel 20 we can start to see data features related to the magnetic soil.

For this example we will solve for the smooth soil model that best fits the soil response. Tikhonov regularization is used to solve the under-determined linear inverse problem, such that the optimal geologic model is obtained through the following optimization problem:

$$\text{Minimize } \|d - Am\|^2 + \lambda \|Wm\|^2$$

where a second derivative operator is chosen for the regularization matrix W to ensure a smooth soil model. This approach is demonstrated using the wrench data from Figure 2.1. Figure 2.2(a) plots a gridded image of the sensor elevation relative to the nominal 30 cm ground clearance for the Geonics EM63. The ground clearance ranges from approximately 25 cm to 38 cm. The region outside the green circle (i.e. tan area without a target response) has a background response ranging from 20 to 60 mV in the EM63 at the first time channel. We see that in areas where there is an increase in the sensor elevation, there is a decrease in the background soil signal (Figure 2.2(b)). In particular, there is a section in the north east corner portion of the grid where the increased ground clearance (red region in (a)) corresponds to a region of lower data magnitude (blue in (b)).

Soundings outside the green circles were used to estimate a background soil model. A soil model was estimated by discretizing the background into 20 cm x 20 cm square cells. A regularized linear inverse problem was solved to obtain the smooth recovered soil model in Figure 2.2(c). The value of the soil model parameters are scaled such that if the deviation from the nominal height and the sensor pitch and roll is zero, then the soil model parameter would be equal to the data. This model is then used to predict the response due to the soil alone (Figure 2.2(d)). The predicted soil response matches the observed data in Figure 2.2(b) very well. In particular, the low magnitude data corresponding to the section of the grid with the largest ground clearance is recovered. The modeled soil response can then be subtracted from the measured data (Figure 2.2(e)). By changing the color scale to -10 mV to 10 mV, we see that the data outside the green circle appears to be random which suggests that the soil model was able to model the spatially correlated signal related to the magnetic soil. The second step of the method is to solve an inverse problem for the dipole polarizabilities of the target. Removal of correlated non-target signal in the data greatly reduces the chances that the recovered model parameters will be biased when obtaining the least squares solution.

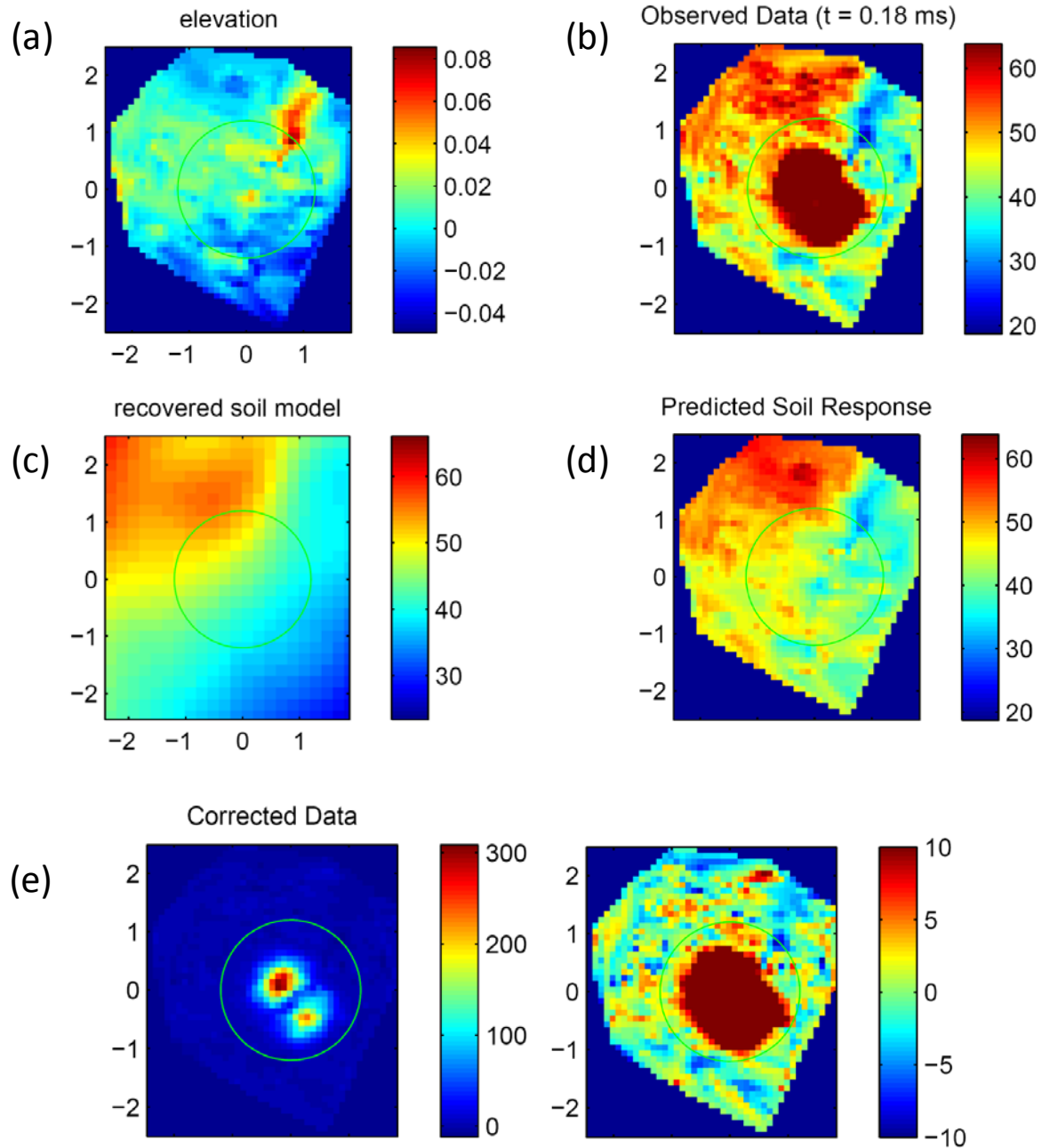
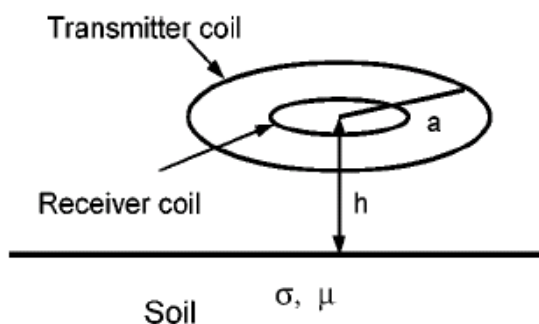
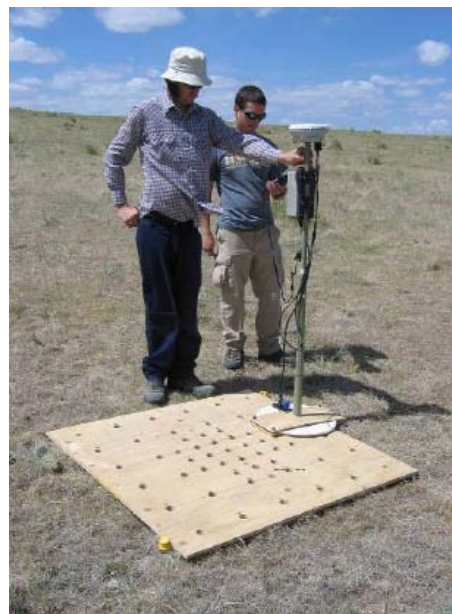


Figure 2.2. Application of a soil fitting procedure to the Geonics EM63 data in Figure 2.1(c). The elevation variations in (a) are correlated with the measured data in (b). A soil model is constructed by discretizing the surface, and then solving an underdetermined inverse problem that constructs a smooth model based on data outside the green circle. The soil model does a good job of predicting the soil response outside the green circle. The corrected data is shown in (e).

*EXAMPLE: APPLICATION OF SEQUENTIAL PROCESSING USING GEOPHEX GEM3
FREQUENCY DOMAIN EMI DATA*



(a) Schematic of the Geophex GEM3 sensor



(b) GEM3 data collection at the Former Lowry Bombing and Gunnery Range

Figure 2.3. The Geophex GEM3 sensor. A schematic of the GEM3 sensor head is shown in (a). A pair of transmitter coils are used to buck the primary field, such that the receiver coil is placed in a region of low transmit field. For the examples in this project, GEM3 were collected on a template. The template used at FLBGR is shown in (b).

The sequential processing approach was tested using a Geophex GEM3 frequency domain EMI instrument. The sensor head contains collocated and circular transmitter and receiver coils with additional bucking coils to cancel out the effect of the primary field in the receiver coils (Figure 2.3). The in-phase (real) and quadrature (imaginary) components of the scattered field are recorded at ten frequencies: 90, 210, 390, 750, 1470, 2910, 5850, 11430, 21690 to 41010 Hz. We tested the sequential processing method using GEM3 data acquired at two sites: (1) the Former Lowry Bombing and Gunnery Range (FLBGR) and (2) the Former Camp Sibert. For both examples we first remove the magnetic soil background with the VRM model, and then we invert the background subtracted data assuming a dipole model to obtain the instantaneous elements of the magnetic polarization tensor of the induced electromagnetic dipole. To assess the potential for discrimination with the GEM3 at the two sites, we fit the principle polarizabilities with the four-parameter model of (Miller et al. 2001) and examine their separation in feature space

We process the GEM3 data with the sequential inversion process. Similar to the time domain case, we use the resistive limit solution for the magnetic soil response. Earlier in this report, we showed that we could represent the secondary field as

$$H_z^s(\omega) \approx \frac{I}{4} \frac{a^2}{[a^2 + (2h)^2]^{3/2}} \frac{\chi_o}{\ln(\tau_2 / \tau_1)} \left(1 - \ln(\omega\tau_2) - i\frac{\pi}{2} \right) \quad (2.4)$$

If the data are acquired at constant ground clearance, then the data can be fit with the following function

$$data = A(x, y) \ln(\omega) + B(x, y) + iA(x, y) \frac{\pi}{2} \quad (2.5)$$

In order to estimate the functions A(x,y) and B(x,y), we assume that A(x,y) and B(x,y) are (1) smoothly varying over the template, and (2) can be exactly determined on the boundary. With these assumption in place, the inversion process is then:

1. *Identify soundings that are due to soil and not a compact metallic object.* Lhomme et al. (2008) describe a method for identifying soil soundings that exploits the characteristics of a VRM soil response.
2. *Use the non-target soundings to calculate A(x,y) and B(x,y).* We determine A(x,y) and B(x,y) over all sounding locations within the template by using a thin plate spline.
3. *Subtract the background soil response from the data, and invert the data for dipole polarizabilities.* Once the data are background corrected, we can then solve for dipole polarizability. Each polarizabilities is then fit for the four parameter function described in Miller et al. (2001)

$$L(\omega) = k \left(s + \frac{(i\omega\tau)^c - 2}{(i\omega\tau)^c + 1} \right) \quad (2.6)$$

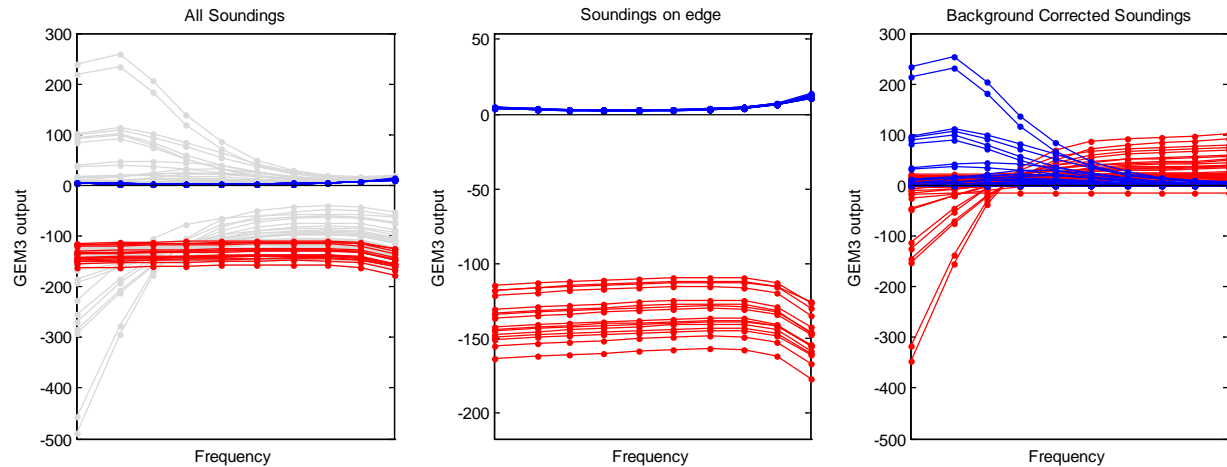
The above methodology was applied to two sets of GEM3 data. We first applied the technique to data collected at the Former Lowry Bombing and Gunnery Range 20 mm Range Fan. We then applied the methodology to data collected at the Former Camp Sibert geophysical prove out site as part of the ESTCP Discrimination Pilot discrimination project.

Application to Former Lowry Bombing and Gunnery Range 20 mm Range Fan

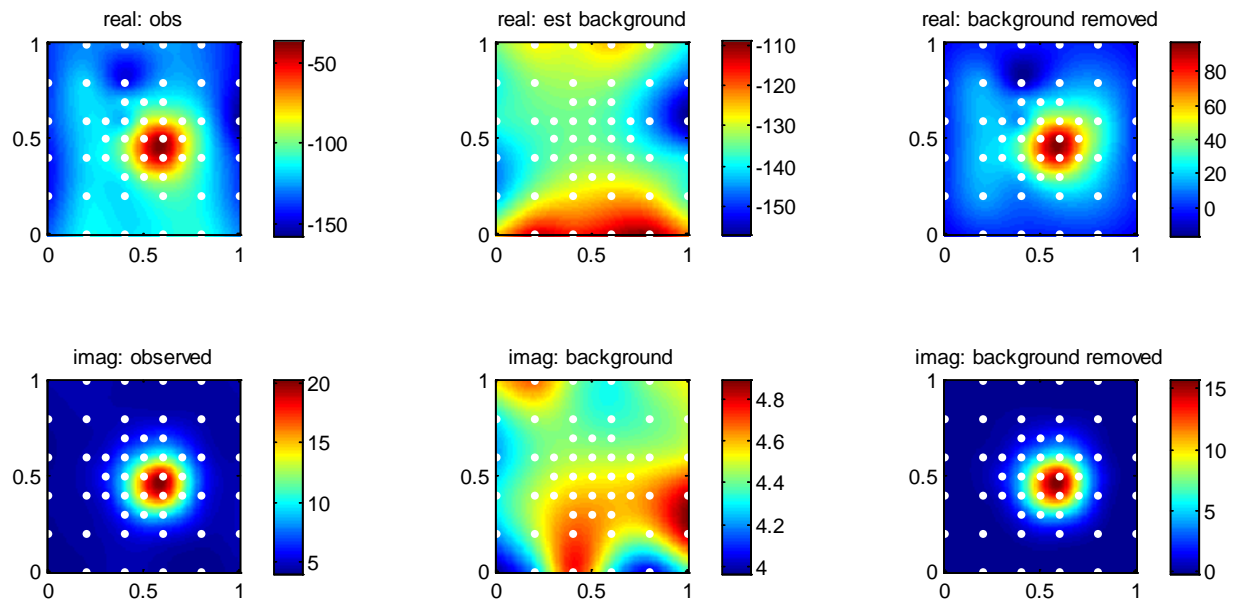
Data were collected with a Geophex GEM3 frequency-domain sensor at FLBGR as part of ESTCP Project 200504 "Practical Discrimination Strategies for Application to Live Sites". The range is located approximately 20 miles southeast of Denver, Colorado, in Arapahoe County. The 20 mm Range Fan was used for air-to-ground target practice from fixed-wing aircraft that fired 0.50 caliber projectiles, 20 mm and 37 mm projectiles. The 37 mm projectile was the target of interest for the remediation effort. Geonics EM61 data were used to identify 59 anomalies for re-collection with the GEM3.

GEM3 measurements were made using a template (Fig. 2.3(b)) to improve positioning accuracy and signal to noise ratio. The template was designed to have 49 positions with 0.10 and 0.20 m spacing, and 16 peripheral positions. The 16 peripheral positions were included for characterizing the background signal. The GEM3 data were drift-corrected using the free-air calibration measurements that were conducted before and after each anomaly was surveyed. Following the free-air calibration, soundings on the periphery deemed to be from soil only were used to solve for the functions $A(x,y)$ and $B(x,y)$. A thin plate spline was used to interpolate the function to all measurement locations.

Examples of the free-air calibrated data and the results of the background removal process are shown in Figures 2.4 and 2.5. Figure 2.4 summarizes the process over a 0.50 cal bullet (cell number 29) and figure 2.5 shows results for a 37 mm projectile in cell 40. All frequency domain soundings collected over the 0.50 cal bullet in cell 29 are plotted in the left panel of figure 2.4(a). The blue lines indicate imaginary (or quadrature) components of the data measured on the edge of the template. Red lines show the real (or in phase) part of the data. A closer look at the soundings recorded on the edge of the template are plotted in the center panel of figure 2.4(a). The soundings in the center panel exhibit the characteristic VRM frequency domain response of a log-linear decay in magnitude of the real components of the data, and a slight offset in the imaginary part of the data. The far right panel of figure 2.4(a) is a plot of the background corrected data. Figure 2.4(b) contains gridded images of the real and imaginary components of the observed data, the estimated background response, and the background corrected data. The most significant difference between the background corrected and raw data is in the real component of the data. Indeed, the magnitude of the background signal is of the same order as the background corrected response.

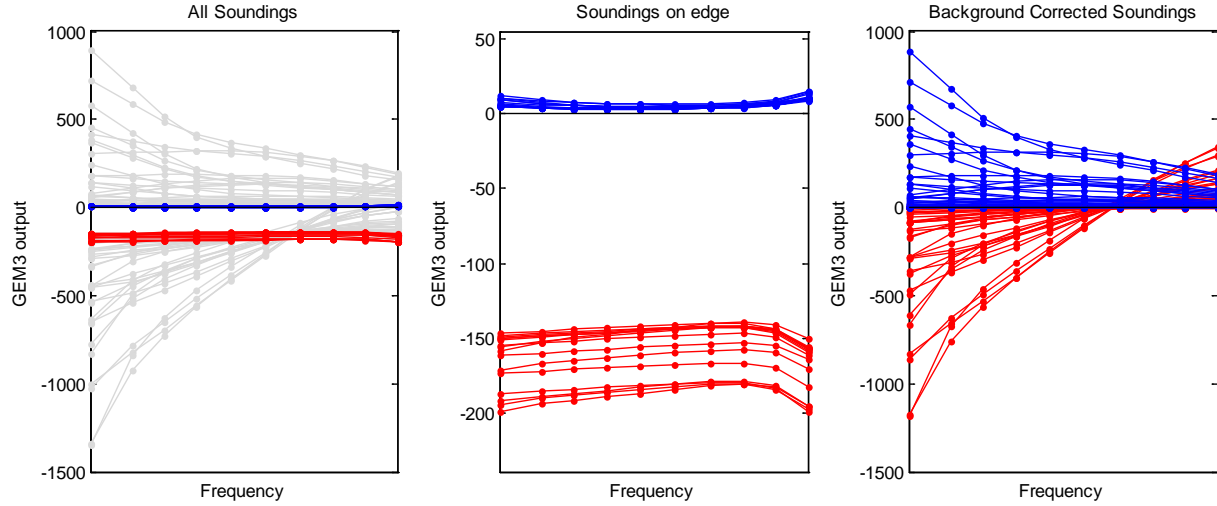


(a) Comparison of soundings before and after background soil correction.

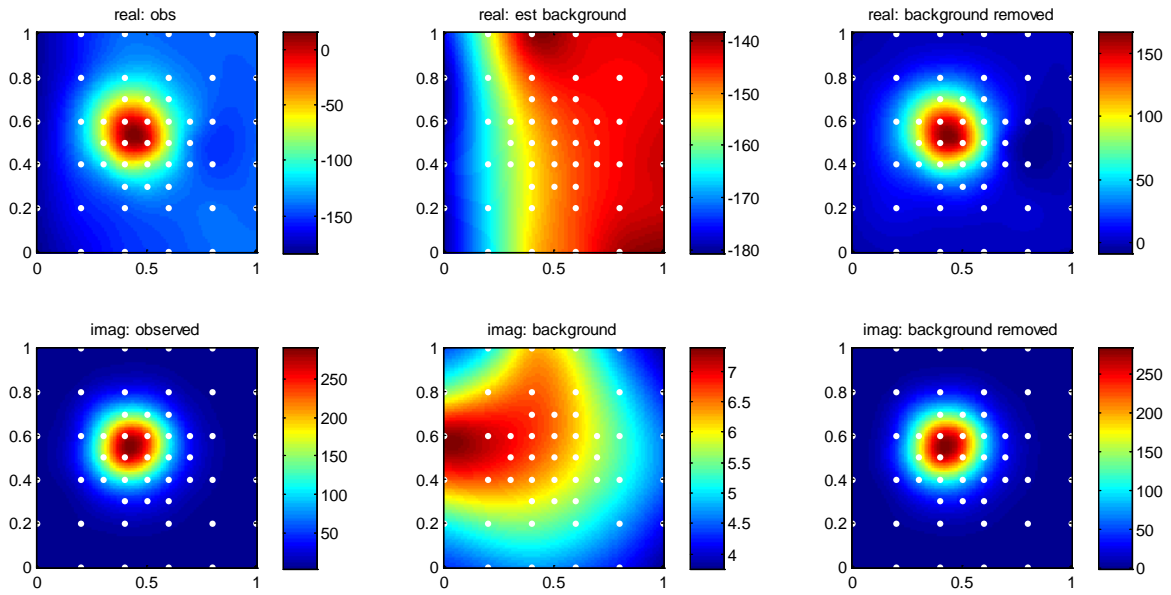


(b) Plan view comparison of data before and after background soil correction procedure

Figure 2.4. Demonstration of soil removal technique applied to Geophex GEM3 frequency domain data. Excavation of this anomaly (Cell 29) produced a 0.50 cal.



(a) Comparison of soundings before and after background soil correction.

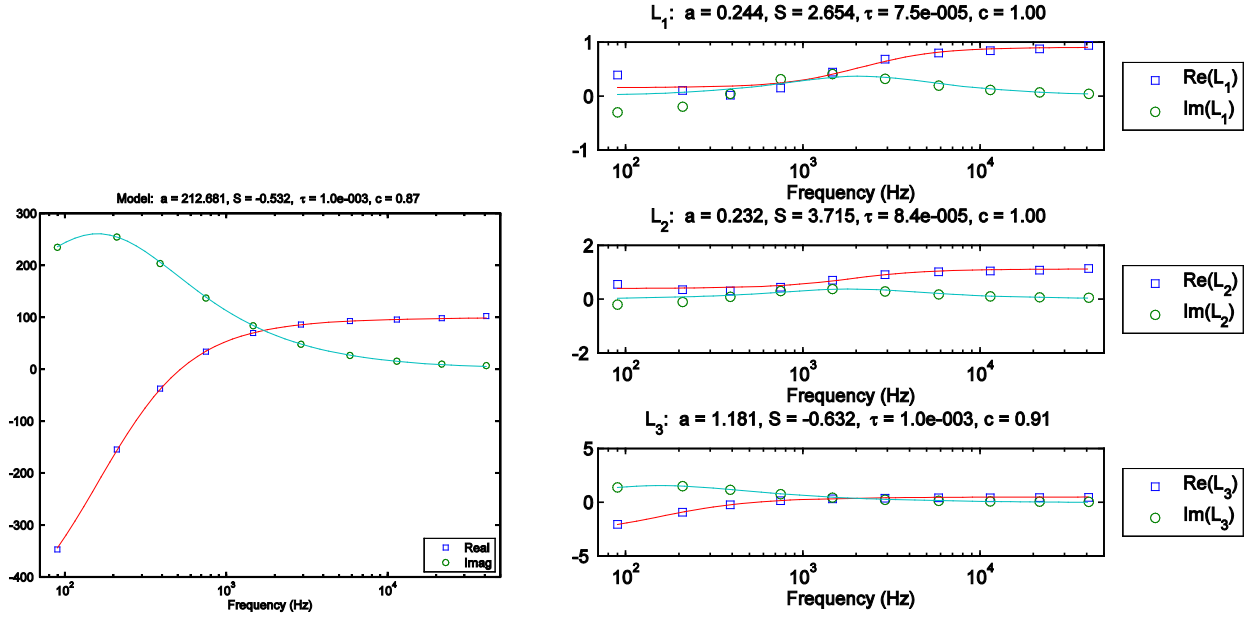


(b) Plan view comparison of data before and after background soil correction procedure

Figure 2.5. Demonstration of soil removal technique applied to Geophex GEM3 Frequency domain data. Excavation of this anomaly (Cell 40) uncovered a 37 mm mortar.

After removing the effect of the background geology with the VRM soil model, the corrected data are inverted for the location, orientation and principle polarizabilities of a buried metallic object. There are only four inversions out of 59 where the depth error exceeds 0.10 m. The amplitude of the signal is weak for all four poor predictions. Three of these correspond to the deepest targets. The estimated principle

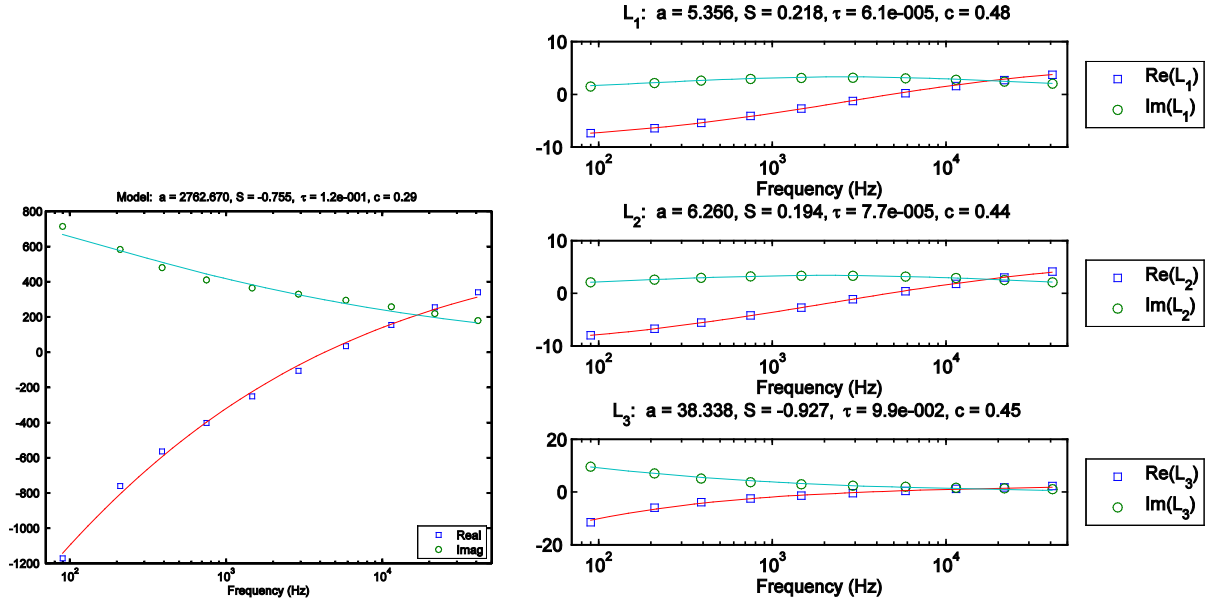
polarizabilities were fit with a four-parameter model (equation 2.6) using a least squares optimization algorithm. Figure 2.6 shows the result of the fitting procedure applied to the data of Figure 2.4, which were acquired over a 0.50 cal bullet. The components of the polarizability amplitude parameter is represented by the variable a , instead of k , and have values of 1.18, 0.23, 0.18. A large primary polarizability and two smaller and approximately equal secondary polarizabilities suggest a rod-like object. The results of the same inversion process applied to the data in Figure 2.5, is plotted in Figure 2.7.



(a) Data fit of a sounding at center of the template.

(b) Result of fitting parameterization of Equation 2.6 to the principle polarizabilities

Figure 2.6. Data fit (left) and fitting recovered polarizabilities with Equation 2.6 (right) for cell 29, which contains a 0.50 cal.



(a) Data fit of a sounding at center of the template.

(b) Result of fitting parameterization of Equation 2.6 to the principle polarizabilities

Figure 2.7. Data fit (left) and fitting recovered polarizabilities with equation 2.6 (right) for cell 40, which contains 37 mm projectile.

The parameters derived for 0.50 cal bullet, 20 mm projectile, and 37 mm projectile anomalies are shown in four lower panels of Fig. 2.8. The four panels plot the amplitude k , offset s , time constant τ and exponent c of both the axial and transverse components of the principle polarizabilities. The endpoints of the vertical line on the plots are defined by the minimum and maximum parameters related to the transverse polarizability. Therefore, an axisymmetric rod-like target would be plotted as a single point since the transverse polarizabilities should be equal. Figure 2.8(a) shows that 37 mm projectiles separate well from the 20 mm projectiles and 50 caliber bullets based on the axial and transverse parameters for the amplitude of the polarization. However, there is little separation between the feature clusters of the 20 mm and 0.50 cal targets. Figure 2.8(c) show that there is also good separation in the time constant τ between the 37 mm and the other targets, with the exception of one of the 0.50 cal anomalies. The discrimination goal of finding 37 mm amongst less harmful smaller munitions is achieved with the amplitude parameter and, to a lesser extent, the time constant parameter τ .

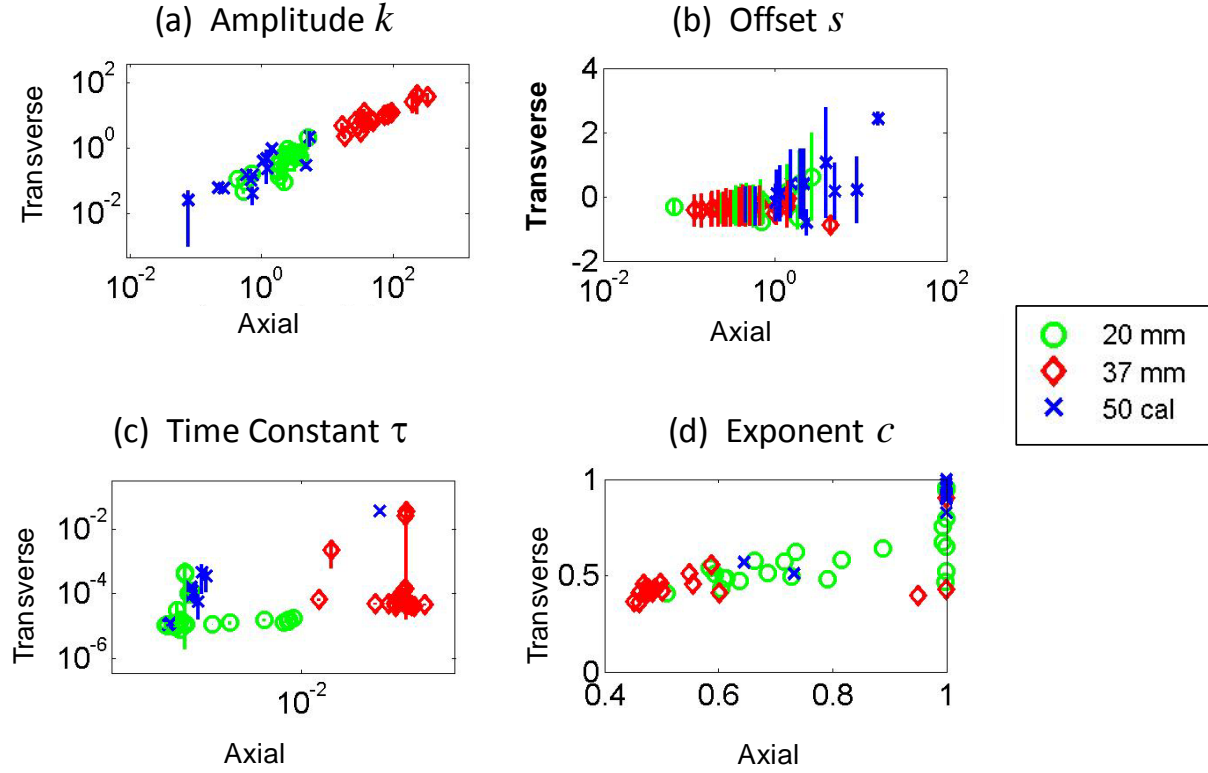


Figure 2.8. A comparison of different model parameters from Equation 2.6 when inverting GEM3 data collected at the FLBGR 20 mm range fan. For the transverse axis, the symbol represents the average of the parameters related to the two secondary polarizabilities and the endpoints of the line indicate the maximum and minimum values of that parameter.

Figure 2.9 compares the effectiveness of the background removal method with results from an earlier study. In the earlier study, the real and imaginary components of the background signal were estimated at each frequency by fitting a low order surface based on all peripheral soundings (right panel). Therefore, the earlier study (1) did not include a step to determine if a sounding was suitable for estimating the soil response, and (2) did not take advantage of the characteristic response of VRM soils (i.e. constant imaginary component that equals the slope of the log-linear real component of the signal). Figure 2.9(a) and (b) plot the amplitude factor k for the new method and earlier method, respectively. The new method shows improved separation of the recovered parameters between the 37 mm projectiles and the other ordnance. In addition, the recovered parameters for the 20 mm projectiles more consistently suggest a rod-like target when using the new method than when the older method is used. By using the soil model to identify soil and propagate its properties in frequency, we achieve a tighter clustering effect of key discriminating parameters, a clearer separation of the 37 mm projectile, and find fewer outliers that could cause ordnance to be incorrectly labeled.

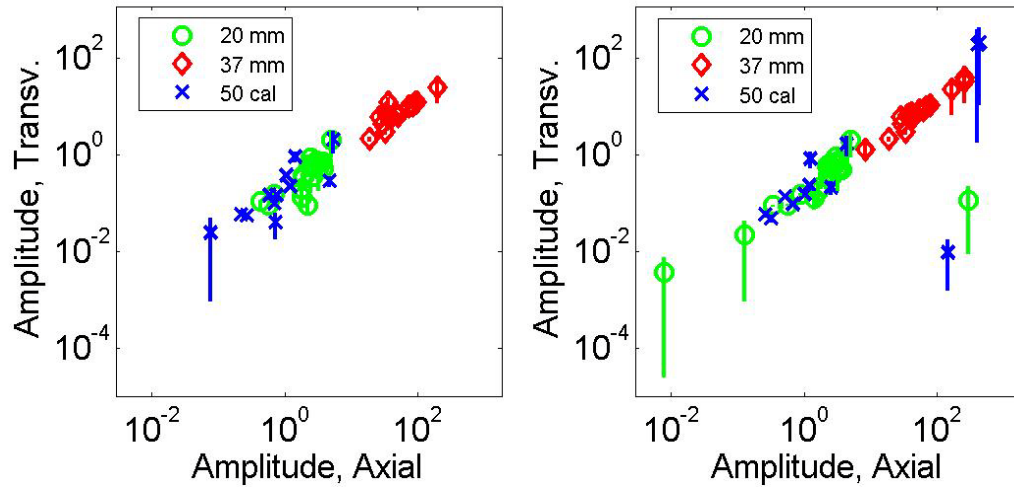


Figure 2.9. A comparison of different model parameters from Equation 2.6 when applied to data corrected using a background soil model, and data corrected by subtracting a low order surface at each frequency.

Application to Former Camp Sibert Geophysical Prove Out GEM3 data

The Former Camp Sibert was the site of the ESTCP Pilot Discrimination Project. The discrimination objective was to identify 4.2 inch mortars from partial mortars. As part of the demonstration, Geophex GEM3 frequency-domain sensor data were acquired on the Geophysical prove-out. Initial analysis by the Program Office on these data suggested that the background soil levels would be too high to perform reliable discrimination on the remainder of the site. In the previous example we showed that the soil response removal technique applied to data collected at FLBGR resulted in sufficient cluster class separation to distinguish between the 37 mm projectiles and the smaller ordnance. Although the target of interest at Camp Sibert is much larger than a 37 mm, the soil response at Camp Sibert GPO is much greater than the soil response at FLBGR. The objective of this analysis was to determine if modeling the background response would be able to improve discrimination at Camp Sibert.

To ensure accurate positioning and increase signal to noise ratio, the data were acquired in a cued (static) mode using a template (Figure 2.10). The template has 29 measurement locations, consisting of a 5x5 uniform grid of points covering a 1 m square region which is surrounded by 4 additional soundings. The four additional soundings were intended to be taken far enough away from the target such that they could be used to characterize the background response.

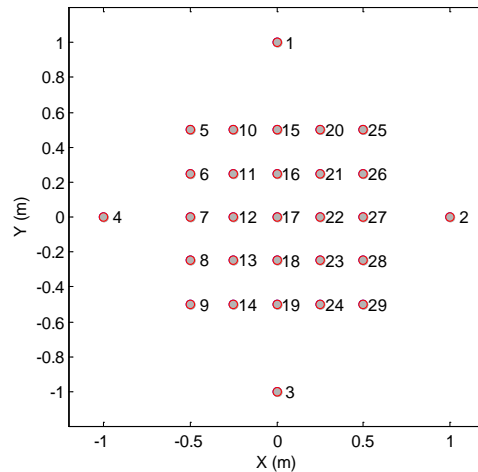


Figure 2.10. Cued pattern for collecting GEM3 data at the Camp Sibert GPO.

Images of gridded Sibert GPO GEM3 data for the 90Hz frequency are plotted in Figure 2.11 (top row). The GEM3 image was created by using the outer four background measurements for gridding. It is clear that the background VRM signal increases from South to North. For comparison, a gridded image of the first time channel of Geonics EM63 data is shown in the bottom left panel of Figure 2.11. As expected, the imaginary component and the time domain signal follow the same spatial pattern. The similar spatial characteristic is because, in the resistive limit, the magnitude of the

time domain response is directly proportional to imaginary part of the frequency domain signal (for example Li et al. 2010).

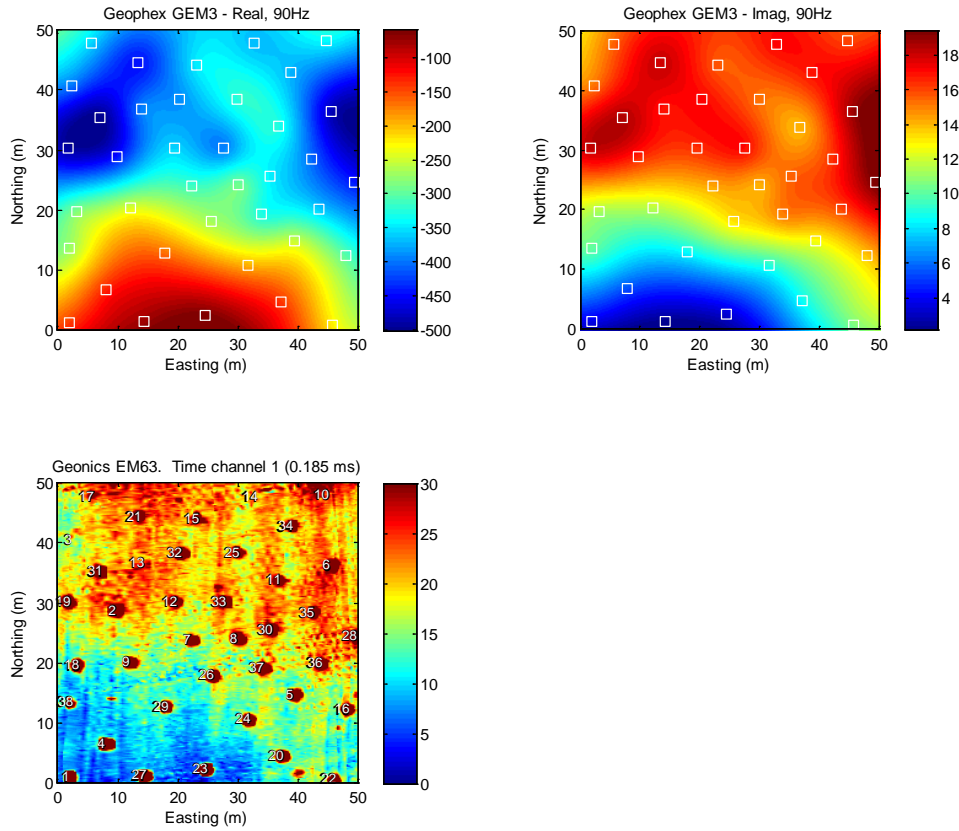
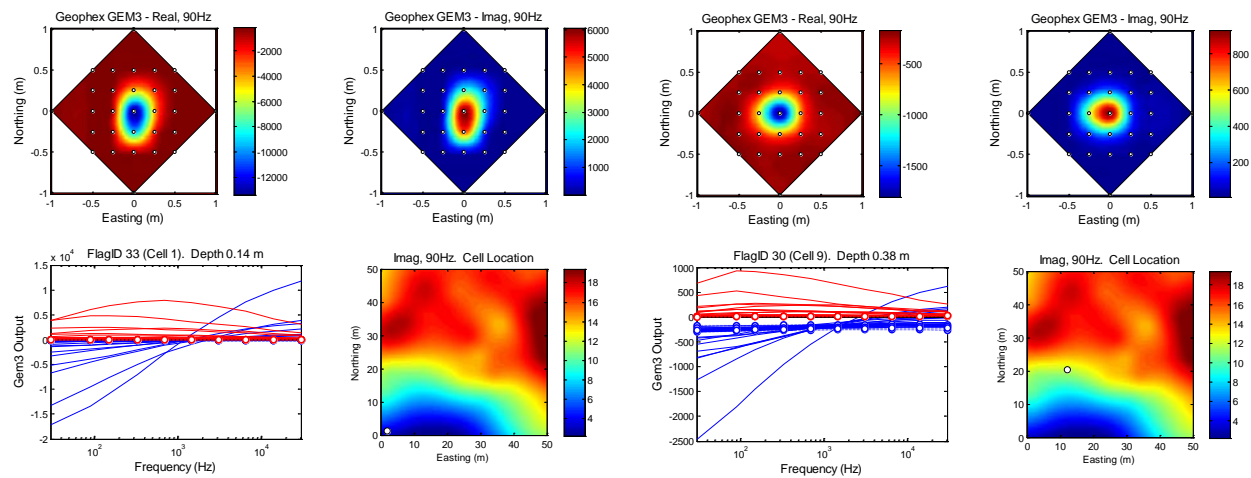


Figure 2.11. Example of EMI data collected on the Camp Sibert GPO. The top two grids show the real and imaginary part of the secondary field at 90 Hz. The bottom left image is of the first time channel of Geonics EM63 time domain data.

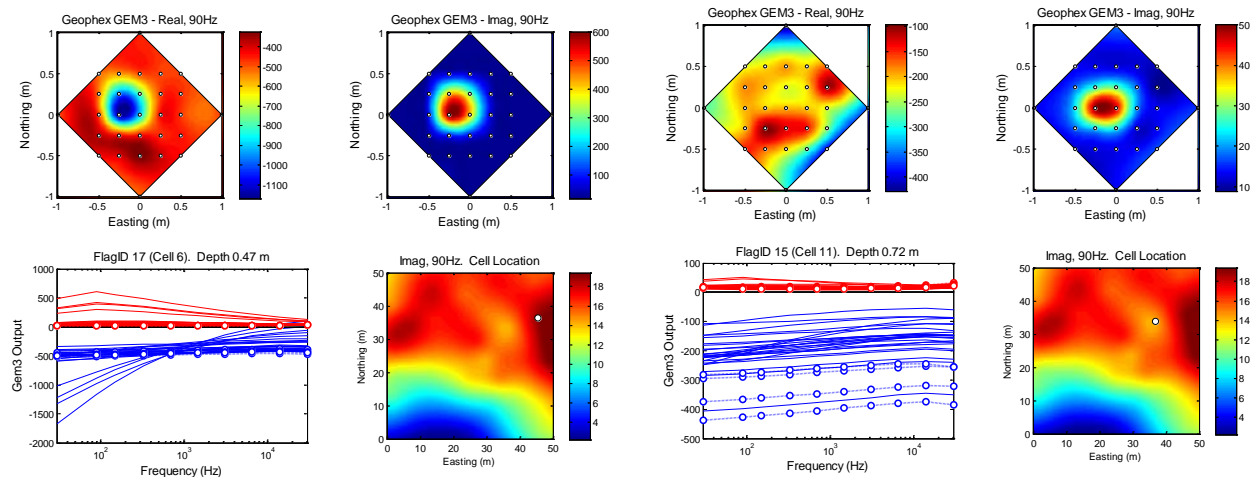
To get a sense of the range of the VRM response across the site, data over four of the anomalies in the GPO are plotted in Figure 2.12. For each anomaly (i.e. Figures 2.12(a)-(d)) there are four plots: the top pair of plot contain a gridded image of the real and imaginary components of the measured data at 90 Hz, the bottom left panel plots all the soundings as a function of frequency on the same axis, and the bottom right panel plots a plan view of the imaginary data at 90Hz with a white circle to indicate where on the grid the GEM3 data were acquired. In the frequency sounding plots, the soundings recorded at the 4 outer locations are plotted using a dotted line and circular symbols, and sounding measured within the 5x5 uniform grid are plotted with solid lines. Figure 2.12(a) plots an anomaly in the Southwest corner of the GPO, where there is a lower level of VRM response. As you move further North and East the amount of soil signal increases. The increased soil signal is most clearly seen in the increased offset in the real component of the data indicated by the dotted blue lines.

Figure 2.12 (d) contains plots of data over a target at a depth of 72 cm and acquired in an area of higher VRM noise. Due to the depth of the target, the anomaly is quite weak, and we see that there is not a very well defined anomaly in the real component of the data. The reason for the poorly defined anomaly can be attributed to the variation in instrument clearance height. When seeding a site with target, the dirt used to cover the target can settle with time which then leaves a depression on the ground. Since data are acquired on a board placed above the depression, the distance between the sensor and the ground will be greatest at the center of the template. Thus, we would expect the ground response to be largest at the edge of the template and smallest at the center of the template. Figure 2.13 plots data acquired over targets with depth greater than 1 m, and thus too deep to be detected by the GEM3 sensor. The plots of soundings as a function of frequency (lower left), all show the characteristic VRM response for frequency domain data. For each of the three examples in Figure 2.13, the signal magnitude is lowest at the center of the template where the greatest ground clearance height would be found, and the largest magnitude sounding is generally found on the edge of the template. Since we will be using soundings on the edge the anomaly to estimate the soil properties - i.e. estimate the functions $A(x,y)$ and $B(x,y)$ - we expect that we will be over estimating the background response when removing it from the data.



(a) Example of data collected in region with lower χ

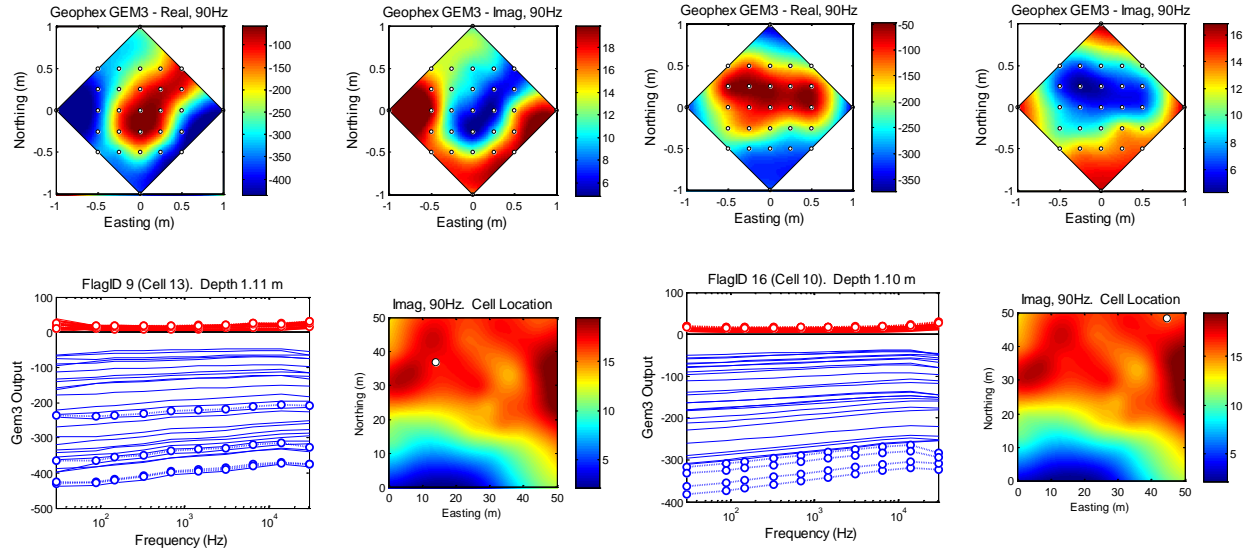
(b) Example of data collected in region with lower χ



(c) Example of data collected in region with higher χ

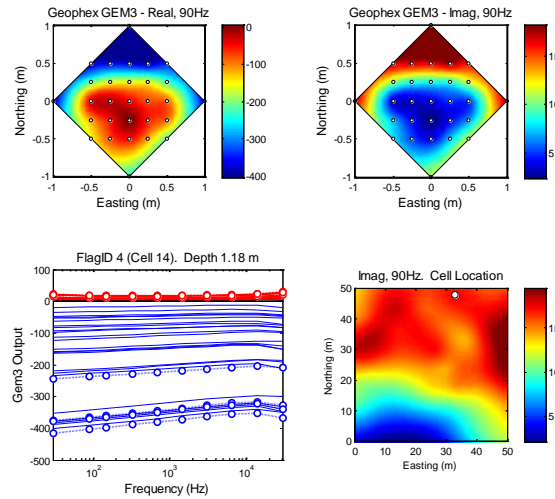
(d) Example of data collected in region with higher χ

Figure 2.12. Example of data collected in areas of the GPO. The presence of VRM soil results in a small offset in the imaginary or quadrature part of the data (red lines) and a large negative offset in the real (or in-phase) part of the data (blue lines).



(a) Cell 13. Depth = 1.11 m

(b) Cell 13. Depth = 1.10 m



(a) Cell 14. Depth = 1.15 m

Figure 2.13. Examples of Geophex GEM3 data acquired over targets buried at a depth greater than 1 m. The location of the data in the GPO is indicated by a white circle on the gridded data. At depths greater than 1 m the Geophex GEM3 is unable to sense the target, and is only sensitive to the soil. Plots of the individual soundings (real component in blue and imaginary component in red) possess the characteristics of viscous remnant magnetized soil.

The Sibert Geophex GEM3 data were processed in the same manner as the FLBGR data of the previous section. Figure 2.14 contain the resulting feature space plots. For the FLBGR example we found that the amplitude k provided the best separation between the cluster classes. For the Sibert data, the intact and partial 4.2 inch mortars cluster classes are not well separated when plotting the amplitude parameter

(Figure 2.14(a)). However, there is a very clear separation in the axial time constant τ . With the exception of a pair of outliers, there is relatively good separation in the offset s parameter. From the GPO analysis, we believe that discrimination performance at Camp Sibert could have been achieved by using GEM3 frequency domain data. We note that, based on analysis of time domain data across the entire site, that the VRM noise were largest on the GPO, and thus GPO performance of the GEM3 processing represent the base level performance for the entire site.

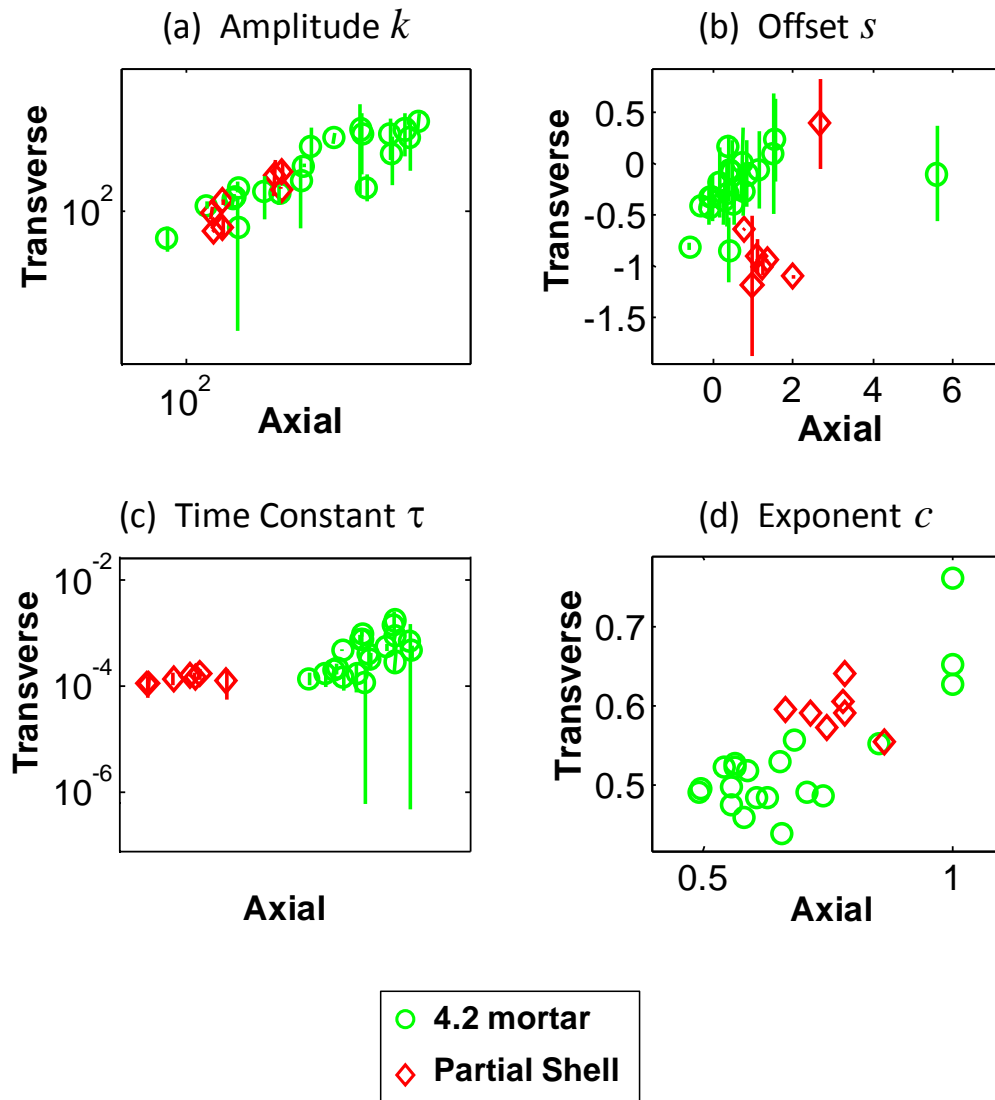


Figure 2.14. Feature space plots when processing the Camp Sibert GEM3 data. For the Sibert data, the intact and partial 4.2 inch mortars cluster classes based on the amplitude k do not have same clear separation as for the FLBGR case. However, there is a very clear separation in the axial time constant τ that would allow for reliable discrimination between the 4.2 inch mortars and partial shells.

METHOD TWO: SIMULTANEOUS INVERSION SOLUTION

This method involves estimating both the soil parameters and target parameters simultaneously from the data. The target parameters we wish to estimate is:

$$\mathbf{m}_{target} = [x, y, z, \theta, \phi, \varphi, \mathbf{p}_1, \mathbf{p}_2, \mathbf{p}_3] \quad (2.7)$$

where the target location is (x, y, z) , the orientation is defined by the angles (θ, ϕ, φ) , and the principle polarizabilities are defined by $\mathbf{p}_1, \mathbf{p}_2$, and \mathbf{p}_3 . For this example we assume that the background soil properties vary spatially as a plane: $G(x, y) = ax + by + c$. The soil parameters in this case are

$$\mathbf{m}_{soil} = [a, b, c] \quad (2.8)$$

The inverse problem for \mathbf{m}_{target} and \mathbf{m}_{soil} is cast as an optimization problem:

$$\text{Minimize } \phi(\mathbf{m}) = \frac{1}{2} \|V_d^{-1/2} (\mathbf{d} - F[\mathbf{m}_{target}] - F[\mathbf{m}_{soil}])\|^2 \text{ subject to } m_i^L \leq m_i \leq m_i^U \quad (2.9)$$

where V_d is the data covariance matrix, m^L and m^U are the lower and upper constraints, respectively. Since a non-linear optimization problem is solved, a good starting guess of the soil and target parameters are essential for avoiding local minima. A starting guess for the soil model is obtained by first drawing a polygon (or circle) around the anomaly to identify soundings related to the target and soundings related to the soil only. The soil only soundings are then used to estimate a constant soil model $G(x, y) = c$. Parameters a and b in the soil model are initially set to zero. The starting guess for the dipole parameters are estimated by, first subtracting the response predicted by the initial guess of the soil model, and then using the background corrected data to invert for an initial guess of the dipole parameters.

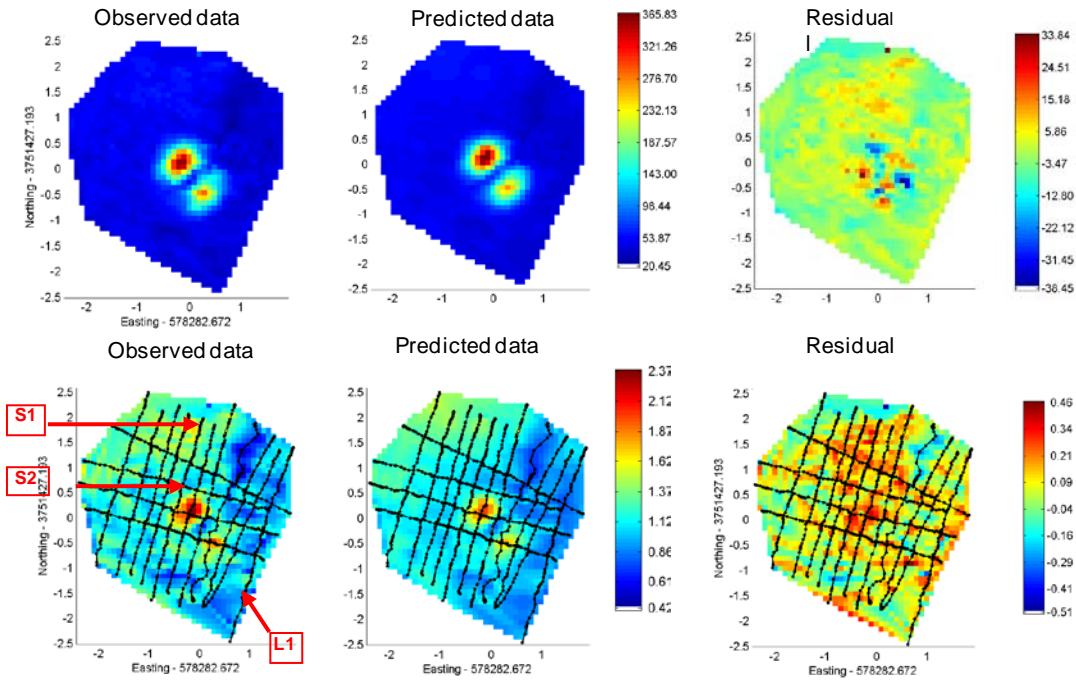
EXAMPLE: DYNAMIC, CUED INTERROGATION EM63 DATA FROM THE CAMP SIBERT GEOPHYSICAL PROVEOUT

Figure 2.15 demonstrates the simultaneous inversion using Geonics EM63 data acquired over a wrench at Camp Sibert, AL (Figure 2.1). For this example we parameterize the dipole model as

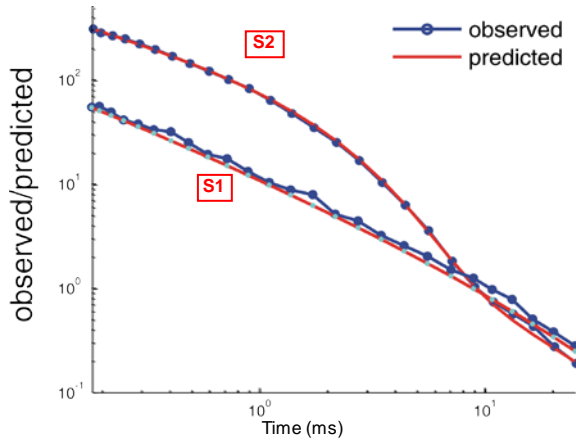
$$\mathbf{m}_{target} = [x, y, z, \theta, \phi, \varphi, k_1, \beta_1, \gamma_1, k_2, \beta_2, \gamma_2, k_3, \beta_3, \gamma_3] \quad (2.10)$$

Figure 2.15(a) compares the observed and predicted data during the first and twentieth time channel. In the grid of the predicted data we see that both the soil response and the response from the wrench are modeled very well. Figure 2.15(b) compares observed and predicted soundings at a location away from the target anomaly (S1) and directly over the target (S2). The approximately $f(t)=1/t$ decay that characterizes the step-off response for viscous remnant magnetic (VRM) soils is clearly seen in sounding S1. In sounding S2, we see that at early times the decay characteristics are dominated by the wrench. At late times, the signal is dominated by

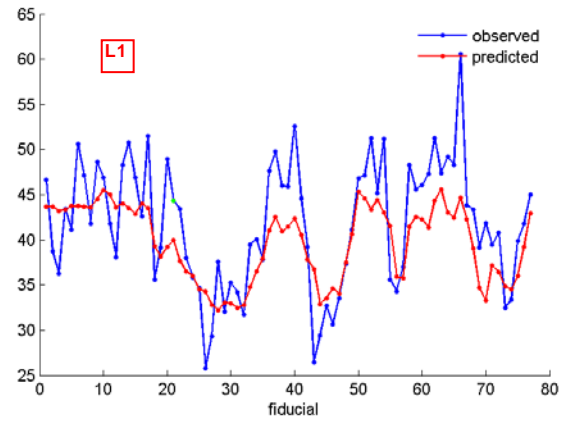
the VRM soil response. Figure 2.15(c) compares the first time channel of observed and predicted data along the eastern-most line of data.



(a) Plan view comparison of data fit (time channel 1)



(b) Comparison of a pair of soundings



(c) Data fit comparison along a line during first time channel

Figure 2.15. Simultaneous fitting example. The data from Figure 2.1 is inverted for dipole parameters and background soil model simultaneously. The background soil model is $G(x,y)=ax+by+c$. The top set of plots in (a) are for the first time channel, and the results for the 20th time channel are plotted in the lower set of plots. (b) Observed and predicted soundings are plotted at a couple of locations in the grid. (c) Comparison of observed and predicted data in the first time channel.

Figure 2.16 plots the polarizations recovered from the inversion process. The black lines are the polarizations obtained from controlled lab measurements using the TEMTADS time domain sensor. Simultaneous inversions were carried out assuming an axial symmetric target (i.e. 2 polarizabilities constrained to be equal, red lines) and without symmetry assumptions (i.e. 3 polarizabilities, blue lines). We see that the polarizations estimated by simultaneously inverting the data for both the dipole parameters and soil parameters can accurately recover the parameters when assuming an axial symmetric target. The data recovered polarizabilities when assuming 3 unique polarizabilities does a good job of recovering the primary polarizability. However, the data did not constrain one of the secondary polarizabilities to be equal to the polarizabilities obtained from the lab measurements.

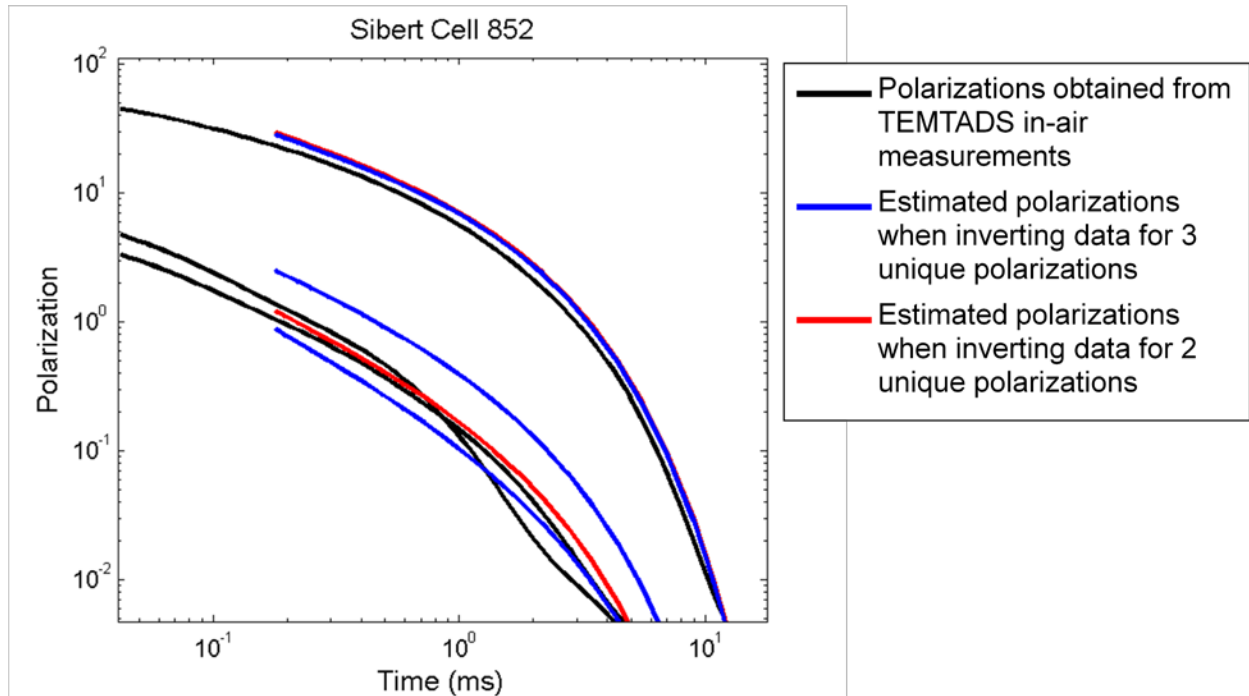


Figure 2.16. Comparison of polarizabilities recovered using simultaneous inversion of background and dipole parameters with polarizabilities derived using TEMTADS in-air measurements. The data were inverted assuming axial symmetry (2 unique polarizabilities) and without any assumptions on symmetry (3 unique polarizabilities). For the 3 polarizability case, the primary polarizability is well constrained, but there is a difference in magnitude in one of the two secondary polarizabilities.

EXAMPLE: DYNAMIC EM63 DATA FROM THE CAMP SIBERT GEOPHYSICAL PROVEOUT

In the first year annual report, we tested the simultaneous inversion method using dynamically collected, full coverage Geonics EM63 data acquired at the Camp Sibert GPO. We direct readers to Appendix 1, which contains a copy of the annual report for details.

SIMULATIONS FOR DETERMINING THE EFFECTIVENESS OF SIMULTANEOUS ESTIMATION OF TARGET AND BACKGROUND

Simulations were used to determine the improvements of inverting data while taking into account the background response. In this section, we compare results of inverting synthetic data from three target types (1) a 37 mm projectile at a depth of 20 cm, (2) a 60 mm mortar at a depth of 40 cm, and (3) an 81 mm mortar at a depth of 40 cm. For each target 200 anomalies were generated, with the orientation of the targets randomly chosen. In order to have realistic IMU and GPS data, we used the IMU and GPS recordings from the Geonics EM63 data acquisition at Camp Sibert. A Gaussian error with a standard deviation of 1 degree and 1 cm was applied to the IMU and GPS data, respectively. Figure 2.17(a) contains data synthetically generated for 60 mm mortar data when buried at a depth of 40 cm in a host with a 30 mV background response.

Two different magnitudes of magnetic soil noise are added to the data. In the first set of simulations, a magnetic soil noise with a mean magnitude of 15 mV in the first time channel is added. The magnetic soil signal follows the $1/t$ decay over the 26 EM63 time channels. A magnetic soil noise with a mean magnitude of 30 mV was used in the second set of simulations. The 30 mV level of noise is representative of the noisiest magnetic geology conditions at Camp Sibert. For these simulations we assumed that the magnetic properties of the soil were spatially uniform. Of course, the simulated data due to the magnetic properties will not be uniform due to the movement of the sensor relative to the magnetic ground. In addition to magnetic soil noise, sensor noise characteristic to the EM63 was added to the simulated data. The sensor noise is proportional to $1/\sqrt{t}$.

Three processing techniques are compared:

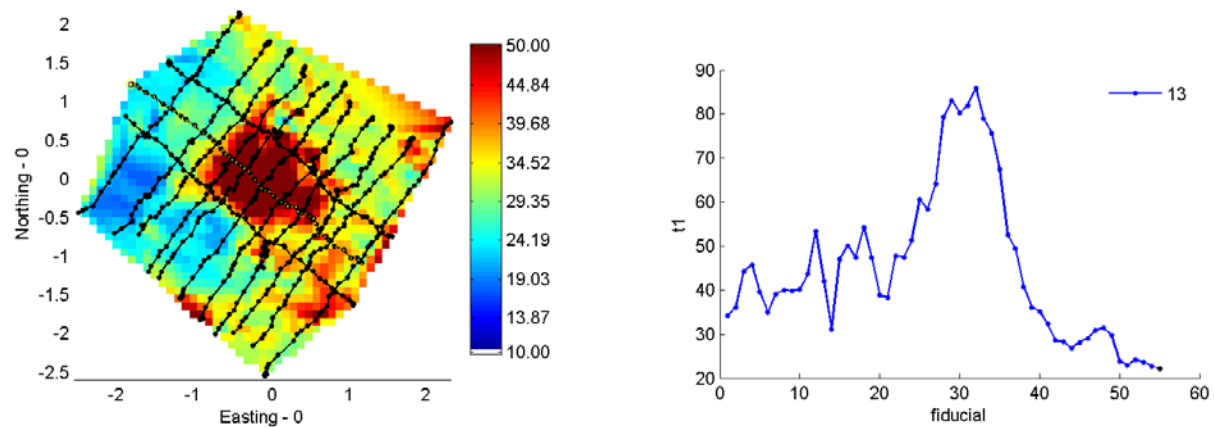
1. Application of a de-median filter on each time channel, followed by inversion for recovered parameters
2. Fitting a soil model to the data surrounding the anomaly, then subtracting the soil response from the measured data. The background corrected data were then inverted.
3. Simultaneous estimation of a soil model and dipole parameters. Unfiltered data is inverted.

A soil model of $G(x,y) = ax+by+c$ is assumed. Figure 2.17 compares 60 mm mortar data when buried in a host with a 30 mV background response. The different plots are: (a)

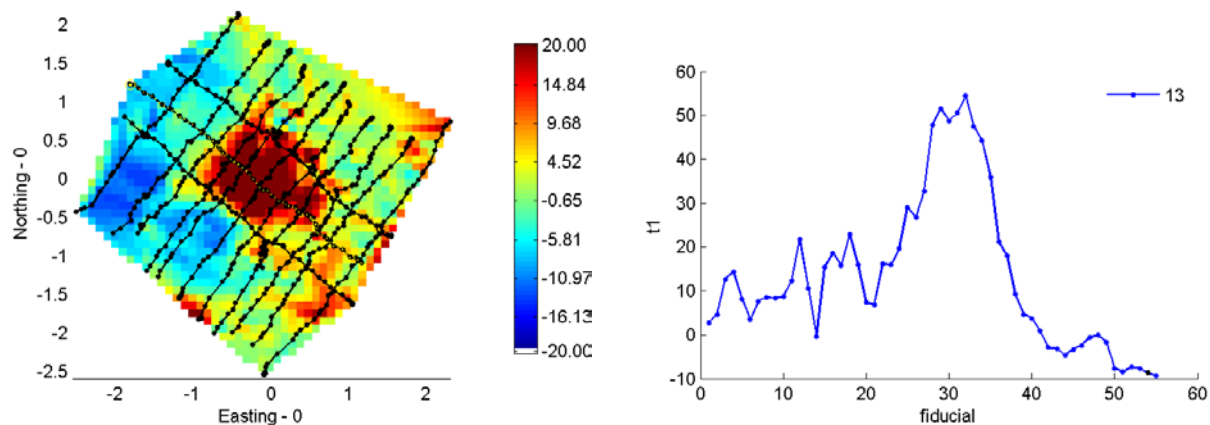
unfiltered data with (b) the data filtered using a de-median filter and (c) the data with a background response removed by solving for a soil model. We see in Figure 2.17(c) that, in addition to having lower magnitude of noise, that the background response has less spatially correlated structure in the data. This is important, because correlated noise tends to bias solutions to inverse problems that use an L2-norm (which is assumed when solving for least squares solutions).

Figure 2.18 plots the recovered polarizations for the 60 mm mortars buried in a host with a background response of 30 mV. Figure 2.18(a) shows the result of inverting the de-median filtered data. In the top panels, the green and black dotted lines indicate the polarizations of the 60 mm mortar that were used to generate the synthetic data. There is a spread in the recovered polarizations, with the inversions more accurately recovering the primary polarization $L_1(t)$ than the secondary polarizations $L_2(t)$ and $L_3(t)$. A measure of the spread in recovered polarizations is found in the lower panels of Figure 2.18(a). The standard deviation of the recovered polarizations divided by the true polarization is calculated at each time channel and plotted. Although the primary polarization does have some spread in the recovered magnitudes, the decay characteristics are recovered well, and would provide a robust feature for discrimination.

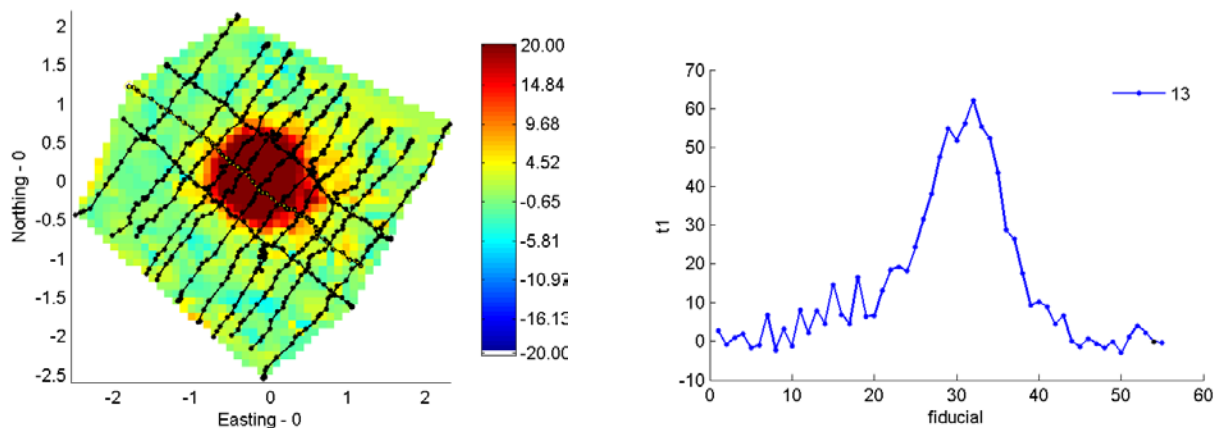
Figure 2.18(b) shows the result of inverting data where a soil model was estimated, then subtracted from the data. The upper panels clearly show an improvement in constraining the recovered polarizations is achieved by modeling the soil response. There is a decrease in the error both in the recovered primary and secondary polarizations. This improvement is quantified in the bottom panels of Figure 2.18(b). The standard deviation of the recovered polarizations is approximately 10 percent at early times. At late times the error increases due to decreasing signal-to-noise ratio of the data. The increasing error is particularly evident in the secondary polarizations since the secondary polarizations contribute much less to the total signal at late times.



(a) Unfiltered data

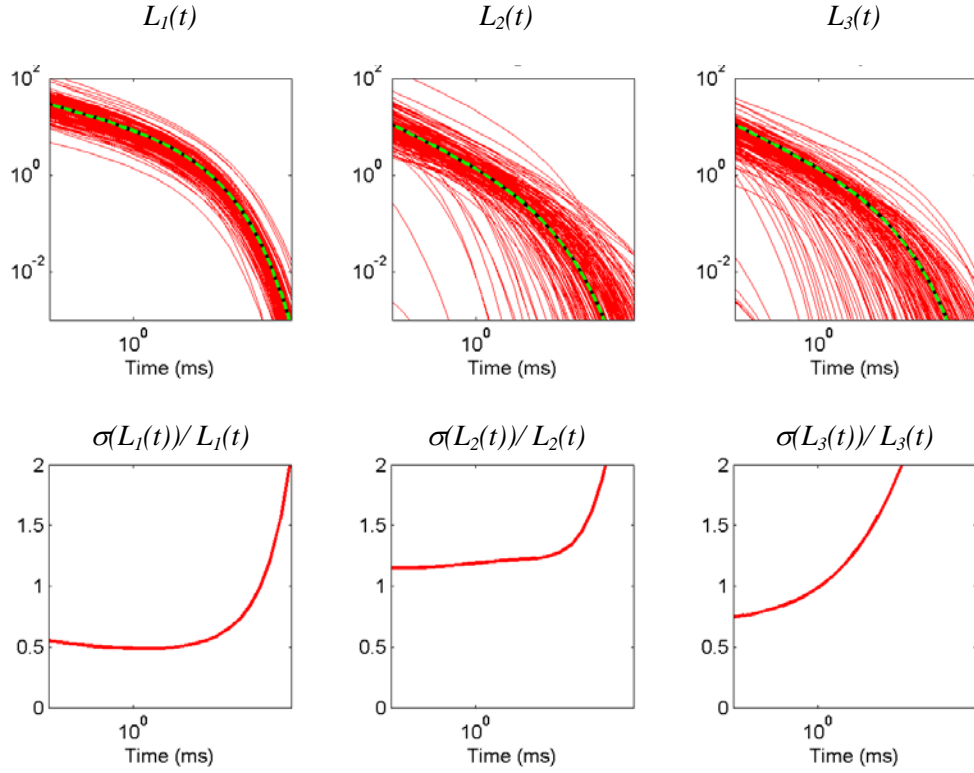


(b) Median removed

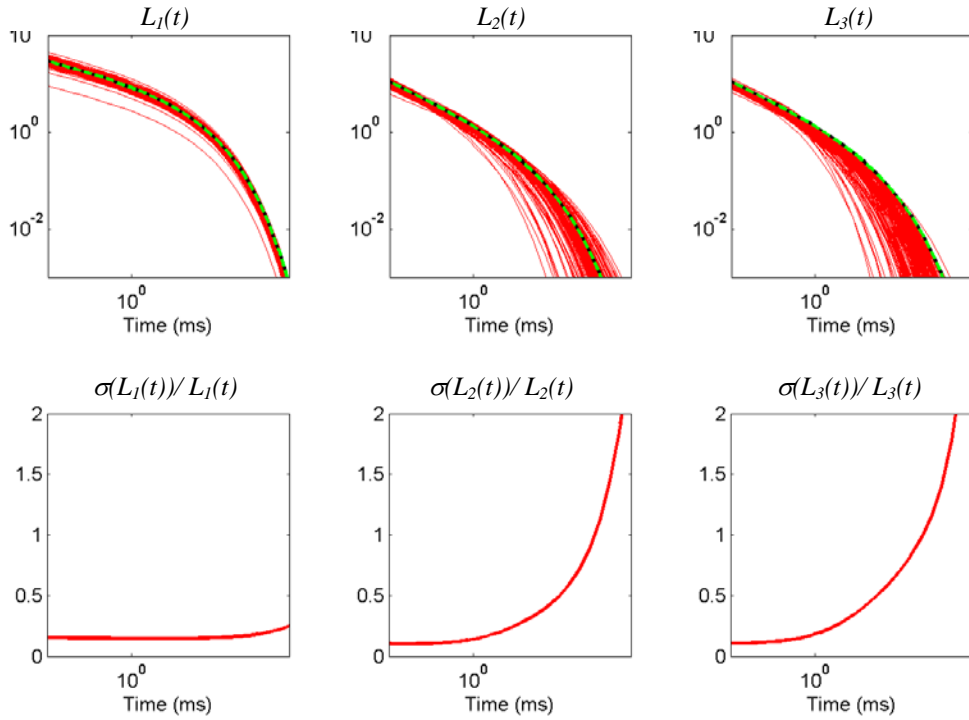


(c) Soil model $G(x,y)$ estimated, then soil response subtracted

Figure 2.17. Examples of synthetic 60 mm mortar data. For this example the 60 mm mortar was buried at a depth of 40 cm, and pointed 20 degrees from North and 56 degrees from vertical. The first time channel is shown here. The data profiles are taken along the middle line of the three East-West lines. The data filtered by estimating a soil model (c) has less correlated noise in the data.



(a) Recovered polarizabilities when applying a median filter on the data



(b) Recovered polarizabilities when fitting a soil model

Figure 2.18. A comparison of recovered polarizabilities for the 60 mm mortar buried in a host with a background response of 30 mV in the first time channel.

DEFINING METRICS FOR COMPARING DISCRIMINATION PERFORMANCE

Discrimination is the process of determining, for each anomaly in the target list, the likelihood that the anomaly was due to a UXO. The objective is to minimize the number of unnecessary excavations. UXO discrimination is achieved by extracting parameters from geophysical data that reflect characteristics of the target that generated the measured signal. These parameters come in two forms: (1) data-based parameters that are directly inferred from the data, such as amplitude and energy and (2) model-based parameters that are variables of a mathematical forward model (such as the dipole model) that can reproduce the data. Data and model based parameters can then be used as input to statistical classification methods (such as support vector machines and neural networks) to determine the likelihood that the target is a UXO. The parameters are related to the physical properties of an object and we refer to them as physics-based forward models. The recovered polarization tensor components plotted in Figure 2.16 are examples of model based parameters.

Discrimination features are graphically presented in feature space plots. Figure 2.19 gives an example of features plotted based on dipole parameters estimated from Camp Sibert Geonics EM63 data. The discrimination problem at this Camp Sibert site involved identifying buried 4.2 inch mortars. The top plot compares the integrated primary polarization (i.e. the integral of $L_1(t)$) to the integral of the secondary polarizations (i.e. $L_2(t)$ and $L_3(t)$). The clusters for the mortars and base plates fall below the $L_1(t) = L_2(t)$ since these targets are rod-like, axisymmetric ($L_1(t) > L_2(t) = L_3(t)$). The cluster for the partial mortars is centered above the line since those targets are plate-like, and thus the primary (or axial) polarization is the smallest. In the lower plot, the magnitude and decay of the primary polarization are plotted. Both pairs of features plotted in Figure 2.19 show good separation between the 4.2 inch mortars and the non-UXO clusters.

Effective discrimination performance was achieved at Camp Sibert due to the good separation of clusters of UXO and non-UXO. Clearly the type of clutter and targets present at a site affect discrimination success. For example, if there are large scrap items and ordnance of a similar size, such that the measured data between the large scrap items and ordnance are nearly the same, then we would expect discrimination would be difficult to achieve. In addition the data acquired at Camp Sibert was of very high quality, and thus the variance in the class cluster was small relative to the distance between clusters.

To summarize, there are a number of factors affecting discrimination performance:

- The separation between targets of interest in feature space. Targets that are physically and electromagnetically similar will have cluster classes that are close together in feature space
- The ability to constrain parameters, i.e. the cluster class variance. As the quality of the data decreases, the ability to accurately recover parameters

decreases. Data quality factors include positional accuracy, spatial coverage of the measured signal, ability to remove noise due to geology, etc.

A meaningful measure of an algorithm's discrimination ability should reflect the cluster class separation and variance. Figure 2.20 contains examples of synthetically generated clusters with different levels of cluster separation.

We propose a simple method of comparing discrimination potential between a pair of data processing techniques. The method seeks to quantify the ability to distinguish between two targets as a function of different survey parameters (such as data noise, spatial coverage, etc.). First a pair of test targets is chosen. The discrimination problem becomes more difficult if the polarization curves for the pair of targets are similar. Once the test targets are chosen, they are used to forward model multiple data sets. We then invert each set of data for dipole model parameters. A set of feature vectors based on these parameters can then be formed. Each feature is shifted to be centered on the arithmetic mean of the two cluster centers and normalized by a single standard deviation estimated from the features of both classes. The normalized and shifted parameters are then projected onto a line that connects the center of the parameter clusters for the two targets. A parameter λ indicates where on the line the projected location occurs. The parameter λ is similar to the output of a classification algorithm, in the sense that λ is used to form a ranked list. The area under the curve (AUC) is then calculated

$$AUC = \int_0^1 TPF d(FPF) \quad (2.11)$$

where FPF is the false positive fraction and TPF is the true positive fraction. The AUC quantifies the ability correctly rank randomly chosen UXO and non-UXO anomalies. The ideal discrimination algorithm will have and $AUC = 1$.

This technique is demonstrated in Figure 2.20. In each of the four cases, clusters are generated using a Gaussian distribution with unit standard deviation in two dimensions. The distance between the red and blue clusters decrease from (a) to (d). In Figure 2.20(a), the left panels indicate there is good separation between parameter clusters. The center of each cluster is marked by a white circle. In the center panel, a histogram is generated by binning along the parameter λ . The feature vectors are sorted according to their λ values. The rightmost panel plots the ROC curve generated by "digging" according to the sorted λ values. The AUC of 1 reflects the good separation of the clusters and suggests that discrimination would be successful. In Figure 2.20(d), there is virtually no separation between the red and blue clusters. As a result the histograms of the two target types also overlap. The ROC curve nearly follows the unit slope line and the AUC is almost equal to 0.5. In this case, discrimination algorithms would be no more successful than flipping a coin. For a much more complete treatment on the interpretation of ROC curves applied to UXO discrimination, we direct the reader to [2] (Beran and Oldenburg 2008),

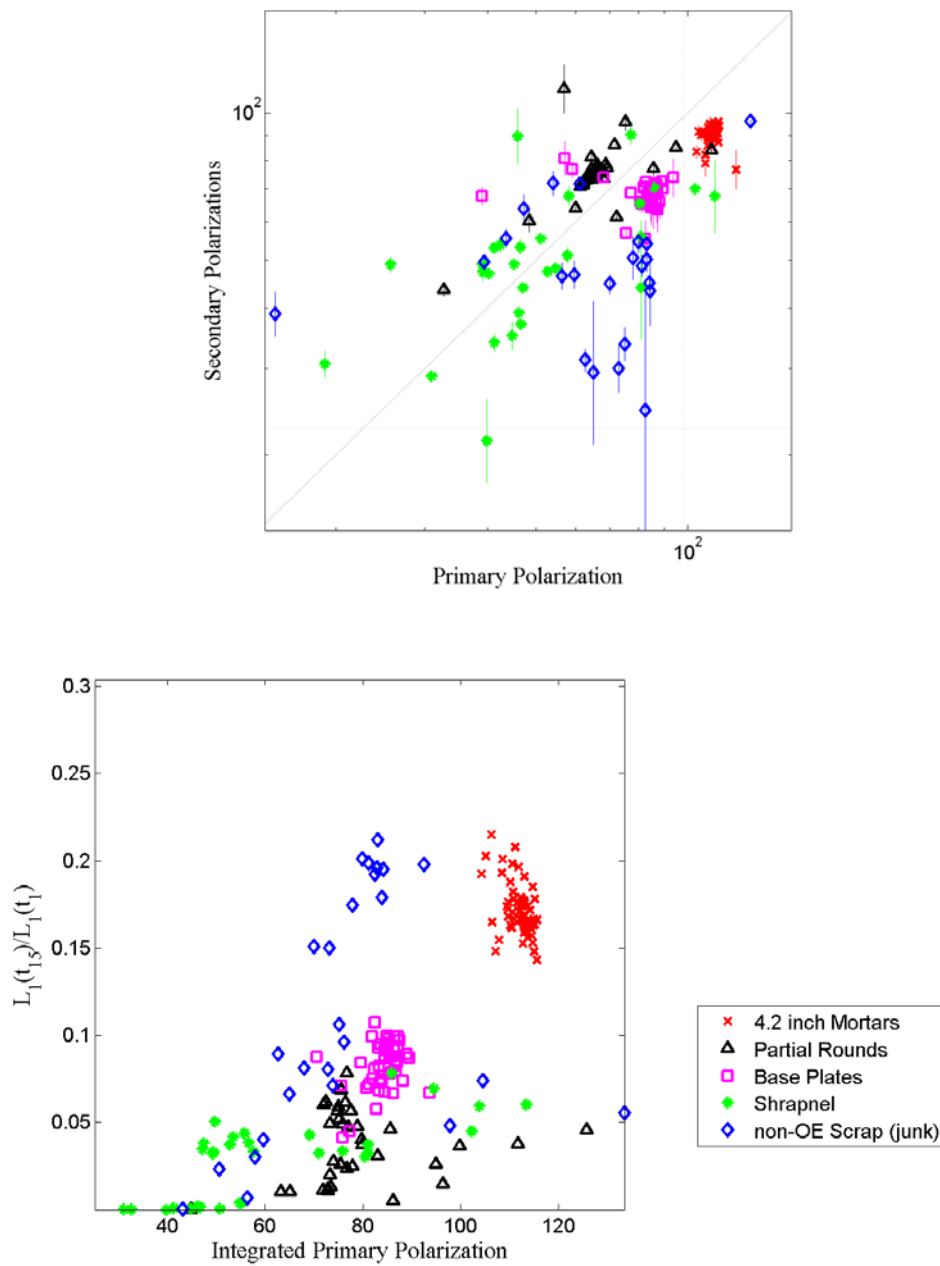


Figure 2.19. Feature space plots based on the inversion of Geonics EM63 data acquired at Camp Sibert.

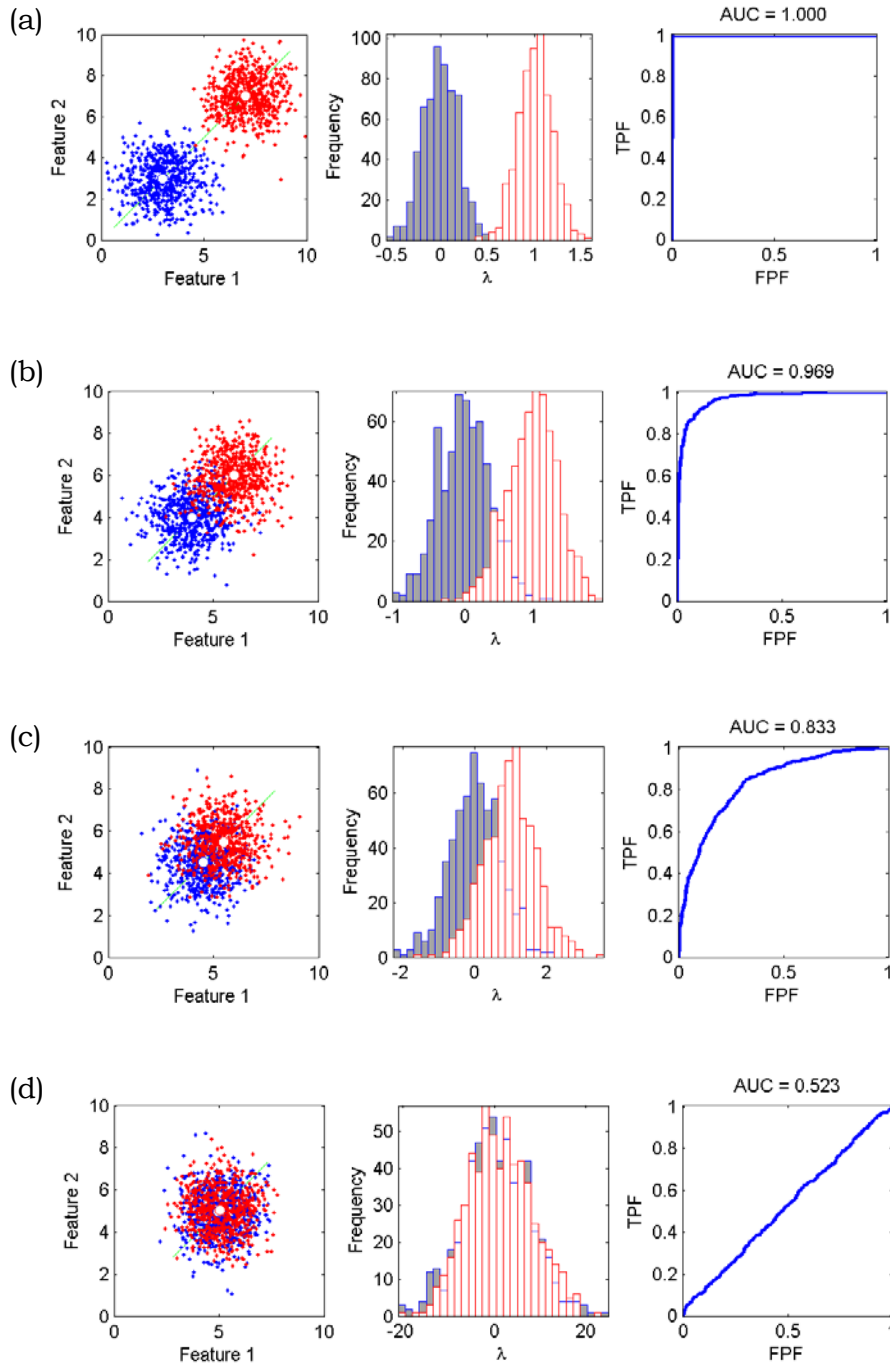


Figure 2.20. Synthetic examples of characterizing the separation of cluster classes using an ROC curve. Clusters are generated by generating Gaussian distributions with unit standard deviation. The separation between clusters decreases from (a) to (d). The panels on the left plot a pair of features for two different target types (red and blue). The middle panels are histograms when projecting the clusters onto a line that connects the true parameters of the two target types

Application of metrics to Geonics EM63 Simulations

Let us consider the following 3 features derived from the polarization tensor:

$$\text{Feature 1: } \text{int}(L1) = \int_{t_A}^{t_B} L_1(t) dt$$

$$\text{Feature 2: } \text{int}(L2) = \int_{t_A}^{t_B} L_2(t) dt \quad (2.12)$$

$$\text{Feature 3: } \text{int}(L3) = \int_{t_A}^{t_B} L_3(t) dt$$

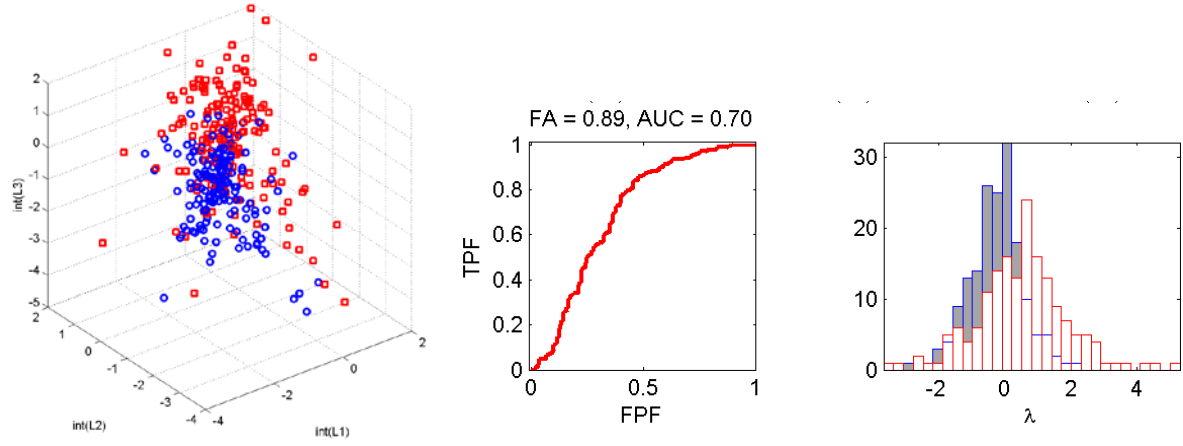
These features provide a measure of the magnitude of the 3 polarizations. Figure 2.21 compares the separation in clusters when using the different processing techniques for the case of 37 mm projectiles and 60 mm mortars buried in a host with 30 mV background response in the first time channel. The features in (2.11) define the feature space. Figure 2.21(a) summarizes the results when inverting data that were median filtered. For the median filtered data case there is substantial overlap between the 37 mm cluster (blue symbols) and 60 mm cluster (red symbols) (Figure 2.21(a) leftmost plot). The AUC for this method is 0.70 suggesting that there is only a 70 percent probability that you would correctly identify a 37 mm projectile from a 60 mm mortar.

Figure 2.21(b) summarizes the results when inverting data whose soil response was removed by fitting a soil model. By taking into account the variations in the soil response due to the movement of the sensor above the ground there is an improved separation between the 37 mm projectile and 60 mm mortar clusters. The AUC for this method is 0.98.

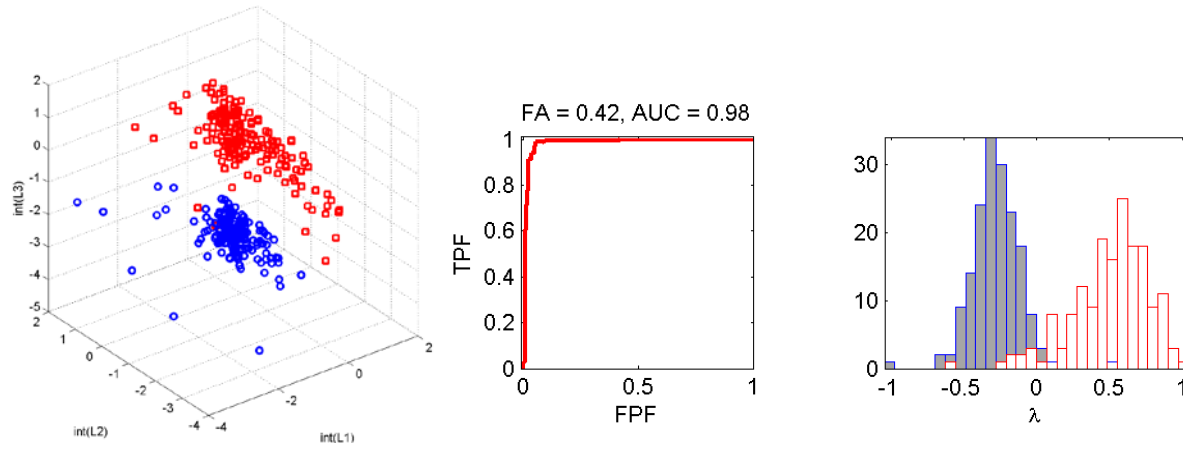
Figure 2.21(c) shows the results of simultaneously inverting the data for dipole parameters and soil model parameters. The separation between clusters is again improved. The AUC is 1.0, suggesting that discrimination would be very successful using these particular feature vectors.

Table 2.1 summarizes the AUC when trying to discrimination between a 37 mm and 60 mm mortar, as well as between a 60 mm and 81 mm mortar, when the targets are buried in a host with a background response of either 15 mV or 30 mV in the first time channel. Methods that include determining a soil model have superior performance relative to applying a de-median filter to each time channel.

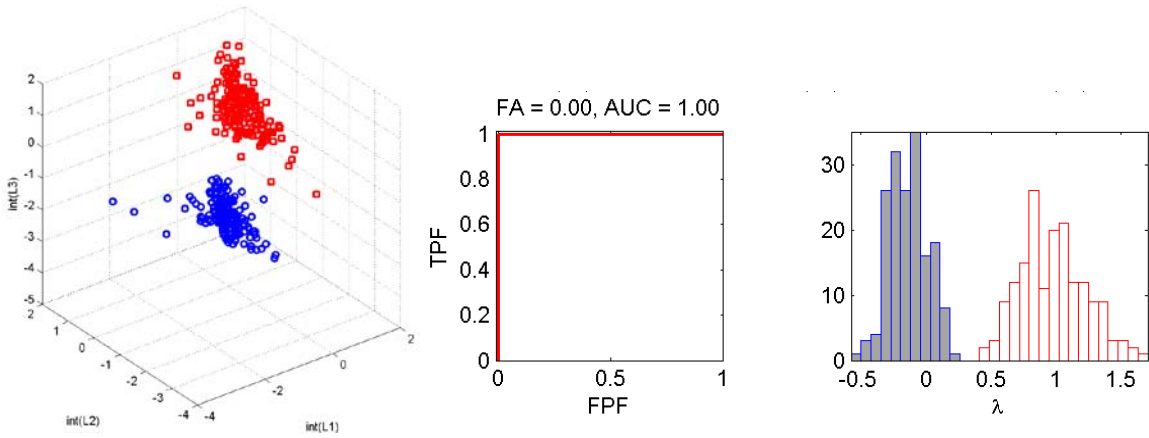
The last row of Table 2.1 summarizes the ability to correctly distinguish a 37 mm projectile and an 81 mortar when there is a background response of 30 mV. Recall that it was difficult to distinguish a 37 mm from a 60 mm mortar when the background response was 30 mV if a median filter was used. In this case, regardless



(a) Median filter applied to each time channel



(b) Filtering using a $G(x,y) = ax+by+c$



(c) Simultaneous inversion result

Figure 2.21. Comparison of processing data where there is a 30 mV background soil response. The blue cluster contains feature vectors from a 37 mm projectile. The red cluster contains feature vectors from 60 mm mortars.

of the processing method the two targets are very well separated in feature space. This is due to the two targets being sufficiently different that the spread in the cluster class due to soil noise is not large enough to cause an overlap in the two clusters.

Target 1	Target 2	Background in First time channel (mV)	Median Filter data	Area Under the Curve (AUC)	
				Method 1: Subtract soil, then invert	Method 2: Simultaneous Inversion
FLBGR 37 mm	ATC 60 mortar	15	0.84	1	1
ATC 60 mortar	ATC 81 mm mortar	15	0.99	1	1
FLBGR 37 mm	ATC 60 mortar	30	0.7	0.98	1
ATC 60 mortar	ATC 81 mm mortar	30	0.94	1	1
FLBGR 37 mm	ATC 81 mm mortar	30	1	1	1

Table 2.1. Summary of performance when inverting simulated data for a 37 mm projectile buried at 20 cm, a 60 mm mortar buried at 40 cm, and an 81 mm mortar buried at 40 cm.

SUMMARY

In this chapter, we presented results from applying two different processing techniques that incorporate the modeling of the geologic response. The first approach is a sequential approach, where the soil magnetic susceptibility is estimated, then the soil response calculated using the estimated magnetic susceptibility is subtracted. The second approach is a simultaneous inversion approach, where target and background soil parameters are simultaneously estimated from electromagnetic induction sensor data.

These inversion methods are demonstrated using both cued interrogation and dynamically acquired Geonics EM63 pulse induction sensor data and cued interrogation Geophex GEM3 frequency domain data collected at the FLBGR and the Former Camp Sibert. We showed that estimating the background response may improve our ability to classify UXO.

Simulations using Geonics EM63 data were also used to demonstrate the performance of the processing methods. We demonstrated a metric for determining if there are improvements to discrimination ability when applying processing methods that include a model for the soil. We proposed a method that quantifies the ability to distinguish between two targets. This method involves projecting feature vectors along a line that connects the true feature vectors for the two targets. A ROC curve is formed by sorting the feature vectors according to the location along the line. The AUC quantifies the ability to correctly distinguish a pair of targets. Using this metric

we showed that utilizing positioning information of the sensor to model the electromagnetic response of the soil can lead to improvements in discrimination ability. However, for lower levels of magnetic susceptibility, a median filter may be sufficient.

Although accurate modeling of the soil response will, in general, produce more diagnostic feature vectors, quantifying discrimination performance by modeling the soil response is sensor dependent. Different sensors will have different transmitter and receiver geometries and different spatial coverage of the secondary field response. Quantifying how the soil modeling methods proposed here would improve discrimination performance, requires simulations and analysis on data specific to that sensor.

3. A METHOD FOR PROCESSING DATA FROM ADVANCED EMI SENSORS

The examples of the previous section were developed and tested using mono-static sensors. These sensors featured coaxial, horizontal loop transmitters and receivers. Although this geometry produces the maximum possible signal over buried compact metallic objects when surveying an area, this arrangement also produces the maximum coupling between the sensor and the ground.

Over the course of this project, SERDP and ESTCP funded programs developed a new generation of EMI sensors designed specifically for target characterization. In order to produce data that are better able to localize the target and constrain dipole polarizabilities, these advanced EMI instruments feature multiple transmitter coils for illuminating a target in a variety of directions and have numerous receiver coils that record the secondary field at multiple locations. For mono-static sensors (more specifically, sensors that only measure the vertical component of the secondary field due to a vertical field transmitter), all soundings are well coupled to the ground. In addition to the coaxial transmitter/receiver geometry, advanced EMI instruments also have receiver/transmitter combinations that are poorly coupled to magnetic soils. That is, there are soundings that are relatively insensitive to the presence of magnetic soils. In Figure 3.1, we plot the vertical and horizontal components of the magnetic field due to a half-space of magnetic material being illuminated by a horizontal loop. At the center of the transmitter loop there is a maximum coupling to the ground in the vertical component of the data and a minimum coupling in the horizontal component of the data. As the distance from the center of the transmitter loop increases, the vertical component decreases and the horizontal component increases with a maximum at approximately 70 cm from the transmitter loop center.

Figure 3.2 shows how the ground coupling varies for different transmitter and receiver combinations of the TEMTADS 2x2 sensor. The data were collected as part of the Camp Beale ESTCP Live-Site Demonstration. The TEMTADS 2x2 consists of 4 transmitters, with a 3 component receiver cube at the center of each transmitter (Figure 3.2(a)). Figure 3.2 plots the measured data when transmitter Tx0 fires. Figure 3.2(b) shows that the z-component measured by each receiver cube approximately follows the characteristic decay of VRM, with the magnitude decreasing as a function of distance away from transmitter Tx0, i.e. the coaxial receiver Rx0 has the largest response, Rx1 and Rx3 have a lower magnitude response than Rx0, and Rx3 has the smallest magnitude response since it is furthest from Tx0. Figures 3.2(c) and (d), plot the horizontal component soundings, with green lines being used to indicate azimuthal components which are poorly coupled to the ground response. Red and blue lines are used to indicate components that would measure some response

from the soil. The blue lines are lower magnitude since the Rx2 receiver is farthest away from Tx0.

The symmetry of the ground response and the multi-static, multi-component nature of the advanced sensors suggest the following two step inversion process:

1. Invert for dipole parameters by using data components that are least sensitive to magnetic soil
2. Refine the model from step one by fitting all components of the data for all time channels to a model consisting of dipole parameters and the background magnetic properties.

The ability to provide a good starting model greatly improves the robustness of the non-linear inversion process.

In this section we first compare data measured by a few advanced EMI sensors over magnetic earth with modeled data. We then test the two stage inversion algorithm by inverting simulated MPV-MARK 1 data. Finally, we present results of processing MPV-MARK 1 field data acquired at the Defense Research and Development Center magnetic soils test site in Suffield, Alberta, Canada.

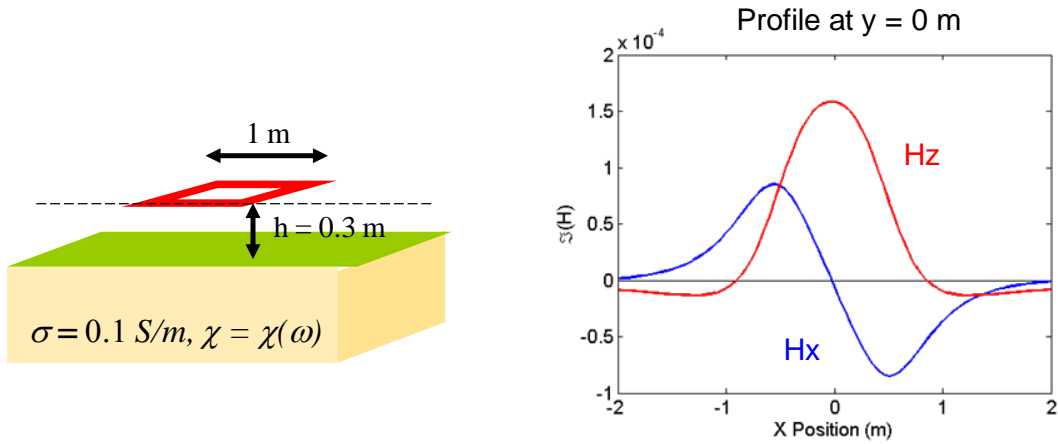
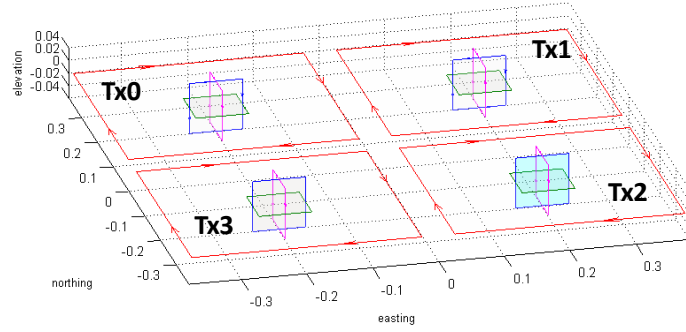
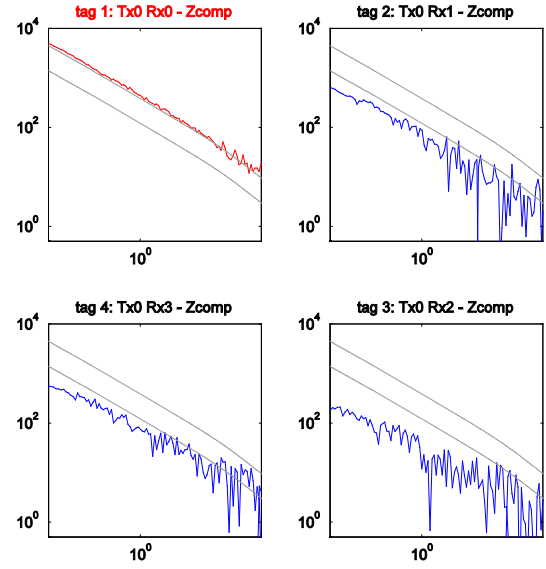


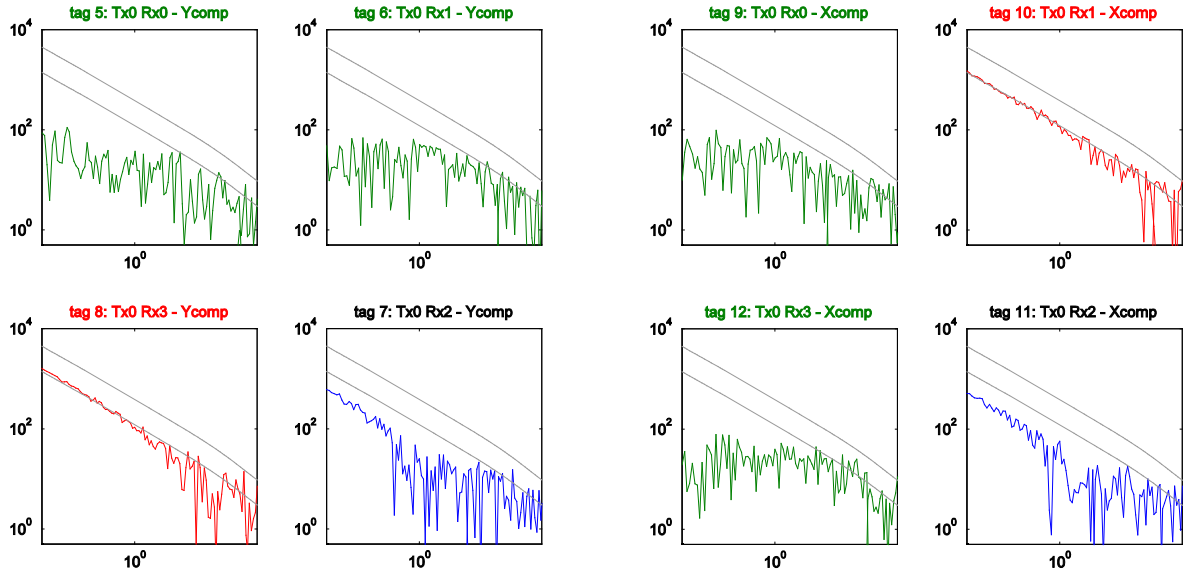
Figure 3.1. The geologic response of horizontal loop transmitters.



(a) Geometry of the TEMTADS 2x2 sensor transmitter



(b) Z component response to the Tx0



(c) Y component response to the Tx0 transmitter

(d) X component response to the Tx0

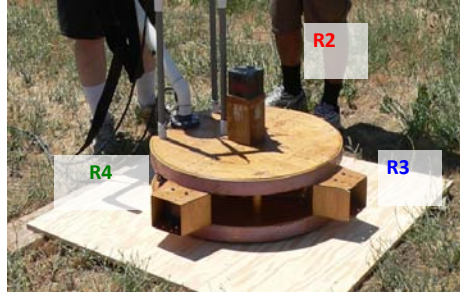
Figure 3.2. TEMTADS 2x2 data collected at Camp Beale, CA.

EXAMPLE OF MODELING DATA FROM MULTI-STATIC SENSORS: MPV-MARK 1 MEASUREMENTS AT THE ASHLAND, OREGON AIRPORT

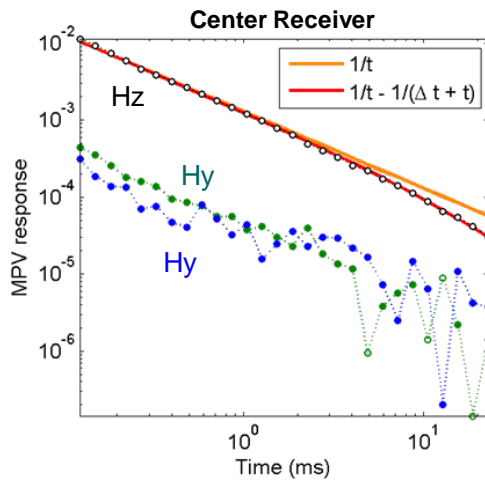
The MPV-MARK 1 consists of a pair of coaxial 75 cm diameter circular transmitter coils (Figure 3.3(a)). The MPV-MARK 1 has 5 receiver cubes, with one cube centered between the two transmitters, one cube above the transmitters and coaxial to the transmitters, and three receivers located on the edge of the coils. Each cube measures the 3 components of the secondary field.

Data were acquired at the Sky research UXO test site using the MPV MK1 sensor. Previous EMI surveys with the Geophex GEM3 and Geonics EM63 showed evidence magnetic soils (for example Pasion et al. 2005). As Figure 3.3(a) indicates, the MPV-MARK 1 was placed on a small piece of plywood that lay on the ground. Figure 3.3(b) compares the response of the center receiver. The result is consistent with the modeled result of Figure 3.1, with a soil response in the vertical component of the data (labeled Hz), and much less response in the horizontal components (Hy). The low level signal in the secondary components may be due to the MPV-MARK 1 deviating slightly from horizontal. In Figure 3.3(c) shows the response of the outer receivers (labeled Rx2 - Red, Rx3 - Blue, and Rx4 - Green). At the edge of the loop there are both vertical and radial components of the secondary field measured. The azimuthal components of the soil response are within the noise levels of the instrument,. The components of the MPV-MARK 1 response that are poorly coupled with the magnetic soil response (i.e. the horizontal components of the coaxial receivers and the azimuthal components of the edge receivers) will be used in the first step of the inversion process.

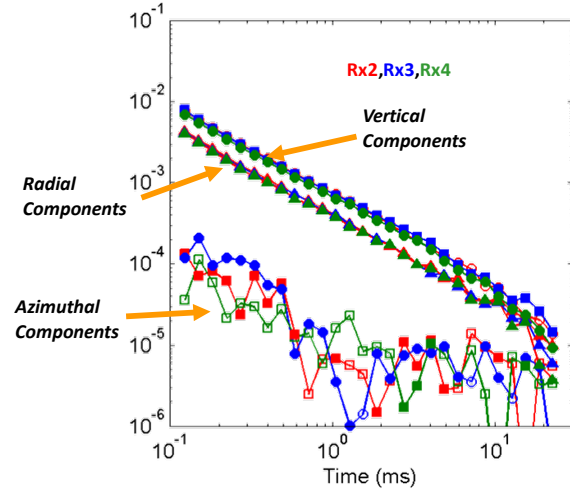
The MPV-MARK 1 response at the Sky Research site was measured as a function of height and tilt (Figure 3.4). Instrument height was adjusted by placing foam pieces beneath the MPV-MARK 1. For the tilt test the rear edge of the receiver remained in contact with the ground and tilt angle was adjusted by placing foam pieces beneath the front edge of the MPV-MARK 1. In Figure 3.4 we plot the 3 components of the secondary field in the center (coaxial) receiver and front receiver (labeled R3 in Figure 3.3(a)) measured in the second time channel of the MPV-MARK 1. The MPV-MARK 1 response was calculated using the soil modeling technique introduced in the previous chapter. Within the error introduced by the uncertainty in the height and tilt of the MPV-MARK 1, the modeled response produces a good estimate of the sensor response.



(a) MPV-MARK 1 sensor



(b) Response of the 3 receivers on the edge.



(c) Response of the center receiver.

Figure 3.3. MPV-MARK 1 measurements made at the Ashland Municipal Airport.

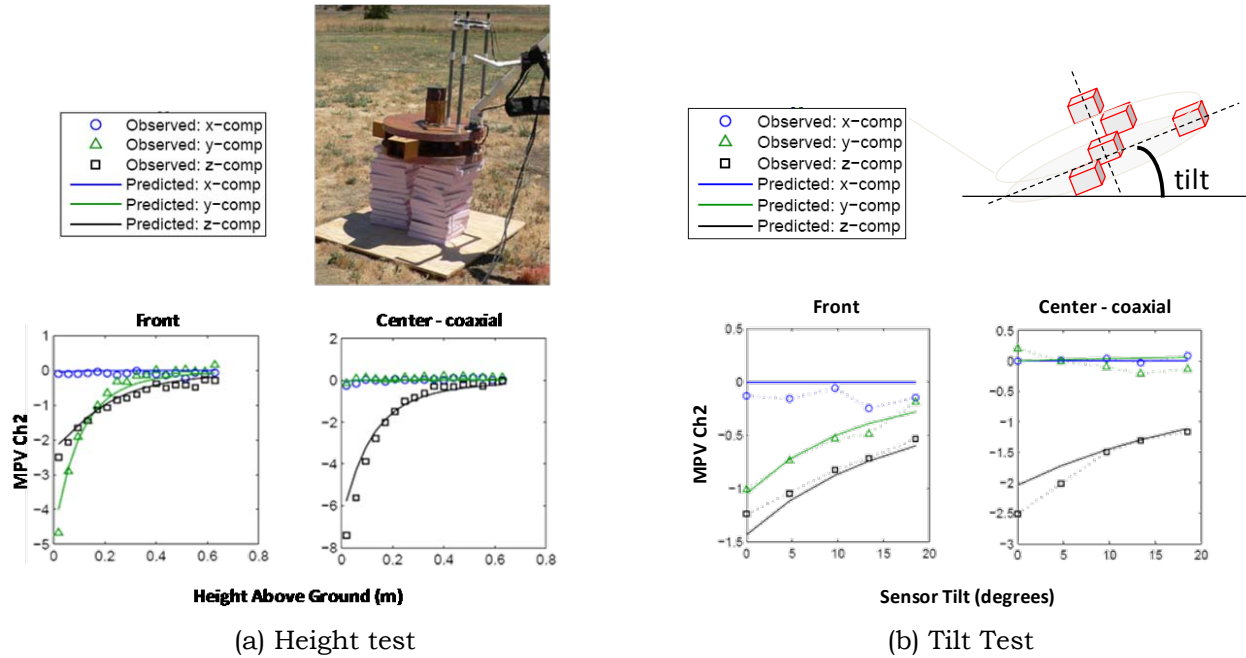


Figure 3.4. Height and tilt test measurements using the MPV-MARK 1 sensor.

A METHOD FOR PROCESSING DATA FROM ADVANCED SENSORS

The simultaneous inversion method described earlier in this report was developed for traditional mono-static static sensors. For the new generation of advanced EMI sensors, we propose a two step inversion process that modifies the mono-static sensor simultaneous inversion method:

1. Invert for dipole parameters by using data components that are least sensitive to magnetic soil.
2. Refine the model from step one by fitting all components of the data for all time channels to a model consisting of dipole parameters and the background magnetic properties.

The primary difference when applying the simultaneous inversion method to advanced sensors is the manner in which the starting model is chosen (Step 1). The simultaneous inversion method inverts for position, orientation, quadrature susceptibility, and dipole polarizabilities simultaneously using a Newton-type, non-linear optimization algorithm. In order to avoid local minimum, a good starting model is necessary. To improve our starting guess from mono-static data, we identify soundings near the anomaly that are due to soil only (i.e. no contribution from the buried target) and use these soundings to provide an initial estimate of the soil model. We then subtract the soil contribution from the data, and invert the soil corrected data for an initial guess at the dipole parameters. The soil model and dipole model are then refined by inverting for all model parameters, using all data.

When working with advanced sensors in a cued mode, data are often acquired at only a single location. The location is chosen to be as close as possible to being directly above the target to be interrogated. Thus it is often not possible to make an initial estimate of soil properties using soundings that are not sensitive to the target. However, when working with advanced sensor data we are able to select soundings that are less contaminated by soil noise. This subset of data can then be used to produce an initial guess of the dipole model. Again, both soil and dipole parameters are then refined by simultaneously inverting for all model parameters, using all data.

To demonstrate the method we present a series of simulations using MPV-MARK 1 data collected over soil with a viscous remnant magnetization approximately twice as strong as the Cambodian soil found at the Defense Research and Development Center Soil Test Facility in Suffield, Alberta. The magnetic susceptibility of the Cambodian soil can be found in Table 3.1. We choose a 4 inch long steel cylinder (Figure 3.5(a)) as a target. The polarizabilities for the cylinder were determined using in-air MPV-MARK 1 measurements carried out at the Sky Research office located in Vancouver (Figure 3.5(b)). The cylinder is randomly oriented and placed at a depth of 25 cm below the surface. Figure 3.6 shows the sawtooth pattern used to collect the data. The path taken by the MPV-MARK 1 is made more realistic by adding some random

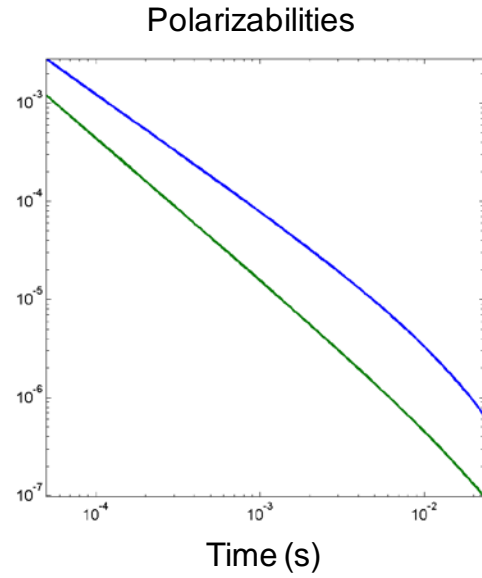
motion such that the MPV-MARK 1 path deviates from the sawtooth pattern. The same type of random walk-type motion is applied to the MPV-MARK 1's pitch, roll, and azimuth information. A normally distributed error with a standard deviation of 0.5 cm is applied to the easting, northing, and elevation of the sensor location information. A normally distributed error with a standard deviation of 0.5 degrees is applied the sensor position, pitch, roll and azimuth information.

An example of the data created for these simulations is shown in 3.7. The three components of the secondary field measured during the first time gate from a receiver co-axial to the MPV-MARK 1 transmitter (Rx1 in Figure 3.7(a)) and a receiver located at the edge of the transmitter (Rx2) are gridded. The data produced by the target only (top row) and the target plus soil response (bottom row) are compared. Comparison of the signals in the top and bottom rows of Figure 3.7(b) confirms that at the center of the transmitter coil, the horizontal components of the data are insensitive to magnetic soil, while the vertical component of the data is most sensitive to the soil. Data components that are more sensitive to magnetic soil are indicated by a red dashed line surrounding their gridded data image. For the non-coaxial receivers (i.e. Rx2, Rx3, and Rx4), only the azimuthal component (i.e. the component parallel to the transmitter loop) of the field is insensitive to the soil signal. Therefore, we invert 7 of the 15 total soundings when inverting the MPV-MARK 1 data components least sensitive to the soil response.

The simultaneous inversion method described above was applied to the simulated data (Figure 3.8). The first step was to invert the 7 of 15 soundings that were least sensitive to the soil response. Figure 3.8(b) plots the principle polarizabilities after inverting the less sensitive soundings. The true polarizabilities are also plotted with a black dashed line. Figure 3.8(c) plots the principle polarizabilities when inverting all of the 15 soundings. For this second step, the model estimated in step 1 is used as a starting model for the non-linear inversion. It is clear that using all soundings are required to better constrain the target polarizabilities.

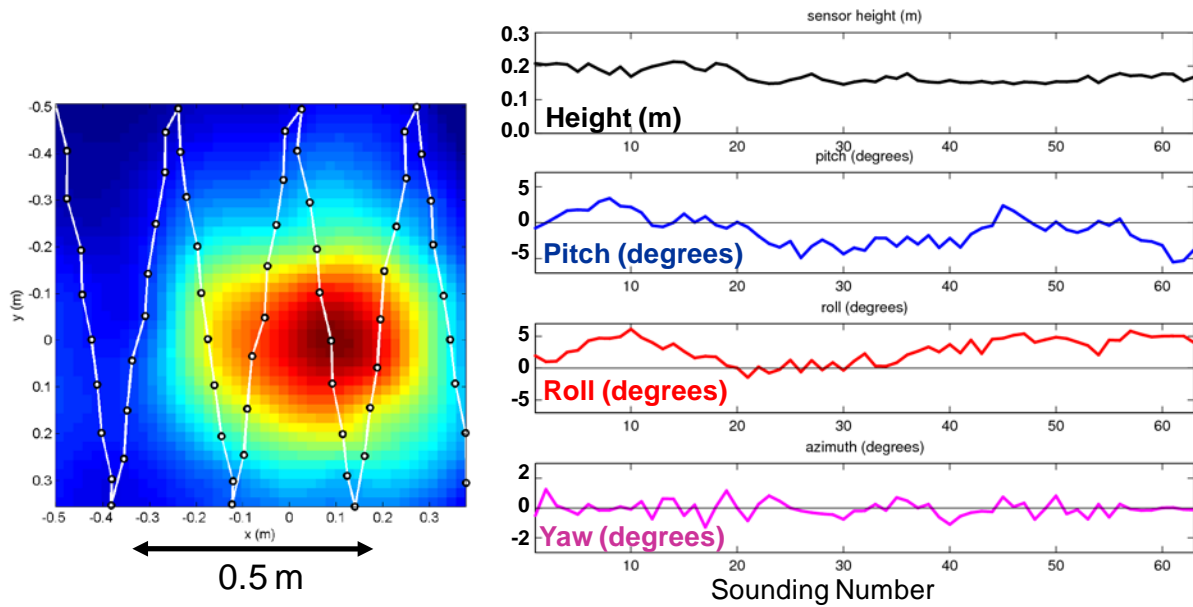


a) Four inch long steel cylinder



b) Cylinder polarizability estimated from in air measurements

Figure 3.5. Steel cylinder used for simulations

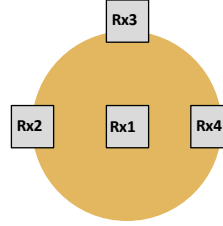


(a) Sawtooth pattern used for collecting data

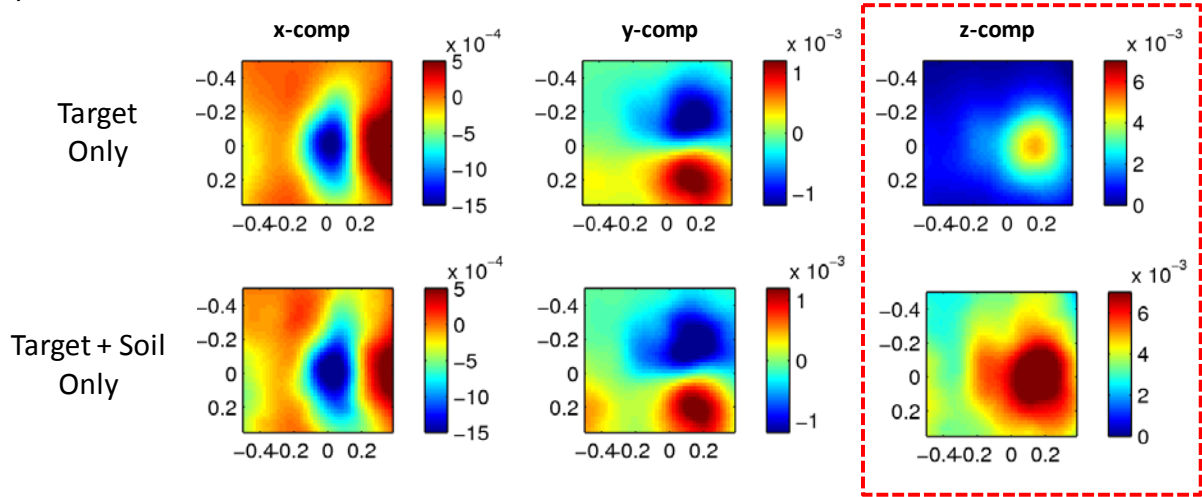
(b) A sample realization of simulated sensor height, pitch, roll, and yaw

Figure 3.6. An example of a survey used during MPV- Mark 1 simulations

(a) Receiver labeling for MPV



(b) Receiver Rx1: Co-axial receiver



(c) Receiver Rx2: Receiver at edge of transmitter

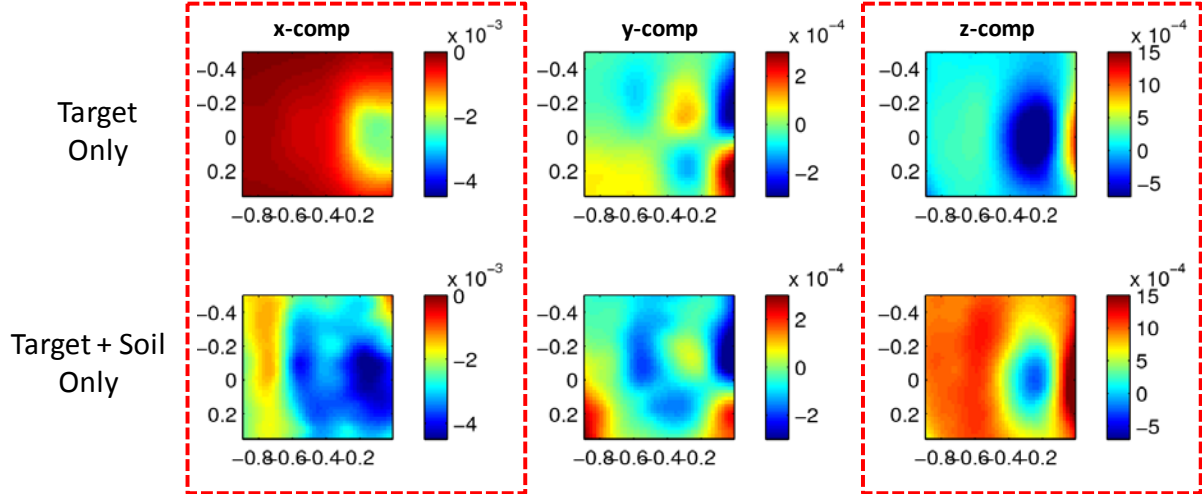
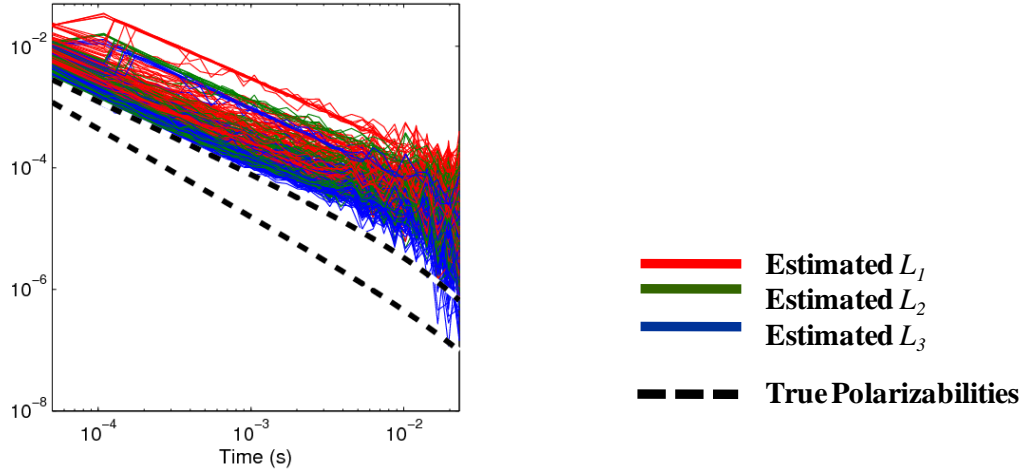
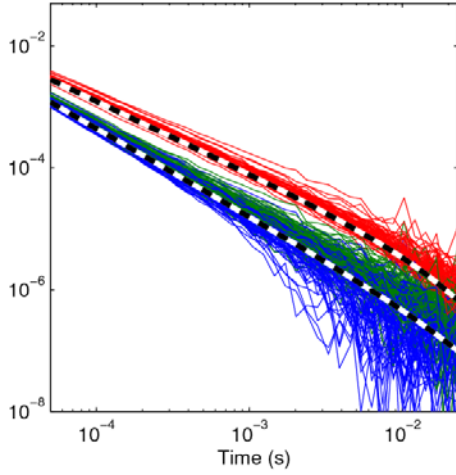


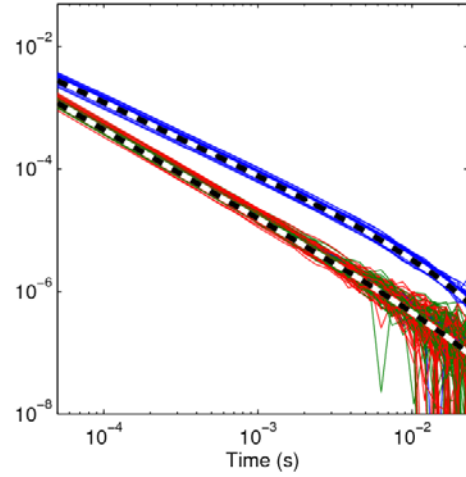
Figure 3.7. An example of synthetically generated data as part of the MPV-Mark 1 simulations. The red dashed boxes indicate the components most sensitive to soil.



(a) Results when inverting all data components.



(b) Recovered polarizabilities when inverting soundings that are not well coupled to the ground



(c) Recovered polarizabilities when using the models in (b) as start models and all soundings.

Figure 3.8. A comparison of recovered polarizabilities when inverting the simulated data.

PROCESSING FIELD DATA COLLECTED AT THE DEFENCE RESEARCH AND DEVELOPMENT CENTRE MAGNETIC SOIL TEST FACILITY

In order to test and evaluate our inversion methods, EMI data were collected between February 8 and 12, 2010 at the Defense Research and Development Canada (DRDC) facility located at Canadian Armed Forces Base at Suffield, Alberta. The DRDC Suffield soil testing facility consists of a large heated greenhouse structure which house a number of soil pits with natural occurring and synthetic soils. The majority of our EMI measurements were taken on a 4m x 4m x 2m pit containing soil that originated from Cambodia (Figure 3.9). The red color of the soil is reminiscent of the Kaho'olawe soil seen in Figure 0.1(a). In both Kaho'olawe and Cambodia, old volcanoes subjected to long term weathering have led to high levels of VRM in the soils. The magnetic susceptibility of the different soil types have been well characterized using a number of different multiple frequency magnetic susceptibility meters (Cross 2008). Additional measurements and analysis were carried out on the soil pits containing synthetic soils with different levels of magnetite content (1%, 3%, 5%, and 15% magnetite by weight). Table 3.1 contains the Bartington MS2D magnetic susceptibility meter measurements that we made on site.

DESCRIPTION OF MEASUREMENTS

Data were acquired at the Suffield site with the MPV-MARK 1 and Geophex GEM3 sensors. For this report we will focus on data collected with the MPV-MARK 1. Collecting data within the greenhouse structure produced a pair of challenges. The first challenge was obtaining accurate positioning of the instruments. Since the soil pits were located inside a large greenhouse, GPS was not a viable option for positioning. Therefore, a positioning template was created by marking a sheet of plywood with a 7 x 7 uniform grid with a station spacing of 15 cm (see Figure 3.11). The MPV-MARK 1 was positioned by placing it on a small piece of plywood, then sliding the small piece of plywood to the marked locations on the full size piece of plywood. The clearance between the surface and the plywood was adjusted by adding 2x4's beneath the plywood.

The MPV-MARK 1 sensor was sensitive to the metal framing of the greenhouse structure. MPV-MARK 1 soundings were acquired at numerous points within the greenhouse structure. These measurements showed that the magnitude and direction of the background response varied throughout the interior of the greenhouse. In order to remove this background signal from subsequent measurements, a data set was collected on a horizontal plain at a height of approximately 50 cm above the site where the data were collected. We assumed that the response of the greenhouse would be approximately the same 50 cm above the soil as the response would be if recorded near the surface of the soil. The background measurement was subtracted from all data collected on the Cambodian soil pit. When using this background removal method a small portion of the soil response is removed through this background

correction. However, we were reluctant to acquire the background measurement at the greater height since we were worried that the measured background signal would be less characteristic of the greenhouse background signal recorded by the MPV-MARK 1 in survey data mode.

There were several data sets acquired at the Cambodian soil pit. We focused on two targets: a 4 inch steel cylinder and a 3.5 inch aluminum cylinder (Figure 3.12). These targets were chosen as simulants for a 37 mm projectile and a 40 mm aluminum projectile. Since the simulants are solid cylinder instead of shells, the targets will have longer time constants than the actual 37 mm and 40 mm projectiles. Two different ground clearance heights - corresponding to having one 2x4 or a pair of stacked 2x4s beneath the plywood - were used during the measurements. Data were also taken with a simulated mound beneath the plywood and near to the buried cylinder (Figure 3.13). Figure 3.14 contains an example of data collected over the aluminum. For this example the aluminum target was horizontal, with the top of the target flush with the top of the surface. In Figure 3.14(c) a plan view grid of the first time channel of data and a plot of the soundings are shown for the center receiver.

INVERSION RESULTS

We first tested the simultaneous inversion method using data from the Cambodian soil pit. We used the two step procedure defined earlier. The first step is to use components of the MPV-MARK 1 receivers that are least affected by the soil to provide an initial estimate of the dipole parameters. Only the horizontal components in the center receiver and the azimuthal components of the receivers at the edge of the MPV-MARK 1 are inverted in this first step. This inversion produces an estimate of the optimal dipole location and the polarizability matrix. The trace and eigenvalues of the polarizability matrix are then calculated. The second step is to refine this initial model by simultaneously estimating dipole parameters and the background magnetic properties using all components and time channels of the data. For these experiments we assumed that the magnetic background was constant over the 90 cm x 90 cm area of the survey, such that the model could be characterized by a single parameter.

Figure 3.15 compares the inverted polarizabilities for the 4 inch steel cylinder. The recovered polarizabilities when inverting data least affected by the magnetic soil are plotted in Figure 3.15(a). The subset of data not significantly affected soil are able to constrain the primary polarizability, but has some difficulty with the secondary polarizabilities when the cylinder is vertical. Since the MPV-MARK 1 illuminates targets with a horizontal loop, the primary field is predominantly vertical when the MPV-MARK 1 is positioned directly above the target. Therefore, the poorest orientation for exciting the secondary polarizabilities is when the target is vertical. The subset of data that was poorly coupled to the ground was insufficient for constraining the secondary polarizabilities during the inversion. Figure 3.15(b) plots the recovered polarizabilities when using the estimated locations in the previous step as a start model when performing the simultaneous inversion of all data for both

background parameters and polarizabilities. Using all data resulted in being able to correctly recover the primary and secondary polarizabilities. Figures 3.15(c) and (d) plot the total polarizability (or trace of the polarizability matrix, when inverting components of the data that are insensitive to the soil and all data, respectively). We found that the total polarizability is a robust measure, and that its recovery was very stable for all datasets.

Figure 3.16 compares the inverted polarizabilities for the 3.5 inch aluminum cylinder. The performance of the algorithm was similar to the steel cylinder case. An aluminum cylinder is characterized by having two large equal polarizabilities and a small polarizability corresponding to the axis of symmetry. During the first step of the method, the inversion was able to recover the primary polarizability well, and the secondary polarizability was not as well constrained when the cylinder was vertical (Figure 3.16(a)). For the vertical case (red lines) the three polarizabilities are nearly equal. Figure 3.16(b) shows that the simultaneous inversion successfully recovered all polarizabilities for all cases. In Figures 3.16(c) and (d) the recovered total polarizability is calculated for the non-soil component case and simultaneous inversion case. In both stages, the total polarizability was well constrained.

In Figures 3.15 and 3.16, black lines represent the recovered responses when a mound of dirt is present. The geometry of the experimental setup is sketched in Figures 3.13 (c) and (e). For both the aluminum and steel cylinder cases, the presence of the mound does not negatively affect our ability to recover target polarizabilities. Figure 3.17 (c) plots the third time channel of z component center receiver data acquired above the mound without a target present. Due to the relatively large size of the MPV-MARK 1 transmitter loops, the MPV-MARK 1 is not well coupled to the mound and only a weak anomaly is produced by the mound. There is a slight increase in the magnitude of the data when the MPV-MARK 1 passes over the mound. However, the increase in magnitude of the signal due to the mound is quite small and thus does not affect the dipole inversion.

Up until this point, all the measurements were made with a constant ground clearance and sensor orientation. Although our original intention was to acquire data sets with variable ground clearance and orientation, we were limited by our inability to use GPS at the site. In addition, the background removal process used a calibration measurement where the MPV-MARK 1 was level. We were concerned that applying the background removal to a dataset where the MPV-MARK 1 was not level would not sufficiently remove the background structure response. We acquired two data sets with non-zero pitch and variable sensor height. Figure 3.18(a) shows the setup for the two data sets. A 4x4 piece of wood was used to elevate one end of the plywood template, which gave the MPV-MARK 1 a platform with a 3 degree incline to move on. Data were acquired with both a positive and negative pitch.

Figure 3.18(d) plots the recovered polarizabilities when inverting the components of the data least affected by the magnetic soil. Some of the data components that are poorly coupled with the soil when the MPV-MARK 1 is horizontal will measure some soil response when the MPV-MARK 1 is tilted. When the pitch is +3 degrees, the polarizabilities are accurately recovered. However, when the pitch is -3 degrees, the secondary polarizabilities are poorly constrained. The main difference between the positive and negative pitch datasets are that the lead receiver cube is closer to the ground in the negative pitch case. However, this may not be the cause for the difference in the recovered polarizabilities. As we saw in Figure 3.15, even when the MPV-MARK 1 is level the first step of inverting non-mag soil data components can have difficulties constraining the secondary polarizabilities of a vertical target. Simultaneous inversion for the soil and target parameters improves the polarizability estimates.

Our final tests of the inversion algorithm involved data acquired over the test site's synthetic soil pits (Figure 3.19). The level of instantaneous susceptibility was sufficiently high in the 15% soil pit to saturate the Geophex GEM3 data. The susceptibility of the 15% soil was also too high to be measured by the Bartington MS2B. However, the high levels of real susceptibility did not correlate to a high viscous remnant magnetic component and thus the MPV-MARK 1 was not as sensitive to the synthetic soil response as the GEM3. The resulting polarizabilities are well recovered by the simultaneous inversion (Figure 3.19(d)).

Sample location	Average low freq	Average high freq
synthetic - 0%	23	21.5
synthetic - 1%	438.5	434.5
synthetic - 3%	974.5	970.5
synthetic - 5%	3655	3636.5
Cambodia soil pit: y = 60cm	238.25	227
Cambodia soil pit: y = 100cm	193.75	180.5
Cambodia soil pit: y = 250cm	183.75	169.5

Table 3.1. Bartington MS2D Magnetic Susceptibility measurements. Photos of soil samples at y = 60 cm, 100 cm, and y = 250 cm are presented in Figure 3.9.

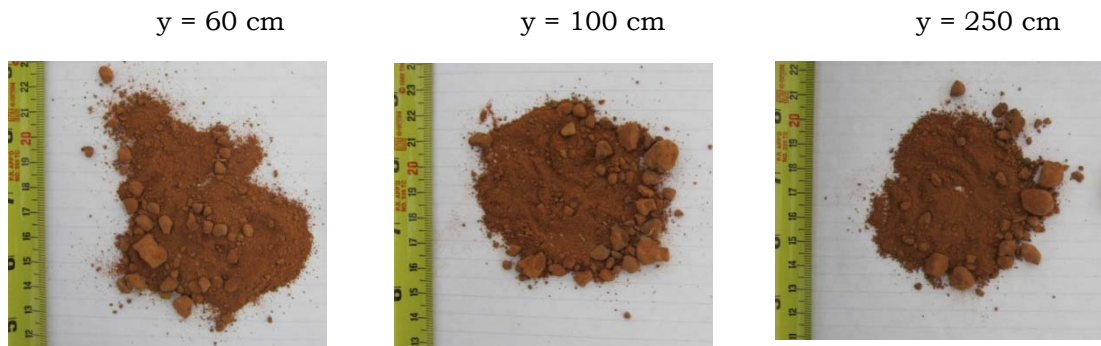


Figure 3.9. Photos of samples taken from Cambodian soil pit for susceptibility measurements.

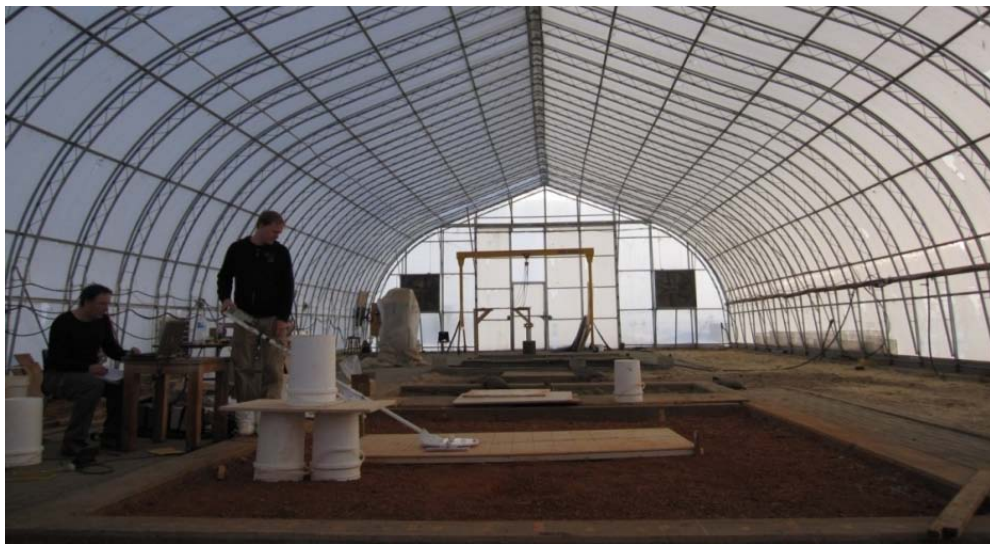
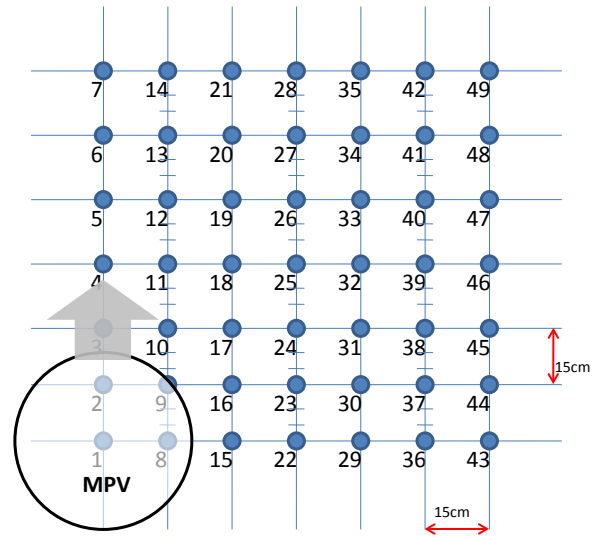
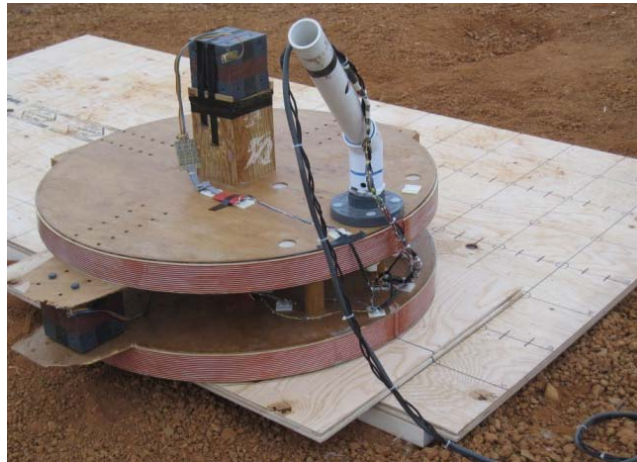


Figure 3.10. The DRDC Suffield magnetic soil test pits. The test pits were located in a heated greenhouse. The greenhouse resulted in two challenges during data collection: (1) GPS positioning was not possible and (2) the EMI sensors were sensitive to the metal frame of the structure. The Cambodian Soil pit is in the foreground.



(a) MPV on plywood template used for positioning (b) Survey grid. Stations are numbered in order of survey and denote position of center of the MPV.

Figure 3.11. Positioning was achieved by placing the MPV-MARK 1 on piece of plywood that was marked with a uniform 7 x 7 grid with a 15 cm spacing. The data acquisition pattern is shown in (b).



(a) Targets: 4" solid steel and 2.75" aluminum cylinders



(b) Photo of MPV-MARK 1 on the Cambodian soil pit at the DRDC test facility

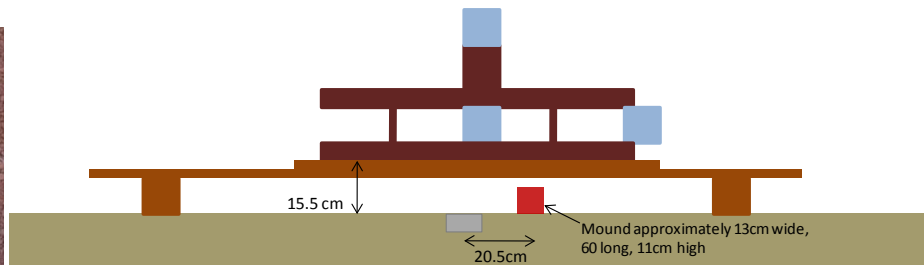
Figure 3.12. Photo of targets measured at the Cambodian soil pit and a photo of the inside of the DRDC magnetic soil test facility greenhouse.



(a) Photos of mound



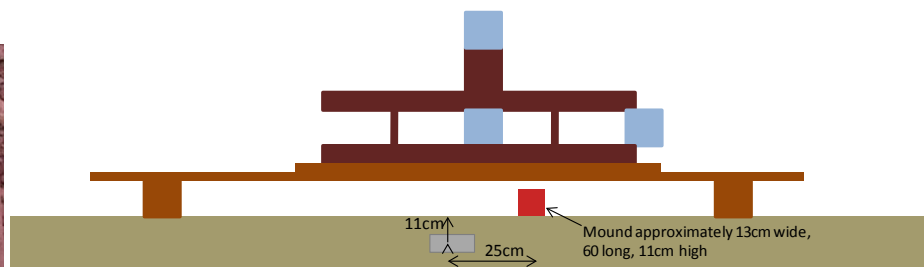
(b) 2.75" solid aluminum horizontal cylinder



(c) Arrangement of simulated mound with 2.75" solid aluminum horizontal cylinder surface, 2cm depth to center of mass

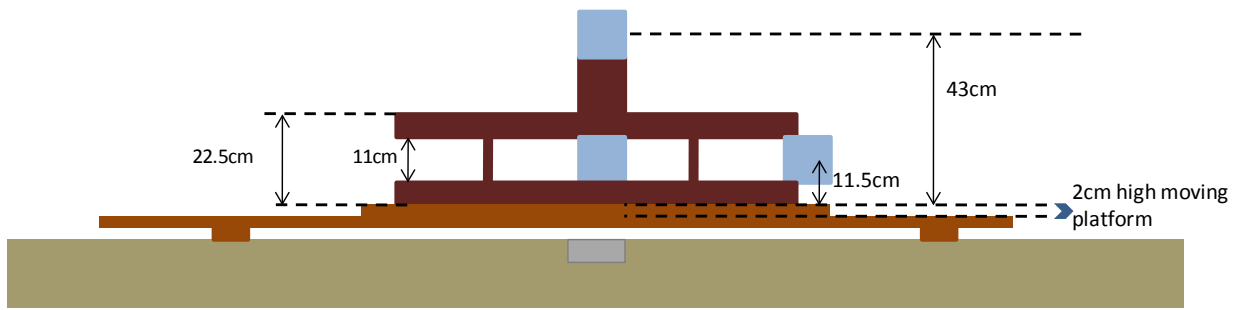


(d) 4" solid steel horizontal cylinder

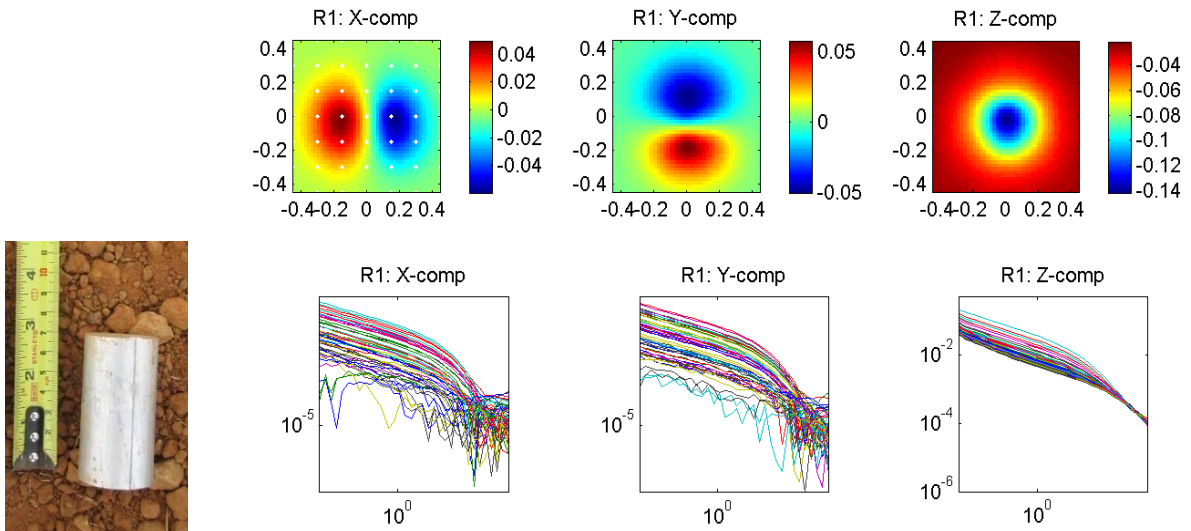


(e) Arrangement of simulated mound with 4" solid steel horizontal cylinder with depth of 11 cm to center of mass

Figure 3.13. Measurements taken with the artificially created mound.



(a) Measurement setup for the aluminum cylinder (cylinder is not to scale)

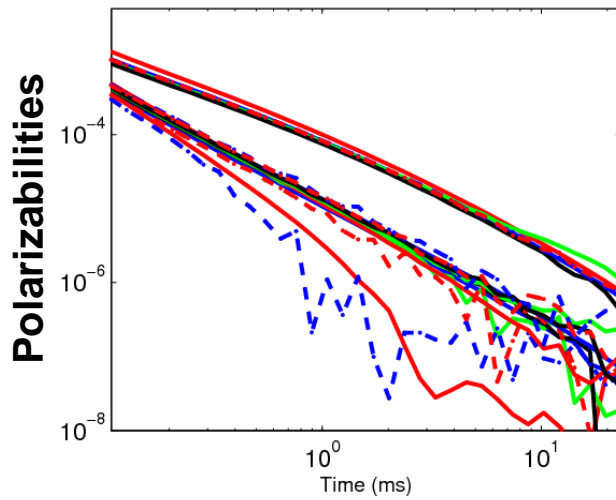


(b) Aluminum cylinder

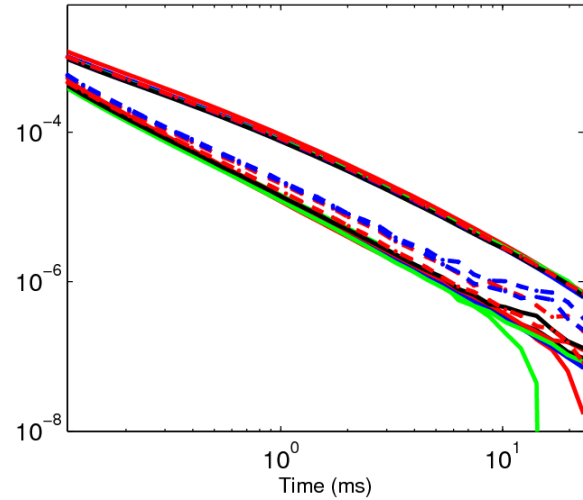
(c) Data from the center receiver

Figure 3.14. Example of MPV-MARK 1 data collected at DRDC Suffield. For this example data were acquired over a 3 inch aluminum cylinder with a 40 mm diameter. The cylinder was horizontal and flush with the surface.

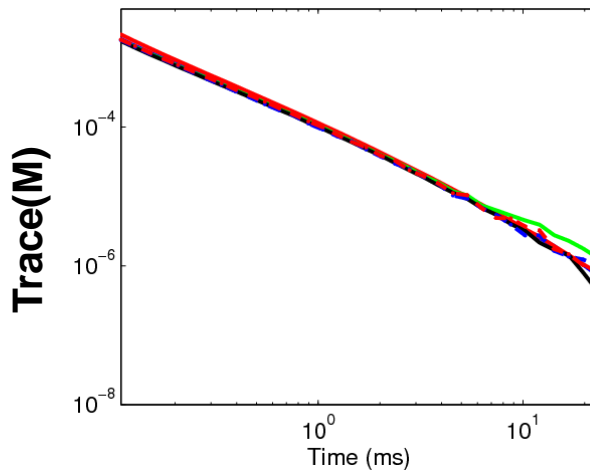
	orient	height	depth		orient	height	depth
—	Horiz.	7.5 cm	2 cm	—	Horiz	15.5 cm	11 cm
—	Vert.	7.5	5	- -	Vert.	15.5	21
—	Horiz.	7.5	22	- -	45	15.5	20



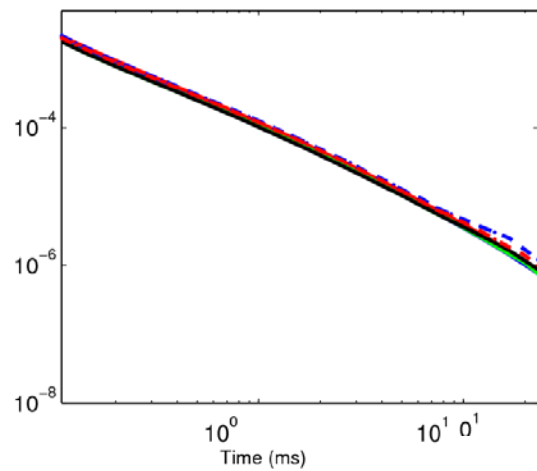
(a) Total polarizabilities when inverting data components least affected by magnetic soil



(b) Simultaneous inversion for dipole and soil parameters using all data components



(c) Total polarizabilities when inverting data components least affected by magnetic soil



(d) Simultaneous inversion for dipole and soil parameters using all data components

Figure 3.15. Results from inverting data acquired over a 4 inch steel cylinder buried in the Cambodian soil pit data.

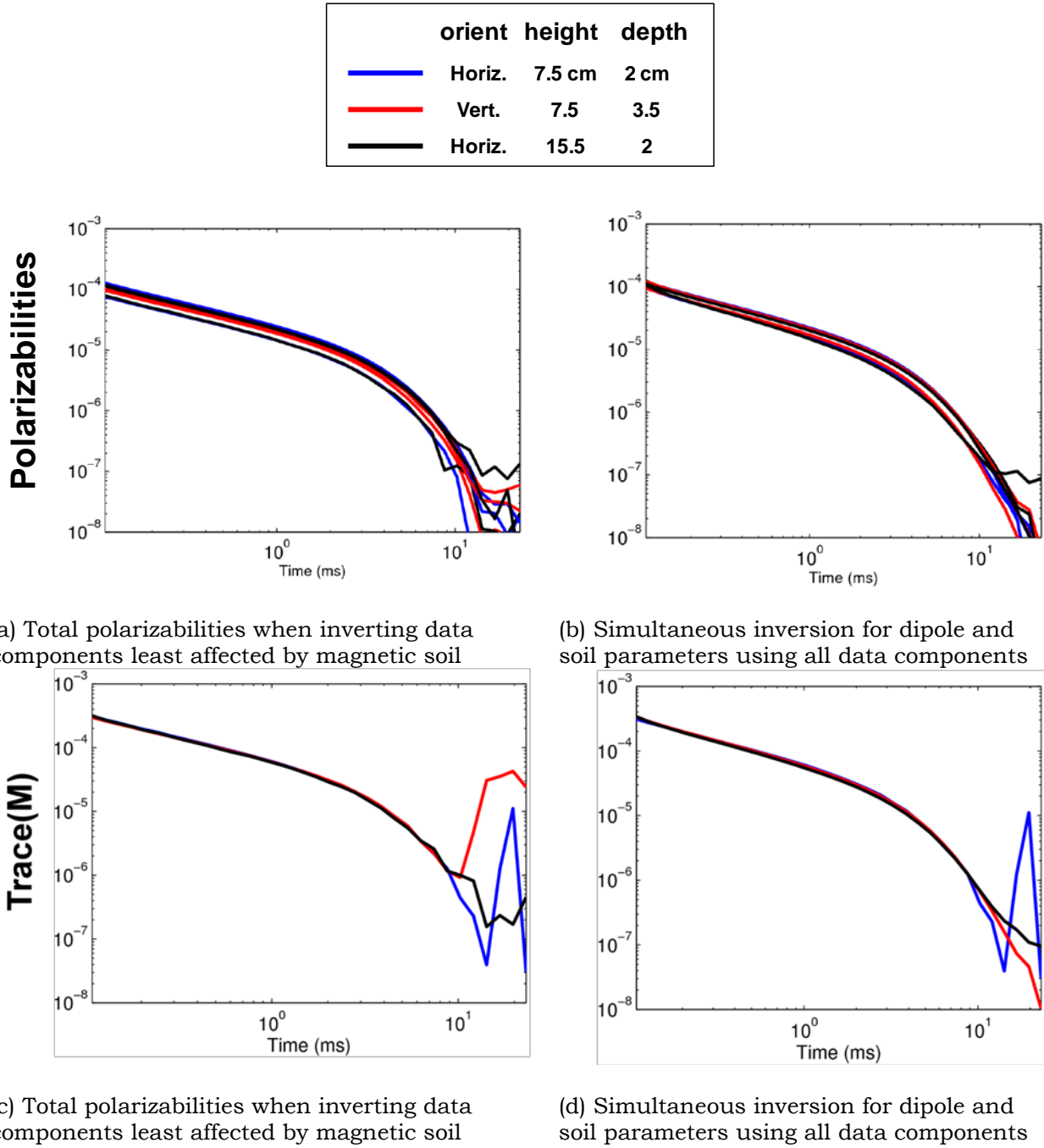


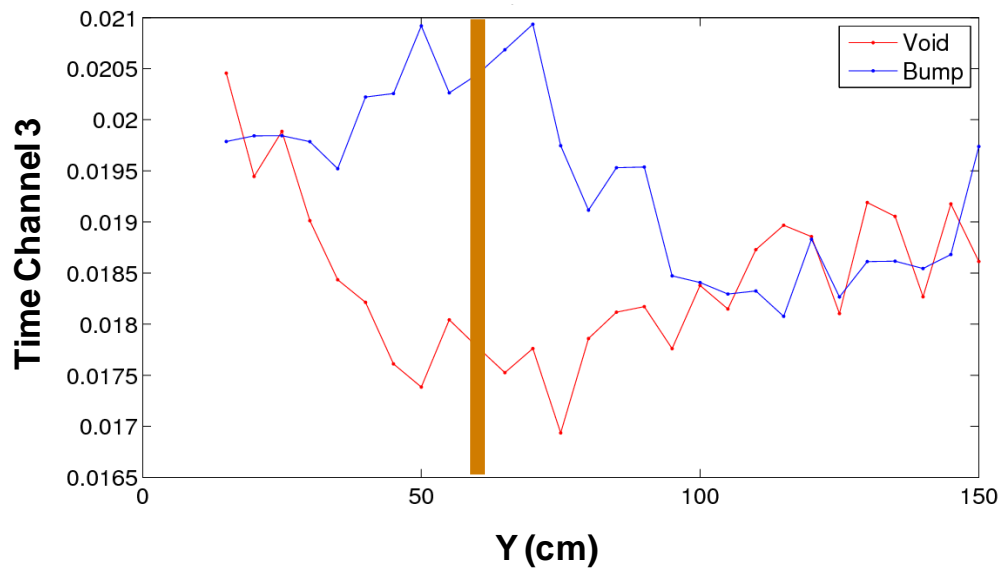
Figure 3.16. Results from inverting data acquired over a 3 inch aluminum cylinder buried in the Cambodian soil pit data.



(a) Simulated mound

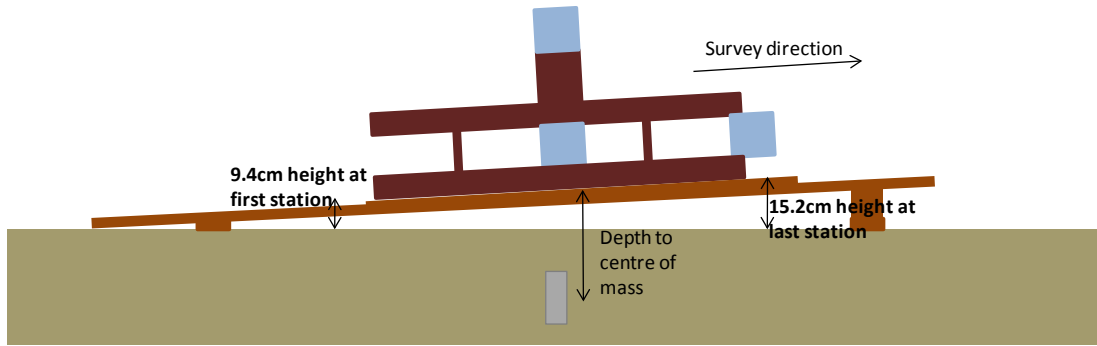


(b) Simulated void

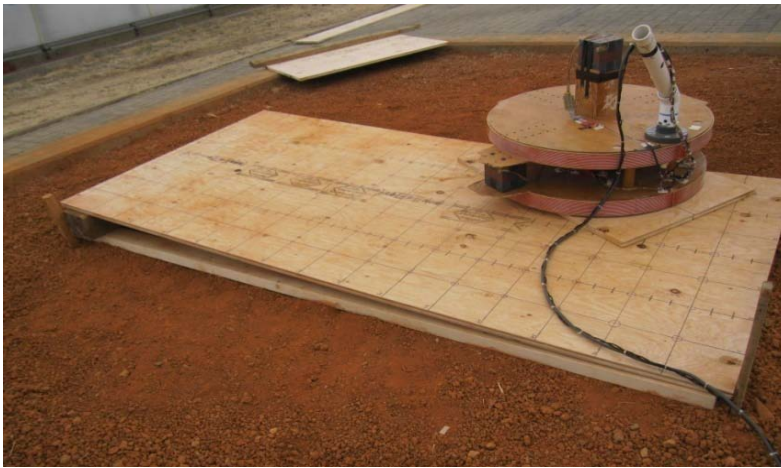


(c) Response due to the simulated void and bump

Figure 3.17. Data acquired over a simulated mound and void. (a) A simulated mound with dimensions of 60 x 13 x 11 cm was created. (b) A void was created by placing pieces of wood in the soil pit. The void measures 61 x 20 x 8 cm. (c) Both the mound and void does not produce a significant anomaly in the data. The brown line indicates the location of the mound and void along the line of data.



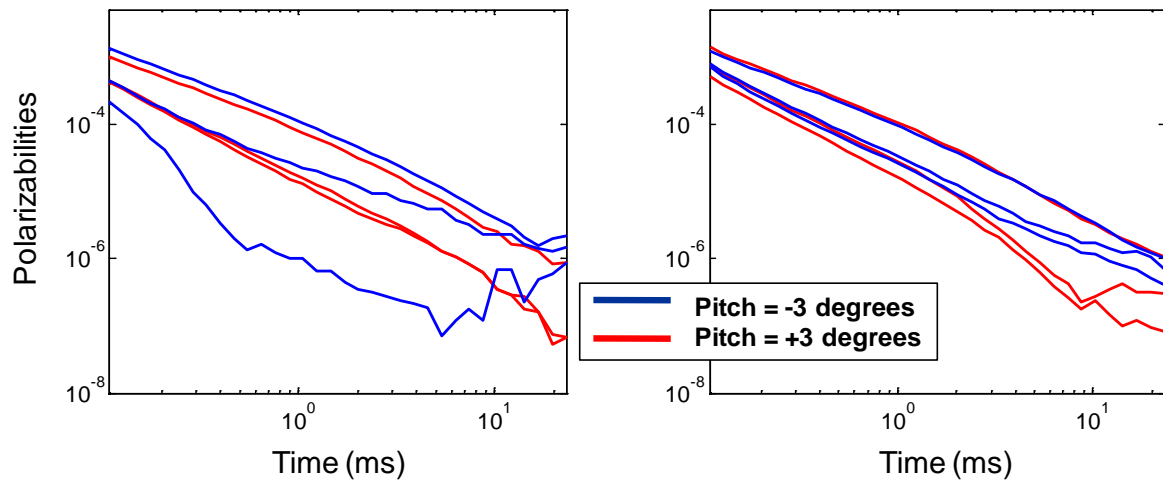
(a) Setup for tilt test. Pitch in this diagram is +3 degrees.



(b) Photo of tilt test. Pitch in this case is +3 degrees.



(c) Buried target.



(d) Inverting data from receivers least affected by soil (e) Inverting all receivers simultaneously

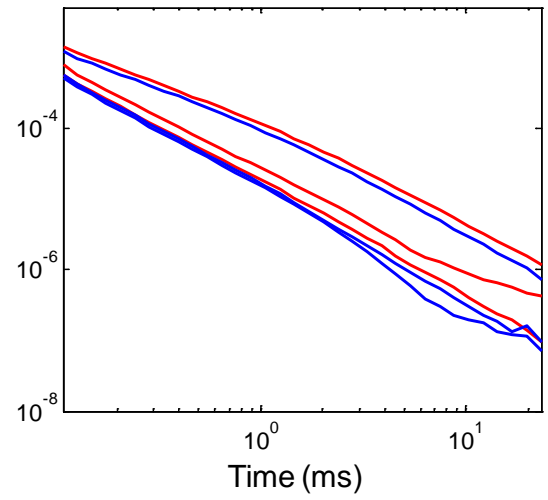
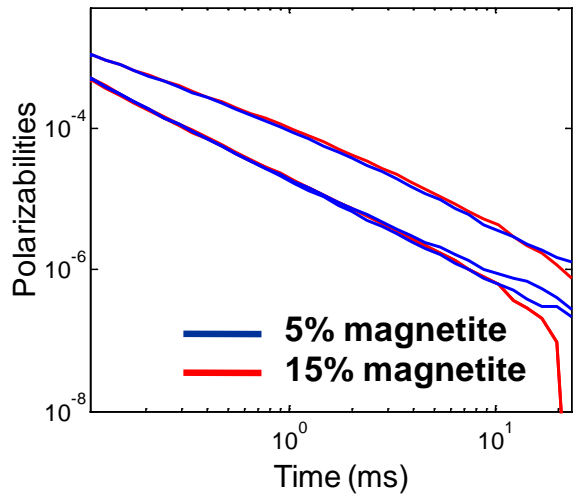
Figure 3.18. Results from a tilt test.



(a) Synthetic soil pit



(b) Buried target



(c) Inverting data from receivers least affected by soil. (d) Inverting all receivers simultaneously

Figure 3.19. Results from inverting data acquired over synthetic soil. The black synthetic soil have large levels of instantaneous susceptibility (see Table 3.1) but a low level of viscous remnant magnetization.

4. INVESTIGATING THE EFFECTS OF SOILS WITH COMPLEX MAGNETIC SUSCEPTIBILITY ON EMI MEASUREMENTS USING NUMERICAL MODELING OF MAXWELL'S EQUATIONS

Remediation of a UXO contaminated site typically involves the detection, discrimination and excavation of anomalies identified with EMI sensors. UXO discrimination is achieved by utilizing features extracted from physics-based model-fits to observed anomalies in order to determine the likelihood that the buried item is a UXO. Standard UXO processing techniques involve estimating the background response which is then subsequently removed from the observed data. In the ideal case, after the background has been successfully removed, the filtered data can be inverted using the physical model of a UXO in free space.

Magnetic soils are a major source of false positives when searching for unexploded ordnance with EMI sensors because of large geologic background signals (Cargile *et al.*, 2004). These signals are a consequence of the sensitivity of EMI sensors to soils where viscous remnant magnetization (VRM) is present (Lee 1983; Billings *et al.* 2003; Das, 2006). It is not uncommon for VRM soils to exhibit geology related responses on the same order as UXO. In addition, movement of the transmitter and receiver relative to magnetic ground can produce significant small wavelength anomalies in the data (Walker *et al.* 2005; Foley *et al.* 2005).

This section investigates the effects of magnetic soils by using numerical solutions to Maxwell's Equations. We do not know of previous numerical modeling studies that represents the soil with a frequency dependent susceptibility. First, we investigate the validity of treating a compact metallic target and the host soil as separate additive responses. That is, we investigate if there is a significant interaction between the target and the host soil.

NUMERICAL MODELING OF MAXWELL'S EQUATIONS USING EH3D

EH3D is a flexible forward modeling program developed at UBC-GIF for calculating the EM fields resulting from a wide range of time domain electromagnetic sources and source waveforms, over a 3D earth that is discretized using a mesh of rectangular cells. The fields are calculated using a finite volume numerical solution to Maxwell's Equations (Haber *et al.* 2004). EH3D can handle 3D variations of frequency dependent magnetic susceptibility and electrical conductivity. The Earth is divided into cuboidal cells each of which has a uniform conductivity and permeability at each frequency. Electric and magnetic fields are computed anywhere in the model studied.

EH3D takes Maxwell's equations which are described in the frequency domain by:

$$\nabla \times \mathbf{E} - i\omega\mu\mathbf{H} = 0 \quad (4.1)$$

$$\nabla \times \mathbf{H} - \hat{\sigma}\mathbf{E} = \mathbf{J}^s \quad (4.2)$$

$$\nabla \times \mathbf{H} = 0 \quad \text{on the boundary} \quad (4.3)$$

where μ is the magnetic permeability, σ is the conductivity ($\hat{\sigma} = \sigma - i\omega\varepsilon$) and \mathbf{J}^s is a known source current density. Using a Helmholtz decomposition of the electric field (i.e. $\mathbf{E} = \mathbf{A} + \nabla\phi$, $\nabla \cdot \mathbf{A} = 0$), to cope with numerical difficulties associated with the null space of the curl operator at low frequencies, produces a system of equations for the vector \mathbf{A} and scalar ϕ .

$$\nabla \times (\mu^{-1} \nabla \times \mathbf{A}) - \nabla (\mu^{-1} \nabla \cdot \mathbf{A}) - i\omega\hat{\sigma}(\mathbf{A} + \nabla\phi) = i\omega\mathbf{J}^s \quad (4.4)$$

$$\nabla \cdot \sigma\mathbf{A} + \nabla \cdot \sigma\nabla\phi = -\nabla \cdot \mathbf{J}^s \quad (4.5)$$

The above system of equations is discretized using a finite volume method on a staggered grid. The variables \mathbf{A} are located at the cell's faces and ϕ are located at the cell's center. The staggered grid implies that \mathbf{H} is measured at the cell's edges while \mathbf{J} (and therefore \mathbf{E}) is measured at the cell's faces as illustrated in Figure 4.1.

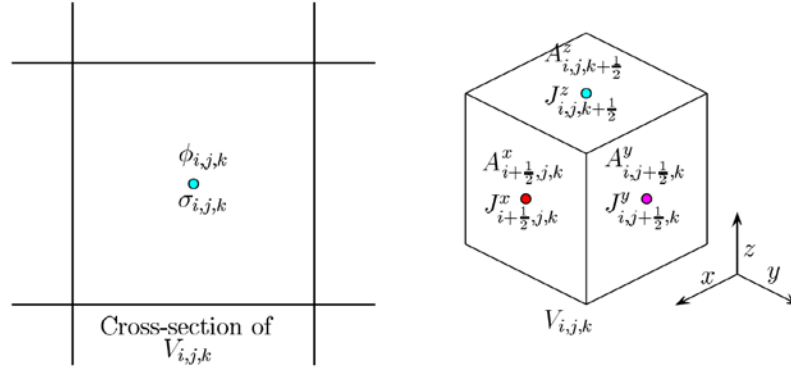


Figure 4.1. The staggered grid used in EH3D finite volume methods.

Consideration is required when designing the mesh to be used. In principle, a finer mesh will produce more accurate computed fields however the mesh size is also limited by computational resources. The area surrounding the target contains the finest mesh with the grid cells gradually becoming larger as we move away from the area of interest. It is necessary to extend the computational domain far beyond the area surrounding the target in order to minimize boundary condition effects. For the validation tests, a mesh with a spacing of 5cm was used for an inner core and the computation domain boundaries were set at 1000m.

The UBC-GIF EH3D codes have been successfully applied to a range of mineral exploration application (Oldenberg *et al.* 2007; Oldenberg *et al.* 2005). Because these codes also capture the physics associated with the electromagnetic response of a UXO

in the presence of an inducing field, we intend to downscale the associated geometries and use the EH3D codes to model the interaction of a UXO with its host medium. We focus on the frequency domain EH3D codes as they are currently the only version capable of handling complex susceptibility values. The range of frequencies selected for modeling was chosen based on typical frequency domain instruments employed for UXO surveying.

Prior to modeling any UXO-like targets, a variety of half-spaces with a range of conductivities were modeled using EH3D. These results were compared with analytical solutions for a loop above a half-space in order to validate the codes. The analytic expression for the radial component (H_ρ) and vertical component (H_z) of the secondary field at the center of a transmitting loop of radius a carrying a current I is well known:

$$H_\rho(\omega) = 0$$

$$H_z(\omega) = \frac{Ia}{2} \int_0^\infty \left[1 + \frac{P_{21}}{P_{11}} e^{-2\mu_o h} \right] \frac{\lambda^2}{\mu_o} J_1(\lambda a) d\lambda \quad (4.6)$$

where J_1 is a first order Bessel function and P_{11} , P_{21} are propagator matrices obtained in the solution for horizontal and vertical dipoles over a conductive and magnetically permeable half-space. Further details on this solution can be found in, for example, Pasion⁹.

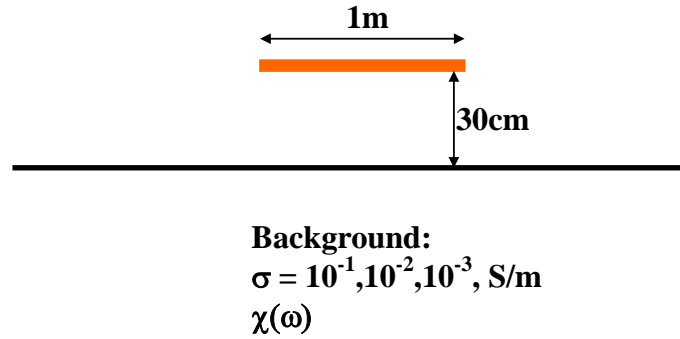


Figure 4.2. The environment modeled in EH3D for validation tests.

A schematic for the EH3D models run during the validation process is illustrated in Figure 4.2. A current source consisting of a 1 m square loop was assumed. Conductivities for the background ranged from 10^{-1} to 10^{-3} S/m. Excellent agreement was found between the analytical response and the EH3D modeled responses for half-spaces over the range of conductivities.

In order to validate the EH3D codes for a half-space environment containing complex susceptibility, an analytical solution was calculated and the results are compared in Figure 4.3. EH3D input files allow the user to specify real and imaginary susceptibility values at each frequency being modeled. Susceptibility values were based on

measurements made at Kaho'olawe, Hawaii. The results were also plotted for a half-space of conductivity 0.1 S/m but with susceptibility values set to zero so that the complex susceptibility effects can be gauged. The susceptible half-space results produced by EH3D are in excellent agreement with the analytic solution. The susceptible half-space also levels off at lower frequencies as the resistive limit is approached and the magnetic response becomes more important while the half-space without complex conductivities continues to fall off at lower frequencies as expected for a purely conductive response.

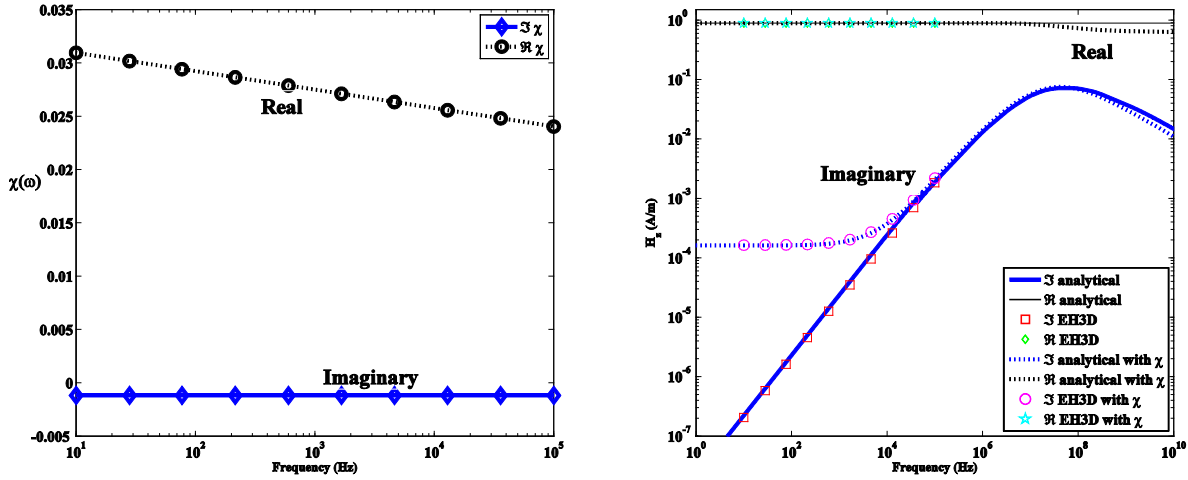


Figure 4.3. EH3D correctly models the viscous remnant magnetization (VRM) response. Panel on the left shows the susceptibility values calculated based on soil measurements made at Kaho'olawe, Hawaii and the panel on the right illustrates both the analytical and EH3D solutions for a conductive only half-space and a conductive half-space with viscous remnant magnetism (VRM).

RESULTS 1: ADDITIVITY OF SOIL AND TARGET RESPONSES

Methods for subtracting the soil response from EMI data often assume that the response of a target in a half-space can be approximated well by adding the response of the target in free space to the response of the half-space, i.e.

$$\text{Response of a target in free space} = (\text{response of target in half-space}) - (\text{half-space response})$$

Das (2006) used an approximate technique to study the effect of the background host material on the response function (for example see Grant and West 1965) of a sphere. By using the Das technique, Pasion (2007) investigated the effect of the half-space using susceptibility values derived from Kaho'olawe Island soil samples. The extent to which the additive assumption is appropriate can only be rigorously tested through the numerical modeling of Maxwell's equations. Having found acceptable agreement between analytic and EH3D responses for half-spaces of varying conductivity, we use EH3D to study additivity by considering a compact target embedded in a half-space.

We chose to consider the highest conductivity ($\sigma=10^{-1}$ S/m) half-space. The UXO-like target and geometry modeled is specified in Figure 4.4. The target was simulated as a region with dimensions 10cm x 10cm x 20cm with a conductivity value of 10^4 S/m. This particular target has a low electromagnetic contrast with the background, because we wanted to investigate scenarios that would have a higher likelihood of producing greater interaction between the target and background. The target was centered beneath the transmit loop in a vertical orientation at a depth of 20cm below the surface.

In order to investigate the validity of the additivity assumption, we compare the response of a target in free space with a residual response obtained by subtracting the half-space response from that generated by the same target in a half-space as shown in Figure 4.5. All fields are obtained using EH3D. The frequency of 1668 hertz (Hz) was chosen to illustrate the additivity concepts of the field as this particular frequency was observed to produce more substantial variations in the H field around the target than other frequencies.

We now choose a point at the center of the loop and show results for both the real and imaginary components of each frequency modeled with EH3D. Again we compare soundings for the free space computed directly from EH3D with a derived half-space achieved by differencing the soundings extracted at the center of the loop for the EHD solutions obtained for the target in a half-space and the half-space only models. There is a small difference between the computed target in free space response and the derived response obtained by differencing the target in a half-space response with the half-space response. This discrepancy can be accounted for by adding a response for the soil that replaces the target when calculating the derived free space response. This concept is illustrated in Figure 4.6. After taking into account this contribution from the extra soil occupying the target void, the agreement is excellent at all frequencies as shown in the bottom two panels of Figure 4.7. Additivity would be expected for the high contrast in electromagnetic properties that are typical of UXO (conductivity $>10^6$ S/m, susceptibility > 100). Even with the low contrast in conductivity and susceptibility between host and target considered here, no interactions between host and target were observed. We conclude that additivity is valid for the model considered (a compact target within a host that has viscous remnant magnetic as well as conductivity). Thus processing that involves subtracting a background EM response from the data to produce a response that can be modeled as a UXO in free space is a reasonable procedure.

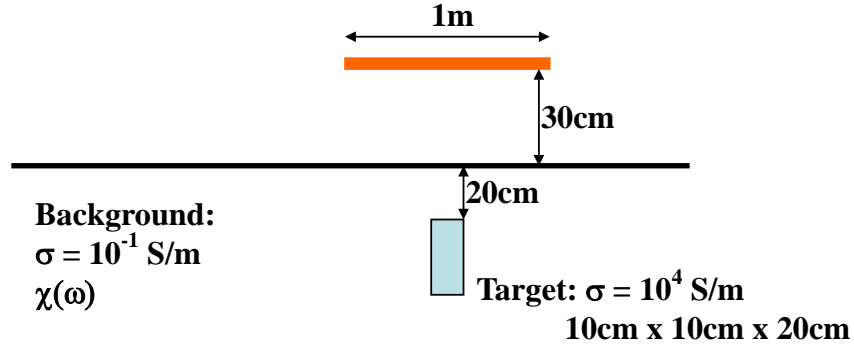


Figure 4.4. The environment modeled in EH3D for additivity tests.

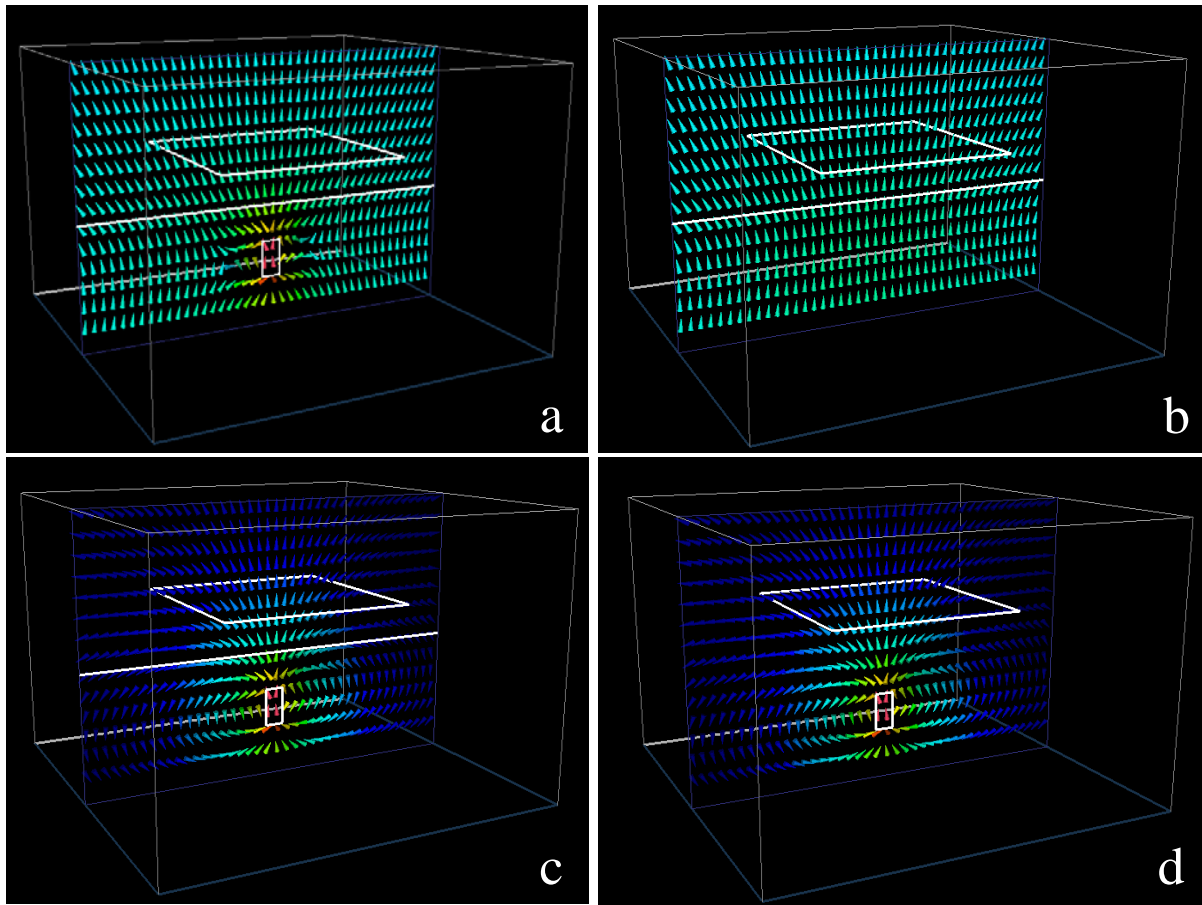


Figure 4.5. Additivity illustrated through the imaginary component of the H field at 1668 Hz. Panel (a) shows the EH3D response generated for a target in a half-space, (b) the EH3D response for a half-space. Panel (c) displays the derived target in free space response obtained by differencing the top 2 panel responses. Finally, panel (d) displays the EH3D response for a target in a free space which is virtually identical to the adjacent derived response of panel (c). All four panels shown have identical limits on color scale. Half-space results used were the 0.1 S/m case.

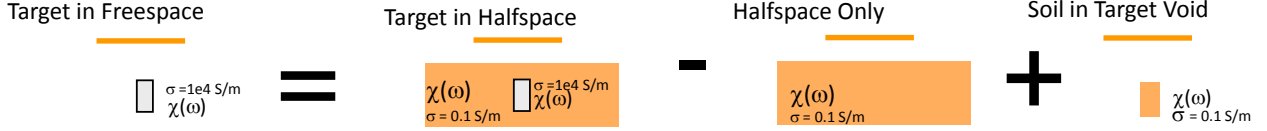


Figure 4.6. Additivity is examined by comparing the response computed for a target in free space with a derived free space response obtained by differencing a target in half space response with a half-space response. There is a small difference between these computed and derived free space solutions due to the soil response from the target void. The error due to the void will be extremely small when compared to target responses for electromagnetic properties that are typical of UXO ($\sigma > 10^6 \text{ S/m}$, $\chi > 100$) but for the low contrast case here ($\sigma = 10^4 \text{ S/m}$, $\chi = 0.1$) it is more substantial.

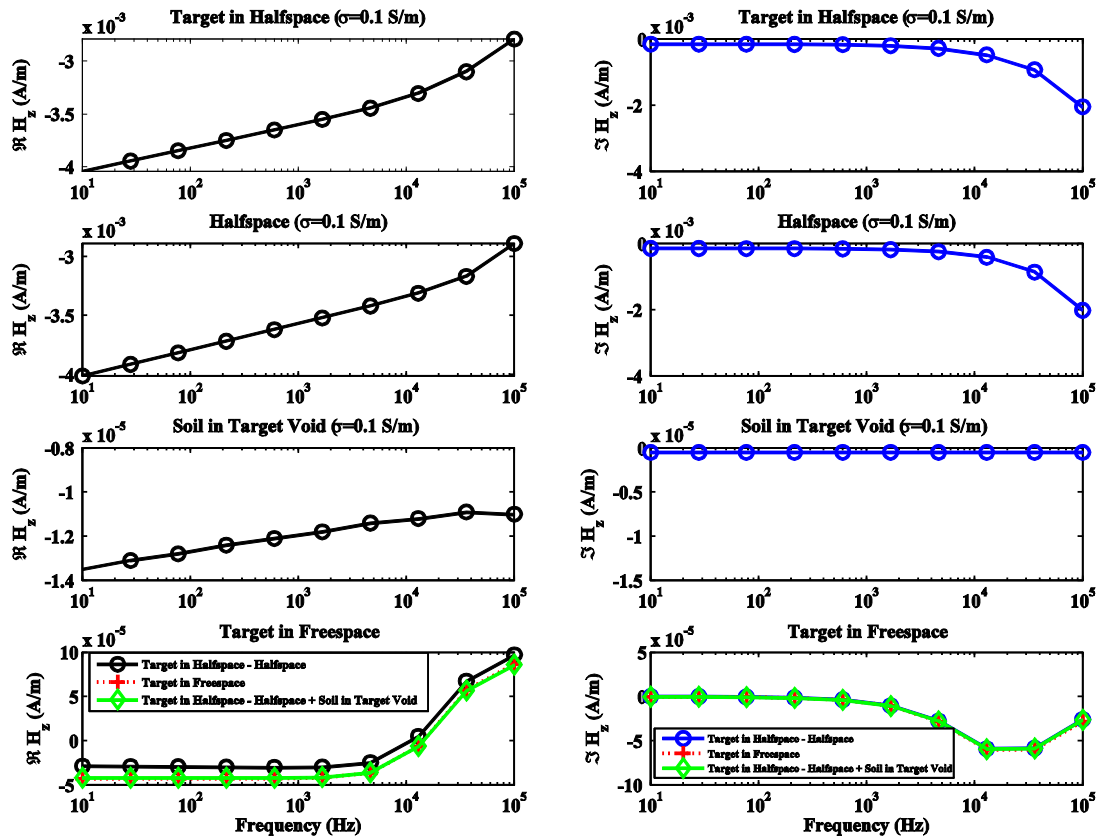


Figure 4.7. Real and imaginary values of the H field for all frequencies modeled in EH3D with a target in a conductive half-space with viscous remnant magnetism (VRM) (top 2 panels) and a half-space with VRM (second row 2 panels). The third row of two panels plots the response due to soil replacing the target volume in free space. The bottom 2 panels plot the derived target in free space solution obtained by differencing the soundings at the center of the loop between the top row of panels and the middle row of panels. The EH3D computed solution for a target in free space is also plotted in the bottom row panels.

RESULTS 2: STUDYING THE EFFECT OF SMALL SCALE TOPOGRAPHY

The next modeling effort was to determine if it is possible to model simple bumps and trenches to quantify the effects of EMI measurements made over a rough surface in environments with magnetic soil.

NUMERICAL MODELING SIMPLE TOPOGRAPHY: COMPARISON WITH FIELD DATA

To establish the validity of modeling small scale topographic features with EH3D, we model a simple bump and trench of dimensions that approximate targets over which field data was acquired using the Man Portable Vector (MPV) sensor. The MPV is a multi-axis, man-portable, ultra-wideband EMI sensor designed for cued interrogation of anomalies. MPV-MARK 1 data were acquired at the Sky Research test plot in Ashland, OR. The site is well characterized having been surveyed with numerous geophysical sensors and the soil has been sampled and analyzed. EH3D is capable of modeling a complex multi-receiver geometry in a relatively straightforward manner because receiver locations can be specified at any location within the computational domain. A number of EH3D runs were completed at varying transmitter offsets to simulate a profile line of data over the trench and bump targets.

The trench and the divot were modeled in EH3D using the schematic shown in Figure 4.8 and Figure 4.9. A current source consisting of a 64 cm square loop was assumed. The MPV-MARK 1 transmitter is composed of two circular loops but for modeling purposes, a square loop with an equivalent moment was assumed. Conductivities for the background were set at 10^{-2} S/m. A bump target was simulated by placing a region of dimensions 10cm x 12cm x 120cm with a conductivity value of 10^{-2} S/m on top of the half-space (Figure 4.8). The trench target was simulated by creating a volume of dimensions 10cm x 12cm x 120cm with a conductivity value of 10^{-9} S/m below the surface of the half-space (Figure 4.9). The bump and trench targets were placed in the center of the computation domain and the transmit loop was moved through a series of offsets to simulate collection of an MPV-MARK 1 survey line collected across the trench or bump. Results are shown for the MPV-MARK 1 receiver located at the center of the transmitter loop to match the geometry of the modeled scenarios. Figures 4.8 and 4.9 illustrate excellent agreement when comparing the EH3D modeling results with data collected using the Man Portable Vector (MPV) sensor.

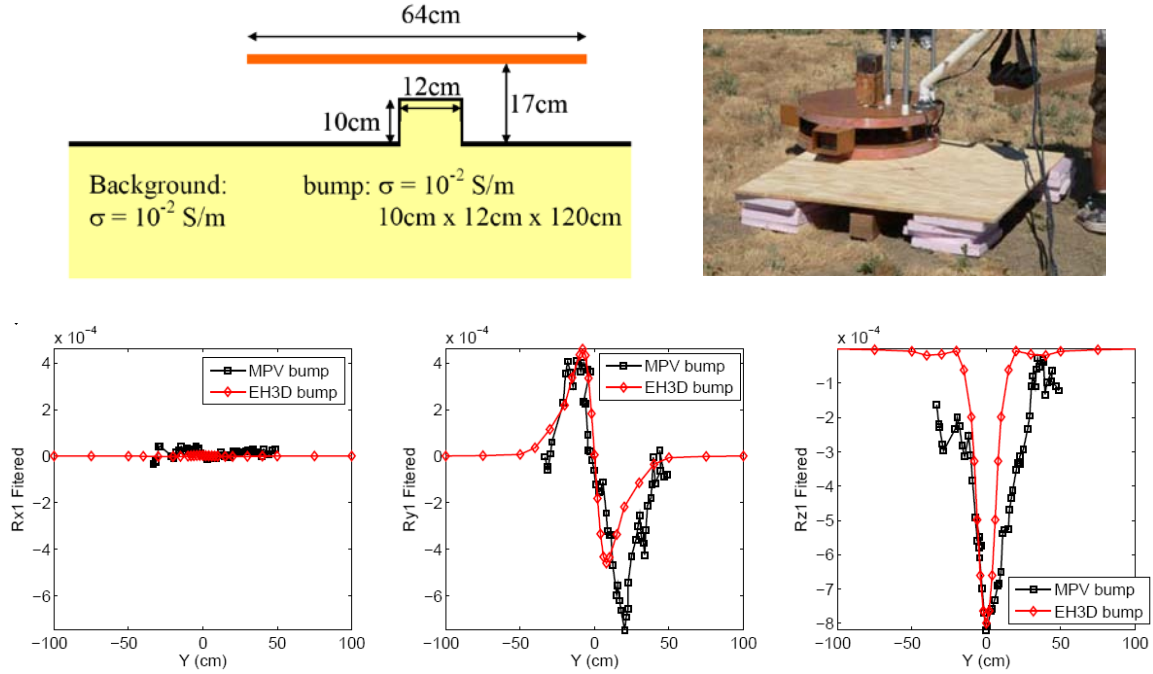


Figure 4.8. EH3D results for modeling MPV-MARK 1 data acquired over a single bump. The upper left panel illustrates the environment modeled in EH3D. The upper right panel shows the MPV-MARK 1 acquiring data over the single bump target. The bottom row of plots shows the three components of the fields both measured with the MPV-MARK 1 and modeled using EH3D.

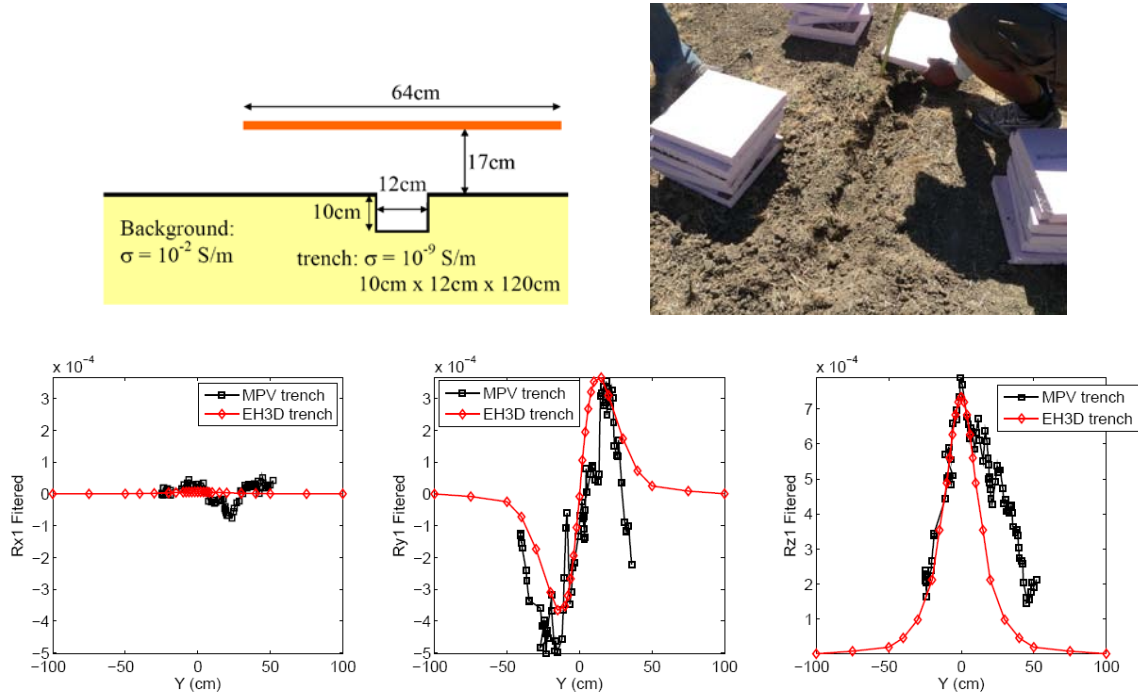


Figure 4.9. EH3D results for modeling MPV-MARK 1 data acquired over a single trench. The upper left panel illustrates the environment modeled in EH3D. The upper right panel shows the single trench target. The bottom row of plots shows the three components of the fields both measured with the MPV-MARK 1 and modeled using EH3D.

4.3 MODELING SIMPLE TOPOGRAPHY: BUMP AND TRENCH OF VARYING SIZE

Detection and identification of UXO at sites with large geologic background signals can be very difficult. In locations where the soil is especially problematic, system responses from local geology can be of the same order as signals due to UXO. Even at sites where the soil is more hospitable, attempts to apply discrimination techniques can be hampered by geology. In order to investigate these effects, two simple geologic scenarios were modeled with EH3D, a bump and a trench as depicted in Figure 4.10. A series of bumps and trenches each 50 cm long and with varying cross sections (6, 10, 12, 14, 18cm square) were modeled. For each scenario, the EH3D codes were run at a range of offsets to simulate a profile line of data crossing directly over the geologic target.

Results for the modeled bumps and trenches are shown in Figure 4.11. The modeled response increases for both the bump and the trench as the cross sectional dimensions are increased from 6cm square up to 18cm square. The peak amplitudes for the bump exceed those of the trench which is expected since the bump target places additional background material in closer proximity to the sensor. The shape of the modeled H_z responses is also narrower for the bump targets, again a consequence of the sensor effectively being placed closer to the target, in this case the bump.

In order to further investigate the effects of loops size relative to small scale geology on EM measurements, a number of simple bumps and trenches of increasing dimensions were modeled with both 40cm and 1m square loops. Both of the loops were located at a height of 30cm above the surface. In order to determine the contribution from the bump/trench itself, a half-space was also run and the half-space results were subtracted from the run for a bump/trench on the surface of a half-space to produce the results due to the bumps and trenches shown in Figure 4.12. The response from the trench is an order of magnitude less than the response of the bump, a result of the magnetic material being closer to the sensor for the bump case and hence producing a stronger response. The bump response observed for the 40cm loop is slightly larger than that produced by modeling the same environment with a 1m loop. The induced currents in the bump are going to be long extended loops in horizontal planes because of the orientation of the transmitter loop giving a magnetic field that is mostly vertical. The pattern of the current loops in the bump are almost completely a result of the geometry of the bump, and not much to do with the exact size of the transmitter loop. Also, for the two different sizes of transmitter loops, because the current is the same in both, there's the same number of magnetic field lines passing through each loop. But these lines for the smaller loop are concentrated in a smaller area. So for the smaller loop there's a more intense magnetic field when crossing the bump.

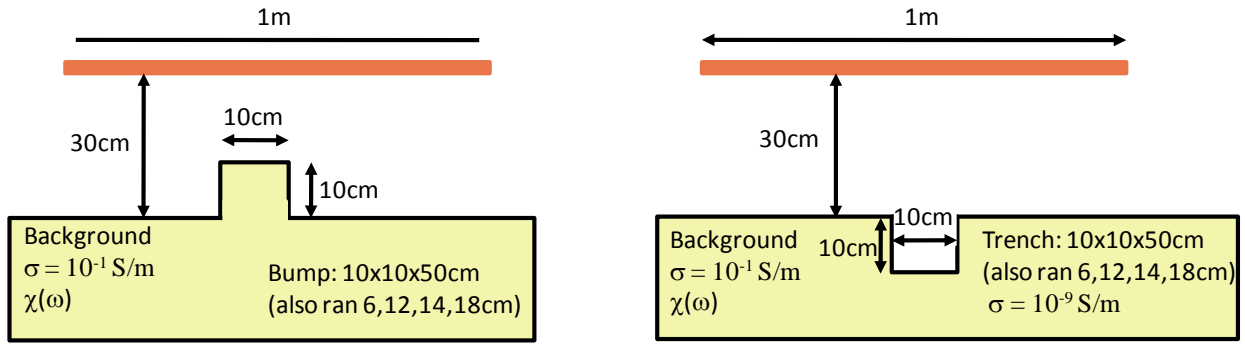


Figure 4.10. EH3D model environment for two simple variations in topography including a bump (left panel) and trench (right panel).

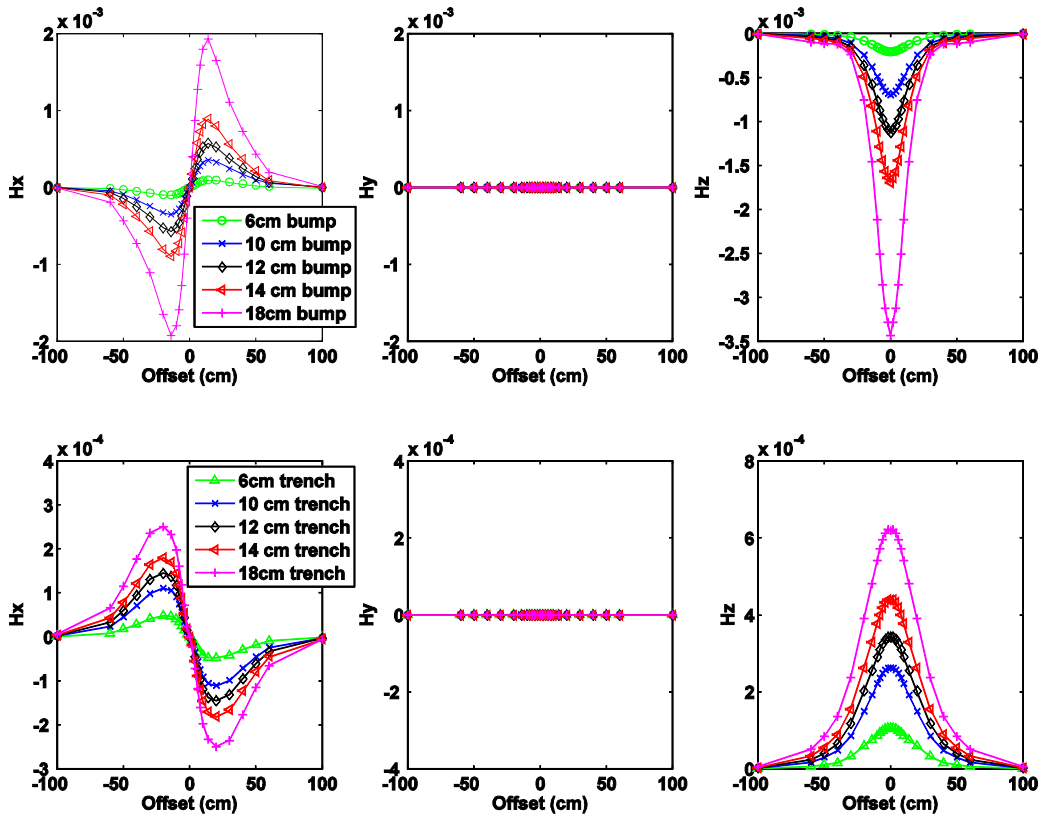


Figure 4.11. EH3D results for modeling simple geologic variations. The top three panels illustrate the three components of the H fields for a series of bumps of increasing size. The bottom three panels the same fields for trenches of increasing dimensions. Physical properties and dimensions used for the modeling are described in Figure 4.10.

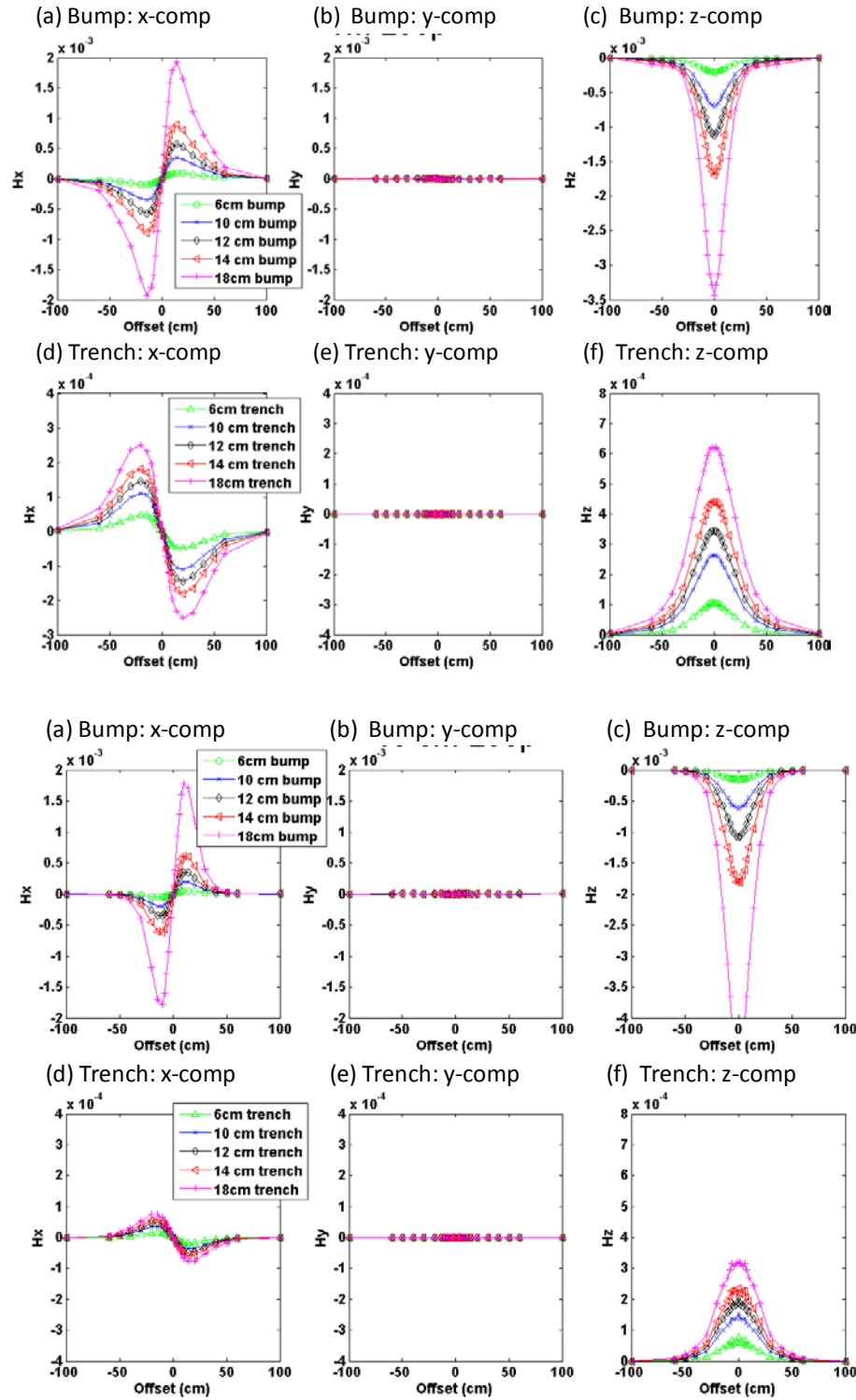


Figure 4.12. Plots comparing the simulated profiles over bumps and trenches for a 1m loop and 40cm loop. Y axes in the 40cm loop plots forced to match those of the 1m plots to help comparing the two loop sizes.

MODELING EXAMPLE: TEMTADS DATA

Having obtained confidence in the code's capability to numerically compute the effects of complex magnetic susceptibility and topography, attempts were made to model sensor types beyond a simple single loop configuration. In Figure 4.14, the variation in modeled response is shown for a single bump of dimensions 14cm x 14cm x 50cm centered in the middle of a sensor comprised of twenty five 40cm coincident receivers and transmitters in a 5 by 5 configuration (similar to the TEMTADS EMI array) as depicted in Figure 4.13. This result indicates that the subtle effects of a simple change in geology represented by a magnetic soil can be modeled for next generation sensors using the EH3D code.

EH3D was also utilized to investigate soil effects observed in TEMTADS data acquired at San Luis Obispo (SLO) as part of ESTCP 0504. In the QC of data it was observed that data which was attributed to a soil response (and confirmed as No Contact in the groundtruth) was characterized by the mimicking of a sensor response to the Tx location firing. Results are shown for a 4.2 inch mortar (item 965) and a "No Contact" cell (item 1166) in Figure 4.15. When there is a large target present such as the case with the 4.2 inch mortar, the effects of soil are not immediately apparent as the strong return from the target is the dominant response. For the "No Contact" cell, the observed response is presumed to be due to soil. The plan map images show that the observed response is focused around the Tx locations. This is expected because without a large metallic target present, the recorded response will be entirely due to the soil. Any magnetic effects of the soil are expected to be strongest nearest the receivers closest to the Transmitter firing.

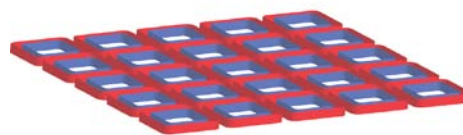


Figure 4.13. TEMTADS EMI Array. The TEMTADS array consists of a 25 transmitters with a receiver at the center of each transmitter. The transmitter fire sequentially and each of the 25 receivers record the secondary field, resulting in a total of 625 soundings measured.

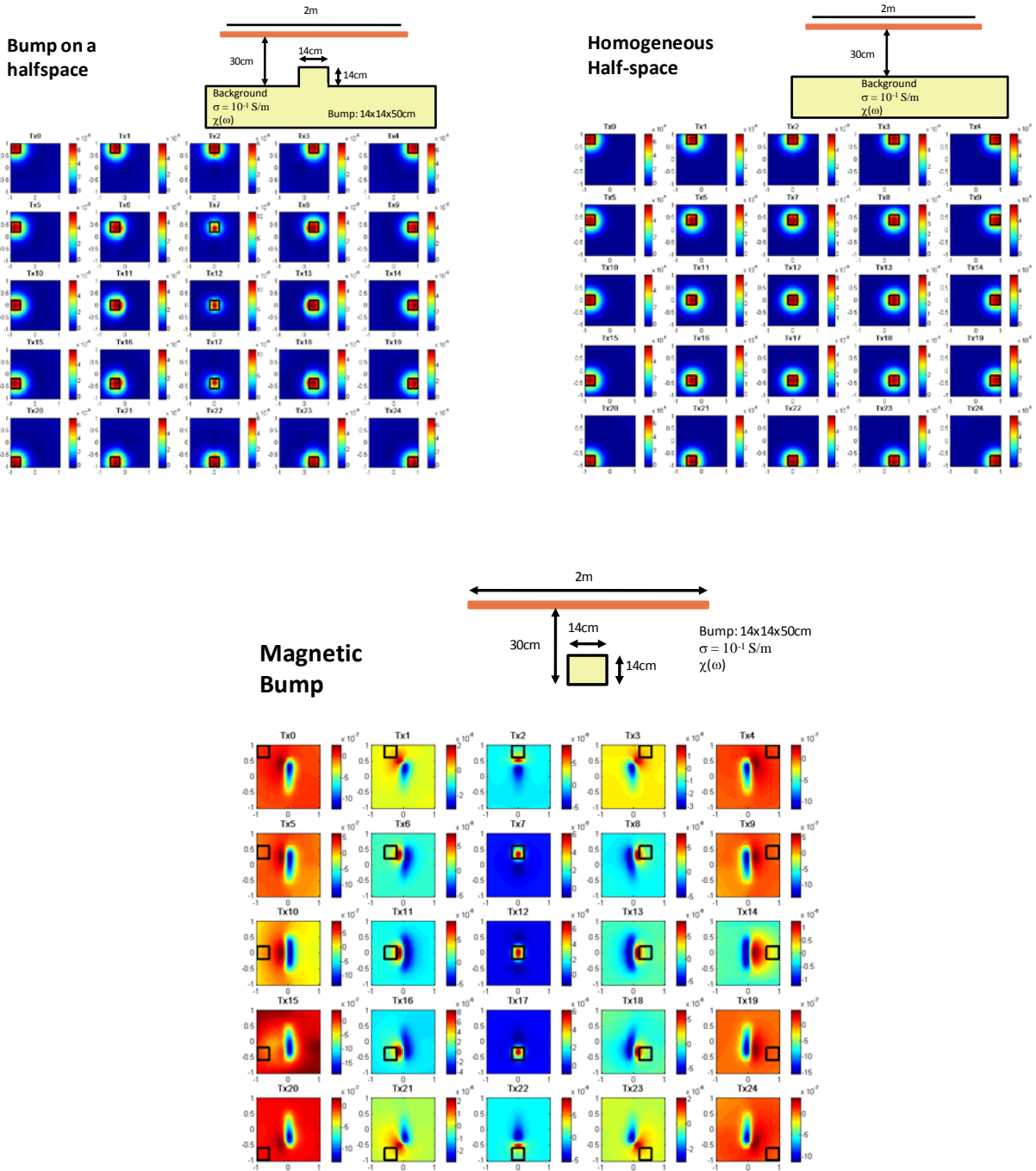


Figure 4.14. EH3D results for three different Tx locations over a bump. Modeled sensor was comprised of 5 x 5 array of 40cm square loops with coincident Tx/Rx. The Tx locations are overlaid on the images of the real part of H. Tx locations correspond to center, middle right and lower right Rx/Tx loops. Target was a bump of dimensions 14cm x 14cm x 50cm.

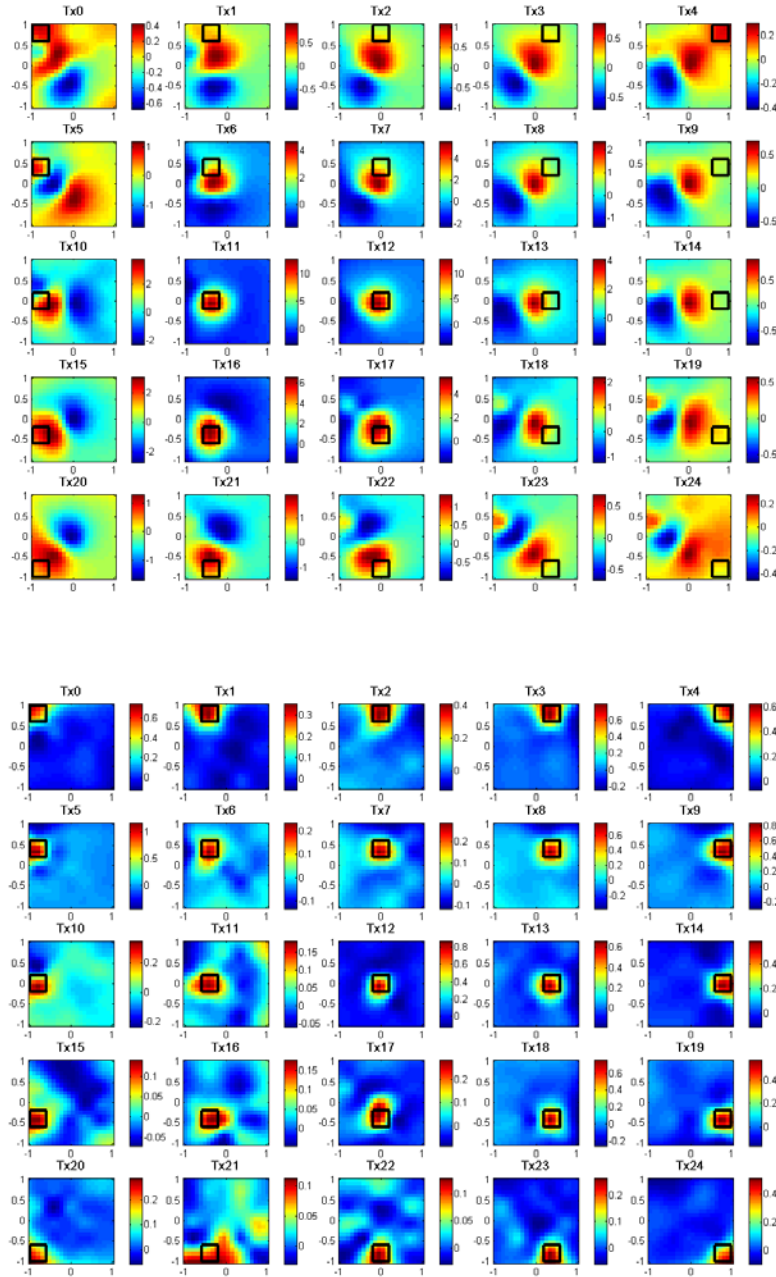


Figure 4.15. TEMTADS data from SLO illustrating the difference between the observed response for a significant metallic target, a 4.2 inch mortar (on top) and a no contact cell presumed to be due to soil effects (on bottom).

SIMULATIONS FOR TESTING THE EFFECT OF TOPOGRAPHY ON DISCRIMINATION

Once we verified our ability to model topography using EH3D, we proceeded with using simulations to study the impact of topography on recovering dipole polarizabilities. For this example, we test the ability to recover polarizabilities of targets buried underneath a mound of magnetic soil. For this example, we choose an aluminum 40 mm projectile and a 37 mm projectile for targets. Figure 4.16(a) has a sketch of the projectile and bump geometry. The 40 mm projectile is buried in a random orientation at a depth of 15 cm, and the 37 mm projectile is buried in a random orientation at a depth of 20 cm.

The MPV Mark1 data is acquired in a saw-tooth pattern over a 50 cm by 50 cm area (Figure 4.16(c)). A random error with a standard deviation of 0.5 cm is added to the position data, and a random error of 0.5 degrees is added to the orientation data. Data from the first time channel for the three components of the secondary field measured by the central receiver is shown in Figure 4.16(c) for one of the 100 realizations. Added to the target's dipole response is the response from a mound of magnetic dirt Figure 4.16(d). The mound is 14 cm tall x 14 cm wide x 50 cm long and oriented North-South. We do not include the response of the magnetic soil half-space. By omitting the half-space response, we are assuming perfect subtraction of the background not related to the mound of dirt. For the simulations, we model three levels of magnetic soil signal strength: (1) no magnetic soil (i.e. target only), (2) magnetic soil response approximately equal to that at the Sky Research hangar (low magnetic soil noise), and (3) magnetic soil response slightly larger than the Cambodian soil pit at the DRDC magnetic soil test site (larger magnetic soil noise). The data from the mound or dirt is shown in Figure 4.16(e). The response clearly indicates the North-South strike of the mound.

The simulated data are inverted for dipole polarizabilities. Figure 4.17 plots the recovered polarizabilities for the 40 mm projectile buried beneath a mound with the three different levels of magnetic soil strength. Figure 4.17(a)-(c) plot the three recovered principle polarizabilities, with the primary polarizability plotted in red, the secondary polarizability in green, and the tertiary polarizability in blue. Since the 40 mm projectile is rod-like and aluminum, there are two larger and equal polarizabilities and one smaller polarizability. This is seen for the case of no magnetic soil present. At late times the recovered polarizabilities are not well constrained due to a low signal to noise ratio. When the soil mound has magnetic properties comparable to that found in Ashland (Figure 4.17(b)), we see that the ability to recover shape is lost since the primary and secondary polarizabilities are no longer equal. In addition, the recovered polarizabilities appear to deviate from the true polarizabilities (plotted as a black and white dashed line) at early and late time. At late times the recovered polarizabilities have the decay rate that is characteristic of viscous remnant magnetization. This effect is even more prominent in Figure 4.17(c), where the results of having a soil mound with the magnetic properties slightly greater than those found at the DRDC Cambodian soil pit. At late time there is a clear deviation from the

polarizabilities of a 40 mm projectile, to a target with a decay that is characteristic of viscous remnant magnetization. Figure 4.17(d)-(f) plots the recovered total polarizabilities (or trace of the polarizability matrix) for the different levels of mound magnetization. The total polarizability is nearly the same regardless of mound magnetization, and thus is a very robust feature to estimate in the presence of magnetic topography.

Figure 4.18 plots the recovered polarizabilities for a 37 mm projectile buried 20 cm below the surface. The recovered polarizabilities are not greatly affected by the magnetic mound. At the larger magnetic susceptibility level there is a slight deviation of the secondary polarizability (plotted in green, Figure 4.18(c)) from the true secondary polarizability due to the influence of the magnetic mound response. The total polarizability (Figure 4.18(d)-(f)) is very well constrained for all but the latest time channels.

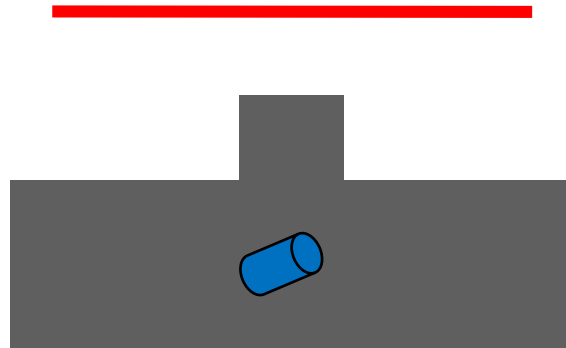
We have shown that a small targets could have their polarizabilities accurately estimated in the presence of relatively strong magnetic soil signals due topography. In particular, the total polarizability would be a very robust feature for inversion. We believe that the most significant factor to be modeled when considering magnetic soil noise is the signal due to variations in ground clearance and orientation variations.

SUMMARY

The ability to accurately forward model soil and UXO responses is a powerful tool, especially in scenarios where data can be degraded due to the presence of magnetic soils. We've been able to numerically compute in 3D the effects of complex magnetic susceptibility and find excellent agreement with analytic results. It was also confirmed that a compact target and a host soil that is complex susceptible as well as conductive can be treated as separate, additive responses. We modeled simple changes in topography which, in a magnetic soil environment, can lead to false positives if they are not accounted for. The potential for sensor characterization via forward modeling was also illustrated based on the agreement between data acquired over a simple bump and trench target using the MPV-MARK 1. The codes were also used to model a multi loop sensor similar to the TEMTADS and results modeled over small bumps were compared with "No Contact" (soil) responses from SLO.

Simulations were used to investigate the ability to estimate polarizabilities when a magnetic mound is in the near vicinity of the target. The numerical modeling code was used to generate responses of a magnetic mound of soil. These responses were added to dipole responses for a 37 mm and a 40 mm projectile, and subsequently inverted for dipole parameters. We found that even for relatively strong levels of viscous remnant magnetic soils (i.e. stronger than the VRM signal of the red Cambodian soils in Table 3.1), the polarizabilities of the targets are well constrained. The effect of magnetic topography is a much less significant effect to model than the

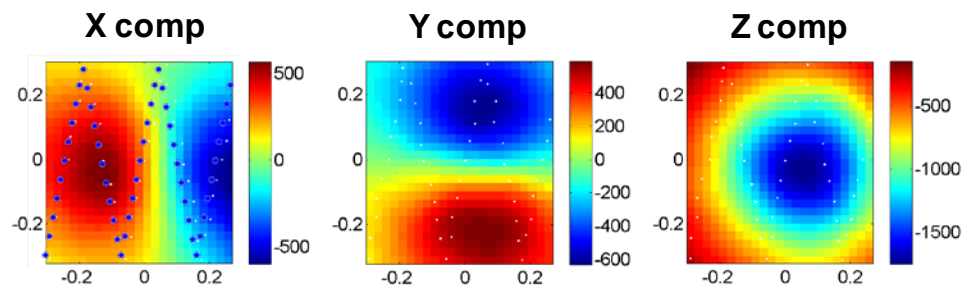
changes in signal to the changes in the sensor height and orientation relative to the ground.



(a) Target buried under a mound of dirt.



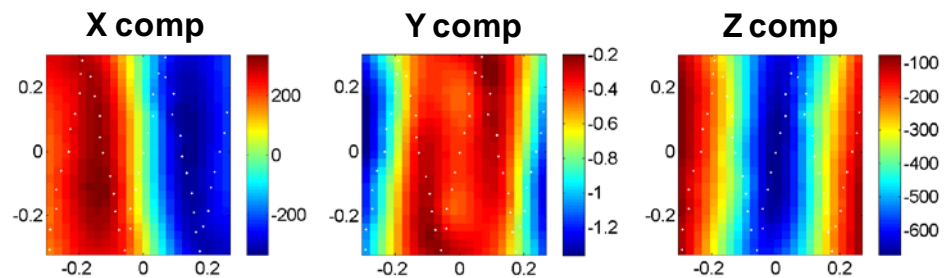
(b) 40 mm projectile



(c) Data measured by the center receiver



(d) Mound of dirt



(e) Data measured by the center receiver

Figure 4.16. Setup for testing effect of a mound of magnetic soil above a buried target. The mound runs North-South. The blue dots in (c) indicate the stations at which data soundings are acquired.

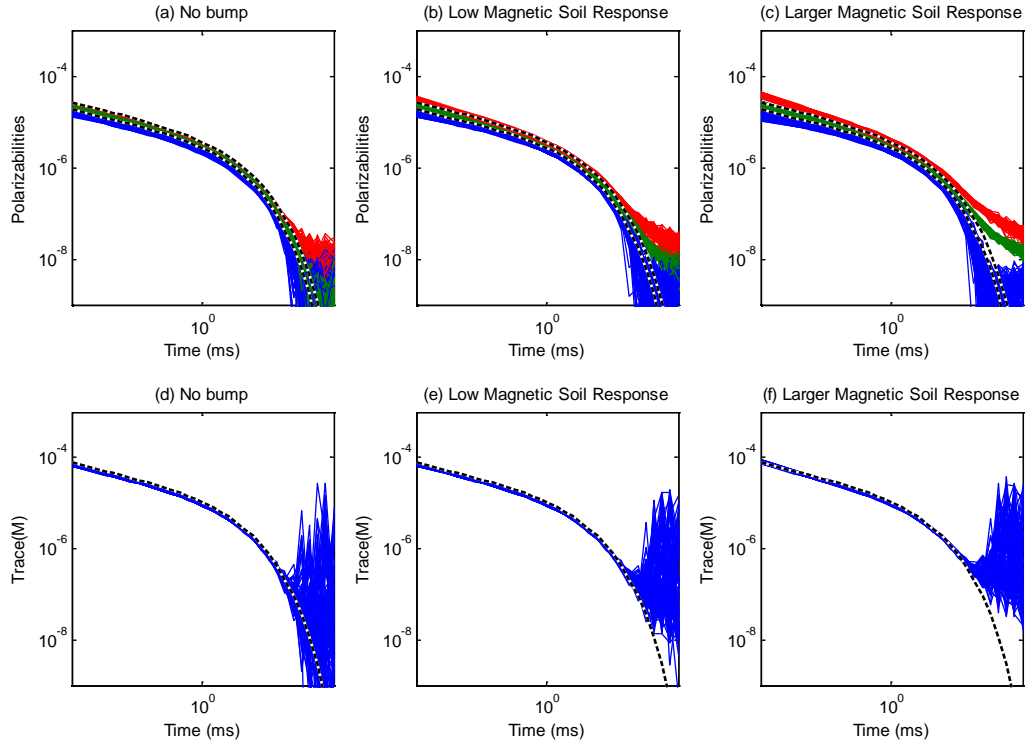


Figure 4.17. Recovered polarizabilities for a 40 mm projectile buried beneath a mound of magnetic soil.

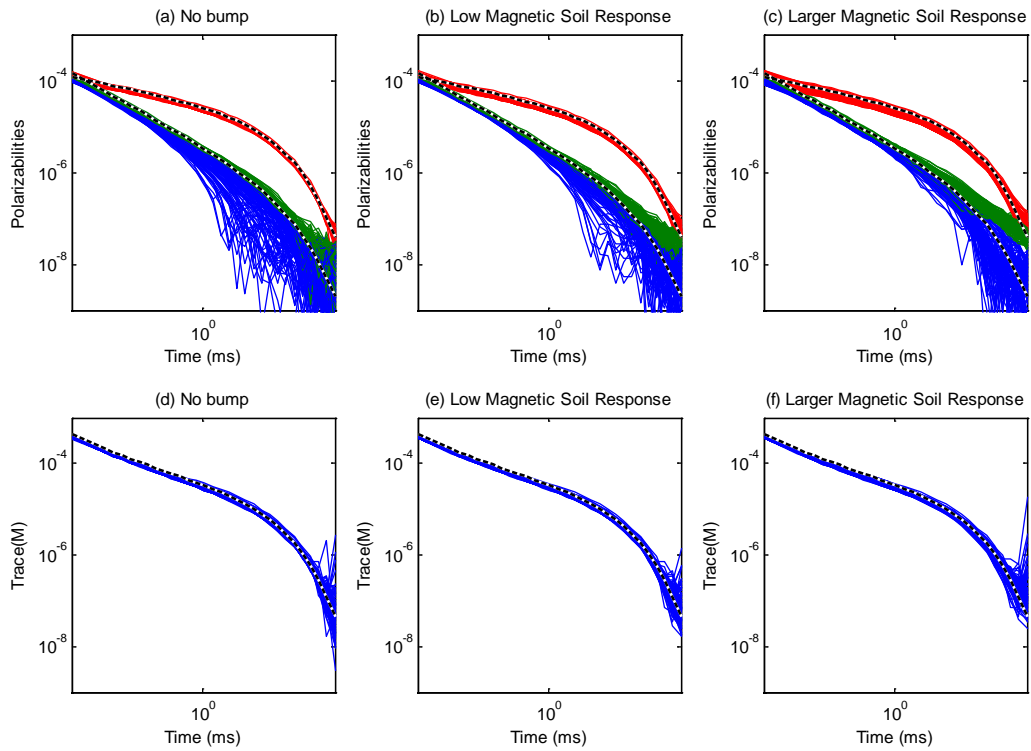


Figure 4.18. Recovered polarizabilities for a 37 mm projectile buried beneath a mound of magnetic soil.

5. MODELING THE BACKGROUND RESPONSE WITH DIPOLE SOURCES

Dynamically acquired, full coverage MetalMapper data were acquired as part of the ESTCP Live-Site Demo at Camp Butner (Figure 5.1). When collecting data in dynamic mode, the MetalMapper only fires the vertical component transmitters but still records all 3 components of the secondary field with the seven receivers. Regions of elevated soil response were observed in the dynamic MetalMapper data collected at Camp Butner. This response appears in the vertical components of the response. Figure 5.2 show gridded images of the different MetalMapper components and, for comparison, an image of the leveled EM61 cart full coverage data. Not surprisingly, the horizontal components of the data are minimally affected by the soil. In order to minimize the effect of the magnetic soils, we used the horizontal components only for inversions.

Figure 5.3(a) plots the anomalies picked using the Geonics EM61 data. At each of these anomalies, cued interrogation MetalMapper data were acquired. We inverted these data using a single source and a two source inversion algorithm. We noticed that for many of the anomalies we were recovering targets with depths greater than 40 cm and with polarizabilities similar to the M48 fuzes found on site. When the locations of these anomalies are plotted on the grid, we see that they correlate to regions of higher magnetic soil response. The deeper sources with M48 polarizabilities were modeling the magnetic soil response.

Figure 5.4 contains recovered polarizabilities for anomalies A, B, and C indicated in Figure 5.3. On the left is the recovered polarizability. The center panel indicates the location of the anomaly in size/decay feature space with a yellow circle. On the right is a plot of the predicted source location and depth. Anomalies A and C (Targets 2362 and 3879, respectively) are small scrap items and anomaly B is an empty hole. In each case a source is estimated that is approximately 50 cm deep with the polarizabilities of an M48 fuse. This source models the background response.

These results suggest that it might be possible to represent the background soil response with dipole sources. In the following sections we investigate the use of a multi-dipole source inversion to model both target and background response. By modeling the background separately with an additional source, we investigate if the source modeling the target has improved recovery of target polarizabilities. We test this method using Geonics EM63 data and MetalMapper data.



Figure 5.1. The MetalMapper (left) and Geonics EM61 (right) at Camp Butner.

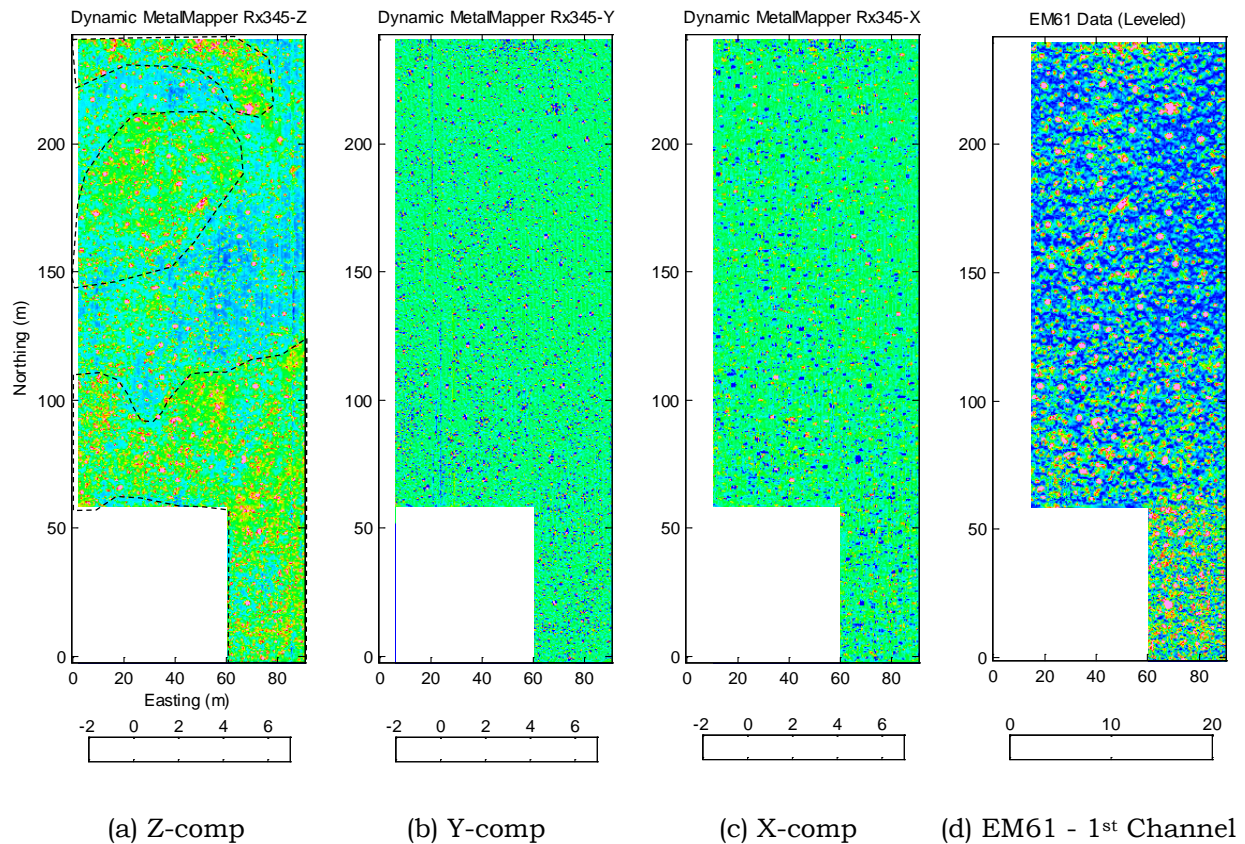


Figure 5.2. Dynamic MetalMapper data and Geonics EM61 data acquired at Camp Butner. Only the middle 3 receivers of the MetalMapper are gridded above. The black dashed lines in (a) highlight the elevated levels of magnetic soil response at the site. The horizontal components of the signal are unaffected by the magnetic soils (gridded in (b) and (c)). The Geonics EM61 data in (d) were leveled using a demedian filter.

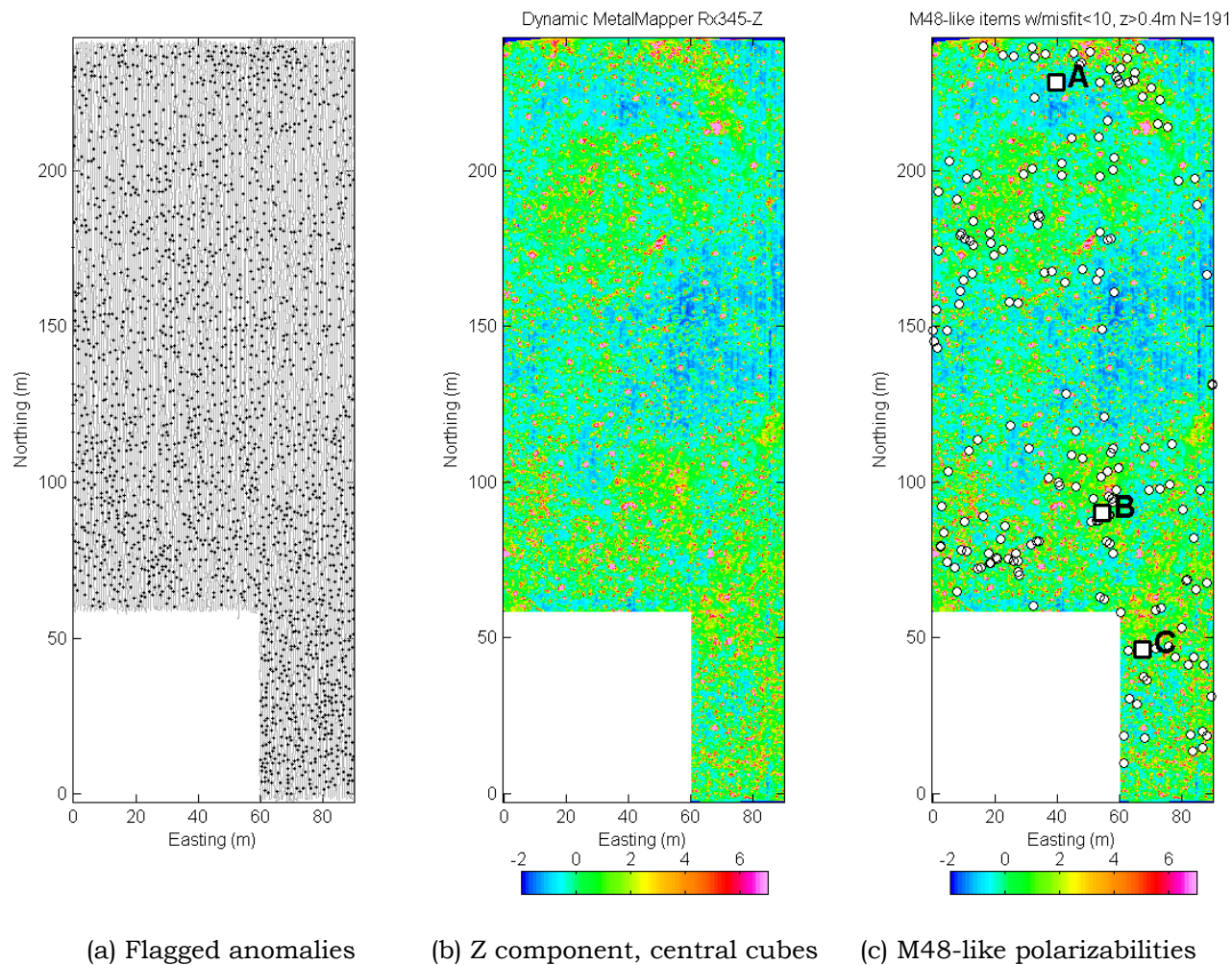


Figure 5.3. Flagged anomalies for the Camp Butner site are shown in (a). The anomalies that produced estimated polarizabilities that are similar to the characteristic M48 polarizabilities and estimated depths greater than 40 cm are plotted in (c).

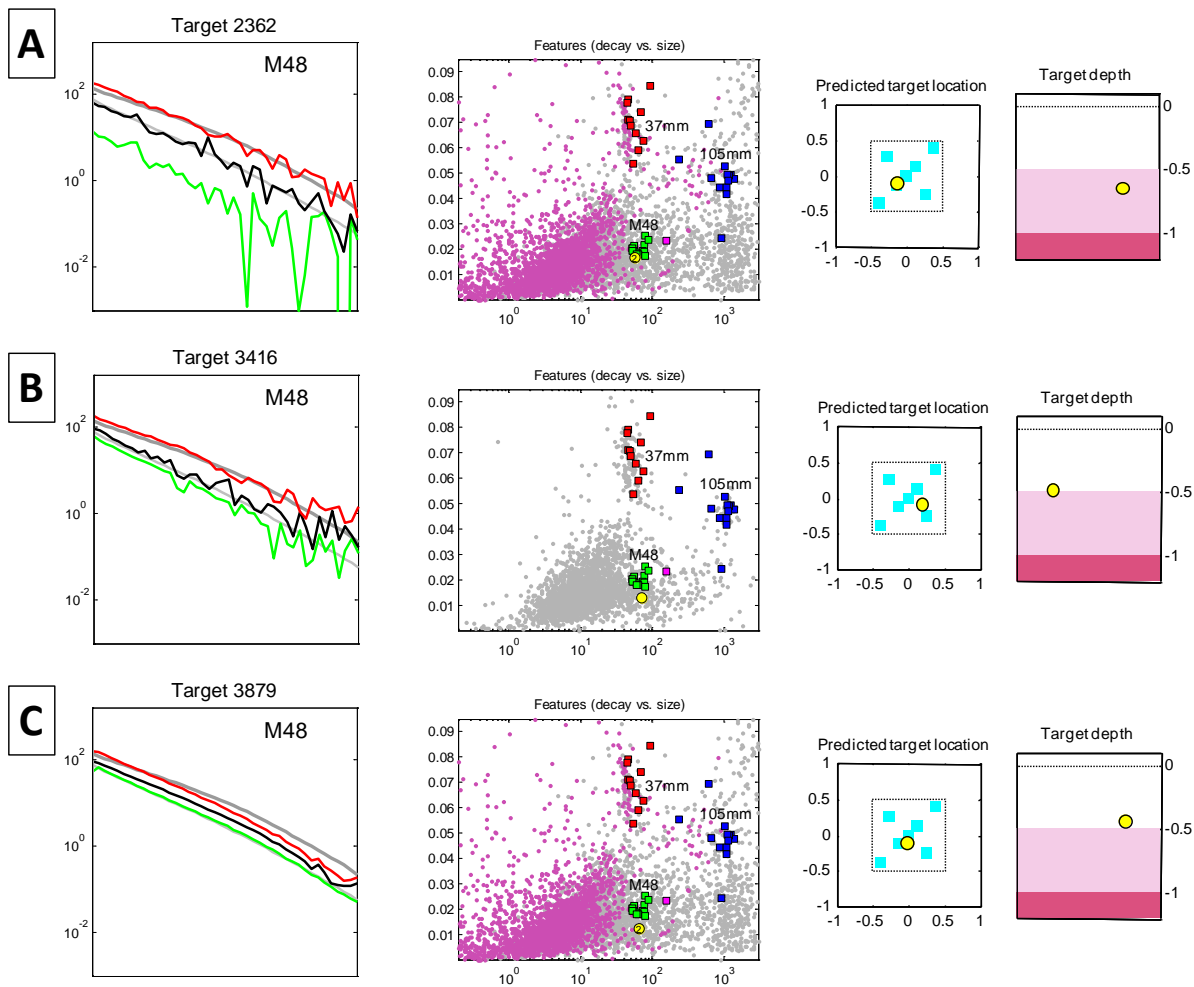


Figure 5.4. Examples of M48 type polarizabilities recovered from cued MetalMapper acquired at Camp Butner. The locations of the three anomalies are indicated in Figure 5.3. On the left is the recovered polarizability. The center panel indicates the location of the anomaly in size/decay feature space with a yellow circle. For the size/decay plot, the x axis has the size which is defined as the integrated value of the total polarizability, and the decay rate - ratio of total polarizability at early and late time - is plotted on the y axis. On the right is the predicted source location and depth. In each case the source depth is approximately 50 cm.

CAMP SIBERT EM63 MULTI OBJECT INVERSION

Multi Object inversions were examined with the intention of improving the single object inversion results in areas where there is a background soil response. The investigation would treat the target and the soil responses as separate, additive responses with one dipole of the multi object inversion representing the target and another representing the soil response. As an initial investigation, items from the Camp Sibert GPO (Figure 5.5) were inverted with both a single object and a two object inversion.

Recovered polarizabilities for single object and two object inversions of 4.2 inch mortars at Camp Sibert GPO are compared in Figure 5.6. The multi object inversions do a better job of constraining the recovered polarizabilities. In setting up the multi object inversion, one of the dipoles was constrained to be deep and in doing so the deeper dipole effectively modeled the soil response while the unconstrained second dipole modeled the target response. The single object polarizabilities which deviate furthest from the reference polarizability for the 4.2 inch mortar correspond to targets with a significant background soil response. The success of the multi object inversions in modeling a background soil response for the GPO data led to further investigations on some cued targets from the Camp Sibert field data.

The field data was examined and two cued targets were chosen for further analysis. The first item, target 852 was a pair of pliers. The topography around this target included a bump that raised the sensor further from the surface and created a low amplitude region in the recorded data as shown in Figure 5.7. Selecting a larger mask allows both a representative background response and the target to be contained within the mask. However, a mask that includes the response resulting from topographical changes over the survey area for target 852 was problematic for a single object inversion and could potentially benefit from one of two approaches:

1. A multi object (2 or 3) inversion which simultaneously fits the target of interest with one dipole and additional dipole(s) used to fit the background soil response.
2. Modeling the soil response (either as a single, 2 or 3 object inversion) using an exclusive mask to isolate the background soil response then subsequently removing the background soil response and reinverting the (background soil removed) target response as a single object inversion.

MODELING BACKGROUND, REMOVING BACKGROUND, SINGLE OBJECT TARGET INVERSION

The background soil response was modeled with a single, two object, and three object inversion. Results for these backgrounds are illustrated in the inversion results shown in the top rows of Figures 5.8 to 5.10. An exclusive mask was used around the target response in an attempt to model only the background response. For the two object inversion, one of the dipoles was constrained to be deep (i.e. between 5m and 10m)

and for the three dipole inversion, 2 of the dipoles were constrained to be deep in attempts to model the soil response as a deep dipole(s).

Modeling the background soil response with a single dipole (Figure 5.8) does produce a background response with a slightly lower amplitude in the region where the topography lifted the sensor and produced a lower amplitude in the recorded data. The two and three dipole backgrounds (Figures 5.9 and 5.10, respectively) produce a slightly better fit to the topography induced response in the background.

The main difficulty in removing the modeled background response from the data prior to inverting for the target response is the use of the exclusive mask in calculating the background. Because the data within the mask is not constrained, the modeled response of the background tends to overestimate the data within the mask and the background removal also tends to eliminate part of the target response. This is evident in comparing the observed and residual plots for each of the three backgrounds calculated (single, 2 object, 3 object) where the residual target response is smaller than the observed response. In inverting the background removed response with a single object inversion (bottom row of Figure 5.8) it is also evident from the substantial residual that the background removal process has also affected the target response. Comparing the background removed inversions of Figures 5.8 to 5.10 with the approach in Figure 5.11 which illustrates a 3 object inversion that simultaneously inverts for background and target response with two dipoles forced deep (between 5 and 10m) to model the background response suggests that the all at once method is better. Figure 5.13 shows improvements in the recovered secondary polarizabilities with the methods that don't remove background response prior to inverting.

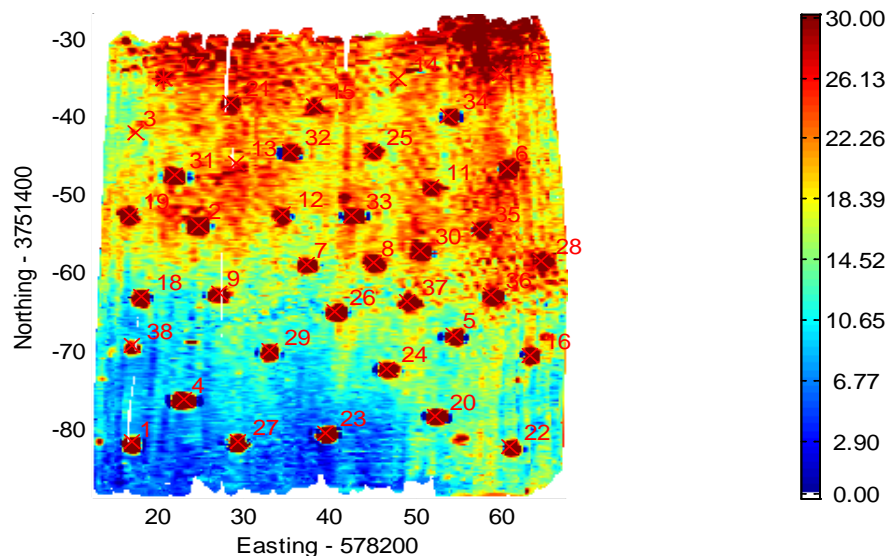
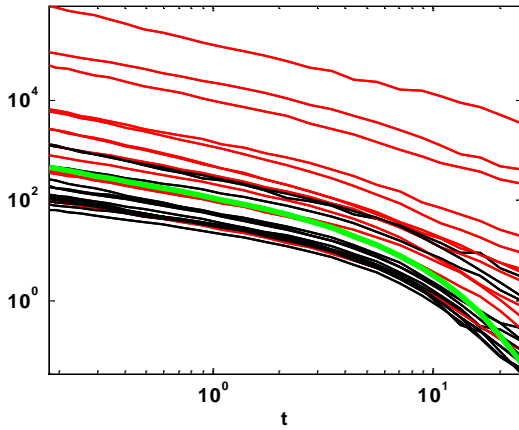


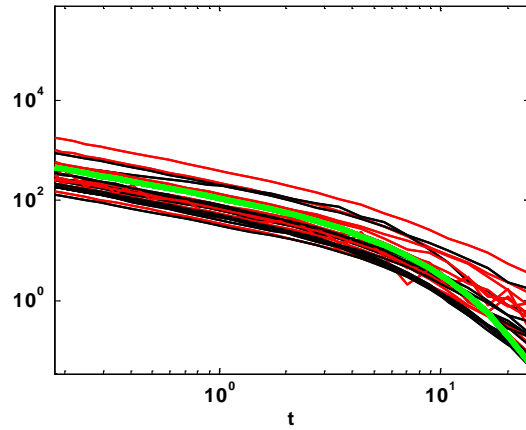
Figure 5.5. Camp Sibert GPO, background soil response is more problematic in the northeast portion of the grid.

Total Polarizability – Single Object Inversion



(a) Single Object Inversion

Total Polarizability – Multi-Object Inversion



(b) Multi Object Inversion

Figure 5.6. Recovered polarizabilities from single object inversion (left) and multi object inversion (right) from the Camp Sibert GPO. Only detectable 4.2 inch mortars were included in the analysis. Green plot represents the library polarizability for a 4.2 inch mortar, the red curves indicate items that fall into the northeastern portion of the GPO where a stronger soil response is evident while the black curves are GPO items in the more benign southwest portion of the GPO.

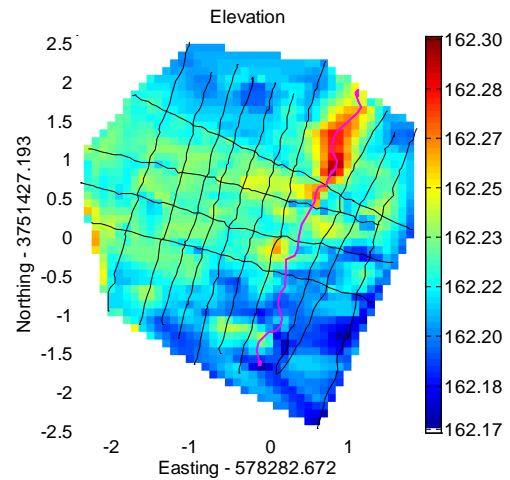
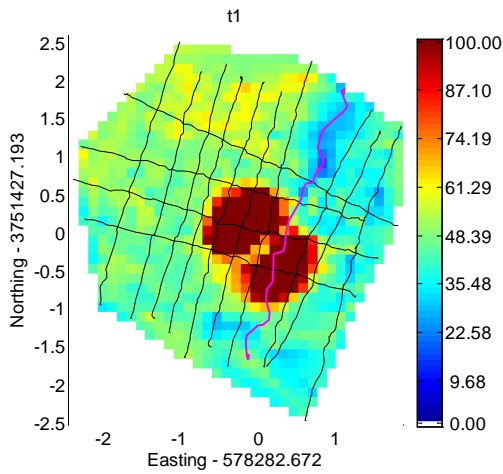


Figure 5.7. First time channel and elevation for target 852. A moderate bump in the topography (along the line shown in magenta colour) leads to a lower amplitude in the data.

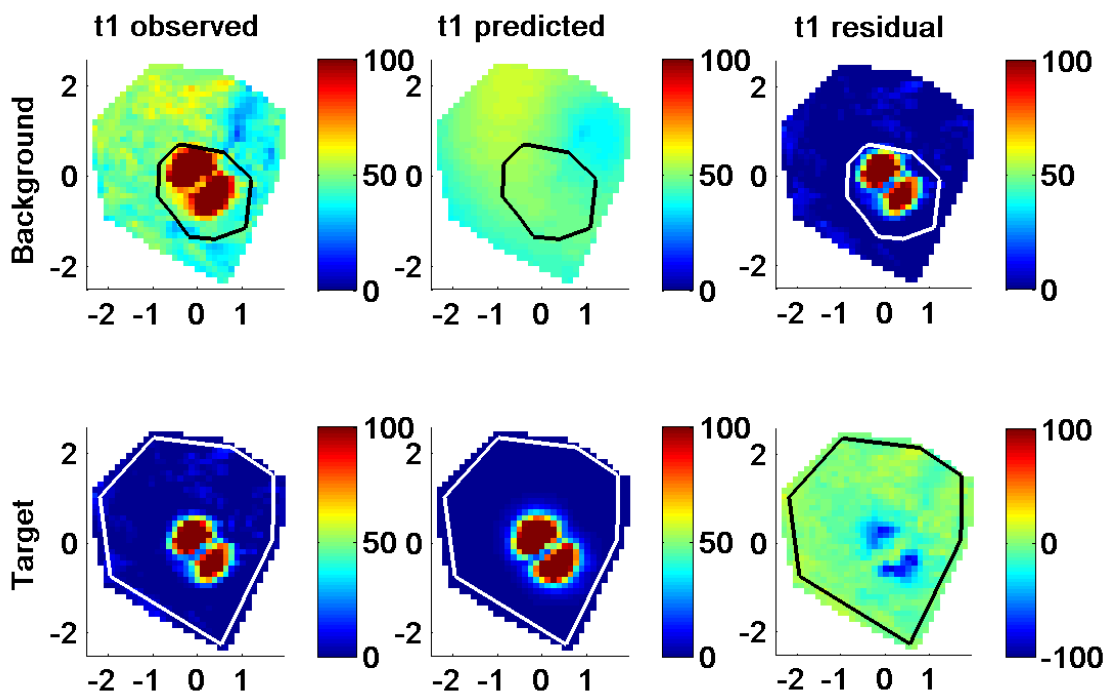


Figure 5.8. Modeling the background response for Camp Sibert target 852 using a single object inversion with an exclusive mask (top row). Once the background response is removed, reinvert with a single object inversion for the target response (bottom row).

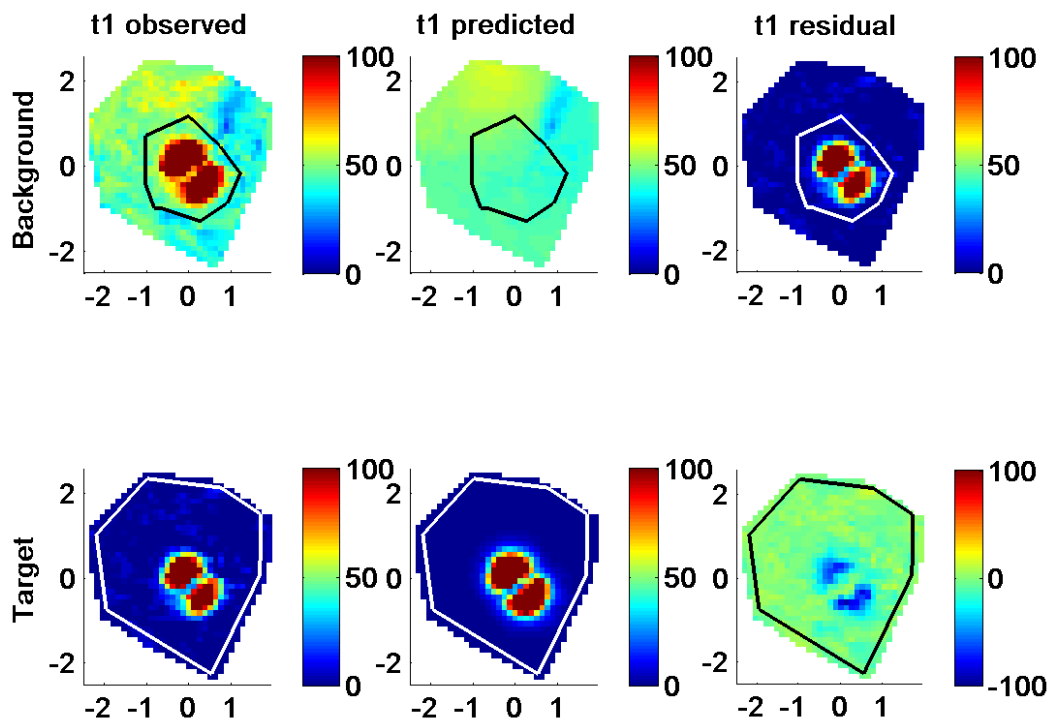


Figure 5.9. Modeling the background response for Camp Sibert target 852 using a two object inversion with an exclusive mask (top row). Once the background response is removed, reinvert with a single object inversion for the target response (bottom row).

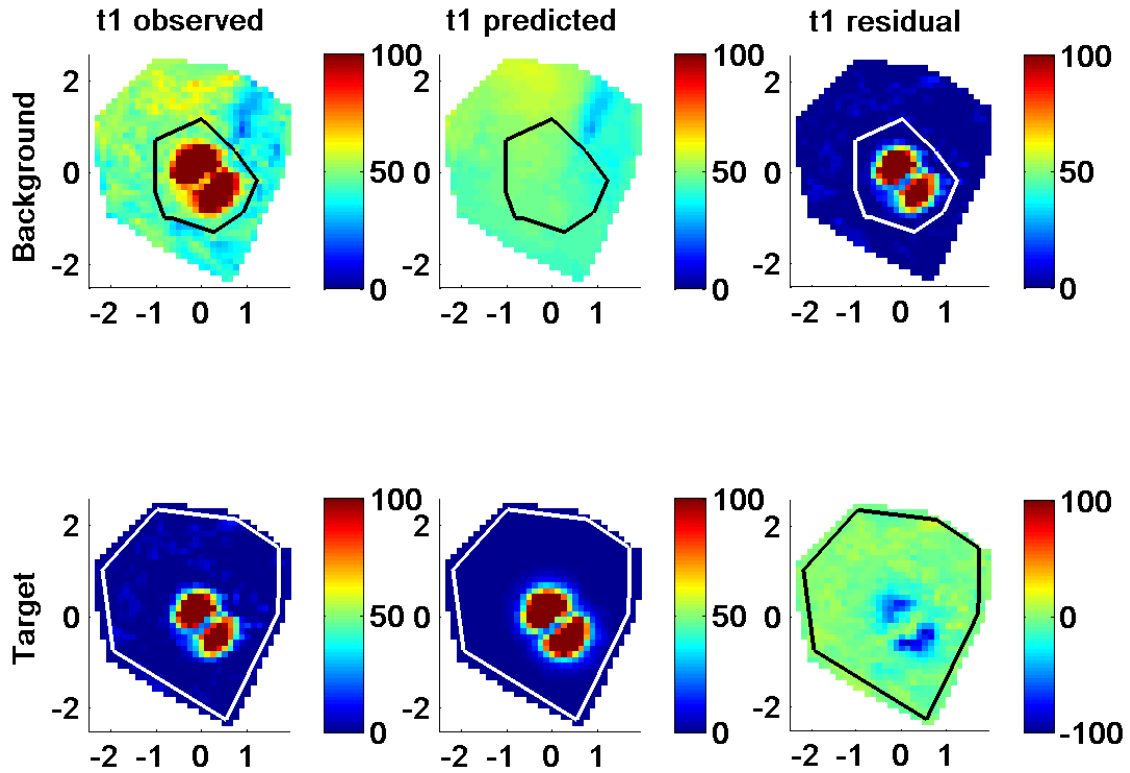


Figure 5.10. Modeling the background response for Camp Sibert target 852 using a three object inversion with an exclusive mask (top row). Once the background response is removed, reinvert with a single object inversion for the target response (bottom row).

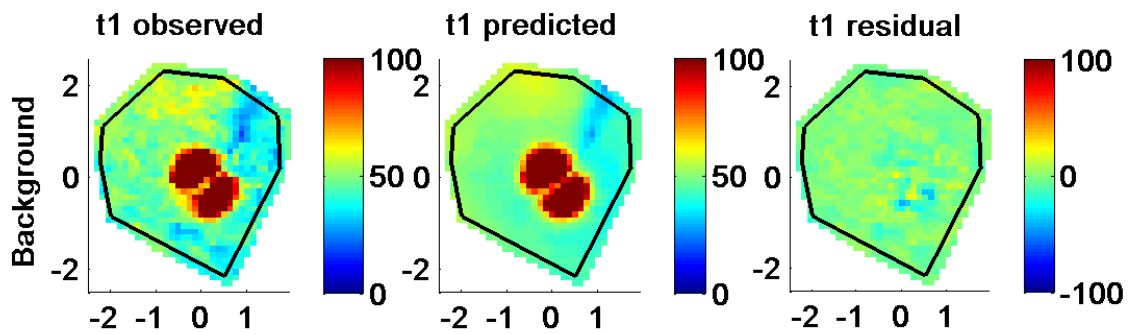


Figure 5.11. Modeling target and background response for Camp Sibert target 852 simultaneously using a three object inversion with two dipoles constrained to depths between 5 and 10m to model the soil response.

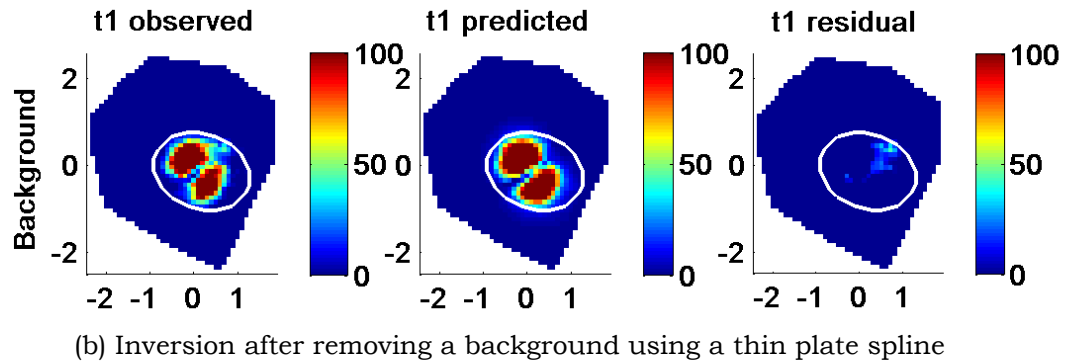
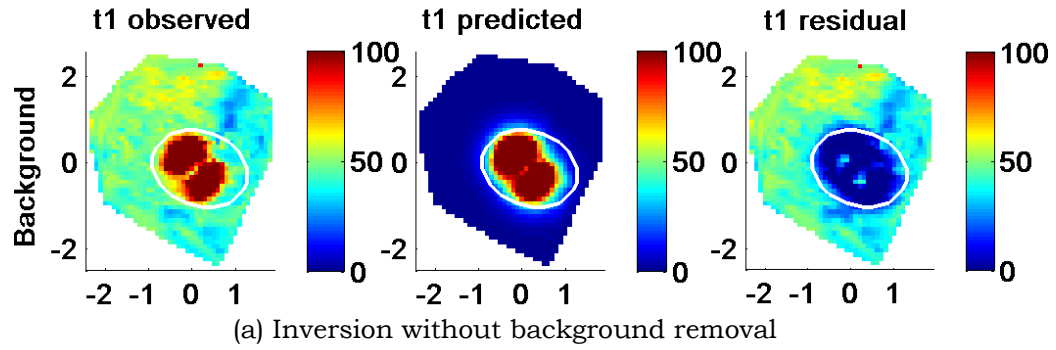


Figure 5.12. Modeling the background response for Camp Sibert target 852 using a thin plate spline to calculate background values within the mask region. Single object inversions are shown with no background removed (top row) and after removing a background using a thin plate spline across the masked target region (bottom row).

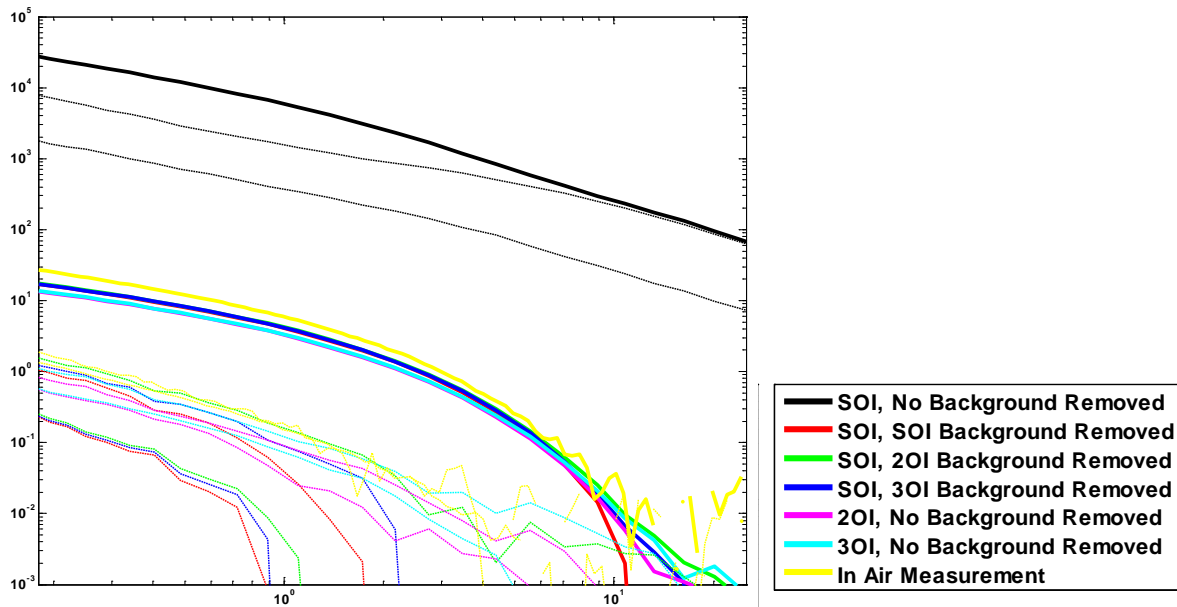


Figure 5.13. Recovered polarizabilities for different inversion scenarios. Secondary polarizabilities are better resolved for the two and three object inversions where one unconstrained dipole models the target and remaining dipole(s) are constrained to be 5 to 10m deep to model the soil response.

Target 1032

An additional target from the Camp Sibert dataset, 1032 also contains a significant background soil response. Unlike cell 852, the variation in background response for 1032 is not due to small scale change in topography but rather a uniform increase in the background likely due to a viscous magnetic response in the surrounding soil. Based on the observations for target 852, optimal results are obtained with a multi-object inversion rather than attempting to model the background response and remove it prior to inverting for the target response. The top two rows in Figure 5.14 show single object inversions both for a mask that is tight around the target and for a larger mask that incorporates the background response. Not surprisingly the large mask results in a poor fit, with a single object inversion one dipole cannot simultaneously model both the target response and the soil response. Tightening the mask to isolate the target response results in an improved fit but still displays a significant residual response.

A large mask coupled with a multi object inversion (bottom two rows of Figure 5.14) produces the best fits. The two object inversion is shown in the second last row and the three object inversion is in the bottom row. There is little difference between two object and three object inversion results indicating that for target 1032, the background response can be successfully modeled with a single constrained deep (5-10m) dipole.

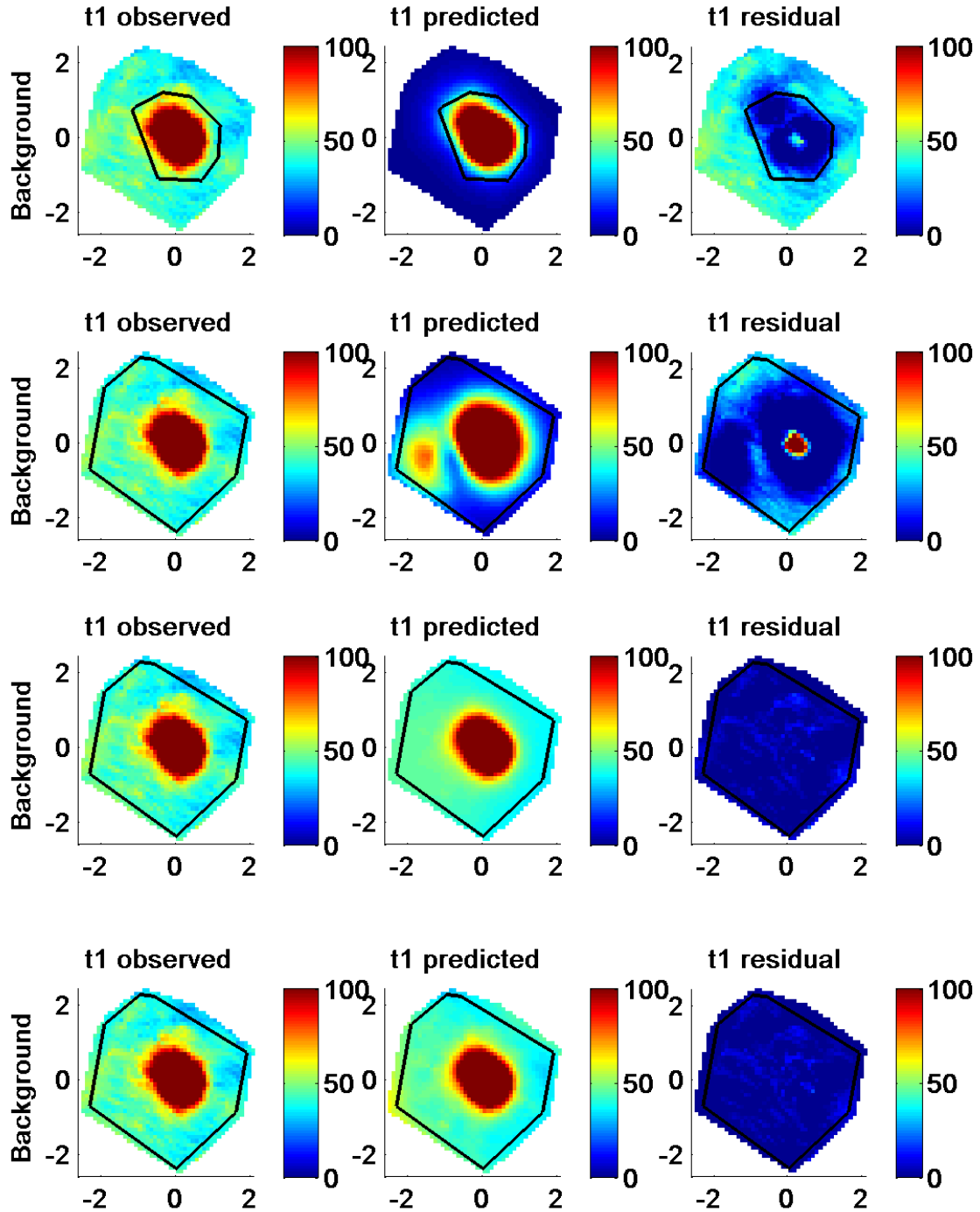


Figure 5.14. Modeling target response for Camp Sibert target 1032 using a single object inversion with different masks (top 2 rows) and two and three object inversions (bottom 2 rows) with one unconstrained dipole modeling the target and additional dipole(s) constrained to depths between 5 and 10m modeling the soil response (bottom).

Targets 808, 954, and 997

Three additional targets from Camp Sibert were identified that had significant background response. Those three targets were inverted as a single object inversion for a benchmark and with the two most promising results based on analysis for targets 852 and 1032. First inverting after removing background values outside of the mask and using a thin plate spline to approximate the background values within the mask. Secondly a two object inversion was applied with no back ground removed but a large mask was used and one dipole was forced deep (between 5-10m) to model the background. Inversion results are shown in Figures 5.15 to 5.17.

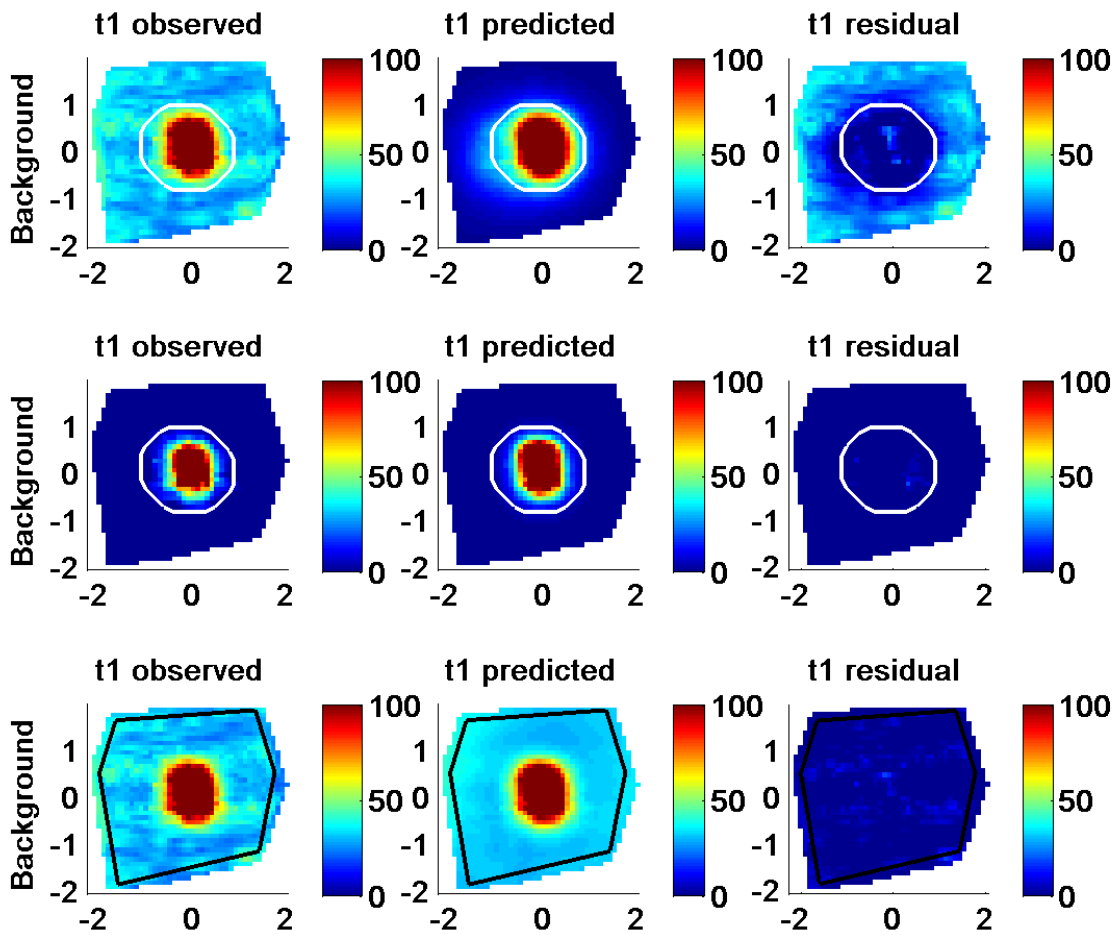


Figure 5.15. Target 808. Inverting Camp Sibert target 808 with different approaches to compensate for an elevated background response. Top row shows the single object inversion with no background removed. The middle row depicts results after removing a background response using a thin plate spline to calculate background values within the mask region. The bottom row shows a two object inversion with no background removed and one dipole forced deep between 5 and 10m.

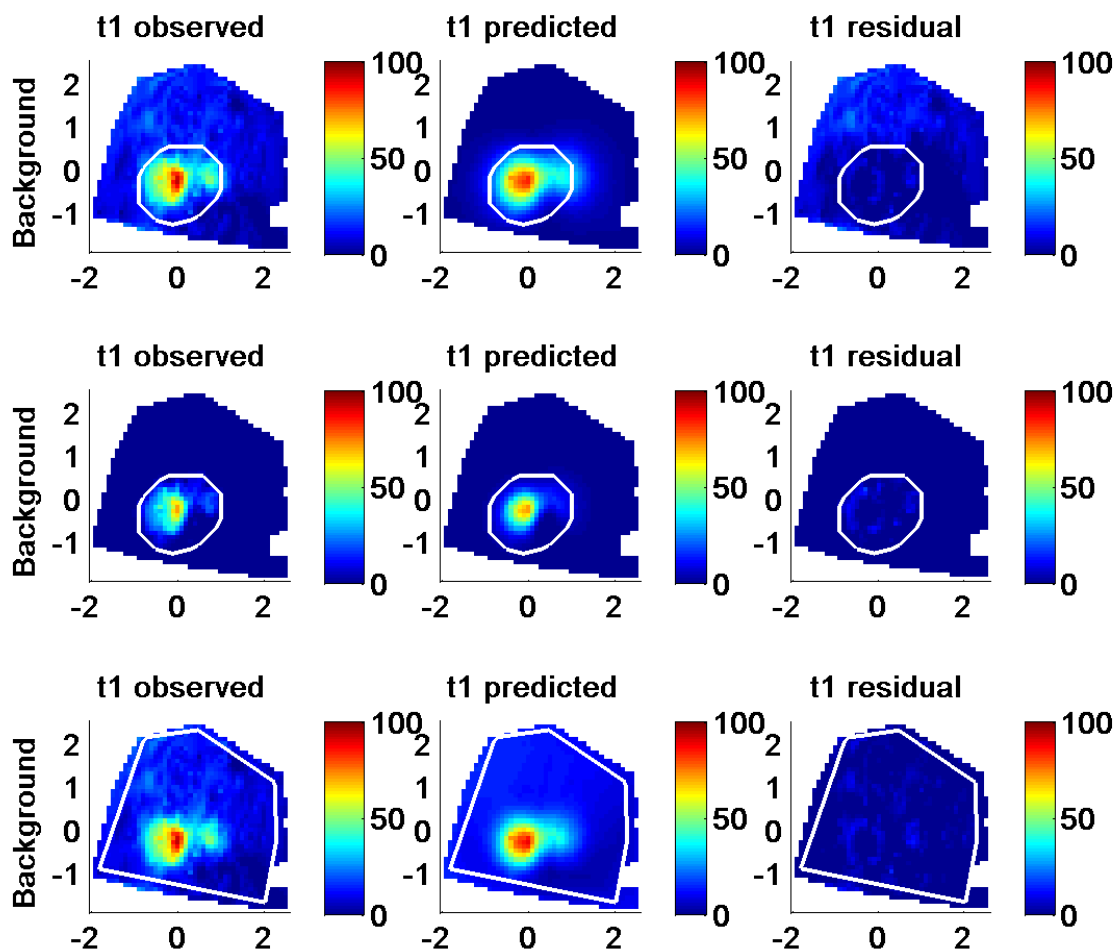


Figure 5.16. Target 954. Inverting Camp Sibert target 954 with different approaches to compensate for background response. Top row shows the single object inversion with no background removed. The middle row depicts results after removing a background response using a thin plate spline to calculate background values within the mask region. The bottom row shows a two object inversion with no background removed and one dipole forced deep between 5 and 10m.

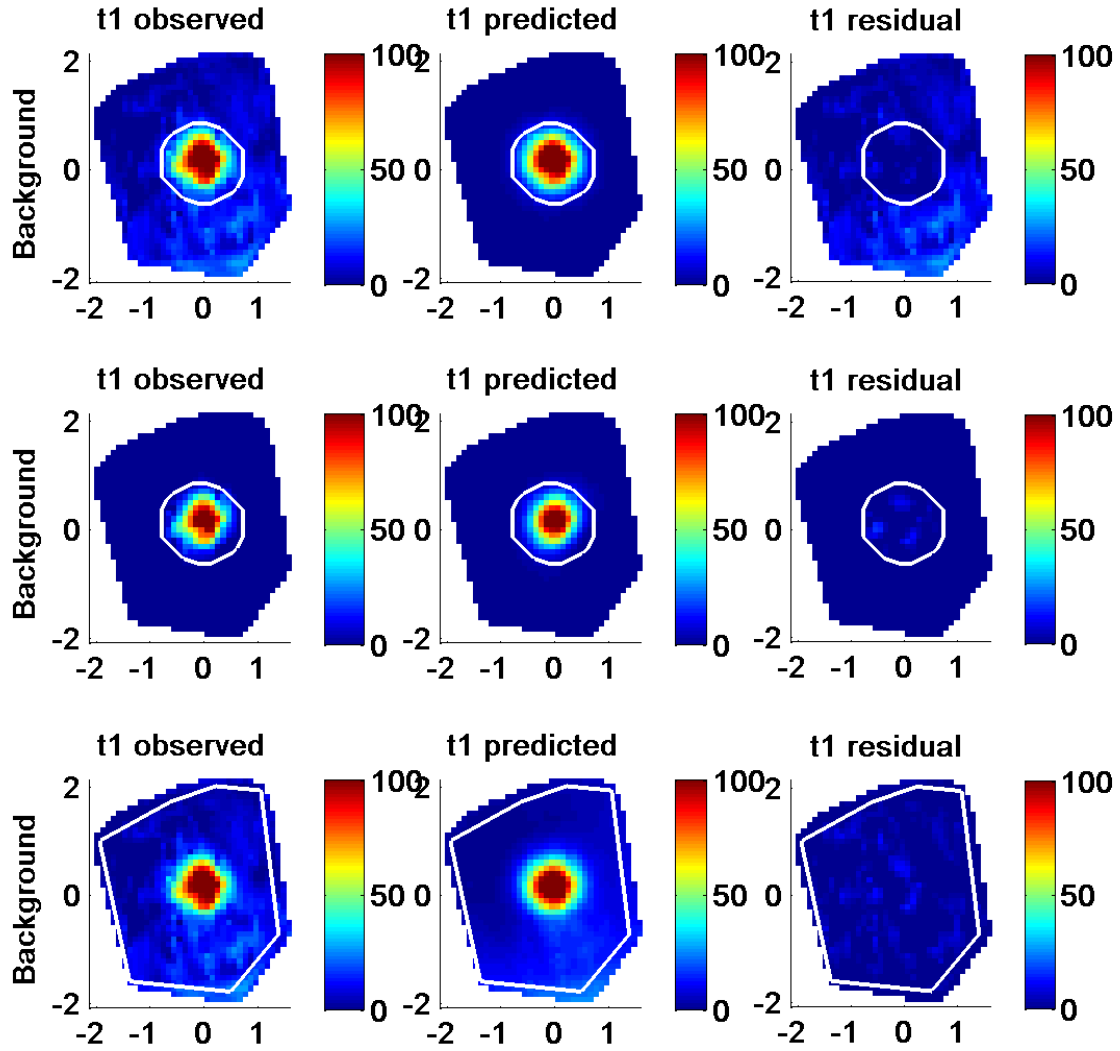


Figure 5.17. Target 997. Inverting Camp Sibert target 997 with different approaches to compensate for background response. Top row shows the single object inversion with no background removed. The middle row depicts results after removing a background response using a thin plate spline to calculate background values within the mask region. The bottom row shows a two object inversion with no background removed and one dipole forced deep between 5 and 10m.

CAMP BUTNER – M48 LIKE TARGETS

In the initial analysis a number of targets were identified with polarizabilities that closely resembled the M48. Recovered depths for these items were consistently deeper than would be expected for such a small target, typically around 0.5 m. The depths indicated that these were unlikely to be a TOI however the recovered polarizabilities so closely matched the M48 library that they were selected as TOI. Three specific M48-like anomalies were examined to investigate if multi object inversions with dipole(s) constrained deep can improve the ability to identify these responses as non TOI items.

Target 2362 and 3879 were both small pieces of scrap (see Figure 5.18) and target 3416 produced no contact. In all three cases, recovered polarizabilities matched a deep M48. Results are compared for single, two and three object inversions for both dynamic and cued data collected over each target.



Figure 5.18. Groundtruth for Camp Butner targets 2362 and 3879. Both items were small pieces of frag that when inverted produced polarizabilities that closely matched the M48 library polarizability

Comparisons were made between the recovered polarizabilities for the soil responses which produce M48 like polarizabilities (2362, 3416, 3879) with a high SNR M48 (35) and the deepest M48 (272). For target 2362 shown in Figure 5.19, the single object inversion produced a recovered polarizability that matched the M48 reference polarizability. The two object inversion produced a polarizability that resembles a small piece of scrap but the second source still produced a polarizability similar to the M48 reference. Forcing one dipole deep in the two object inversion successfully recovered a polarizability representing a small piece of scrap and the second source forced deeper no longer matches the M48 reference. The three object inversions were also able to identify a small piece of scrap without producing a false match to the M48 reference polarizability.

The second piece of small scrap (3879) that recovered a polarizability matching the M48 for a single object inversion showed that it was not always possible to eliminate

the ambiguity of false positive M48 polarizabilities with multi object inversion methods. While the multi object inversions shown in Figure 5.21 do recover a polarizability that matches a small piece of scrap, a second source still produces a polarizability matching the M48 reference.

Figure 5.20 shows the polarizabilities recovered for the no contact cell, 3416. The single object inversion again produces a polarizability matching the M48. The multi object inversions produce polarizabilities distinct from the M48 reference.

In general, the three object inversions provide little improvement over the two object inversions. The actual M48 targets produce consistently better M48 polarizability matches over the range of inversion scenarios attempted. The soil and small scrap responses generally only produce a good M48 polarizability match for one of single, two or three object inversions while the actual M48 targets (272, figure 5.23 and 35, figure 5.25) recover a model that is a good fit to the reference polarizabilities for all of the single and multi source inversions. It may be possible to use this information to exclude some false positive responses from a TOI list.

2362: Frag

The MetalMapper cued data for this target shown in Figure 5.19 produces polarizabilities that closely resemble the M48 for both single and 2 object inversions (with no dipole forced deep). When one of the dipoles is forced deep, the recovered polarizabilities are distinct from the M48. A three object inversion also produces distinct polarizabilities both for the case with no dipoles forced deep and when two dipoles were forced deep.

2362	X1	Y1	Z1	X2	Y2	Z2	X3	Y3	Z3
Static									
SOI original	0.21	-0.01	-0.23						
2OI original	-0.14	-0.10	-0.65	0.25	-0.01	-0.17			
2OI, none deep	-0.14	-0.09	-0.65	0.25	-0.01	-0.17			
2OI, 1 deep	-2.00	-0.33	-5.00	0.23	-0.01	-0.22			
3OI, none deep	-0.28	0.25	-0.44	-0.15	-0.58	-0.03	0.23	-0.00	-0.19
3OI, 2 deep	0.23	-0.01	-0.22	-2.00	-0.32	-5.00	-0.76	1.75	-5.00

Table 5.1. Recovered positions for different inversion scenarios attempted for target 2362.

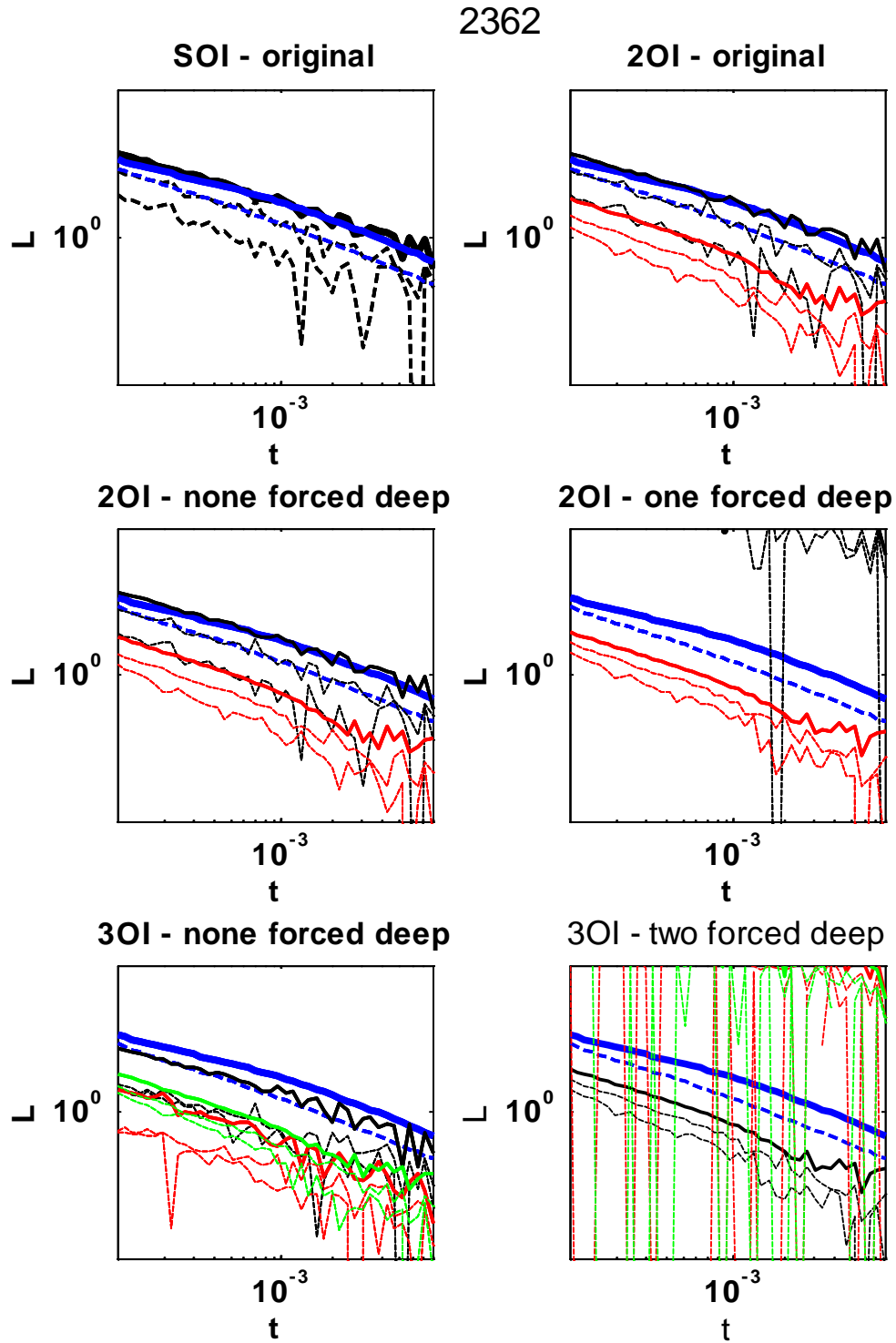


Figure 5.19. Target 2362. Recovered polarizabilities for MetalMapper cued data over target 2362. The original single and 2 object inversions are shown as well as two and three object inversions where the modeled dipoles are not constrained and again when one dipole is unconstrained and remaining dipole(s) are constrained to be deep (5-10m) to model the background soil response. Library polarizability is shown in blue with black, red, green illustrating single, two object and three object inversions.

3416: No contact

The MetalMapper cued data for this target shown in Figure 5.21 produce polarizabilities that resemble the M48 for the single object inversions. Two object inversions do not produce good matches for polarizabilities for the M48. An unconstrained three object inversion also produces a better match for the M48 polarizabilities however when two dipoles were forced deep, the three object inversion did not result in polarizabilities matching the M48.

3416	X1	Y1	Z1	X2	Y2	Z2	X3	Y3	Z3
Static									
SOI original	0.20	-0.09	-0.49						
2OI original	0.08	-0.12	-1.01	0.21	-0.05	-0.15			
2OI, none deep	0.07	-0.08	-1.02	0.20	-0.05	-0.15			
2OI, 1 deep	0.03	0.36	-5.00	0.19	-0.06	-0.30			
3OI, none deep	1.59	2.00	-0.91	0.21	-0.14	-0.56	0.24	-0.00	-0.02
3OI, 2 deep	0.19	-0.06	-0.29	-2.00	-0.31	-5.00	0.10	1.09	-5.00

Table 5.2. Recovered positions for different inversion scenarios attempted for target 3416.

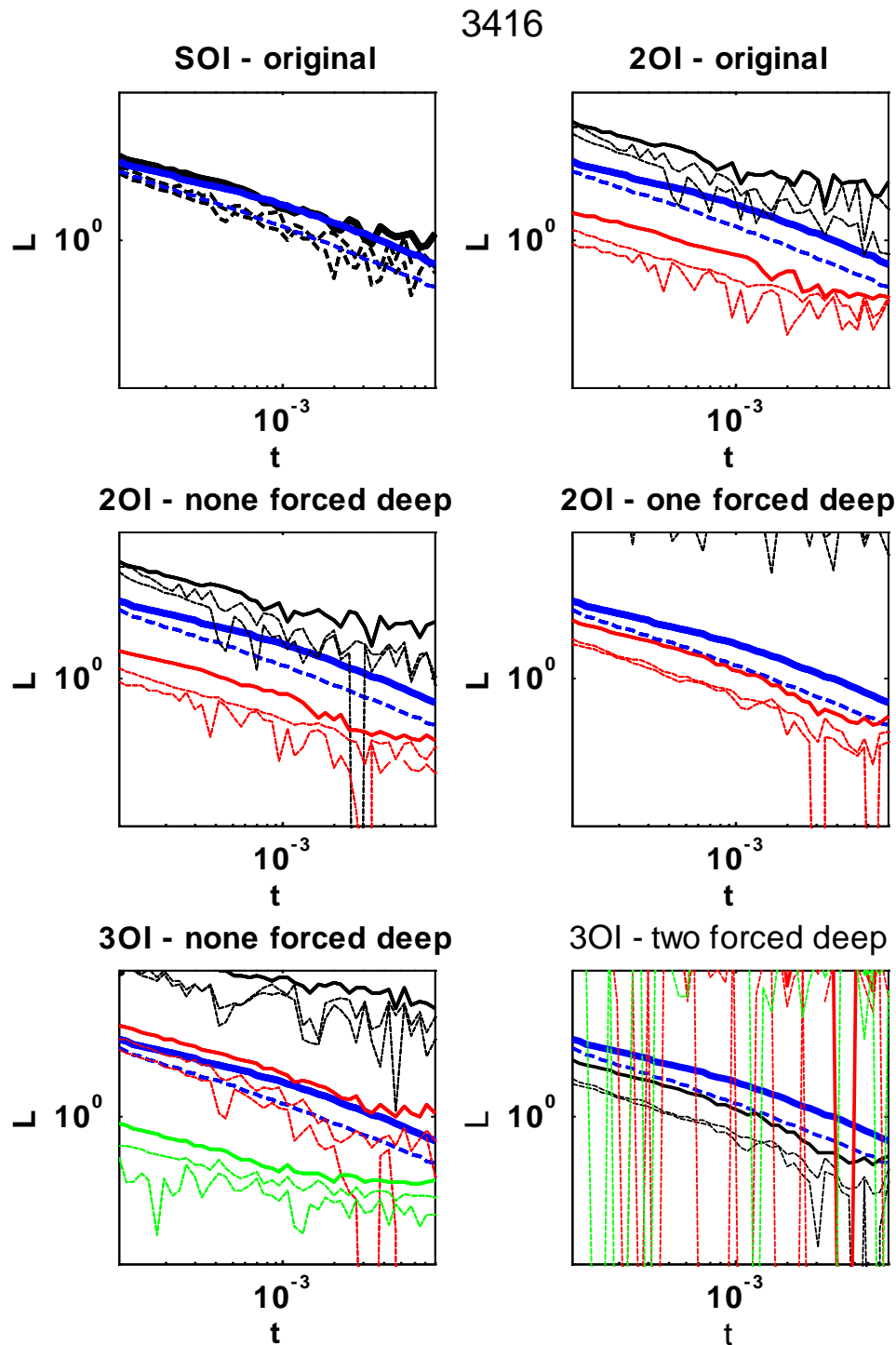


Figure 5.20. Target 3416. Recovered polarizabilities for MetalMapper cued data over target 3416. The original single and 2 object inversions are shown as well as two and three object inversions where the modeled dipoles are not constrained and again when one dipole is unconstrained and remaining dipole(s) are constrained to be deep (5-10m) to model the background soil response. Library polarizability is shown in blue with black, red, green illustrating single, two object and three object inversions.

3879: Frag

The MetalMapper cued data for this target (Figure 5.23) produce polarizabilities that resemble the M48 for the two and three object inversions but not the single object inversion.

3879	X1	Y1	Z1	X2	Y2	Z2	X3	Y3	Z3
Static									
SOI original	-0.02	-0.04	-0.54						
2OI original	-0.01	-0.11	-0.44	0.42	0.15	-0.07			
2OI, none deep	0.01	-0.10	-0.42	0.39	0.15	-0.00			
2OI, 1 deep	0.75	2.00	-5.00	0.04	-0.06	-0.47			
3OI, none deep	0.07	0.27	-0.19	-0.06	-0.25	-0.19	0.50	0.39	-0.13
3OI, 2 deep	0.04	-0.07	-0.45	-0.55	0.83	-5.00	1.84	2.00	-5.00

Table 5.3. Recovered positions for different inversion scenarios attempted for target 3879.

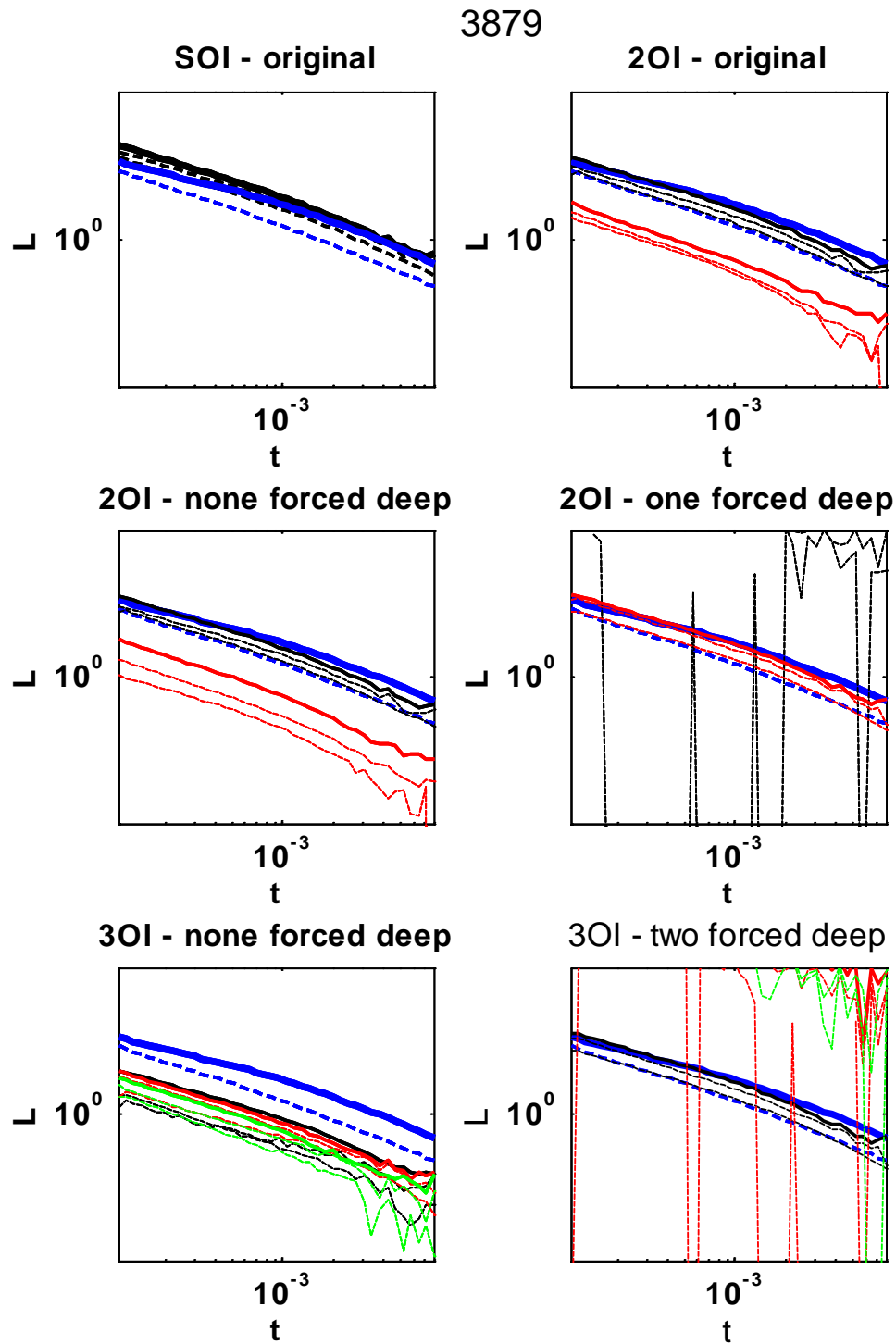


Figure 5.21. Target 3879. Recovered polarizabilities for MetalMapper cued data over target 3879. The original single and 2 object inversions are shown as well as two and three object inversions where the modeled dipoles are not constrained and again when one dipole is unconstrained and remaining dipole(s) are constrained to be deep (5-10m) to model the background soil response. Library polarizability is shown in blue with black, red, green illustrating single, two object and three object inversions.

272: Deep, Low S2N M48 Fuze

The MetalMapper cued data for this target produce a set of polarizabilities that resemble the M48 for all of the single, two and three object inversions.

272	X1	Y1	Z1	X2	Y2	Z2	X3	Y3	Z3
Static									
SOI original	0.06	-0.25	-0.35						
2OI original	0.27	-0.5	-0.59	0.04	-0.22	-0.31			
2OI, none deep	0.2	-0.59	-0.58	0.04	-0.22	-0.31			
2OI, 1 deep	-1.17	-2.0	-5.0	0.05	-0.24	-0.34			
3OI, none deep	0.05	-0.23	-0.34	-1.44	-0.66	-6.58	-0.03	-0.54	-0.05
3OI, 2 deep	0.05	-0.24	-0.34	0.5	-1.35	-8.57	0.71	-2.0	-5.0

Table 5.4. Recovered positions for different inversion scenarios attempted for target 272.

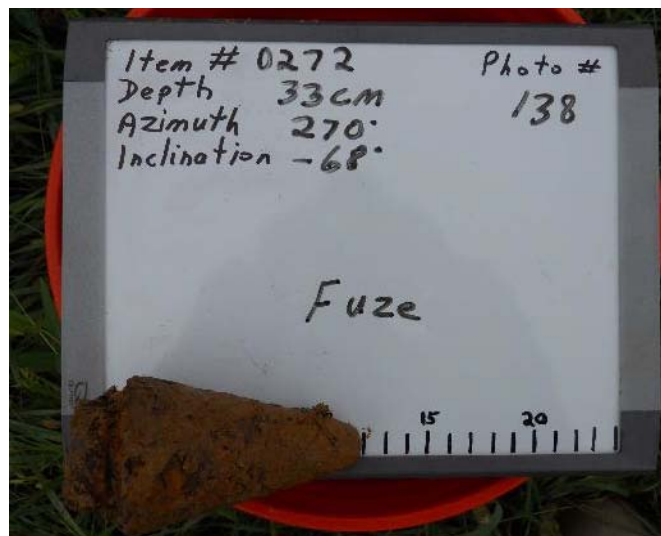


Figure 5.22. Groundtruth for Camp Butner target 272. This was the deepest M48 at the site and is shown for comparison purposes with the soil responses that emulate M48 polarizabilities.

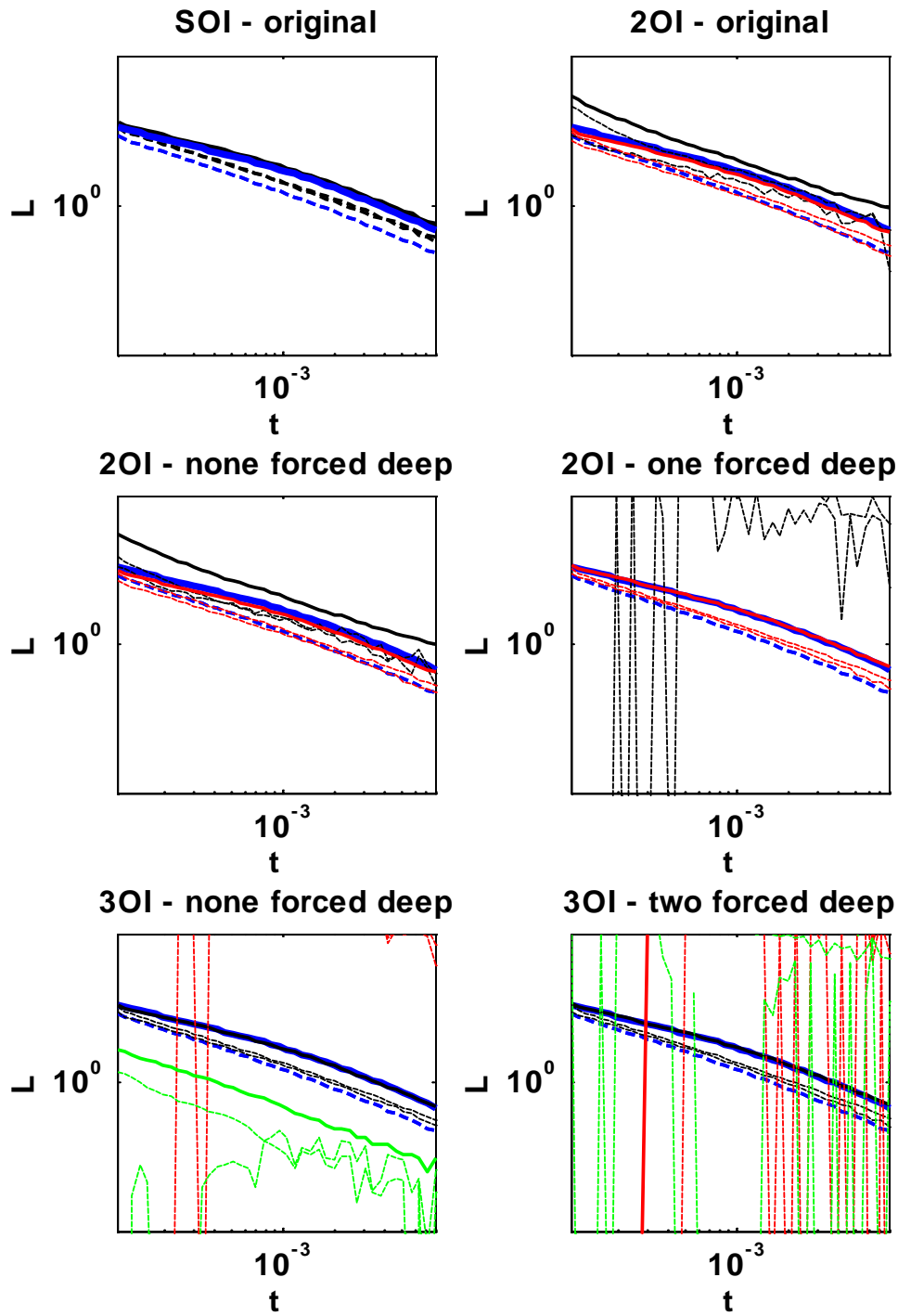


Figure 5.23. Recovered polarizabilities for MetalMapper cued data over target 272. The original single and 2 object inversions are shown as well as two and three object inversions where the modeled dipoles are not constrained and again when one dipole is unconstrained and remaining dipole(s) are constrained to be deep (5-10m) to model the background soil response. Library polarizability is shown in blue with black, red, green illustrating single, two, and three object inversions.

35: Shallow, High SNR M48 Fuze

The MetalMapper cued data for this target produces a set of polarizabilities that resemble the M48 for all of the single, two and three object inversions.

35	X1	Y1	Z1	X2	Y2	Z2	X3	Y3	Z3
Static									
SOI original	-0.11	-0.1	-0.12						
2OI original	-0.11	-0.1	-0.12	-0.1	-0.09	-0.12			
2OI, none deep	-0.11	-0.11	-0.12	-0.1	-0.09	-0.12			
2OI, 1 deep	-0.11	-0.1	-0.12	1.71	0.0	-5.0			
3OI, none deep	-0.09	-0.07	-0.1	0.69	0.16	-0.29	-0.11	-0.11	-0.12
3OI, 2 deep	-0.11	-0.1	-0.12	-1.86	-2.0	-6.48	1.72	0.15	-5.0

Table 5.5. Recovered positions for different inversion scenarios attempted for target 35.

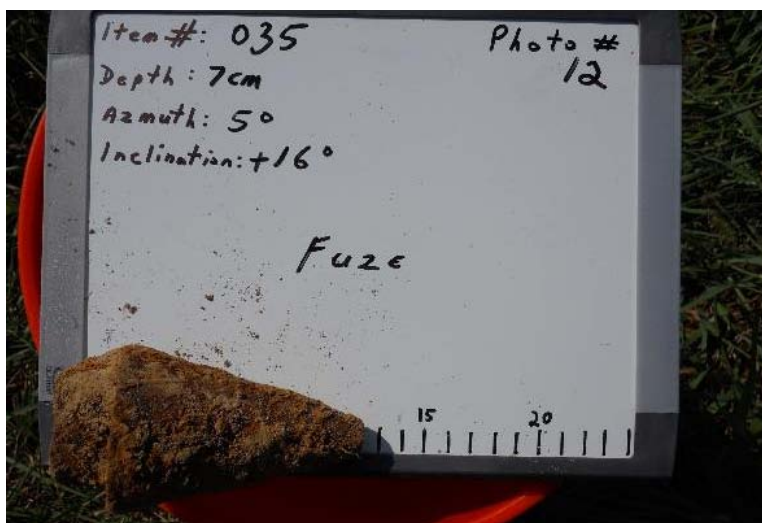


Figure 5.24. Groundtruth for Camp Butner target 35. This was a high SNR M48 at the site and is shown for comparison purposes with the soil responses that emulate M48 polarizabilities.

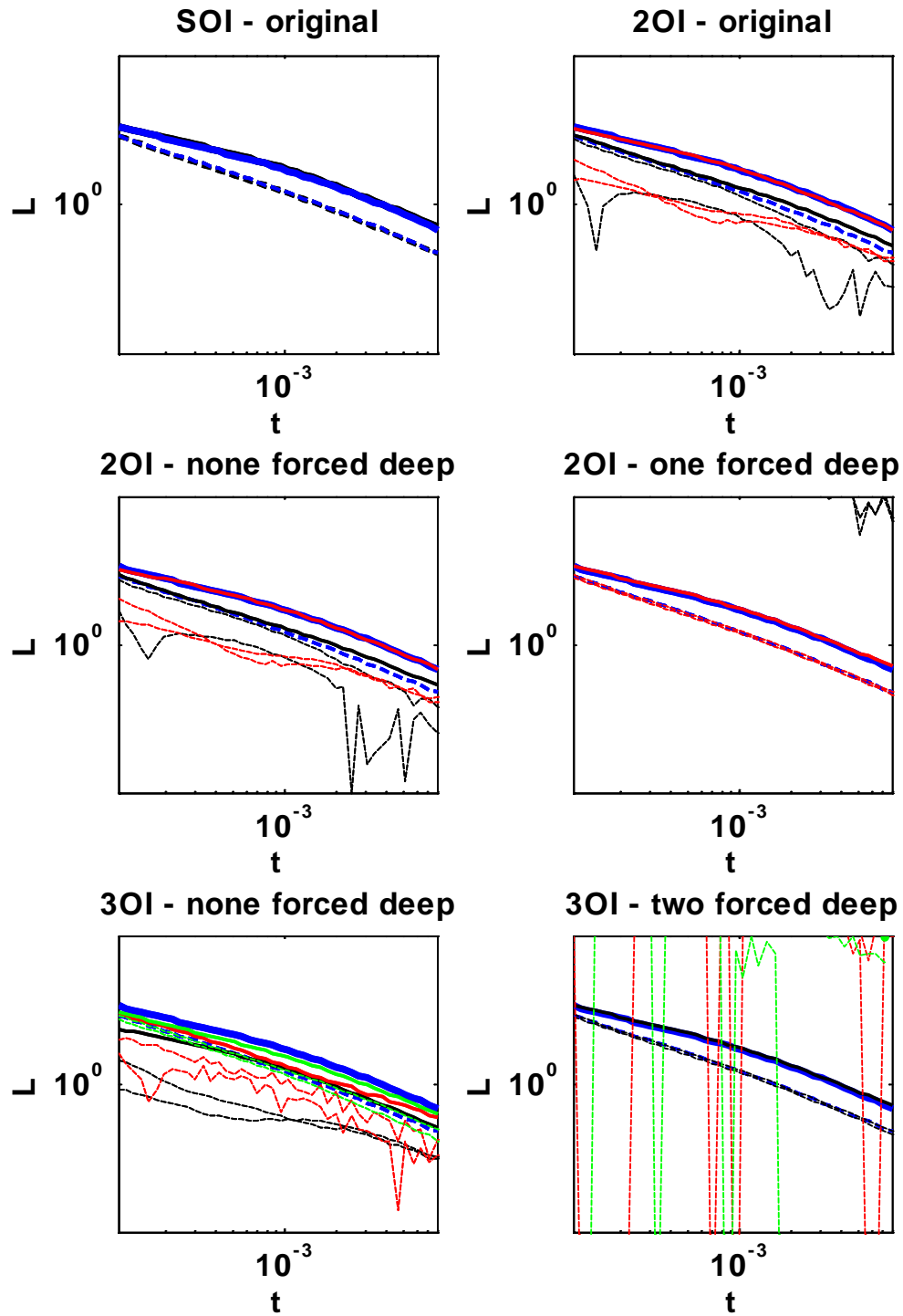


Figure 5.25. Recovered polarizabilities for MetalMapper cued data over target 35. The original single and 2 object inversions are shown as well as two and three object inversions where the modeled dipoles are not constrained and again when one dipole is unconstrained and remaining dipole(s) are constrained to be deep (5-10m) to model the background soil response. Library polarizability is shown in blue with black, red, green illustrating single, two, and three object inversions.

CAMP BEALE METALMAPPER AND TEMTADS 2x2 MULTI OBJECT INVERSION

During the ESTCP Live Site demonstration at the Former Camp Beale, several participants noted that magnetic soil response may be affecting the accuracy of polarizability estimates. When processing the Camp Beale data, participants generally used both a single source solver and a multi-source solver to process the data. A multi-source solver is necessary for obtaining accurate polarizability estimates when (1) there are multiple pieces of metal in the field of view of the instrument or (2) if a target is large, heterogeneous (e.g. steel body, with aluminum fins) and close enough to the surface that multiple sources are required to model the different components of the target. In this section we present examples of how using a multi-source solver can have the added benefit of modeling background soil response and improving the accuracy of the polarizability estimates.

For these examples we look at cued interrogation data acquired with the MetalMapper and TEMTADS 2x2 instruments at Camp Beale. We will focus on anomalies 438 and 1553, which were found to be 0.50 cal bullets upon excavation (Figure 5.26). These anomalies were inverted using a single source solver, a two source solver, and a three source solver. For all cases, no constraints were placed on the depth with which any of the sources could sit in the subsurface.

The recovered polarizabilities from MetalMapper data acquired over anomaly 438 is shown in Figure 5.27. When inverting for a single source (top row of Figure 5.27), a dipole is placed at a depth of 16 cm. The recovered polarizabilities suggest a target with axial symmetry. The dashed line is the characteristic decay for VRM soil. We notice that the decay characteristics of the polarizability follow the VRM decay at early and late times. This effect can be clearly observed in the secondary polarizabilities after 1 ms. When the data are inverted for a pair of sources (middle row of Figure 5.27), we observe that there is one source placed at a depth of 64 cm that models the non-target data (Model 1/2) and the 0.50 cal is modeled with an anomaly at a depth of 10 cm (Model 2/2). The recovered polarizabilities of the first source has a decay that is slightly faster than the characteristic VRM soil decay, and the polarizabilities of the second source do not transition to the soil decay, but rather decay into the noise floor. This suggests that the data components related to the soil are being modeled by other sources, and not the source related to the 0.50 cal bullet. Figure 5.28 compares the data fit when modeling with a single source to modeling with two sources. The data fit for a single source inversion does not fit the data as well as the two source inversion since the single source model is too simplistic to replicate all the features in the data. We note that the dipole location in the single source case unsuccessfully tried to model data components from both the soil and the 0.50 cal, and is thus deeper than the 0.50 cal dipole in the two source case.

A three source inversion was also carried out on the anomaly (bottom row of Figure 5.27). The source representing the 0.50 cal (Model 2/3) is not much different than the source in the two source case, and therefore a three source inversion was not

necessary from the standpoint of improving the ability to recover target polarizabilities. However, the additional source may be modeling a piece of small scrap (Model 1/3, $d=0.17\text{m}$) because we notice that the deeper source that models the background soil signal now follows the decay of VRM soil more closely than in the two source case.

Figure 5.28 contains results of processing TEMTADS 2x2 data over the same anomaly. We again invert for one, two, and three source models. The recovered polarizabilities of the single source model have similar characteristics to the MetalMapper derived polarizabilities. That is, at later time the polarizabilities start to follow the VRM decay rate (dashed line). When an additional source is added to the modeling (Model 1/2 at a depth of 55 cm), there is only marginal improvement in the polarizabilities of the 0.50 cal; the secondary polarizabilities of the source modeling the 0.50 cal (Model 2/2, depth = 10 cm) still follow the VRM decay rate after 1 ms and the secondary polarizabilities are not equal after 1 ms, thus not accurately representing the axial symmetry of the target. The three source inversion does appear to provide an improvement to the recovered polarizability for the 0.50 cal. For the three source case, the recovered source location polarizabilities of the 0.50 cal better reflect the axial symmetry of the bullet (i.e. secondary polarizabilities are equal), and the target polarizabilities do not follow the VRM decay. Interestingly, the source modeling the background response (Model 2/3) is slightly shallower (36 cm) and the source modeling a potential scrap or frag item is at a depth that is within 2 cm of the additional source obtained by processing the MetalMapper data (i.e. Model 1/3 in Figure 5.27).

The final example we present here is for anomaly 1553. Figure 5.29 contains polarizabilities estimated from MetalMapper data. Accurate recovery of the 0.50 cal bullet polarizabilities is only possible with the three source inversion. This is not surprising since excavation of the anomaly unearthed a small piece of scrap in addition to the 0.50 cal bullet. Although the recovered polarizability for the small scrap (Model 1/3) is quite noisy, the addition of this source is still very useful as it models parts of the data that were biasing the 0.50 cal estimated polarizabilities for the one and two source cases. The background soil in this case is modeled with a deep source (Model 3/3, depth = 1.2 m).



Figure 5.26. Photos of anomalies 438 and 1553. The red soil in the background of the anomaly 438 photo suggest the presence of iron rich, magnetic soil.

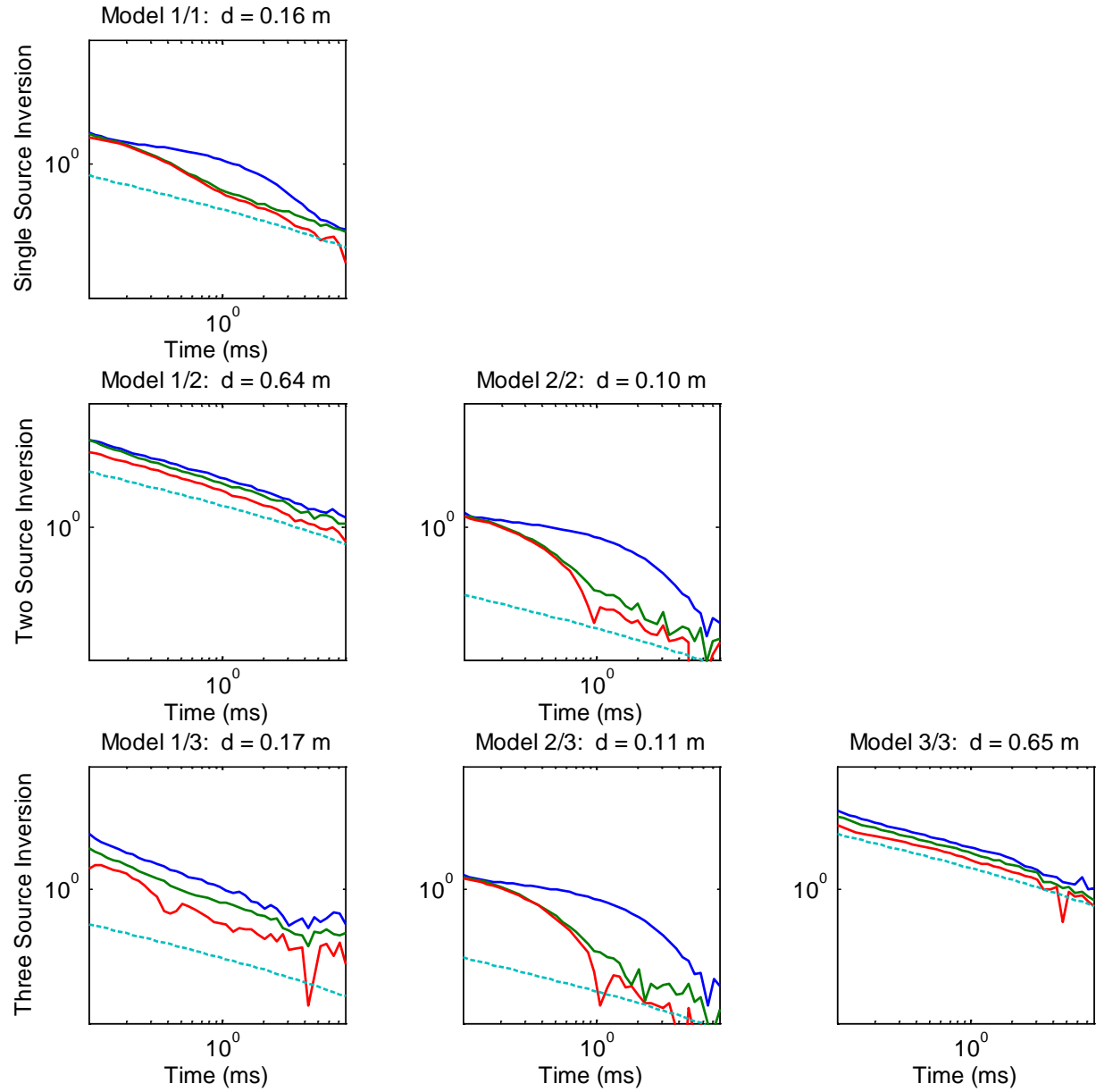
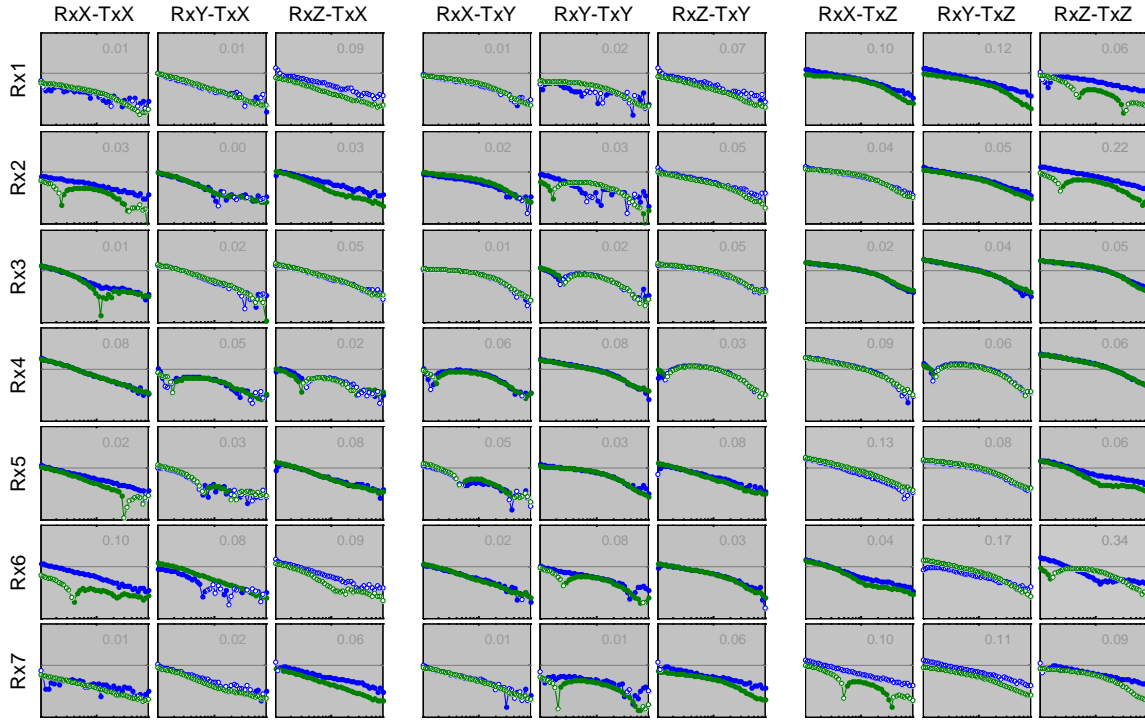
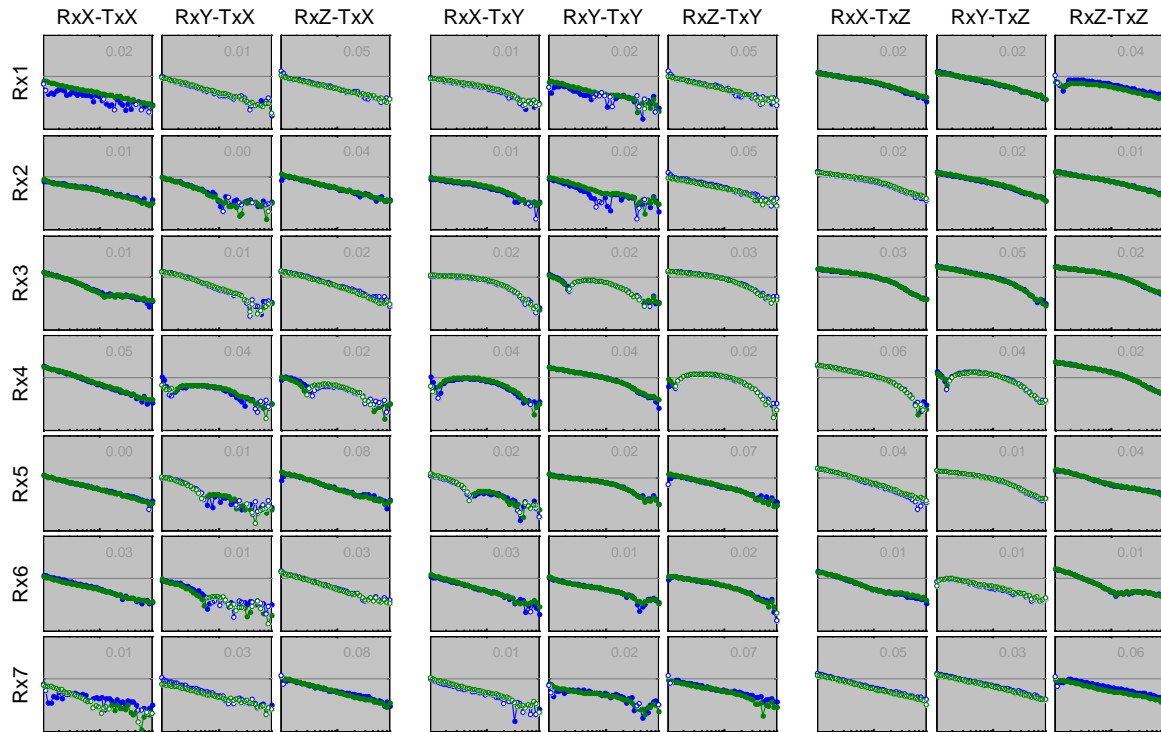


Figure 5.27. Anomaly 438. MetalMapper inversion results. An additional source to model the background soil improves the recovered polarizabilities for the 0.50 cal. The source that models the background soil is located at a depth of 65 cm.



(a) Data fit when using a single source inversion.



(b) Data fit when using a two source inversion.

Figure 5.28. MetalMapper data fit when inverting anomaly 438. The data fit for a single source inversion is much worse, since the single source model is too simplistic to replicate all the features in the data. A two source model fits the data.

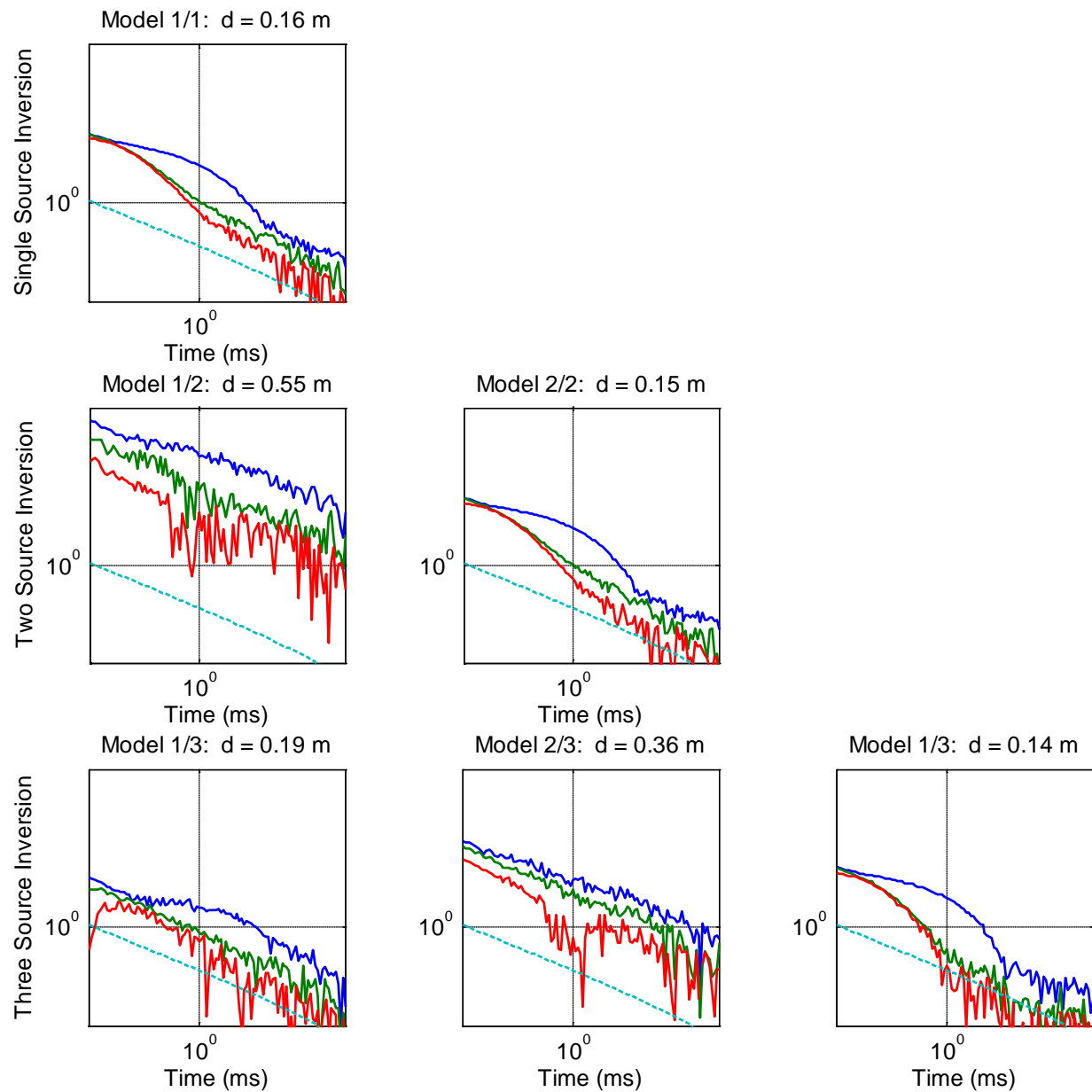


Figure 5.29. Anomaly 438. Polarizabilities estimated from TEMTADS 2x2 data. Three sources produce the best estimates for the 0.50 cal polarizabilities.

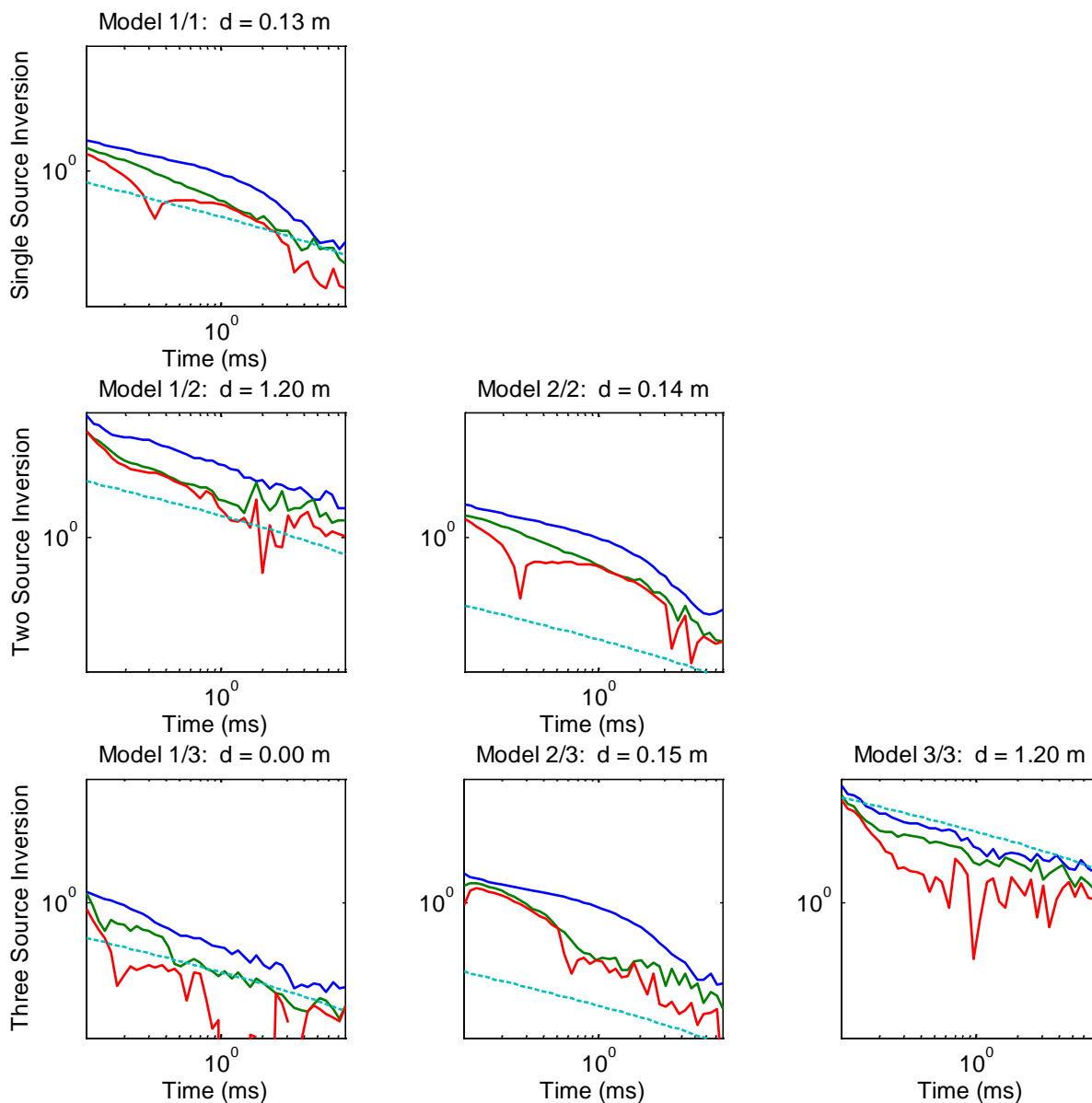


Figure 5.30. Anomaly 1553. Polarizabilities estimated from MetalMapper data. A three source model (bottom row) is required to extract the correct polarizabilities for the 0.50 cal bullet. The background response is modeled by a deep (1.2 m) and large dipole source (Model 3/3).

6. CONCLUSIONS

Detection and identification of UXO at geologically hostile sites can be unreliable. In this project we investigated different approaches for improving discrimination of UXO at these sites. The processing methods we developed are characteristically different from those adopted as the standard state of practice because each method includes a step where the background soil properties in the vicinity of the UXO are estimated. Having an estimate for the background soil properties enables us to model variations in sensor response resulting from changes in sensor height and orientation relative to the surface. We believe that by modeling these data effects, that the bias in the estimated dipole parameters resulting from spatially correlated signals resulting from variable sensor position would be reduced.

In order to calculate the background response due to changes in sensor height and orientation relative to the ground, we developed a forward model based on the analytic solution for a dipole over a conductive and magnetically susceptible half-space. The two main assumptions of the model are (1) small scale topography does not need to be modeled and (2) there is no significant EM interaction between the host material and the UXO, such that the two signals could be treated as additive. These assumptions were investigated using numerical modeling of Maxwell's equations, and shown to only result in smaller, second order data effects that would be unlikely to significantly affect inversion results. The accuracy of our approach was verified by comparing modeling results with measurements from a number of field sensors. The accuracy of the model, combined with the speed in which it can calculate the soil response, makes the modeling method an ideal candidate for inverse problems where numerous forward model calculations are required.

The first inversion methods developed and tested in this project were for the Geonics EM63 and Geophex GEM3 instruments. The EM63 and GEM3 are mono-static, multi-channel sensors with coaxial transmitter and receiver geometries that are optimally coupled with geology. Since these instruments only have a single transmitter, multiple angles of target illumination are achieved by recording soundings at multiple locations spatially distributed above the target. By moving the instrument to different locations, the amount of soil response has the potential of spatially varying background responses, depending on the ground clearance, orientation variations, and geologic properties.

The first approach we investigated subtracted the soil response prior to inverting for dipole parameters. This method requires a background susceptibility model to be constructed from soundings located far enough away from the target such that the signal is due to soil only, while being close enough to the target such that the susceptibility model near the target could be characterized. Once the susceptibility model is constructed, then ground clearance height and IMU information is used to calculate the soil response in the vicinity of the target. This soil response is then subtracted from the data and then inverted with a dipole model. An important step in

this process is the ability to determine if a sounding is due to soil only (and thus should be used for estimating the background geology) or if a sounding has a significant target component (and should be excluded when determining the geology).

The second approach we developed estimated the geology and target dipole parameters simultaneously. This approach is useful when there are an insufficient number of soil-only soundings acquired at the edge of the target to constrain the soil model. Field data and synthetic data were used to show that at highly magnetic sites, the simultaneous inversion technique could be used to reliably extract target parameters using mono-static sensors.

During this project's period of performance, ESTCP funded the development of advanced EMI sensors that featured multiple transmitters and receivers to improve the ability to constrain target parameters. For some of these advanced sensors (e.g. MetalMapper, TEMTADS and BUD sensors), data are acquired in a cued mode where data are acquired from a single position directly over the target. The processing method designed for mono-static sensors – i.e. utilizing data taken far enough away to be insensitive to soil in order to help constrain an initial background soil model – is not possible with cued mode data collection. Therefore, we designed a processing specifically for the multi-static data of advanced sensors. The technique utilizes data components not sensitive to the ground which are used to make an initial guess at the target's dipole parameters. This initial guess is then refined by performing a simultaneous inversion for the soil and target parameters. This technique was successfully tested using MPV-MARK 1 synthetic data and field data collected at the DRDC Suffield magnetic soil facility.

A study was carried out that investigated the extent to which the background modeling algorithms improved classification performance relative to the standard median filtering approach. Simulations showed that improvements in classification could be realized at sites with soil susceptibility levels similar to those found at Camp Sibert for mono-static sensors used in a cued mode. For mono-static data acquired in a dynamic mode, we showed techniques accounting for background response variations will also improve discrimination, though we only tested the method on field data collected at Camp Sibert.

Unfortunately, a similar study was not carried out for multi-static, advanced EMI sensors. A study should be considered for future research. We developed some sense of the importance of the modeling techniques applied to advanced sensors by processing two field datasets: MPV data collected at the DRDC Suffield soil test facility, and MetalMapper data collected at Camp Beale. Soil modeling techniques were essential for reliable polarizability estimates using the MPV sensors over the Cambodian soil at the DRDC test facility. However, modeling the background response is less important for advanced multi-static EMI sensors than for mono-static sensors. The non-ground coupled data soundings of new sensors, combined with the careful subtraction of background measurements, are often sufficient for reliable

extraction with magnetic soil responses when acquiring cued data. This was the case for the recent ESTCP Live-Site demonstration held at Camp Beale. Although the classification performance at Camp Beale was satisfactory, the recovery of polarizabilities was much better during the recent Pole Mountain demonstration. The ability of Pole Mountain data to better constrain polarizabilities can partially be attributed to the presence of magnetic soil noise at Camp Beale.

Advanced sensors are now being tested in a dynamic, full coverage mode in order to further reduce the cost of discrimination (e.g. OPTEMA, TEMTADS 2x2). Dynamically acquired, full coverage data types from sites with a significant background response are candidates for applying some of the different methods tested in this project. Full coverage data at highly magnetic sites would be required to determine if background response modeling is necessary. The techniques developed in this project, combined with the addition of ground clearance sensors and high quality IMU data for accurate sensor positioning relative to magnetic soils can improve discrimination and classification at highly magnetic sites.

REFERENCES

- Baum, C.E. Detection and Identification of Visually Obscured Targets, Chapter: The Magnetic Polarizability Dyadic and Point Symmetry, pages 219–242. Taylor and Francis, 1999.
- Bell, T., B. Barrow, J. Miller, 2001. “Subsurface discrimination using electromagnetic induction sensors”. IEEE Transactions Geoscience and Remote Sensing 39, 1286–1293.
- L. Beran and D.W. Oldenburg, Selecting a Discrimination Algorithm for Unexploded Ordnance Remediation. IEEE Transactions on Geoscience and Remote Sensing, 46(9): 2547-2557, 2008.
- Billings, S., Pasion, L., Oldenburg, D., and Foley, J., 2003. “The influence of magnetic viscosity on electromagnetic sensors,” in Proceedings of EUDEM-SCOT2, International Conference on Requirements and Technologies for the Detection, Removal and Neutralization of Landmines and UXO.
- Billings, S., Data Modeling, Feature Extraction, and Classification of Magnetic and EMI Data, ESTCP Discrimination Study, Camp Sibert, AL. ESTCP Project Final Report, MM-0504, 2008
- Cargile, D., Bennet, H., Goodson, R., DeMoss, T. and Cespedes, E., 2004. “Advanced UXO detection/discrimination technology demonstration – Kaho’olawe, Hawaii,” Technical Report U.S. Army Research and Development Center, Vicksburg, MS. ERDC/EL TR-04-1.
- Das, Y., “Effects of soil electromagnetic properties on metal detectors.” IEEE Transactions on Geoscience and Remote Sensing 44(6), pp. 1444-1453, 2006.
- Fernandez, J.P., Barrowes, B.E., Grzegorzcyk, T.M., Lhomme, N., O'Neill, K., Shubitidze, F., 2011. "A Man-Portable Vector Sensor for Identification of Unexploded Ordnance." IEEE Sensors Journal. vol 11, issue 10. P. 2542 – 2555.
- Foley, J., Billings, S., Pasion, L., Walker, S., and Pasion, C., UXO Target Detection and Discrimination with Electromagnetic Differential Illumination. Technical Report, Strategic. .
- Gasperikova, E., Smith, J. T., Morrison, H. F., Becker, A., 2007, Berkeley UXO Discriminator (BUD) at Camp Sibert, AL, Partners in Environmental Technology Technical Symposium & Workshop, Washington D.C.
- Grant, F.S. and West, G.G. Interpretation Theory in Applied Geophysics. McGraw-Hill Book Company, 1965.

- Haber, E., Ascher, U. M., and Oldenburg, D. W., 2004. "Inversion of 3D electromagnetic data in frequency and time domain using an inexact all-at-once approach." *Geophysics*, 69, 1216–1228.
- Lee, T., 1983. "The effect of a superparamagnetic layer on the transient electromagnetic response of a ground." *Geophysical Prospecting* 32, pp. 480-496,.
- Li, Y., Krahenbuhl, R., Meglich, T., Oldenburg, D.W., Pasion, L.R., Billings, S., van Dam, R. , Harrison, B., 2010. "Improving UXO Detection and Discrimination in Magnetic Environments." SERDP Project MM-1414 Final Report, Strategic Environmental Research and Development Program (SERDP).
- Miller, J.T.; Bell, T.H.; Soukup, J.; Keiswetter, D., 2001. "Simple phenomenological models for wideband frequency-domain electromagnetic induction." *IEEE Transactions on Geoscience and Remote Sensing*, 39-6, pp. 1294 – 1298.
- Lhomme, N., Pasion, L.R., Billings, S.D, Oldenburg, D.W., 2008. "Inversion of frequency domain data collected in a magnetic setting for the detection of UXO (Proceedings Paper)". *Proceedings Vol. 6953. Detection and Sensing of Mines, Explosive Objects, and Obscured Targets XIII*, Russell S. Harmon; John H. Holloway, Jr.; J. Thomas Broach, Editors, The International Society for Optical Engineering.
- Cross, G., 2008. "Soil Electromagnetic Properties and Metal Detector Performance Theory and Measurement." *Contract Report for Defense R&D Canada, Contract Report DCDC Suffield CR 2009-062*.
- Pasion, L., Oldenburg, D. W., Billings, S. D., and Sinex, D., 2007. "Soil compensation techniques for the detection of buried metallic objects using electromagnetic sensors," in *SPIE Conference on Detection and Remediation Technologies for Mines and Minelike Targets XII*, R. S. Harmon, J. T. Broach, and J. H. Holloway, eds., 6553, The International Society for Optical Engineering.
- Pasion, L. and Oldenburg, D. W., 2001, "A Discrimination Algorithm for UXO Using Time Domain Electromagnetics. *Journal of Engineering and Environmental Geophysics*, 28, no. 2, pages 91-102.
- Walker, S. E., Pasion, L. R., Billings, S. D., Oldenburg, D. W., and Li, Y, 2005. "Examples of the effect of magnetic soil environments on time domain electromagnetic data." In *Proceedings from SAGEEP 2005*. Oldenburg, D. W., and Pratt, D.A., 2007. "Geophysical inversion for mineral exploration: a decade of progress in theory and practice." In *Fifth Decennial International Conference on Geology, Geochemistry, Geophysics and Remote Sensing, Exploration 07 Proceedings*, pp. 61-96.
- Oldenburg, D.W., Eso, R., Napier, S., and Haber, E., 2005. "Controlled source electromagnetic inversion for resource exploration." *First Break*, Vol 23, p 41-48.

Pasion, L. R., 2007. "Inversion of Time Domain Electromagnetic Data for the Detection of Unexploded Ordnance, PhD Thesis, University of British Columbia.

Prouty, M., George, D.C., Snyder, D.D., 2011. "MetalMapper: A Multi-Sensor TEM System for UXO Detection and Classification." ESTCP Project MR-200603 Final Report, Environment and Security Technology Certification Program (ESTCP).

Steinhurst, D.A., Harbaugh, G.R., Kingdon, J.B., Furuya, T., Keiswetter, D.A., George, D.C., 2010. "EMI Array for Cued UXO Discrimination." ESTCP Project MR-200601 Final Report, Environment and Security Technology Certification Program (ESTCP).

APPENDICES

We include relevant reports, conference proceedings and presentations related to this project.

A1. Year One Annual Report. This report includes a detailed summary of the soil modeling technique, as well as examples of applying the soil modeling to dynamically acquired Geonics EM63.

A2. Improving detection and discrimination of buried metallic objects in magnetic geologic settings by modeling the background soil response (SPIE Defense Security and Sensing Proceedings Paper).

Authors: Leonard R. Pasion, Stephen D. Billings, et al. Published 29 April 2008

A3. Inversion of frequency domain data collected in a magnetic setting for the detection of UXO (SPIE Defense Security and Sensing Proceedings Paper).

Authors: Nicolas Lhomme, Leonard R. Pasion, et al. Published 29 April 2008

A4. Investigating the effects of soils with complex magnetic susceptibility on EMI measurements using numerical modeling of Maxwell's equations (SPIE Defense Security and Sensing Proceedings Paper).

Authors: Kevin A. Kingdon, Leonard R. Pasion, et al. Published 4 May 2009

A5. Simultaneous inversion of electromagnetic induction data for target and soil parameters (SPIE Defense Security and Sensing presentation).

Authors: Leonard R. Pasion, Kevin Kingdon, Jon Jacobson, Stephen Billings and Douglas W. Oldenburg. Presented 26 April 2011

A1. Year One Annual Report. This report includes a detailed summary of the soil modeling technique, as well as examples of applying the soil modeling to dynamically acquired Geonics EM63.



Simultaneous Inversion of UXO Parameters and Background Response

Project UX-1573

2007 Annual Report

January 2008

*Lead Principal Investigator: Leonard R. Pasion, Sky Research Inc.
Partners: Nicolas Lhomme and Douglas Oldenburg, University of British Columbia Geophysical
Inversion Facility*

This research was supported wholly (or in part) by the US Department of Defense, through the Strategic Environmental Research and Development Program (SERDP).

REPORT DOCUMENTATION PAGE			Form Approved OMB No. 0704-0188	
Public reporting burden for this collection of information is estimated to average 1 hour per response, including the time for reviewing instructions, searching existing data sources, gathering and maintaining the data needed, and completing and reviewing the collection of information. Send comments regarding this burden estimate or any other aspect of this collection of information, including suggestions for reducing this burden, to Washington Headquarters Services, Directorate for Information Operations and Reports, 1215 Jefferson Davis Highway, Suite 1204, Arlington, VA 22202-4302, and to the Office of Management and Budget, Paperwork Reduction Project (0704-0188), Washington, DC 20503.				
1. AGENCY USE ONLY (Leave blank)		2. REPORT DATE 01-04-2008		3. REPORT TYPE AND DATES COVERED Annual report 2007
4. TITLE AND SUBTITLE Project MM-1573: Simultaneous Inversion of UXO Parameters and Background Response, 2007 Annual Progress Report			5. FUNDING NUMBERS W912HQ-07-C-0012	
6. AUTHOR(S) Leonard Pasion, Steve Billings, Kevin Kingdon, Jon Jacobson (Sky Research, Inc.) Nicolas Lhomme (Sky Research, Inc./UBC-GIF), Douglas Oldenburg (UBC-GIF)				
7. PERFORMING ORGANIZATION NAME(S) AND ADDRESS(ES) Sky Research, Inc. 445 Dead Indian Memorial Road Ashland, OR 97520			8. PERFORMING ORGANIZATION REPORT NUMBER	
9. SPONSORING/MONITORING AGENCY NAME(S) AND ADDRESS(ES) Strategic Environmental Research and Development Program 901 North Stuart Street, Suite 303 Arlington, VA 22203-1821			10. SPONSORING/MONITORING AGENCY REPORT NUMBER	
11. SUPPLEMENTARY NOTES				
12a. DISTRIBUTION/AVAILABILITY STATEMENT Unclassified/Unlimited			12b. DISTRIBUTION CODE	
13. ABSTRACT (Maximum 200 words) This project focuses on the accurate recovery of target parameters from geophysical sensor data, even in cases when targets of interest occur in a magnetic or conductive host. Simultaneous modeling of dipole parameters and background properties has been conducted for both magnetic and electromagnetic field data. For magnetics data, several implementations of an equivalent layer code have been developed. We have shown that the depth and size of a buried object can be recovered when using an equivalent layer as a filter prior to the inversion, even at low signal to noise ratios. For electromagnetic induction data, an inversion methodology has been developed to simultaneously estimate geologic and dipole parameters. A method of modeling the geologic response as a result of sensor movement has been developed and looks promising. A finite volume numerical solution of Maxwell's equation has been used to model the response of a compact metallic target and a host that has viscous remnant magnetic as well as conductivity. To our knowledge, this is the only example of 3D numerical modeling of complex susceptibility and conductivity.				
14. SUBJECT TERMS Simultaneous inversion, background response, UXO, EMI, magnetics			15. NUMBER OF PAGES 78	
			16. PRICE CODE	
17. SECURITY CLASSIFICATION OF REPORT Unclassified	18. SECURITY CLASSIFICATION OF THIS PAGE Unclassified	19. SECURITY CLASSIFICATION OF ABSTRACT Unclassified	20. LIMITATION OF ABSTRACT Unlimited	

Table of Contents

Executive Summary	9
1 Introduction.....	10
1.1 Objective	10
2 Task 1.1: Development of an Equivalent Layer Methodology for Magnetics Processing ..	12
2.1 Effect of Parameterization	14
2.2 Effect of Grid Size	16
2.3 Effect of Depth.....	17
2.4 Stability of the Dipole Distribution.....	18
2.5 Constraints	19
2.6 Effect of Masking	20
2.6.1 Masking Data	21
2.6.2 Masking Data and Layer Dipoles	21
2.7 Inversion Strategy With A Dipole Layer	23
2.8 Filtering With an Equivalent Layer	23
2.9 Conclusion	29
3 Task 1.2: Develop Methodology for Inverting EMI Data for the Properties of The Background Host	31
3.1 Modeling Geologic Signal Due To Sensor Motion	35
3.2 Modeling Geology Related Sensor Noise with a Slowly Spatially Varying Background Geology Model	41
3.3 Simultaneous Inversion of Geonics EM-63 data for Dipole Parameters and Geology Parameters	45
4 Task 2.1: Studying The Amount of Interaction Between a Compact Metallic Target and Host Using Numerical Modeling of Maxwell's Equations.....	67
4.1 EH3D Details	67
4.2 Details on mesh design	68
4.3 EH3D Frequency Domain Investigations	69
4.4 Additivity	70
4.5 EH3D Modeling with Complex Susceptibilities.....	72
4.6 EH3D Time Domain Investigations.....	75
4.7 Future Modeling Efforts	77
5 Concluding Summary	78
6 References	79

List of Figures

Figure 2-1. Magnetic soil at Chevallier Ranch, MT and Camp Sibert, AL (unit: nT).	13
Figure 2-2. Equivalent layer of discrete dipoles. Left panel: Gridded Chevalier Ranch data. Right panel: Gridded residual. Units in sidebar: nT.	14
Figure 2-3. Linear representation.....	15
Figure 2-4. Power spectrum of original and predicted data, taking a FFT along the lines on which the data were collected after interpolating by distance to get a regular spacing.....	16
Figure 2-5. Effect of grid resolution. Residual of magnetic data for soil from Chevallier Ranch (Axes in m, colors in nT)	17
Figure 2-6. Effect of grid resolution, Camp Sibert, AL.....	17
Figure 2-7. Effect of depth, Chevallier Ranch.	17
Figure 2-8. Stability of equivalent layer when noise is added (square grid with 0.5 m spacing at 2 m depth). Axes: Northing and Easting, m; Magnetic data in nT	18
Figure 2-9. Effect of applying a constraint on the equivalent charge distribution for a 1 m grid. Error defined in percent has the ratio of the norms of the residual (original minus predicted data) and the original data.	19
Figure 2-10. Effect of applying a constraint on the equivalent charge distribution for a 0.5 m grid. Error defined has the ratio of the norms of the residual and the original data. Although the non-constrained visually shows the best fit, its error is the largest – this is due to the non-uniform spatial distribution of the original data.	20
Figure 2-11. Effect of mask size on the inversion of a buried dipole. Each panel shows the equivalent layer obtained with the data outside the mask for different masks (black contour). As the mask reduces the layer predicts an increasing signal inside the mask, similar to an overshooting interpolation and possibly taking away signal from a buried item. For each mask and layer a dipole model is inverted for the residual data. The title of each window indicates the contour level taken to define the mask (as a fraction of peak amplitude) and the result of the inversion for the buried item: amplitude of dipole moment m in Am^2 and depth z in meter. In this example a synthetic dipole of moment $m=0.1 \text{ Am}^2$ was buried at $z=-0.8 \text{ m}$ in real soil at Camp Sibert, AL. The dipole layer sits at $z=-2 \text{ m}$ with a spacing of 1 m on a square grid.....	21
Figure 2-12. 1m grid	22
Figure 2-13. 0.5 m grid	22
Figure 2-14. Modeling method and mask size for identifying a buried dipole. Assume a buried dipole with moment $m=0.15 \text{ Am}^2$, depth $z=-0.8 \text{ m}$, position $x=0 \text{ m}$ and $y=0 \text{ m}$. Left panel: magnetic soil, buried dipole and mask size (black contour). Right panel: Model error relative to depth and moment for different methods and mask sizes.....	24
Figure 2-15. Same test as in Figure 2-11, here $m = 0.10 \text{ Am}^2$	24
Figure 2-16. Same as before, here $m = 0.05 \text{ Am}^2$. Right panel shows the misfit.	25
Figure 2-17. Dipole with $m=0.05 \text{ Am}^2$, depth $z=-0.8 \text{ m}$ and $x=1 \text{ m}$ (displacement to the right). ..	25
Figure 2-18 Moment $m = 0.1 \text{ Am}^2$, $z=-0.8 \text{ m}$	26
Figure 2-19. Moment $m = 0.05 \text{ Am}^2$, $z=-0.8 \text{ m}$	26
Figure 2-20. Moment $m = 0.05 \text{ Am}^2$, $z=-0.8 \text{ m}$. Target off-center.....	27
Figure 2-21. Moment $m = 0.05 \text{ Am}^2$, $z=-0.8 \text{ m}$. Target off-center.....	27
Figure 2-22. Simulations testing the ability to recover a UXO against a strong magnetic background.....	29

Figure 3-1. Geonics EM-63 Time domain electromagnetic data acquired over the Camp Sibert Geophysical GPO. (a) The Geonics EM-63 was instrumented with a Crossbow 400 IMU for coil orientation measurements and a Leica Robotic Total Station. (b) Thirty intact 4.2 in mortars and 8 partial mortars were seeded in the GPO. Dynamically acquired data were taken along North-South lines with approximately 50 cm line spacing. (c) Time domain soundings of the background soil display the characteristic viscous remnant magnetization (VRM) decay.	33
Figure 3-2. Comparison of the first time channel of data collected along a line located at an Easting of approximately $x = 43$ m. Along this line there were no emplaced items and no known metallic targets. Variations in the measured data are correlated with the sensor elevation and orientation.	34
Figure 3-3. Tilt and height testing modeling results. A Geonics EM-61 Mark 2 sensor was used to collect data on Kaho'olawe, Island at a number of different heights and tilt angles. The signal was calculated by representing the transmitter loop with 8 dipoles.	39
Figure 3-4. Representing a 1m square loop with multiple transmitters.	39
Figure 3-5. Approximating the field produced by a 1 m square loop by dipoles.	40
Figure 3-6. Numerical modeling of field from a square Tx loop over a conductive and viscous remnant magnetic half-space.	41
Figure 3-7. Fitting raw (i.e. non-detrended) data with a slowly spatially varying background geology.	44
Figure 3-8. Fitting detrended data using a slowly varying background geology.	45
Figure 3-9. Dipole polarizations for a 60 mm mortar and a 4.2 inch mortar from Camp Sibert, AL. The 60 mm mortar polarization was derived from measurements acquired on the US Army Corps of Engineers (USACE) Engineer Research and Development Center (ERDC) test stand in Vicksburg, MS. The 4.2 inch mortar polarizations plotted here represent the average recovered polarizations from EM-63 inversions completed as part of ESTCP project MM-0504. The table lists decay parameters when modeling the polarization with the function $L(t) = kt^{\beta} \exp(-t/\gamma)$	47
Figure 3-10. Synthetically generated Geonics EM-63 data. Sensor elevation and IMU data are taken from lines $Y = 45$ to $Y = 53$ m of the Sibert GPO survey. The response of five 60 mm mortars is included. The detrended data were obtained by applying a 5 m median filter along each line and time channel.	50
Figure 3-11. Comparison of data fits when fitting data with and without geology modeling included.	51
Figure 3-12. Comparison of data fits when inverting synthetic data using simultaneous estimation of dipole and geology ((a)-(b)) and dipole only ((c)-(d)).	52
Figure 3-13. Modeling results assuming the spatial distribution of the geology can be represented by a plane. The top row of plots compares the observed and predicted data for the first time channel. The bottom row compares the true and predicted geology. The black dots at $z=0$ represent the locations at which data are modeled.	53
Figure 3-14. Comparison of recovered polarization parameters. Clearly, the secondary polarizations are not well resolved when inverting for a dipole only.	54
Figure 3-15. Depth comparison. Parameter estimation techniques	57
Figure 3-16. Depth comparison. Library fitting Techniques	58
Figure 3-17. Items included in the ordnance library.	59
Figure 3-18. Recovered primary polarizations.	60
Figure 3-19 Recovered primary polarizations normalized.	61
Figure 3-20. Parameter plots when not modeling a geology response	62

Figure 3-21. Recovered parameters when simultaneously inverting detrended data for dipole parameters and geology parameters.....	63
Figure 3-22. Parameter plots when modeling unfiltered data with a geology response	64
Figure 3-23. Library based inversion example. Examples (a) and (b) are for the same anomaly.	65
Figure 3-24. Summary of library fitting results. Anomalies with no signal or poor coverage are not included in this list.....	66
Figure 3-25. Comparison of polarizations for an ATC 2.75 and a Camp Sibert 4.2 inch mortar. Although the magnitudes of the polarizations are different, the polarizations decay in a similar manner.....	66
Figure 4-1. The staggered grid used in EH3D finite volume methods.	68
Figure 4-2. The environment modeled in EH3D.	68
Figure 4-3 A typical mesh used for modeling with EH3D. Extra padding cells have been omitted so that the fine mesh of the inner core is visible. The mesh is shown sliced 30cm above the surface where the 1m square transmit loop is indicated in red.	69
Figure 4-4. Validation tests for the EH3D frequency domain codes. Half-spaces with conductivities of 10^{-1} , 10^{-2} , 10^{-3} S/m were modeled using EH3D and compared with analytical solutions.	70
Figure 4-5. Additivity illustrated through the imaginary component of the H field at 1668 Hz. Top left shows the EH3D response generated for a target in a half-space, the top right the EH3D response for a half-space. The bottom left panel displays the derived UXO in free-space response obtained by differencing the top 2 panel responses. Finally the bottom right panel displays the EH3D response computer for a target in a free-space which is virtually identical to the adjacent derived response. All four panels shown have identical limits on color scale. Half-space results used were the 0.1 S/m case.	71
Figure 4-6. The results obtained for real and imaginary values of the H field for all frequencies modeled in EH3D for a target in a half-space (top 2 panels) and a half-space (middle 2 panels). The bottom 2 panels plot the derived target in free-space solution obtained by differencing the soundings at the center of the loop between the top row of panels and the middle row of panels. The EH3D computed solution for a target in free-space is also plotted in the bottom row panels.	72
Figure 4-7. Complex susceptibility values used for the frequency domain EH3D results incorporating non-zero susceptibility values.	73
Figure 4-8. Comparison of analytic and EH3D responses for half-spaces with complex susceptibilities and for half-spaces that have no susceptibility. Numerical solutions from EH3D have been limited to the range 10 – 100,000 Hz which is the range for our UXO studies.....	74
Figure 4-9. Comparison of the real components for analytic and EH3D responses generated by a half-space containing complex susceptibilities.....	75
Figure 4-10. Comparisons of analytical, 1D and EH3D solutions for three half-spaces of varying conductivity produced during the validation of the time domain EH3D codes.....	76
Figure 4-11. Example from previous UBC-GIF testing of EH3DTD against the method of auxiliary sources (MAS) formulation. Results illustrate a high-contrast case for a half-space: $3 \times 10^4 = \sigma_s / \sigma_b$ where $\sigma_s = 3000$ S/m, $\sigma_b = 0.1$ S/m. Vertical magnetic field is measured on the surface $y_r = z_r = 0$ m for $x_r = 0$ m (on the left) and $x_r = 0.5$ m (on the right).	77

Acronym List

Am ²	Amperes meters squared (unit of dipole moment)
ATC	Aberdeen Test Center
cm	centimeter
dB	Decibels
DC	Direct current
DoD	Department of Defense
EM	Electromagnetic
EMI	Electromagnetic induction
EqL	Equivalent layer
ERDC	Engineer Research and Development Center
ESTCP	Environmental Security Technology Certification Program
FEM	Frequency domain electromagnetic
FFT	Fast Fourier transform
GPO	Geophysical prove-out
Hz	Hertz
IMU	Inertial measurement unit
MAS	Method of Auxiliary Sources
m	meter
mm	millimeter
mV	millivolt
SERDP	Strategic Environmental Research and Development Program
SNR	Signal-to-noise ratio
TEM	Time domain electromagnetic
UBC-GIF	University of British Columbia – Geophysical Inversion Facility
USACE	United States Army Corps of Engineers
UXO	Unexploded ordnance
VRM	Viscous remanent magnetization

Acknowledgements

Camp Sibert data processed in this report were collected as part of ESTCP project MM-0504 “Practical Discrimination Strategies for Application to Live Sites”.

We thank Dr. Greg Oldenborger for his help in running the EH3D numerical modeling code. We also thank Roman Shekhtman for preparing a version of EH3D that models complex susceptibility and also for providing support when running the code on the University of British Columbia Geophysical Inversion Facility computer cluster.

EXECUTIVE SUMMARY

This is the first annual report for the Strategic Environmental Research and Development Program (SERDP) Project MM-1573 and covers the research results accomplished during calendar year 2007. This project focuses on the accurate recovery of target parameters from geophysical sensor data, even in cases when targets of interest occur in a magnetic or conductive host. Specific technical objectives are as follows:

- 1) Develop improved recovery of target parameters by simultaneously inverting for both target parameters and the properties of the host material (Task 1).
- 2) Determine the extent to which a highly conductive or magnetic host interacts with a buried metallic target (Task 2).

The research completed to date has progressed according to the project plan. Simultaneous modeling of dipole parameters and background properties has been conducted for both magnetic and electromagnetic field data. Numerical modeling using frequency domain formulations has been able to accurately calculate the response of a conductive and complex magnetic susceptible soil. All codes are performing as expected, and we can confidently proceed with additional simulations and testing specific aspects of the different algorithms.

This report is organized such that three primary research tasks for the first year are summarized in individual sections:

- Task 1.1: Develop an equivalent layer methodology for magnetics data processing
- Task 1.2: Develop methodology for inverting electromagnetic induction (EMI) data for the properties of the background host
- Task 2.1: Evaluate the interaction between a compact metallic target and host using numerical modeling of Maxwell's equations

The report concludes with a summary section outlining the accomplishments and research plans for the upcoming year.

INTRODUCTION

This research addresses one of the Department of Defense's (DoD) most pressing environmental problems; that is, the efficient and reliable identification of unexploded ordnance (UXO) without the need to excavate large numbers of non-UXO. The task of discriminating UXO from non-UXO items is more difficult when sensor data are collected at sites where an electromagnetically active host contributes a large background signal that masks the response of UXO. These include sites contaminated with geological noise originating from magnetic soil, and sites requiring detection of UXO in conductive sea water. In regions of highly magnetic soil, magnetic and electromagnetic sensors often detect large anomalies that are of geologic, rather than metallic, origin.

OBJECTIVE

This project focuses on the accurate recovery of target parameters from geophysical sensor data, even in cases when targets of interest sit in a magnetic or conductive host. Specific technical objectives are as follows: 1) Determine the extent to which a highly conductive or magnetic host interacts with a buried metallic target. 2) Develop improved recovery of target parameters by simultaneously inverting for both target parameters and the properties of the host material.

Process Summary

This research concerns the process of extracting physically realistic models of buried unexploded ordnance from magnetic, time-domain electromagnetic (TEM) and frequency-domain electromagnetic (FEM) data. In particular, methodologies for modeling and simultaneous inversion of objects and background host material are being evaluated.

For magnetic data, non-linear high-pass filters are typically used to remove the larger scale host material or background geological effects and the remaining dipolar anomalies are inverted either individually or simultaneously by an efficient bound-constrained optimization algorithm. This process works well when the geological variations are at larger scales than the UXO anomalies, but it is ineffective when this is not the case. Therefore, we proposed to couple our inversion scheme with an equivalent layer that attempts to model the background geology. The equivalent layer will then act as a high-pass filter with a cut-off value that depends on the grid spacing and depth below the observation surface.

For EMI data, we will simultaneously fit the background response and a target's dipolar response. Including the parameters of the background response in the model vector will help reduce filtering artifacts that bias estimates of the target parameters. However, the introduction of a more complex model results in a more difficult inverse problem that must be solved. We will carry out an

extensive investigation of the inverse problem to determine the extent with which data can constrain the parameters of the forward model.

In addition to developing improved parameter estimation techniques, we will determine if, and under what conditions, the interaction between the target and the host is important. With that understanding, we can develop inversion tools to take this interaction into account.

TASK 1.1: DEVELOPMENT OF AN EQUIVALENT LAYER METHODOLOGY FOR MAGNETICS PROCESSING

In magnetic data, UXO items and other metallic debris generally appear as dipolar anomalies overprinting larger scale features due to near-surface magnetite variations and the regional geology. Non-linear high-pass filters are typically used to remove the larger scale effects and the remaining dipolar anomalies are inverted either individually or simultaneously by an efficient bound-constrained optimization algorithm. This process works well when the geological variations are at larger scales than the UXO anomalies, but is ineffective when this is not the case. We proposed to model the background geology with an *equivalent layer*, a fictitious distribution of dipolar sources that lie at or below the observation surface and which can potentially reproduce any magnetic field.

The following study shows some of the properties of an equivalent layer and presents our first attempts at inverting magnetic data over an item buried in a magnetic host using an equivalent layer.

METHOD

The equivalent source technique (Dampney, 1969) was first introduced to map a potential field on a regular grid, in particular when magnetic or gravity data are collected over variable topography in an airborne survey (e.g., Hansen and Miyasaki, 1984; Ivan, 1994; Li and Oldenburg, 1999). The method is based on the inherent ambiguity in determining the source of a potential field from its values outside of the source region and is most useful when interpreting data where distance to the source varies.

We assume that the magnetic signal of a soil and any geologic artifacts can be modeled by a distribution of magnetic dipoles placed on an equivalent layer below the observation level. To separate the contribution of the magnetic host from a buried item of interest, we further assume that there is no interaction between the host and item and that the host is located below the item so that the equivalent layer can also be placed below it.

Due to the computational intensity of the process, we propose to define an equivalent layer on a cell by cell basis as opposed to modeling the equivalent layer of an entire grid. We perform a series of tests using data collected over soils with large amounts of magnetization. We consider a cell from the site of Chevallier Ranch, MT, where a magnetic survey was conducted as part of SERDP project MM-1414 and from former Camp Sibert, AL, where data were collected for the UXO Discrimination Pilot Study (Environmental Security Technology Certification Program (ESTCP) project MM-0504). The first data set is characterized by long scale features whereas the second one shows variability at shorter scales (Figure 2.1).

The following steps are taken to build and use an equivalent layer:

1. Define the relationship between the equivalent layer and the observations: build a matrix \mathbf{A} such that $\mathbf{A} \mathbf{x} = \mathbf{d}_{\text{obs}}$
2. Get equivalent layer \mathbf{x}_{out} based on the data away from magnetic anomaly of interest; \mathbf{x}_{out} is the initial guess for equiv layer when inverting all data
3. Invert simultaneously all the magnetic data to characterize the soil and the buried item.

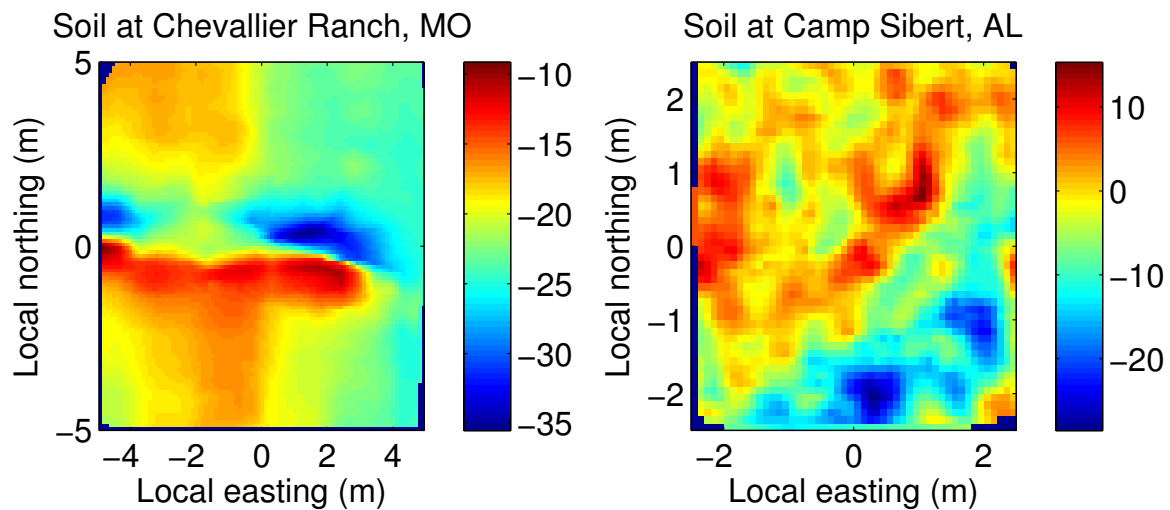


Figure 0.1. Magnetic soil at Chevallier Ranch, MT and Camp Sibert, AL (unit: nT).

PROPERTIES OF EQUIVALENT LAYERS

The fidelity with which an equivalent layer of dipoles can predict magnetic data depends on the type of parameterization of the layer, the grid size used for discretization, the depth of the layer, and the method used for inverting the dipole distribution. In this section we test those different effects in the context of applying an equivalent layer for filtering out geology, not necessarily for accurately mapping all detailed features of a magnetic data set.

We test two types of parameterizations for the distribution of dipoles:

- Discrete dipoles placed at grid nodes, following the original method of Dampney (1969);
- Linear dipoles over cell faces, adapting the method of Ivan (1994).

In both cases we assume that the layer is a flat surface and that dipoles are vertically oriented.

EFFECT OF PARAMETERIZATION

DISCRETE REPRESENTATION

Figure 2.2 shows gridded data over a magnetic soil at Chevallier Ranch, MT and the residual when predicting the magnetic data at observation locations with an equivalent layer. The layer is made of discrete vertical dipoles on a 1 meter (m) square grid placed on a horizontal plane at 2 m below the average surface elevation and is inverted with a straightforward least square solver.

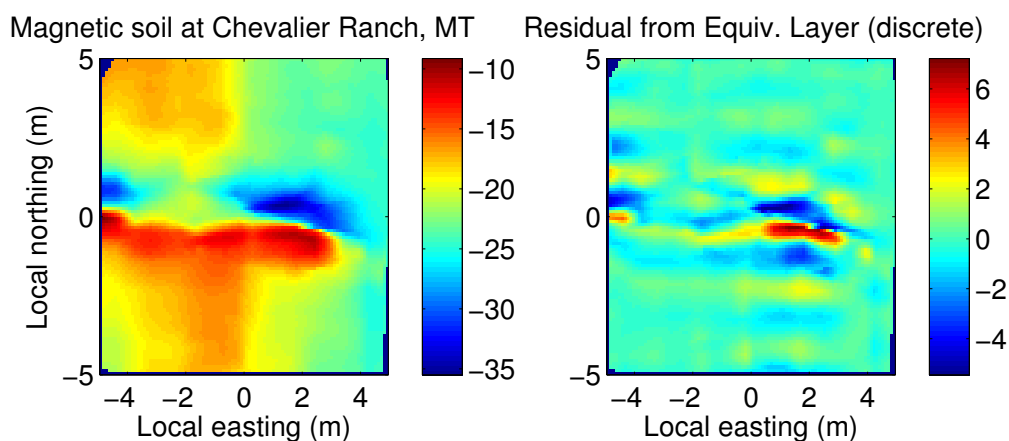


Figure 0.1. Equivalent layer of discrete dipoles. Left panel: Gridded Chevallier Ranch data. Right panel: Gridded residual. Units in sidebar: nT.

LINEAR DISTRIBUTION:

Figure 2.3 (left panel) shows the residual when using a distribution of dipoles that linearly varies over cells: $m(x,y) = Mx + Ny + P$.

The algorithm extends the method of polyhedral surfaces of Ivan (1994) to squares.

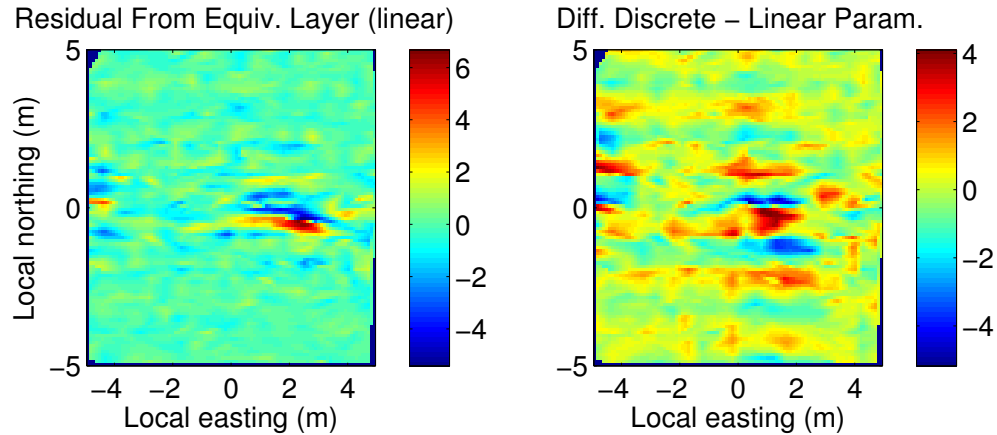


Figure 0.3. Linear representation.

A COMPARISON OF LINEAR AND DISCRETE DIPOLE DISTRIBUTIONS:

The linear method provides a better fit than the discrete one for a same discretization grid (25% in this example). In effect, the linear method uses three times as many variables as the discrete one for the same discretization and requires a significantly longer time to build the modeling matrix that maps the layer onto the observations.

Figure 2.4 shows that neither method captures much of the power below 0.3 m. Between 0.3-1 m the linear method best resolves the original data with possible addition of extra noise (may introduce some power at medium lengths not present in original data), whereas the discrete method best performs in the 1-3 m range.

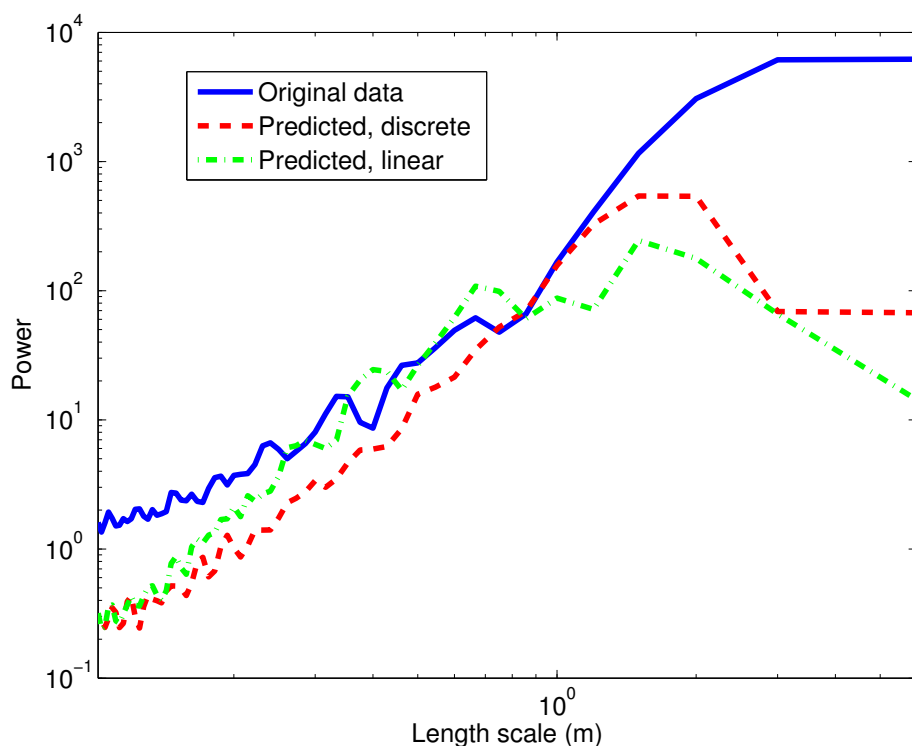


Figure 0.4. Power spectrum of original and predicted data, taking a fast Fourier transform (FFT) along the lines on which the data were collected after interpolating by distance to get a regular spacing.

EFFECT OF GRID SIZE

Figures 2.5 and 2.6 show the residual when modeling magnetic soil at different grid resolutions. Using a discrete parameterization of a layer at 2 m depth, we find, as expected, that the finer the grid the better the fit.

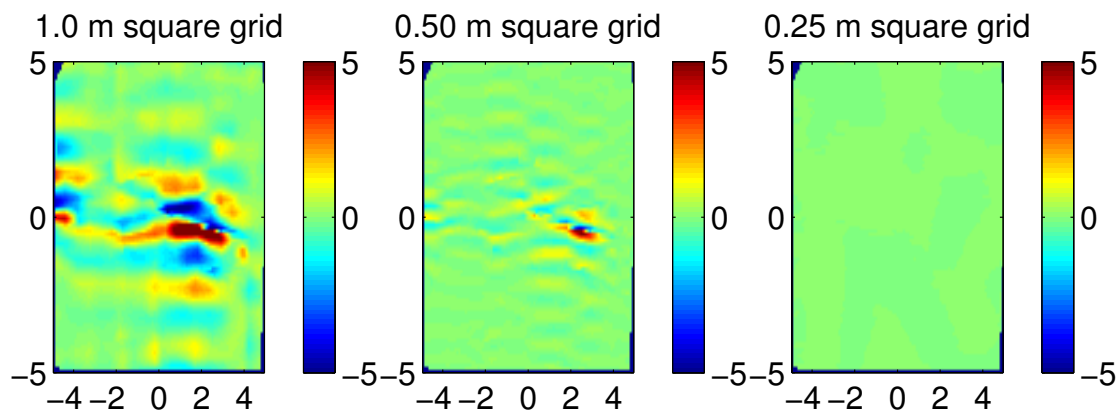


Figure 0.5. Effect of grid resolution. Residual of magnetic data for soil from Chevallier Ranch (Axes in m, colors in nT)

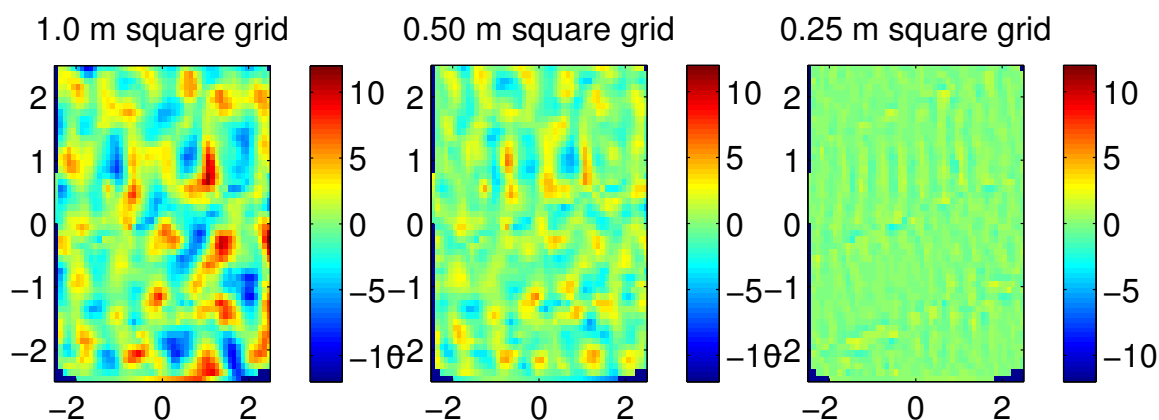


Figure 0.6. Effect of grid resolution, Camp Sibert, AL

EFFECT OF DEPTH

Figure 2.7 shows the effect of varying the depth of the equivalent layer on soil from Chevallier Ranch. There is a subtle difference in fit between the layers, with a better fit at shallow depth.

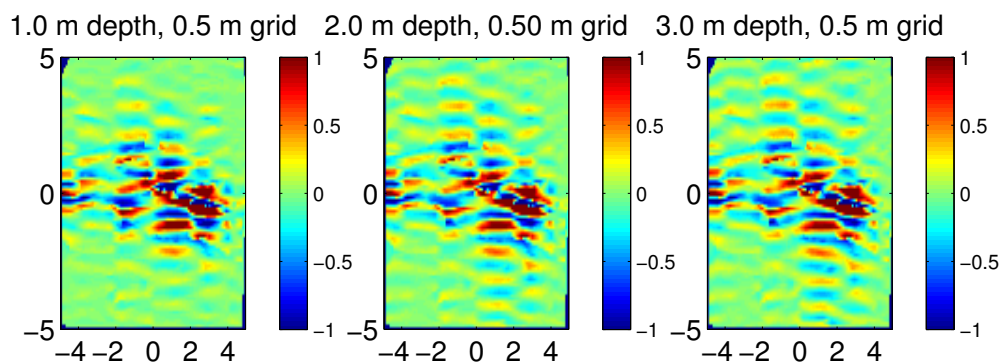


Figure 0.7. Effect of depth, Chevallier Ranch.

STABILITY OF THE DIPOLE DISTRIBUTION

Figure 2.8 shows the change in the equivalent layer when noise is added to the original data (Gaussian noise with $\text{std}=0.5$ nT). The lower panels show how the distribution of dipoles on the new equivalent layer (right panel) varies significantly and non-linearly to a small perturbation. It is therefore unstable. This result has significant repercussions for the inversion of a buried item and equivalent layer. In an iterative search for an equivalent layer, two layers could be significantly different, and the final layer could not bear any similarities with the initial layer, thus tight bounds would not be recommended.

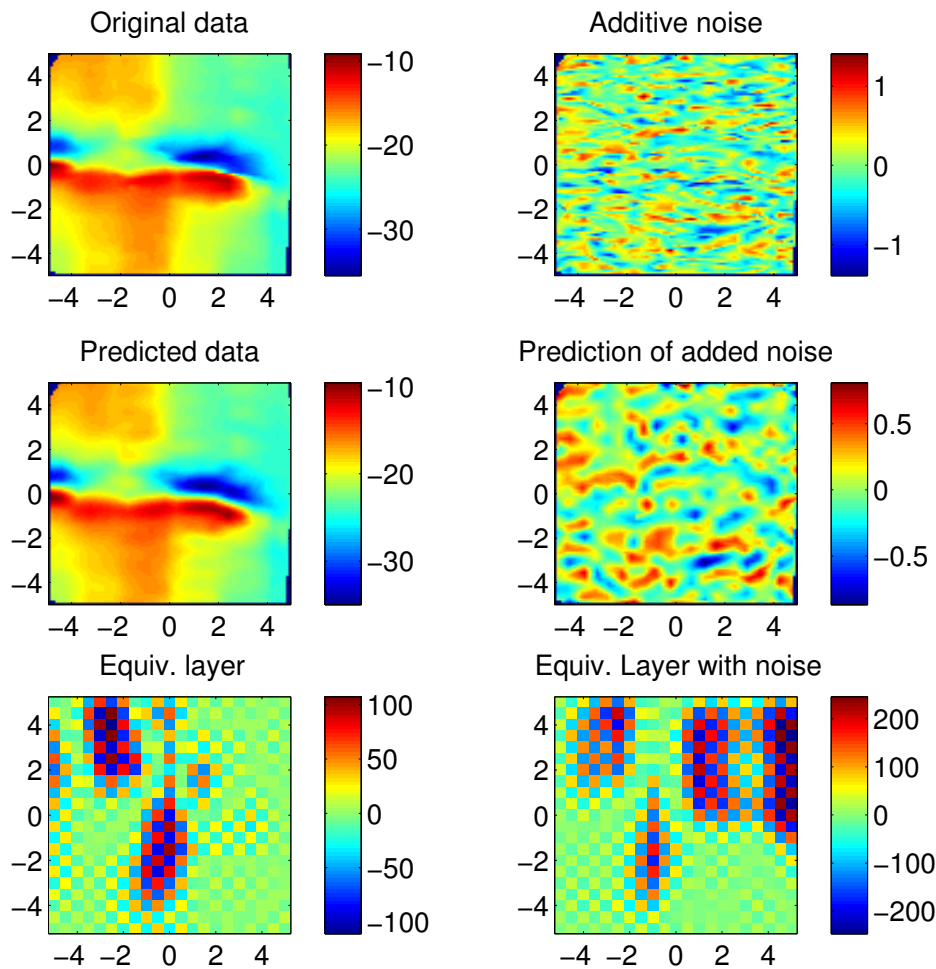


Figure 0.8. Stability of equivalent layer when noise is added (square grid with 0.5 m spacing at 2 m depth). Axes: Northing and Easting, m; Magnetic data in nT

We note that the equivalent layer has a great deal of high frequency variation that is characteristic of an unregularized data inversion. A formulation that includes regularization is required to help stabilize the dipole distribution.

CONSTRAINTS

One would be tempted to apply some sort of regularization or constraints to stabilize the solution of the equivalent layer problem. Thus far we used the pseudo-inverse of a matrix to solve for the equivalent layer, based on the Moore-Penrose algorithm in MatLab (*pinv*). Positivity or negativity can be imposed on the solution by using a linear solver (MatLab function *lsqlin*). Using data over a soil at Camp Sibert, Figures 2-9 and 2-10 show the fits and errors associated with each method for a 1 m grid and a 0.5 m grid, respectively. For this dataset the constraints have negligible effect on the fit with a 1 m grid. At 0.5 m the non-constrained solution provides a significantly better fit whereas the constrained solutions have fits similar to those achieved at lower resolution, thus defeating the purpose of a finer grid. Positive or negative constraints are therefore not recommended for this data set. This reinforces the claim made in the previous section about the inapplicability of positivity and negativity bounds.

We note that the equivalent layer will need both positive and negative values, so neither positivity nor negativity will likely be successful. However, bounding the amplitudes (having both a positive and negative limit) may help. Also, the deeper the equivalent layer, the greater the bounds will likely have to be.

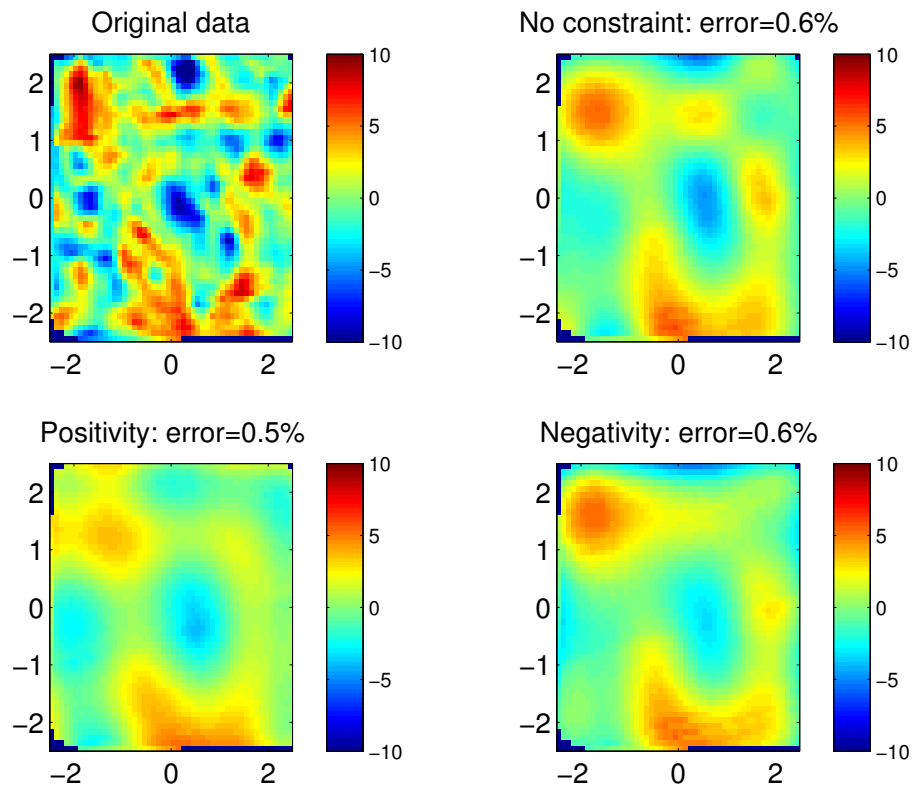


Figure 0.9. Effect of applying a constraint on the equivalent charge distribution for a 1 m grid. Error defined in percent has the ratio of the norms of the residual (original minus predicted data) and the original data.

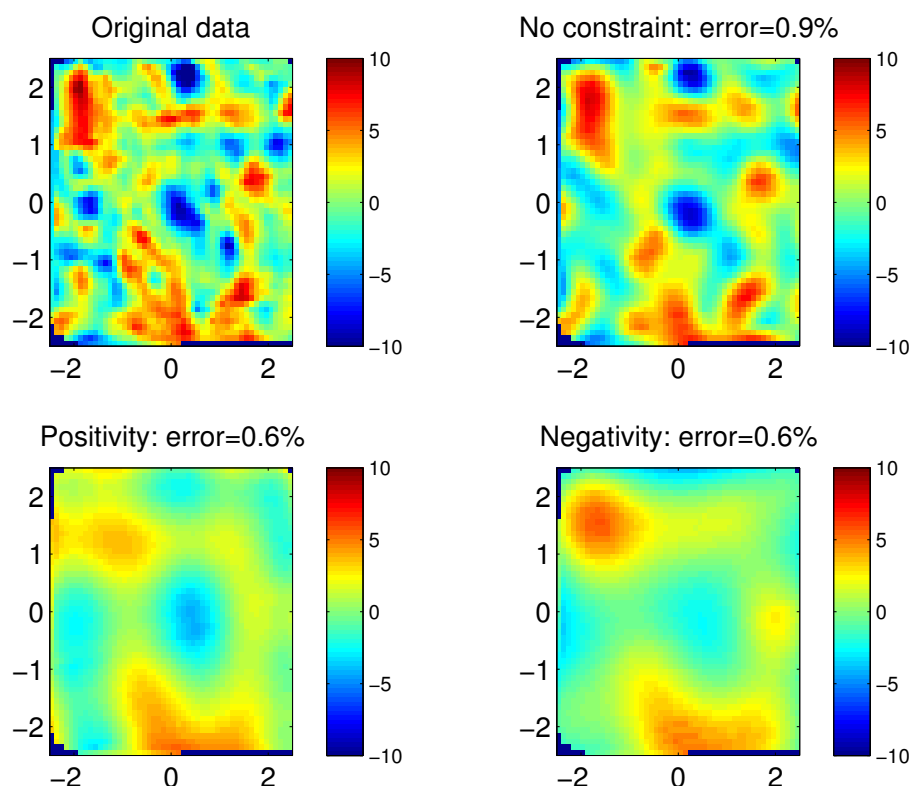


Figure 0.10. Effect of applying a constraint on the equivalent charge distribution for a 0.5 m grid. Error defined as the ratio of the norms of the residual and the original data. Although the non-constrained visually shows the best fit, its error is the largest – this is due to the non-uniform spatial distribution of the original data.

EFFECT OF MASKING

When an item is buried in a magnetic soil, we propose to identify that item by assuming that a model with a single dipole accounts for its signature while a model of equivalent layer represents the soil. To separate the domains within which each entity is dominant, a mask can be defined around the anomaly caused by the object of interest. Outside of the mask, most of the magnetic signal is assumed to be soil and modeled with the equivalent layer. Inside the mask the object of interest is preponderant, although there remains a contribution from the soil. The main challenge of characterizing the object of interest lies in the difficulty to separating each contribution. As a first pass, one can assume that the data outside of the mask can be used to characterize the soil inside and outside of the mask, as the equivalent layer of magnetic dipoles predicts data everywhere, regardless of the mask.

MASKING DATA

The size of the mask determines the characteristic length scale and intensity of the signal that the equivalent layer predicts inside the mask. A large mask contains little fraction of the signal originating from the buried object of interest and therefore predicts a smooth magnetic field with low intensity, as illustrated in the figure below. As the mask tightens up, data from the anomaly is taken into account by the equivalent layer, which then predicts signal with larger amplitude and shorter length scale – in the limit case the equivalent layer predicts the anomaly caused by the buried item.

In Figure 2.11 the smaller the mask (higher fraction of maximum value), as more signal is taken into account by the equivalent layer, less remains to be inverted for the buried item, and therefore the amplitude of the predicted dipole becomes smaller and the depth is shallower because the wide spatial decay, characteristic of deep item, is already accounted for by the equivalent layer. By contrast, if the mask is too large it contains signal from the soil where the anomaly caused by the buried item has vanished. Thus there is a trade-off on the size of the mask.

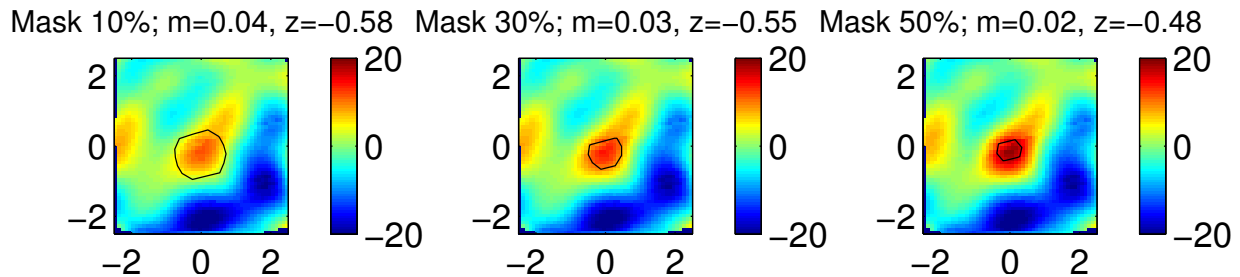


Figure 0.11. Effect of mask size on the inversion of a buried dipole. Each panel shows the equivalent layer obtained with the data outside the mask for different masks (black contour). As the mask reduces the layer predicts an increasing signal inside the mask, similar to an overshooting interpolation and possibly taking away signal from a buried item. For each mask and layer a dipole model is inverted for the residual data. The title of each window indicates the contour level taken to define the mask (as a fraction of peak amplitude) and the result of the inversion for the buried item: amplitude of dipole moment m in Am^2 and depth z in meter. In this example a synthetic dipole of moment $m=0.1 \text{ Am}^2$ was buried at $z=-0.8 \text{ m}$ in real soil at Camp Sibert, AL. The dipole layer sits at $z=-2 \text{ m}$ with a spacing of 1 m on a square grid.

MASKING DATA AND LAYER DIPOLES

One possible issue with the previous method is caused by portion of the equivalent layer that lies inside the mask. Dipoles there are poorly constrained as the distance between the dipole and the magnetic data outside the mask gets too large. To avoid that issue we propose to remove all dipoles of the layer inside the mask. For the same example as the previous section, Figure 2.12 shows that the resulting magnetic map predicts weaker amplitudes inside the mask and improves the recovery of the buried dipole at all mask sizes, although the best result remains significantly

different than the true model. The inversion improves in Figure 2.13 when the grid spacing is reduced to 0.5 m.

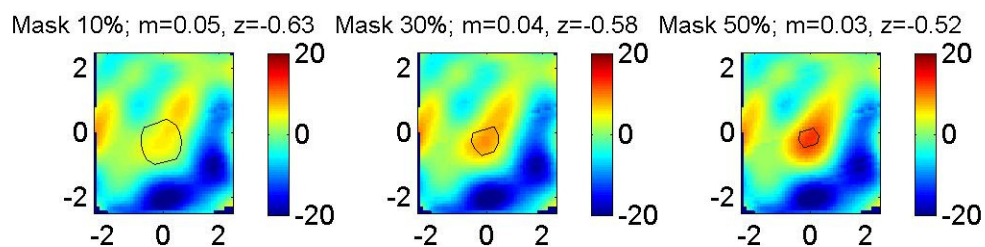


Figure 2.12. 1m grid

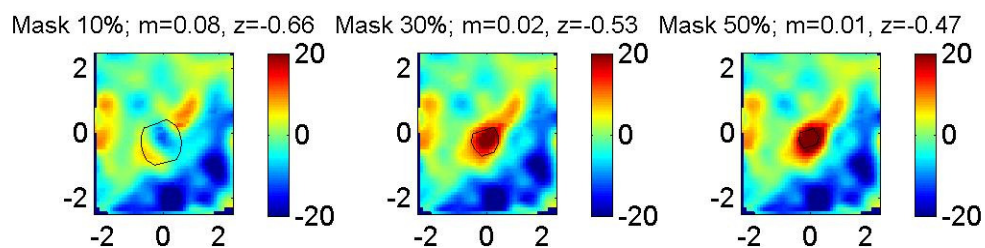


Figure 2.13. 0.5 m grid

INVERSION STRATEGY WITH A DIPOLE LAYER

When inverting for a buried item, the components of the dipole model are the position, orientation, and amplitude of the moment and a direct current (DC) shift that accounts for the presence of a background (noise, soil). With a dipole layer that DC shift can be taken into account by the layer and therefore the dipole model for the buried object can be reduced. We test the success rate of inverting with a single dipole and an equivalent layer, with and without a DC shift parameter.

As the choice of the size of a mask is critical, we test the effect of setting the contour limit of the mask to 2.5, 5, 10, 20 and 30 % fraction of the peak signal for the synthetic dipole before it is added to the soil. This choice is made to study the effect of mask size while circumventing the crucial issue of establishing a masking strategy for an item embedded in a magnetic host. We choose a discrete parameterization of the layer with a square grid with 0.5 or 1 m spacing at 2 m depth and ignore the layer inside the mask.

FILTERING WITH AN EQUIVALENT LAYER

We propose a series of examples to illustrate the effect of mask size, grid spacing and model type for different soils and sizes of buried ordnance. We choose soils from Chevallier Ranch, MT and Camp Sibert, AL, where a strong magnetization caused difficulties in identifying buried ordnance. To control the experiment and vary the size and depth of the target of interest we place a synthetic dipole instead of relying on real data.

For these examples we first invert for the dipole layer outside of the mask then invert for a buried single dipole using the residual of the magnetic data after the contribution from the equivalent layer has been removed. The following notations are applied:

- EqL: Inversion with equivalent layer and a single dipole for the buried ordnance;
- DC: Invert directly for dipole with soil taken into account by DC shift (no equivalent layer); and,
- EqL+DC: equivalent layer + dipole model + DC shift.

SOIL FROM CHEVALLIER RANCH, MT:

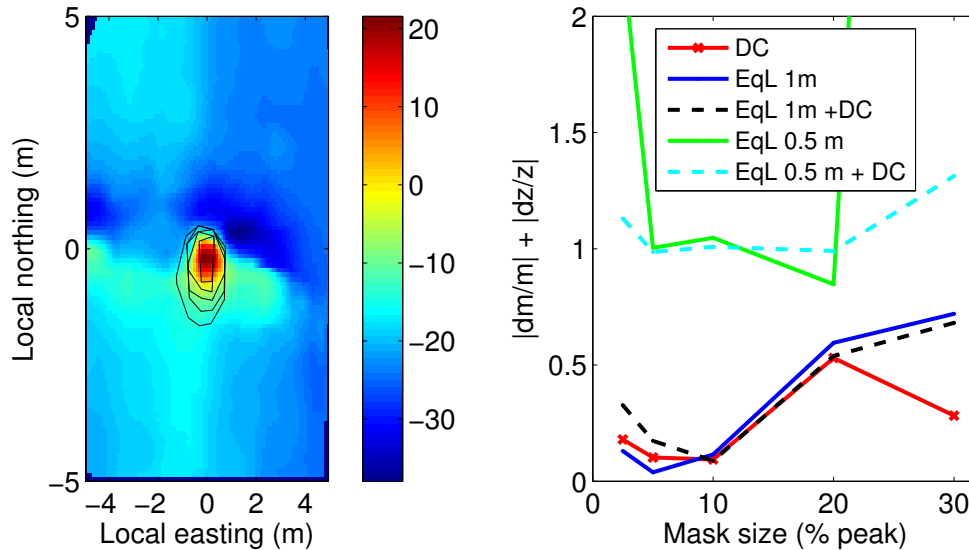


Figure 2.14. Modeling method and mask size for identifying a buried dipole. Assume a buried dipole with moment $m=0.15 \text{ Am}^2$, depth $z=-0.8 \text{ m}$, position $x=0 \text{ m}$ and $y=0 \text{ m}$. Left panel: magnetic soil, buried dipole and mask size (black contour). Right panel: Model error relative to depth and moment for different methods and mask sizes.

Figure 2.14 shows the example of an item that stands out in a magnetic environment. The best results are achieved with a large mask and coarse grid spacing. Direct inversion without explicit modeling of the soil also yields acceptable results. In Figure 2.15 the size of the item is reduced and the coarse-grid layer outperforms all other methods.

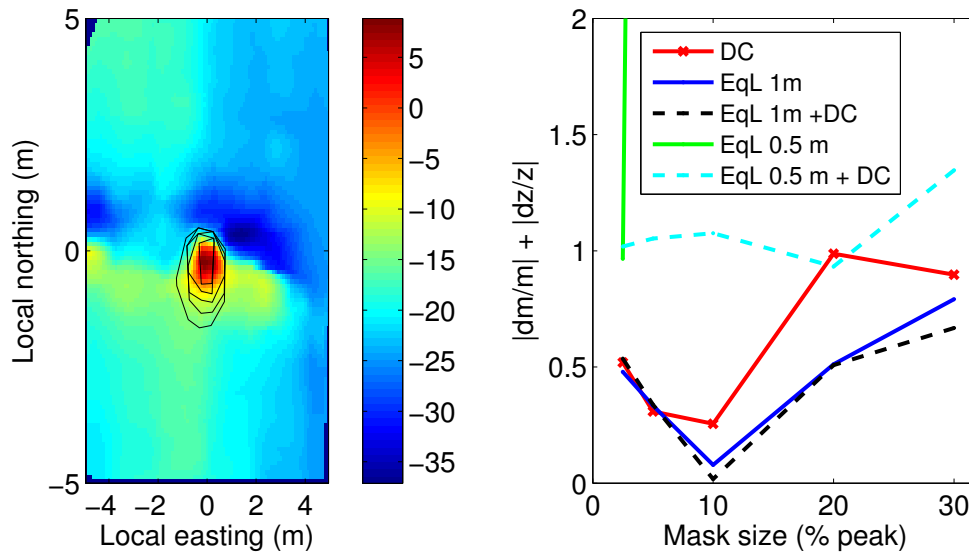


Figure 2.15. Same test as in Figure 2.11, here $m = 0.10 \text{ Am}^2$

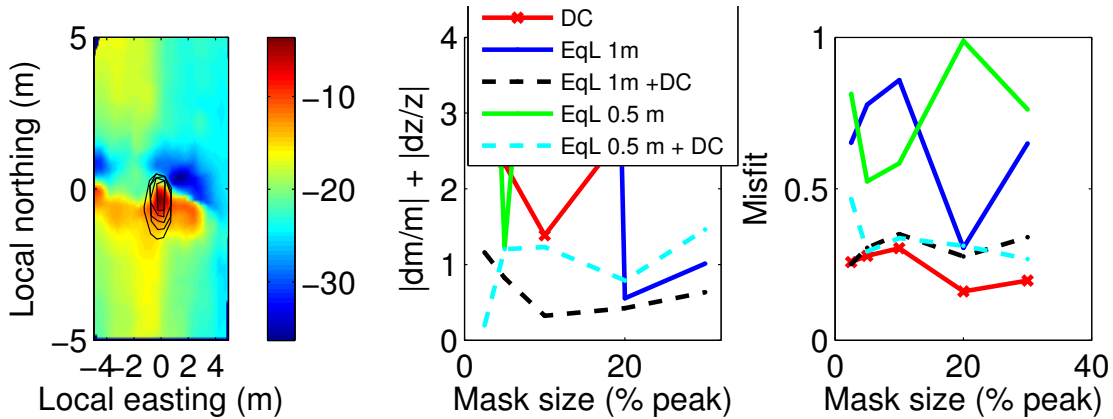


Figure 2.16. Same as before, here $m = 0.05 \text{ Am}^2$. Right panel shows the misfit.

Figure 2.16 shows the same soil with an item half the size of the previous test. The anomaly originating from that item is barely noticeable against the background. In that case an equivalent layer with an additional DC shift for the dipole yields the best results, in particular with 1 m grid and a 10-20%-level mask. The misfit does not convey any useful information for choosing the best model. On the contrary, the simple dipole without an equivalent layer yields the best fit even though the recovered model strongly differs from the actual model. A similar result is presented in Figure 2.17, where direct inversion is completely inappropriate. In summary we find for this Chevallier Ranch data set that the 1 m grid with a mask at 10% of the peak anomaly best suits the case of a small UXO in geology where long-scale features dominate.

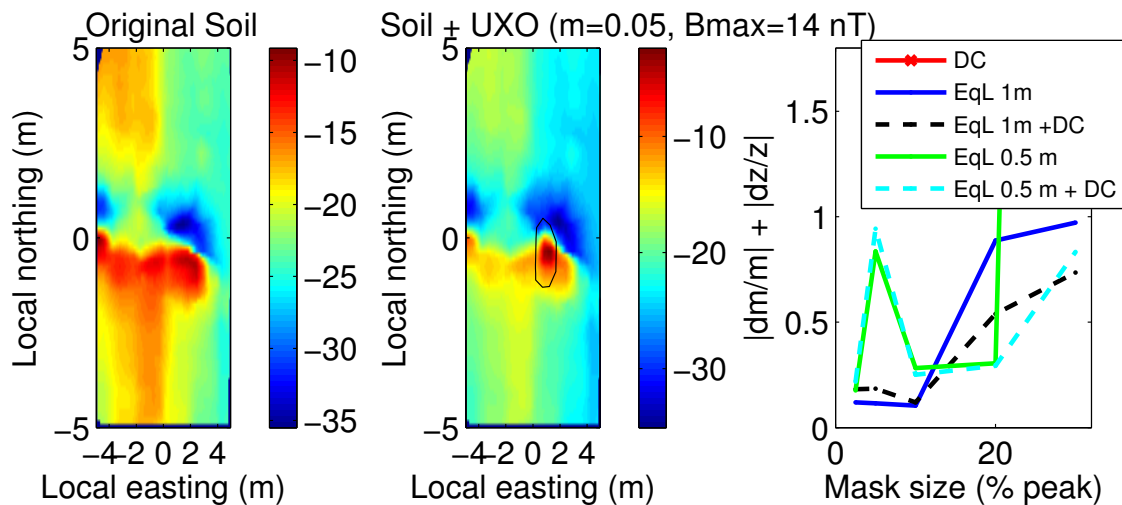


Figure 2.17. Dipole with $m=0.05 \text{ Am}^2$, depth $z=-0.8 \text{ m}$ and $x=1 \text{ m}$ (displacement to the right).

SOIL FROM CAMP SIBERT, CELL 725 (ORIGINAL ANOMALY CAUSED BY SOIL).

Similar to the previous site, we add a synthetic dipole of amplitude 0.10 or 0.05 amperes meters squared (Am^2) to a data set where the magnetic signal is characterized by shorter length scale than that of Chevallier Ranch.

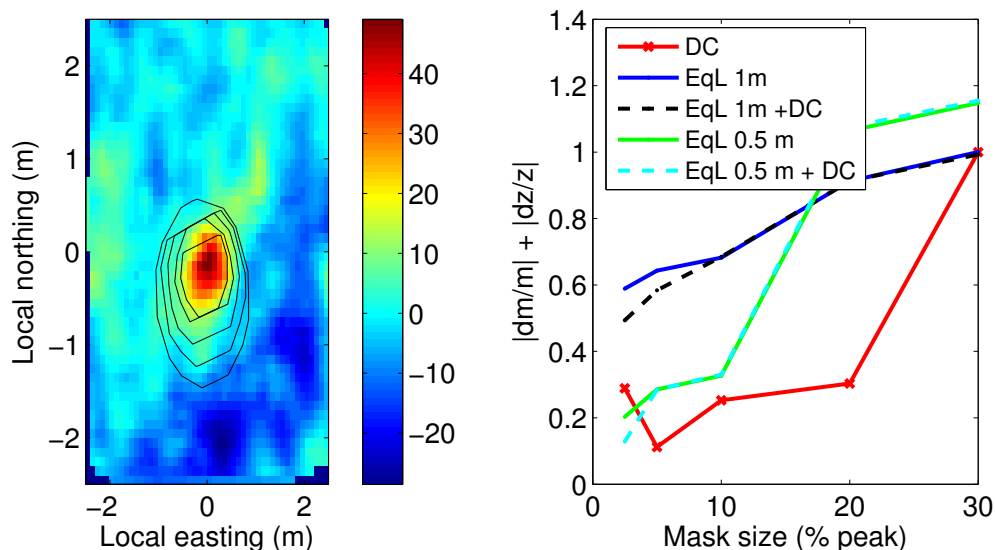


Figure 2.18. Moment $m = 0.1 \text{ Am}^2$, $z = -0.8 \text{ m}$.

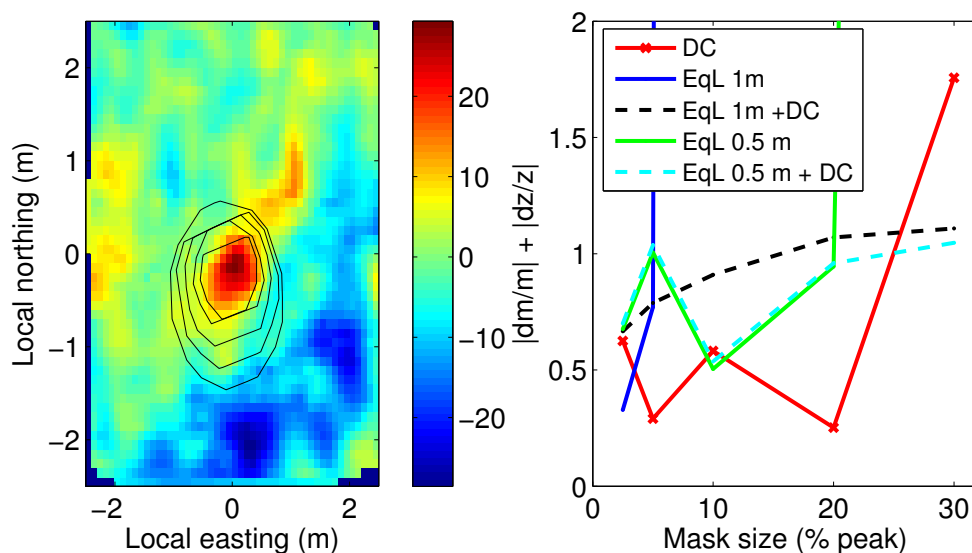


Figure 2.19. Moment $m = 0.05 \text{ Am}^2$, $z = -0.8 \text{ m}$

In Figures 2.18 and 2.19 the best results are achieved with the simple dipole model. In Figure 2.18 the fine grid also provides satisfactory results; results degrade rapidly with decrease in

mask size. In Figure 2.19, results are highly unstable because the signal from the buried item is weak relative to the original background (Figure 2.1).

In Figures 2.20 and 2.21 the same small dipole is displaced off the center of the cell to illustrate the effect of the nearby surroundings on the performance of the different methods. Results differ significantly. In those cases the method with 1 m grid plus DC shift yields the best success.

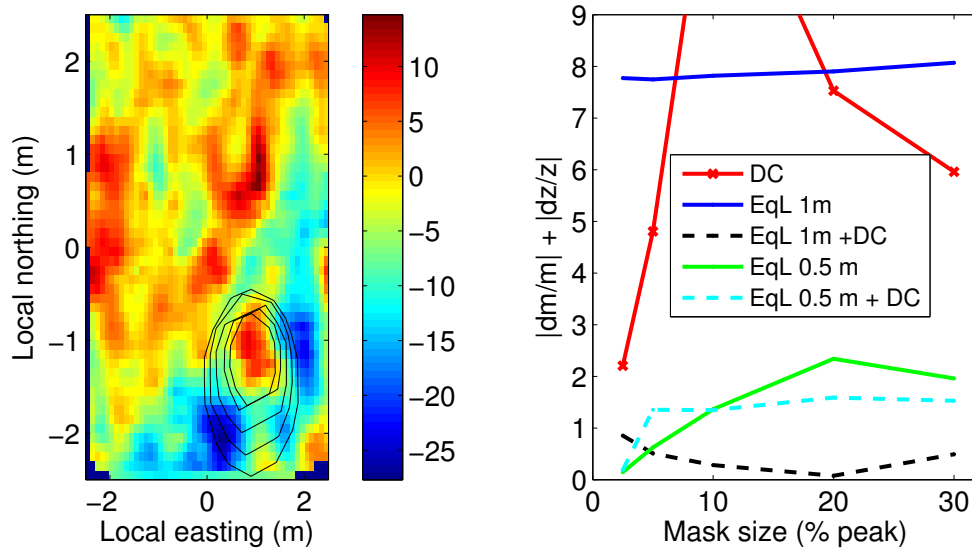


Figure 2.20. Moment $m = 0.05 \text{ Am}^2$, $z=-0.8 \text{ m}$. Target off-center

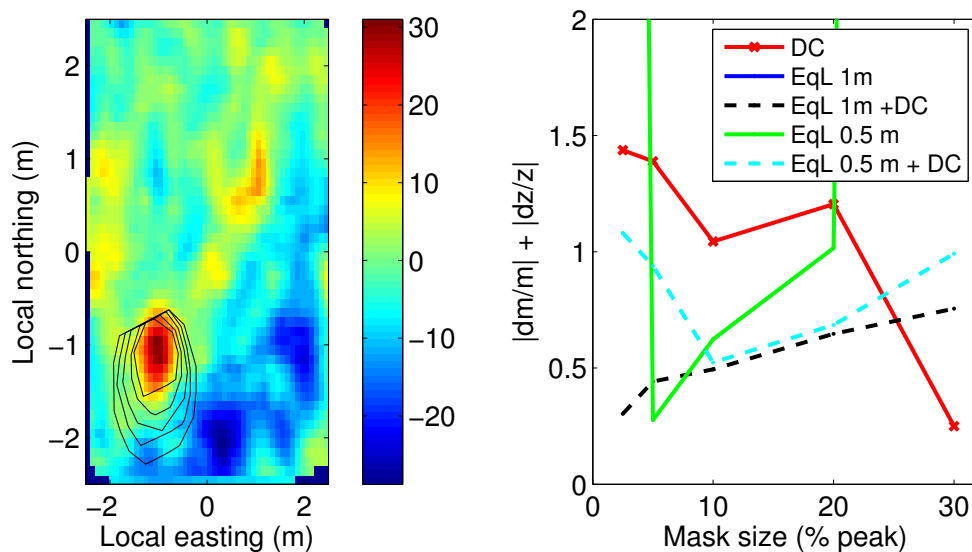


Figure 2.21. Moment $m = 0.05 \text{ Am}^2$, $z=-0.8 \text{ m}$. Target off-center

This study with soil from Camp Sibert shows that there is no emerging best method for that data set, as the 0.5 m spacing fits best the first two examples, whereas the 1 m grid is better for the

last two. This suggests that optimal spacing and mask size depend on the location of the target with respect to anomalies caused by soil. This implies that knowledge of the typical length scales of the soil inside a cell is not sufficient to guide the choice of grid spacing and mask size. Additionally, we find that misfits do not provide any clear indication for identifying the best method.

For Chevallier Ranch data, the soil is long wave and the anomaly sits near a large contrast: 1m spacing works best, as expected. For Camp Sibert data, it depends on whether there are variations in soil response immediately around the target:

- if small variations are of short length (1st 2): 0.5 m spacing work best
- if a target lies near a large contrast (last 2): 1 m spacing seems to perform better, similar to Chevallier Ranch data.

SIMULATIONS:

We run simulations to test the ability to recover a UXO against a strong background signal to noise ratio (SNR) as low as 20 decibels (dB)). We use magnetic soils from Chevallier Ranch and Camp Sibert as background. We assume a buried synthetic UXO of moment $m = 0.05, 0.10$ and 0.15 Am^2 at $z=0.8, 1.2$ and 1.6 m below the magnetic sensor at a random location within 1 m of cell center. We invert for the best combinations of a dipole and DC shift, dipole and equivalent layer, and dipole and EqL + DC shift, for a grid of 0.5 m and 1 m, with a mask at 5, 10 and 20% of the peak value of the anomaly. The measure of success is $|dm/ml| + |dz/z|$. To measure the variability near the anomaly, the standard deviations of the data inside a 1-m-radius circle (std1) and the surrounding 1-to-2-m ring (std2) are compared.

We find that the dipole model with equivalent layer at 1 m plus additional DC shift consistently performs well, usually within 20% of the true model, and is always the best model when $\text{std1}/\text{std2} > 1.5$ (and with a mask at 5% of the peak anomaly) (Figure 2.22). Additional simulations, not presented here, show that success of inversions becomes less predictable for all methods when the signal to noise ratio becomes less than 20 dB in a strongly magnetic environment.

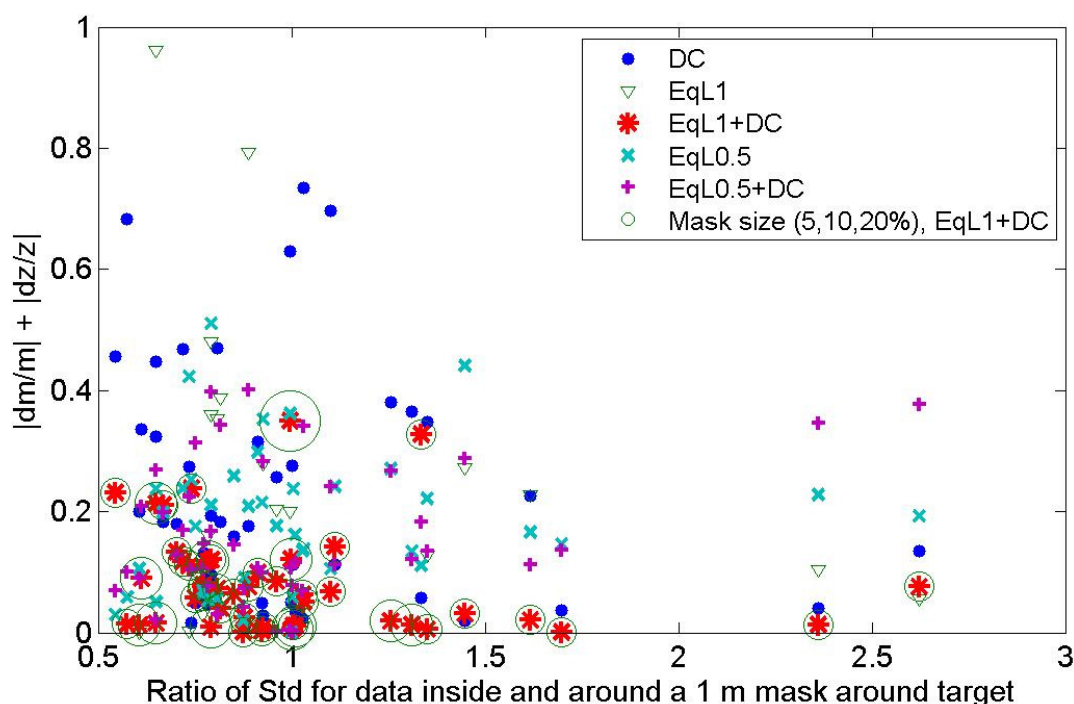


Figure 2.22. Simulations testing the ability to recover a UXO against a strong magnetic background

CONCLUSION

Inverting magnetic data to identify a buried item in a magnetic host is a difficult task that we propose to address by modeling the host with an equivalent layer of dipoles. The inverse problem is complex because it mixes the linear problem of inverting for a layer and the non-linear one of inverting for the depth and size of a buried dipole. There is a tradeoff between the amounts of signal that are to be balanced between the equivalent layer and the dipole used for the buried object of interest. This tradeoff can be controlled by either:

- The parameters of the layer (resolution, size, depth, parameterization), the choice of a mask and its size, the use of the mask on the data or on the data and the layer; or
- By a method of regularization and choice of a norm.

The key issue is to determine the critical length scales of the signal pertaining to the buried object in a host where geology and noise (instrument, positioning) add a broad range of scales to the signal spectrum.

For this initial effort we have focused on characterizing the properties of an equivalent layer in the context of filtering out the main features of a magnetic soil, as opposed to reproducing a magnetic map with high fidelity. We have tested the effects of the parameterization of the layer,

the grid size, depth, inversion method and use of constraints, and the size and method of application of a mask. This preliminary study lays the foundation for more advanced inversion methods. We have shown that the depth and size of a buried object can be recovered when using an equivalent layer as a filter prior to the inversion of a buried object of interest, even at signal to noise ratios as low as 20 dB. Below that level results are less stable.

Attempts at using the inversion of a layer and buried item in a perturbation scheme have shown limited success and are not presented here. We also have tried simultaneous inversion of the soil and buried object using the Matlab *lsqnonlin* solver with different mask sizes and constraints, using the non-simultaneous solution as an initial guess and building on our preliminary study on the equivalent layer. However, results were less accurate in terms of recovering the buried dipole than the initial guess. More work will follow to explore possible formulations of the inverse problem and a regularization to address the tradeoff issue.

TASK 1.2: DEVELOP METHODOLOGY FOR INVERTING EMI DATA FOR THE PROPERTIES OF THE BACKGROUND HOST

Detection and identification of UXO at sites with large geologic background signals can be very difficult. With the large frequency-dependent component of susceptibility of Kaho`olawe soils, detection of UXO can be compromised due to geology-related sensor responses of the same order of magnitude of UXO. In less hostile settings, detection may be possible, but discrimination may be difficult due to geology-related sensor noise reducing the ability with which target parameters can be accurately estimated. An example of such a scenario is the geophysical prove-out (GPO) located at Camp Sibert, AL (Figure 3.1).

Consider a target buried in a setting where the background geology is not negligible. The measured sensor data can be written as:

$$\mathbf{d}^{\text{obs}} = F[\text{target}, \text{host}] + \text{noise}$$

where \mathbf{d}^{obs} is the observed sensor data and $\mathbf{d}^{\text{obs}} = F[\text{target}, \text{host}]$ represent the forward model that is a function of the target and host. If the responses of the target and host are approximately additive, we can write:

$$\begin{aligned}\mathbf{d}^{\text{obs}} &= F^{\text{bg}}[\text{host}] + F^{\text{t}}[\text{target}] + \text{noise} \\ &= \mathbf{d}^{\text{bg}} + \mathbf{d}^{\text{target}} + \text{noise}\end{aligned}$$

where $\mathbf{d}^{\text{obs}} = F^{\text{bg}}[\text{host}]$ is the response due to the background host, $\mathbf{d}^{\text{target}} = F^{\text{t}}[\text{target}]$ is the response due to the target, $F^{\text{int}}[\text{target}, \text{host}]$ represents the interaction between target and host. In most cases $F^{\text{t}}[\text{target}]$ is chosen to be a dipole model representation of the target.

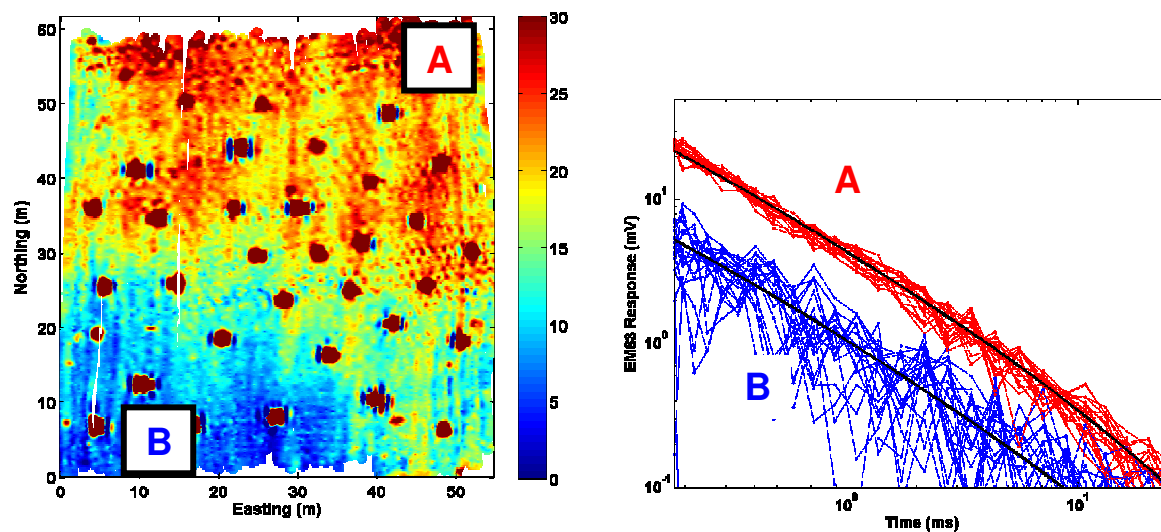
The most common approach to processing is to develop filtering techniques such that the background response \mathbf{d}^{bg} can be estimated, and subsequently subtracted from the data. These filtering methods assume that the geologic, and therefore electromagnetic, properties of the host material are spatially slowly varying, while the anomalies of compact targets have a relatively smaller spatial wavelength. The filtered data are then inverted with the physical model $F^{\text{T}}[\text{target}]$ for the UXO response in free space.

One of the major difficulties with this approach is the accuracy with which filtering can remove the background response $\mathbf{d}^{\text{bg}} = F^{\text{bg}}[\text{host}]$. In particular, movement of the transmitter and receiver relative to magnetic ground can produce significant small wavelength anomalies in the data (Walker et al., 2005; Foley et al., 2005). Figure 3.2 contains a single line of Geonics EM-63 and inertial measurement unit (IMU) data collected on the Camp Sibert GPO. Along this line there are no known UXO. The EMI and IMU sensor data are clearly correlated. Of particular interest are the approximately 10 millivolt (mV) peaks in the first time channel between a Northing of 20 and 30 m. These peaks appear to be well correlated with “valleys” in the elevation, i.e. where the sensor was closer to the ground surface. High pass filters will have limited success in cases

where the geologic response has spatially correlated anomalies. Rather than using a filter to eliminate the geologic response, our preferred approach to process these data by estimating a smoothly varying



(a) Geonics EM-63 time domain sensor and a 4.2 inch mortar



(b) A gridded image of the first time channel (c) Time domain soundings Figure 3.1. Geonics EM-63 Time domain electromagnetic data acquired over the Camp Sibert Geophysical GPO. (a) The Geonics EM-63 was instrumented with a Crossbow 400 IMU for coil orientation measurements and a Leica Robotic Total Station. (b) Thirty intact 4.2 in mortars and 8 partial mortars were seeded in the GPO. Dynamically acquired data were taken along North-South lines with approximately 50 cm line spacing. (c) Time domain soundings of the background soil display the characteristic viscous remnant magnetization (VRM) decay.

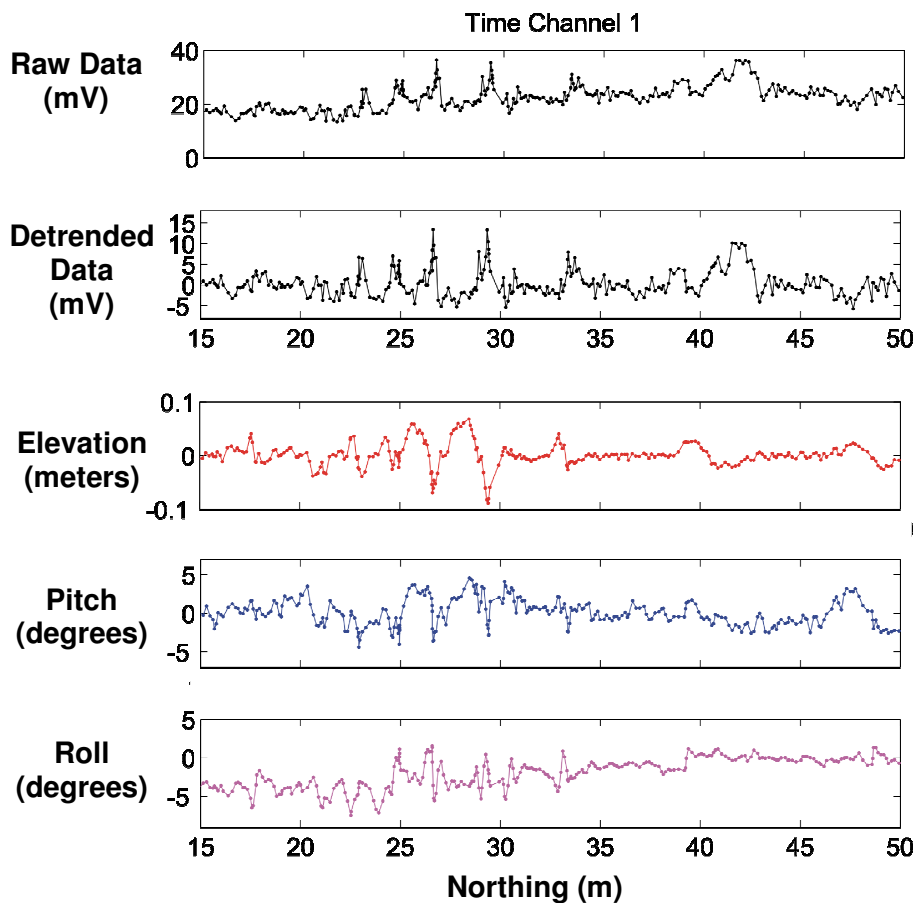


Figure 3.2. Comparison of the first time channel of data collected along a line located at an Easting of approximately $x = 43$ m. Along this line there were no emplaced items and no known metallic targets. Variations in the measured data are correlated with the sensor elevation and orientation.

background geology. This approach requires accurate sensor positioning and orientation information to model the small wavelength variations.

Techniques for processing data collected at remediation sites with large geologic background signals are considered in this section. A number of synthetic data will be used to demonstrate filtering, target picking, and parameter estimation of data collected in a magnetic geology setting. The objective is to determine what type of information can be recovered from electromagnetic data collected in regions with highly magnetic geology.

MODELING GEOLOGIC SIGNAL DUE TO SENSOR MOTION

Let us assume that the response of the background geology and the target are additive.

$$\mathbf{d}^{obs} = \mathbf{d}^{bg} + \mathbf{d}^{target} + noise \quad (3.1)$$

The background geology response \mathbf{d}^{bg} is a function of the position (i.e. location and orientation) of the EMI sensor relative to the ground surface, topography, and the spatial distribution of the subsurface electromagnetic properties (i.e. conductivity and magnetic susceptibility). An analytic solution for the response of a loop at an arbitrary orientation over a conductive and magnetic subsurface is not available. For the case of a single loop over a complex permeable, but non-conducting, half-space, the solution for the magnetic field at the center of the loop is given by:

$$H_z^s(\omega) = \frac{I}{4} \frac{a^2}{[a^2 + (2h)^2]^{3/2}} \chi(\omega). \quad (3.2)$$

where the radius of the loop is a , the frequency dependent magnetic susceptibility of the half-space is $\chi(\omega)$, and the height of the loop over the half-space is h . If we assume a complex susceptibility defined by log-uniform distribution of time constants (where $\tau_2 \gg \tau_1$), then:

$$H_z^s(\omega) = \frac{I}{4} \frac{a^2}{[a^2 + (2h)^2]^{3/2}} \frac{\chi_o}{\ln(\tau_2 / \tau_1)} \left(1 - \ln(\omega\tau_2) - i \frac{\pi}{2} \right) \quad (3.3)$$

A Fourier transform of the above expression can then be used to calculate the step-off response in the time domain:

$$\frac{\partial H}{\partial t} = -\frac{I}{4} \frac{a^2}{[a^2 + (2h)^2]^{3/2}} \frac{\chi_o}{\ln(\tau_2 / \tau_1)} \frac{1}{t} \quad (3.4)$$

Therefore, for the simple case of a loop over a complex permeable, but non-conductive half-space, the response can be written as the product of three components:

$$V_s = A(h)G(\chi)f(t) \quad (3.5)$$

where $A(h)$ is a function of the sensor geometry and relative position to the half-space and is independent of the susceptibility, $G(\chi)$ is a function of the half-space susceptibility, and $f(t)$ is the temporal response of the geology.

In the absence of an analytic solution for an arbitrarily oriented loop, we construct an approximate forward model by making some assumptions:

1. We assume that the response measured by a sensor moving over the ground can be approximated by assuming that the Tx and Rx loop is stationary at any instant. That is, we assume that the receiver loop is moving slowly enough, that the signal due to a change in flux through the receiver loop due to the Rx loop's movement through the earth's field is small.
2. The geologic response will primarily be due to viscous remnant magnetization (VRM), and not conductivity. Modeling and field measurements at sites with VRM have shown that this assumption is valid for the geometry of transmitter loops used in UXO sensors. We note that this assumption is not necessary for carrying out the modeling, but it will improve the speed at which the forward modeling can be carried out.
3. The response for a loop with an arbitrary orientation can be approximated to have the same form as (3.5). That is, the function relating to the sensor position and orientation and the function related to the geologic properties are separable.

$$V_s = A(h, pitch, roll, yaw)G(\chi)f(t)$$

This assumption greatly simplifies our calculations, as the functions A and $f(t)$ are function of survey and sensor parameters, and not the geologic properties of the subsurface. The function A needs to be calculated only at the start of processing, and $f(t)$ is the convolution of the VRM response with the transmitter waveform.

4. Topography does not need to be modeled. We note that a ground clearance correction may be applied to the data (Walker *et. al.*, 2005) which could be introduced into the function A .
5. The transmitter loop can be approximated as multiple dipole moments.

APPROXIMATING THE SENSOR WITH MULTIPLE DIPOLES

We will use the propagator matrix solution for horizontal or vertical dipoles over a conductive and magnetically permeable half-space to construct the approximate modeling. For a small transmitter loop, the primary field can be approximated by a dipole. This assumption is inaccurate for the sensor and survey geometries of UXO EMI surveys. Therefore, we compute the electromagnetic response of the background geology by representing the instrument transmitter by a number of dipoles and sum the response for each dipole. Each transmitter dipole, whose orientation is known from IMU data, is decomposed into vertical and horizontal components. We use the analytic solutions for a horizontal and vertical dipole over a half-space to calculate the secondary fields for each dipole, and sum the secondary fields generated by each dipole over the half-space.

The expressions for the magnetic field H at a measurement point (X, Y, Z) due to a Z -directed magnetic dipole source located at $(0, 0, h)$ over a layered earth is:

$$H_x(x, y, z, \omega) = \frac{1}{4\pi r} \int_0^\infty \left(e^{-\lambda|z+h|} - \frac{P_{21}}{P_{11}} e^{\lambda(z-h)} \right) \lambda^2 J_1(\lambda r) d\lambda$$

$$\begin{aligned}
 H_y(x, y, z, \omega) &= \frac{1}{4\pi} \frac{y}{r} \int_0^\infty \left(e^{-\lambda|z+h|} - \frac{P_{21}}{P_{11}} e^{\lambda(z-h)} \right) \lambda^2 J_1(\lambda r) d\lambda \\
 H_z(x, y, z, \omega) &= \frac{1}{4\pi} \int_0^\infty \left(e^{-\lambda|z+h|} + \frac{P_{21}}{P_{11}} e^{\lambda(z-h)} \right) \lambda^2 J_0(\lambda r) d\lambda
 \end{aligned} \tag{3.6}$$

where J_i is the i^{th} order Bessel function. For an X-directed magnetic dipole source at (0,0,h):

$$\begin{aligned}
 H_x(x, y, z, \omega) &= -\frac{1}{4\pi} \left(\frac{1}{r} - \frac{2x^2}{r^3} \right) \int_0^\infty \left(e^{-\lambda|z+h|} - \frac{P_{21}}{P_{11}} e^{\lambda(z-h)} \right) \lambda J_1(\lambda r) d\lambda \\
 &\quad - \frac{1}{4\pi} \frac{2x^2}{r^2} \int_0^\infty \left(e^{-\lambda|z+h|} - \frac{P_{21}}{P_{11}} e^{\lambda(z-h)} \right) \lambda^2 J_0(\lambda r) d\lambda \\
 H_y(x, y, z, \omega) &= \frac{1}{2\pi} \frac{xy}{r^3} \int_0^\infty \left(e^{-\lambda|z+h|} - \frac{P_{21}}{P_{11}} e^{\lambda(z-h)} \right) \lambda J_1(\lambda r) d\lambda \\
 &\quad - \frac{1}{4\pi} \frac{xy}{r^2} \int_0^\infty \left(e^{-\lambda|z+h|} - \frac{P_{21}}{P_{11}} e^{\lambda(z-h)} \right) \lambda^2 J_0(\lambda r) d\lambda \\
 H_z(x, y, z, \omega) &= \frac{1}{4\pi} \frac{x}{r} \int_0^\infty \left(e^{-\lambda|z+h|} + \frac{P_{21}}{P_{11}} e^{\lambda(z-h)} \right) \lambda^2 J_1(\lambda r) d\lambda,
 \end{aligned} \tag{3.7}$$

For a half-space, the ratio of elements in the propagator matrix P_{21}/P_{11} simplifies to:

$$\frac{P_{21}}{P_{11}} = \frac{\mu_1 u_o - \mu_o u_1}{\mu_1 u_o + \mu_o u_1}, \tag{3.8}$$

Where:

$$\begin{aligned}
 u_1 &= \sqrt{\lambda^2 - (\mu \epsilon \omega^2 - i \mu \sigma \omega)} \\
 u_o &= \sqrt{\lambda^2 - \mu_o \epsilon_o \omega^2}
 \end{aligned}$$

The Hankel transforms are computed using the digital filtering routine of Anderson.

Figure 3-3 contains data measured using a Geonics EM-61 Mark2 sensor that was modified to have a 10 mV transmitter on time (as part of SERDP UX-1355). The data were taken on Kaho'olawe Island, Hawaii with the sensor at a number of heights and dip angles. We found that using 8 dipoles to model the transmitter sensor was sufficient to model the measured data. Not surprisingly, data collected with the transmitter loop close to the ground were less closely modeled. When the loop is greater than 10 centimeters (cm) above the ground surface and less than 50 degrees the data are well modeled.

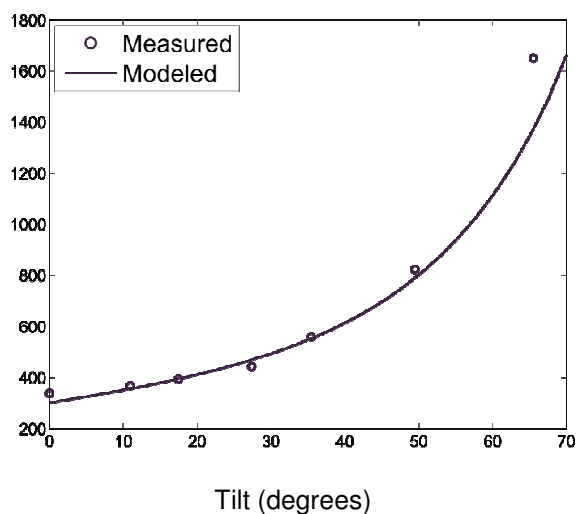
In this report we will be focusing on Geonics EM-63 data. The Geonics EM-63 transmitter consists of a 1 m square loop. Figure 3.4 contains some possible dipole configurations for modeling the transmitter field. Figure 3.5 compares the field on a plane 30 cm below a square loop to approximations of the field by using multiple dipoles. From these figures, it appears that a minimum of 9 dipoles would be appropriate for modeling the field of a 1 m square loop. Additional lab measurements and numerical modeling (see Figure 3.6) should be used to determine the minimum number of dipoles for modeling EM-63 data. For this report we will use

only 4 dipoles to model the loop. This choice was motivated by increasing computational speed such that testing of the algorithm could be carried out in a timely manner.

(a) Setup for the Tilt test



(b) Tilt test modeling result



(c) Setup for the height test



(d) Height test modeling result

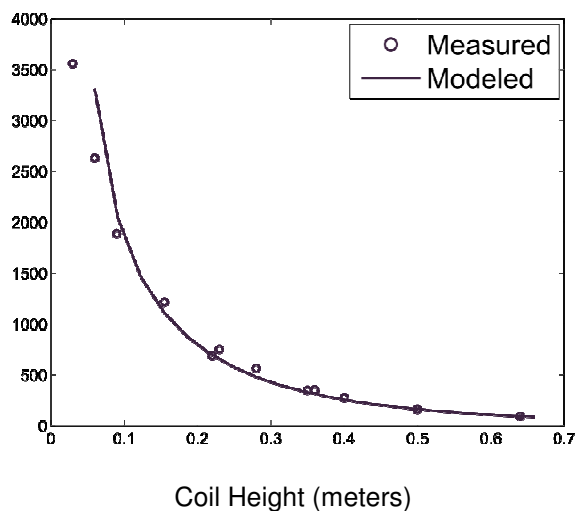


Figure 3.3. Tilt and height testing modeling results. A Geonics EM-61 Mark 2 sensor was used to collect data on Kaho'olawe, Island at a number of different heights and tilt angles. The signal was calculated by representing the transmitter loop with 8 dipoles.

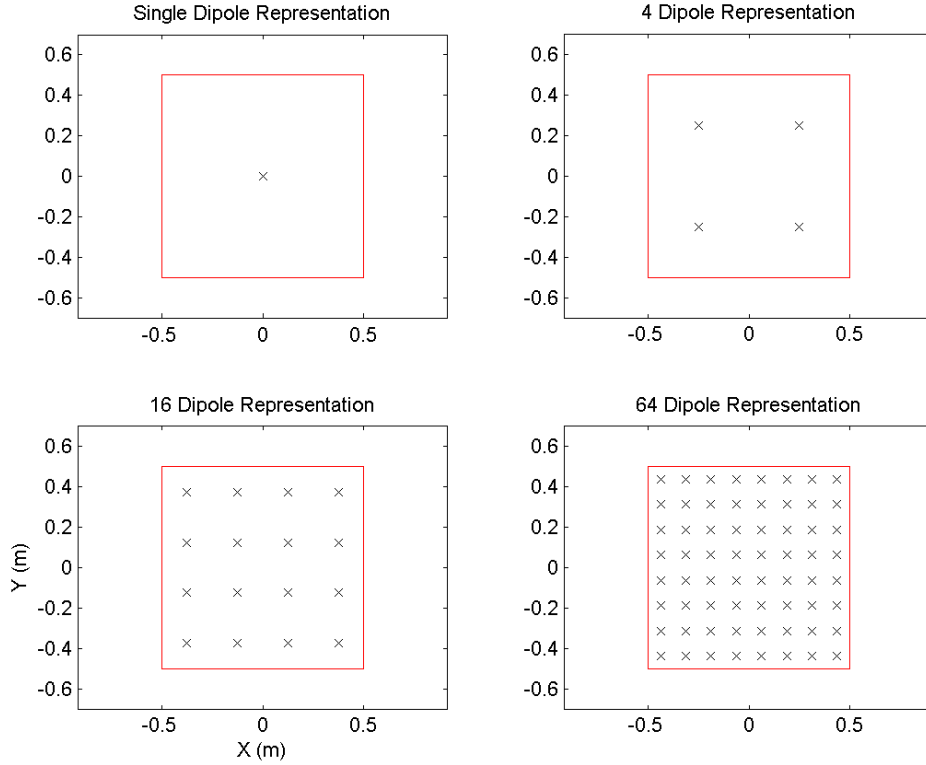


Figure 3.4. Representing a 1m square loop with multiple transmitters.

PROCESSING FILTERED DATA

In some cases, a median filter may be required to remove the sensor drift. It may still be possible to fit a geology response to such data. If we substitute Equation (3.5) into (3.1), and include the sensor drift, then the observed data can be written as:

$$\mathbf{d}^{obs}(t) = A(h)G(\chi)f(t) + \mathbf{d}^{t\ arg et} + drift + noise \quad (3.9)$$

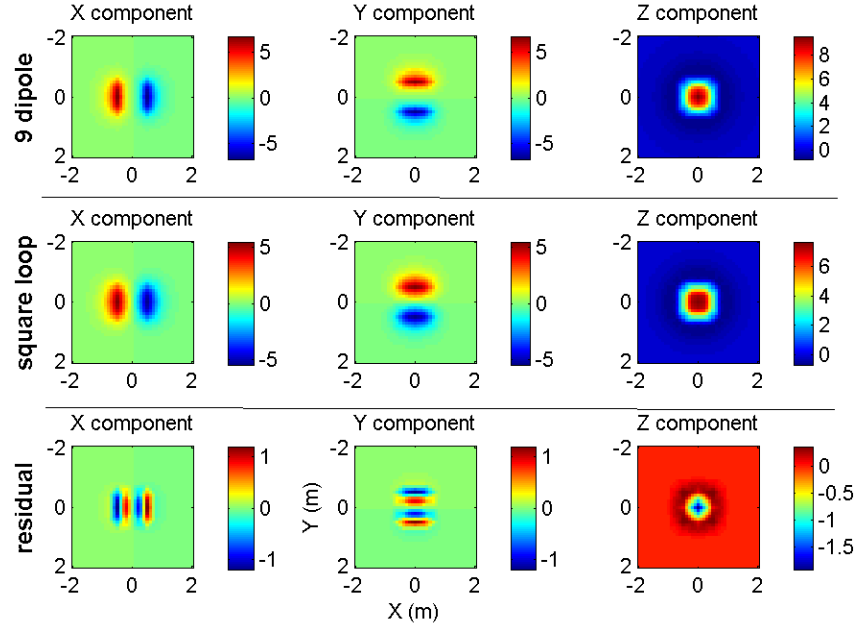
The function $A(h)$ can be rewritten:

$$\begin{aligned} \mathbf{d}^{obs}(t) &= [A(h_o) + p(\Delta h)]G(\chi)f(t) + \mathbf{d}^{t\ arg et} + drift + noise \\ &= A(h_o)G(\chi)f(t) + drift + p(\Delta h)G(\chi)f(t) + \mathbf{d}^{t\ arg et} + noise \end{aligned} \quad (3.10)$$

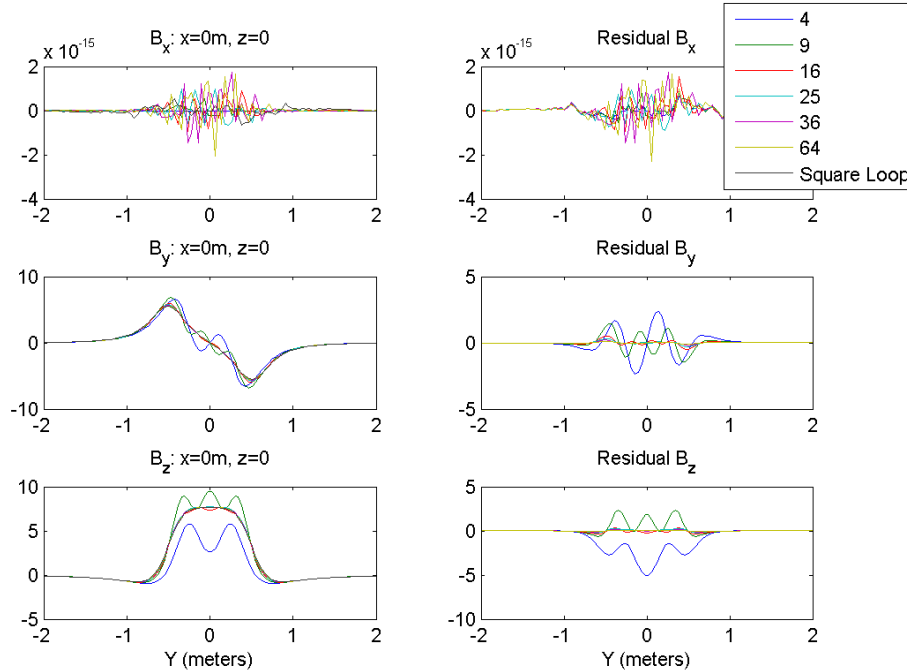
We can re-group the terms (3.10) into components with a long spatial wavelength, and shorter:

$$\mathbf{d}^{obs}(t) = \{A(h_o)G(\chi)f(t) + drift\} + \{p(\Delta h)G(\chi)f(t) + \mathbf{d}^{target} + noise\} \quad (3.11)$$

= Long spatial wavelength + Shorter spatial wavelength

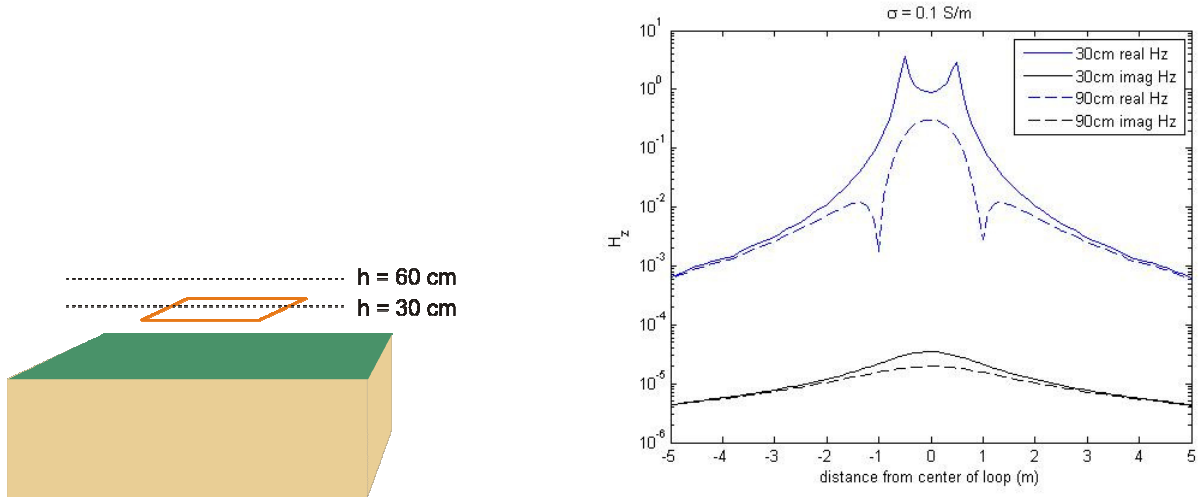


(a) The field of a square loop calculated on a horizontal plane that is parallel to, and 30 cm below, the loop



(b) Comparison of the accuracy of the dipole approximation of a square loop as a function of the number of dipoles. The data taken on the line y=0, and 30 cm below the loop.

Figure 3.5. Approximating the field produced by a 1 m square loop by dipoles.



(a) Geometry for measurements in (b). (b) Numerical calculations of field at two heights

Figure 3.6. Numerical modeling of field from a square Tx loop over a conductive and viscous remnant magnetic half-space.

In cases where instrument drift can only be removed through the application of a high-pass filter, we have two possible approaches. The first approach is to (1) solve for the geologic properties $G(\chi)$, (2) subtract the geologic response from the data, and (3) invert the geology corrected data set \mathbf{d}^+ for dipole parameters.

$$\mathbf{d}^+ = \mathbf{d}_{filt}^{obs}(t) - p(\Delta h)G(\chi)f(t) = \mathbf{d}^{target} + noise \quad (3.12)$$

The second approach is to solve for the geology and target parameters simultaneously from the filtered data. We can rearrange the above equation as

$$\begin{aligned} \mathbf{d}_{filt}^{obs}(t) &= p(\Delta h)G(\chi)f(t) + \mathbf{d}^{target} + noise \\ &= F[\mathbf{m}_s] + F[\mathbf{m}_{dip}] + noise \end{aligned} \quad (3.13)$$

In this report we will attempt to solve for the geologic properties \mathbf{m}_s and dipole parameters \mathbf{m}_{dip} simultaneously. In future work, we will compare the performance of the two different options.

MODELING GEOLOGY RELATED SENSOR NOISE WITH A SLOWLY SPATIALLY VARYING BACKGROUND GEOLOGY MODEL

In this project we assume that the electromagnetic properties of the subsurface are slowly spatially varying. That is, small spatial wavelength features in the data can be attributed to the sensor motion $A(h, pitch, roll, yaw)$ (or topography, which we are ignoring in this report) rather than sudden changes in the mineralogy (modeled by $G(\chi)$). In order to test this assumption, let

us again consider the line of EM-63 and IMU data plotted in Figure 3.2. Recall that the forward model for the soil can be written as:

$$\mathbf{d} = A(h, pitch, roll, yaw)G(\chi)f(t) \quad (3.14)$$

The data \mathbf{d} is linearly dependent on the model $G(\chi)$, i.e.

$$\mathbf{A}\mathbf{m} = \mathbf{d} \quad (3.15)$$

where the variation in the data due to changes in sensor position and orientation is contained in the modeling matrix \mathbf{A} , and the spatial behavior of the geology is contained in the model vector $\mathbf{m}=G(\chi)$. Let us parameterize the geologic model $G(\chi)$ with 2 cm constant cells along the N-S direction. Since data are taken at approximately 10 cm intervals along each line, we have an under-determined problem for the model.

Tikhonov regularization is used to solve the under-determined linear inverse problem. The optimal geologic model is obtained through the following optimization problem:

$$\min \|\mathbf{d} - \mathbf{A}\mathbf{m}\|^2 + \lambda \|\mathbf{W}_m \mathbf{m}\| \quad (3.16)$$

where λ is the trade-off parameter and \mathbf{W}_m is the regularization matrix. The regularization matrix allows us to introduce features of the model that we know *a-priori*. Common choices for the regularization matrix are flatness, which is enforced using the first order finite difference matrix

$$\mathbf{W}_m^1 = \begin{bmatrix} 1 & -1 & & \\ & \ddots & \ddots & \\ & & 1 & -1 \end{bmatrix}. \quad (3.17)$$

Regularization for this choice of \mathbf{W}_m thus balances the data fit with a measure of the slope of the recovered model. Another common choice for regularization is smoothness, which is enforced using the second order finite difference matrix:

$$\mathbf{W}_m^2 = \begin{bmatrix} 1 & -2 & 1 & & \\ & \ddots & \ddots & \ddots & \\ & & & \ddots & \\ & & & & 1 & -2 & 1 \end{bmatrix} \quad (3.18)$$

which minimizes the curvature of the recovered model. Once a \mathbf{W}_m is chosen, the solution for \mathbf{m} is:

$$\mathbf{m} = (\mathbf{A}^T \mathbf{A} + \lambda \mathbf{W}_m^T \mathbf{W}_m)^{-1} \mathbf{A}^T \mathbf{d} \quad (3.19)$$

Figures 3.7 and 3.8 contain examples of fitting the data using either smooth or flat models to a line of Geonics EM-63 data collected on the Camp Sibert GPO (Figure 3.1). At this point the details of how the trade-off parameter λ is selected is not important, as our objective is to determine if the geologic properties in \mathbf{m} can be slowly spatially varying while still being able to model the small wavelength variations in the data. Figure 3.7 plots the results of fitting the non-detrended (i.e. unfiltered, raw) data with a flat model in (a) and a smooth model in (b). In both (a) and (b), the upper panel shows the fit to the first time channel of data and the lower panel plots the recovered geology model. As expected, the estimated background geology increases from South to North. The flat model is nearly linear with Northing, while still fitting the main features in the data. The smooth model is similar to the flat model in magnitude. Figure 3.8 contain examples of fitting detrended data. Although the data fits in Figure 3.8 appear to be slightly better than when inverting the raw, unfiltered data, the recovered models have slightly more structure. The models are similar in magnitude to those recovered by inverting raw data.

These results suggest that it may be possible to:

- (1) work with either raw or detrended data, and
- (2) model the geologic response by assuming slowly varying background geology.

The first result is important since the data from many EMI sensors require filtering to remove sensor drift. The second result will allow us to parameterize the background geology with simple models, such as a plane, within small spatial subsets of the data.

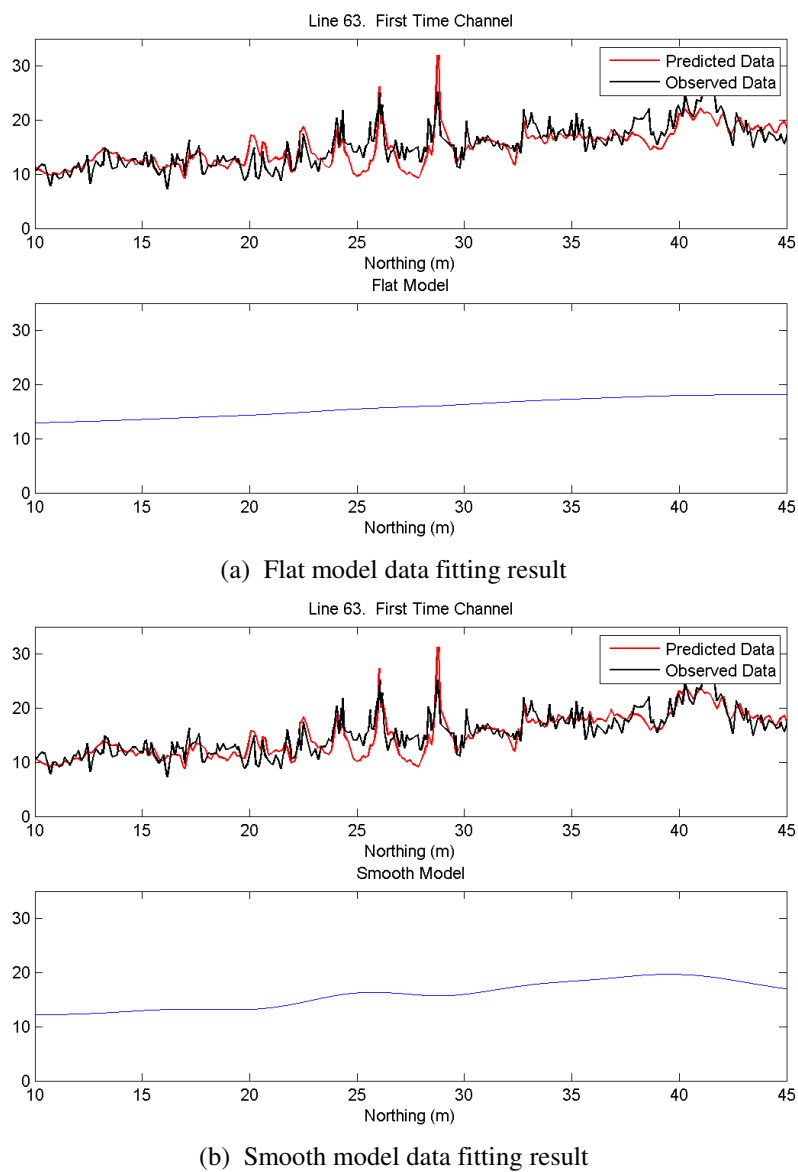


Figure 3.7. Fitting raw (i.e. non-detrended) data with a slowly spatially varying background geology.

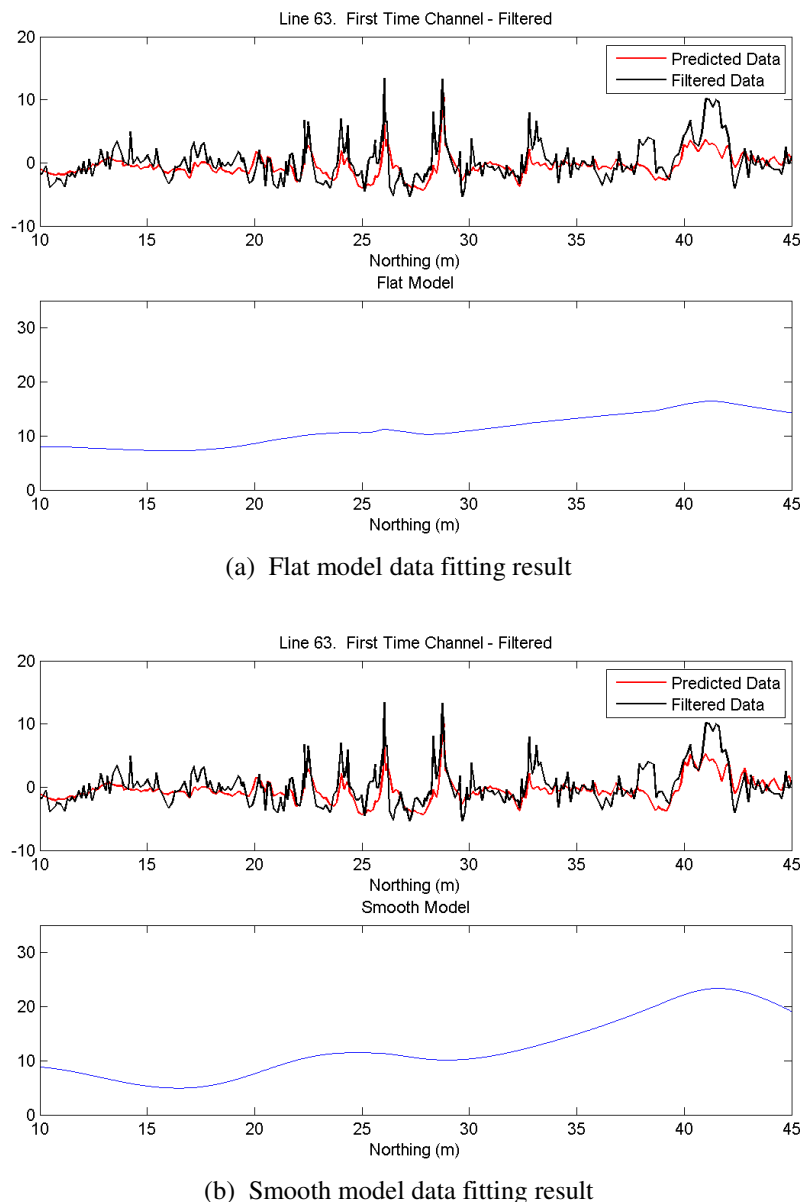


Figure 3.8. Fitting detrended data using a slowly varying background geology.

SIMULTANEOUS INVERSION OF GEONICS EM-63 DATA FOR DIPOLE PARAMETERS AND GEOLOGY PARAMETERS

In this section we present results from inverting Geonics EM-63 data simultaneously for geology parameters and target dipole parameters. The objective of inversion is to estimate parameters \mathbf{m} of a forward model $F[\mathbf{m}]$ from observed data. The choice of the model is based on the ability of the parameters to predict the observed data and any prior knowledge we have of the model parameters.

The forward modeling can be written as:

$$\begin{aligned}\mathbf{d} &= F[\mathbf{m}] \\ &= F[\mathbf{m}_{soil}] + F[\mathbf{m}_{target}]\end{aligned}\tag{3.20}$$

We will model the soil response as

$$F[\mathbf{m}_{soil}] = A(h, pitch, yaw, roll)G(x, y)f(t).\tag{3.21}$$

The function A is dependent on sensor positioning and orientation, i.e. parameters that are extrinsic to the target and geology. Therefore A can be calculated prior to the inversion process using the dipole approximation to the sensor outlined earlier. In this report, we assume that the contribution of conductivity to the measured response will be small relative to the effect of viscous remnant magnetic soil. Therefore, the function $f(t)$ is the characteristic response of viscous remnant soil convolved with the sensor waveform.

The function $G(x,y)$ defines the magnetic characteristics of the background geology. When processing data we, in general, identify and then isolate individual anomalies in data “cells” that are of the order of a few meters square. Within these data “cells”, the background geology $G(x,y)$ does not appear to vary significantly (See Figure 3.7). In the previous section the subsurface was finely discretized, and the slowly varying characteristics of the background were introduced through regularization of the inverse problem. Rather than solve an underdetermined inverse problem, we will parameterize the background geology as a plane:

$$G(x, y) = a + b(x - x_o) + c(y - y_o)\tag{3.22}$$

where the (x_o, y_o) is the center of each data cell. Therefore, for each anomaly we solve for an additional 3 soil parameters:

$$\mathbf{m}_{soil} = [a, b, c]\tag{3.23}$$

In our modeling, we define the function $G(x,y)$ to be equal to the background response measured in the first time channel of the Geonics EM-63.

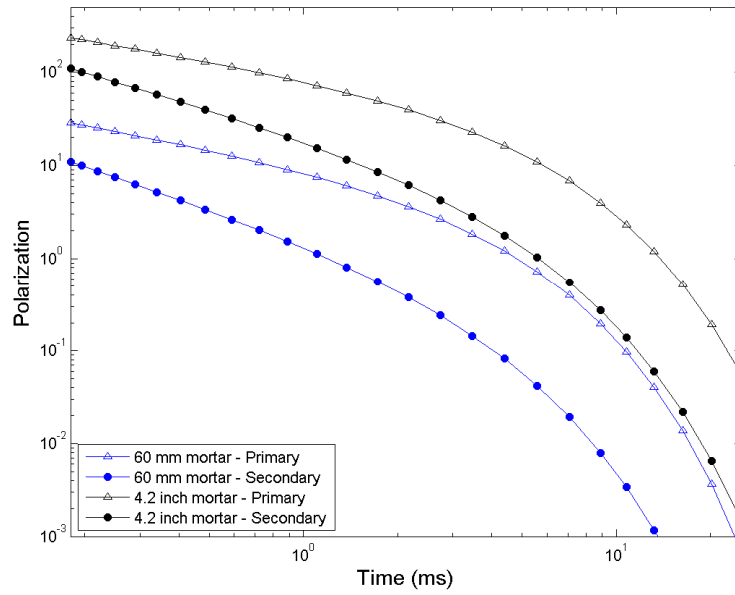
The response of the target $F[\mathbf{m}_{target}]$ is assumed to be dipolar. The dipole polarization tensor is:

$$\mathbf{F}(t) = \begin{bmatrix} L_3(t) & 0 & 0 \\ 0 & L_2(t) & 0 \\ 0 & 0 & L_1(t) \end{bmatrix}.\tag{3.24}$$

Where we parameterize the decay of the polarization tensor with the function:

$$L_i(t) = k_i t^{-\beta_i} \exp(-t / \gamma_i).\tag{3.25}$$

Examples of polarizations for an Aberdeen Test Center (ATC) 60 millimeter (mm) mortar and a 4.2 inch mortar found at Camp Sibert are shown in Figure 3.9.



	60 mm ATC mortar		4.2 inch Camp Sibert Mortar	
	Primary	Secondary	Primary	Secondary
k	11.2	1.8	98.3	22.6
β	0.58	1.1	0.53	0.95
γ	3.2	2.9	4.3	3.8

Figure 3.9. Dipole polarizations for a 60 mm mortar and a 4.2 inch mortar from Camp Sibert, AL. The 60 mm mortar polarization was derived from measurements acquired on the US Army Corps of Engineers (USACE) Engineer Research and Development Center (ERDC) test stand in Vicksburg, MS. The 4.2 inch mortar polarizations plotted here represent the average recovered polarizations from EM-63 inversions completed as part of ESTCP project MM-0504. The table lists decay parameters when modeling the polarization with the function $L(t)=kt^\beta \exp(-t/\gamma)$.

The target parameters are:

$$\mathbf{m}_{target} = [x, y, z, \theta, \phi, \varphi, k_1, \beta_1, \gamma_1, k_2, \beta_2, \gamma_2, k_3, \beta_3, \gamma_3] \quad (3.26)$$

where the target location is (x,y,z) and the orientation is defined by the angles (θ, ϕ, φ). We will also present modeling results where we assume an axi-symmetric target. When inverting for an axi-symmetric target we set $\varphi = 0$ and $L_2(t)=L_3(t)$ such that:

$$\mathbf{m}_{target} = [x, y, z, \theta, \phi, k_1, \beta_1, \gamma_1, k_2, \beta_2, \gamma_2] \quad (3.27)$$

The inverse problem for \mathbf{m}_{target} and \mathbf{m}_{soil} is cast as an optimization problem:

$$\text{Minimize } \phi(\mathbf{m}) = \frac{1}{2} \left\| V_d^{-1/2} (\mathbf{d} - F[\mathbf{m}_{target}] - F[\mathbf{m}_{soil}]) \right\|^2 \text{ subject to } m_i^L \leq m_i \leq m_i^U \quad (3.28)$$

where V_d is the data covariance matrix, m^L and m^U are the lower and upper constraints, respectively.

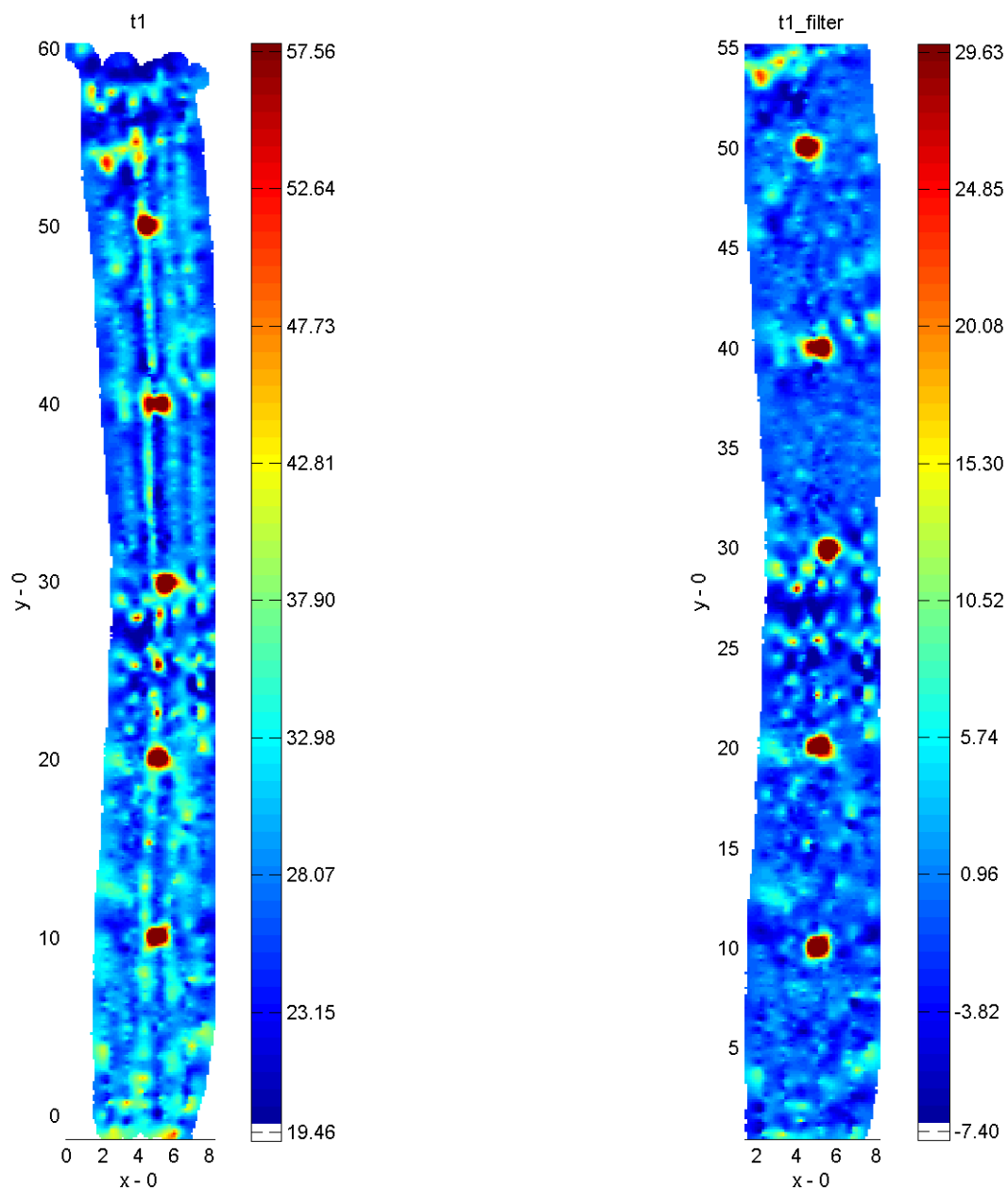
Two versions of the simultaneous inversion methodology are implemented. The first method is a parameter estimation approach where the location, orientation, and polarization tensor parameters are estimated from the data (for example Pasion and Oldenburg, 2001). The second method is a library based method where we have a library consisting of the polarization curves for a number of difference ordnance items, and we invert for the optimal location and orientation for each item in the library (Pasion *et. al.*, 2006). We determine which ordnance item in the library most likely generated the observed data.

Simultaneous Inversion Example 1: Synthetically generated 60 mm data

A large component of this project is the use of simulations for determining the effectiveness of the simultaneous fitting technique as a function of data fidelity. We present here an example of data simulated for a 60 mm mortar buried at a depth of 40 cm. Figure 3.9 contains a plot of the polarization curves that we use to forward model the data. For this example, we assume a viscous remnant background response that has a magnitude of 30 mV in the first time channel. We use a subset of elevation and IMU data (lines $X=45\text{m}$ to $X=52\text{m}$ in Figure 3.1) collected during the Geonics EM-63 survey collected on the Camp Sibert GPO (Figure 3.1). A gridded image of the first time channel of simulated data is shown in Figure 3.10(a). Figure 3.10(b) contains a gridded image of the first time channel of data after a 5 m median filter had been applied along each data line and on each time channel. Not surprisingly, there are small scale, spatially correlated (non-ordnance related) features in the synthetic data that are similar to those found in the section of data from which we extracted the elevation and IMU data (Figure 3.1, $X=45\text{ m}$ to $X = 52\text{ m}$).

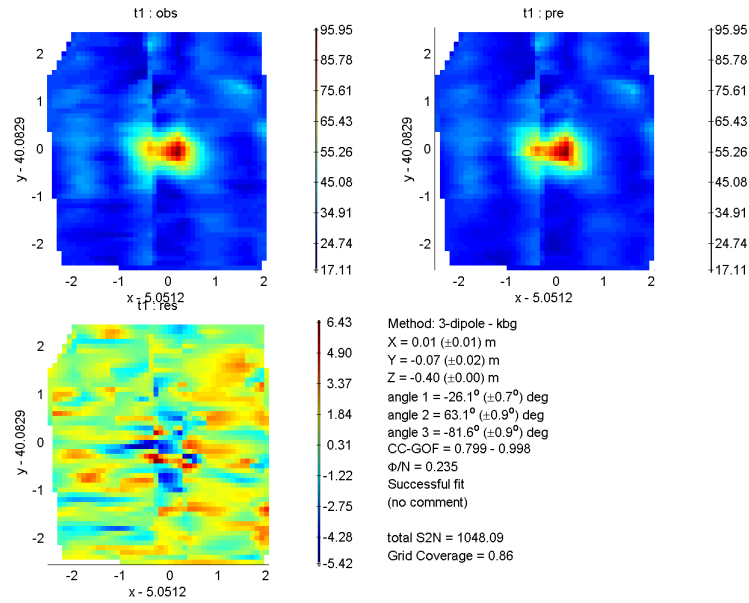
We will focus on the inversion of the anomaly located at $(x,y) = (5.05, 40.08)$. We compare the standard method of processing data where we fit a dipole model to detrended data to simultaneous estimation of the background geology and the dipole parameters. The simultaneous inversion will use the unfiltered sensor data. A random error with a standard deviation of 1 cm was added to elevation data. No noise was added to the IMU (i.e. accurate IMU information was input into the inversion algorithm). When inverting the data for target and geology parameters simultaneously, a 5 m square of data centered on the target is inverted. When inverting the detrended data, a 3 m diameter circular mask defined the data to be inverted. For this example, we invert the data using 3 unique polarizations (Equation 3.26) and the background geology will be modeled using a plane (Equation 3.22).

Figure 3.11 compares the first time channel of the observed and predicted data. The fit when modeling the anomaly using both a geology and dipole response is plotted in (a), and the fit using a dipole only is plotted in (b). Both models appear to fit the data reasonably well. Of note is the how the residual of the fit without geology (in (b)) appears to have some spatially correlated features, while the fit using geology and a dipole results in a random resulting residual. The spatially correlated features in (b) are important to note, as our inversion approach is optimized for Gaussian noise in the data. Spatially correlated signals have the potential to bias the recovered parameters.



(a) Raw Data (b) Detrended Data
 Figure 3.10. Synthetically generated Geonics EM-63 data. Sensor elevation and IMU data are taken from lines $Y = 45$ to $Y = 53$ m of the Sibert GPO survey. The response of five 60 mm mortars is included. The detrended data were obtained by applying a 5 m median filter along each line and time channel.

(a) Simultaneous fit using raw (not filtered data).



(b) Fitting filtered data using a dipole model (no geology)

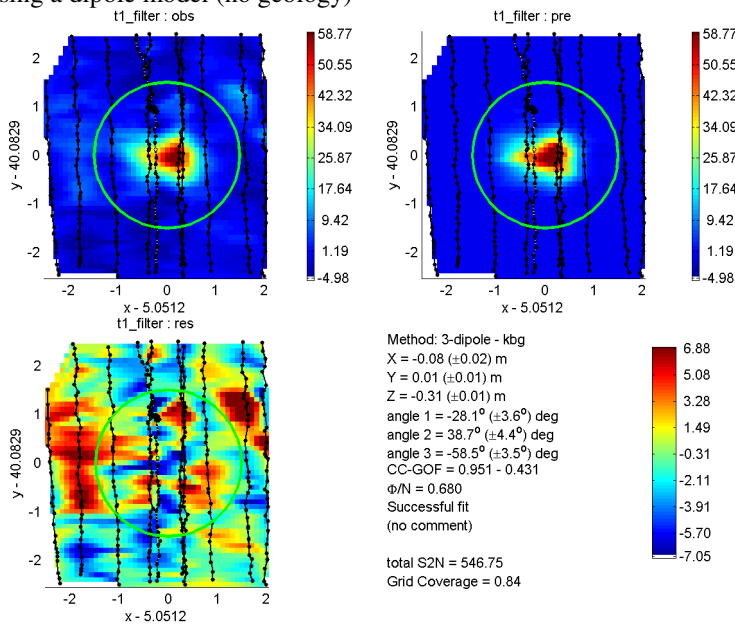
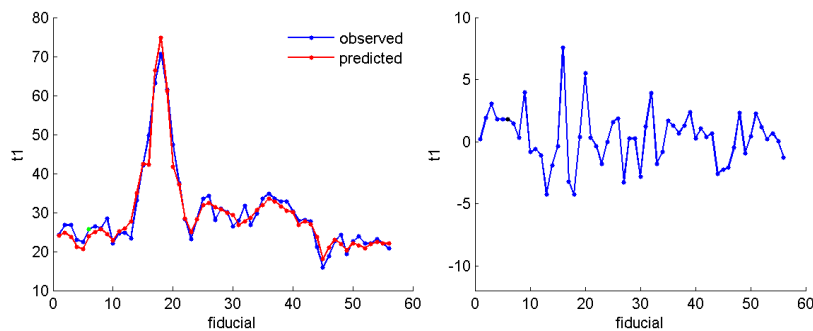
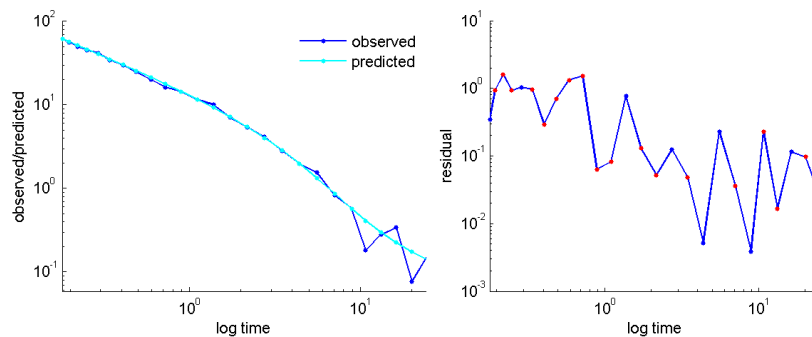


Figure 3.11. Comparison of data fits when fitting data with and without geology modeling included.

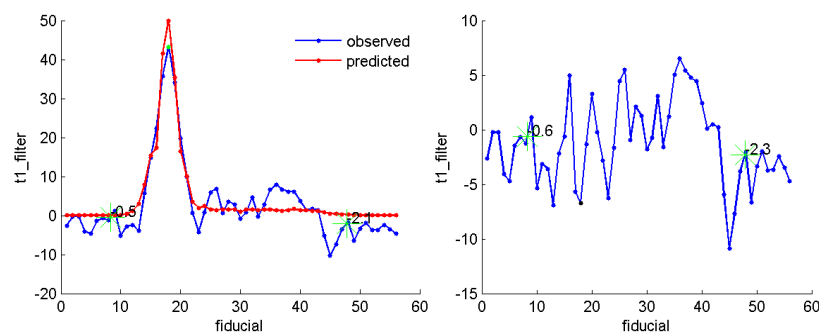
Figures 3.12(a) and (b) compare the observed and predicted data along a spatial profile and at a station above the ordnance when applying the simultaneous inversion approach. Figures 3.12(c) and (d) provide the same comparison when fitting the data using a dipole only. When looking at the residual along the spatial profile we see that the residual is smaller when modeling the geology. As a result, the signal to noise ratio is smaller when modeling geology. The



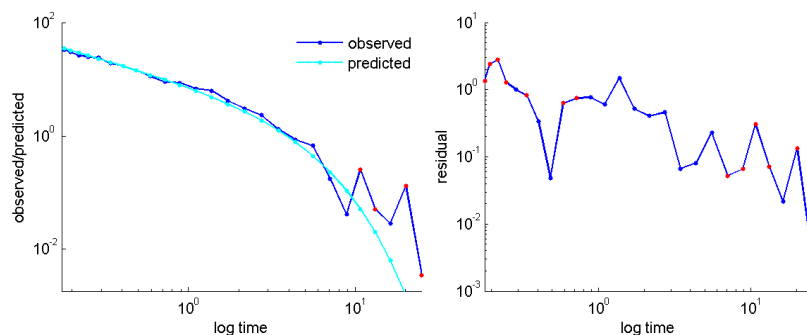
(a) Raw Data, Plane Geologic background – Profile.



(b) Raw Data, Plane Geologic background - Time Decay



(c) Detrended Data - Profile



(d) Detrended Data – Time Decay

Figure 3.12. Comparison of data fits when inverting synthetic data using simultaneous estimation of dipole and geology ((a)-(b)) and dipole only ((c)-(d)).

improvement in parameter estimates that we would expect from a lower SNR could possibly be offset by the more complex (an additional 3 parameters in this case) required for modeling the geology.

A comparison of the true and recovered geology model is shown in the lower panels of Figure 3.13. The true geology model was defined to be $G(x,y)=30$, and is accurately estimate. The recovered geology model is $G(x,y)=29.26 - 0.15(x-x_o) + 0.07(y-y_o)$. A summary of the recovered dipole parameters are found in Figure 3.14(a). Without modeling the geology, the inversion was unable to accurately predict the data. The accuracy with which the polarization parameters were recovered can more easily be seen in plots of Figures 3.14(b) and (c). In both cases, the primary polarization is well recovered (although the simultaneous inversion result is better). Not including the geology resulted in a much poorer recovery of the secondary polarizations.

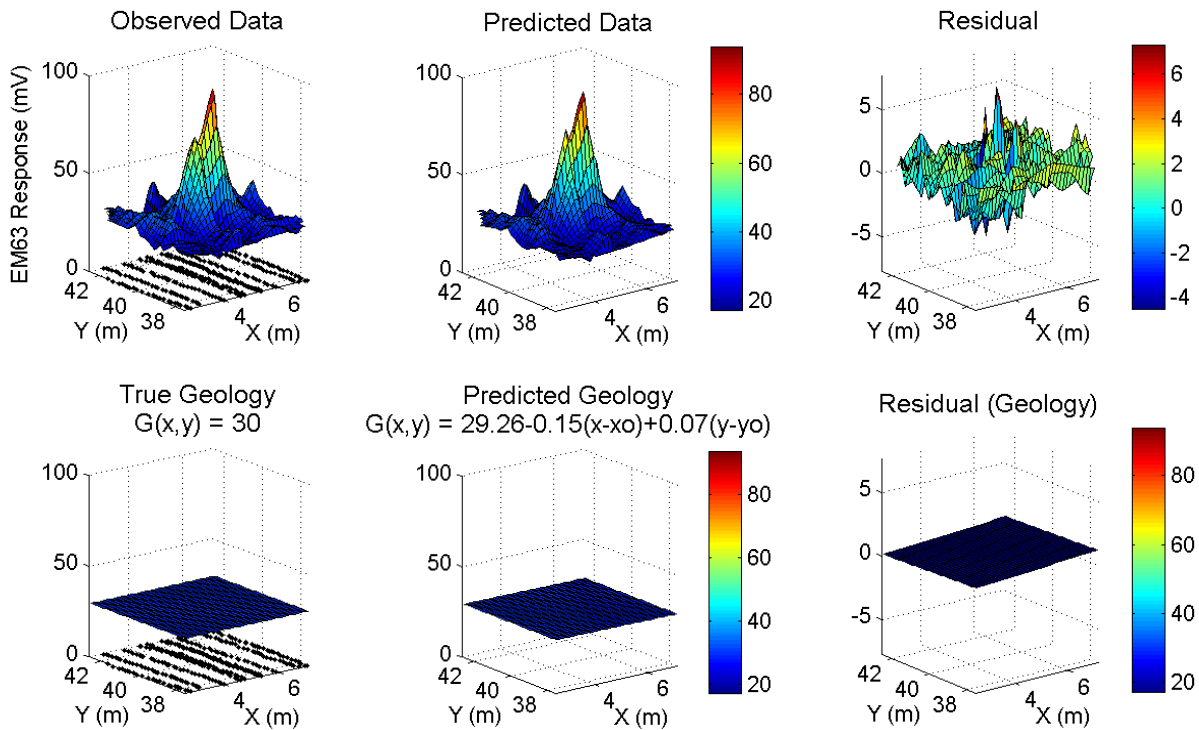
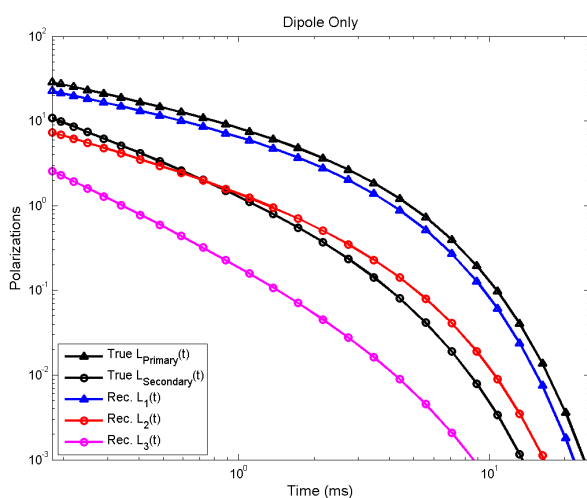


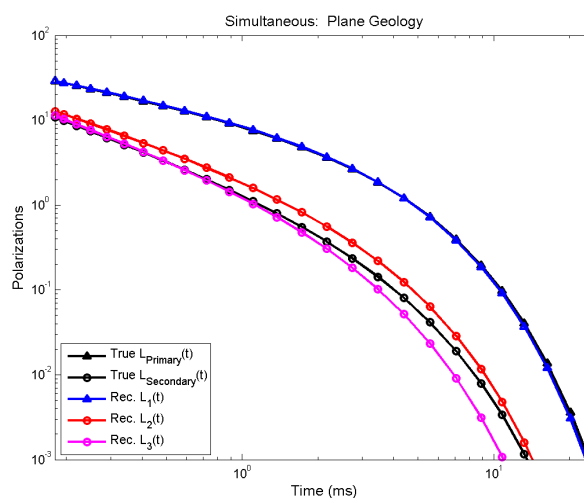
Figure 3.13. Modeling results assuming the spatial distribution of the geology can be represented by a plane. The top row of plots compares the observed and predicted data for the first time channel. The bottom row compares the true and predicted geology. The black dots at $z=0$ represent the locations at which data are modeled.

Parameter	Expected	No Geology	Plane Geology
X	5.05	4.98	5.06
Y	40.08	40.09	40.01
Z	0.40	0.31	0.40
k_1	11.2	9.00	11.56
β_1	0.58	0.57	0.57
γ_1	3.2	2.96	3.09
k_2	1.8	1.90	2.63
β_2	1.08	0.82	0.96
γ_2	2.9	3.16	2.68
k_3	1.8	0.25	1.89
β_3	1.08	1.39	1.09
γ_3	2.9	3.42	2.21

(a) Recovered Parameters



(b) No Geology model included (dipole only)



(c) Simultaneous dipole and geology

Figure 3.14. Comparison of recovered polarization parameters. Clearly, the secondary polarizations are not well resolved when inverting for a dipole only.

Simultaneous Inversion Example 2: Camp Sibert GPO data

The simultaneous dipole and geology parameter inversion technique described in the previous section was applied to dynamically collected Geonics EM-63 data acquired at the Camp Sibert geophysical prove-out (Figure 3.1). In this section we compare the standard approach of estimating dipole parameters from detrended data, to different variations of the simultaneous inversion approach. We will fit unfiltered and filtered data using library and parameter estimation inversion methodologies, with either plane or uniform parameterizations of the geology properties. For these parametric inversions, we will invert for an axi-symmetric target. That is we will solve for dipole model where the two secondary polarizations are equal (Equation 3.27).

Figure 3.15 plots a comparison of estimated and ground truth depths for the parameter estimation inversions. Depth estimate comparisons are useful, since accurate size estimates of ordnance require accurate estimates of depth. The red 'x' symbols indicate intact 4.2 inch mortars and the black triangles indicate partial mortars. A gray dot overlaying a symbol indicates that the data anomaly had either known signal above the noise, or the data coverage was very poor. Estimates that fall within the gray band indicate that the error in the depth estimate was less than 20 cm. The standard method of only fitting a dipole model has more inaccurate depth estimates than the other methods, with 4 mortars with good data coverage that have a depth error greater than 20 cm. Although there are only 38 total anomalies, this result suggests that including a soil model in the fitting may improve the estimation of size-based dipole parameters.

The depth analysis was repeated for results from the library based fitting method (Figure 3.16). The 4.2 inch mortar dipole polarization curves are shown in the Figure 3.9. An additional 20 ordnance items were included in the ordnance library (Figure 3.17). The accuracy of the depths is much better when using the library based fitting method. Including the geology response did not significantly improve the performance of the library based method.

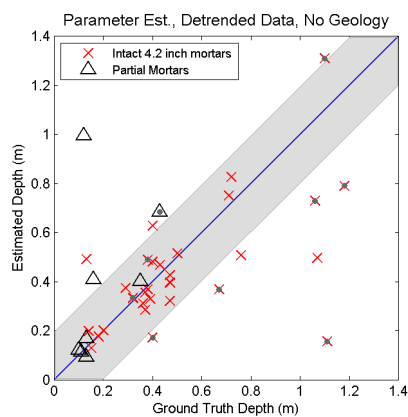
Figure 3.18 plots the primary polarization $L_1(t)$ recovered from the inversion. Recovered polarizations for intact 4.2 inch mortars are plotted in red and partial mortar polarizations are plotted in black. Polarizations derived from anomalies with poor coverage or signal in the noise are plotted with a dotted line. The blue dashed line indicates the 4.2 inch mortar primary polarization from Figure 3.9. Methods that include geology appear to have a slightly better ability to cluster the recovered primary polarization close to the blue dashed line. Using raw data and plane geology (Figure 3.18, lower left) probably has the best ability to cluster the 4.2 inch mortar polarizations. Figure 3.19 re-plots the recovered primary parameterizations, but normalizes to be equal to unity at the first Geonics EM-63 time channel. Presented in this manner, including the geology again appears to slightly improve results.

Figure 3.20 plots the magnitudes of the primary and secondary polarizations (i.e. k_1 vs. k_2) and the magnitude vs. time constant of the primary polarization (i.e. k_1 vs. γ_1) for the dipole fitting without a geology model. Similar plots for the simultaneous geology and dipole inversions of detrended data included are shown in Figure 3.21, and plots for the simultaneous geology and dipole inversions using raw/non-detrended data are in Figure 3.22. There appears to be a marginal improvement in the size based parameter clustering (k_1 vs. k_2) when including the

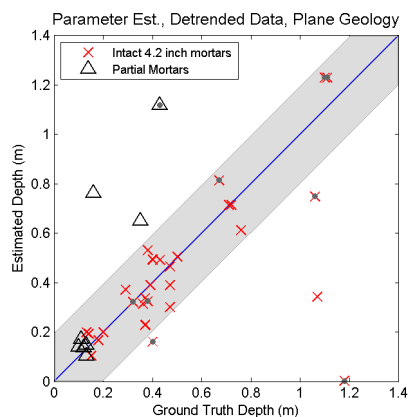
geology model. The k_1 vs γ_1 parameter space provides a good separation between partial and intact mortars, regardless of whether a geologic model is used. The separation is largely due to the much smaller time constants γ_1 of the partial mortars. Again, we note that since there are only 38 anomalies in the Camp Sibert GPO it is difficult to make any statistically significant conclusions.

The library based method was very successful when applied to the data. Figure 3.23 summarizes the library based classification results for the different methods. Three or fewer misclassifications resulted for each of the methods. The application of the library method to non-detrended data and assuming a planar geology resulted in all 4.2 inch mortars being correctly classified. For all but one of the misclassifications, the incorrectly predicted item was an ATC 2.75 inch rocket. A comparison of the polarizations for the ATC 2.75 inch rocket and the Camp Sibert 4.2 inch mortar can explain these misclassifications (Figure 3.24). Figure 3.24(a) clearly shows that the magnitudes of the polarizations are quite different. However, the decay behavior is quite similar, as can be seen by plotting the normalized polarizations (Figure 3.24(b)). It is likely that some anomalies, particularly those with poor spatial coverage, would have been fit with an ATC 2.75 inch mortar that is shallower than the true depth.

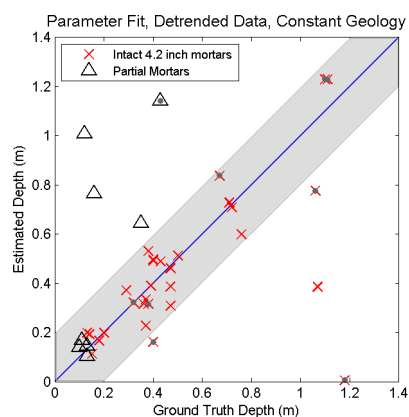
Of particular interest is the misclassification of a 4.2 inch mortar as a 37 mm projectile. The depth of this particular 4.2 inch mortar was 1.07 m, and thus the anomaly has a low signal to noise ratio. Figure 3.25 compares the data fit at the first time channel. By including a geology response, the small wavelength anomalies due to sensor movement were modeled, and depth was more accurately predicted.



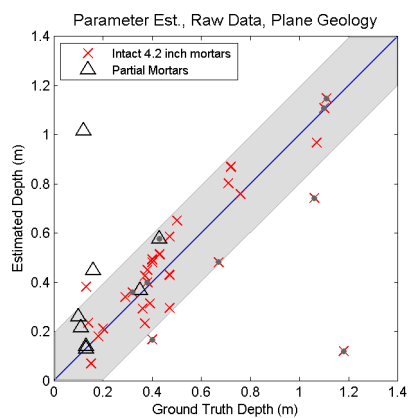
(a) 4 mortars with good data coverage that have a depth error >0.2 m



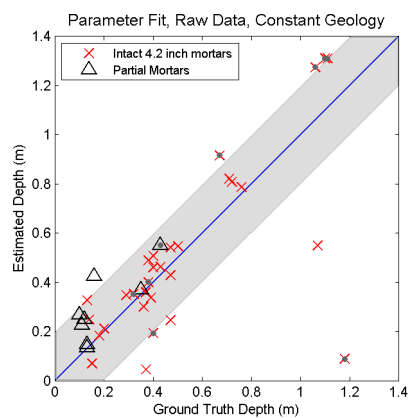
(b) 1 mortars with depth error >0.2 m



(c) 1 mortars with depth error >0.2 m



(d) 1 mortars with depth error >0.2 m



(e) 3 mortars with depth error >0.2 m

Figure 3.15. Depth comparison. Parameter estimation techniques

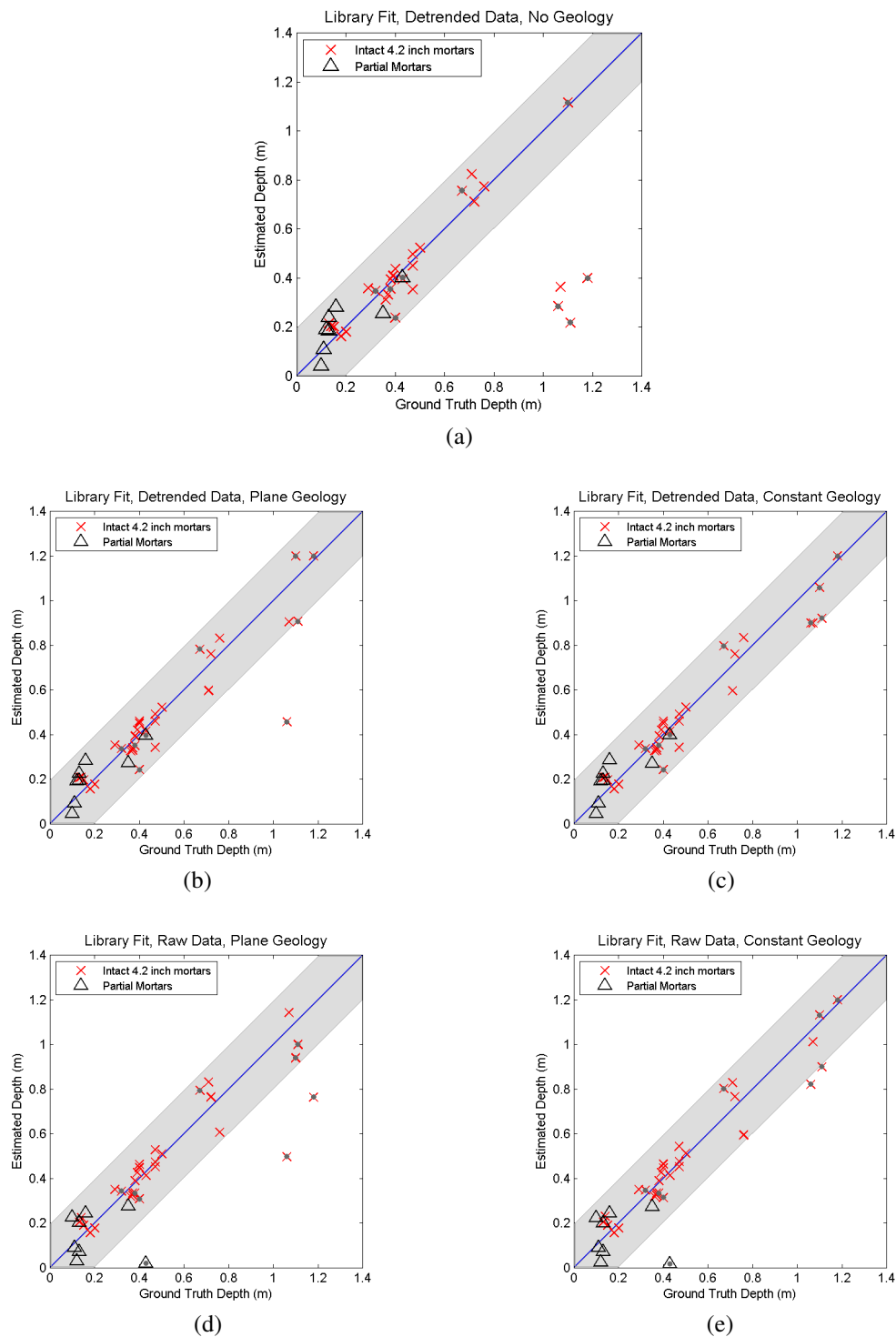


Figure 3.16. Depth comparison. Library fitting Techniques

U.S. Army Aberdeen Test Center	Montana Army National Guard	Former Lowry Bombing and Gunnery Range	Marine Corps Base Camp Lejeune
20 mm	76 mm projectile	3 lb bomb	3.5 inch with fins
40 mm projectile	81 mm mortar	37 mm	3.5 inch without fins
60 mm mortar	90 mm		Aluminum adapter
81 mm mortar			105 mm
105 mm			
155 mm			
2.75 inch Rocket			
BDU28 submunition			
BLU26 submunition			
M42			
MK118			

Figure 3.17. Items included in the ordnance library.

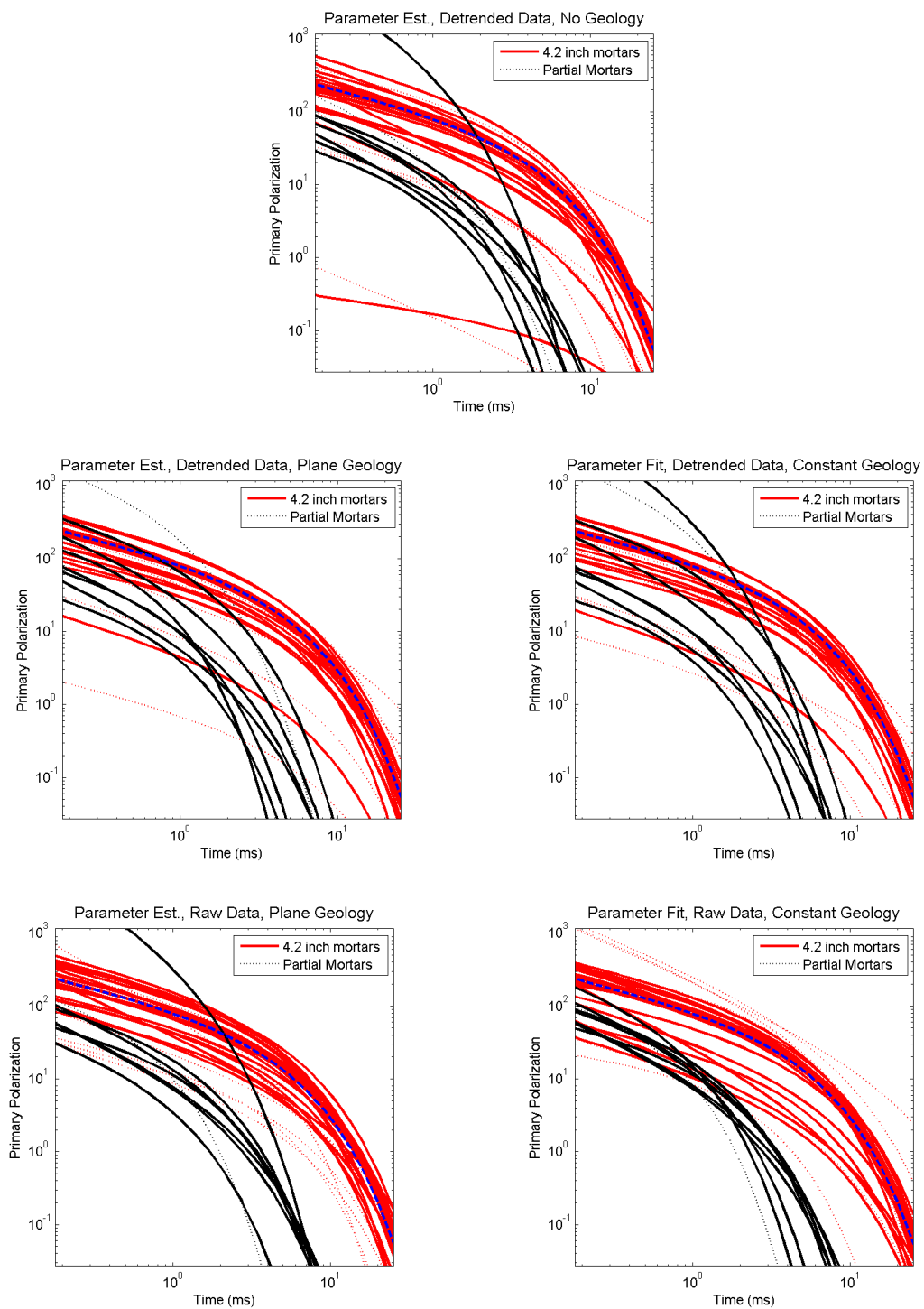


Figure 3.18. Recovered primary polarizations.

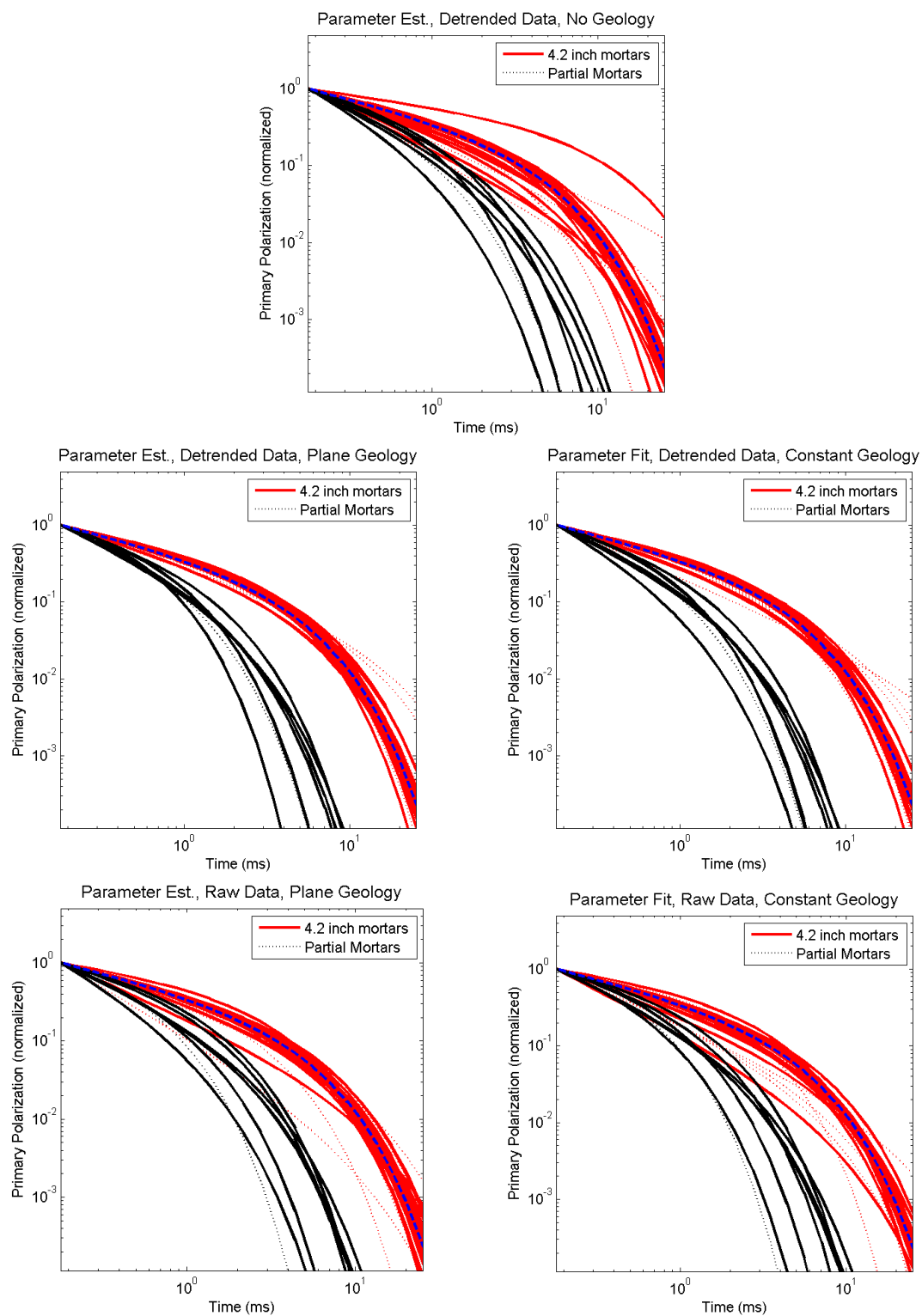


Figure 3.19. Recovered primary polarizations normalized.

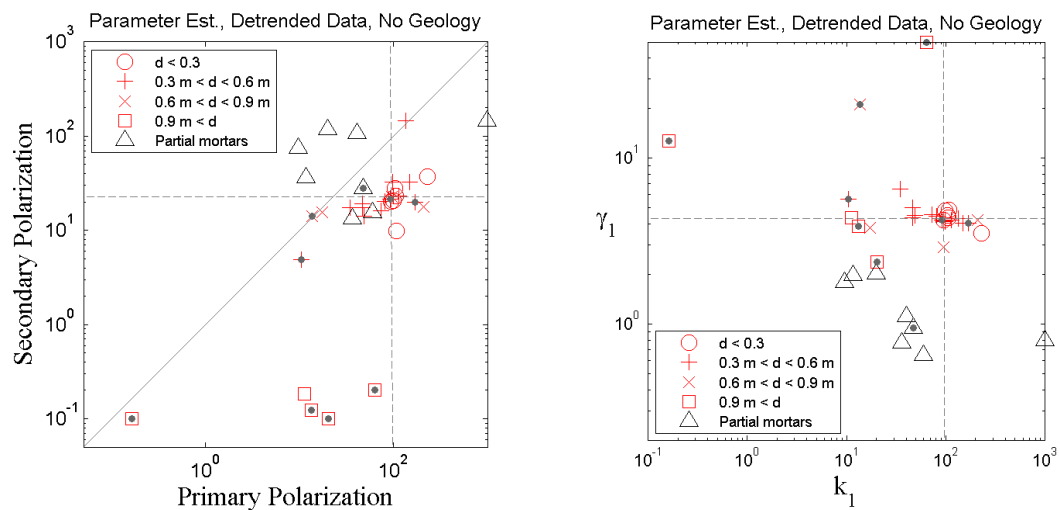
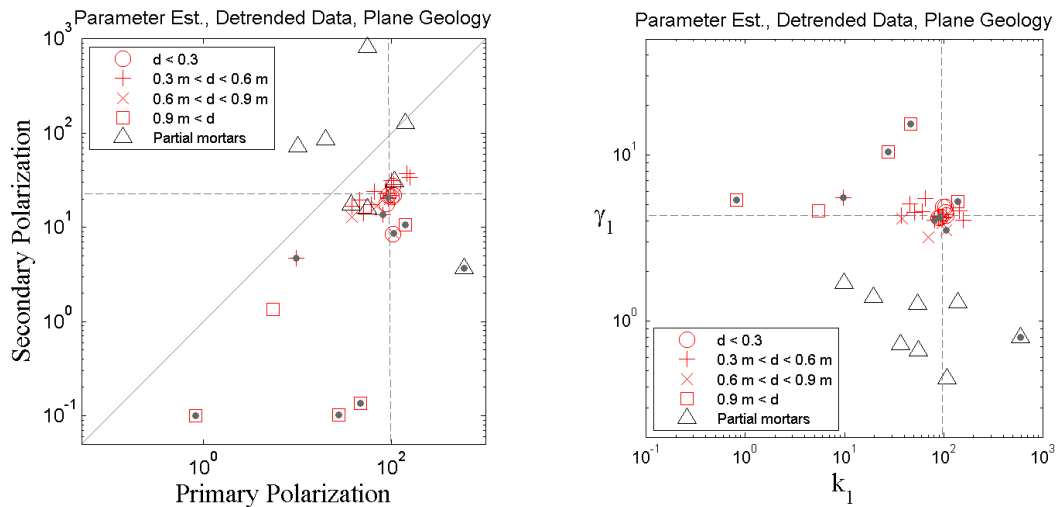
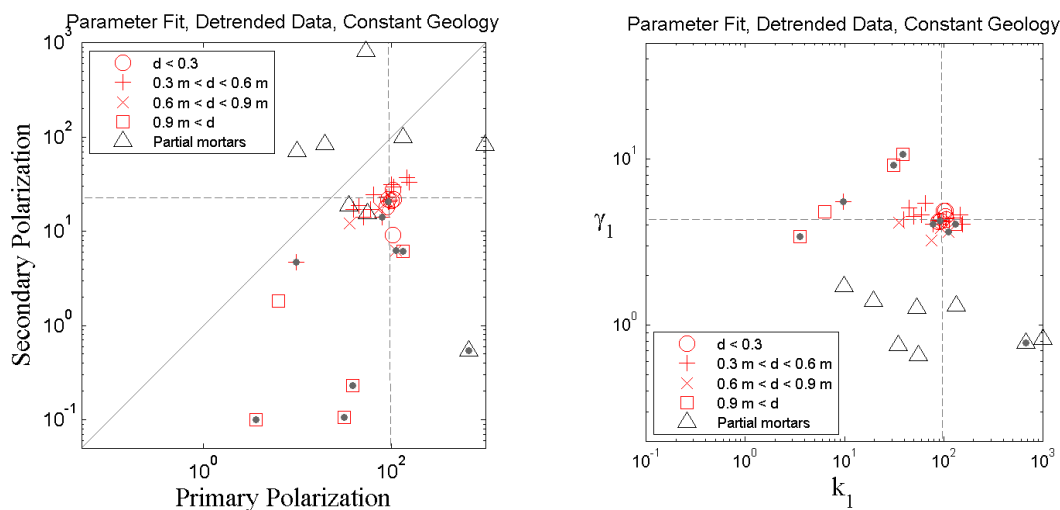


Figure 3.20. Parameter plots when not modeling a geology response

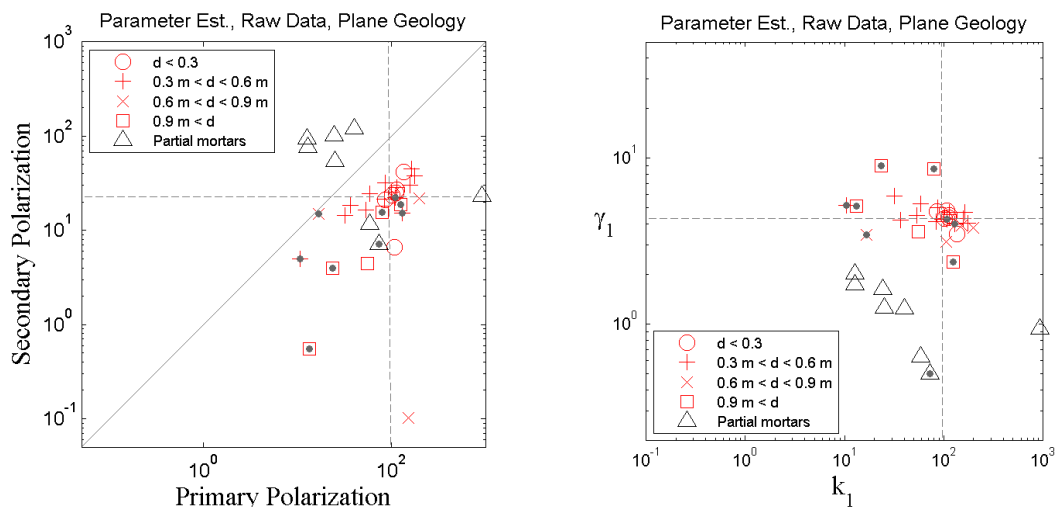


(a) Simultaneous inversion of detrended data when assuming a plane geology model: $G(x,y) = a + b(x-x_o) + c(y-y_o)$

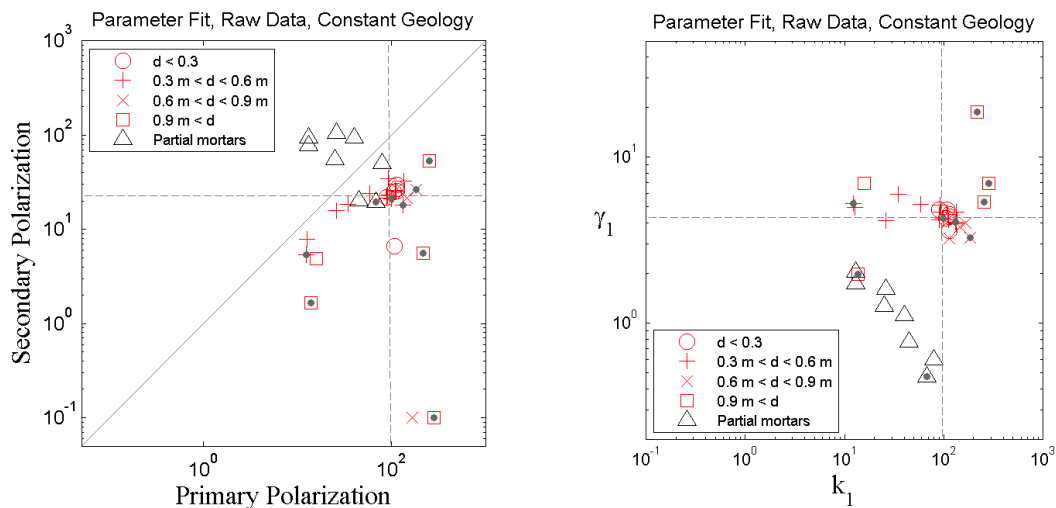


(b) Simultaneous inversion of detrended data assuming a uniform geology model, $G(x,y) = a$.

Figure 3.21. Recovered parameters when simultaneously inverting detrended data for dipole parameters and geology parameters.

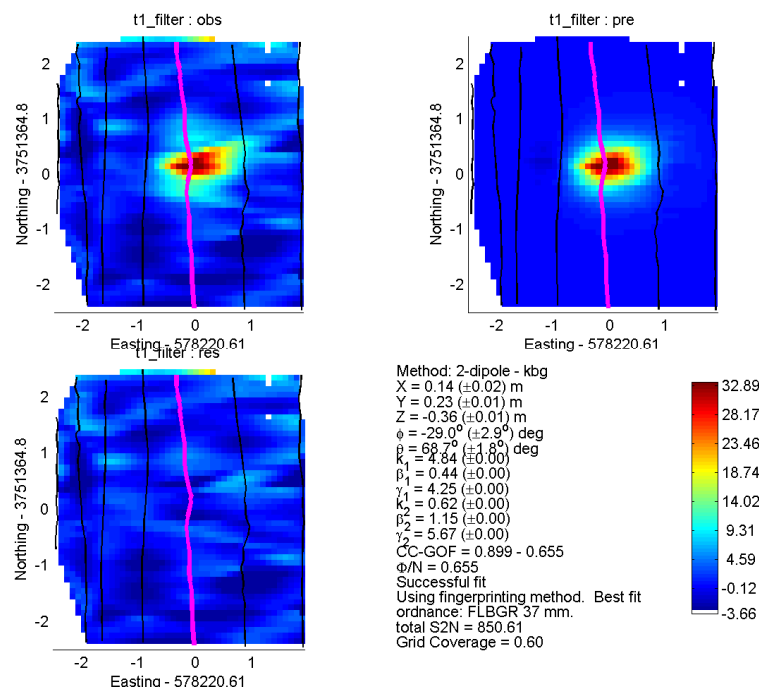


(a) Simultaneous inversion of raw data when assuming a plane geology model: $G(x,y) = a + b(x-x_o) + c(y-y_o)$

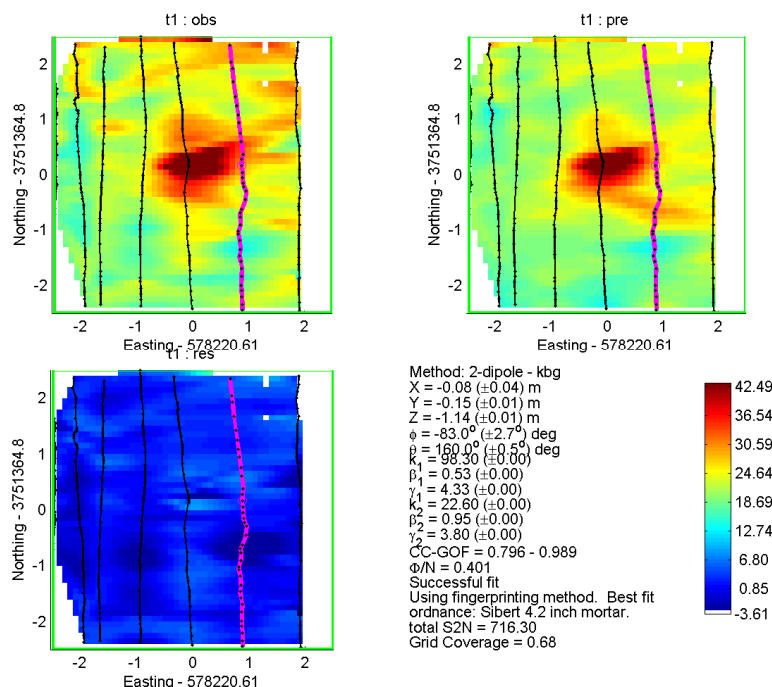


(a) Simultaneous inversion of raw data when assuming a uniform geology model: $G(x,y) = a$

Figure 3.22. Parameter plots when modeling unfiltered data with a geology response



(a) Library based method without a geology model. A 37 mm projectile is the best fit ordnance.



(b) Library based method assuming a plane geology. The method correctly determines that the anomaly is from a 4.2 inch mortar.

Figure 3.23. Library based inversion example. Examples (a) and (b) are for the same anomaly.

Data Type	Geology Model	Comments
Detrend	No	2 misclassifications (1 37 mm , 1 2.75 inch)
Detrend	Constant	3 misclassifications (all 2.75 inch)
Detrend	Plane	2 misclassification (2.75 inch)
Raw data	Constant	1 misclassification (2.75 inch)
Raw data	Plane	No misclassified mortars

Figure 3.24. Summary of library fitting results. Anomalies with no signal or poor coverage are not included in this list.

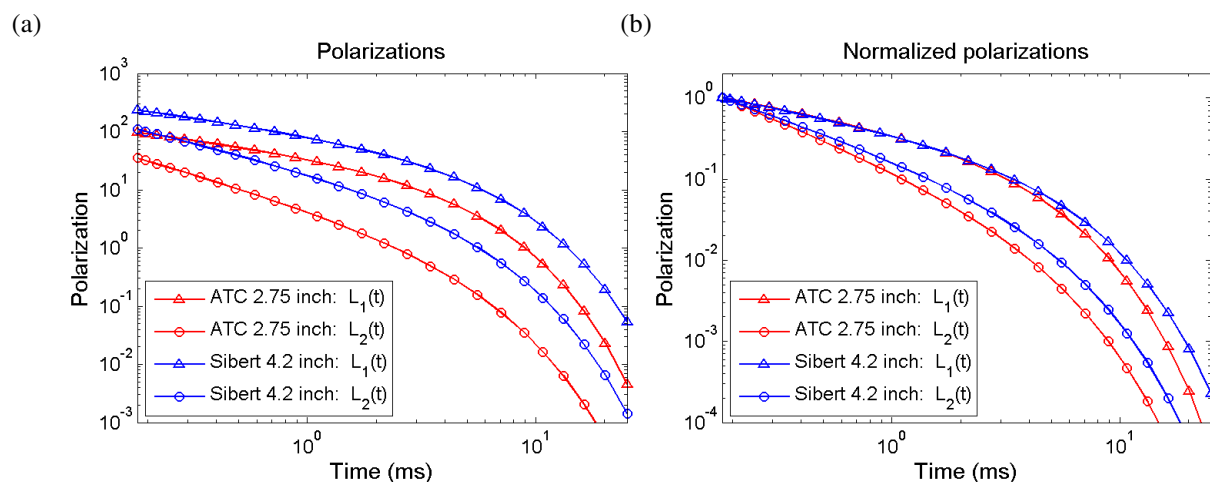


Figure 3.25. Comparison of polarizations for an ATC 2.75 and a Camp Sibert 4.2 inch mortar. Although the magnitudes of the polarizations are different, the polarizations decay in a similar manner.

TASK 2.1: STUDYING THE AMOUNT OF INTERACTION BETWEEN A COMPACT METALLIC TARGET AND HOST USING NUMERICAL MODELING OF MAXWELL'S EQUATIONS

Inversion for the object parameters in an interacting background assumes that the EMI response from a target in a host medium is modeled by a superposition of the host and target responses. In this research we use the University of British Columbia Geophysical Inversion Facility (UBC-GIF) electromagnetic (EM) forward modeling code EH3D (Haber *et al.*, 2004). This code has been previously validated on UXO-types of problems by comparing the responses of EH3D with analytic solutions. The code has also been used to successfully model the effects of complex susceptibility in a conductive half-space environment.

EH3D DETAILS

EH3D is a flexible forward modeling program developed at UBC-GIF for calculating the EM fields resulting from a frequency domain electromagnetic source of arbitrary geometry. The 3D earth which can have substantial complexity, is discretized using a mesh of rectangular cells. Each cell has a uniform conductivity and permeability at each frequency. The fields are calculated using a finite volume numerical solution to Maxwell's Equations. Electric and magnetic fields are computed anywhere in the model.

EH3D takes Maxwell's equations which are described in the frequency domain by:

$$\begin{aligned}\nabla \times E - i\omega\mu H &= 0 \\ \nabla \times H - \sigma E &= J^s \\ n \times H &= 0, \quad \partial\Omega\end{aligned}$$

Then, using a Helmholtz decomposition of the electric field to cope with numerical difficulties associated with the quasi static assumptions, EH3D produces a system of equations for the vector A and scalar ϕ .

$$\begin{aligned}\nabla \times (\mu^{-1} \nabla \times A) - \nabla (\mu^{-1} \nabla \cdot A) - i\omega\sigma(A + \nabla\phi) &= i\omega J^s \\ \nabla \cdot \sigma A + \nabla \cdot \sigma \nabla \phi &= -\nabla \cdot J^s\end{aligned}$$

The above system of equations is discretized using a finite volume method on a staggered grid. The variables A are located at the cell's faces and ϕ is located at the cell's center. The staggered grid implies that H is measured at the cell's edges while J (and therefore E) is at the cell's faces as illustrated in Figure 4.1.

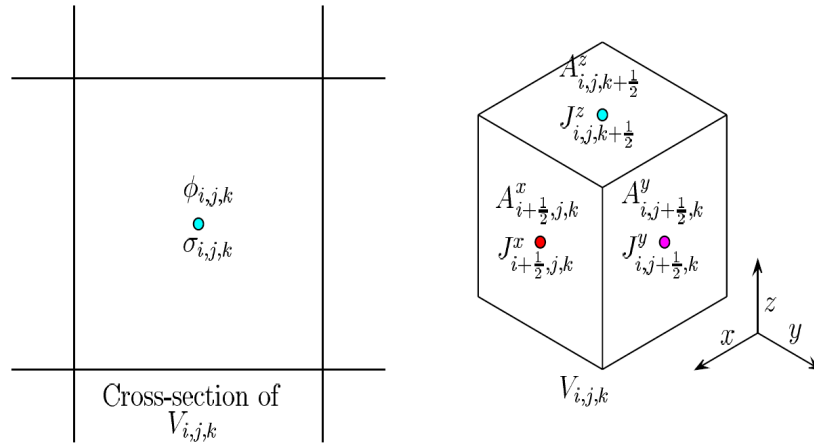


Figure 4.1. The staggered grid used in EH3D finite volume methods.

DETAILS ON MESH DESIGN

A schematic for the models run in the examples that follow is indicated in Figure 4.2. A current source consisting of a 1 m square loop was assumed. Conductivities for the background ranged from 10^{-1} to 10^{-3} S/m. A UXO-like target was simulated as a region on dimensions 10cm x 10cm x 20cm with a conductivity value of 10^4 S/m. The target was centered beneath the transmit loop in a vertical orientation at a depth of 20cm below the surface.

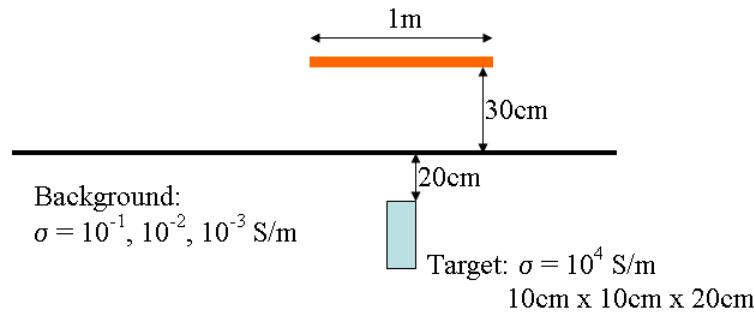


Figure 4.2. The environment modeled in EH3D.

Consideration is required when designing the mesh to be used. In principle, a finer mesh will produce more accurate computed fields, however the mesh size is also limited by computational resources. The area surrounding the target contains the finest mesh with the grid cells gradually becoming larger as we move away from the area of interest. It is necessary to extend the computational domain far beyond the area surrounding the target in order to minimize boundary conditions effects. For the examples presented here, a mesh with a spacing of 5cm was used for an inner core and the computation domain boundaries were set at 1000m. A typical mesh used for results presented here is shown in Figure 4.3

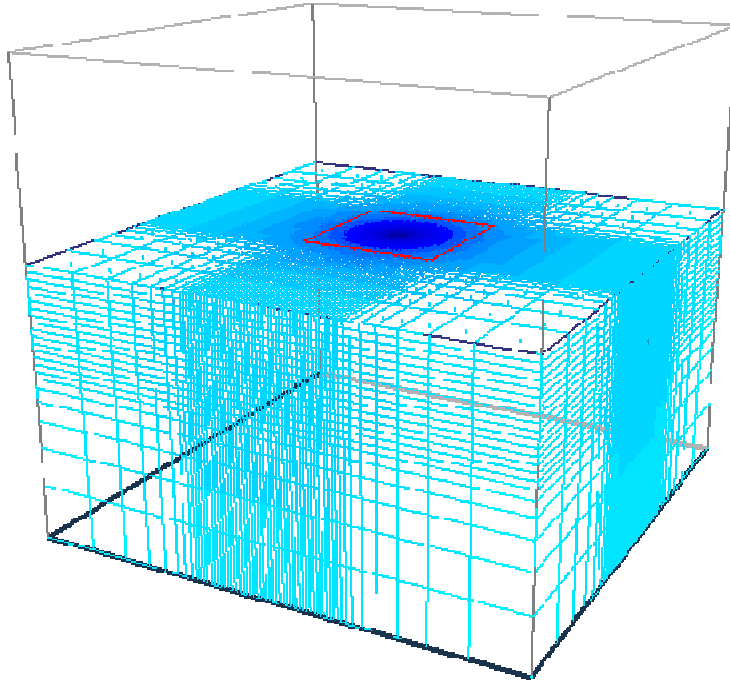


Figure 4.3. A typical mesh used for modeling with EH3D. Extra padding cells have been omitted so that the fine mesh of the inner core is visible. The mesh is shown sliced 30cm above the surface where the 1m square transmit loop is indicated in red.

EH3D FREQUENCY DOMAIN INVESTIGATIONS

The UBC-GIF EH3D codes have been successfully applied to a range of mineral exploration applications. Because these codes also capture the physics associated with the electromagnetic response of a UXO in the presence of an inducing field, we intend to downscale the associated geometries and use the EH3D codes to model the interaction of a UXO with its host medium. We will primarily focus on the frequency domain EH3D codes as they are currently the only version capable of handling complex susceptibility values. The range of frequencies selected for modeling was chosen based on typical frequency domain instruments employed for UXO surveying.

The analytic expression for the radial component (H_ρ) and vertical component (H_z) of the secondary field at the center of a transmitting loop of radius a carrying a current I is given by:

$$H_\rho(\omega) = 0$$

$$H_z(\omega) = \frac{Ia}{2} \int_0^\infty \left[1 + \frac{P_{21}}{P_{11}} e^{-2\mu_o h} \right] \frac{\lambda^2}{\mu_o} J_1(\lambda a) d\lambda$$

where J_1 is a first order Bessel function and P_{11}/P_{21} are as defined earlier in this report.

Prior to modeling any UXO-like targets, a variety of half-spaces with varying conductivities were modeled using EH3D and compared with analytical solutions for a loop above a half-space to validate the codes. Results of these tests are shown in Figure 4.4. The quadrature responses exhibit excellent agreement between the analytical and EH3D solutions.

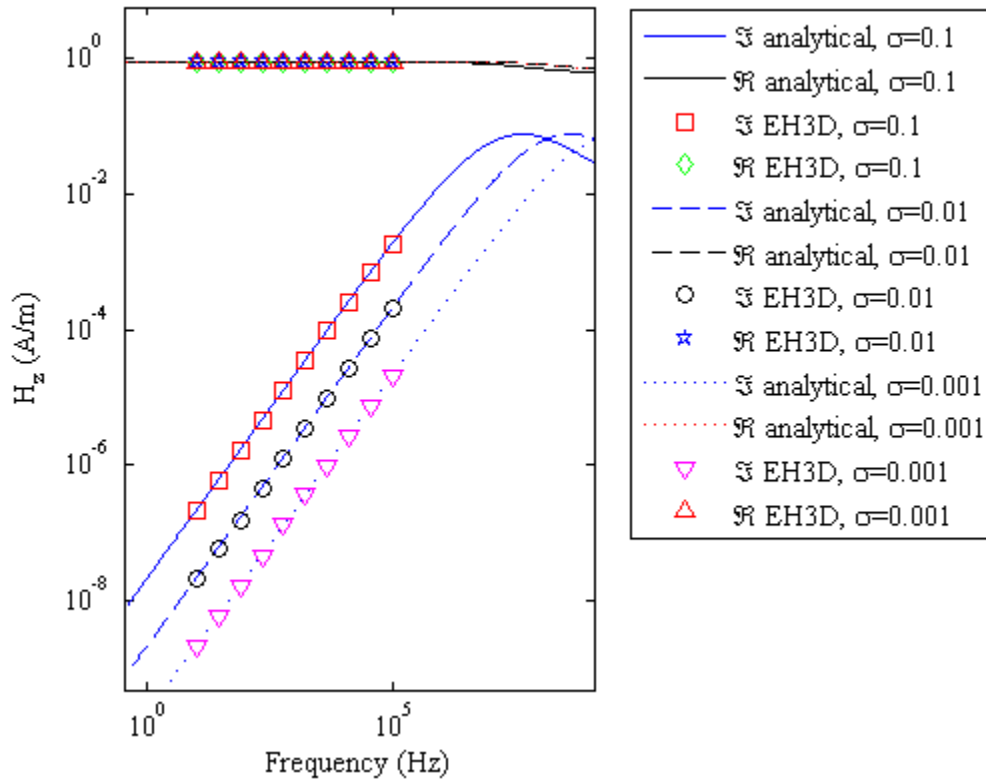


Figure 4.4. Validation tests for the EH3D frequency domain codes. Half-spaces with conductivities of 10^{-1} , 10^{-2} , 10^{-3} S/m were modeled using EH3D and compared with analytical solutions.

ADDITIVITY

Having found acceptable agreement between analytic and EH3D responses for half-spaces of varying conductivity, we consider a UXO-like target embedded in a half-space. We chose to consider the highest conductivity ($\sigma=10^{-1}$ S/m) half-space as that is the scenario most likely to produce current channeling which would pose the most difficulties in the assumption that a target and host soil response can be treated as separate, additive responses.

EH3D is equipped with utilities that allow the extraction and plotting of the fields contained within the computational volume (Figure 4.5). Additionally, routines are available that allow the difference of two fields to be computed. In order to investigate the validity of the additivity assumption, we compare the response of a UXO-like target in free space with a residual response obtained by subtracting the half-space response from that generated by the target in a half-space.

All fields are obtained using EH3D. The UXO-like target and geometry is specified in Figure 4.2. The frequency of 1668 hertz (Hz) was chosen to illustrate the additivity concepts of the field as this particular frequency was observed to produce more substantial variations in the H field around the target than other frequencies.

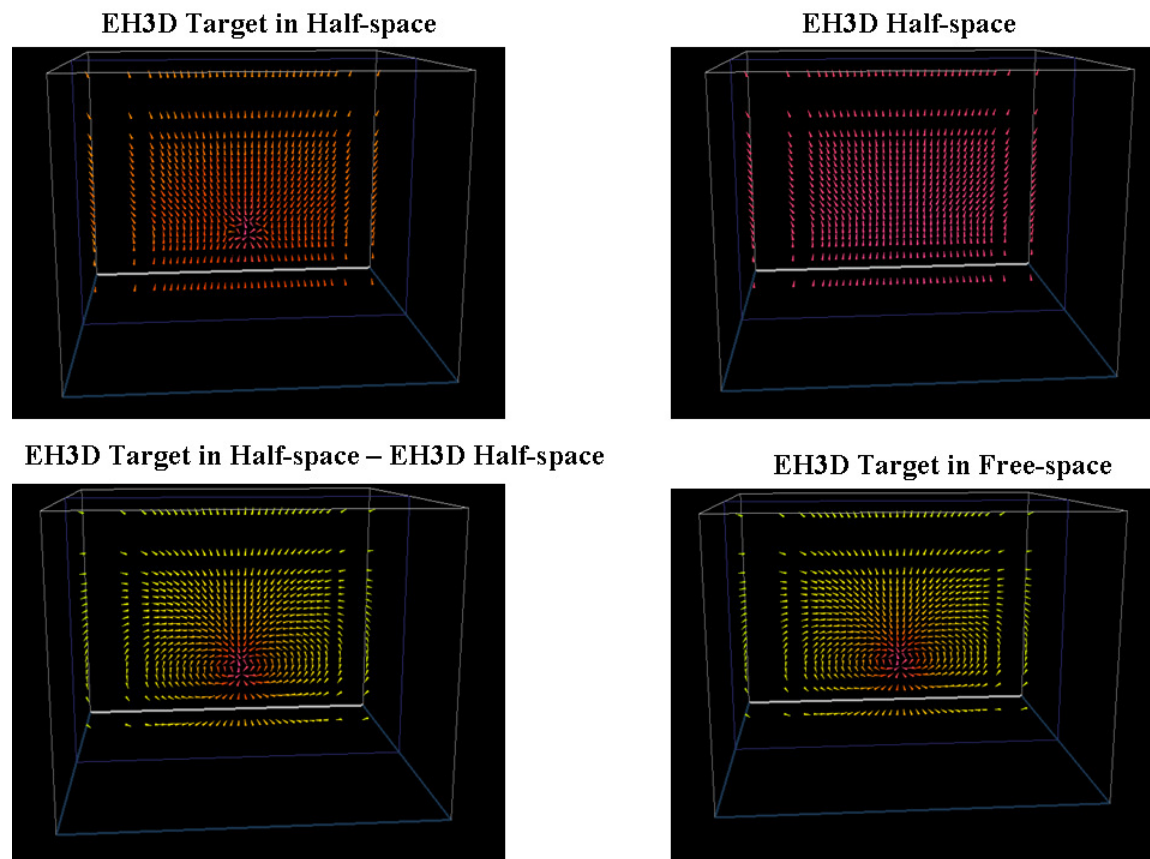


Figure 4.5. Additivity illustrated through the imaginary component of the H field at 1668 Hz. Top left shows the EH3D response generated for a target in a half-space, the top right the EH3D response for a half-space. The bottom left panel displays the derived UXO in free-space response obtained by differencing the top 2 panel responses. Finally the bottom right panel displays the EH3D response computer for a target in a free-space which is virtually identical to the adjacent derived response. All four panels shown have identical limits on color scale. Half-space results used were the 0.1 S/m case.

In addition to intuitively illustrating the additivity via visual inspection EH3D field values, another EH3D utility allows values to be extracted from the solutions at arbitrary locations to produce a collection of soundings. We now choose a point at the center of the loop and show results for both the real and imaginary components of all the frequencies modeled with EH3D. Again we compare soundings for the free-space computed directly from EH3D with a derived half-space achieved by differencing the soundings extracted at the center of the loop for the EHD solutions obtained for the target in a half-space and the half-space only models. The agreement is

excellent at all frequencies as shown in the bottom two panels of Figure 4.6. We conclude that additivity is valid for the model considered. Thus a processing procedure that involves subtracting a background EM response from the data to produce a response that can be modeled as a UXO in free-space is a reasonable procedure.

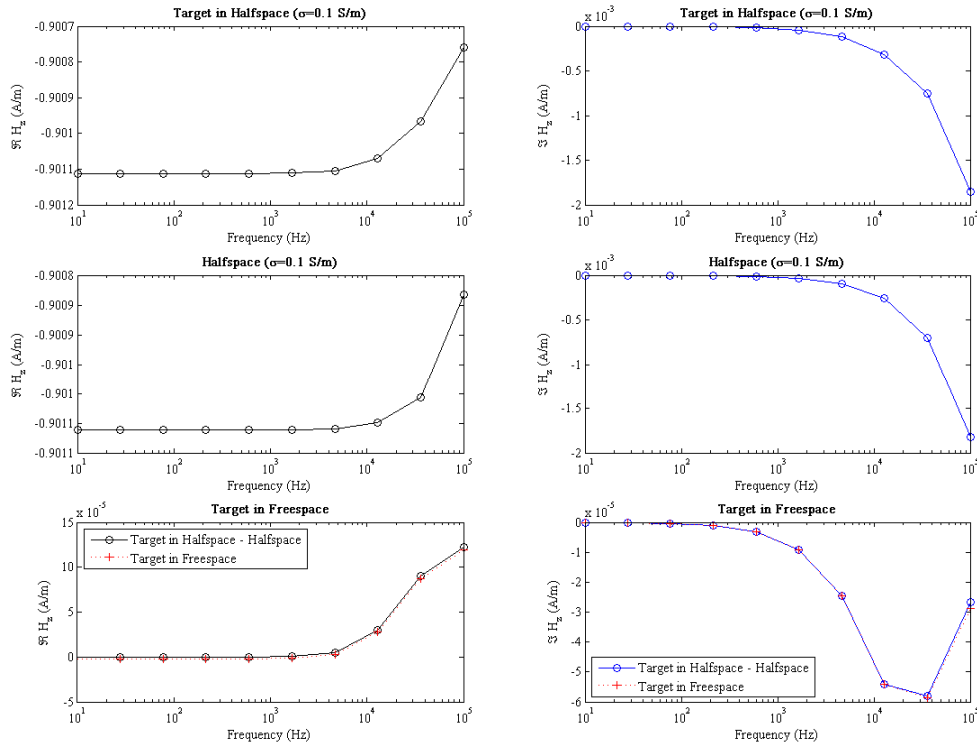


Figure 4.6. The results obtained for real and imaginary values of the H field for all frequencies modeled in EH3D for a target in a half-space (top 2 panels) and a half-space (middle 2 panels). The bottom 2 panels plot the derived target in free-space solution obtained by differencing the soundings at the center of the loop between the top row of panels and the middle row of panels. The EH3D computed solution for a target in free-space is also plotted in the bottom row panels.

EH3D MODELING WITH COMPLEX SUSCEPTIBILITIES

An important aspect of our research is to model the effects of magnetic soils (particularly VRM) for frequency and time domain sensors. The EH3D frequency domain code can model responses in an environment with complex susceptibility values. EH3D input files allow the user to specify a real and imaginary susceptibility value for each cell and for each frequency being modeled. We calculated susceptibility values (see Figure 4.7) based on measurements made at Kaho'olawe, Hawaii. Note that the imaginary part has a negative bias and the real part displays a linear decrease with frequency.

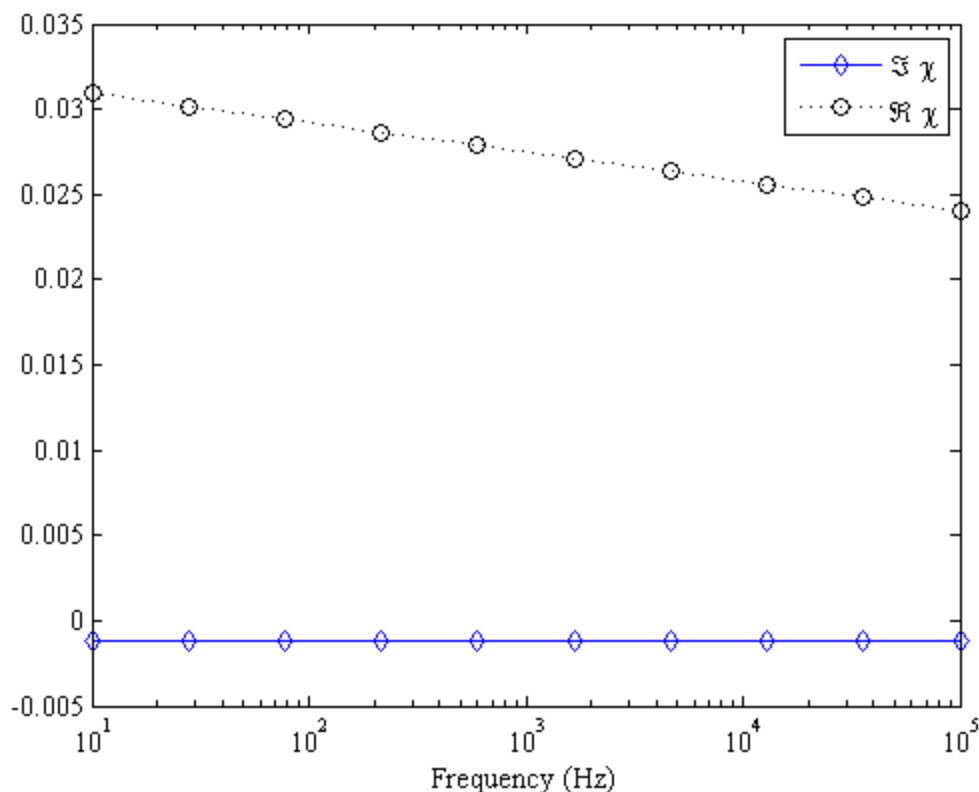


Figure 4.7. Complex susceptibility values used for the frequency domain EH3D results incorporating non-zero susceptibility values.

In order to validate the EH3D codes for a half-space environment containing complex susceptibility, an analytical solution was calculated and the results are compared in Figure 4.8. The results were also plotted for a half-space of equal conductivity (0.1 S/m) but with susceptibility values set to zero so that the effects of complex susceptibility effects can be gauged. The susceptible half-space results produced by EH3D are in excellent agreement with the analytic solution. The susceptible half-space also levels off at lower frequencies as the resistive limit is approached and the magnetic response becomes more important while the half-space without complex conductivities continues to fall off at lower frequencies as expected for a purely conductive response.

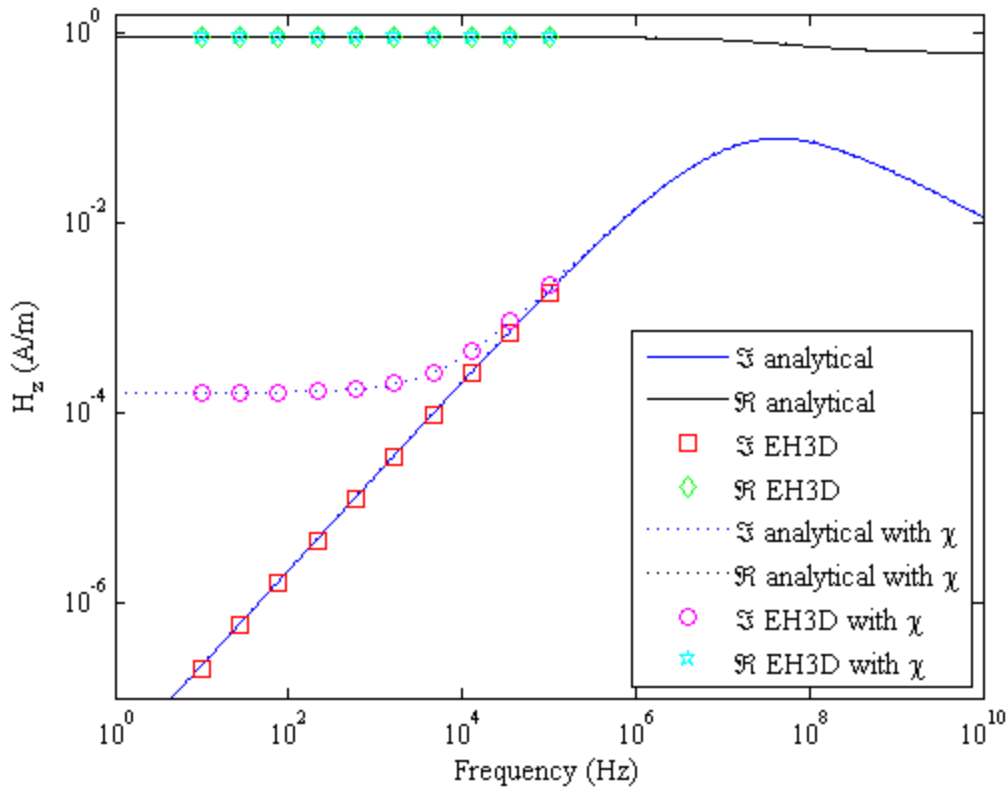


Figure 4.8. Comparison of analytic and EH3D responses for half-spaces with complex susceptibilities and for half-spaces that have no susceptibility. Numerical solutions from EH3D have been limited to the range 10 – 100,000 Hz which is the range for our UXO studies.

While the real part of the analytical and EH3D responses are plotted in Figure 4.8, a finer scale is required to visualize the in-phase components. Figure 4.9 displays the real components at a scale that offers additional insights. The half-space only response displays excellent agreement between the analytical and EH3D solutions. There is also reasonable agreement between analytical and EH3D responses for the complex susceptibility. However, the real component of the EH3D result has a smaller slope than does the analytical solution. The cause for this, and the

assessment about whether the difference is important in our research will be further investigated.

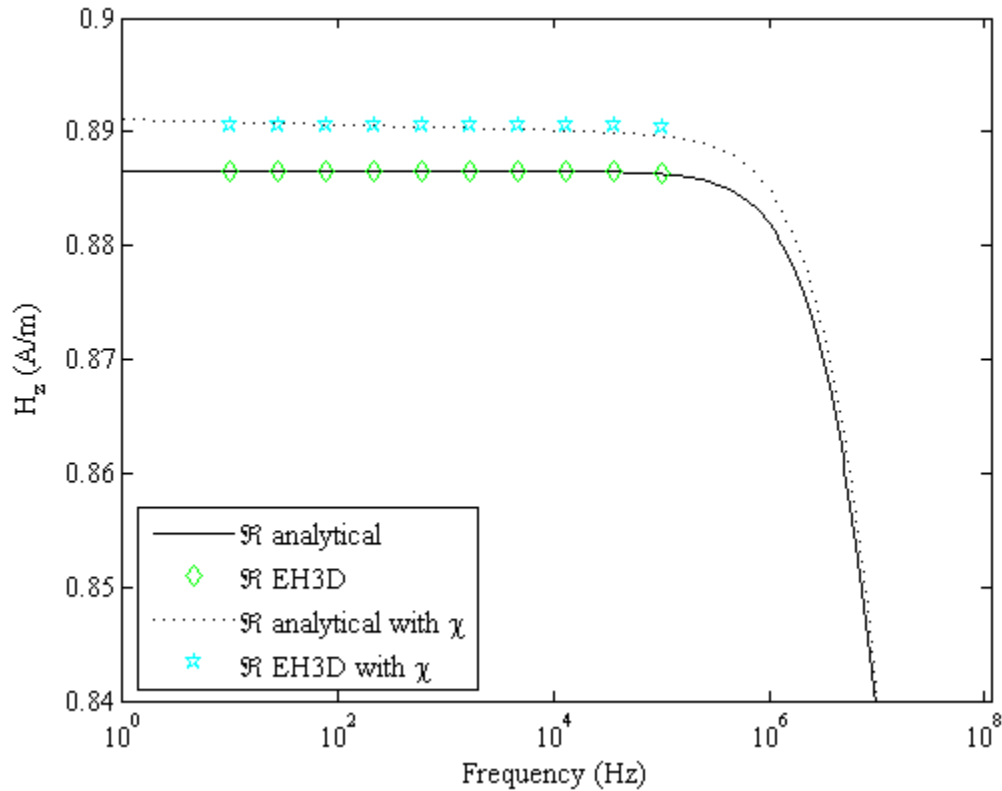


Figure 4.9. Comparison of the real components for analytic and EH3D responses generated by a half-space containing complex susceptibilities.

EH3D TIME DOMAIN INVESTIGATIONS

Efforts have also focused on the testing the time domain modeling code, EH3DTD. This is a time marching algorithm that can handle arbitrary waveforms. Because many of the EM sensors employed acquire data in the time domain, these codes will be useful for comparison with existing time domain datasets. Like the frequency domain codes, in order to be confident in applying the time domain code to obtain responses from a UXO-like target, verification was sought by running EH3DTD on half-spaces of varying conductivities. The results produced by EH3DTD were subsequently compared with both analytic and 1D solutions.

Figure 4.10 shows analytical and 1D solutions along with results obtained from EH3DTD for three half-spaces with conductivities of 0.1, 0.01 and 0.001 S/m. The analytical and 1D solutions are in excellent agreement, appearing indistinguishable when plotted on top of one another and both following the expected $t^{-5/2}$ falloff for a half-space in the time domain. However, the EH3DTD results differ from the analytic and 1D solutions in a manner that is not yet understood. The main discrepancy is for the late time behavior. For the two lower conductivities (0.01, 0.001 S/m), the EH3DTD results both tend to tail off from the expected $t^{-5/2}$ response at late times with

this effect being more pronounced for the lower conductivity. The highest conductivity half-space modeled (0.1 S/m) also does not decay with the expected $t^{-5/2}$ behavior.

These results have been shared with members of the UBC-GIF group and they will pursue this issue. Should they develop modifications to the code that address the discrepancies observed here, we will revisit the use of EH3DTD. However, modeling efforts to this point indicate that the frequency domain EH3D code will be sufficient for the proposed modeling studies.

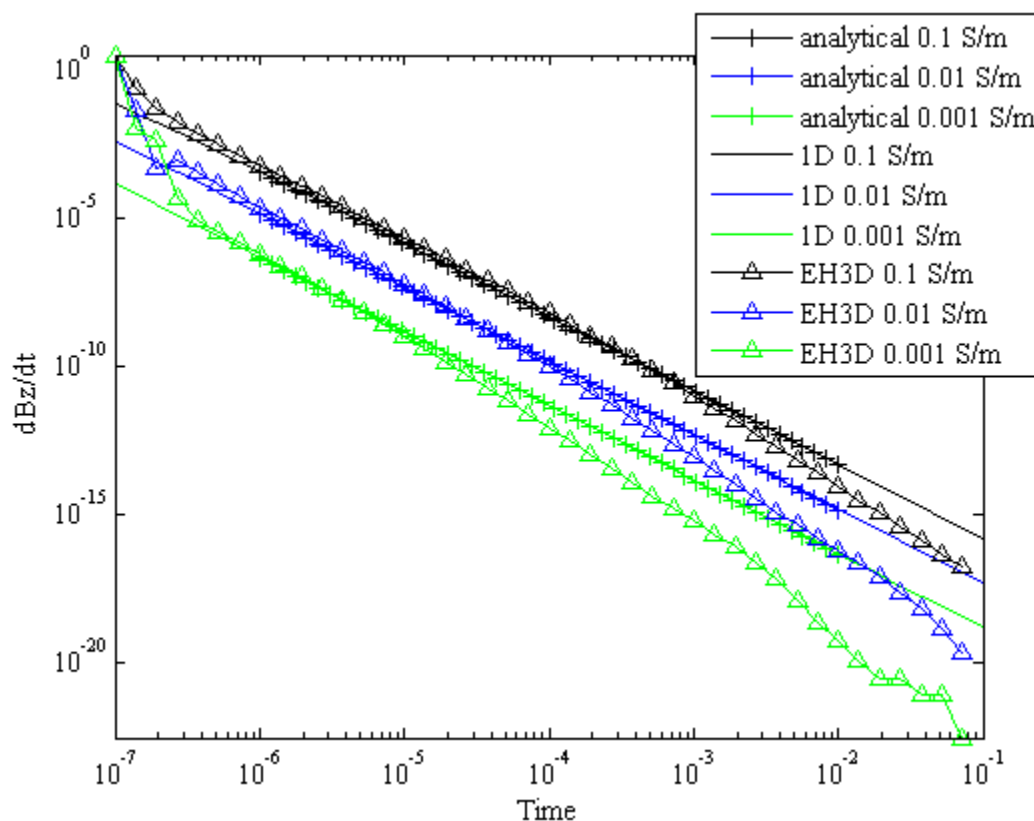


Figure 4.10. Comparisons of analytical, 1D and EH3D solutions for three half-spaces of varying conductivity produced during the validation of the time domain EH3D codes.

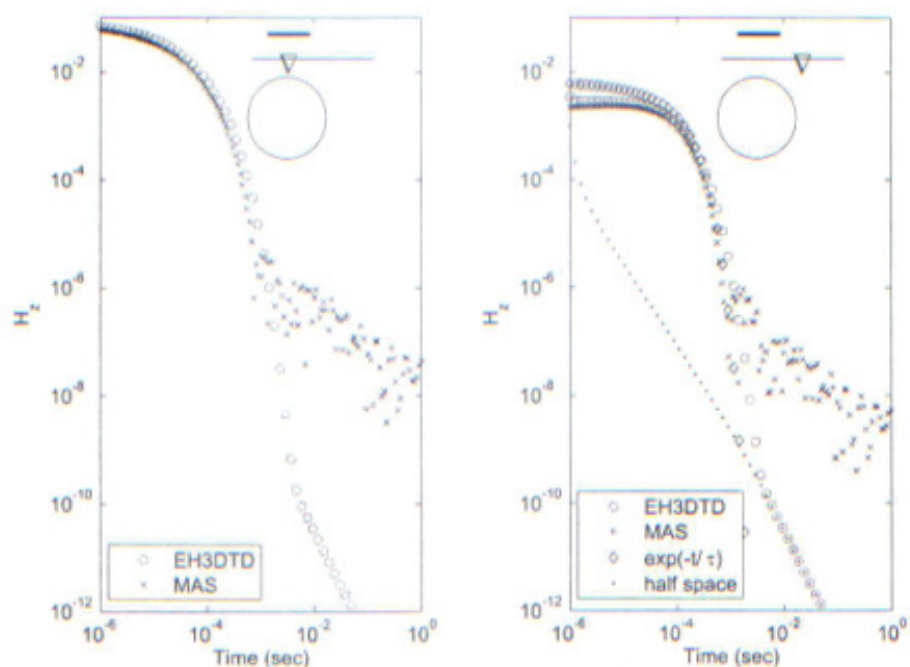


Figure 4.11. Example from previous UBC-GIF testing of EH3DTD against the method of auxiliary sources (MAS) formulation. Results illustrate a high-contrast case for a half-space: $3 \times 10^4 = \sigma_s / \sigma_b$ where $\sigma_s = 3000$ S/m, $\sigma_b = 0.1$ S/m. Vertical magnetic field is measured on the surface $y_r = z_r = 0$ m for $x_r = 0$ m (on the left) and $x_r = 0.5$ m (on the right).

FUTURE MODELING EFFORTS

Tasks for the future include the addition of a UXO-like target to the models being run for the complex susceptibility frequency domain code. Now that we are confident we can model the physics of complex susceptibility processes, a suite of results will be obtained for varying conductivities and susceptibilities. This will allow us to see if the additivity assumption is valid as indicated by the results shown for the conductive half spaces shown earlier. The simulations will therefore identify under what range of target and soil parameters the concept of additivity is valid and when it might break down.

We will also perform comparisons with the Method of Auxiliary Sources (MAS) code provided by Fridon Shubitidze at the Thayer School of Engineering at Dartmouth College. Preliminary comparisons have been completed (Figure 4.11).

CONCLUDING SUMMARY

This is the first annual report for the SERDP Project MM-1573 and covers the research results accomplished for the calendar year of 2007. The research completed to this time has progressed according to the project plan.

Several different versions of an equivalent layer code have been developed for magnetics data processing. We have developed better understanding of the filtering properties of different layer implementations. We have shown that the depth and size of a buried object can be recovered when using an equivalent layer as a filter prior to the inversion of a buried object of interest, even at signal to noise ratios as low as 20 dB. This study lays the foundation for more advanced inversion methods that incorporate the layer formulation.

An inversion methodology has been developed to simultaneously estimate geologic and dipole parameters. A method of modeling the geologic response as a result of sensor movement has been developed and looks promising. We have shown that a background with slowly spatially varying geologic properties can model the observed small spatial wavelength features in the data. This is a useful development as, by removing the background response, we hope to reduce the amount of noise that is included in the data. In addition, anomalies due to the bouncing of EMI sensors could be eliminated, thereby reducing geology-related false positives.

The EMI simultaneous inversion algorithms have been tested on synthetic data and field data acquired on the Camp Sibert GPO. There are a number of different aspects of the algorithm we will address:

- Accuracy of geologic modeling. A combination of numerical forward modeling and field measurements need to be completed to optimize the location and number of dipoles used to model the sensor.
- Accuracy of sensor positioning. A study is needed to determine the required accuracy of IMU and positioning for accurate background modeling.
- Sensitivity to data coverage
- Optimizing starting models and model weighting parameters when minimizing the data misfit function.

A frequency domain formulation of a finite volume numerical solution of Maxwell's equation has been used to model the response of a compact metallic target and a host that has viscous remnant magnetic as well as conductivity. To our knowledge, this is the only example of 3D numerical modeling of complex susceptibility and conductivity. We will now proceed to use this code to quantify the interaction effects of compact targets and a complex susceptible and conductive host. The code will also be used to help optimize the dipole modeling of EMI sensors and to help quantify the effect of topography.

REFERENCES

1. Dampney, C. N. G., 1969. The equivalent source technique. *Geophysics*, 34 (1), pp 39-53.
2. Hansen, R. O. and Miyazaki, Y., 1984. Continuation of potential fields between arbitrary surfaces. *Geophysics*, 49 (6), pp 787-795.
3. Ivan, M., 1994. Upward continuation of potential fields from a polyhedral surface. *Geophysical Prospecting*, 42, pp 391-404.
4. Li, Y., and Oldenburg, D. W., 1999, Stable reduction to the pole at the magnetic equator. *Geophysics*, 66, pp 571-578
5. S.E. Walker, L.R. Pasion, S.D. Billings, D.W. Oldenburg, and Y. Li. Examples of the effect of magnetic soil environments on time domain electromagnetic data. In proceedings from SAGEEP 2005.
6. J. Foley, S. Billings, L. Pasion, S. Walker, and C. Pasion, UXO Target Detection and Discrimination with Electromagnetic Differential Illumination. Technical Report, Strategic Environmental Research and Development Program (SERDP) 2005.
7. L. Pasion, S. Billings, D. W. Oldenburg, and S. E. Walker. Application of a Library Based Method to TEM data for the Identification of UXO. *Journal of Applied Geophysics*, 61(3): 279-291, 2006.
8. L. Pasion and D. Oldenburg. A Discrimination Algorithm for UXO using Time Domain Electromagnetics. *Journal of Engineering and Environmental Geophysics*, 6(2): 91-102, 2001.
9. E. Haber, U. Ascher, and D. W. Oldenburg, 2004. Inversion of 3D electromagnetic data in frequency and time domain using an inexact all-at-once approach. *Geophysics*, Vol. 69, No.5, p 1216-1228.

A2. Improving detection and discrimination of buried metallic objects in magnetic geologic settings by modeling the background soil response (SPIE Defense Security and Sensing Proceedings Paper).

Authors: Leonard R. Pasion, Stephen D. Billings, et al. Published 29 April 2008

Improving Detection and Discrimination of Buried Metallic Objects in Magnetic Geologic Settings by Modeling the Background Soil Response

Leonard R. Pasion^{a,b}, Stephen D. Billings^b, Douglas W. Oldenburg^a

^aUniv. of British Columbia Geophysical Inversion Facility,
6339 Stores Road, Vancouver, BC, V6T-1Z4, CANADA;

^bSky Research Inc., 112A/2386 East Mall, Vancouver, BC, V6T-1Z3, CANADA

ABSTRACT

Magnetic soils are a major source of false positives when searching for unexploded ordnance with electromagnetic induction sensors. In adverse areas up to 30% of identified electromagnetic induction anomalies have been attributed to geology. In the presence of magnetic soil, sensor movement and surface topography can cause anomalies in the data that have similar size and shape to those from compact metallic targets. In areas where the background geological response is small relative to the response of metallic targets, electromagnetic induction data can be inverted for the dipole polarization tensor. However, spatially correlated noise from the presence of a geologic background greatly reduces the accuracy of dipole polarization estimates. In this presentation we examine the effects of sensor movement on the measured EM response of a magnetic background signal. We demonstrate how sensor position and orientation information can be used to model the background soil response and improve estimates of a target's dipole polarization tensor.

Keywords: unexploded ordnance, magnetic soils

1. INTRODUCTION

Detection and identification of unexploded ordnance (UXO) at sites with large geologic background signals can be very difficult. With the large frequency-dependent component of susceptibility at a "geologically hostile" site like Kaho'olawe Island, Hawaii, detection of UXO can be compromised due to geology-related sensor responses of the same order of magnitude as those from UXO. In less hostile settings, detection may be possible, but discrimination difficult due to geology-related sensor noise biasing the recovered polarization tensor.¹

The standard approach to processing data collected in a magnetic geologic setting is to develop filtering techniques such that the background response can be estimated, and subsequently subtracted from the data. These filtering methods generally assume that the geologic, and therefore electromagnetic, properties of the host material are spatially slowly varying, while the anomalies of compact targets have a smaller spatial wavelength. The filtered data are then inverted assuming a physical model of the UXO in free space.

One of the major difficulties with the data filtering approach is the accuracy with which a high pass filter can remove the background response. In particular, movement of the transmitter and receiver relative to magnetic ground can produce significant small wavelength anomalies in the data.^{2,3} The Geonics EM63 is a pulse-based multi-gate time domain electromagnetic induction instrument. The system consists of a 1 m x 1 m square transmitter coil and three coaxial 0.5 m x 0.5 m square receiver loops mounted on a two-wheel trailer. Measured decays are averaged over 26 geometrically spaced time gates, spanning the range from 177 μ s to 25.01 ms. Figure 1 contains a single line of Geonics EM-63, elevation data measured using GPS, and inertial measurement unit (IMU) data collected on the Camp Sibert Geophysical Proveout Area (GPO). Along this data line there were no known UXO or metallic items. The EMI, elevation and IMU sensor data are clearly correlated. Of particular interest are the approximately 10 millivolt (mV) peaks in the first time channel between a Northing of 20 and 30 m. These peaks appear to be well correlated with "valleys" in the elevation, i.e. where the sensor

Further author information: (Send correspondence to L.R.P.)

L.R.P.: E-mail: len.pasion@skyresearch.com, Telephone: 1 505 123 1234

was closer to the ground surface. High pass filters will have limited success in cases where the geologic response produces anomalies of comparable wavelength to those from buried metallic objects. Least-squares inversion procedures are sensitive to correlated noise and can produce biased estimates of target parameters.

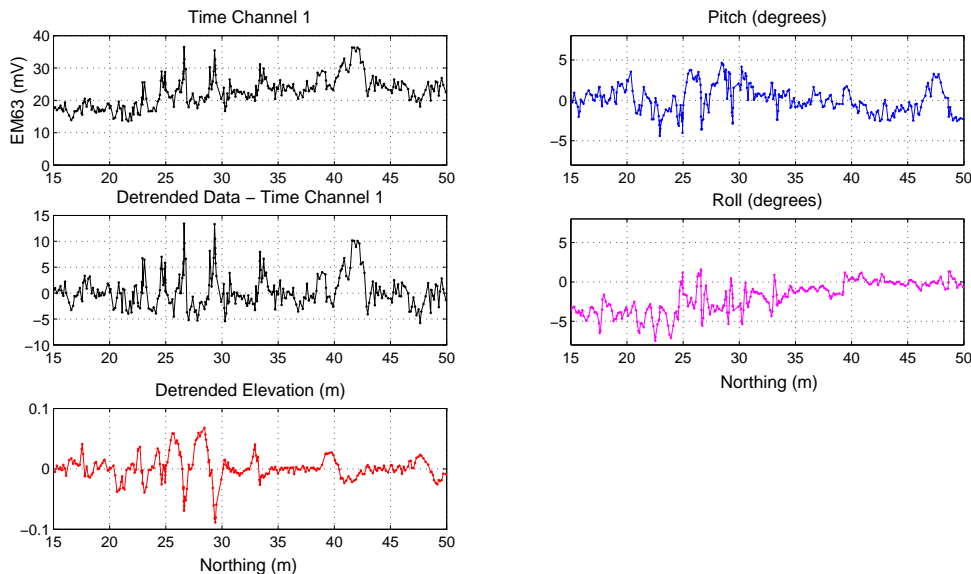


Figure 1. Comparison of the first time channel of data collected along a line located at an Easting of approximately $x = 43$ m. Along this line there were no emplaced items and no known metallic targets. Variations in the measured data are correlated with the sensor elevation and orientation.

Rather than using a filter to eliminate the geologic response, we propose to use GPS and IMU information to directly model the small spatial wavelength features caused by sensor movement. In this presentation, we outline a method of modeling the background geology response by assuming the underlying geology has smoothly varying magnetic characteristics. Parameters describing the amplitude and spatial variation of the geology and parameters characterizing a buried compact target are simultaneously estimated from electromagnetic induction sensor data. The simultaneous inversion methodology is demonstrated using both simulated and field data sets acquired with a Geonics EM63 pulse induction sensor.

2. MODELING GEOLOGIC SIGNAL DUE TO SENSOR MOTION OVER A MAGNETIC EARTH

The background geology response is a function of the position (i.e. location and orientation) of the EMI sensor relative to the ground surface, topography, and the spatial distribution of the subsurface electromagnetic properties (i.e. conductivity and magnetic susceptibility). Accurate modeling of the electromagnetic response of the geology requires numerical modeling of Maxwell's equations, which can be computationally intensive and unsuitable for processing large numbers of target anomalies. Unfortunately, an analytic solution for the response of a loop at an arbitrary orientation over a conductive and magnetic subsurface is not available. Therefore we develop an approximate solution that has the same form as the solution for a horizontal circular transmitter loop over a half-space with viscous remnant magnetization.

For the case of a single loop over a complex permeable, but non-conducting, half-space, the solution for the magnetic field at the center of the loop is given by¹

$$H_z^s(\omega) = \frac{I}{4} \frac{a^2}{[a^2 + (2h)^2]^{3/2}} \chi(\omega). \quad (1)$$

where the radius of the loop is a , the frequency dependent magnetic susceptibility of the half-space is $\chi(\omega)$, and the height of the loop over the half-space is h . If we assume a complex susceptibility defined by log-uniform distribution of time constants (where $\tau_2 \gg \tau_1$), then:

$$H_z^s(\omega) = \frac{I}{4} \frac{a^2}{[a^2 + (2h)^2]^{3/2}} \frac{\chi_o}{\ln(\tau_2/\tau_1)} \left(1 - \ln(\omega\tau_2) - i\frac{\pi}{2}\right). \quad (2)$$

A Fourier transform of the above expression can then be used to calculate the step-off response in the time domain:

$$\frac{\partial H}{\partial t} \approx \frac{I}{4} \frac{a^2}{[a^2 + (2h)^2]^{3/2}} \frac{1}{t}. \quad (3)$$

Therefore, for the simple case of a loop over a complex permeable, but non-conductive half-space, the response can be written as the product of three components:

$$V_s = A(h) G(\chi) f(t) \quad (4)$$

where $A(h)$ is a function of the sensor geometry and relative position to the half-space and is independent of the susceptibility, $G(\chi)$ is a function of the half-space susceptibility, and $f(t)$ is the temporal response of the geology (i.e. $f(t)$ is the convolution of the VRM response with the transmitter waveform).

An approximate forward model can be constructed under the following assumptions:

1. The response measured by a sensor moving over the ground can be approximated by a stationary receiver loop. That is, we assume that the receiver loop is moving slowly enough, that the signal due to a change in flux through the receiver loop due to the Rx loop's movement through the earth's field is small.
2. The geologic response will primarily be due to viscous remnant magnetization (VRM), and not conductivity. Modeling and field measurements at sites with VRM have shown that this assumption is valid for the time range and geometry of transmitter loops used in UXO sensors. We note that this assumption is not necessary, but does simplify the modeling,
3. The response of a loop with an arbitrary orientation can be approximated by Equation 4. That is, the function related to the sensor position and orientation can be separated from the function related to the geologic properties:

$$V_s = A(h, \text{pitch}, \text{roll}, \text{yaw}) G(\chi) f(t)$$

This assumption simplifies our calculations, since A and $f(t)$ are dependent only on survey and sensor parameters, and not the geologic properties of the subsurface. Therefore, when fitting data, the function A needs to be calculated only once at the start of processing rather than at each iteration when the inversion process searches model space.

4. Topography does not need to be modeled. We note that it is possible to introduce a ground clearance correction² into the function A . However, information on surface topography is not usually available at the scale or resolution required.
5. The transmitter loop can be approximated as multiple dipole moments.

3. APPROXIMATING AN ELECTROMAGNETIC SENSOR WITH MULTIPLE DIPOLES

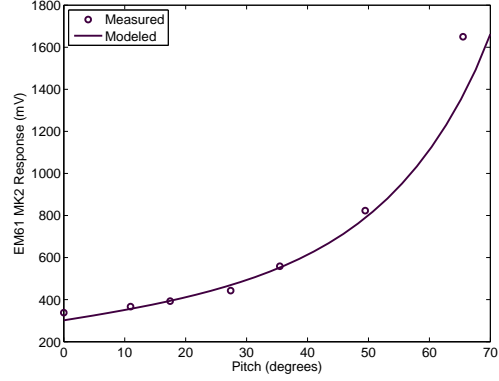
For a small transmitter loop, the primary field can be approximated by a dipole. This assumption is inaccurate for the sensor and survey geometries of UXO EMI surveys. Therefore, we compute the electromagnetic response of the background geology by representing the instrument transmitter by a number of dipoles and sum the response for each dipole. Each transmitter dipole, whose orientation is known from IMU data, is decomposed

into vertical and horizontal components. We use the analytic solutions for a horizontal and vertical dipole over a half-space⁴ to calculate the secondary fields for each dipole, and sum the secondary fields generated by each dipole over the half-space.

Figure 2 contains data measured using a Geonics EM-61 Mark2 pulse induction sensor that was modified to have a 10 mV transmitter on time. The data were taken on Kaho’olawe Island, Hawaii with the sensor at a number of heights and dip angles. We found that using 8 dipoles to model the transmitter sensor was sufficient to model the measured data. Not surprisingly, data collected with the transmitter loop close to the ground were less accurately modeled. When the loop is greater than 10 cm above the ground surface and less than 50 degrees from horizontal the data are accurately modeled using the multiple-dipole method



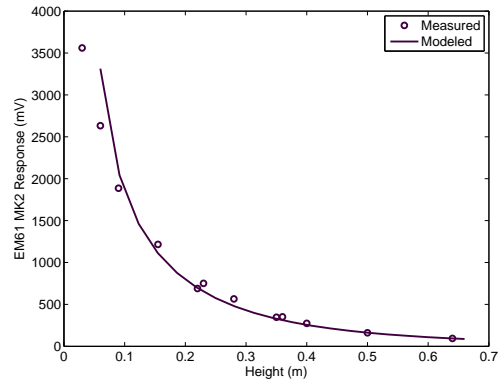
(a) Tilt test setup.



(b) First time channel data measured as a function of pitch.



(c) Height test setup.



(d) First time channel data measured as a function of height.

Figure 2. Tilt and height testing modeling results. A Geonics EM-61 Mark 2 sensor was used to collect data on Kaho’olawe, Island at a number of different heights and tilt angles. The signal was calculated by representing the transmitter loop with 8 dipoles.

4. MODELING GEOLOGY RELATED SENSOR NOISE WITH A SLOWLY SPATIALLY VARYING BACKGROUND GEOLOGY MODEL

In this paper we assume that the electromagnetic properties of the subsurface are slowly spatially varying. That is, small spatial wavelength features in the data can be attributed to the sensor motion $A(h, pitch, roll, yaw)$

rather than sudden changes in the mineralogy (modeled by $G(\chi)$). In order to test this assumption, we again consider the line of EM-63 and IMU data plotted in Figure 1. Recall that the forward model for the soil can be written as:

$$\mathbf{d} = A(h, \text{pitch}, \text{roll}, \text{yaw}) G(\chi) f(t) \quad (5)$$

The data \mathbf{d} is linearly dependent on the model $G(\chi)$, i.e. $\mathbf{A}\mathbf{m} = \mathbf{d}$ where the variation in the data due to changes in sensor position and orientation is contained in the modeling matrix \mathbf{A} , and the spatial behavior of the geology is contained in the model vector $\mathbf{m} = G(\chi)$. Let us parameterize the geologic model $G(\chi)$ with 2 cm constant cells along the N-S direction. Since data are taken at approximately 10 cm intervals along each line, we have an under-determined problem for the model.

Tikhonov regularization is used to solve the under-determined linear inverse problem. The optimal geologic model is obtained through the following optimization problem:

$$\text{minimize } \|\mathbf{d} - \mathbf{A}\mathbf{m}\|^2 + \lambda \|\mathbf{W}_m \mathbf{m}\|^2 \quad (6)$$

where λ is the trade-off parameter and \mathbf{W}_m is the regularization matrix. The regularization matrix allows us to introduce features of the model that we know a-priori. Common choices for the regularization matrix are flatness, which is enforced using the first order finite difference matrix. Regularization for this choice of \mathbf{W}_m thus balances the data fit with a measure of the slope of the recovered model. Another common choice for regularization is smoothness, which is enforced using the second order finite difference matrix. Once a \mathbf{W}_m is chosen, the solution for \mathbf{m} is:

$$\mathbf{m} = (\mathbf{A}^T \mathbf{A} + \lambda \mathbf{W}_m^T \mathbf{W}_m)^{-1} \mathbf{A}^T \mathbf{d} \quad (7)$$

Figure 3 contain examples of fitting the data using either smooth or flat models to a line of Geonics EM-63 data collected on the Camp Sibert GPO. We do not here discuss how the trade-off parameter λ is selected, as our primary objective is to determine if the geologic properties in \mathbf{m} can be slowly spatially varying while still being able to model the small wavelength variations in the data. Figure 3 plots the results of fitting the data with a flat model in (a) and a smooth model in (b). In both (a) and (b), the upper panel shows the fit to the first time channel of data and the lower panel plots the recovered geology model. The flat model is nearly linear with Northing, while still fitting the main features in the data. The smooth and flat models have similar magnitudes. These results suggests that it may be possible parameterize the background geology with simple models, such as a plane, within small spatial subsets of the data while still modeling small wavelength features.

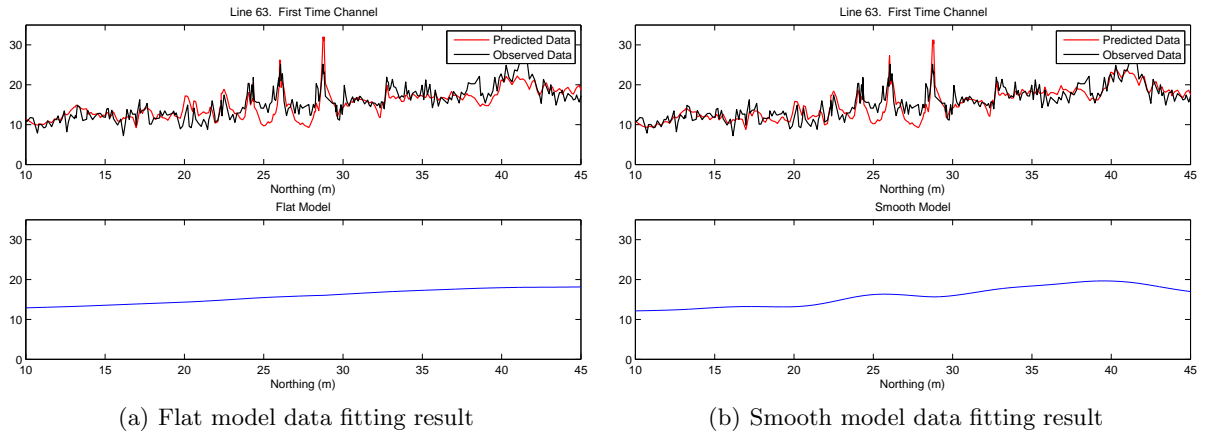


Figure 3. Fitting raw (i.e. non-detrended) data with a slowly spatially varying background geology.

5. SIMULTANEOUS INVERSION OF DATA FOR DIPOLE AND GEOLOGY PARAMETERS

In this section we present results from inverting Geonics EM-63 data simultaneously for geology parameters and target dipole parameters. The objective of inversion is to estimate parameters \mathbf{m} of a forward model $F[\mathbf{m}]$ from

observed data. The choice of the model is based on the ability of the parameters to predict the observed data and any prior knowledge we have of the model parameters.

The forward modeling can be written as

$$\mathbf{d} = F[\mathbf{m}_{soil}] + F[\mathbf{m}_{target}] \quad (8)$$

We will model the soil response as

$$F[\mathbf{m}_{soil}] = A(h, pitch, roll, yaw) G(x, y) f(t) \quad (9)$$

The function A is dependent on sensor positioning and orientation, i.e. parameters that are extrinsic to the target and geology. Therefore A can be calculated prior to the inversion process using the dipole approximation to the sensor outlined earlier. In this paper, we assume that the contribution of conductivity to the measured response will be small relative to the effect of viscous remnant magnetic soil. Therefore, the function $f(t)$ is the characteristic response of viscous remnant soil convolved with the sensor waveform.

The function $G(x, y)$ defines the magnetic characteristics of the background geology. When processing data we, in general, identify and then isolate individual anomalies in data "cells" that are of the order of a few meters square. Within these data "cells", the background geology $G(x, y)$ does not appear to vary significantly. In the previous section the subsurface was finely discretized, and the slowly varying characteristics of the background were introduced through regularization of the inverse problem. Rather than solve an underdetermined inverse problem, we will parameterize the background geology as a plane:

$$G(x, y) = a + b(x - x_o) + c(y - y_o) \quad (10)$$

where the (x_o, y_o) is the center of each data cell. Therefore, for each anomaly we solve for an additional 3 soil parameters: $\mathbf{m}_{soil} = [a, b, c]$.

In our modeling, we define the function $G(x, y)$ to be equal to the background response measured in the first time channel of the Geonics EM-63. The background response at time-channel t_n is then $G(x, y)f(t_n)$.

The response of the target $F[\mathbf{m}_{target}]$ is assumed to be dipolar. The dipole polarization tensor is:

$$\mathbf{L}(t) = \begin{bmatrix} L_3(t) & 0 & 0 \\ 0 & L_2(t) & 0 \\ 0 & 0 & L_1(t) \end{bmatrix}. \quad (11)$$

where we parameterize the decay of the polarization tensor with the function $L_i(t) = k_i t^{-\beta_i} \exp(-t/\gamma_i)$. Examples of polarizations for an Aberdeen Test Center (ATC) 60 millimeter (mm) mortar and a 4.2 inch mortar found at Camp Sibert are shown in Figure 4.

The target parameters are:

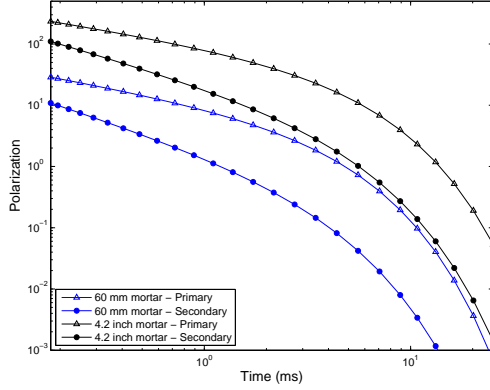
$$\mathbf{m}_{target} = [x, y, z, \theta, \phi, \psi, k_1, \beta_1, \gamma_1, k_2, \beta_2, \gamma_2, k_3, \beta_3, \gamma_3] \quad (12)$$

where the target location is (x, y, z) and the orientation is defined by the angles (θ, ϕ, ψ) . The inverse problem for \mathbf{m}_{target} and \mathbf{m}_{soil} is cast as an optimization problem:

$$\text{minimize} \quad \phi(\mathbf{m}) = \frac{1}{2} \|V_d^{-1/2} (\mathbf{d}^{obs} - F(\mathbf{m}_{target}))\|^2 \quad \text{subject to} \quad m_i^L \leq m_i \leq m_i^U \quad (13)$$

where V_d is the data covariance matrix, m_i^L and m_i^U are the lower and upper constraints, respectively.

Two versions of the simultaneous inversion methodology are implemented. The first method is a parameter estimation approach where the location, orientation, and polarization tensor parameters are estimated from the data (for example⁵). The second method is a library based method where we have a library consisting of the polarization curves for a number of difference ordnance items, and we invert for the optimal location and orientation for each item in the library.⁶ We determine which ordnance item in the library most likely generated the observed data.



(a) 60 mm mortar and 4.2 inch mortar polarizations.

	60 mm ATC mortar		4.2 inch Camp Sibert Mortar	
	Primary	Secondary	Primary	Secondary
k_1	11.2	1.8	98.3	98.3
β_1	0.58	1.1	0.53	0.95
γ_1	3.2	2.9	4.3	3.8

(b) Table of decay parameters

Figure 4. Dipole polarizations for a 60 mm mortar and a 4.2 inch mortar from Camp Sibert, AL. The 60 mm mortar polarization was derived from measurements acquired on the US Army Corps of Engineers (USACE) Engineer Research and Development Center (ERDC) test stand in Vicksburg, MS. The 4.2 inch mortar polarizations plotted here represent the average recovered polarizations from EM-63 inversions completed as part of ESTCP project MM-0504. The table lists decay parameters when modeling the polarization with the function $L(t) = kt^{-\beta} \exp(-t/\gamma)$.

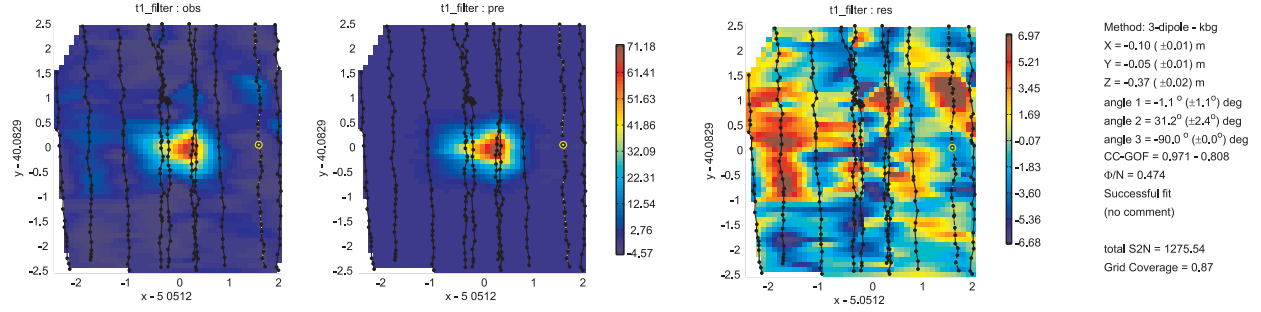
5.1. Simultaneous Inversion Example 1: Synthetically Generated 60 mm Data

As a first test of the simultaneous inversion technique, we invert Geonics EM63 data simulated for a 60 mm mortar buried at a depth of 40 cm. The nominal height of the Geonics EM63 transmitter coil is 30 cm above the ground. Figure 4 contains a plot of the polarization curves that we use to forward model the data. For this example, we assume a viscous remnant background response that has a magnitude of 30 mV in the first time channel. We use a subset of elevation and IMU data collected during the Geonics EM-63 survey collected on the Camp Sibert GPO.

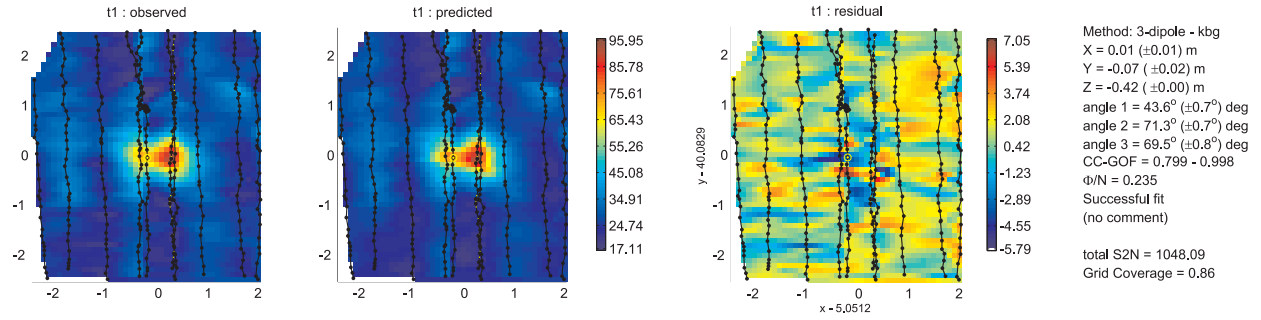
We compare the standard method of processing data where we fit a dipole model to detrended data with simultaneous estimation of the background geology and the dipole parameters. A 51 point median filter was used along lines to detrend the data. The length of the filter was chosen to remove as much of the background as possible, while preserving the shape of anomalies from buried targets. The simultaneous inversion will use the unfiltered sensor data. A random error with a standard deviation of 1 cm was added to elevation data. No noise was added to the IMU (i.e. accurate IMU information was used as input to both the inversion of the detrended data and the raw data). When inverting the data for target and geology parameters simultaneously, a 5 m square of data centered on the target is inverted. When inverting the detrended data, a 3 m diameter circular mask defined the data to be fit. For this example, we invert the data using 3 unique polarizations (Equation 12) and the background geology will be modeled using a plane (Equation 10).

Figure 5 compares the first time channel of the observed and predicted data. The fit when modeling the anomaly using both a geology and dipole response is plotted in (a), and the fit using a dipole only is plotted in (b). Both models appear to fit the data reasonably well. Of note is the how the residual of the fit without geology (in (b)) appears to have some spatially correlated features, while the fit using geology and a dipole results in a random resulting residual. The spatially correlated features in (b) are important to note, as our inversion approach is optimized for Gaussian noise in the data. Spatially correlated signals have the potential to bias the recovered parameters.

The true geology model was defined to be $G(x, y) = 30$, and is accurately estimate. The recovered geology model is $G(x, y) = 29.26 - 0.15(x - x_0) + 0.07(y - y_0)$. A summary of the recovered dipole parameters are found in Figure 6(a). Without modeling the geology, the inversion was unable to accurately predict the data. The accuracy with which the polarization parameters were recovered can more easily be seen in plots of Figures 6(b) and (c). In both cases, the primary polarization is well recovered (although the simultaneous inversion result is better). Not including the geology resulted in a much poorer recovery of the secondary polarizations.



(a) Fitting filtered data using a dipole model (no geology)

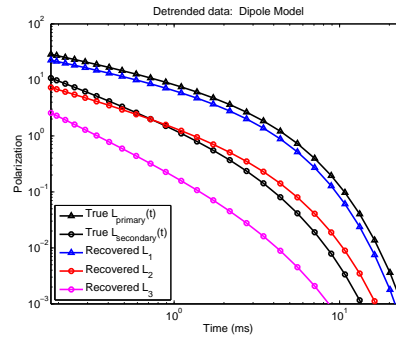


(b) Simultaneous fit using raw (not filtered) data).

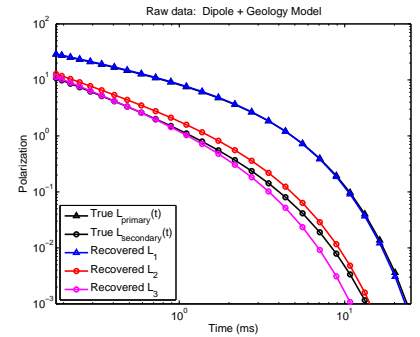
Figure 5. Comparison of data fits when fitting data with and without geology modeling included.

	True Model	Dipole Only	Dipole+ Geology
X	5.05	4.98	5.06
Y	40.08	40.09	40.01
Z	0.40	0.31	0.40
k_1	11.2	9.00	11.56
β_1	0.58	0.57	0.57
γ_1	3.2	2.96	3.09
k_2	1.8	1.90	2.63
β_2	1.08	0.82	0.96
γ_2	2.9	3.16	2.68
k_3	1.8	0.25	1.89
β_3	1.08	1.39	1.09
γ_3	2.9	3.42	2.21

(a) Recovered Parameters



(b) No geology model included



(c) Simultaneous dipole and geology

Figure 6. Comparison of recovered polarization parameters. Clearly, the secondary polarizations are not well resolved when inverting for a dipole only.

5.2. Simultaneous Inversion Example 2: Camp Sibert GPO data

The simultaneous dipole and geology parameter inversion technique described in the previous section was applied to dynamically collected Geonics EM-63 data acquired at the Camp Sibert geophysical prove-out. In this section we compare the standard approach of estimating dipole parameters from detrended data to the simultaneous inversion approach. For these parametric inversions, we will invert for an axi-symmetric target. That is we will solve for dipole model where the two secondary polarizations are equal (i.e. $k_2 = k_3$, $\beta_2 = \beta_3$, and $\gamma_2 = \gamma_3$).

Figures 7(a) and (b) compare the ground truth depths to the depths estimated from the parameter estimation inversions. Depth estimate comparisons are important, since accurate size estimates of ordnance require accurate estimates of depth. The red 'x' symbols indicate intact 4.2 inch mortars and the black triangles indicate partial mortars. A gray dot overlaying a symbol indicates that the data anomaly had either no signal above the noise, or the data coverage was very poor. Estimates that fall within the gray band indicate that the error in the depth estimate was less than 20 cm. The standard method of only fitting a dipole model has a greater number of inaccurate depth estimates than the other methods, with 4 mortars with good data coverage that have a depth error greater than 20 cm. Although there are only 38 total anomalies, this result suggests that including a soil model in the fitting may improve the estimation of size-based dipole parameters. The depth analysis was repeated for results from the library based fitting method (Figures 7(c) and (d)). The 4.2 inch mortar dipole polarization curves were shown in Figure 4. An additional 20 ordnance items were included in the ordnance library. The accuracy of the depths is much better when using the library based fitting method. Including the geology response did not significantly improve the performance of the library based method.

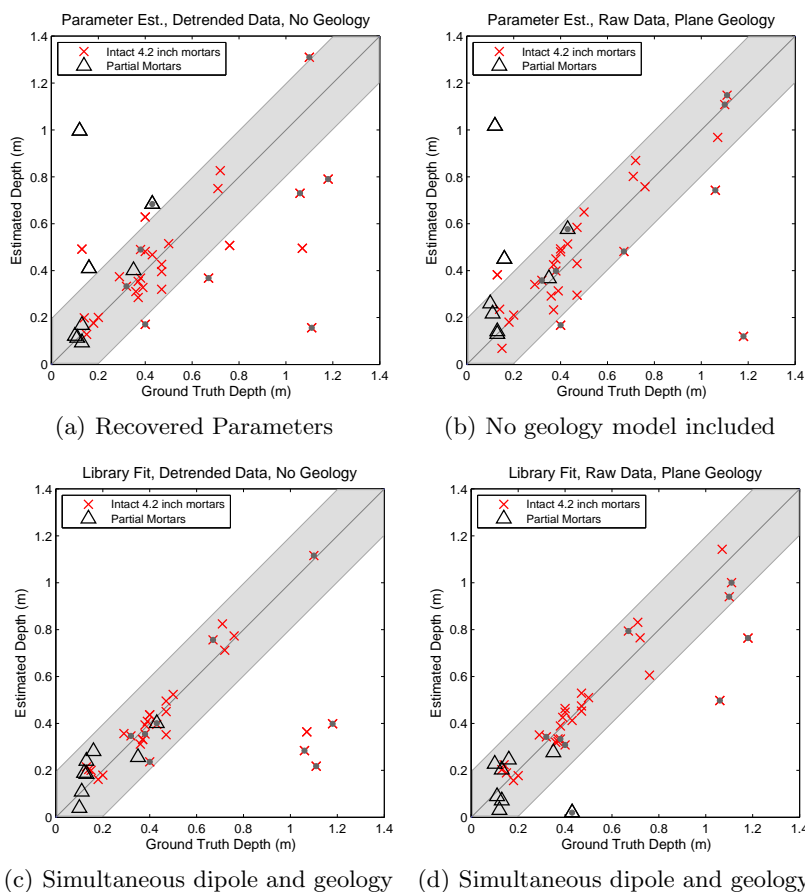


Figure 7. Depth comparison. The top row summarizes results when inverting for dipole parameters. The bottom row (c-d) contains summarizes results from applying the library fitting method.

Figure 8 summarizes the recovered parameters. Figures 8(a) and (d) plots the primary polarization $L_1(t)$ recovered from the inversion with and without geologic modeled. Recovered polarizations for intact 4.2 inch mortars are plotted in red and partial mortar polarizations are plotted in black. Polarizations derived from anomalies with poor coverage or low signal-to-noise levels are plotted with a dotted line. The blue dashed line indicates the 4.2 inch mortar primary polarization from Figure 4. When inverting for dipole parameters from detrended data, there are a couple anomalies from which there is inaccurate recovery of the primary polarization. By including the geology response, the polarizations are more robustly recovered.

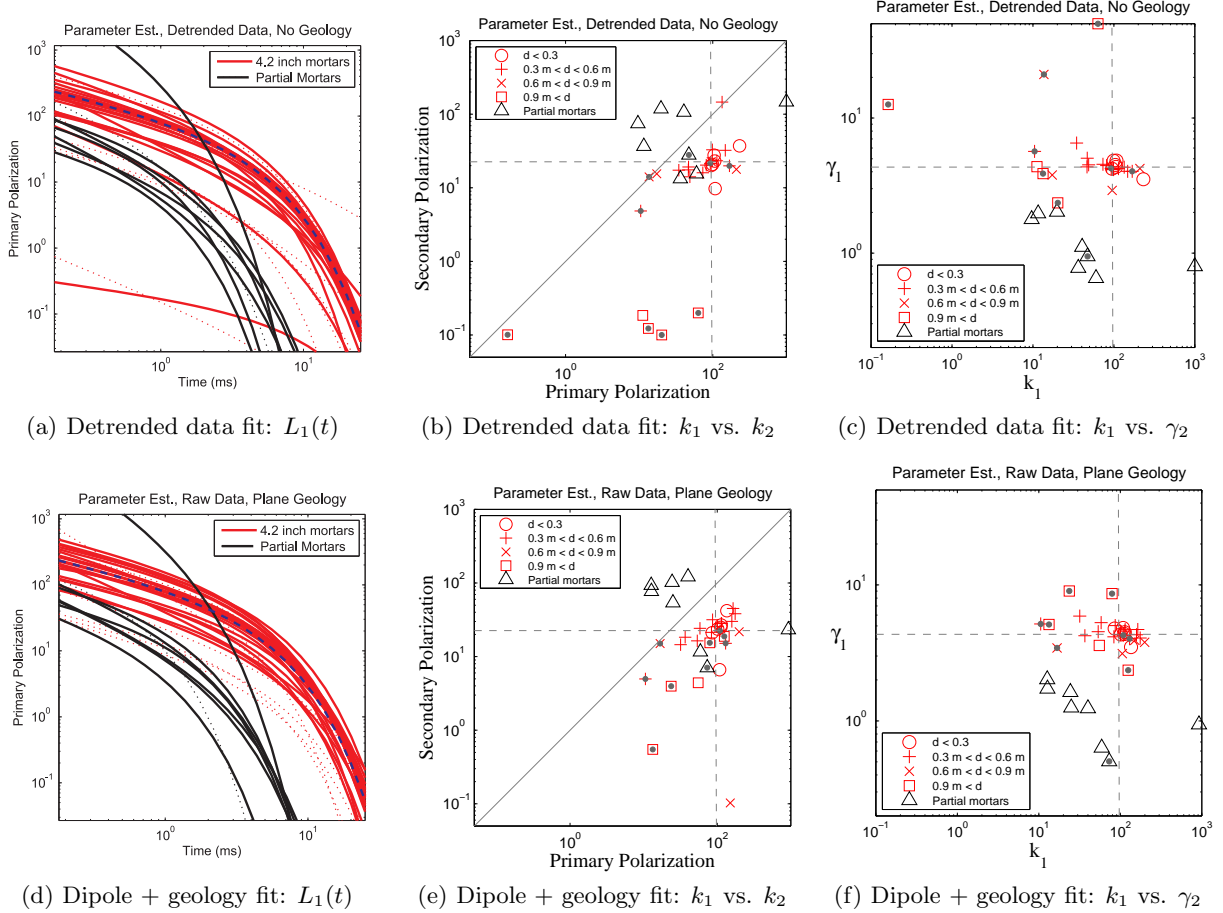


Figure 8. Recovered primary polarizations. The top row summarizes results when inverting detrended data for dipole parameters. The bottom row summarizes results when including background geology in the modeling.

Figure 8(b) plots the magnitudes of the primary and secondary polarizations (i.e. k_1 vs. k_2) and the magnitude vs. time constant of the primary polarization (i.e. k_1 vs. γ_1) for the dipole fitting without a geology model. Plots for the simultaneous geology and dipole inversions using raw/non-detrended data are in Figure 8(e). There appears to be a marginal improvement in the size based parameter clustering (k_1 vs. k_2) when including the geology model. The k_1 vs. γ_1 parameter space provides a good separation between partial and intact mortars, regardless of whether a geologic model is used (Figures 8(c) and (f)). The separation is largely due to the much smaller time constants γ_1 of the partial mortars. Again, we note that since there are only 38 anomalies in the Camp Sibert GPO it is difficult to make any statistically significant conclusions.

The library based method performed well when applied to the data. When applying the library method to detrended data, there were two anomalies from a 4.2 inch mortar that were misclassified. One anomaly was classified as a 2.75 inch rocket, and the other incorrect anomaly was classified as a 37 mm projectile. The application of the library method to non-detrended data and assuming a planar geology resulted in all 4.2 inch

mortars being correctly classified. A comparison of the polarizations for the ATC 2.75 inch rocket and the Camp Sibert 4.2 inch mortar can explain the misclassifications (Figure 9). Figure 9(a) shows that the magnitudes of the polarizations are quite different. However, the decay behavior is quite similar, as can be seen by plotting the normalized polarizations (Figure 9(b)). It is likely that some anomalies, particularly those with poor spatial coverage, would have been fit with an ATC 2.75 inch mortar that is shallower than the true depth.

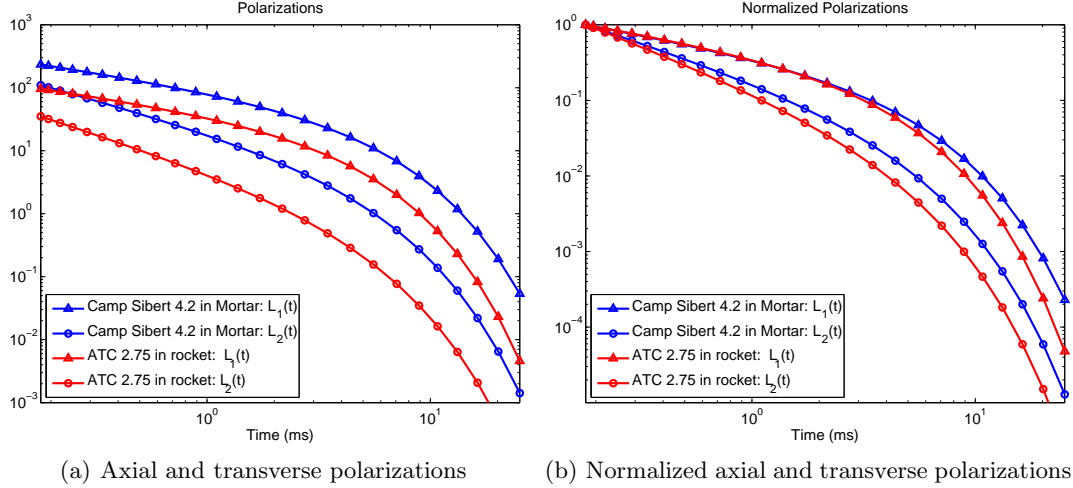


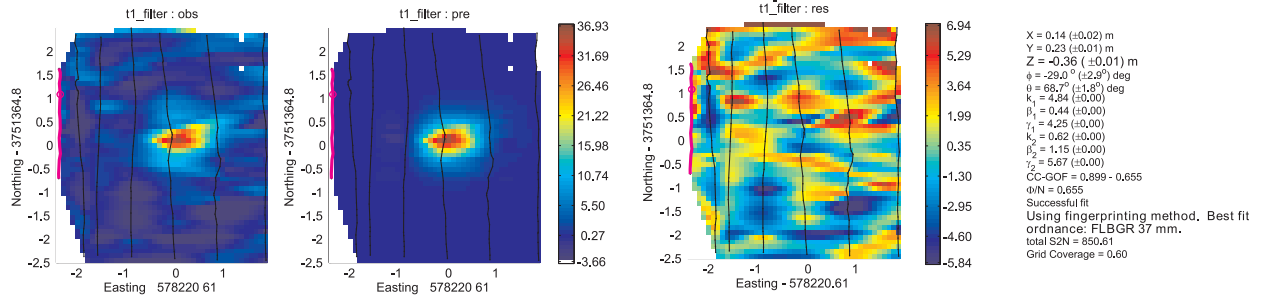
Figure 9. Comparison of polarizations for an ATC 2.75 and a Camp Sibert 4.2 inch mortar. Although the magnitudes of the polarizations are different, the polarizations decay in a similar manner.

Of particular interest is the misclassification of a 4.2 inch mortar as a 37 mm projectile. The depth of this particular 4.2 inch mortar was 1.07 m, and thus the anomaly has a low signal to noise ratio. Figure 10 compares the data fit at the first time channel. By including a geology response, the small wavelength anomalies due to sensor movement were modeled, and depth was more accurately predicted.

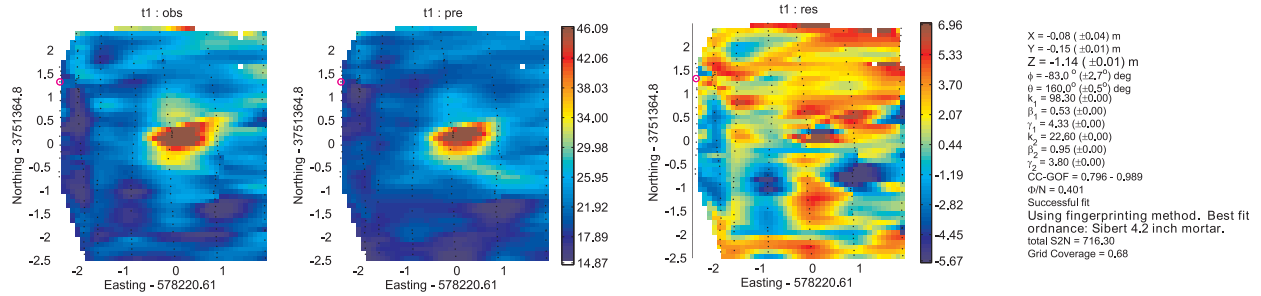
6. CONCLUSIONS

The most common approach to processing data collected at site with significant geologic noise is to: (1) develop filtering techniques such that the background response can be estimated, and subsequently subtracted from the data, and (2) invert the spatially filtered data using a physical model for the UXO response in free space. In this paper, we presented a data inversion method that included the background geology in the forward model. Our objective was to remove the small spatial wavelength correlated signal due to sensor movement relative to magnetic soils. By modeling the geological signal, we are attempting to increase the signal to noise ratio of the data, and therefore improve the accuracy of the recovered parameters. We showed that the response of the background could be approximated by modeling the transmitter as a number of dipoles and by assuming that the background geology varies slowly. By inverting synthetic and field data collected at Camp Sibert, we demonstrated that including a background response may improve the ability with which parameters can be recovered.

While the results presented here are promising we feel that several aspects of the simultaneous inversion procedure should be investigated before the technique is applied to production cleanup projects. A study needs to be carried out to determine the accuracy of the geologic modeling. A combination of numerical forward and field measurements need to be completed to optimize the location and number of dipoles used to model the sensor. The improvement in parameter estimates that we would expect from a higher SNR could possibly be offset by the more complex (an additional 3 parameters in this case) required for modeling the geology. Therefore, a study is needed to determine the required accuracy of the IMU and positioning for reliable parameter estimation.



(a) No geology model. A 37 mm projectile is the best fitting ordnance from the library.



(b) Assuming a plane geology. The method correctly identifies the anomaly is from a 4.2 inch mortar.

Figure 10. Library based inversion example. Examples (a) and (b) are for the same anomaly.

ACKNOWLEDGMENTS

Funding of this work is provided through the Strategic Environmental Research and Development Program (SERDP) funded project "Simultaneous Inversion of UXO Parameters and Background Response (SERDP Project MM-1573)". Geonics EM61 MK2 data acquired on Kaho'olawe Island, Hawaii were collected as part of the SERDP project "UXO Target Detection and Discrimination with Electromagnetic Differential Illumination (SERDP Project-1355)".

REFERENCES

1. L. Pasion, D. W. Oldenburg, S. D. Billings, and D. Sinex, "Soil compensation techniques for the detection of buried metallic objects using electromagnetic sensors," in *SPIE Conference on Detection and Remediation Technologies for Mines and Minelike Targets XII*, R. S. Harmon, J. T. Broach, and J. H. Holloway, eds., **6553**, The International Society for Optical Engineering, 2007.
2. S. Walker, L. Pasion, S. Billings, D. Oldenburg, and Y. Li, "Examples of the effect of magnetic soil environments on time domain electromagnetic data," in *Proceedings from SAGEEP 05*, 2005.
3. J. Foley, S. Billings, L. Pasion, S. Walker, and C. Pasion, "Uxo target detection and discrimination with electromagnetic differential illumination," tech. rep., Strategic Environmental Research and Development Program (SERDP), 2005.
4. S. H. Ward and G. W. Hohmann, *Electromagnetic Methods In Applied Geophysics: Theory*, vol. 1, ch. Electromagnetic Theory for Geophysical Applications, pp. 131–311. Society of Exploration Geophysicists, 1991.
5. L. R. Pasion and D. W. Oldenburg, "A discrimination algorithm for uxu using time domain electromagnetics," *Journal of Engineering and Environmental Geophysics* **6**(2), pp. 91–102, 2001.
6. L. R. Pasion, S. D. Billings, D. W. Oldenburg, and S. E. Walker, "Application of a library based method to tem data for the identification of uxu," *Journal of Applied Geophysics* **61**(3), pp. 279–291, 2005.

A3. Inversion of frequency domain data collected in a magnetic setting for the detection of UXO (SPIE Defense Security and Sensing Proceedings Paper).

Authors: Nicolas Lhomme, Leonard R. Pasion, et al. Published 29 April 2008

Inversion of frequency domain data collected in a magnetic setting for the detection of UXO

Nicolas Lhomme^{*ab}, Leonard R. Pasion^{ab}, Stephen D. Billings^a, Douglas W. Oldenburg^b

^aSky Research Inc., Suite 112A, 2386 East Mall, Vancouver, BC, Canada, V6T1Z3

^bGeophysical Inversion Facility, Dept. of Earth & Ocean Sc., The University of British Columbia, 6339 Stores Rd, Vancouver, BC, Canada, V6T 1Z4

ABSTRACT

Magnetic soils are a major source of false positives when searching for landmines or unexploded ordnance (UXO) with electromagnetic induction sensors. The viscosity effects of magnetic soil can be accurately modeled by assuming a ferrite relaxation with a log-uniform distribution of time constants. The frequency domain response of ferrite soils has a characteristic negative log-linear in-phase and constant quadrature component. After testing and validating that assumption, we process frequency domain electromagnetic data collected over UXO buried in a viscous remanent magnetic host. The first step is to estimate a spatially smooth background magnetic susceptibility model from the sensor. The response of the magnetically susceptibility background is then subtracted from the sensor data. The background removed data are then inverted to obtain estimates of the dipole polarization tensor. This technique is demonstrated for the discrimination of UXO with hand-held Geophex GEM3 data collected at a contaminated site near Denver, Colorado.

Keywords: UXO, soil compensation, metal detector, magnetic viscosity

1. INTRODUCTION

The task of discriminating buried UXO from other objects is complicated when sensor data are contaminated with geological noise originating from magnetic soils. The magnetic properties of soils are mainly due to the presence of iron, in particular in the form of ferrimagnetic minerals such as maghaemite ($\alpha\text{Fe}_2\text{O}_4$) and magnetite (Fe_3O_4). Maghaemite is considered the most important of the minerals within archaeological remote sensing circles (for example [1]). Magnetite is the most magnetic of the iron oxides, and is the most important mineral when considering the effects of magnetic soils on electromagnetic induction (EMI) measurements. Hydrated iron oxides such as muscovite, dolomite, lepidocrocite, and goethite are weakly paramagnetic, and play a minor role in determining the magnetic character of the soil.

Electromagnetic sensors are sensitive to the presence of magnetite due to the phenomenon of magnetic viscosity. In the presence of a magnetic field H , the magnetization vector of a magnetic soil tries to align itself with the exciting field. At the instant the magnetic field is applied there is an immediate change in magnetization and, possibly, an additional time dependent change in magnetization. This time dependent phenomenon is referred to as magnetic viscosity or magnetic after-effect. A time constant T is used to characterize the time for the magnetization vector to rotate from its original orientation, which minimizes the energy prior to application of the field, to its new orientation. For a sample of magnetic grains with a large range of relaxation times that are distributed uniformly over their spectrum, the magnetic moment of the soil sample will decay logarithmically [2]. Consequently, the time derivative of the decaying magnetic field produced by the magnetization decays as t^{-1} . This t^{-1} decay have been observed in archaeological prospecting [3], time domain electromagnetic (TEM) surveys carried out over laeateritic soils for mineral exploration [4], and also in TEM surveys carried out on Kaho'olawe Island, Hawaii [5].

Perturbations in signal due to a magnetic soil affect the ability to detect, locate and identify an ordnance buried in a magnetic host, whatever the model used for representing the properties of that ordnance ([6]; [7]). It is therefore critical to account for the effect of the soil on EMI sensors. Pasion et al. [8] studied in detail the effects of magnetic soils and magnetic viscosity on time domain electromagnetic sensor data and proposed a Viscous Remnant Magnetization (VRM)

model. We propose to test that model to recognize and compensate the effect of a magnetic soil on Frequency-Domain Electro-Magnetic (FDEM) data. We propose to apply that method to data collected at the Former Lowry Bombing and Gunnery Range (FLBGR), where the UXO problem consists in finding 37 mm projectiles among pervasive 20 mm and 50 caliber projectiles in a magnetically active soil. After removal of the magnetic soil background with the VRM model, we invert the data assuming a dipole model ([6]; [9]) to obtain the instantaneous elements of the magnetic polarization tensor of the induced electromagnetic dipole. For discrimination of the different items in the ground, we apply a classification based on the four-parameter model [10] that we use to relate the instantaneous polarizations, then proceed to identifying the 37 mm projectiles at the FLBGR site.

2. DATA DESCRIPTION

The data were collected with a Geophex GEM3 frequency-domain sensor [11] at FLBGR. The range is located approximately 20 miles southeast of Denver, Colorado, in Arapahoe County. We choose the site of the 20 mm Range Fan (RF), which was used for air-to-ground target practice from fixed-wing aircraft firing 50 caliber projectiles, and 20 and 37 mm projectiles. The latter ones were the particular object of the remediation effort.

The measurements were made using a template (Fig. 1), in a cued interrogation mode, to ensure accurate positioning and high signal to noise ratio. The template has 49 positions with 0.10 and 0.20 m spacing and includes 16 peripheral positions that can be used to determine the intensity of the background signal. The template was generally centered near the peak of the anomaly. Here we focus on a data set of 59 anomalies surveyed in that manner.

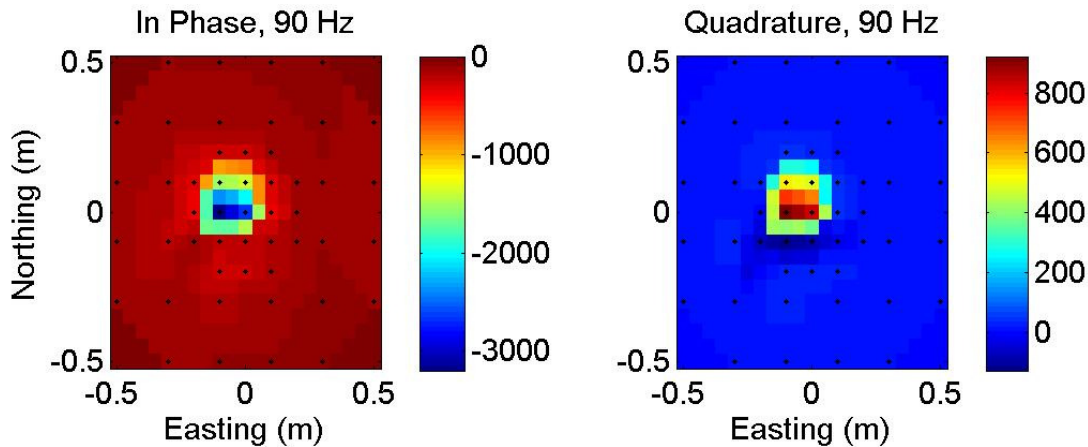


Figure 1: Spatial profile for an anomaly with weak background effect from the soil (first frequency channel, 90 Hz; anomaly caused by a 20 mm projectile). Left: Real part of the signal. Right: Imaginary part. Black dot marks indicate the locations of the soundings on the survey template, with a greater sampling density at the center of the cell, right above the target. Signal intensity in ppm.

The Geophex GEM3 sensor with a 0.40 m circular head was used for the survey. The sensor head contains collocated and circular transmitter and receiver coils with additional bucking coils to cancel out the effect of the primary field in the receiver coils. The scattered field can be recorded at ten frequencies with a measurement of the In-Phase (real) and Quadrature (imaginary) part of the signal. The selected frequencies span a range from 90, 210, 390, 750, 1470, 2910, 5850, 11430, 21690 to 41010 Hz.

For processing, the GEM-3 data were drift-corrected using the free-air calibration measurements that were conducted before and after each anomaly was surveyed. The drift-corrected data still had a significant background shift due to the response of the soil in the vicinity of the detector head.

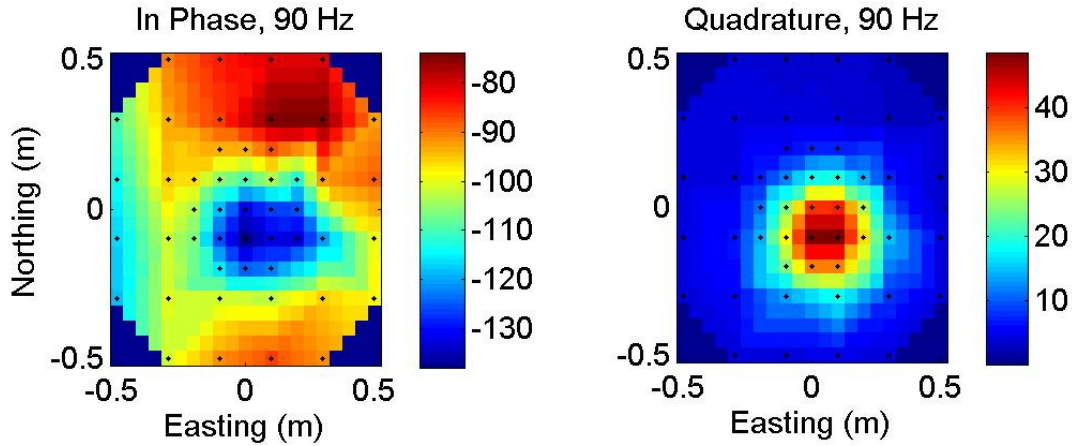


Figure 2: Spatial profile for an anomaly with significant background effect from the soil (first frequency channel, 90 Hz; anomaly caused by a 37 mm projectile). Signal intensity in ppm.

There are instances where the signal from the background has amplitude similar to that of the anomaly, as seen in the horizontal profile in Fig. 2 and the frequency decay in Fig. 3. It is critical to acknowledge and model the effect of the soil for those anomalies. The background signal is not spatially uniform: in Fig. 3 the real part has amplitude of -120 to -80 ppm, similar to that of background measurements collected at the site. In Fig. 3 we also note that the signal gains energy at high frequencies (above 10 kHz). This effect was modeled and identified [8] with a two layer soil model and more recently confirmed [12] by explicitly modeling on a fine grid the EMI properties of a conductive infinite half space, using UBC's EH3D.

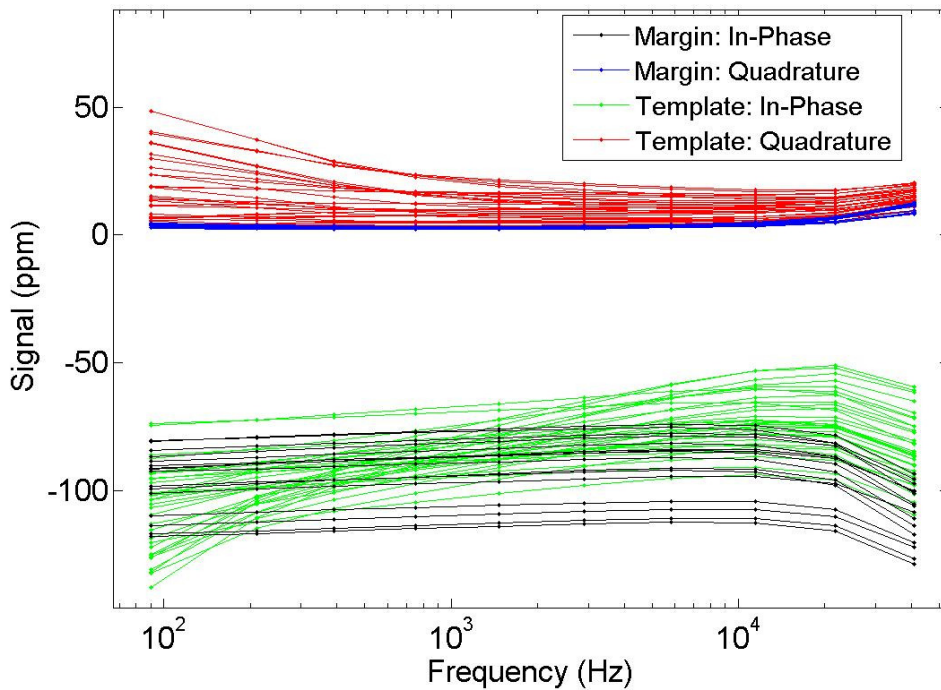


Figure 3: Frequency profile for the same anomaly as in Fig. 2. The data collected at the margin of the template and on the rest of the template are shown in different colors.

3. MODEL DESCRIPTION

3.1. Geology Model

The background geology response is a function of the position (i.e. location and orientation) of the EMI sensor relative to the ground surface, topography, and the spatial distribution of the subsurface electromagnetic properties (i.e. conductivity and magnetic susceptibility). For this survey any variations in the background response is due to subsurface heterogeneities because the elevation and orientation of the sensor are kept constant.

An analytic solution for the response of a loop at an arbitrary orientation over a conductive and magnetic subsurface is not available. For the case of a single loop over a complex permeable, but non-conducting, half-space, the solution for the magnetic field at the center of the loop is given by:

$$H_z^s(\omega) = \frac{I}{4} \frac{a^2}{[a^2 + (2h)^2]^{3/2}} \chi(\omega) \quad (1)$$

where the radius of the loop is a , the frequency dependent magnetic susceptibility of the half-space is $\chi(\omega)$, and the height of the loop over the half-space is h . If we assume a complex susceptibility defined by log-uniform distribution of time constants (where $\tau_2 \gg \tau_1$), then the susceptibility model [13] simplifies to:

$$H_z^s(\omega) = \frac{I}{4} \frac{a^2}{[a^2 + (2h)^2]^{3/2}} \frac{\chi_o}{\ln(\tau_2 / \tau_1)} \left(1 - \ln(\omega \tau_2) - i \frac{\pi}{2} \right) \quad (2)$$

This sets a Viscous Remanent Magnetization model to represent the EM properties of a magnetic soil.

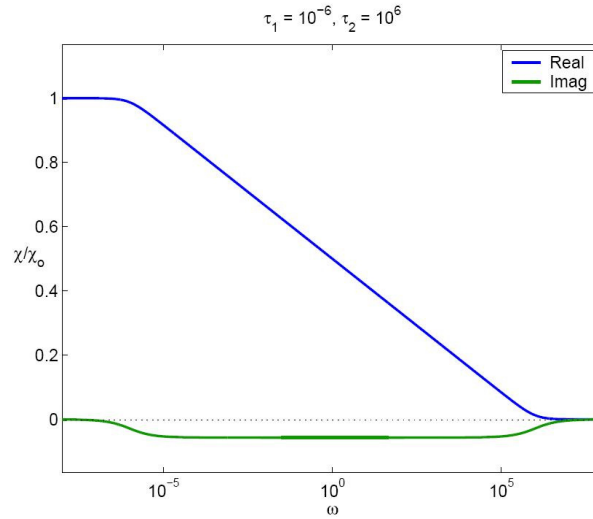


Figure 4: Susceptibility model [13].

Figure 4 shows that the real part of the relative susceptibility for a magnetic soil has a log-linear frequency decay in the 10^{-5} to 10^5 Hz frequency range, while the imaginary part is constant with an opposite sign. In Fig. 3 we also find that, at first order, EMI data from the background collected on the template margin have a log-linear decay real part and constant imaginary part (Note that the signs are reversed as one figure shows the susceptibility while the other shows GEM3 data, which are normalized).

For filtering out the effect of a magnetic soil on GEM3 data we propose to apply the VRM to identify the soundings on the margins of the template for which (1) the real part has log-linear decay, and (2) the imaginary part is constant, and use those properties to define the geologic background for all the data collected over an anomaly.

3.2. Dipole model

In time or frequency domain EMI a loop of wire generates a time varying magnetic field that is used to illuminate a conducting target. This primary field induces surface currents on the target which then generate a secondary magnetic field that can be sensed above ground. With time, surface currents diffuse inward, and the observed secondary field consequently decays. The rate of decay and the spatial behavior of the secondary field are determined by the target's conductivity, magnetic permeability, shape, and size. The electromagnetic response of the target will be primarily dipolar for the target/sensor geometries of UXO surveys. The induced dipole is

$$M(\omega) = V/\mu_o A^T P(\omega) A \cdot b^P \quad (3)$$

where V is the volume of the object, μ_o is the permeability of free space, A is the Euler rotation tensor, b^P is the primary field generated by the sensor transmitter loop, and P is the magnetic polarization tensor. The shape, size, and material properties (i.e., conductivity and magnetic susceptibility) of a target are contained in P . The frequency-dependent polarization tensor $P(\omega)$ has the form

$$P = \begin{bmatrix} L3 & 0 & 0 \\ 0 & L2 & 0 \\ 0 & 0 & L1 \end{bmatrix} \quad (4)$$

with $L1$ the largest eigenvalue, $L3$ the smallest, and $L2(\omega)=L3(\omega)$ for axi-symmetric targets. In a typical survey, EMI soundings are acquired at a number of different locations by moving the transmitter and receiver along the surface, thereby illuminating the target at a number of different angles. This, in turn, causes different components of the polarization tensor to be preferentially excited.

The Geophex GEM3 sensor records the decay of the scattered EM field at ten frequency channels. Thus the polarization tensor is to be resolved at ten frequencies. The orientation of the dipolar object remains the same at all frequencies; the rotation matrix A is constant and determined by three angles: ϕ , θ , and γ . The model m , for the UXO parameterization, can be written with 36 parameters (3 for position, 3 for orientation and 3×10 for polarization), under the form

$$m = [X; Y; Z; \phi; \theta; \gamma; L1(\omega_1), L1(\omega_2), L1(\omega_3), \dots, L2(\omega_1), \dots] \quad (5)$$

where X and Y denote the surface projection of the centre of the body and Z is the depth of the object below the surface. The problem of solving for the model m is non-linear for the position-orientation, and linear for the polarization. The model is recovered by solving a least squares non-linear inverse problem that consists in minimizing the data misfit function

$$\Phi(m) = || W (F[m] - d^{obs}) ||, \quad (6)$$

subject to constraints if provided. The matrix W contains the standard deviations of the data (estimated noise and errors in the data), F is the forward modeling operator and d^{obs} is the observed data (details in [14]).

3.3. Two-step process

Inversions are carried out in two steps. First the dipole model presented above is used to recover the position, orientation and components of the polarization tensor at all frequencies. Then, the instantaneous amplitudes $L(\omega)$ at frequency ω for the 3-dipole inversions are fit to the four-parameter model [10]:

$$L(\omega) = k \left(s + \frac{(i\omega\tau)^c - 2}{(i\omega\tau)^c + 1} \right) \quad (7)$$

where k is the object amplitude, τ is a response time-constant, s is a factor that controls the magnitude of asymptotes at high and low-frequency, and c is a parameter that controls the width of the in-phase peak response (Figure 3). This approach is preferred to directly inverting for the four-parameter model because our experience has shown that this method is more successful at recovering the position of the buried target and the inversion is less likely to be stalled at a non-optimum solution (local minimum).

4. RESULTS

4.1 Verification and application of the soil model

Because the data were collected on a template at constant elevation there is no elevation dependency in equation (2). If the VRM model is valid for this site then the data can be fit with a function of the type

$$H(x,y, \omega) = [A(x,y) \log(\omega) + B(x,y)] + [pi/2 A(x,y)] i \quad (8)$$

where $i = \sqrt{-1}$, (x, y) is the geographic location, and $A(x,y)$ and $B(x,y)$ are 2 functions that need to be solved for. We assume that $A(x,y)$ and $B(x,y)$ are (1) smoothly varying over the template, and (2) can be exactly determined on the boundary.

We propose the following protocol to verify the above two hypotheses for each anomaly surveyed:

- The soundings at the margins of the template are tested to check whether their signal corresponds to a magnetic soil. With the VRM model this implies that:
 - i. The imaginary part is constant with frequency at a given location: The assumption is valid if the variability is smaller than a threshold. Given that background soundings from the margins are used to interpolate the background over the entire template, we require similar variability across soil samples on the margin and define the following stability rule:
We compute

$$s(x,y) = std(\text{Imag}\{H(x,y, \omega), \text{ for all } \omega\})$$
 to measure local stability,

$$S_anom = median(\{s(x,y), \text{ for all } (x,y) \text{ at the margin}\})$$
 to compare soundings,
 and require similar variability

$$s(x,y) \leq 2 S_anom$$
 for (x,y) to belong to the background.
 Where the above is true, $\text{Imag}(H(\omega))$ has little variation so we can define

$$A(x,y) = 2/pi \text{ mean}(\{ \text{Imag}(H(x,y, \omega)), \text{ for all } \omega\})$$
, which corresponds to the least squares solution, or

$$A(x,y) = 2/pi \text{ min}(\{ \text{Imag}(H(x,y, \omega)), \text{ for all } \omega\})$$
 to ensure that $\text{Imag}(H)$ remains positive after correction from the background.
 - ii. The residual of the real part of H , defined as

$$Res(H(x,y, \omega)) = Real(H(x,y, \omega)) - A(x,y) * \log(\omega)$$

 follows the same stability rule as the imaginary part. Where stability is achieved we define the least square solution

$$B(x,y) = \text{mean}(\{ Real(H(x,y, \omega)) - A(x,y) * \log(\omega), \text{ for all } \omega\})$$
.
 - iii. The amplitude of the background geology signal is stable spatially. We consider that the background signal should have limited spatial variability near an anomaly. Considering the stable soundings defined from steps (i) and (ii), we require that the amplitude of the signal be within 50% of the mean background defined by those stable soundings.
- The interpolated background defined for the template should have the properties of a magnetic soil and remain within the range observed at the periphery of the anomaly. The interpolation is based on a tensioned spline with basis the margin of the template, where the background model is already validated. The interpolation works best if the functions A and B are well defined on the entire perimeter of the template. The value of $A(x,y)$ and $B(x,y)$ at peripheral soundings that are recognized as non soil is corrected using an inverse distance weighted interpolation [15] computed with the stable soundings of the margin. In that manner the In-Phase and Quadrature of the interpolated background remain within the values at the margins and follow the same frequency variations.

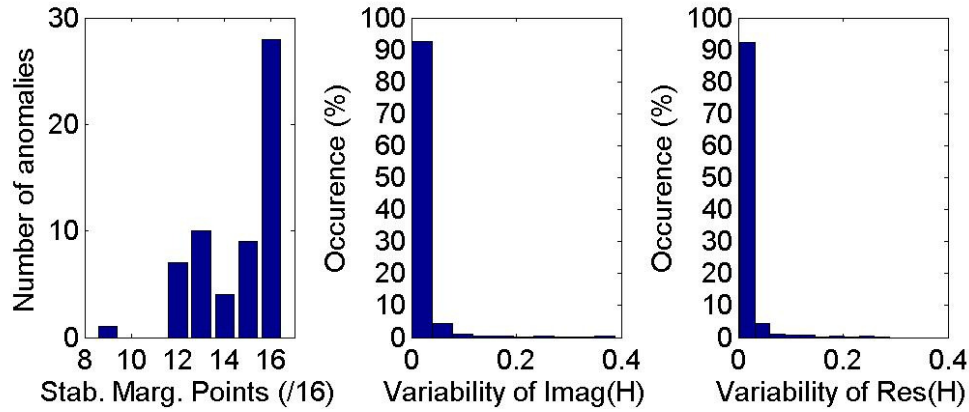


Figure 5: Variability at the margins of the template (16 peripheral points for 59 anomalies).

Left panel: Number of stable peripheral soundings per anomaly, for a template with 16 peripheral points.

Center panel: Spatial variability of $Imag(H(x,y,\omega))$, all ω / $mean(Abs(H(x,y,\omega))$, all ω).

Right panel: Spatial variability of $Std(Res(H(x,y,\omega))$, all ω / $mean(Abs(H(x,y,\omega))$, all ω).

Applying that methodology we identify the peripheral soundings that correspond to a soil with VRM by estimating the relative variability of $Imag(H)$ and $Res(H)$. Presented in the center and right panels in Fig. 5, the variability of all the peripheral soundings at the site is less than 10% in 97% of all cases. This shows that the conditions (i) and (ii) are verified over most peripheral soundings.

The left panel in Fig. 5 counts, for each anomaly, the number of soundings identified as magnetic soil among the 16 peripheral stations of the survey template. For every anomaly we find that over half of the peripheral soundings verify the VRM model. There are, however, numerous anomalies for which some peripheral soundings do not fit the soil model. These are unlikely to be of geologic origin. For instance, the anomaly with 9 stable peripheral points (left panel of Fig. 5) has multiple UXO in its vicinity; therefore its surrounding background is not purely geologic. The correction of the background would be misleading there without the use of a soil model to distinguish soil from other electromagnetically active material around that anomaly.

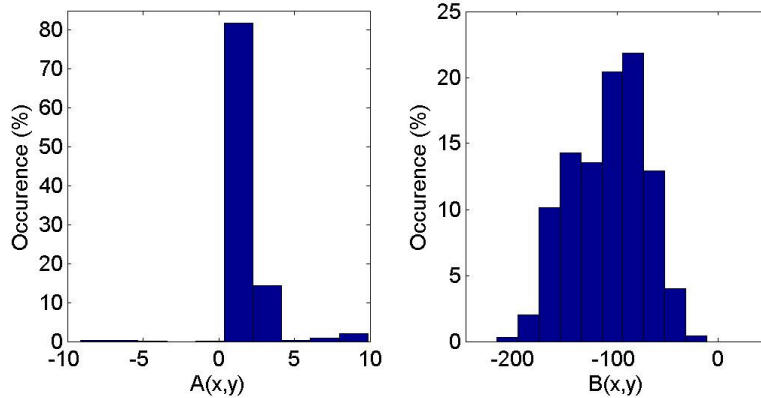


Figure 6: Distribution of the soil parameters A and B for the peripheral soundings that verify the soil model for the FLBGR site. A and B are expressed in ppm.

Figure 6 shows the distribution of the parameters A and B for all the soundings identified as soil around the surveyed anomalies. These distributions show that the soil has relatively homogenous magnetic properties over most of the surveyed area. The magnetic effect is relatively weak compared to other sites (e.g., GEM3 data from Camp Sibert, personal communication). A constant background is not appropriate though, as we find that the In-Phase signal from the soil varies by 30-40 ppm near most anomalies. Figure 7 show a spatial profile for the same anomaly as in Fig. 2 after the background is removed. The difference with Fig. 2 is particularly significant for the In-Phase part of the data and the signal from the buried target is more clearly delineated.

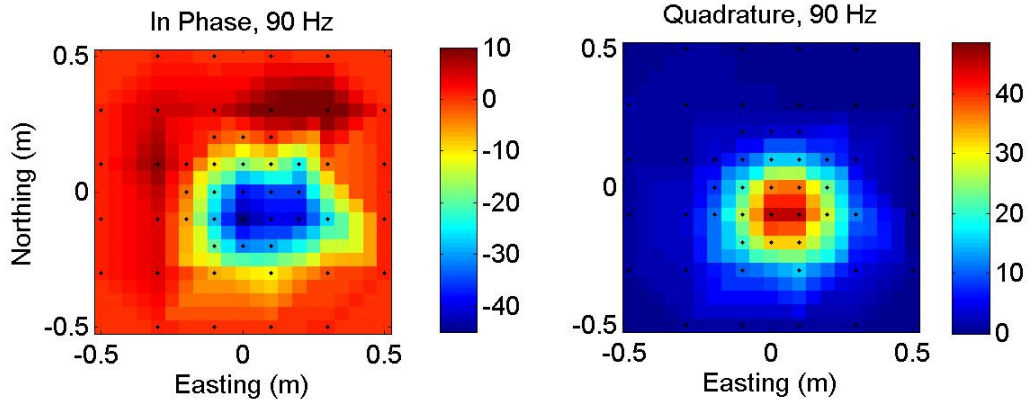


Figure 7: Spatial profile after the background is removed with the VRM model. Same anomaly as in Fig. 2.

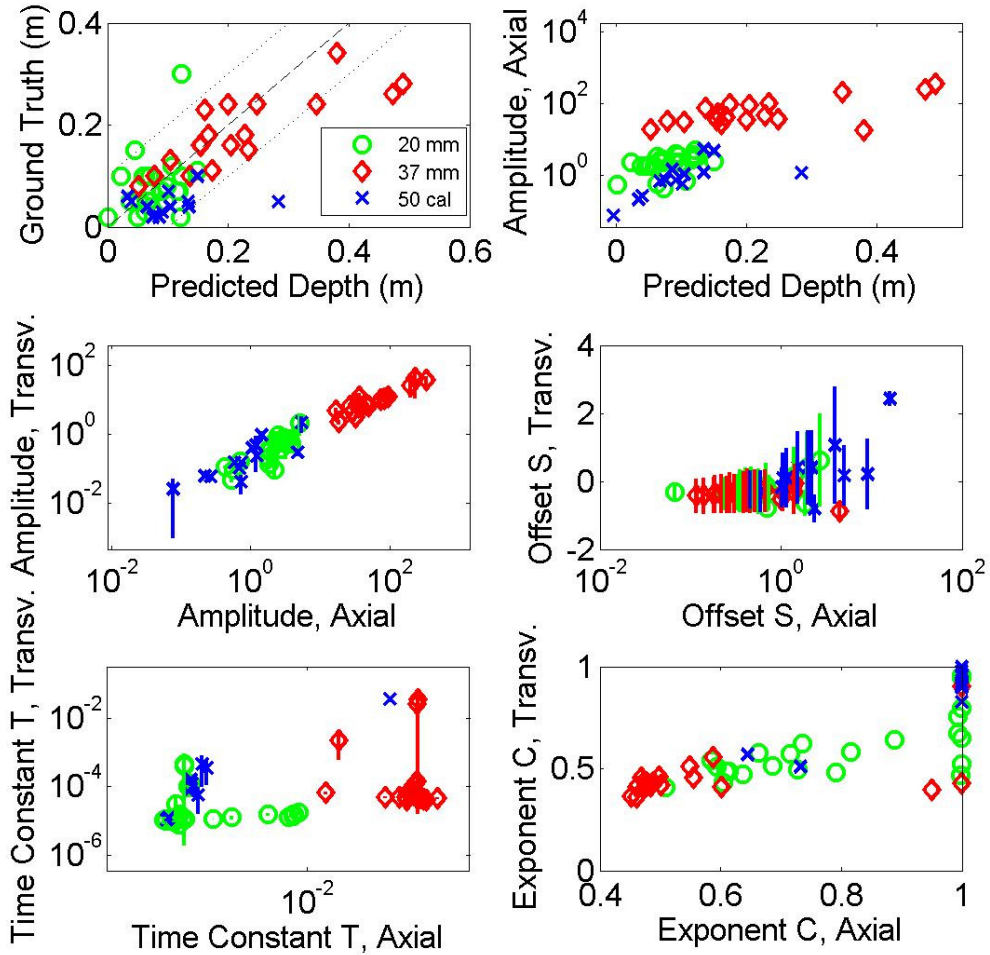


Figure 8: Parameter plots for FLBGR for all inversions. In the upper panels the predicted depth is compared to the ground truth and to the amplitude of the axial polarization, which relates the most to the size of the object. In the four lower panels, graphs compare the axial and transverse parameters with a bar plot that corresponds to the amplitude between the transverse parameters.

4.2 Inversion results with a soil model

After removing the effect of the background geology with the VRM soil model, the corrected data are inverted for the location, orientation and instantaneous polarization of a buried metallic object. The recovered depth of the buried UXO is accurately predicted in most cases (Fig. 8, upper left panel). There are only four inversions out of 59 where the depth error significantly exceeds 0.10 m. The amplitude of the signal is weak for all four poor predictions. Three of these correspond to the deepest targets. With a weak signal there is a large ambiguity among solutions with similar misfit but different depth and polarizations parameters, therefore the results are less reliable, and here erroneous.

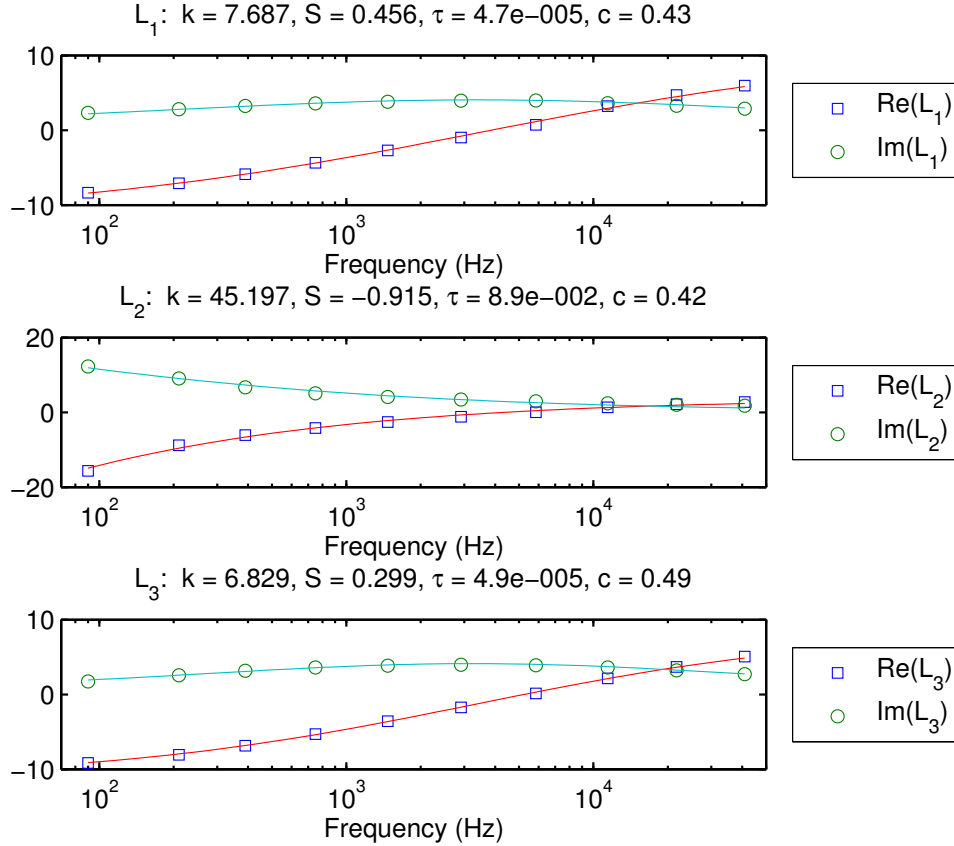


Figure 9: Fitting with the four-parameter model the polarizations from an inversion with a dipole model over a 37 mm projectile. The red and green line show the four-parameter model, the squares and circles indicate the instantaneous polarizations from the inversion with a dipole model. The parameter k relates to the semi-axes of an ellipsoidal body.

The four-parameter model [10] is recovered from the instantaneous polarizations by solving a non-linear optimization problem. An example of a good fit for those parameters is shown in Fig. 9 for a 37 mm. The three components of the polarization amplitude parameter k have values of 45, 7.7 and 6.8 (L_1 ~ L_3), which suggests an object with the shape of a prolate spheroid. The parameters derived for all the inverted anomalies are shown in four lower panels of Fig. 8. The center left panel shows that the 37 mm projectile separate well from the 20 mm and 50 caliber projectiles based on the axial and transverse parameters for the amplitude of the polarization. The discrimination goal for FLBGR is therefore attained with the amplitude parameters, although the separation is less clear for the remaining three parameters.

To illustrate the benefits of this new background removal method we compare in Fig. 10 the amplitude parameters for this method (left panel) and those from an earlier study, where the background was independently estimated for each frequency with a polynomial fit based on all peripheral soundings (right panel). The new method shows clearer separation between the recovered parameters. The difference in method and the resulting correction may be subtle, especially for a soil that has relatively weak magnetic susceptibility (compared to Hawaii, for instance). However, the effect on the recovered parameters is significant. By using the soil model to identify soil and propagate its properties in

frequency, we achieve a tighter clustering effect of key discriminating parameters, a clearer separation of the 37 mm projectile, and find less outliers that could have caused an ordnance to be misidentified.

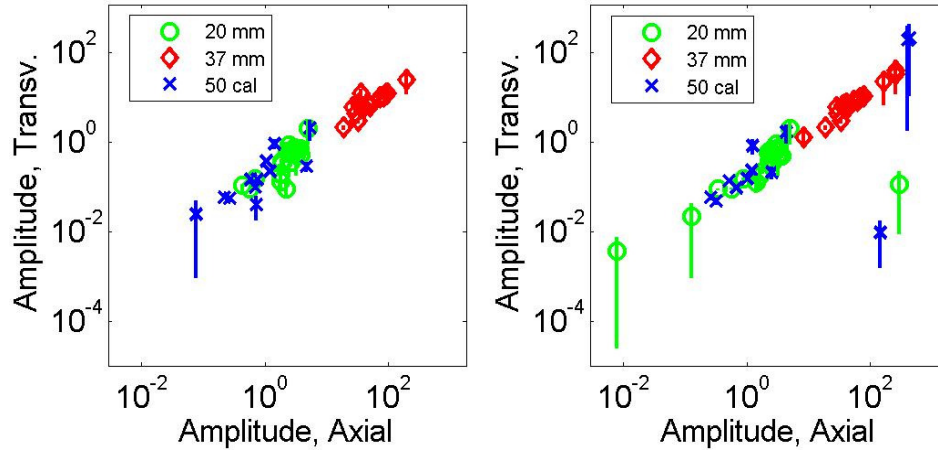


Figure 10: Comparison of polarization parameters for two different background removal methods. Only the successful inversions (with a low misfit) using the method presented in this paper are shown. Left panel: With the soil model. Right panel: With *ad hoc* background estimation.

5. CONCLUSION

The presence of a magnetic soil is often an obstacle for detecting and identifying buried ordnance, unless features of the soil can be recognized and predicted. Analyzing data collected with a Geopex GEM3 sensor, we show that a viscous remanent magnetic soil model can explain the background signal observed at the FLBGR site. This result demonstrates that the soil model developed [8] and applied thus far only on time-domain EMI data [16] is also valid for hand-held frequency-domain EMI data.

Using a soil model to compensate the effect of a magnetic background has clear advantages over other methods. Firstly this framework identifies geologic features in a survey, as opposed to simply assuming that a given set of points are part of the geologic background. Secondly the correction is physically based and allows removal of a well defined and characterized property, as opposed to any *ad hoc* correction process. The benefits of that method are demonstrated in a practical setting and show better performance than previous studies. The parameters recovered from the inversion of field data with a dipole model show that 37 mm projectiles can be clearly separated from 20 mm and 50 caliber projectiles at the FLBGR site and thus solve the UXO problem there. This method suggests that hand-held frequency-domain data can be analyzed and interpreted for discrimination even in a magnetically active soil. Further developments will test the method at sites with stronger magnetic susceptibility and with data where the distance to the ground varies.

REFERENCE

- [1] Scollar, I., Tabbagh, A., Hesse, A., and Herzog, I., [Archaeological Prospecting and Remote Sensing]. Cambridge University Press, Cambridge (1990).
- [2] Chikazumi, S., [Physics of Ferromagnetism], 2nd ed.: Oxford University Press (1997).
- [3] Colani, C. and Aitken, M.J., "Utilization of Magnetic Viscosity Effects in Soils for Archaeological Prospection," Nature, 212, 1446-1447 (1966).

- [4] Buselli, G., "The effect of near surface superparamagnetic material on electromagnetic measurements," *Geophysics*, 47, 1315-1324, (1982).
- [5] Ware, G.H., "EM-63 Decay Curve Analysis for Ordnance Discrimination," *Proc. Partners in Environmental Technology Technical Symposium and Workshop*, Washington D.C. (2001).
- [6] Pasion, L. R., Oldenburg, D. W., "A Discrimination Algorithm for UXO Using Time Domain Electromagnetics," *Journal of Engineering and Environmental Geophysics* 6 (2), 91–102 (2001).
- [7] Shubitidze, F., O'Neill, K., Shamatava, I., Sun, K., and Paulsen, K. D., "Fast and accurate calculation of physically complete EMI response by a heterogeneous metallic object," *IEEE Transactions on Geoscience and Remote Sensing* 43 (8), 1736-1750 (2005).
- [8] Pasion, L. R., Billings, S. D. and Oldenburg, D. W., "Evaluating the effects of magnetic susceptibility in UXO discrimination problems," *Proc. SAGEEP* (2002).
- [9] Bell, T., Barrow, B., Miller, J., "Subsurface Discrimination Using Electromagnetic Induction Sensors," *IEEE Transactions Geoscience & Remote Sensing* 39, 1286–1293 (2001).
- [10] Miller, J. T., Bell, T. H. and Soukup, J., "Simple phenomenological models for wideband frequency-domain electromagnetic induction". *IEEE Transactions Geoscience & Remote Sensing* 39, 1294-1298 (2001).
- [11] Huang, H., Won, I. J., "Characterization of UXO-like targets using broadband electromagnetic induction sensors," *IEEE Transactions Geoscience & Remote Sensing* 41, 652–663 (2003).
- [12] Pasion, L. R., Lhomme, N. and Oldenburg, D. W., "Simultaneous inversion of UXO parameters and background response," *SERDP UX-1573 Annual Report* (2007).
- [13] Lee, T., "The Effect of a Superparamagnetic Layer on the Transient Electromagnetic Response of a Ground", *Geophysical Prospecting*, 32, 480-496 (1983).
- [14] Pasion, L. R., [Inversion of Time Domain Electromagnetic Data for the Detection of Unexploded Ordnance], Ph.D. Thesis, The University of British Columbia (2007).
- [15] Shepard, D., "A two-dimensional interpolation function for irregularly-spaced data," *Proceedings of the 1968 ACM National Conference*: 517–524 (1968).
- [16] Billings, S. D., Pasion, L. R. and Oldenburg, D. W., "The influence of magnetic viscosity on electromagnetic sensors," *EUDEM-SCOT2, International Conference on Requirements and Technologies for the Detection, Removal and Neutralization of Landmines and UXO*, Brussels (2003).

Acknowledgement

The work reported here was sponsored by the Strategic Environmental Research and Development Program (SERDP) through project MM-1414 and MM-1573 and assistance from the Engineering Research and Development Center (ERDC).

A4. Investigating the effects of soils with complex magnetic susceptibility on EMI measurements using numerical modeling of Maxwell's equations (SPIE Defense Security and Sensing Proceedings Paper).

Authors: Kevin A. Kingdon, Leonard R. Pasion, et al. Published 4 May 2009

Investigating the Effects of Soils with Complex Magnetic Susceptibility on EMI Measurements Using Numerical Modelling of Maxwell's Equations

Kevin A. Kingdon^{*a}, Leonard R. Pasion^(a,b), Douglas W. Oldenburg^b

^aSky Research, Suite 112A, 2386 East Mall, Vancouver, BC, CANADA, V6T 1Z3;

^bDept. of Earth and Ocean Sciences, University of British Columbia, 6339 Stores Rd., Vancouver, BC, CANADA, V6T 1Z4

ABSTRACT

Soils that exhibit strong Viscous Remanent Magnetization (VRM) have a major effect on time- and frequency-domain data collected by electromagnetic induction (EMI) sensors. Small scale topography in the form of bumps or troughs will also distort the EM signal due to UXO. If these components of “geologic noise” are not adequately accounted for in the inversion process, then the ability to carry out discrimination will be marginalized. Our long-term goal is to include these effects into the inversion but the chosen methodology depends upon some crucial issues. Foremost, we need to be certain that we can numerically compute the effects of complex magnetic susceptibility and topography that would be encountered in field surveys. Second, we need to investigate whether there is significant electromagnetic interaction between the UXO and its host material or whether the signals are additive. If the total signal can be adequately represented by the superposition of the two individual signals (ie the field of a UXO in free space, and the effect of a conductive host with topography and complex magnetic susceptibility) then there are many avenues by which data can be preprocessed to remove contaminating effects, or by which joint inversion of UXO and host parameters can be carried out. In this paper we concentrate upon the issues of modeling and the possibility of additivity. We first validate our EM numerical modeling code for halfspaces having VRM. We then show that EM interaction between the host and a compact metallic object is minimal for a specific example which is typical of a buried ordnance in a highly magnetic soil such as on Kaho’olawe, Hawaii. We also model soil responses for simple variations of surface roughness including both a single bump and a single trench and compare those results with field data acquired over similar environments.

Keywords: Unexploded ordnance, magnetic soils

1. INTRODUCTION

Remediation of a UXO contaminated site typically involves the detection, discrimination and excavation of anomalies identified with EMI sensors. UXO discrimination is achieved by utilizing features extracted from physics-based model-fits to observed anomalies in order to determine the likelihood that the buried item is a UXO. Standard UXO processing techniques involve estimating the background response which is then subsequently removed from the observed data. In the ideal case, after the background has been successfully removed, the filtered data can be inverted using the physical model of a UXO in free space.

Magnetic soils are a major source of false positives when searching for unexploded ordnance with EMI sensors because of large geologic background signals¹. These signals are a consequence of the sensitivity of EMI sensors to soils where viscous remnant magnetization (VRM) is present²⁻⁴. It is not uncommon for VRM soils to exhibit geology related responses on the same order as UXO (Figure 1). In addition, movement of the transmitter and receiver relative to magnetic ground can produce significant small wavelength anomalies in the data⁵⁻⁶.

This presentation investigates the effects of magnetic soils by using numerical solutions to Maxwell's Equations. We do not know of previous numerical modelling studies that represents the soil with a frequency dependent susceptibility.

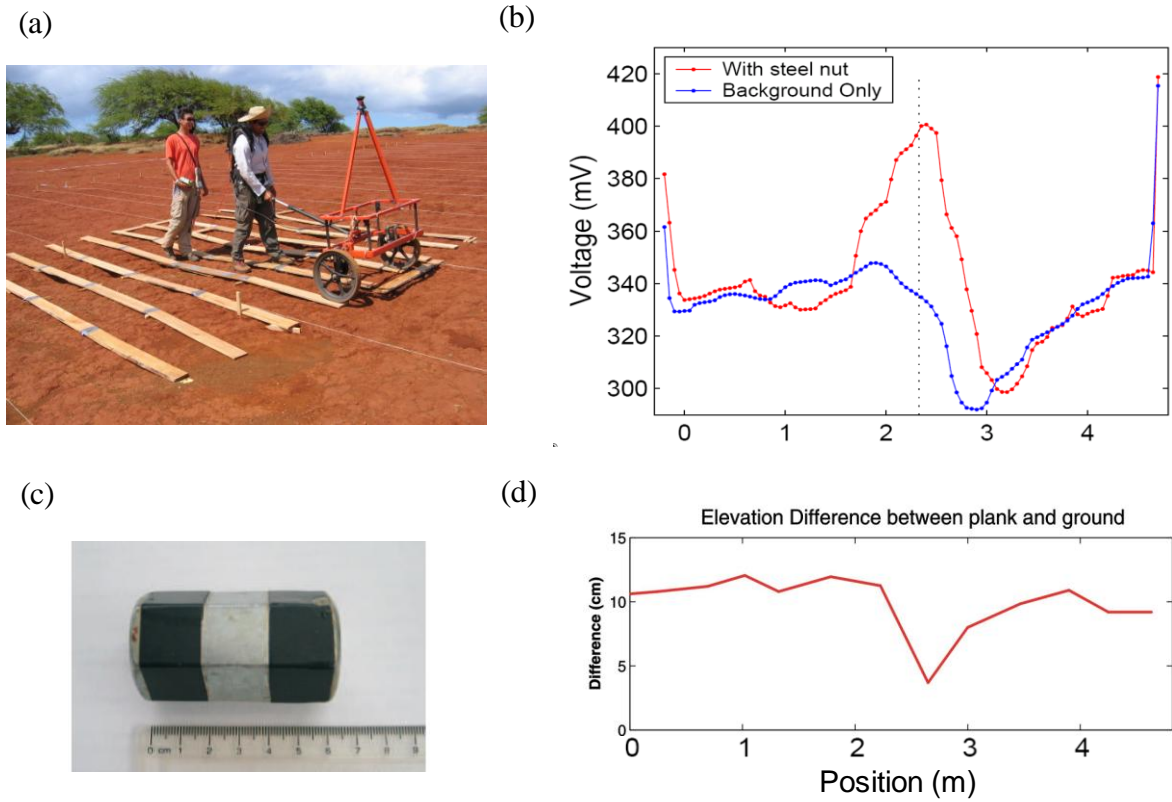


Fig 1. Geonics EM61 MKII time domain data acquired on Kaho'olawe Island, Hawaii. (a) In order to study the effect of topography, the instrument was placed on planks. (b) Data was taken with and without a steel nut placed in a small rivulet that ran underneath the planks. The large increases in magnitude at the ends of the line of data are due to the sensor moving from the planks to the ground. (c) The steel nut used in this experiment. (d) Distance from the top of the planks and the ground.

Two issues are addressed. First, we investigate the validity of treating a compact metallic target and the host soil as separate additive responses. That is, we investigate if there is a significant interaction between the target and the host soil. Second, we determine if it is possible to model simple bumps and trenches to quantify the effects of EMI measurements made over a rough surface in environments with magnetic soil.

2. FREQUENCY DOMAIN FORMULATION OF A FINITE VOLUME NUMERICAL SOLUTION OF MAXWELL'S EQUATIONS

EH3D is a flexible forward modelling program developed at UBC-GIF for calculating the EM fields resulting from a wide range of time domain electromagnetic sources and source waveforms, over a 3D earth that is discretized using a mesh of rectangular cells. The fields are calculated using a finite volume numerical solution to Maxwell's Equations¹¹. EH3D can handle 3D variations of frequency dependent magnetic susceptibility and electrical conductivity. The Earth is divided into cuboidal cells each of which has a uniform conductivity and permeability at each frequency. Electric and magnetic fields are computed anywhere in the model studied.

EH3D takes Maxwell's equations which are described in the frequency domain by:

$$\nabla \times \mathbf{E} - i\omega\mu\mathbf{H} = 0 \quad (1)$$

$$\nabla \times \mathbf{H} - \hat{\sigma}\mathbf{E} = \mathbf{J}^s \quad (2)$$

$$\nabla \times \mathbf{H} = 0 \quad \text{on the boundary} \quad (3)$$

where μ is the magnetic permeability, σ is the conductivity ($\hat{\sigma} = \sigma - i\omega\epsilon$) and \mathbf{J}^s is a known source current density. Using a Helmholtz decomposition of the electric field (i.e. $\mathbf{E} = \mathbf{A} + \nabla\phi$, $\nabla \cdot \mathbf{A} = 0$), to cope with numerical difficulties associated with the null space of the curl operator at low frequencies, produces a system of equations for the vector \mathbf{A} and scalar ϕ

$$\nabla \times (\mu^{-1} \nabla \times \mathbf{A}) - \nabla (\mu^{-1} \nabla \cdot \mathbf{A}) - i\omega\hat{\sigma}(\mathbf{A} + \nabla\phi) = i\omega\mathbf{J}^s \quad (4)$$

$$\nabla \cdot \hat{\sigma}\mathbf{A} + \nabla \cdot \hat{\sigma}\nabla\phi = -\nabla \cdot \mathbf{J}^s \quad (5)$$

The above system of equations is discretized using a finite volume method on a staggered grid. The variables \mathbf{A} are located at the cell's faces and ϕ are located at the cell's center. The staggered grid implies that \mathbf{H} is measured at the cell's edges while \mathbf{J} (and therefore \mathbf{E}) is measured at the cell's faces as illustrated in Figure 2.

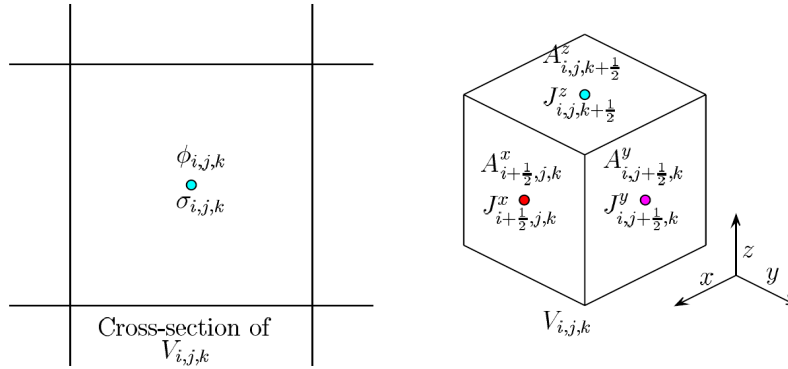


Fig. 2. The staggered grid used in EH3D finite volume methods.

Consideration is required when designing the mesh to be used. In principle, a finer mesh will produce more accurate computed fields however the mesh size is also limited by computational resources. The area surrounding the target contains the finest mesh with the grid cells gradually becoming larger as we move away from the area of interest. It is necessary to extend the computational domain far beyond the area surrounding the target in order to minimize boundary condition effects. For the validation tests, a mesh with a spacing of 5cm was used for an inner core and the computation domain boundaries were set at 1000m.

The UBC-GIF EH3D codes have been successfully applied to a range of mineral exploration applications^{7,8}. Because these codes also capture the physics associated with the electromagnetic response of a UXO in the presence of an

inducing field, we intend to downscale the associated geometries and use the EH3D codes to model the interaction of a UXO with its host medium. We focus on the frequency domain EH3D codes as they are currently the only version capable of handling complex susceptibility values. The range of frequencies selected for modelling was chosen based on typical frequency domain instruments employed for UXO surveying.

3. VALIDATION

Prior to modelling any UXO-like targets, a variety of halfspaces with a range of conductivities were modeled using EH3D. These results were compared with analytical solutions for a loop above a halfspace in order to validate the codes. The analytic expression for the radial component (H_ρ) and vertical component (H_z) of the secondary field at the center of a transmitting loop of radius a carrying a current I is well known:

$$H_\rho(\omega) = 0$$

$$H_z(\omega) = \frac{Ia}{2} \int_0^\infty \left[1 + \frac{P_{21}}{P_{11}} e^{-2\mu_o h} \right] \frac{\lambda^2}{\mu_o} J_1(\lambda a) d\lambda \quad (6)$$

where J_1 is a first order Bessel function and P_{11}, P_{21} are propagator matrices obtained in the solution for horizontal and vertical dipoles over a conductive and magnetically permeable halfspace. Further details on this solution can be found in, for example, Pasion⁹.

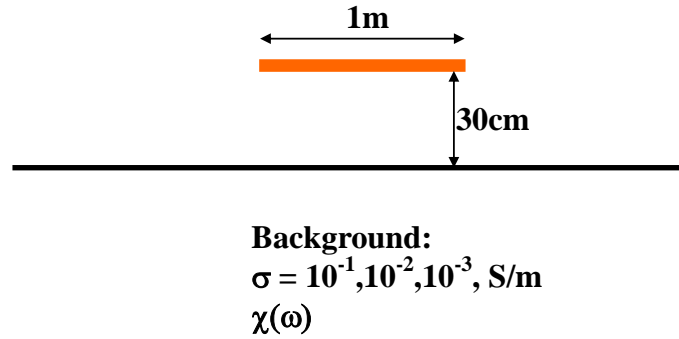


Fig. 3. The environment modeled in EH3D for validation tests.

A schematic for the EH3D models run during the validation process is illustrated in Figure 3. A current source consisting of a 1 m square loop was assumed. Conductivities for the background ranged from 10^{-1} to 10^{-3} S/m. Excellent agreement was found between the analytical response and the EH3D modeled responses for halfspaces over the range of conductivities.

In order to validate the EH3D codes for a halfspace environment containing complex susceptibility, an analytical solution was calculated and the results are compared in Figure 4. EH3D input files allow the user to specify real and imaginary susceptibility values at each frequency being modeled. Susceptibility values (see Figure 4) were based on measurements made at Kaho’olawe, Hawaii. The results were also plotted for a halfspace of conductivity 0.1 S/m but with susceptibility values set to zero so that the complex susceptibility effects can be gauged. The susceptible halfspace results produced by EH3D are in excellent agreement with the analytic solution. The susceptible halfspace also levels off at lower frequencies as the resistive limit is approached and the magnetic response becomes more important while the halfspace without complex conductivities continues to fall off at lower frequencies as expected for a purely conductive response.

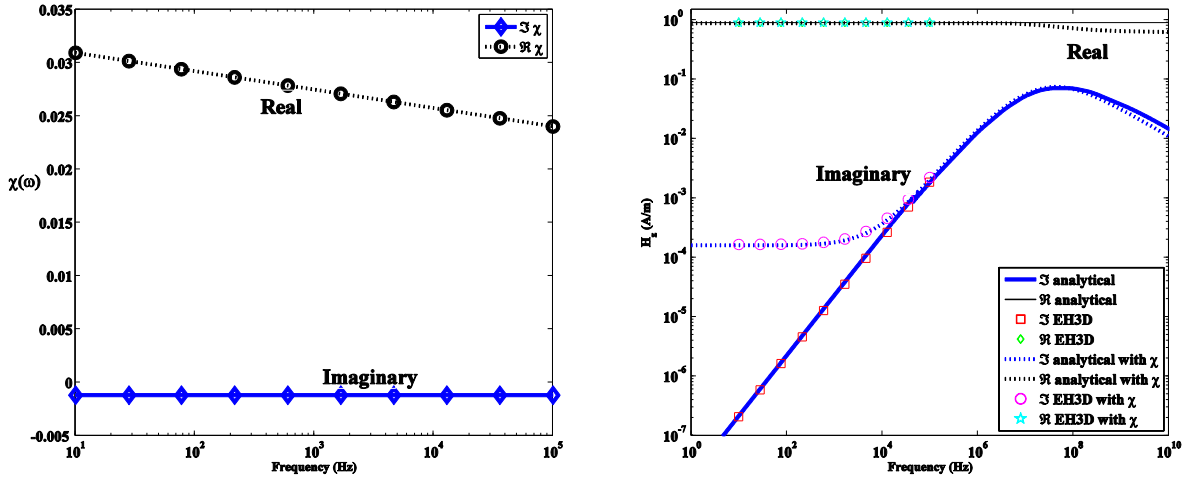


Fig. 4. EH3D correctly models the viscous remnant magnetization (VRM) response. Panel on the left shows the susceptibility values calculated based on soil measurements made at Kaho'olawe, Hawaii and the panel on the right illustrates both the analytical and EH3D solutions for a conductive only halfspace and a conductive halfspace with viscous remnant magnetism (VRM).

4. RESULTS

4.1 Additivity of Soil and Target Responses

Methods for subtracting the soil response from EMI data often assume that the response of a target in a halfspace can be approximated well by adding the response of the target in free space to the response of the halfspace, i.e.

$$\text{Response of a target in freespace} = (\text{response of target in halfspace}) - (\text{halfspace response})$$

Das⁴ used an approximate technique to study the effect of the background host material on the response function (for example see Grant and West¹⁰) of a sphere. By using the Das technique, Pasion⁹ investigated the effect of the halfspace using susceptibility values derived from Kaho'olawe Island soil samples. The extent to which the additive assumption is appropriate can only be rigorously tested through the numerical modelling of Maxwell's equations. Having found acceptable agreement between analytic and EH3D responses for halfspaces of varying conductivity, we use EH3D to study additivity by considering a compact target embedded in a halfspace. We chose to consider the highest conductivity ($\sigma=10^{-1}$ S/m) halfspace. The UXO-like target and geometry modeled is specified in Figure 5. The target was simulated as a region with dimensions 10cm x 10cm x 20cm with a conductivity value of 10^4 S/m. This particular target has a low electromagnetic contrast with the background, because we wanted to investigate scenarios that would have a higher likelihood of producing greater interaction between the target and background. The target was centered beneath the transmit loop in a vertical orientation at a depth of 20cm below the surface.

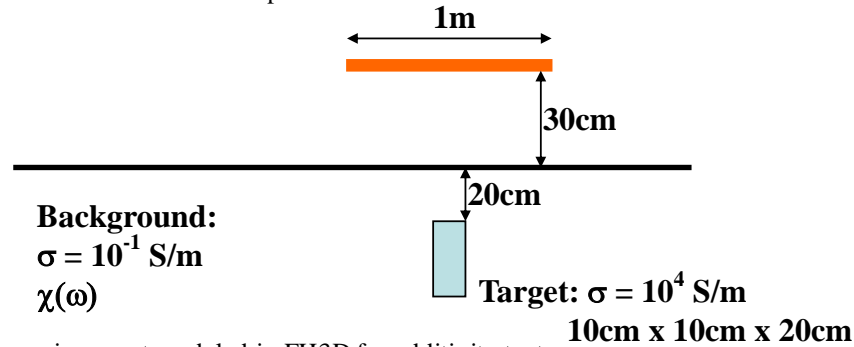


Fig. 5. The environment modeled in EH3D for additivity tests.

In order to investigate the validity of the additivity assumption, we compare the response of a target in free space with a residual response obtained by subtracting the halfspace response from that generated by the same target in a halfspace as shown in Figure 6. All fields are obtained using EH3D. The frequency of 1668 hertz (Hz) was chosen to illustrate the additivity concepts of the field as this particular frequency was observed to produce more substantial variations in the H field around the target than other frequencies.

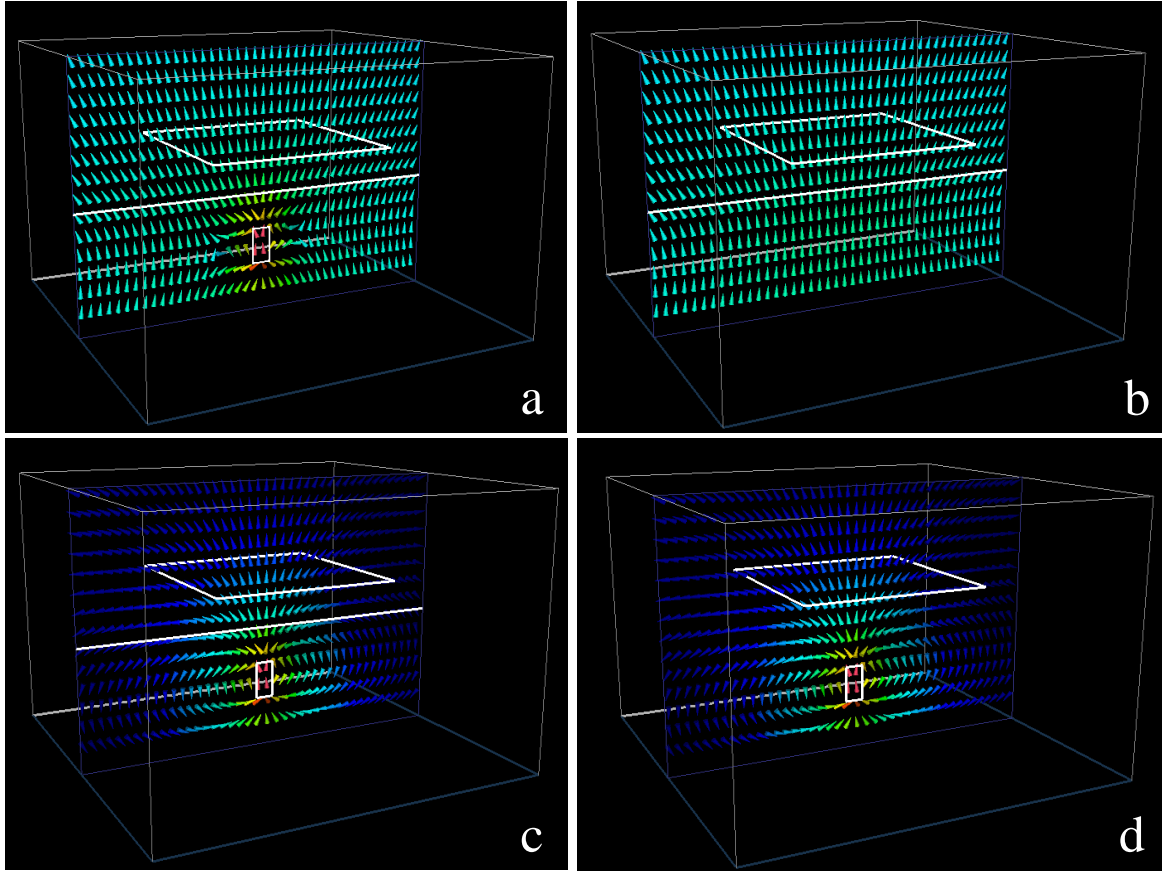


Fig. 6. Additivity illustrated through the imaginary component of the H field at 1668 Hz. Panel (a) shows the EH3D response generated for a target in a halfspace, (b) the EH3D response for a halfspace. Panel (c) displays the derived target in freespace response obtained by differencing the top 2 panel responses. Finally, panel (d) displays the EH3D response for a target in a freespace which is virtually identical to the adjacent derived response of panel (c). All four panels shown have identical limits on color scale. Halfspace results used were the 0.1 S/m case.

We now choose a point at the center of the loop and show results for both the real and imaginary components of each frequency modeled with EH3D. Again we compare soundings for the freespace computed directly from EH3D with a derived halfspace achieved by differencing the soundings extracted at the center of the loop for the EHD solutions obtained for the target in a halfspace and the halfspace only models. There is a small difference between the computed target in free space response and the derived response obtained by differencing the target in a halfspace response with the halfspace response. This discrepancy can be accounted for by adding a response for the soil that replaces the target when calculating the derived freespace response. This concept is illustrated in Figure 7. After taking into account this contribution from the extra soil occupying the target void, the agreement is excellent at all frequencies as shown in the bottom two panels of Figure 8. Additivity would be expected for the high contrast in electromagnetic properties that are typical of UXO (conductivity $>10^6$ S/m, susceptibility > 100). Even with the low contrast in conductivity and

susceptibility between host and target considered here, no interactions between host and target were observed. We conclude that additivity is valid for the model considered (a compact target within a host that has viscous remnant magnetic as well as conductivity). Thus processing that involves subtracting a background EM response from the data to produce a response that can be modeled as a UXO in freespace is a reasonable procedure.

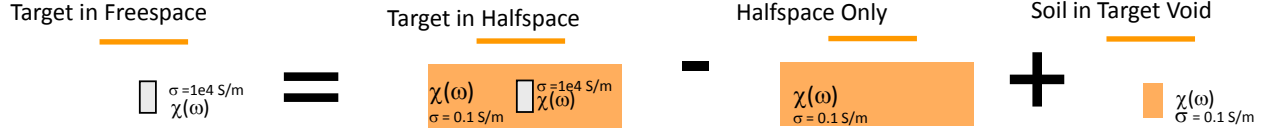


Fig. 7. Additivity is examined by comparing the response computed for a target in freespace with a derived freespace response obtained by differencing a target in half space response with a halfspace response. There is a small difference between these computed and derived freespace solutions due to the soil response from the target void. The error due to the void will be extremely small when compared to target responses for electromagnetic properties that are typical of UXO ($\sigma > 10^6 \text{ S/m}$, $\chi > 100$) but for the low contrast case here ($\sigma = 10^4 \text{ S/m}$, $\chi = 0.1$) it is more substantial.

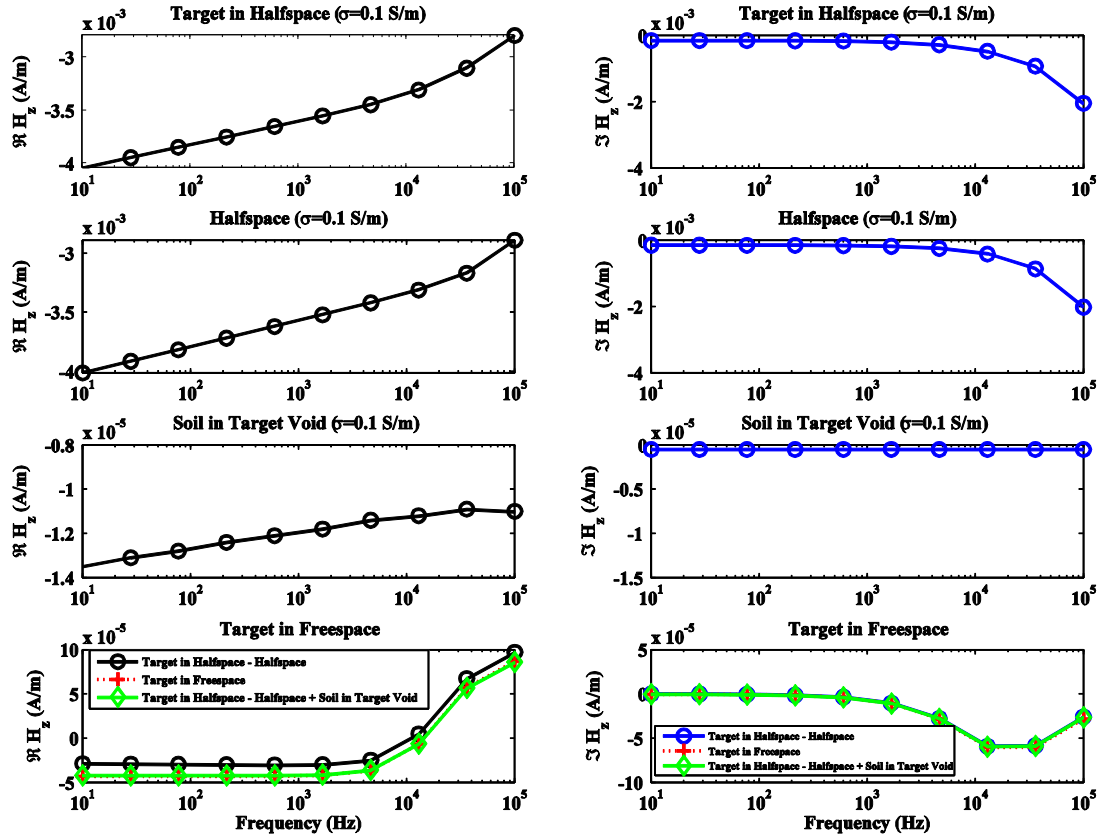


Fig. 8. Real and imaginary values of the H field for all frequencies modeled in EH3D with a target in a conductive halfspace with viscous remnant magnetism (VRM) (top 2 panels) and a halfspace with VRM (second row 2 panels). The third row of two panels plots the response due to soil replacing the target volume in freespace. The bottom 2 panels plot the derived target in freespace solution obtained by differencing the soundings at the center of the loop between the top row of panels and the middle row of panels. The EH3D computed solution for a target in freespace is also plotted in the bottom row panels.

4.2 Modeling Simple Topography: Comparison with Field Data

To establish the validity of modelling small scale topographic features with EH3D, we model a simple bump and trench of dimensions that approximate targets over which field data was acquired using the Man Portable Vector (MPV) sensor. The MPV is a multi-axis, man-portable, ultra-wideband EMI sensor designed for cued interrogation of anomalies. MPV data were acquired at the Sky Research test plot in Ashland, OR. The site is well characterized having been surveyed with numerous geophysical sensors and the soil has been sampled and analyzed. EH3D is capable of modeling a complex multi-receiver geometry in a relatively straightforward manner because receiver locations can be specified at any location within the computational domain. A number of EH3D runs were completed at varying transmitter offsets to simulate a profile line of data over the trench and bump targets.

The trench and the divot were modeled in EH3D using the schematic shown in Figure 9 and Figure 10. A current source consisting of a 64 cm square loop was assumed. The MPV transmitter is composed of two circular loops but for modeling purposes, a square loop with an equivalent moment was assumed. Conductivities for the background were set at 10^{-2} S/m. A bump target was simulated by placing a region of dimensions 10cm x 12cm x 120cm with a conductivity value of 10^{-2} S/m on top of the halfspace (Figure 9). The trench target was simulated by creating a volume of dimensions 10cm x 12cm x 120cm with a conductivity value of 10^{-9} S/m below the surface of the halfspace (Figure 10). The bump and trench targets were placed in the center of the computation domain and the transmit loop was moved through a series of offsets to simulate collection of an MPV survey line collected across the trench or bump. Results are shown for the MPV receiver located at the center of the transmitter loop to match the geometry of the modelled scenarios. Figures 9 and 10 illustrate excellent agreement when comparing the EH3D modelling results with data collected using the Man Portable Vector (MPV) sensor.

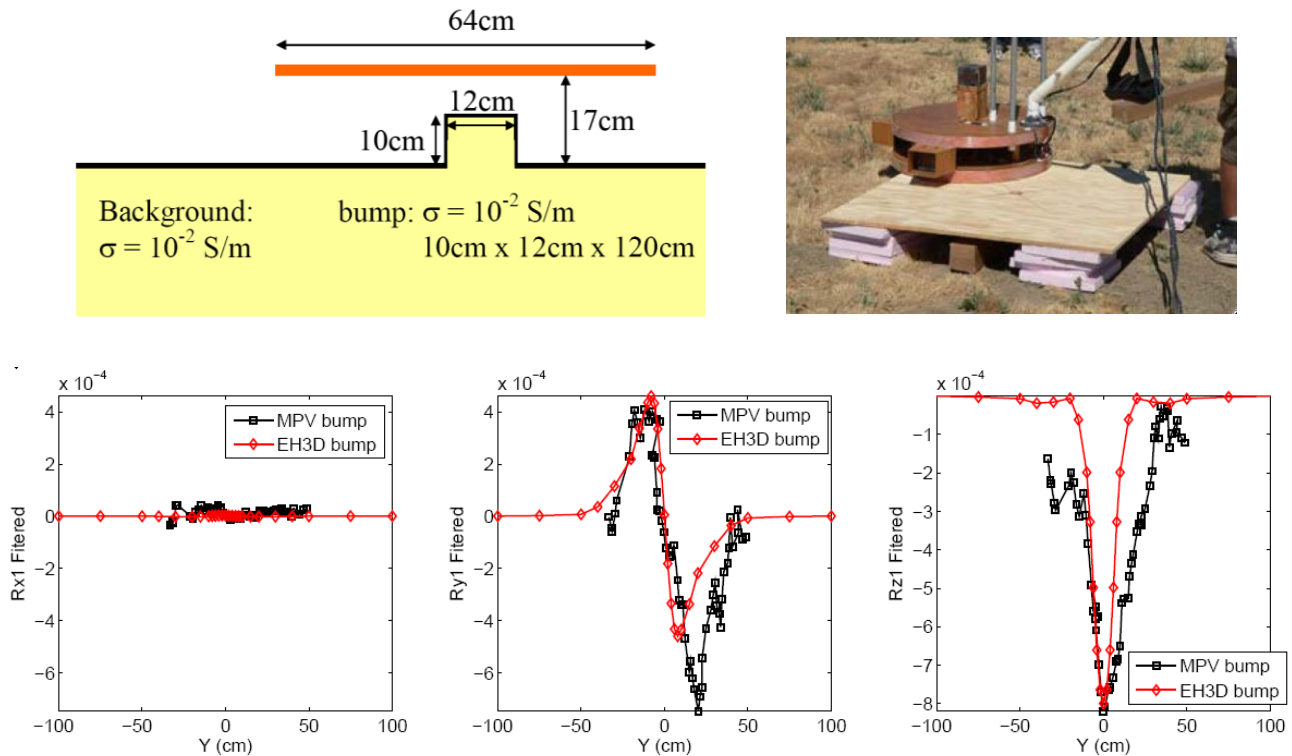


Fig. 9. EH3D results for modeling MPV data acquired over a single bump. The upper left panel illustrates the environment modeled in EH3D. The upper right panel shows the MPV acquiring data over the single bump target. The bottom row of plots shows the three components of the fields both measured with the MPV and modeled using EH3D

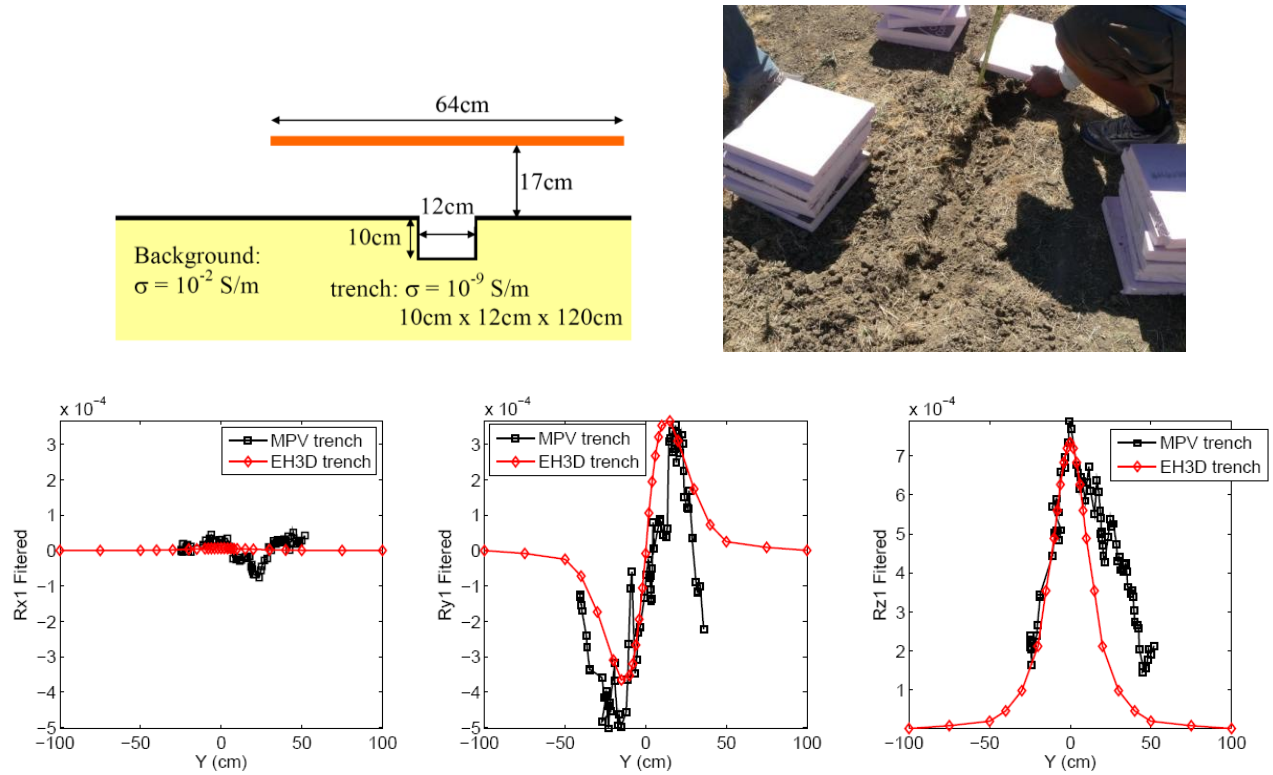


Fig. 10. EH3D results for modeling MPV data acquired over a single trench. The upper left panel illustrates the environment modeled in EH3D. The upper right panel shows the single trench target. The bottom row of plots shows the three components of the fields both measured with the MPV and modeled using EH3D.

4.3 Modeling Simple Topography: Bump and Trench of Varying Size

Detection and identification of UXO at sites with large geologic background signals can be very difficult. In locations where the soil is especially problematic, system responses from local geology can be of the same order as signals due to UXO. Even at sites where the soil is more hospitable, attempts to apply discrimination techniques can be hampered by geology. In order to investigate these effects, two simple geologic scenarios were modeled with EH3D, a bump and a trench as depicted in Figure 11. A series of bumps and trenches each 50 cm long and with varying cross sections (6, 10, 12, 14, 18cm square) were modeled. For each scenario, the EH3D codes were run at a range of offsets to simulate a profile line of data crossing directly over the geologic target.

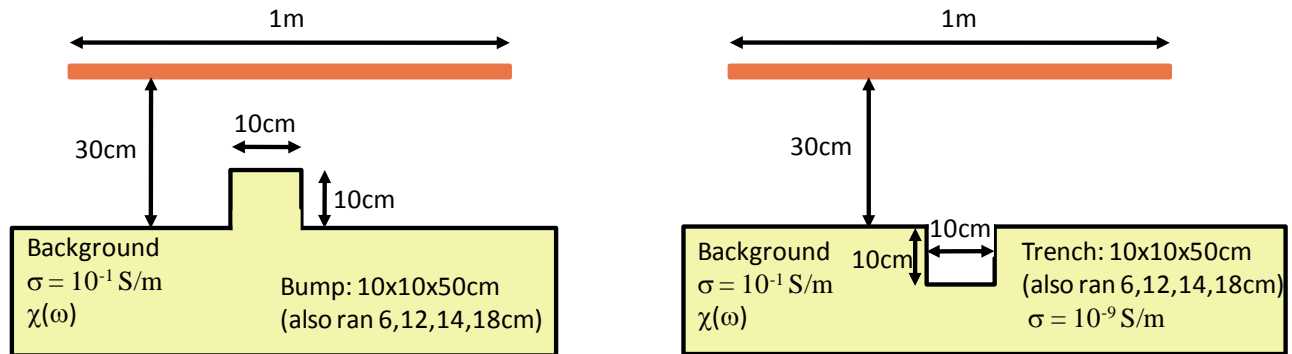


Fig. 11. EH3D model environment for two simple variations in topography including a bump (left panel) and trench (right panel).

Results for the modeled bumps and trenches are shown in Figure 12. The modeled response increases for both the bump and the trench as the cross sectional dimensions are increased from 6cm square up to 18cm square. The peak amplitudes for the bump exceed those of the trench which is expected since the bump target places additional background material in closer proximity to the sensor. The shape of the modeled H_z responses is also narrower for the bump targets, again a consequence of the sensor effectively being placed closer to the target, in this case the bump.

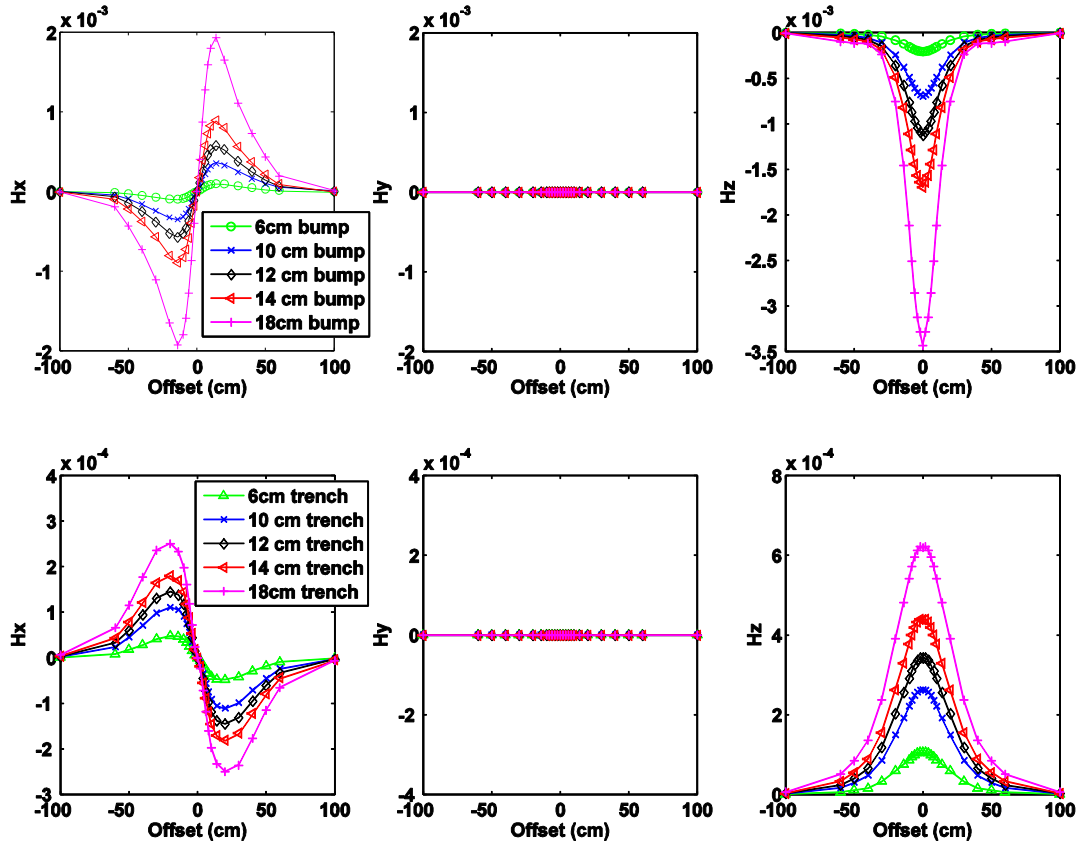


Fig. 12. EH3D results for modeling simple geologic variations. The top three panels illustrate the three components of the H fields for a series of bumps of increasing size. The bottom three panels the same fields for trenches of increasing dimensions. Physical properties and dimensions used for the modeling are described in Figure 8.

5. CONCLUSIONS

The ability to accurately forward model soil and UXO responses is a powerful tool, especially in scenarios where data can be degraded due to the presence of magnetic soils. We've been able to numerically compute in 3D the effects of complex magnetic susceptibility and find excellent agreement with analytic results. It was also confirmed that a compact target and a host soil that is complex susceptible as well as conductive can be treated as separate, additive responses. We model simple changes in topography which, in a magnetic soil environment, can lead to false positives if they are not accounted for. The potential for sensor characterization via forward modeling was also illustrated based on the agreement between data acquired over a simple bump and trench target using the MPV. The code will continue to be used to help optimize the dipole modeling of EMI sensors and to help quantify the effects of topography.

6. ACKNOWLEDGEMENTS

Funding of this work is provided through the Strategic Environmental Research and Development Program (SERDP) funded project “Simultaneous Inversion of UXO Parameters and Background Response (SERDP Project MM-1573)”. We thank Dr. Greg Oldenborger for his help in running the EH3D numerical modeling code. We also thank Roman Shekhtman for preparing a version of EH3D that models complex susceptibility and also for providing support when running the code on the UBC-GIF computer cluster

REFERENCES

- [1] Cargile, D., Bennet, H., Goodson, R., DeMoss, T. and Cespedes, E., "Advanced uxo detection/discrimination technology demonstration – Kaho'olawe, Hawaii," tech. rep. U.S. Army Research and Development Center, Vicksburg, MS, 2004. ERDC/EL TR-04-1.
- [2] Lee, T., "The effect of a superparamagnetic layer on the transient electromagnetic response of a ground." *Geophysical Prospecting* **32**, pp. 480-496, 1983.
- [3] Billings, S., Pasion, L., Oldenburg, D., and Foley, J., "The influence of magnetic viscosity on electromagnetic sensors," in *Proceedings of EUDEM-SCOT2, International Conference on Requirements and Technologies for the Detection, Removal and Neutralization of Landmines and UXO*, 2003.
- [4] Das, Y., "Effects of soil electromagnetic properties on metal detectors." *IEEE Transactions on Geoscience and Remote Sensing* **44**(6), pp. 1444-1453, 2006.
- [5] Walker, S. E., Pasion, L. R., Billings, S. D., Oldenburg, D. W., and Li, Y., Examples of the effect of magnetic soil environments on time domain electromagnetic data. In *Proceedings from SAGEEP 2005*.
- [6] Foley, J., Billings, S., Pasion, L., Walker, S., and Pasion, C., UXO Target Detection and Discrimination with Electromagnetic Differential Illumination. Technical Report, Strategic Environmental Research and Development Program (SERDP) 2005.
- [7] Oldenburg, D. W., and Pratt, D.A., Geophysical inversion for mineral exploration: a decade of progress in theory and practice. In *Fifth Decennial International Conference on Geology, Geochemistry, Geophysics and Remote Sensing, Exploration 07 Proceedings*, pp. 61-96, 2007.
- [8] Oldenburg, D.W., Eso, R., Napier, S., and Haber, E., 2005, Controlled source electromagnetic inversion for resource exploration, *First Break*, Vol 23, p 41-48.
- [9] L. R. Pasion, Inversion of Time Domain Electromagnetic Data for the Detection of Unexploded Ordnance, PhD Thesis, University of British Columbia, 2007.
- [10] F.S. Grant and G.G. West. Interpretation Theory in Applied Geophysics. McGraw-Hill Book Company, 1965.
- [11] Haber, E., Ascher, U. M., and Oldenburg, D. W., Inversion of 3D electromagnetic data in frequency and time domain using an inexact all-at-once approach. *Geophysics*, **69**, 1216–1228.

A5. Simultaneous inversion of electromagnetic induction data for target and soil parameters (SPIE Defense Security and Sensing presentation).

Authors: Leonard R. Pasion, Kevin Kingdon, Jon Jacobson, Stephen Billings and Douglas W. Oldenburg. Presented 26 April 2011

Simultaneous Inversion of Electromagnetic Induction data for Target and Soil Parameters

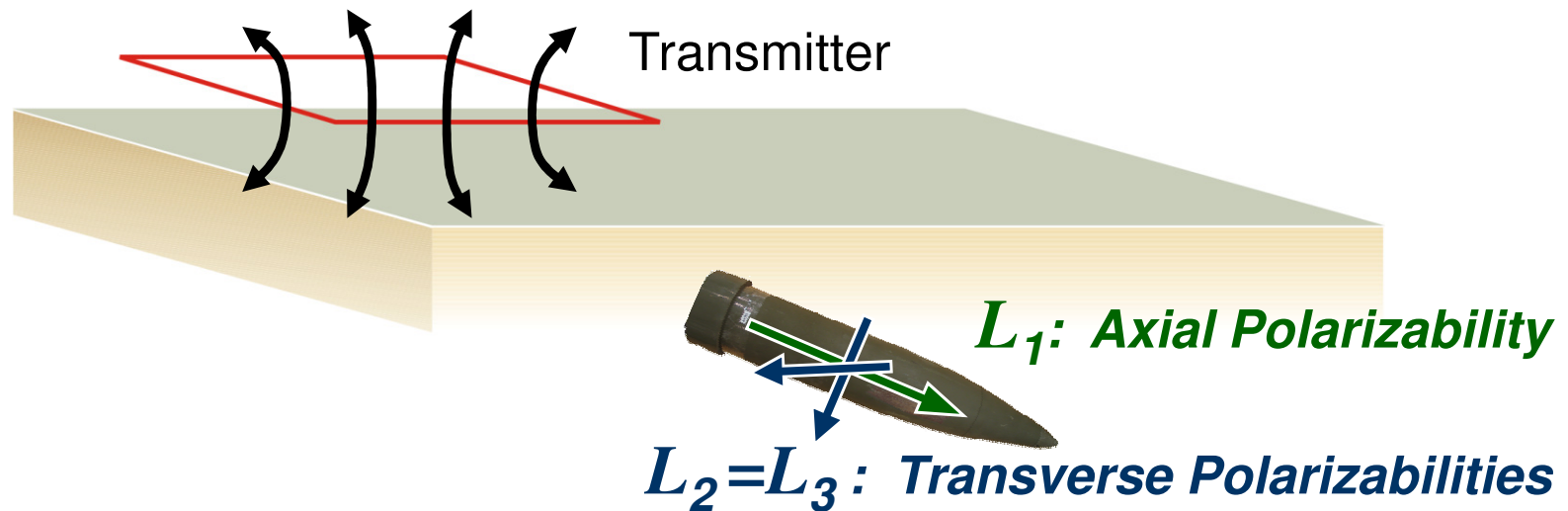
Len Pasion, Kevin Kingdon, Jon Jacobson
Sky Research, Inc.



SPIE Defense, Security and Sensing
APRIL 26, 2011
Orlando, Florida, USA

UXO Discrimination Using a Dipole Model

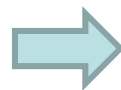
- Most commonly used forward model for UXO processing



Induced Dipole:

$$\mathbf{m}(t) = \frac{1}{\mu_o} \overline{\overline{\mathbf{M}}}(t) \cdot \mathbf{B}_o = \frac{1}{\mu_o} \mathbf{A}^T \overline{\overline{\mathbf{L}}}(t) \mathbf{A} \cdot \mathbf{B}_o$$

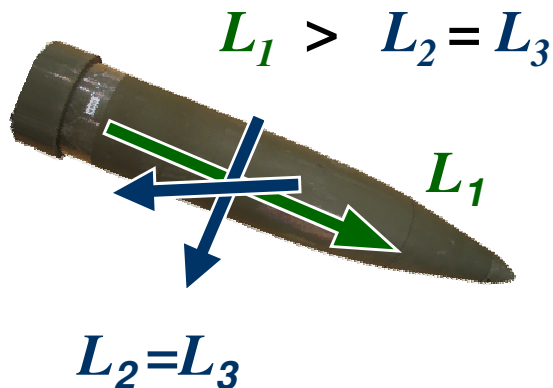
$$\overline{\overline{\mathbf{L}}}(t) = \begin{bmatrix} L_1(t) & 0 & 0 \\ 0 & L_2(t) & 0 \\ 0 & 0 & L_3(t) \end{bmatrix}$$



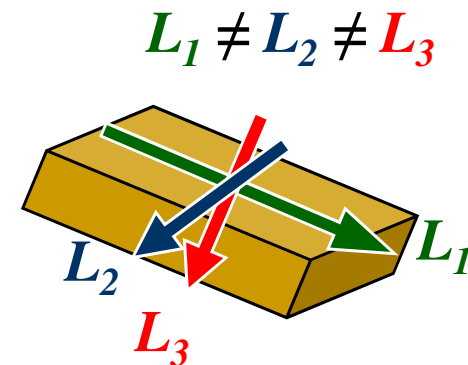
L_1 , L_2 , and L_3 are the **polarizabilities** of the target

- The polarizabilities are *intrinsic* properties of the target, i.e. they are a function of the target properties only and not the orientation, location, and survey parameters.
- Magnitude and decay rate are a function of size
- Relative sizes of elements indicate shape

Axi-symmetric (UXO-like)

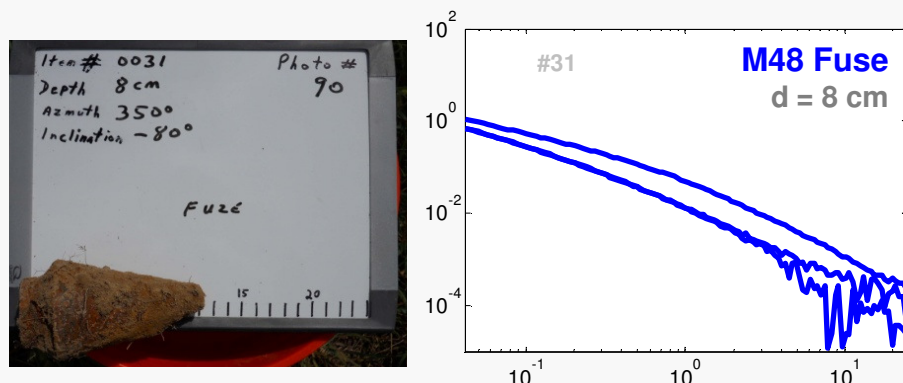
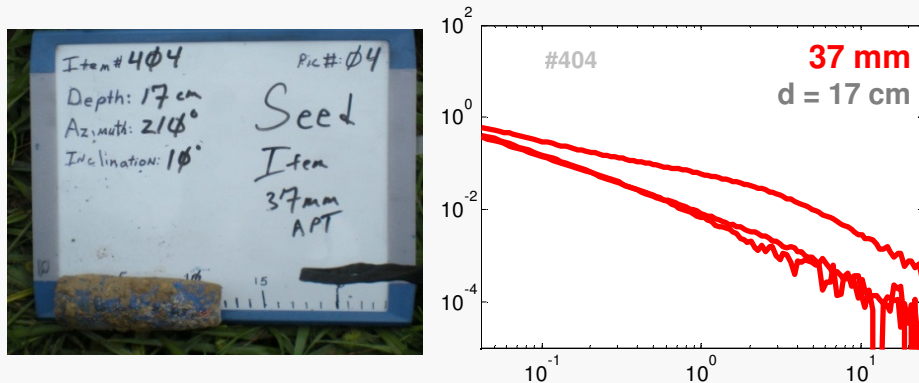
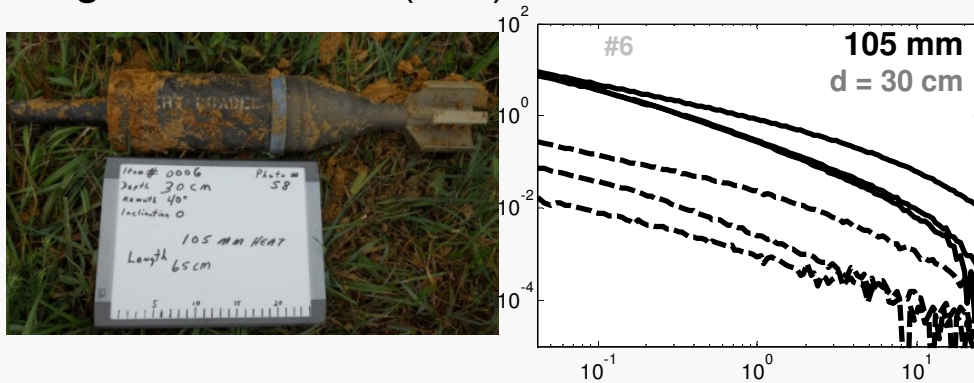


No Axial Symmetry (e.g. some scrap)

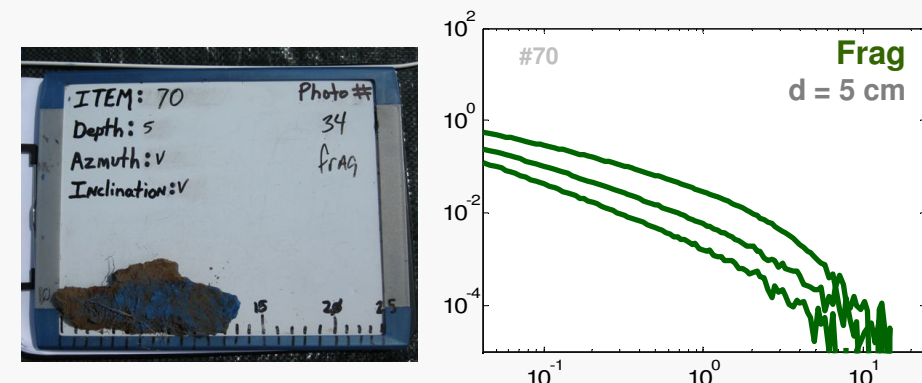
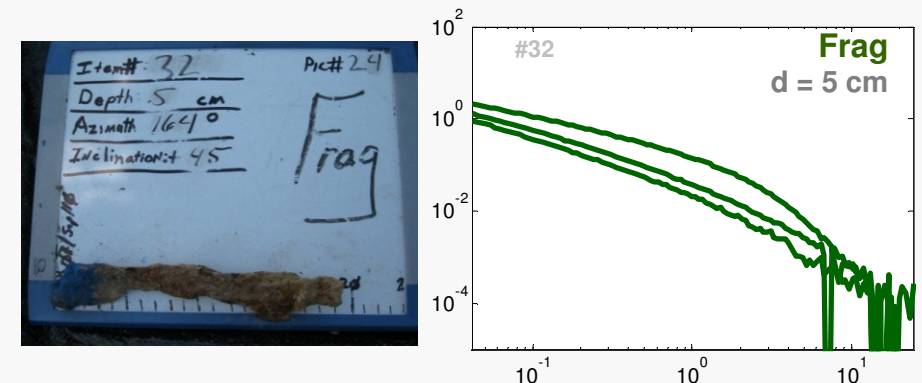
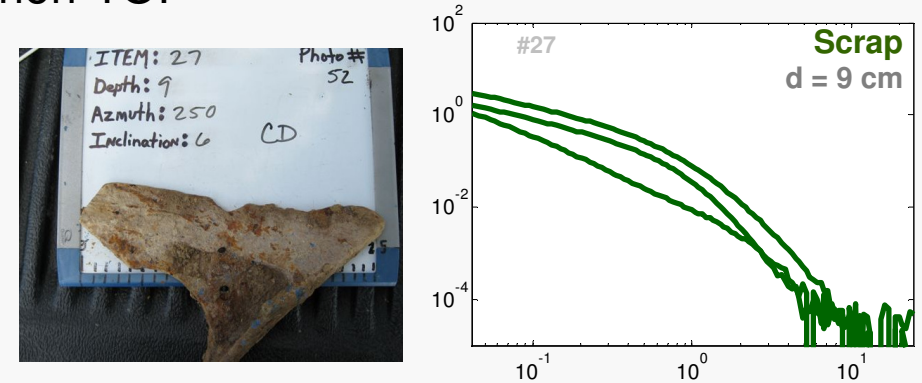


Examples of Principle Polarizabilities

Targets of Interest (TOI)



non-TOI

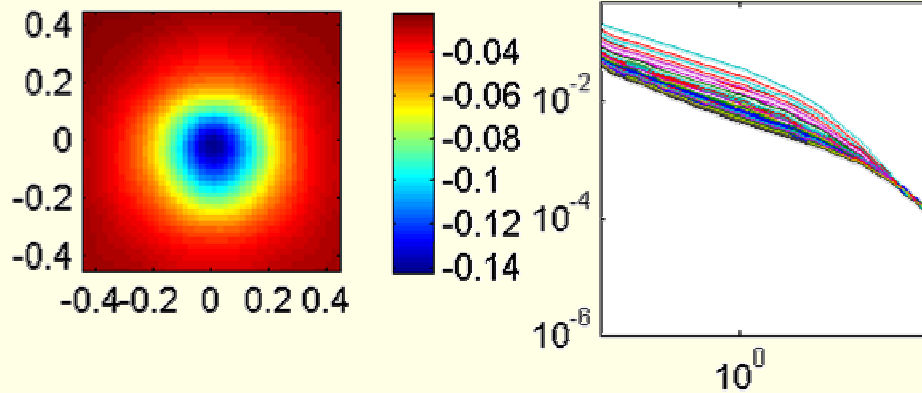


Example: MPV Time Domain EM data inversion

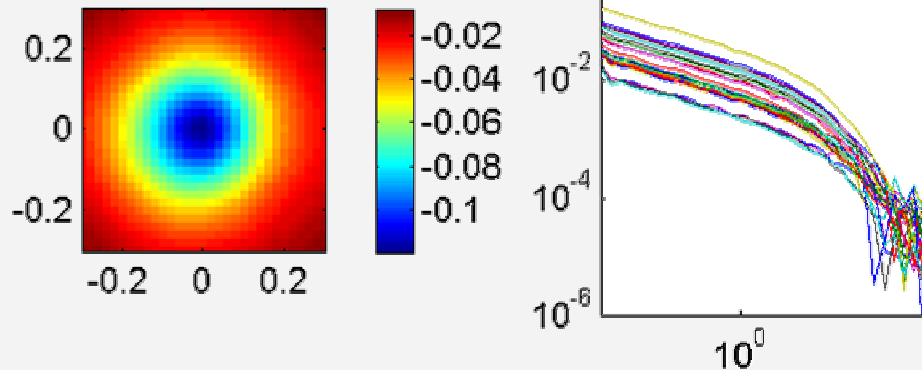
- coaxial receiver, vertical component plotted



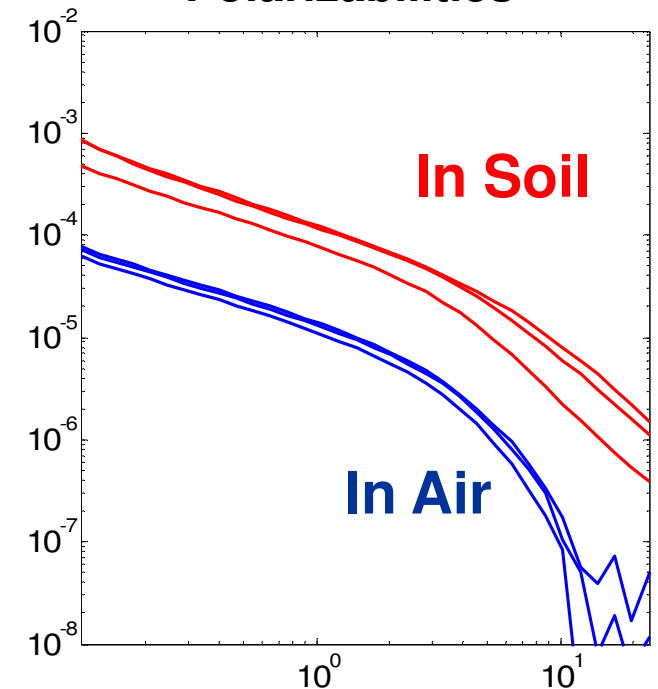
**In
Magnetic
Soil**



In Air



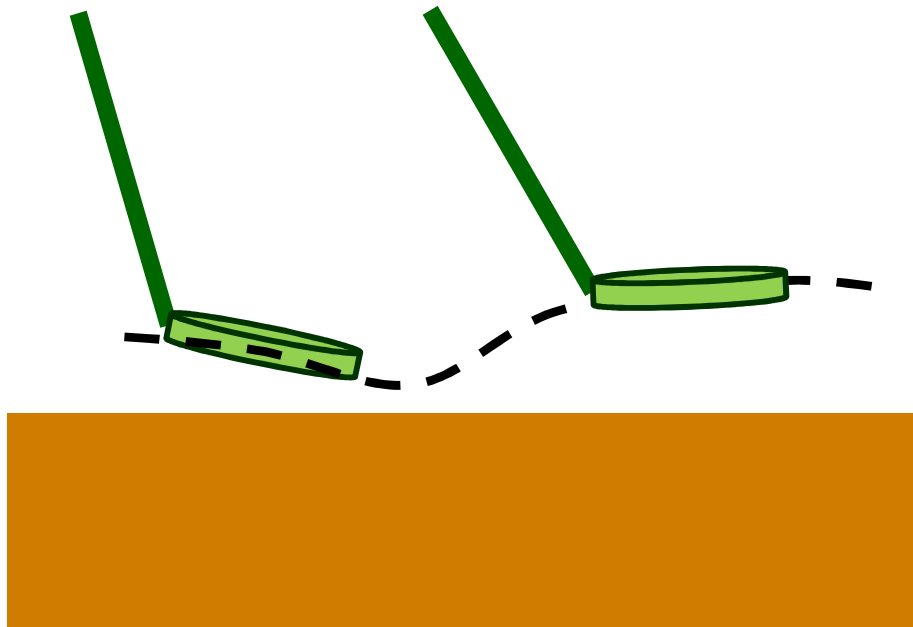
**Recovered
Polarizabilities**



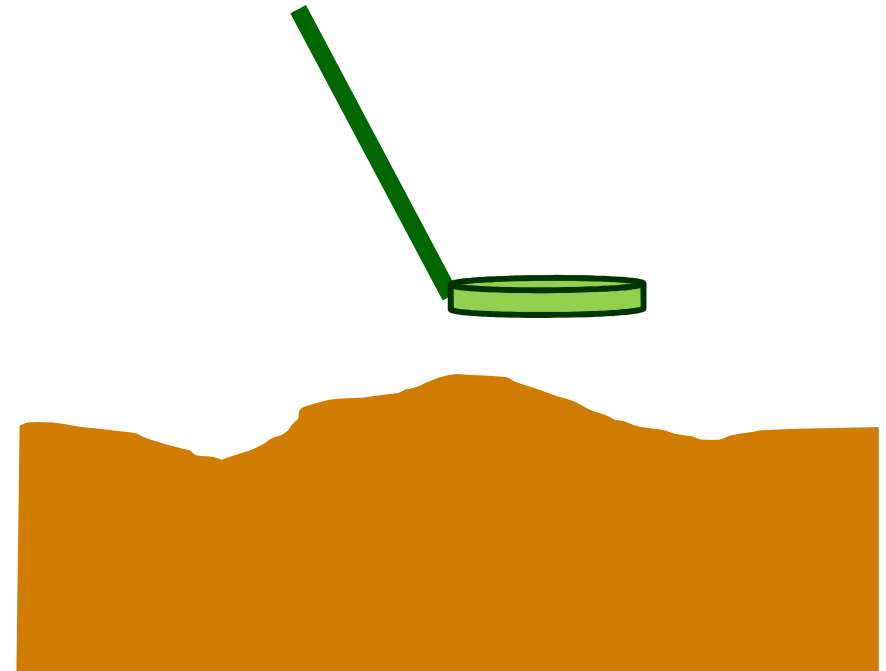
- *Soil signal in data bias recovered polarizabilities* 5

- Examples of sources of spatially varying noise when collected EMI data at sites with magnetic soils.

1. Position of Sensor Above Ground

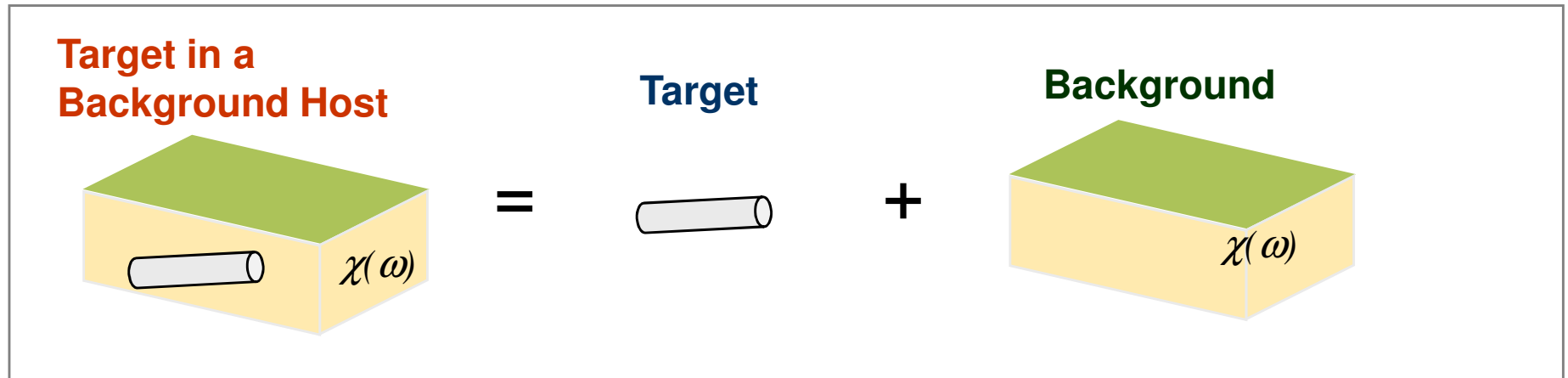


2. Topography



Un-modeled correlated signal will bias the estimated target parameters leading to less reliable classification

Approach: Develop inversion routines for EM data for the dipole polarizabilities *and* the soil background parameters.



- When the target response and background response are additive we can rewrite the forward operator as

$$F[\mathbf{m}] = \underbrace{F^t[\mathbf{r}, \phi, \theta, \mathbf{p}^t]}_{\text{Target}} + \underbrace{F^{bg}[\mathbf{p}^{bg}]}_{\text{Background}}$$

- We will use a dipole model
- The EM parameters of the background can vary laterally

Inverting EMI data for target and geologic properties

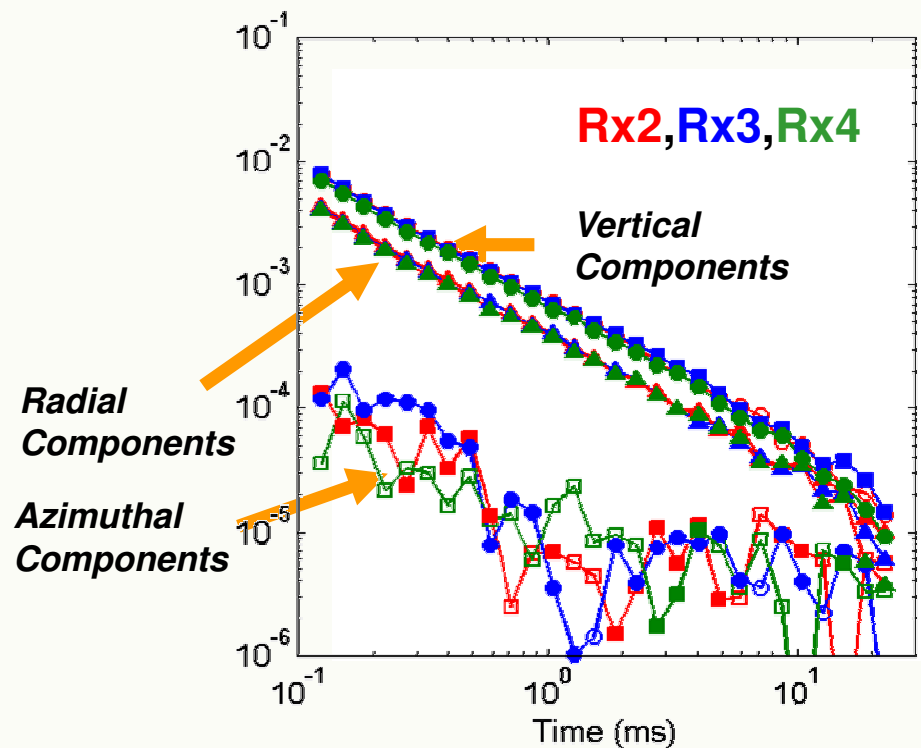
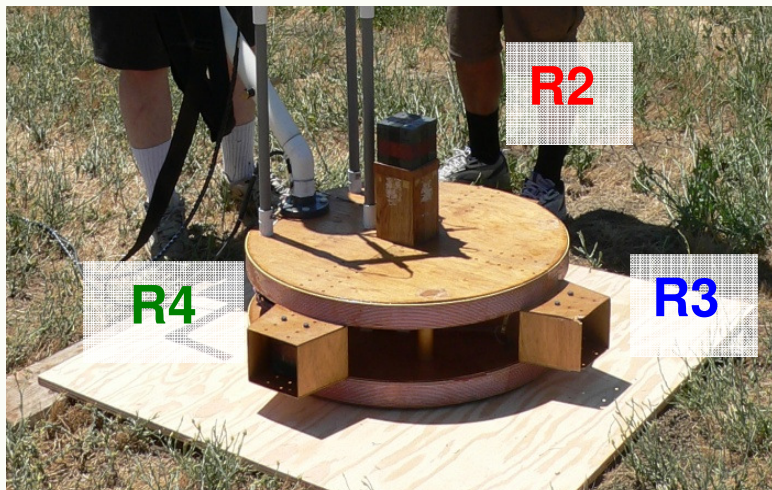
- Methodologies have been developed to estimate geologic and target parameters*.
 - ◆ These methods have been successfully demonstrated using mono-static time domain (Geonics EM63) and frequency domain (Geophex GEM3) data.
- In this presentation:
 - ◆ **Determine if the multi-static, multi-channel nature of newer instruments can be exploited for improved target characterization results.**

* L.R. Pasion, S.D. Billings, and D. W. Oldenburg. *Improving detection and discrimination of buried metallic objects in magnetic geologic settings by modeling the background soil response*: in Proc. of SPIE, Vol. 6953, Detection and Remediation Technologies for Mines and Minelike Targets XII, R. S. Harmon, J. Broach, J. H. Holloway, Jr., Ed., Apr 27, 2008. Paper in proceedings.

Example: Modelling magnetic soil response of the MPV

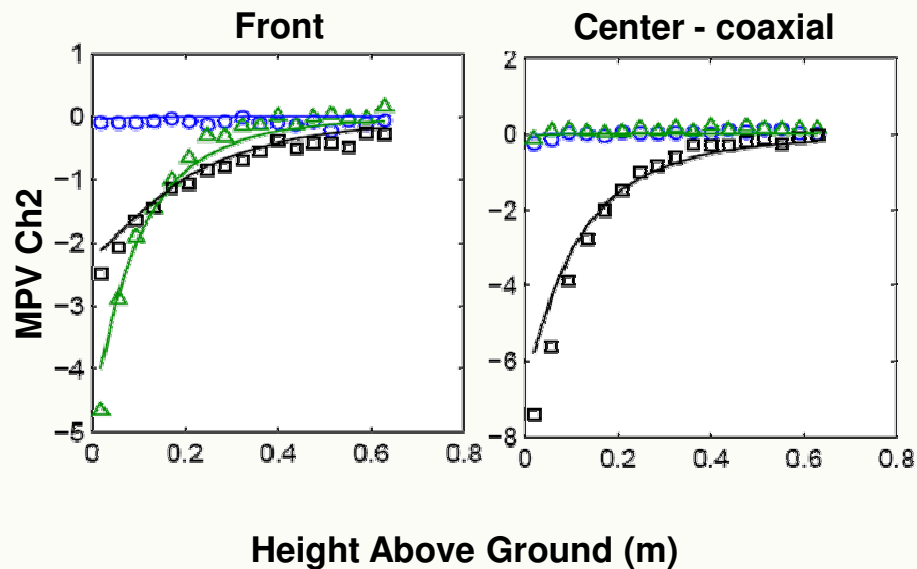
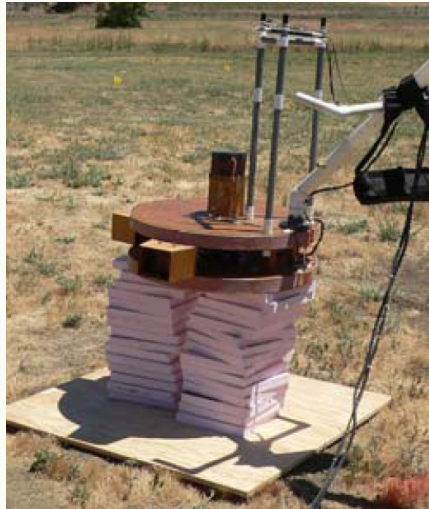
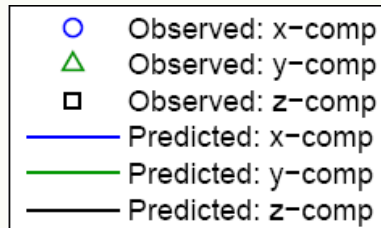
- The Man Portable Vector (MPV) Time Domain EMI sensor developed by G&G Sciences (SERDP MM1443)
- **Multi-time channel:** 35 channels ranging from 0.1 to 23 ms
- **Multi-static:** 5 receiver cubes. Each cube measures 3 orthogonal components of the secondary field

Sky Research UXO test plot in Ashland, OR

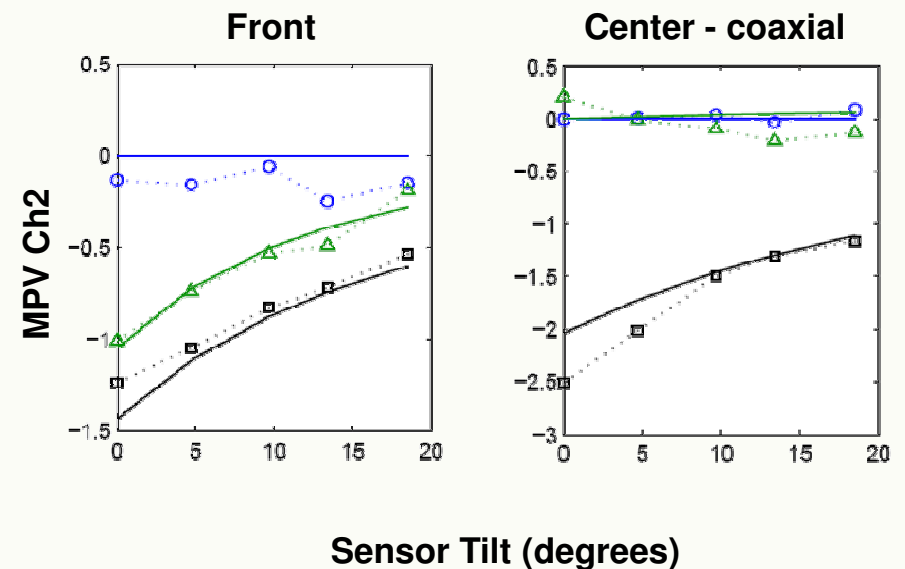
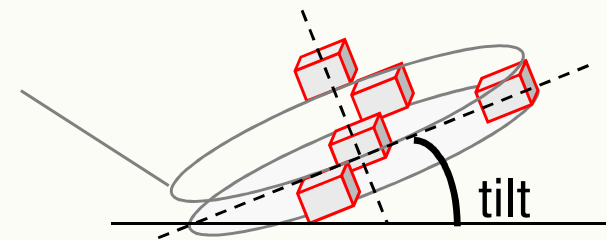


Example: MPV data collected at the Sky Research UXO test site in Ashland, OR

Height Test

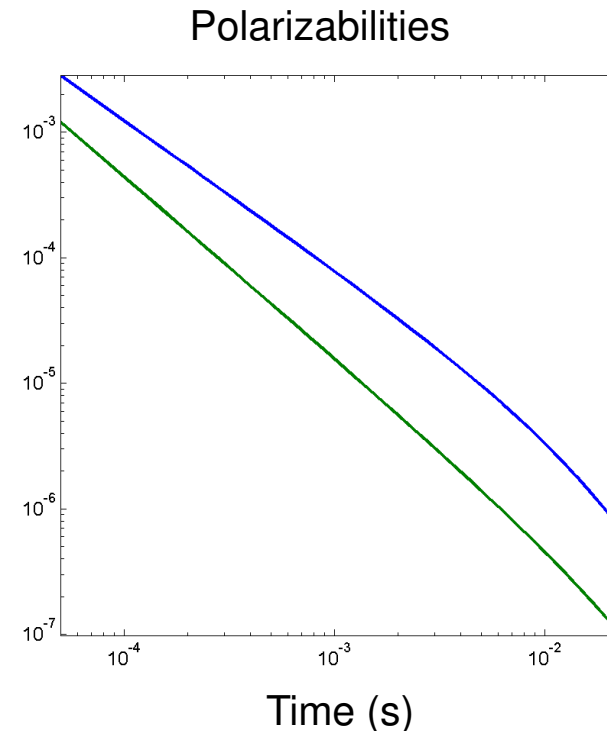


Orientation Test



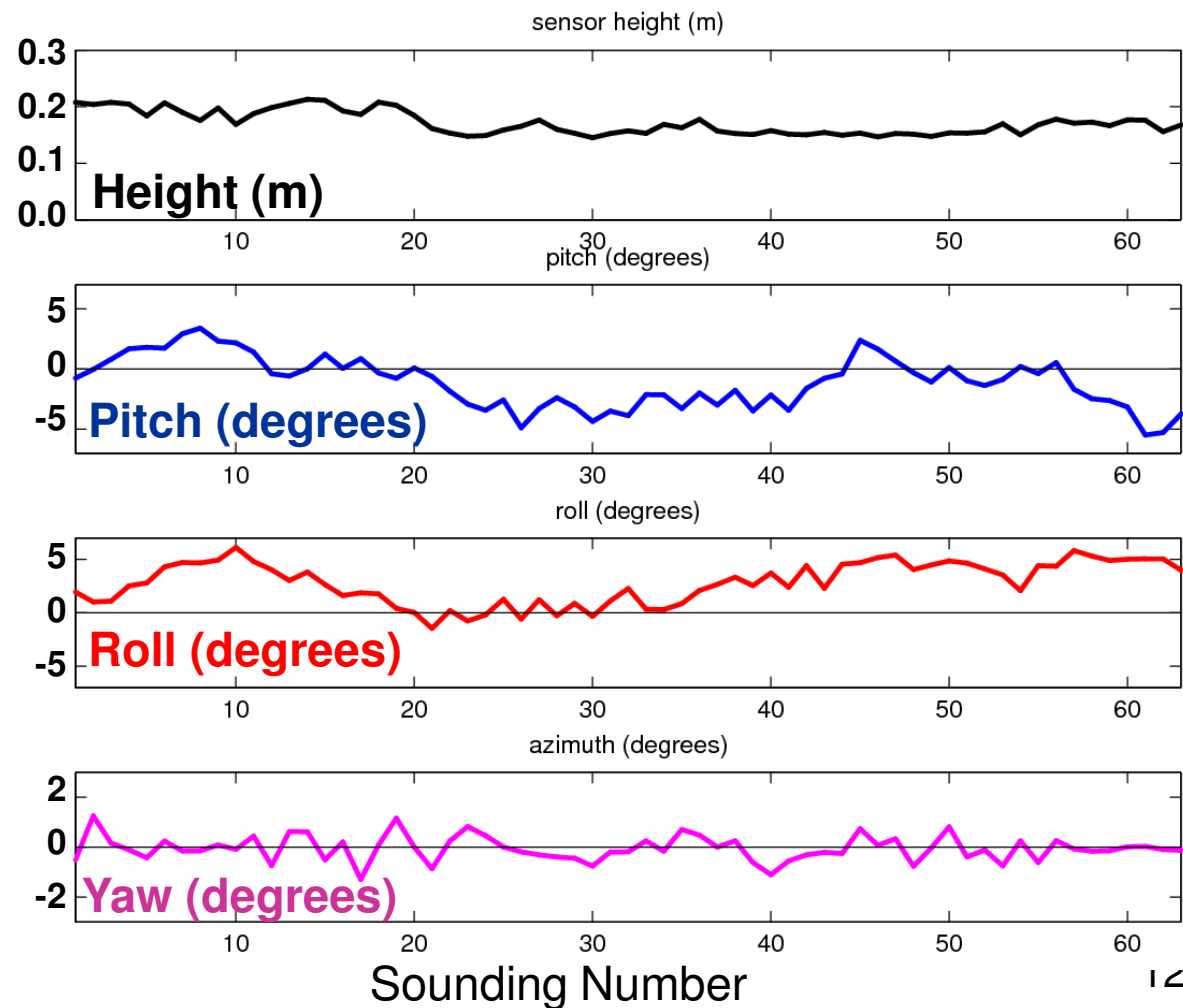
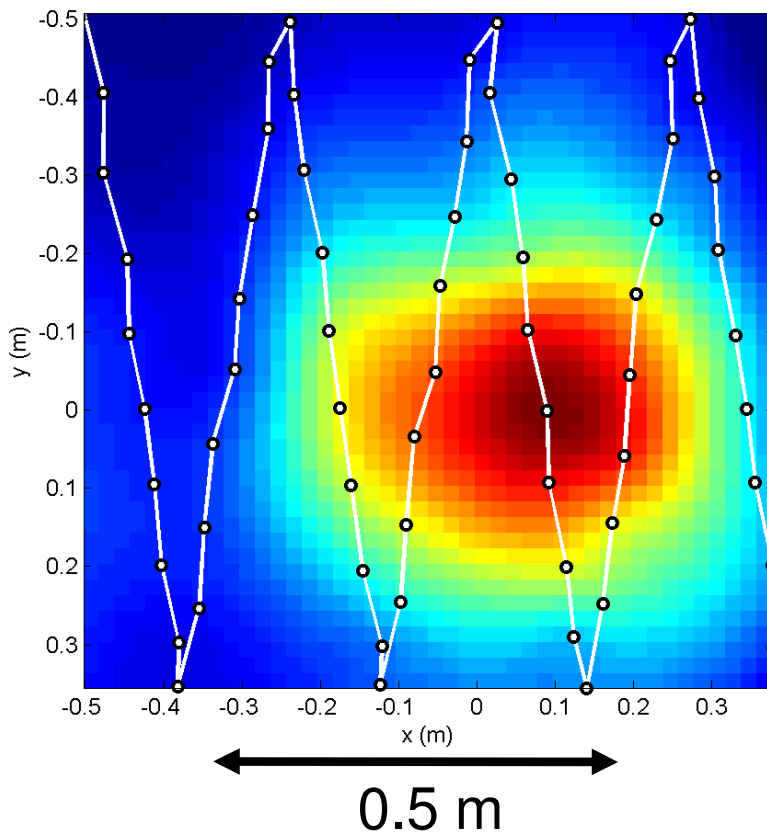
Testing Inversion algorithms using Synthetic MPV Data

- 4 inch x 37 mm steel cylinder
- Depth = 25 cm
- Dipole polarizabilities estimated through in-air, test stand measurements
- Assume a background soil response approximately twice as large as typical Cambodia “hot soil” ($\chi_{lf} \sim 200 \times 10^{-5}$ SI, $\chi_{hf} \sim 180 \times 10^{-5}$ SI)
- Assume laterally uniform soil properties



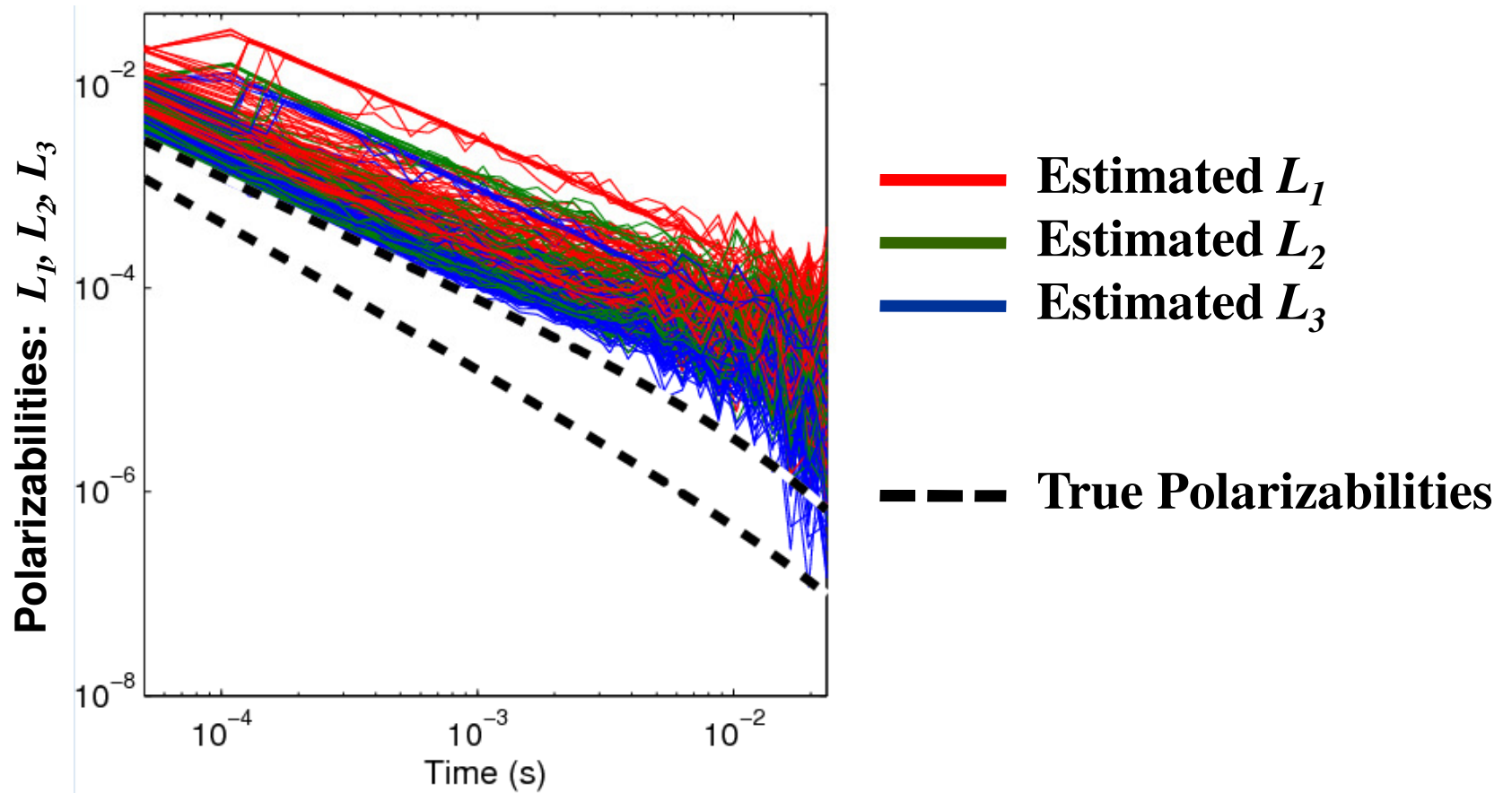
Example: Synthetic MPV data

- Data acquired in a “sawtooth” pattern at 10 cm intervals
- position error: $\sigma = 0.5$ cm
- orientation error: $\sigma = 0.5$ degrees
- Gaussian noise characteristic to the MPV added to data



Example: Synthetic MPV data

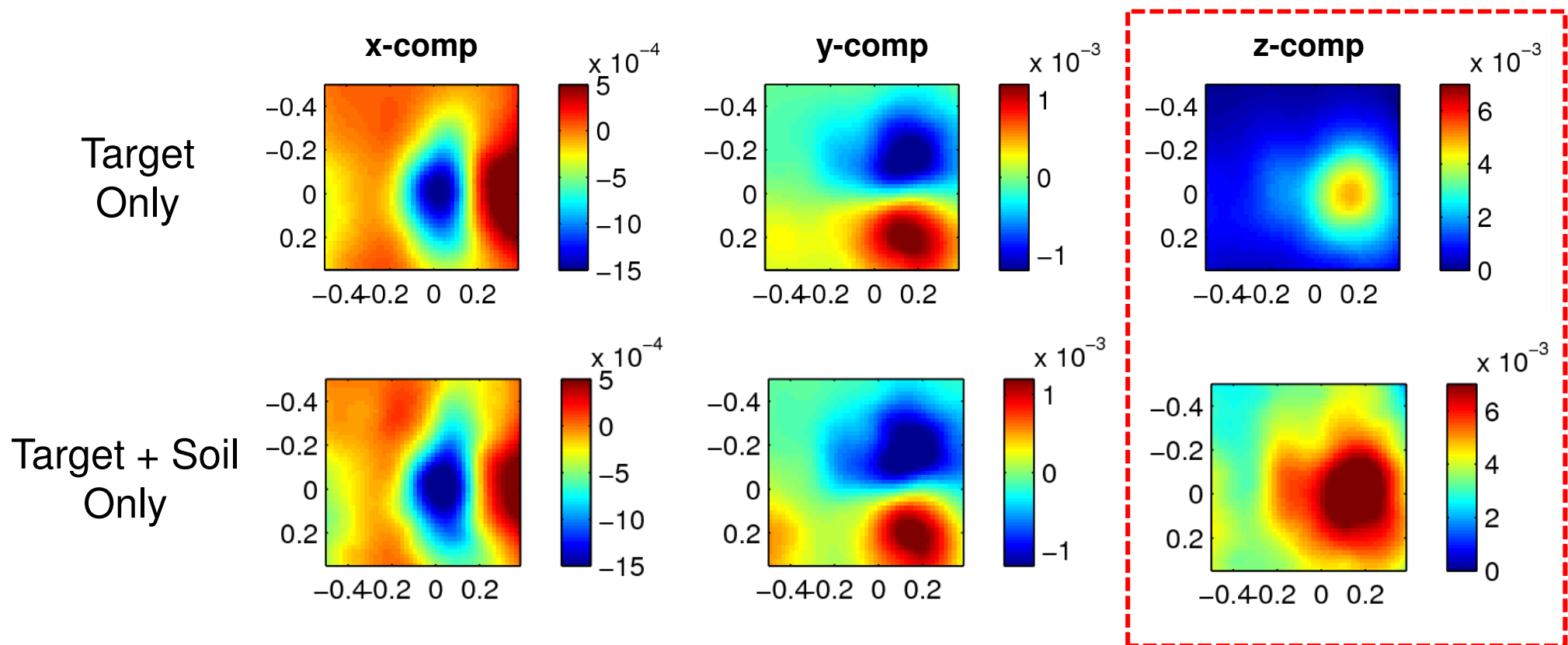
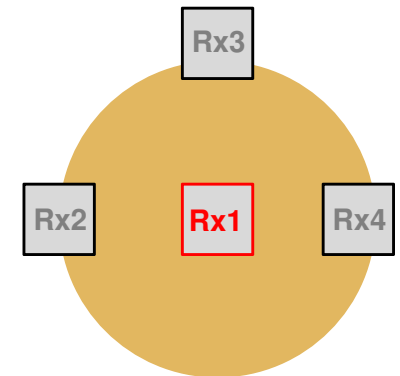
- Invert data for target parameters only (no soil model)



- *Soil signal in MPV data bias recovered polarizabilities resulting in poor estimates*

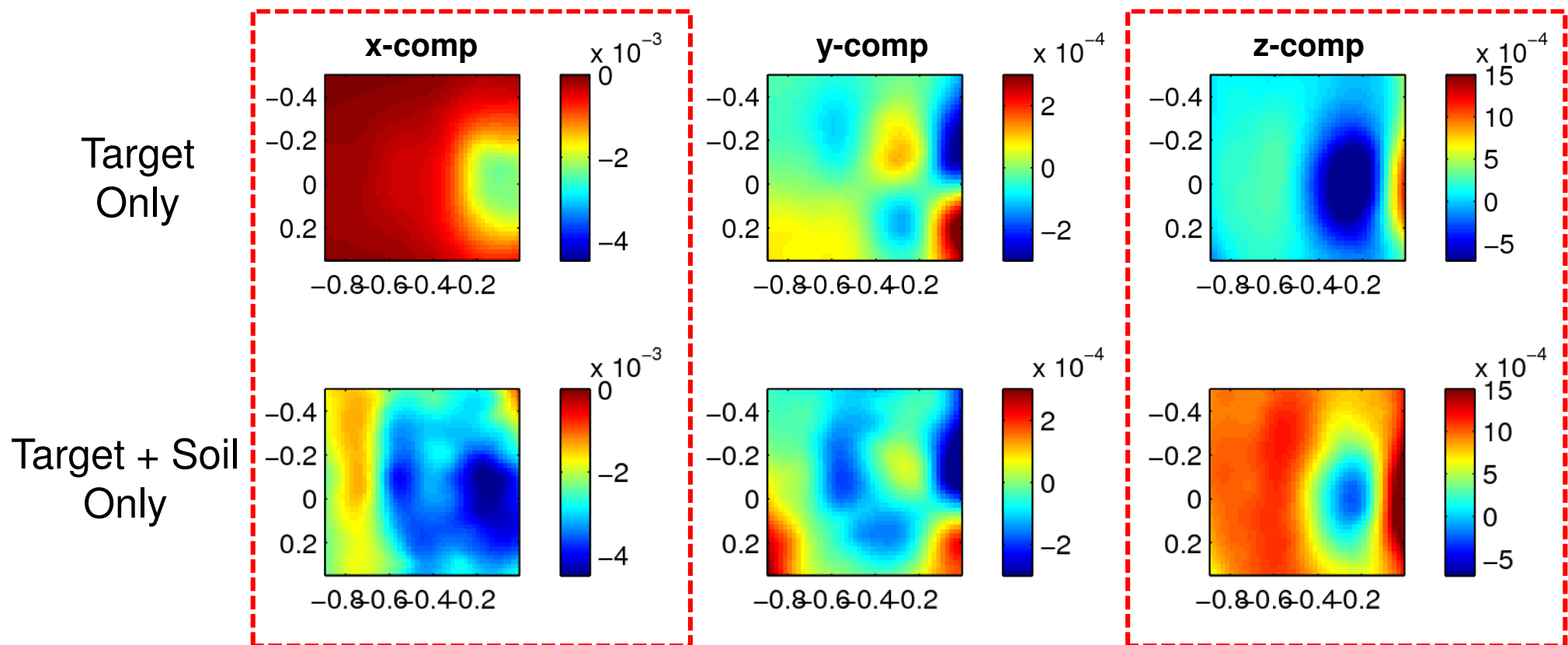
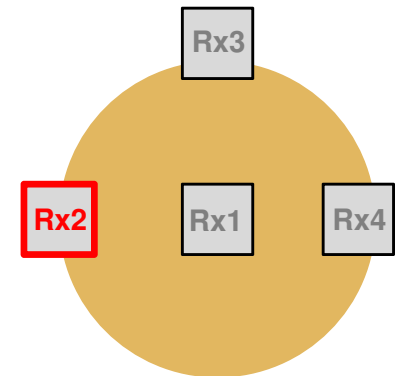
Effect of Magnetic Soils on MPV Data

- Sensor movement distorts the measured response on all components
- For coaxial receiver Rx1, the horizontal components are **least** sensitive to soil



Effect of Magnetic Soils on MPV Data

- Sensor movement distorts the measured response on all components
- For outer receivers, the radial and vertical components are **more** sensitive to soil



Simultaneous Inversion for Host and Target Parameters

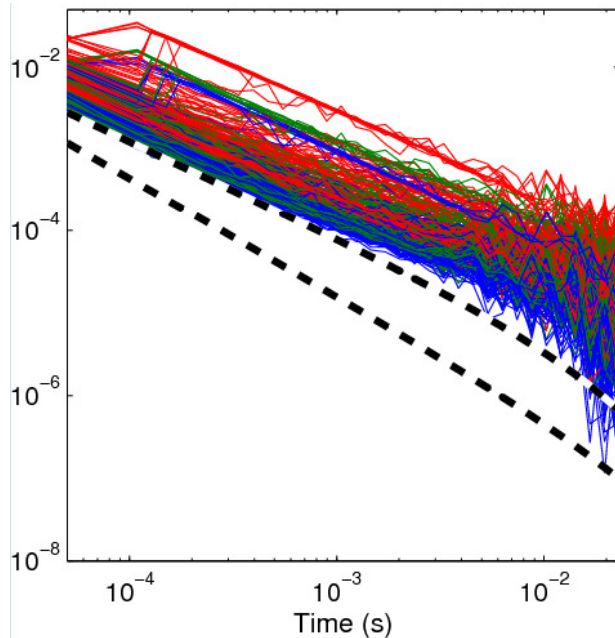
- The symmetry of the ground response and the multi-static, multi-component nature of the MPV suggests the following 2-step inversion process:

Step 1. Invert for dipole parameters by using data components that are least sensitive to magnetic soil

Step 2. Invert for dipole parameters and soil properties simultaneously, using all data components. Use result in step 1 as a starting model.

Example: Synthetic MPV data

**Invert for Target Parameters only
(No Soil Model)**

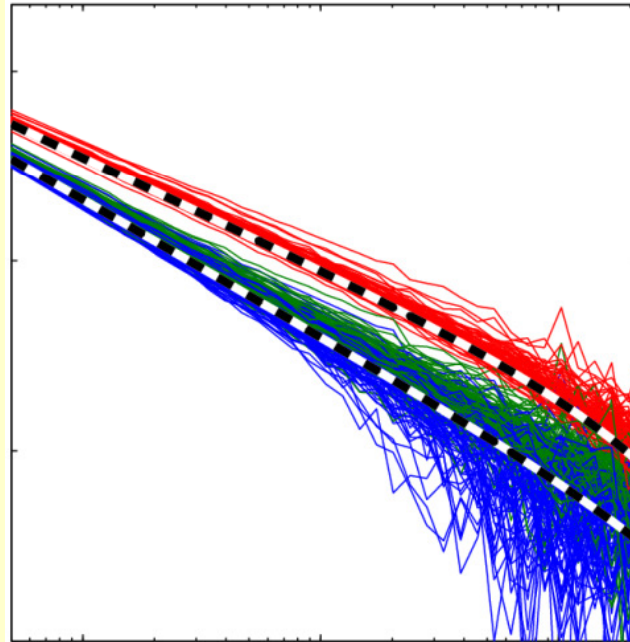


— Estimated L_1
— Estimated L_2
— Estimated L_3
- - - True Polarizabilities

Two-Step Inversion Process

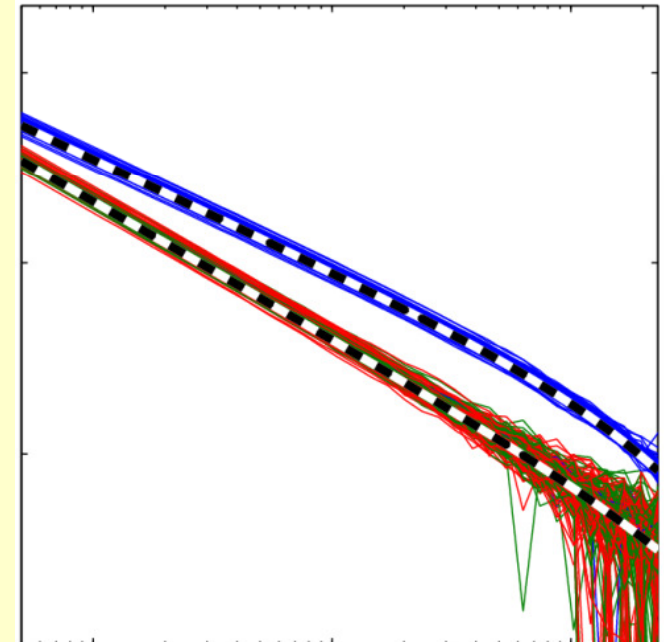
Step 1 :

Invert data components
least affected magnetic soil
for dipole parameters



Step 2:

Simultaneous inversion for
dipole and soil parameters
using all data components



***Accurate polarizability estimates possible
by accounting for the soil response.***

Inversion of MPV data collected at DRDC Suffield

- Measurements were collected the Defense Research and Development Canada (DRDC) test facility at Suffield, Alberta
- Measurements acquired over a pit containing Cambodian red soil and different synthetic soils
- Focused on the response of a 4 inch steel and 3 inch aluminum cylinder

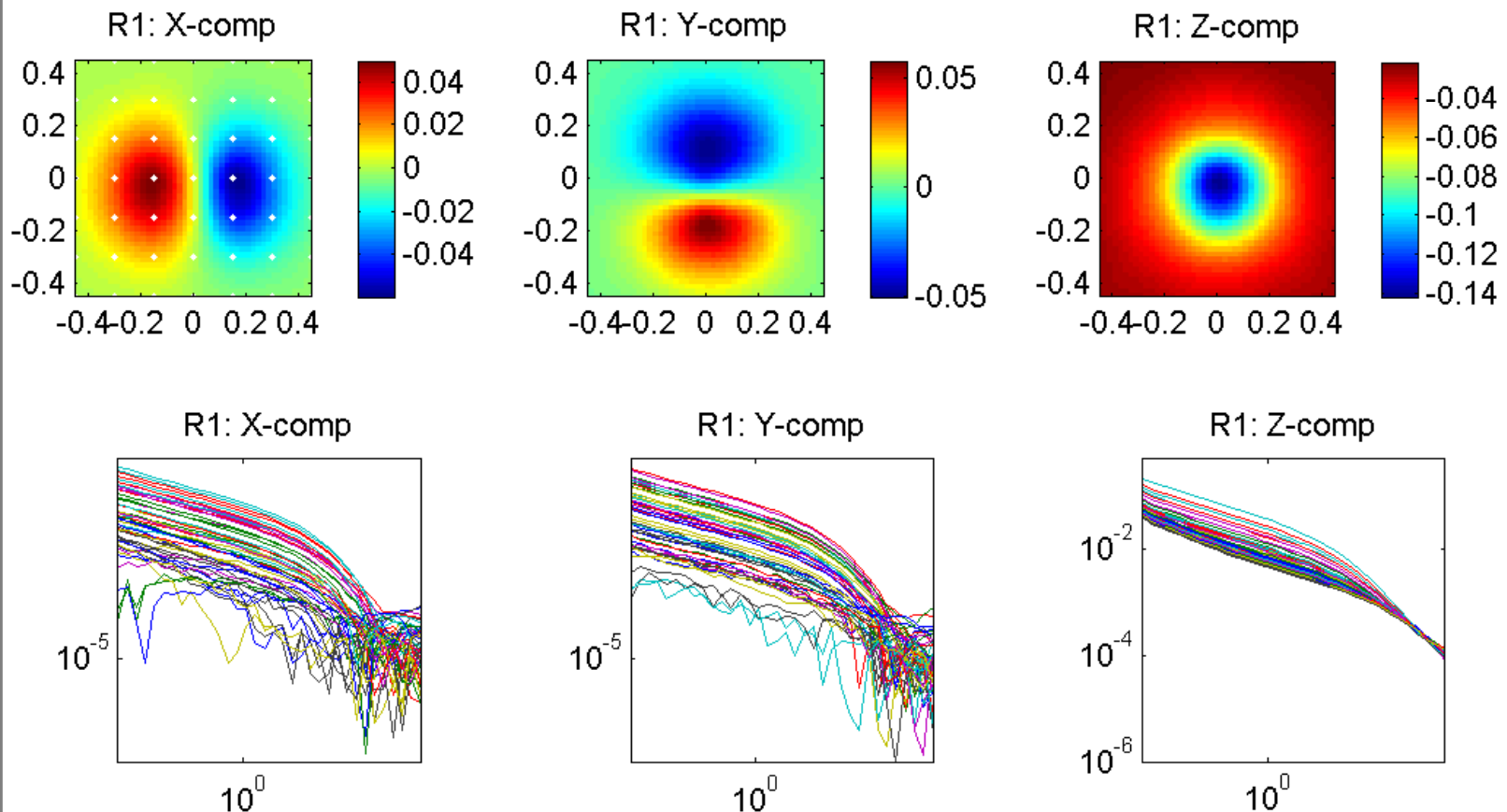


Example of MPV Data collected at DRDC Suffield

- 3 inch aluminum cylinder.
- 40 mm diameter.
- Horizontal , flush with surface



Receiver Rx1 (coaxial receiver):

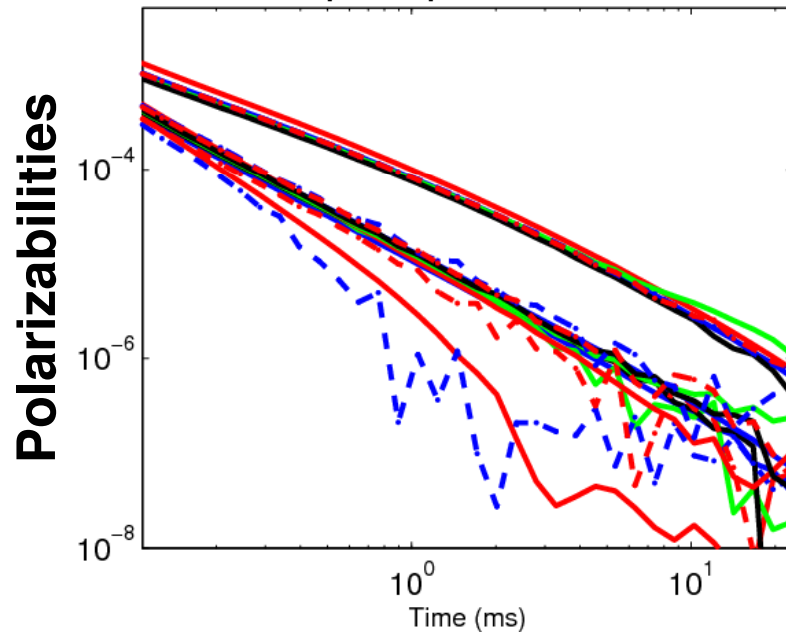


Inversion of data collected at DRDC Suffield: Cambodian Soil Pit

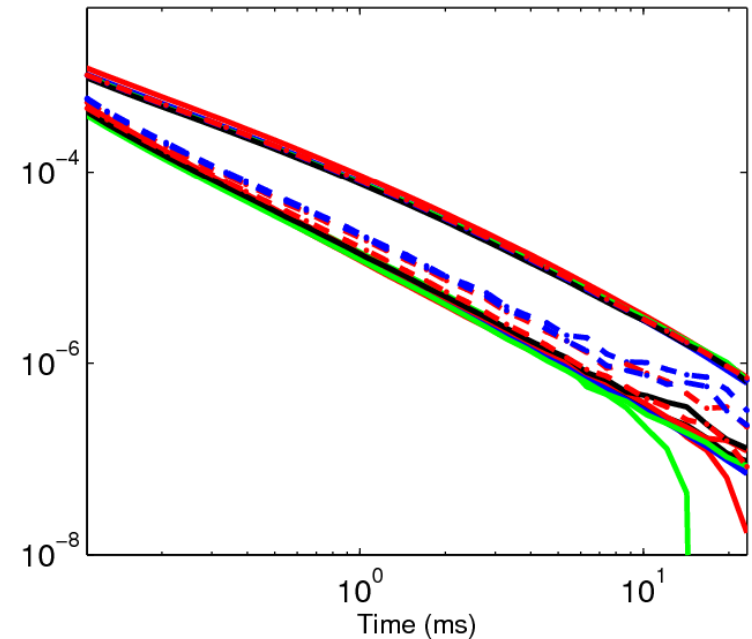
- 4 inch steel cylinder



Step 1 : Invert data components
least affected magnetic soil
for dipole parameters



Step 2: Simultaneous inversion for
dipole and soil parameters
using all data components



	orient	height	depth		orient	height	depth
—	Horiz.	7.5 cm	2 cm	—	Horiz	15.5 cm	11 cm
—	Vert.	7.5	5	- -	Vert.	15.5	21
—	Horiz.	7.5	22	- -	45	15.5	20

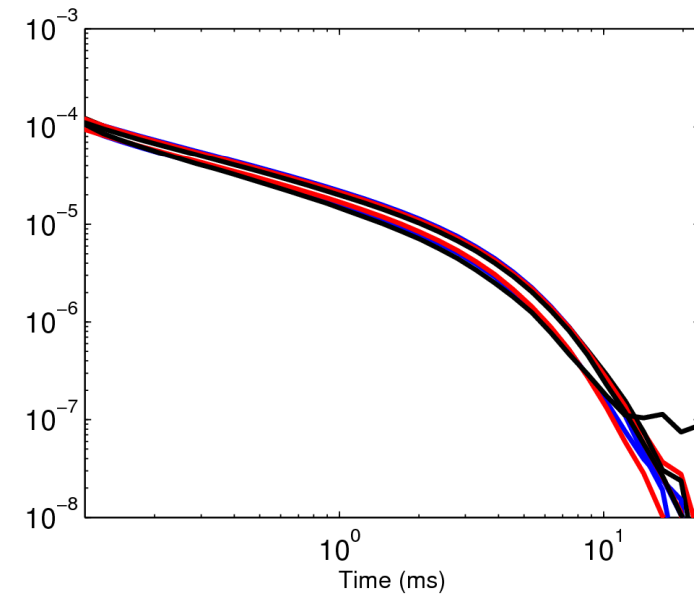
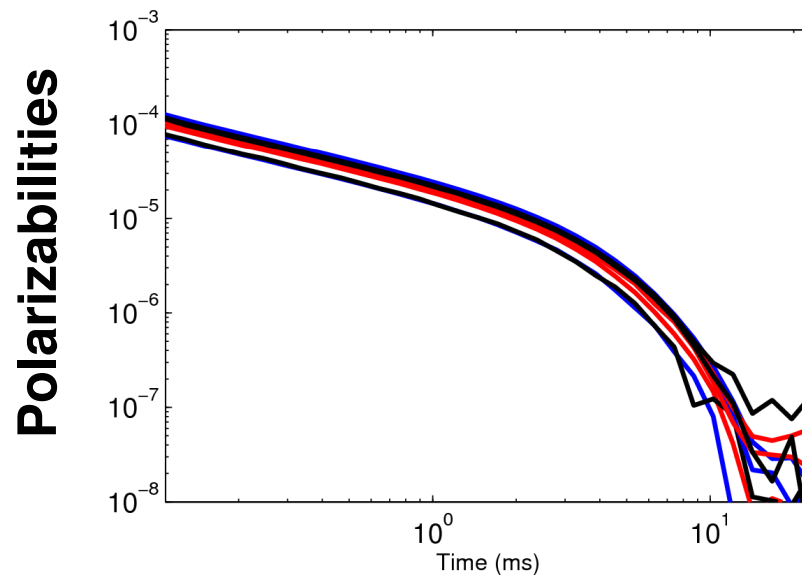
← mound




Inversion of data collected at DRDC Suffield: Cambodian Soil Pit

- 3 inch aluminum cylinder

Step 1: Invert data components
least affected magnetic soil
for dipole parameters

Step 2: Simultaneous inversion for
dipole and soil parameters
using all data components



	orient	height	depth
	Horiz.	7.5 cm	2 cm
	Vert.	7.5	3.5
	Horiz.	15.5	2

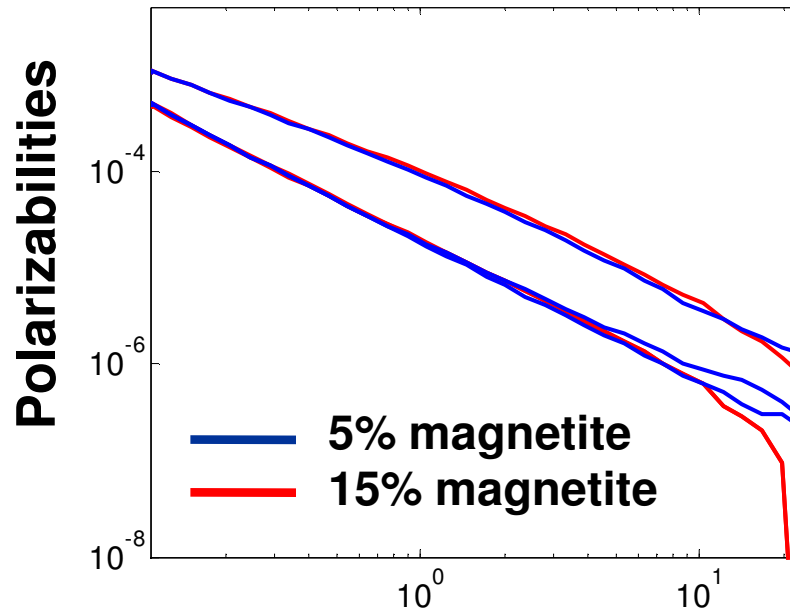
 mound

Inversion of data collected at DRDC Suffield: Synthetic Soil

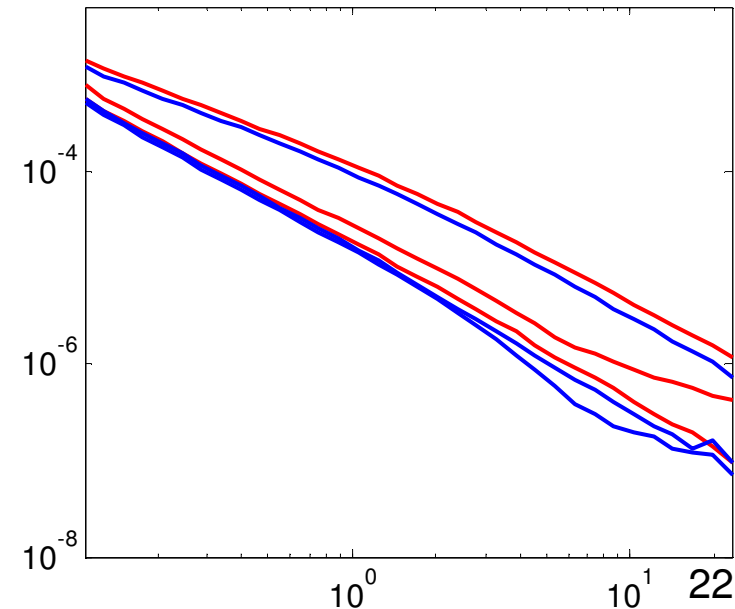
- 4 inch steel cylinder
- depth = 0.22 m
- Two types of soil:
 - 5% and 15% Magnetite by weight.
 - Large static χ ($\chi_{lf} > 3000 \times 10^{-5}$)
 - low frequency dependence



Step 1: Invert data components least affected magnetic soil for dipole parameters

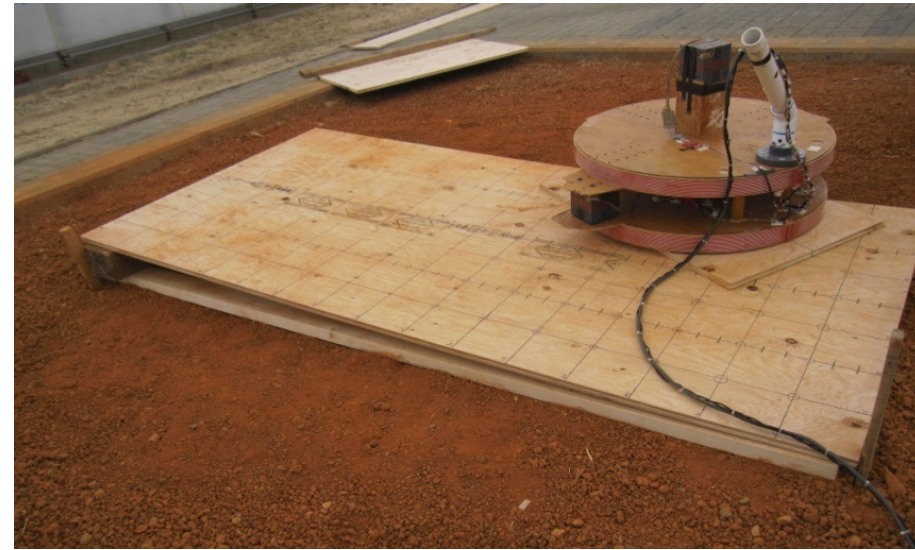


Step 2: Simultaneous inversion for dipole and soil parameters using all data components

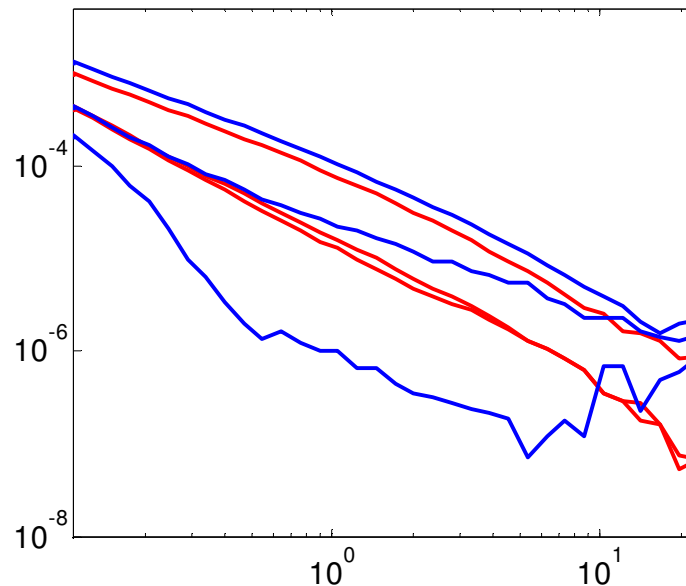


Inversion of data collected at DRDC Suffield: Non-level instrument

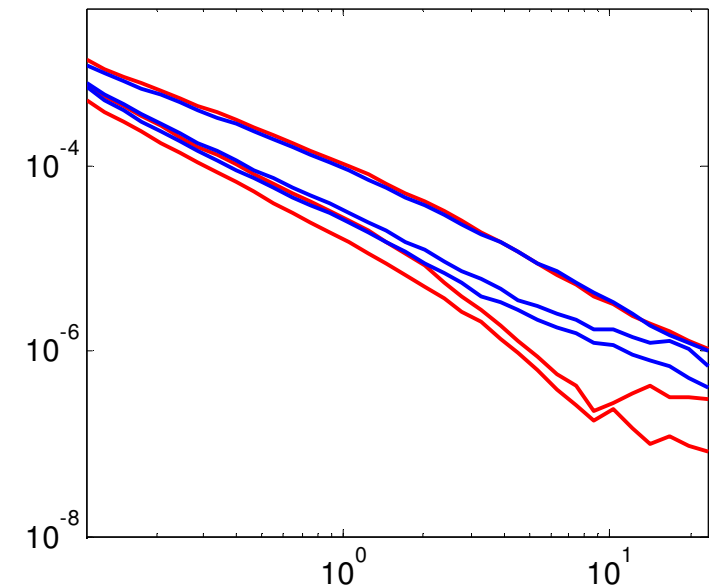
- Cambodian Soil
- 4 inch steel cylinder
- depth = 0.22 m
- Pitch of sensor adjusted



Step 1: Invert data components
least affected magnetic soil
for dipole parameters



Step 2: Simultaneous inversion for
dipole and soil parameters
using all data components



— Pitch = -3 degrees
— Pitch = +3 degrees (see photo above)

Conclusions

- Methodologies have been developed to estimate geologic and target parameters.
- These methods have been applied to both synthetic and field data from newer generation sensors.
- The geometry of a receiver determines the extent of the soil signal
- The ability to correctly estimate the target polarizabilities from data collected in highly magnetic soils was demonstrated on field data collected at the DRDC Suffield Soil test pits facility

Acknowledgements



- Kevin Russell and Wayne Sirovyak at the Defence Research and Development Canada (DRDC) facility in Suffield, Alberta



- This work was funded by the Strategic Environmental Research and Development Program (SERDP)